# "Missing Xenon": experimental and theoretical study of Xe storage in crustal and upper mantle minerals

Céline Crépisson

Sorbonne Université

École doctorale Géosciences, Ressources Naturelles et Environnement – ED 398

*Institut des Sciences de la Terre de Paris (ISTeP)*

# Le “Xénon manquant”: étude expérimentale et théorique du stockage du Xe dans les minéraux de la croûte continentale et du manteau supérieur

# ‘Missing Xenon’: experimental and theoretical study of Xe storage in crustal and upper mantle minerals

Par Céline Crépisson

Thèse de doctorat de Géophysique

Dirigée par Chrystèle Sanloup et Marc Blanchard

Présentée et soutenue publiquement le 19 septembre 2018

Devant un jury composé de :

| | | |
|---|---|---|
| BLANCHARD, Marc | Directeur de Recherche | Directeur |
| DEWAELE, Agnès | Ingénieur-Chercheur | Rapporteur |
| FIQUET, Guillaume | Directeur de Recherche | Examinateur |
| GUYOT, François | Professeur | Rapporteur |
| MARTY, Bernard | Professeur | Examinateur |
| MEHEUT, Merlin | Maître de conférences | Examinateur |
| SANLOUP, Chrystèle | Professeur | Directrice |

**AKNOWLEDGEMENTS**

I would like to thank Chrystèle for sharing so much knowledge, for her enthousiasm and her guidance. I thank Marc for his constant availability and unconditional support, as well as his sharp theoretical eye.
I acknowledged my collaborators: Etienne Balan, Michele Lazzeri, Laurent Cormier and Jessica Hudspeth whose precious work, help and advices made possible this work.
I also aknowledge:
Omar Boudouma, Michel Fialin and Nicolas Rividi from the CAMPARIS centre,
Keevin Beneut for Raman and Infrared spectroscopy, Ludovic Delbes for X-ray diffraction and Yoan Guarnelli from IMPMC,
Jean-Claude Boulliard and the Mineralogical collection of Sorbonne Université,
Lorenzo Paulatto at the IMPMC for his help regarding Quantum ESPRESSO.
Staff from the synchrotron beamlines and in particular Angelika Rosa and Olivier Mathon on BM23, ESRF; Konstantin Glazyrin and Anna Pakhomova on P02.2, Petra, Dominik Daisenberger and Simone Anzellini on I15, Diamond Light Source, and Francesco Capitani on SMIS, SOLEIL synchrotron,
Hélène Bureau, Guillaume Morard, Daniele Antonangeli, Marzena Anna Baron, Francesca Miozzi and Eric Edmund for their wise advice at the IMPMC lab, and Yves Noël, Pauline Thierry and Alain Ragu at ISTeP.

I also thank Mathieu Chassé, Jessica Hudspeth, Marion Harmand, Keevin Béneut and Sarah Figowy for their friendly support throughout PhD hard times.

**SUMMARY**

## RESUME EN FRANCAIS

Le xénon est le plus lourd des gaz rares étudiés (He, Ne, Ar, Kr, Xe). Les gaz rares, relativement inertes chimiquement, très volatils et possédant de nombreux isotopes, sont un outil parfait pour étudier l'évolution du système Terre-atmosphère. En particulier, le xénon possède neuf isotopes stables, dont $^{129}$Xe, issu de la désintégration du radionucléide $^{129}$I aujourd'hui éteint et $^{131,\ 132,\ 134,\ 136}$Xe, issus de la désintégration du radionucléide $^{244}$Pu, lui aussi aujourd'hui éteint et dans une plus faible proportion de la désintégration de $^{238}$U. Les gaz rares ont été accrétés à partir de la nébuleuse solaire lors de la formation de la Terre. Cependant divers apports tardifs (chondrite, comète, ..) ont pu moduler la composition en gaz rare de l'atmosphère et de la terre solide, de même que la décroissance radioactive, le dégazage terrestre (par magmatisme) et la perte potentielle de l'atmosphère primordiale par échappement hydrodynamique (Pépin, 1991, 2006). L'étude de la teneur en gaz rare de différents environnements géologiques permet d'étudier la dynamique mantellique et d'identifier des zones préservées (non dégazées) du manteau, même si le recyclage des gaz rares au niveau des zones de subduction doit également être pris en compte.

Néanmoins le xénon présente ses propres énigmes. Si l'on compare la teneur en gaz rare des météorites de type chondrites (les objets les plus primitifs du système solaires connus à ce jour) avec celle de l'atmosphère terrestre, on constate que le xénon est en déficit d'un facteur 20 dans l'atmosphère terrestre par rapport aux autres gaz rares (figure 1). Le même phénomène est observé pour l'atmosphère martienne (Anders et Owen, 1977). En supposant comme il est communément admis que la composition de l'atmosphère reflète celle de l'ensemble de la Terre alors 90% du xénon s'est « échappé » au moment de la formation de l'atmosphère (Ozima et Podosek, 1999).

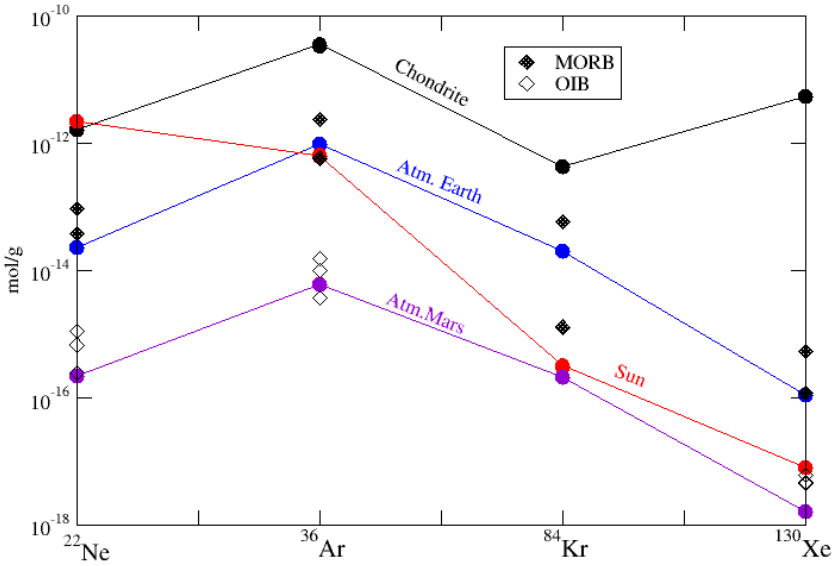


*Figure 1: Teneur en gaz rares en mol/g, MORB (Moreira et al., 1998) et OIB (La Réunion (Hopp and Trieloff, 2005)). Teneur pour les chondrites, l'atmosphère terrestre et le Soleil (compilation Marty (2012)). Atmosphère martienne (Hunten et al., 1987).*

Ce « xénon manquant » est associé à une anomalie de composition isotopique. En effet on observe un déficit en isotopes légers dans les atmosphères terrestre et martienne (figure 2) comparé à la composition isotopique des chondrites (Krummenacher et al., 1962), avec un fractionnement de 3-4 %.amu$^{-1}$ (Hébrard and Marty, 2014). Ce fractionnement est paradoxal : en effet les gaz rares plus légers devraient être plus fractionnés que le xénon, ce qui n'est pas le cas (Kr n'étant par exemple fractionné que de 1 %.amu$^{-1}$ (Hébrard and Marty, 2014)). Enfin, un fractionnement isotopique du xénon dans l'atmosphère est observé tout au long de l'Archéen (Pujol et al., 2011, 2013 ; Avice et al., 2017).

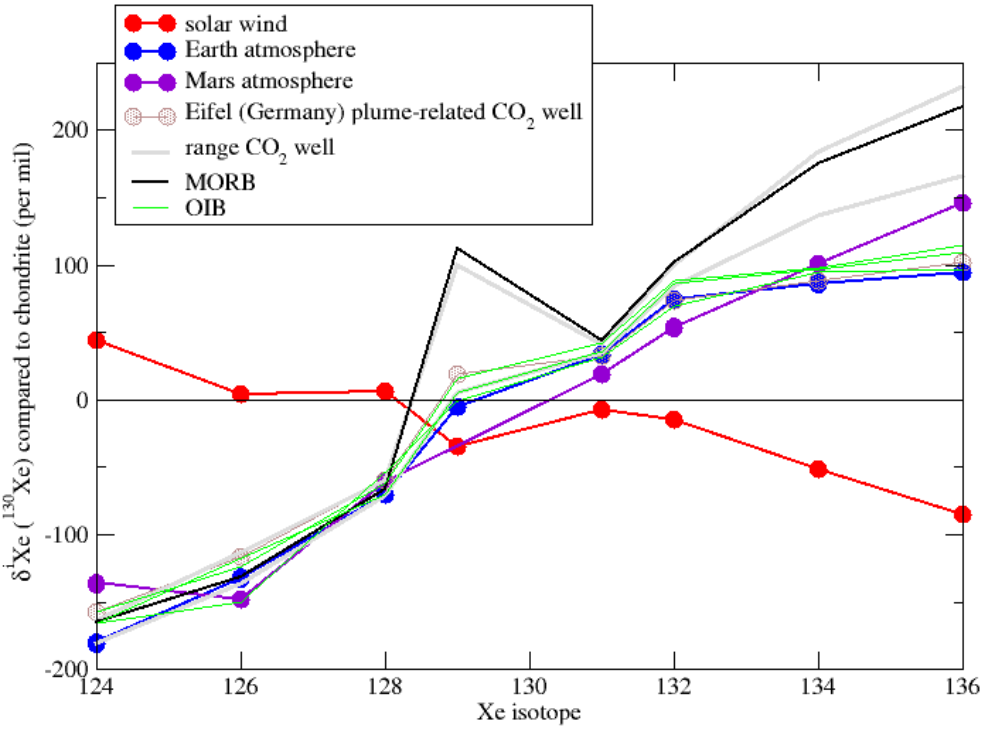


*Figure 2: Composition isotopique du Xe normalisée aux chondrites (Pepin and Phinney, 1978), dans le vent solaire (Meshik et al., 2014), l'atmosphère terrestre (Basford et al., 1973), l'atmosphère martienne (Swindle et al., 2002), les MORBs (Kunz et al., 1998 compilé par Caffee et al., 1999), les OIBs (Yokoshi and Marty, 2005), les puits de $CO_2$ du Colorado, Australie du Sud (Caffee et al., 1999) et du Nouveau Mexique (Caffee et al., 1999; Holland and Ballentine, 2006). La composition isotopique des puits de $CO_2$ dans la région d'Eifel (Allemagne) analysé par Caracausi et al. (2016) est donnée.*

Différentes hypothèses ont été proposées pour expliquer ce xénon manquant et sa composition isotopique particulière, en accord avec un fractionnement au cours de l'Archéen. Ce fractionnement isotopique du xénon au cours de l'Archéen pourrait être lié au flux solaire, plus élevé à l'Archéen (figure 3) entraînant l'ionisation du xénon à environ 120 km d'altitude et son adsorption sur un « brouillard organique » ('organic haze') supposé exister à cette altitude dans l'atmosphère terrestre à l'Archéen (mais qui demeure hypothétique sur Mars), alors que les autres gaz rares ne seraient significativement ionisés qu'à plus haute altitude et donc non adsorbé. Les isotopes lourds étant préférentiellement adsorbés, ce phénomène expliquerait la composition isotopique particulière du xénon. Néanmoins, demeure à comprendre l'élimination des isotopes légers du xénon. Si un échappement hydrodynamique a été proposé, celui-ci aurait également dû influer (et dans une plus grande mesure) les autres

gaz rares et leur composition isotopique (par distillation de Rayleigh), ce qui n'est pas observé.

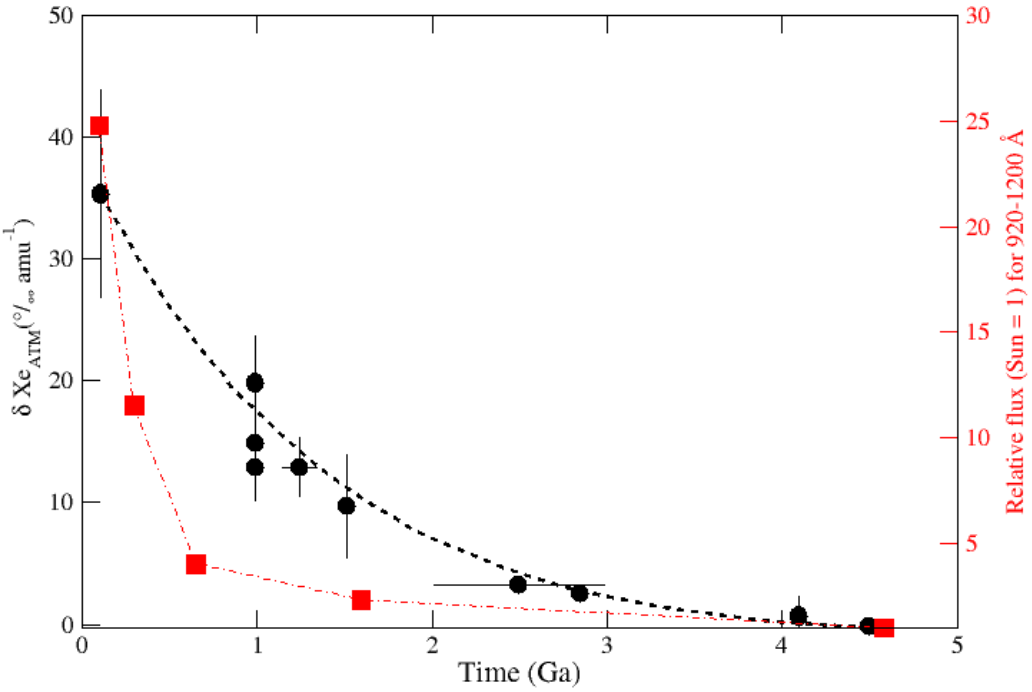


*Figure 3: Le flux UV solaire décroit rapidement comparé au fractionnement isotopique progressif du xénon. Les points noirs pleins montrent le fractionnement du xénon au cours de l'Archéen (références dans Hébrard and Marty (2014) et Avice et al. (2017)), la ligne noire en tirets est le fractionnement isotopique moyen du xénon. Les carrés rouge pleins sont les données de Ribas et al. (2005) pour le flux solaire et la ligne en tiret rouge est un guide pour le lecteur.*

Le stockage du xénon en profondeur sur Terre (et sur Mars) a également été proposé. Le stockage du xénon semble difficile au niveau du noyau et du manteau inférieur : en effet les conditions de pression du noyau martien sont bien inférieures à celles dans le noyau terrestre et Mars est dépourvu de manteau inférieur, or Mars présente une anomalie en xénon similaire à celle de la Terre. Un stockage dans les sédiments ou les glaces (clathrates) s'il est possible, ne peut suffire à abriter la totalité du xénon manquant. Enfin, récemment il a été proposé que le xénon puisse être stocké dans la croûte continentale ou dans le manteau supérieur (Sanloup et al., 2002, 2005, 2011). L'objectif de cette thèse est d'apporter de nouveaux éléments sur l'incorporation du xénon dans les minéraux afin de tester cette dernière hypothèse.

Cette hypothèse se base notamment sur la réactivité du xénon, supérieure à celle des autres gaz rares (Grochala, 2007), en particulier à haute pression. Des oxydes de xénon ont ainsi été synthétisés (Dewaele et al., 2016) et il a été montré que le xénon pouvait être incorporé dans des phases siliceuses (Sanloup et al., 2002, 2005) et dans l'olivine (Sanloup et al., 2011) à des conditions de pression ($P$) et température ($T$) proches de celles de la croûte et du manteau supérieur. Pour l'instant, les données concernant un potentiel fractionnement isotopique lié à l'incorporation du xénon dans les minéraux manquent ; néanmoins des expériences ont déjà montré un fractionnement des gaz lourds lors de leur incorporation dans les glaces d'eau (Notesco et al., 1999).

Dans cette thèse nous avons cherché à résoudre les mécanismes d'incorporation du xénon dans trois minéraux majeurs de la croûte continentale (quartz et feldspath) et du manteau supérieur (olivine), ainsi que dans un verre et magma feldspathique. Pour cela nous avons utilisé de manière complémentaire une approche expérimentale, basée sur l'observation *ex-situ* et *in-situ* (à haute *P*/*T*) d'échantillons enrichis en gaz rares lourds, et une approche théorique, basée sur la théorie de la fonctionnelle de la densité (DFT). Le xénon étant hautement volatil aux conditions *P*/*T* ambiantes, il est indispensable d'étudier son incorporation *in-situ*, puisqu'il s'échappe généralement du réseau cristallin à la trempe, se localisant dans des inclusions fluides.

L'incorporation du xénon dans l'olivine avait été précédemment étudiée par Sanloup et al. (2011) par diffraction des rayons X à haute *P*/*T*. Une augmentation du paramètre de maille *a* avait alors été observée, ainsi que l'apparition d'une nouvelle bande Raman en présence de xénon, au-dessus de la température de fusion de celui-ci. Une étude théorique (DFT) nous a permis de montrer que la substitution du xénon au site du silicium (figure 4) permettait d'expliquer l'augmentation du paramètre de maille *a*, ainsi que la nouvelle bande Raman observée. Près de 0.4 at% Xe pourrait être incorporé dans l'olivine prouvant son importance dans le cadre du « xénon manquant » (Crépisson et al., 2018)..
Il a également été montré que le fer présent dans le matériel de départ lors des expériences en piston cylindre utilisant une capsule de platine est retenu dans l'olivine synthétisée uniquement en présence de Xe. Le cas échéant il forme un alliage métallique avec la capsule en Pt. Enfin, la présence d'eau empêche l'incorporation du Xe dans l'olivine, le xénon se localisant probablement dans la phase fluide.

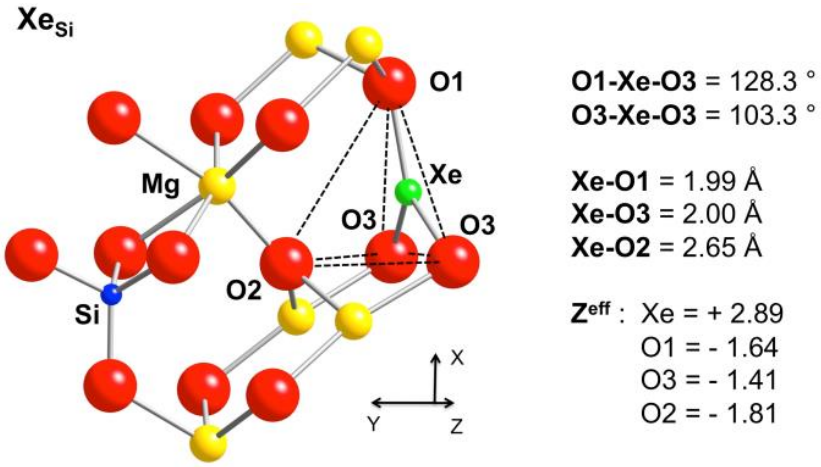


*Figure 4: Structure du site d'incorporation du xénon en substitution avec le silicium dans la forstérite (olivine magnésienne). Les angles O-Xe-O, les liaisons Xe-O sont indiqués ainsi que le tiers de la trace du tenseur de charges efficaces de Born ($Z^{eff}$), donné comme approximation à la charge locale atomique. Les axes a, b et c de la forstérite correspondent respectivement aux axes x, y et z représentés ici.*

L'incorporation du xénon dans le quartz a été étudié à partir de données *in-situ* antérieures de diffractions des rayons X (Sanloup et al., 2005), ainsi qu'à partir de nouvelles données *in situ* de diffraction des rayons X et de spectroscopie infrarouge, acquises en cellule

à enclumes de diamant à chauffage résistif. Il a été montré que le volume de la maille du quartz augmente en présence de xénon. De plus, au-dessus de la température de fusion du xénon, une nouvelle phase apparaît, marquée par la présence de quatre nouveaux pics de diffraction et d'un dédoublement d'une des bandes infrarouges caractéristiques du quartz. Cette nouvelle phase correspond à l'élongation de la maille hexagonale du quartz, en une maille orthorhombique (Crépisson et al., in prep., à soumis à $G^3$).

L'incorporation du xénon dans un feldspath de haute température (la sanidine) a été étudiée par diffraction *in situ* des rayons X en cellule à enclumes de diamant et par l'étude *ex situ* d'échantillons synthétisés en piston cylindre. En présence de xénon une phase riche en fer et en gaz rare, mais appauvrie en aluminium (sans bulle, à l'échelle nanométrique) est observée dans les échantillons récupérés (figure 5), prouvant de nouveau le rôle du fer, potentiellement stabilisé par le xénon. De plus, en-dehors de ces phases ferreuses, une corrélation est observée entre le xénon et l'oxygène (les gaz rares se localisant alors dans des bulles). L'étude *in situ* (à haute P/T) de sanidine enrichie en gaz rares lourds a montré une augmentation du volume de maille de la sanidine en présence de xénon. Néanmoins il demeure difficile d'identifier avec certitude le mécanisme d'incorporation du xénon due à la structure cristallographique complexe de la sanidine (monoclinique). La phase hydratée de haute *P* de la sanidine (K-cymrite) a également été étudiée *in situ* en présence de xénon, mais il demeure impossible de conclure due au manque de données concernant ce minéral à *P* supérieures à 4 GPa et donc l'absence d'équation d'état valide.

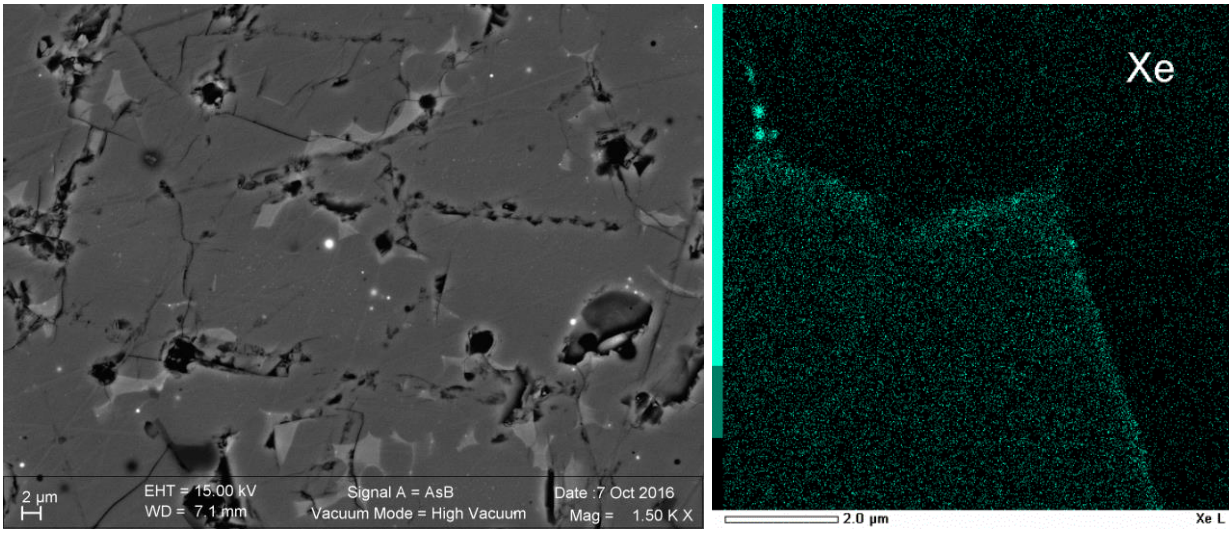


*Figure 5: (gauche) Image MEB en mode rétrodiffusé d'une sanidine enrichie en Xe/Kr. Les zones gris clair sont les zones riches en Fe et gaz rares, et les points brillants sont les bulles de Xe/Kr. (droite) Carte élémentaire (MET) de la zone riche en Fe/Xe.*

Enfin, nous avons étudié l'incorporation des gaz rares lourds dans les verres et magmas feldspathiques (type sanidine). Il existe encore peu de données sur l'incorporation des gaz rares dans les verres et magmas silicatés, et quasi toutes les études sont basées sur des données *ex situ*, pouvant être biaisées par la haute volatilité des gaz rares à conditions ambiantes. Des données récentes, *in situ* par diffraction des rayons X ont ainsi montré

l'existence de liaisons courte Xe-O (2.05 ± 0.05 Å) dans un magma haplogranitique à haute *P* (Leroy et al., 2018).

L'observation des échantillons récupérés montre que, contrairement à l'olivine, même en présence d'une phase fluide, le xénon est incorporé dans le magma. Nous avons également réalisé une étude *in situ*, par spectroscopie d'absorption des rayons X (XAS) aux seuils *K* du xénon (34561 eV) et du krypton (14326 eV) sur un verre riche en Xe (2.18(4) wt%) et Kr (0.52(5) wt%). Les techniques d'analyse ne permettent pas à ce jour de résoudre l'environnement du Xe (le flux n'étant pas assez important à cette énergie), mais le signal indique que le xénon n'est pas localisé dans des nanobulles (comme observé dans le cas d'une implantation ionique, Martin et al., (2008)) mais bien dans le réseau silicaté. Pour le krypton, il a été possible de mettre en évidence deux liaisons Kr-O de longueur 3.32 ± 0.1 Å et 2.49 ± 0.1 Å (figure 6). La présence d'une liaison courte Kr-O (2.49 ± 0.1 Å) associée à une oxydation du krypton, prouve que l'incorporation des gaz rares lourds ne peut être limitée à un simple remplissage des espaces vides (Crépisson et al., 2018, Chemical Geology).

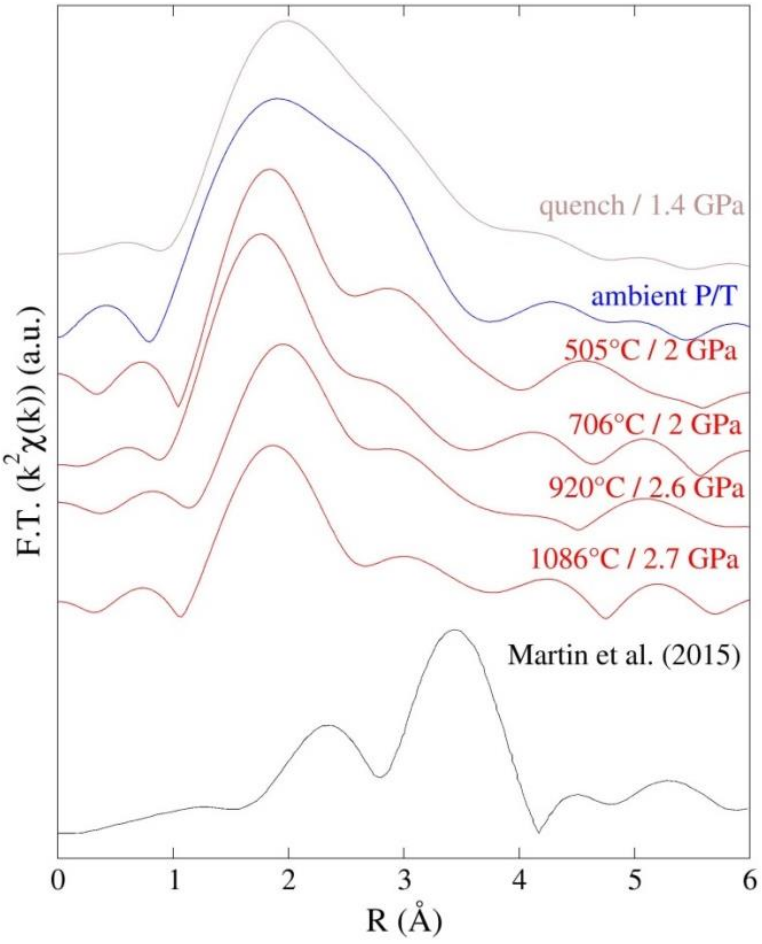


*Figure 6: Valeur absolue de la transformée de Fourier de la function EXAFS du Kr. Le pic observé à ~1.9 Å correspond à la distance Kr-O = 2.49 Å, et le pic à ~2.9 Å à la distance Kr-O = 3.32 Å. L'amplitude décroit de manière générale avec l'augmentation de* T *(Stern et al., 1991).*

## ABSTRACT

Storage of Xe in silicate minerals has been proposed to explain the 'Missing Xenon' issue, i.e. the low Xe abundance in the Earth's and Mars' atmospheres compared to chondrites and to other noble gases. However, data about Xe incorporation in minerals remain scarce due to high Xe volatility preventing studies at ambient conditions. Xe incorporation in silicates has been proposed based on experimental evidences at high pressures (*P*) and temperatures (*T*). Nevertheless Xe incorporation mechanisms remained so far only hypothetical. In this PhD thesis we bring new constraints on Xe incorporation in three major Earth minerals of the continental crust (quartz and feldspar) and upper mantle (olivine). Xe-bearing samples have been synthesized by piston cylinder press, characterized *ex situ* and investigated *in situ* at high *P*-*T* conditions. Significant variations in cell parameters as well as new peaks are retrieved in Xe-bearing quartz, feldspars and olivine by X-ray diffraction, while new bands are observed by infrared spectroscopy on Xe-bearing quartz and olivine. Theoretical calculations (using the density functional theory) have been performed to propose Xe incorporation sites able to reproduce experimental observations. In olivine and quartz, a Xe for Si substitution is likely, with the formation of at least partially covalent Xe-O bonds of 1.98-2.09 Å. Up to 0.4 at% Xe could be potentially stored in olivine at depth, and in quartz a phase transition toward a new $(Xe,Si)O_2$ phase is evidenced at high *T*. In presence of Fe and Xe, a phase separation is observed between a Fe-rich phase and a Fe-poor phase for both feldspars and olivine, with Xe and Fe stabilizing each other. In presence of excess water, Xe is entirely going into the fluid phase for olivine, while it is significantly retained in a feldspathic melt. Eventually Kr and Xe reactivity in feldspathic glass and melt is evidenced by *in situ* X-ray absorption spectroscopy with the observation of Kr oxidation and Kr-O short bonds of 2.49 ± 0.1 Å within the silicate network. These new constraints on Xe incorporation in silicate melts and minerals at depths, often neglected, could be crucial in the 'Missing Xenon' issue.

## ORGANIZATION OF THE PRESENT WORK

In section A/ geochemistry of noble gases, and in particular of xenon is detailed.

In section B/ major physical properties of heavy noble gases are presented, as well as previous results regarding Xe reactivity with major component of the Earth and Mars, in particular silicate minerals.

In section C/ all experimental methods used in this work are detailed.

In section D/ Xe incorporation mechanism in olivine is solved, based on an *ab initio* study and previous *in situ* experimental data at high *P-T* conditions from Sanloup et al. (2011). This work was presented at the 2017 Goldschmidt conference during poster session and published: Crépisson C., Blanchard M., Lazzeri M., Balan E., Sanloup C. (2018) **New constraints on Xe incorporation mechanisms in olivine from first-principles calculations.** *Geochimica et Cosmochimica Acta*, **222**, 146-155. New high *P-T in situ* X-ray diffraction and infrared data on Xe-bearing olivine are presented as well as water and iron impact on Xe incorporation.

In section E/ new and previous *in situ* X-ray diffraction data on Xe-bearing quartz made it possible to identify Xe incorporation as a minor element in quartz as well as a phase transition toward a $(Xe,Si)O_2$ phase at high *T*. This work has been submitted to *Geochemistry, Geophysics, Geosystems*: Crépisson C., Sanloup C., Blanchard M., Hudspeth J., Glazyrin K., Capitani F., **The Xe-$SiO_2$ system at moderate pressure and high temperature.**

In section F/ Xe incorporation in sanidine (a high *T* feldspar) is observed on recovered synthesized samples, showing Xe/Fe-rich phases. Moreover *in situ* X-ray diffraction data on Xe-bearing sanidine confirmed Xe (and possibly Kr) incorporation in sanidine at moderate *P-T* conditions. *In situ* X-ray diffraction data have also been acquired on high-*P* sanidine hydrate (K-cymrite) at high water fugacity on plain and Xe-bearing samples, although results remain inconclusive.

In section G/ Xe and Kr incorporations in sanidine glass are studied by *in situ* X-ray absorption spectroscopy. Results regarding Kr have been published: Crépisson C., Sanloup C., Cormier L., Blanchard M., Hudspeth J., Rosa A., Irifune T., Mathon O., **Kr environment in a feldspathic glass and melt: a high pressure, high temperature X-ray absorption study.** *Chemical Geology*, **493**, 525-531.

In section H/ results are summarized in a final conclusion with further perspectives.

In the Appendix, section I/ and section J/ are reported preliminary results on Xe-bearing haplogranite and on attempt of synthesis of Xe-bearing wavellite.

Results on Xe incorporation in minerals were also presented at the 2017 AGU Fall meeting during a poster session.

## Chapter A: INTRODUCTION (GEOCHEMISTRY)

### I/ Noble gases in geosciences

Noble gases (He, Ne, Ar, Kr, Xe) have been extensively studied by geoscientists. Three recent reviews emphasized their interests and their persistent enigmas (Marty, 2012; Halliday, 2013; Moreira, 2013). Due to their combined relative chemical inertia, volatility and multiple isotopes (Table A1), they are an efficient tool to better understand the Earth-atmosphere system and its evolution since the formation of the Earth. Xenon is the heaviest of the noble gases, and its abundance is generally lower compared to other noble gases in rocks (see Mid Ocean Ridge Basalt (MORB) and Oceanic Island Basalt (OIB) in figure A4). Xe has nine isotopes, including radiogenic isotopes coming from radiogenic decay of extinct $^{129}$I and $^{244}$Pu (Table A1); Xe isotopes can bring further time constraints on early Earth history e.g. Earth formation (Ozima and Podosek, 1999) or formation of the Moon (Avice and Marty, 2014). However Xe has its own enigma.

| | | |
|---|---|---|
| He | $^{3}$He | non radiogenic |
| | $^{4}$He | extant $^{235,238}$U* ($\tau_{1/2}$ = 0.704 Gy, $\tau_{1/2}$ = 4.468 Gy and $^{232}$Th ($\tau_{1/2}$ = 14.01 Gy) |
| Ne | $^{20}$Ne | (rare α-n reaction: $^{17}$O(α,n)) |
| | $^{21}$Ne | α-n reaction: $^{18}$O(α,n) and $^{24}$Mg(n,α) |
| | $^{22}$Ne | (rare α-n reaction: $^{19}$F(α,n)) |
| Ar | $^{36}$Ar | non radiogenic |
| | $^{38}$Ar | non radiogenic |
| | $^{40}$Ar | extant $^{40}$K ($\tau_{1/2}$ = 1.251 Gy). |
| Kr | $^{78}$Kr | non radiogenic |
| | $^{80}$Kr | non radiogenic |
| | $^{82}$Kr | non radiogenic |
| | $^{83}$Kr | extant $^{235,238}$U ** |
| | $^{84}$Kr | extant $^{235,238}$U ** |
| | $^{86}$Kr | extant $^{235,238}$U ** |
| Xe | $^{124}$Xe | non radiogenic |
| | $^{126}$Xe | non radiogenic |
| | $^{128}$Xe | non radiogenic (rare extant $^{128}$Te ($\tau_{1/2} \approx 10^{11}$ Gy)) |
| | $^{129}$Xe | extinct $^{129}$I ($\tau_{1/2}$ =15.7 My) |
| | $^{130}$Xe | non radiogenic (rare extant $^{130}$Te ($\tau_{1/2} \approx 10^{12}$ Gy)) |
| | $^{131}$Xe | extinct $^{244}$Pu ($\tau_{1/2}$ =82 My) and extant $^{235,238}$U |
| | $^{132}$Xe | extinct $^{244}$Pu and extant $^{235,238}$U |
| | $^{134}$Xe | extinct $^{244}$Pu and extant $^{235,238}$U |
| | $^{136}$Xe*** | extinct $^{244}$Pu and extant $^{235,238}$U |

*Table A1: noble gases isotopes and their radioactive origin from natural radionuclides (Ozima and Podosek, 2002, p23). * $^{238}$U is the major U isotope (99.27%), ** very low yield regarding decay of $^{238}$U, *** $^{136}$Xe decays into $^{136}$Ba ($\tau_{1/2} \approx 10^{12}$ Ga).*

The mantle is generally divided into a 'depleted' mantle, which underwent massive degassing and lost its incompatible elements, and an 'enriched' mantle, which did not experience degassing and preserved a primordial composition. Usually MORBs represent the

depleted mantle and OIBs the enriched mantle. Presence of an enriched mantle has first been attributed to a subduction barrier (Allègre et al., 1986/87), although seismic tomography has shown that subduction goes beyond the mantle transition zone (French and Romanowicz, 2015; Van der Hilst, 1997). Becker et al. (1999) argued that blobs of primitive mantle could however be preserved even without subduction barriers, depending on thermal and viscosities parameters of the convection. Other studies attribute mantle heterogeneities to presence of recycled materials at depth (Héber et al., 2007). Study of noble gases at depth can help to better constrain mantle dynamics, i.e. to detect presence of primitive mantle, or recycled material at depth, linking radiogenic isotopes and degassing, but also using non-radiogenic isotopes to trace primitive composition for mantle volatiles.
In the followings, we will focus on the Earth. So far only one Martian meteorite provides information regarding Mars' interior (Mathew and Marti, 2001), with heavy noble gases analyses pointing toward the presence of a solar-like component retained at depth in Mars, differing from the Martian noble gases atmospheric composition.

1/ Helium

He is highly volatile and incompatible, $^{3}He$ is only primordial whereas $^{4}He$ is produced by U and Th radiogenic decay (Table A1). As a consequence high $^{3}He/^{4}He$ ratios in rocks indicate the presence of a primordial, non-degassed component at depth (Clarke et al., 1969). However the ratio is still low compared to the solar wind ratio: around $4.3 - 4.6.10^{-4}$ (data compiled by Ozima and Podosek, 2002, p 88) against $5.5.10^{-5}$ for the highest ratio retrieved in OIB. An extensive record of He ratios in a variety of MORBs and OIBs (Ozima and Igarashi, 2000; Jackson et al., 2007) clearly distinguishes between low homogenous ratios for MORB and high heterogeneous ratios for OIB (Figure A1). It indicates that MORB sources have been extensively degassed whereas OIB sources have been less (and differentially) degassed, or enriched in U and / or Th.

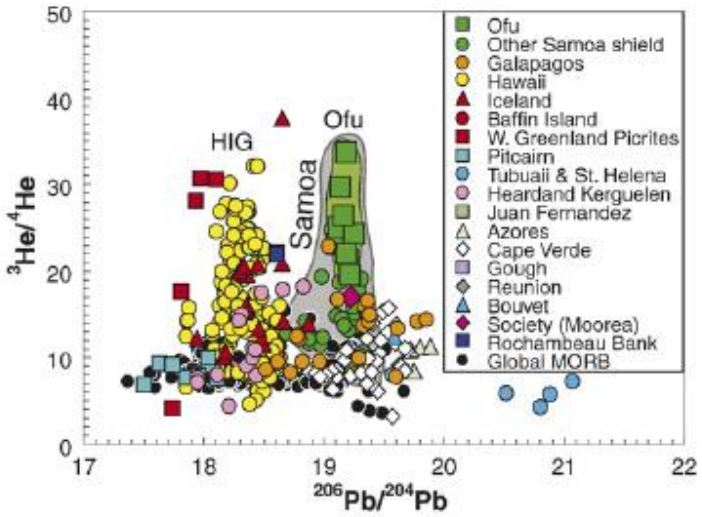


*Figure A1: comparison of He ratios in MORB and OIB, (vertical axis is the helium ratio of the sample divided by the helium ratio of the Earth's atmosphere (e.g. $1.384.10^{-6}$)). Black dots are MORB, color dots are OIB. Figure from Jackson et al. (2007) (see references therein).*

2/ Neon

High $^{20}Ne/^{22}Ne$ ratios retrieved in OIBs, compared to MORBs data are interpreted as preservation of a solar-like component in the enriched mantle (Honda et al., 1991; Yokoshi and Marty, 2004). Indeed, high ratios cannot be explained by α-n reactions involving $^{17}O$ (Table A1), which are likely to be scarce in the mantle and cannot explain high $^{20}Ne$ abundance. Differences with the solar composition[1] have recently been attributed to fractionation during implantation of solar wind based on study of samples from the Genesis mission (Grimberg et al., 2006).

3/ Argon

The $^{40}Ar/^{36}Ar$ ratio is extremely high in MORB ($> 2.5.10^4$ (Moreira and Raquin, 2007)): far higher than the air ratio (295.5) and OIB ratio ($> 3.10^3$ Ozima and Podosek, 2002, p 187). This is linked to a dramatic degassing of the MORB source which would have then only been replenished by radioactive decay of $^{40}K$ (Ozima and Podosek, 2002, p 188).
$^{38}Ar/^{36}Ar$ is similar (= 0.1888, Moreira and Raquin (2007)) in the air and in the mantle (based on MORB, OIB, $CO_2$ wells, diamond analyses) with very little variations observed (Ozima and Podosek, 2000, p 183). Nevertheless this ratio is very different from the solar ratio (0.179, Moreira and Raquin (2007)).

4/ Krypton

None of Kr stable isotopes ($^{78,80,82,83,84,86}Kr$) is purely radiogenic, and Pu and U fission yields are very low for Kr (Table A1). Thus Kr cannot be used to constrain chronology of the atmosphere evolution, and as such has been less studied than other noble gases. However, the small amount of radiogenic Kr makes it suitable to trace air component in fluid inclusions (Böhlke and Irwin, 1992). Earth's atmospheric Kr isotope composition, unchanged since at least 3.3 Gy (Avice et al., 2017), falls in-between solar and chondritic compositions (Pepin, 1991), with a depletion of the atmosphere in heavy isotopes by $1\%.amu^{-1}$ (Hébrard and Marty, 2014). Kr isotopic ratios in $CO_2$ magmatic well gases, measured in the subcontinental lithospheric mantle, show a significant enrichment in $^{84}Kr$ and $^{86}Kr$ compared to the atmosphere (Holland et al. (2009), Figure A2). Mantle-derived samples have an atmospheric Kr isotopic composition for both MORBs and OIBs (Moreira et al., 1998; Trieloff et al., 2000; Graham, 2002), although very few samples have been analyzed for all Kr isotopes due to their very low contents and some complexity of analysis. This homogeneous composition could be due to Kr recycling at subduction zones (Holland and Ballentine, 2006) as previously mentioned.

[1] Previously explained by a 'Neon-B', named after Black (1971) who identified this component in meteorites.

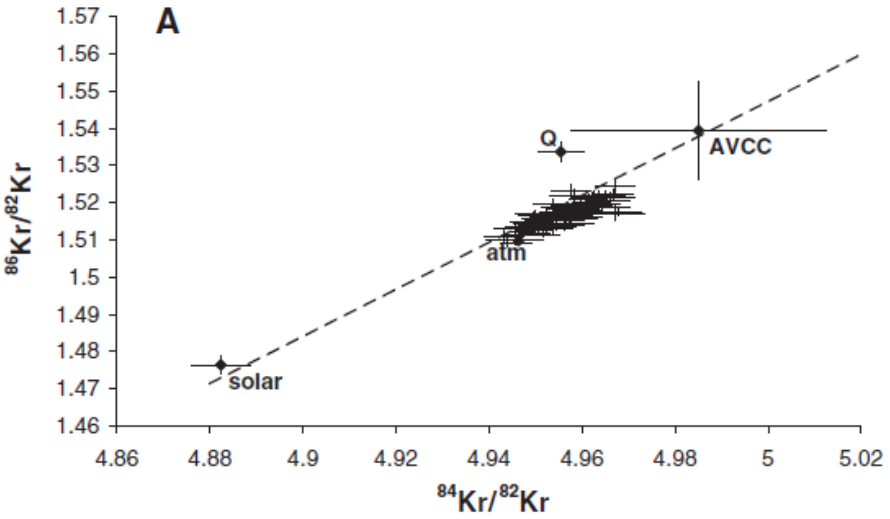


*Figure A2: Isotopic composition of deep magmatic $CO_2$ natural gases representative of the mantle. Samples are on a mixing line between air and AVCC (average carbonaceous chondrite). Figure from Holland et al. (2009).*

5/ Xenon

Measurement of Xe isotopes remains a difficult task, performed in few laboratories in the world, especially regarding light isotopes due to the very low Xe content in samples (around $10^{-12}$ $cm^3$ STP/g: Saito et al. (1984), Moreira et al. (1998)) and the risk of contamination from the air. Crust and sediments have a similar xenon isotopic composition as the air. MORBs (Staudacher and Allègre, 1982; Marty, 1989; Kunz et al., 1998; Moreira et al., 1998 (on popping rock which prevent air contamination); Tucker et al., 2012; Parai et al., 2012; Petö et al., 2013; Parai and Mukhopadhyay, 2015), OIBs (Staudacher and Allègre, 1982; Mukhopadhyay, 2012; Hopp and Trieloff, 2005; Yokoshi and Marty, 2005; Trieloff and Kunz, 2005), diamonds (Ozima and Zashu, 1991; Gautheron et al., 2005), Hadean zircons (Turner et al., 2004) and $CO_2$ well gases (Caffee et al., 1999; Holland and Ballentine, 2006; Holland et al., 2009; Caracausi et al., 2016) have been analyzed. $CO_2$ wells are ideal because of the 'large quantities of sample material available [which] make high-precision measurements possible' (Caracausi et al., 2016). These fluids are linked to magmatism and probe mantellic fluids. Most of analyzed $CO_2$ well gases probed the upper mantle whereas the Eifel $CO_2$ well, recently analyzed by Caracausi et al. (2016), is related to a plume. Study of Xe isotopes in the mantle needs to take into account four components, namely radiogenic $^{129}Xe$, fissiogenic $^{131\text{-}136}Xe$, atmospheric Xe, and possible primordial Xe. Study of light Xe isotopes ($^{124\text{-}128}Xe$) makes it possible to identify primordial component(s), without involving radiogenic correction.

A linear correlation is observed between radiogenic $^{129}Xe$ and fissiogenic $^{136}Xe$ for all available data in various geological environments (Meshik et al., 2000), reflecting at a first-order degassing of the mantle. $^{136}Xe$ is used as a proxy of the fissiogenic Xe components, i.e. of (U)Xe ($^{131,132,134,136}Xe$ coming from decay of $^{238}U$) and (Pu)Xe ($^{131,132,134,136}Xe$ coming from decay of $^{244}Pu$) (Figure A3). Generally a mixing of (U)Xe and (Pu)Xe is assumed or

calculated (Kunz et al., 1998[2]; Caffee et al., 1999; Parai et al., 2012; Petö et al., 2013).
To explain this correlation, Meshik et al., (2000) proposed a chemical fractionation (CFF) of Xe similarly to the one observed in the Okhlo natural nuclear plant (Gabon). In Okhlo, uranite has a low Xe content as most of the Xe produced by U decay has moved to an adjacent aluminophosphate phase (wavellite). The Xe isotopic composition retrieved in wavellite does not match the expected product of U radiogenic decay. A fractionation has occurred during migration of Xe from uranite to wavellite. Inferred fission Xe presents in the atmosphere has the same composition as this Xe-CFF reported by Meshik et al. (2000); therefore authors proposed that current Xe atmospheric composition could be explained via a massive CFF process in the early Earth's history followed by degassing of Xe-CFF in the atmosphere. However Avice et al. (2017) argues that this Xe-CFF fails to account for light Xe isotopic atmospheric composition.

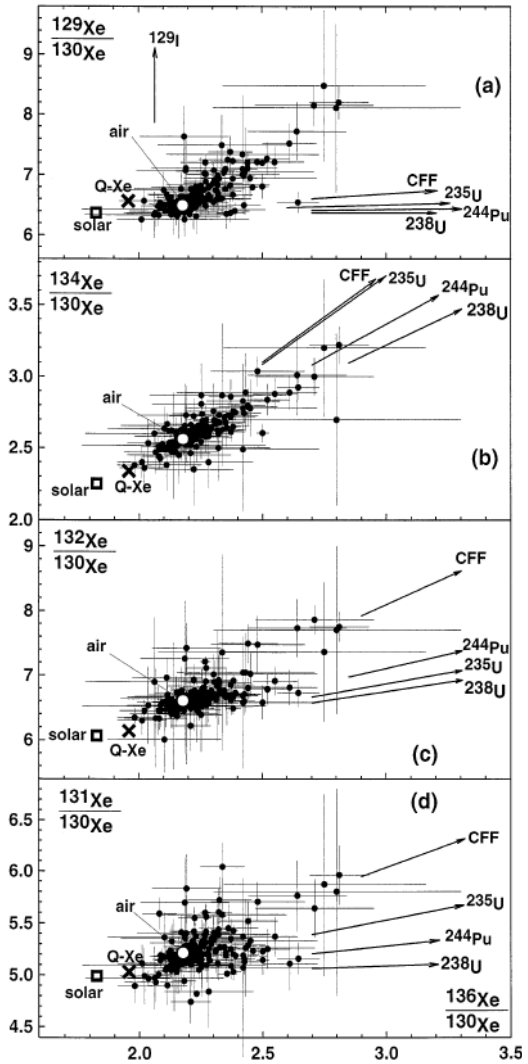


*Figure A3: Compilation of all available data in 2000 (MORB, OIB, diamond). Xe from U or Pu radiogenic decay can be, to some extent, differentiated. CFF refers to the proposed Chemical fractionation of xenon in the Earth, similarly to what is observed in the Okhlo natural nuclear plant. Figure from Meshik et al. (2000).*

[2] They propose that 30% $^{136}$Xe in MORB is coming from radiogenic decay of Pu. In combination with $^{129}$Xe they propose that 80% of the noble gases must have been degassed in the first 20-30 My

6/ Xe and Kr as nuclear fission products

$^{131,133,135}$Xe and $^{85}$Kr are also common radioactive fission products in nuclear fuels. In the frame of long-storage nuclear waste, Xe and Kr have been confined in silica glass (mainly borosilicate and phosphate glasses) for many years via vitrification (Ojovan and Lee, 2011).

$^{131,133,135}$Xe and $^{85}$Kr are also used to detect nuclear underground tests. The Comprehensive Test Ban Treaty (CTBT) organization, created in 1996 (https://www.ctbto.org) has implemented an International Monitoring System (IMS) composed of four networks (detection of seismic, hydroacoustic and infrasound waves as well as detection of atmospheric radionuclides). Amongst atmospheric radionuclides that are monitored, noble gases are particularly relevant to track underground nuclear events. Indeed they do not interact with the soil due to their relative chemical inertia and they rapidly reach the atmosphere due to their volatility. Forty stations of the network are currently measuring noble gases' radionuclides all over the world.

Four metastable Xe isotopes are used to trace nuclear tests (Bowyer et al., 2002, Watrous et al., 2015): $^{131m}$Xe[3], $^{133}$Xe, $^{133m}$Xe and $^{135}$Xe whose half-lives are comprised between 9 hours and 12 days. These isotopes are produced at high yield by nuclear fission of $^{239}$Pu and $^{235}$U. As the ambient atmospheric contents of these isotopes are nearly zero, any release is rapidly identifiable. However complexity arises from 'screening' by other sources of $^{131m,133,133m,135}$Xe such as normal operations of nuclear, medical or industrial facilities. Consequently, models have been developed to take civilian releases into account (see for instance Kalinowski et al., 2011). Transport of Xe throughout the soil i.e. from the underground origin of the nuclear explosion to the atmosphere (Sun et al., 2015) and within the atmosphere (Hourdin and Issartel, 2000) are also investigated and modelled in an effort to better localize the source and determine the timing of an underground nuclear test. The 12$^{th}$ of February 2013 the CTBTO detected $^{131m}$Xe and $^{133}$Xe consistent with the nuclear test announced by North Korea[4].

## II/ Evolution of the Earth-atmosphere system and noble gases

1/ Origin of noble gases

The origin of noble gases, related to the evolution of the Earth-atmosphere system, remains debated. After collapse of the Solar Nebula, planetesimals have been accreted in the first 0.1-1 My (Chambers et al., 2004). Accretion likely lasted 100 My although more than half of the Earth mass was accreted in 20-30 My (Chambers et al., 2004; Wetherill, 1985). Primordial atmosphere is thought to have been acquired by gravitational capture of the surrounding accretion disk of the solar nebula (whose composition is approximated by solar wind composition) as gases remained available for 10 My after solar nebula collapsed (Podosek and Cassen, 1994). Nebular gases may also have been adsorbed at the surface of preplanetesimal dust grains (Pépin, 1991) or ion-implanted. Marrocchi et al. (2011) showed

[3] The exponent $^{m}$ means that it is a metastable nuclear isomer: with a different and metastable spin state.

[4] https://www.ctbto.org/press-centre/press-releases/2013/ctbto-detects-radioactivity-consistent-with-12-february-announced-north-korean-nuclear-test/ (link opened the 31/08/2016).

that Xe isotopic composition of Q-Xe (the C-rich carrier of noble gases in meteorites) can be reproduced by ion-implantation of solar Xe on organic material. Part of the atmosphere could also originate from volatiles and dust carried by planetesimals during accretion (Sasaki, 1991). Returning to 'the Grand Tack Model'[5], Batygin and Laughlin (2015) proposed a formation from small gas-deprived debris of planets. In this case, planets will have acquired volatiles from materials utterly different from the solar nebula. Cometary material could have contributed to the formation of the atmosphere, from the Proto-Earth history till 3.8 Gy, and cometary contribution could reach 22 ± 5% for Xe (Marty et al., 2017) while it may remain smaller than 1% for water, carbon or nitrogen species (Marty et al., 2016). Previous calculations from Dauphas (2003) supported a contribution from cometary material ranging from 19% to 27%.

The discovery of Kr isotopic fractionation in $CO_2$ well gases (Figure A2), taken as a proxy of deep mantle gases, was interpreted as the signature of a primordial Kr chondritic component (Holland et al., 2009). Nevertheless Holland et al. (2009) argue that early degassing of an accreted primordial chondritic composition, followed by mass fractionation during atmosphere loss, fails to explain the composition of the modern atmosphere. Instead, late accretion of cometary material is assumed. Similarly, an excess in Xe light isotopes has been measured in $CO_2$ well gases, compared to the atmospheric Xe (Caffee et al., 1999; Holland and Ballentine, 2006; Holland et al., 2009; Caracausi et al., 2016). The observed variation from the air reveals the presence of a primordial component at depth: solar-like (Caffee et al., 1999) or chondritic (Holland et al., 2009; Caracausi et al., 2016). Origins of mantle Xe could differ from origins of atmospheric Xe. Caracausi et al. (2016) suggests an asteroidal origin for heavy noble gases (Kr, Xe, and possibly Ar) in the mantle, with 16 ± 2% chondritic Xe present at depth.

2/ Atmospheric loss

The Earth's and Mars' primary atmospheres may have been partly or entirely lost throughout their history. The Moon formation impact, at $40^{+20}_{-10}$ My after the formation of the Solar System (Avice and Marty, 2014), could have triggered a catastrophic escape of the primitive atmosphere as well as the Terrestrial Late Heavy Bombardment (TLHB), related to the Late Heavy Bombardment (700 My after formation of the planets) corresponding to a spike of Moon craters (Gomes et al., 2005). These impacts could also have brought late asteroid or cometary volatiles (Marty et al., 2016).

A model of Earth's atmosphere loss relies on hydrodynamic escape (Hunten et al., 1987; Zahnle and Kastling, 1986; Zahnle et al., 1990; Pépin, 1991, 2006). Primordial terrestrial atmosphere was H-rich due to either trapping of nebular gases, or reduction or photodissociation of water. Energy from extreme UV (EUV) radiation from the young Sun or gravitational energy deposited in giant impact could have triggered hot H escape out of the atmosphere with H-fluxes dragging out heavier elements, such as heavy noble gases, inducing mass dependent fractionation. However, very high H-fluxes are required to drag away heavy elements. Considering that EUV flux is only high enough till 50-150 My and that the Moon

[5]Migration inward of Jupiter before its migration in the reverse direction (Walsh et al., 2011)

forming impact occurred at an early stage of the Earth formation, hydrodynamic escapes are thus restricted to early planet history (Pépin, 2006), assuming that H was abundant enough.

3/ Degassing processes

The Earth underwent large degassing events, driving into the atmosphere volatiles located in the solid Earth. Diffusion in solids is too low to explain degassing at the Earth scale, and only happened efficiently through magmatic processes, from the magmatic Ocean era (Elkins-Tanton, 2012) up to nowadays.

Noble gases radiogenic isotopes can be used to study mantle degassing, based on their high volatility and assumed 'infinite' incompatibility. The readiest system is $^{40}K/^{40}Ar$. $^{40}K$, located in the solid Earth, decayed into volatile $^{40}Ar$, the latest representing 99.6% of current atmospheric Ar, whereas there is no $^{40}Ar$ in the primitive atmospheric Ar composition. 40% of radiogenic $^{40}Ar$ has thus been degassed, assuming that the Bulk Silicate Earth has a MORB abundance for K (Porcelli and Ballentine, 2002).

If a similar calculation is done for extinct $^{129}I$ (evaluating initial $^{129}I$ from $^{127}I/^{129}I$ meteoritic ratio), only 0.8 % of radiogenic $^{129}Xe$ is found in the atmosphere. To explain this result, $^{129}Xe$ was assumed to be first entirely lost, before being retained later, defining a closure age for the atmosphere of 97 My (Wetherill, 1985). The same can be done by combining $^{129}I/^{129}Xe$ and $^{244}Pu/^{131\text{-}136}Xe$ systems: assimilating Pu initial abundance to U abundance, and using U-Xe (Pépin, 2000) as a primitive Xe composition. Pépin and Phinney (1976) found a closure age of 82 My. These two closure age estimations did not integrate the fact that 90% Xe is missing in the current atmosphere (Ozima and Podosek, 1999). Avice et al. (2014) built a new model, which took into account the observed isotopic fractionation of Xe throughout the Archean modelled by Rayleigh distillation inducing a mass fractionation and escaping of lighter Xe isotopes from the atmosphere. Authors found a closure age of $40^{+20}_{-10}$ My for the atmosphere, to be related to the Moon formation event[6], and argued that around 77% of the initial volatile elements could have been lost before closure of the atmosphere.

Nevertheless recent results from Marty et al. (2017) showed that 6.8 ± 0.3% of atmospheric $^{129}Xe$ could be related to cometary material accretion thus pointing the need to revise closure ages making use of the $^{129}I/^{129}Xe$ isotopic system.

Within solid Earth, $^{129}Xe/^{130}Xe$ and $^{40}Ar/^{36}Ar$ ratios track the degree of degassing: the higher the ratio is, the more degassed is the source. Indeed high ratios mean that the source has been early degassed and then replenished by decay of $^{129}I$ or $^{40}K$.

Massive mantle degassing has often been invoked to explain the actual current atmosphere composition. However, recent studies of Xe and Kr non–radiogenic isotopes are pointing out the need for two distinct sources to explain on one hand heavy noble gases composition of the atmosphere, and on the other hand heavy noble gases composition of the Earth's mantle (Caffee et al., 1999; Holland et al., 2009; Caracausi et al., 2016).

Eventually, degassing of the solid Earth into the atmosphere is continuing nowadays although

[6] It must be noted that early atmospheric lost till ~ 100 My will not affect degassing results from $^{40}K/^{40}Ar$ (Porcelli and Ballentine, 2002)

at a less extent than in early Earth history: $^{3}He$ flux at oceanic ridges (422 ± 181 mol/year, Saal et al. (2002)) is used to evaluate degassing rate, $^{3}He$ being only a primordial isotope.

4/ Recycling at depth

Recycling at subduction zones, previously neglected, is increasingly invoked as a key process to understand current noble gases elemental and isotopic abundances (Holland and Ballentine, 2006; Smye et al., 2017). Recycled noble gases have been evidenced in Ultra High Pressure terranes brought back to the surface during orogenic collision (Baldwin and Das, 2015; Dai et al., 2016) or in exhumed serpentinites (Kendrick et al., 2011). Kendrick et al. (2013) proposed that 1-10% of subducted Ar could be transferred to the deep mantle.

Recent studies identified deviations from the $^{129}Xe$ and $^{136}Xe$ general correlation (Figure A3) for OIB and $CO_2$ well gases (Caffee et al., 1999; Mukhopadyay, 2012; Peto et al., 2013; Parai and Mukhopadyay, 2015; Caracausi et al., 2016). Deviations are interpreted as early heterogeneities created 4.45 Gy ago, during Earth formation, with different I/Pu and I/Xe ratios within the Earth: MORB source having higher I/Pu ratio (volatile/refractory) and / or lower I/Xe ratio than the 'enriched' reservoir. Recycling could also account for part of the observed deviations from the $^{129}Xe$ and $^{136}Xe$ general correlation, and as a whole could have dramatically shaped current Xe mantle composition (Holland and Ballentine, 2006; Sumino et al., 2010; Kendrick et al., 2011; Parai et al., 2012; Parai and Mukhopadyay, 2015). Up to more than 80% of current Xe could come from recycling material (Holland and Ballentine (2006) based on analysis of a $CO_2$ well in Mexico or Parai and Mukhopadyay (2015) based on analysis from the Southwestern Indian Ridge), while recycling of seawater-derived noble gases could account for 100% of non-radiogenic Ar and Kr (Holland and Ballentine, 2006).

Subduction of seawater-derived noble gases could occur either via unbound seawater filling porous sediments (Holland and Ballentine, 2006), or via retention in hydrous minerals (Kendrick et al., 2011; Smye et al., 2017). Recent experiments showing high He and Ne solubilities in amphibole (Jackson et al., 2013) indicate that noble gases could be transferred into the deep mantle via retention in this mineral in cold subduction contexts (Smye et al., 2017).

## III/ The 'Missing Xenon' and the Xenon Paradox

1/ The 'Missing Xenon'

Noble gases abundances for different cosmochemical planetary end-members are given on figure A4. Noble gases are supposed to be mostly present in atmospheres due to their high volatility. Chondrites are used as a proxy of undifferentiated telluric planets (though it can be challenged especially for volatiles); if absolute abundances of noble gases vary amongst chondrites, relative abundances and isotopic compositions are similar.

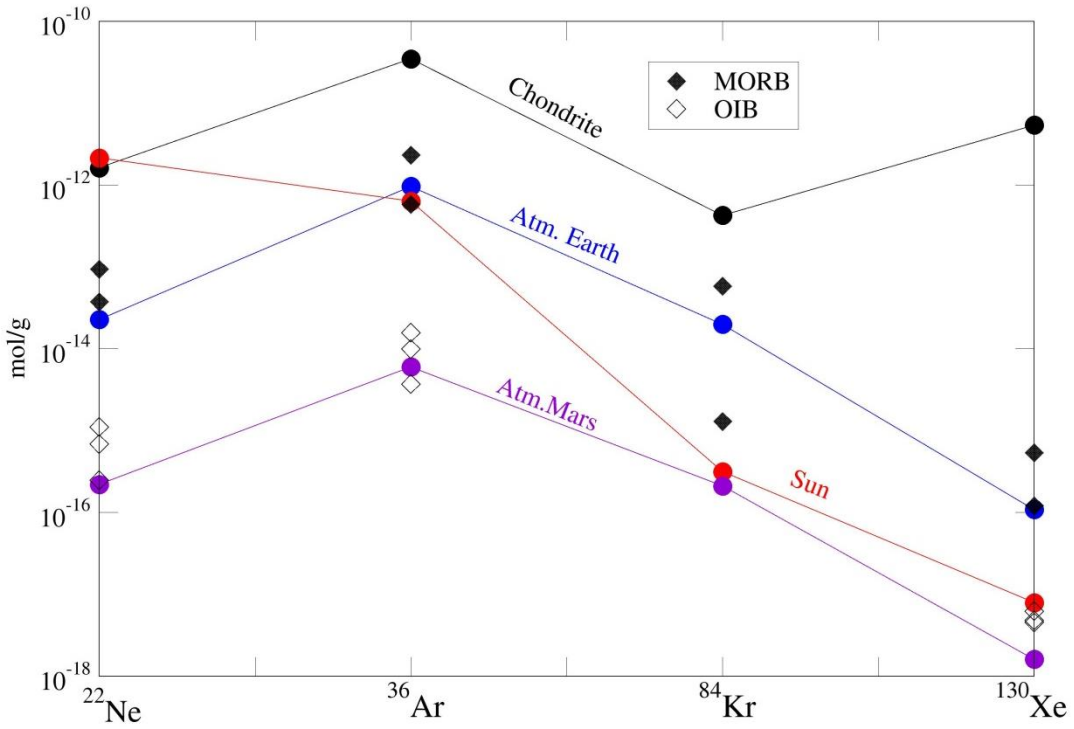


*Figure A4: Noble gases abundances in mol/g[7], MORB (Moreira et al., 1998) and OIB (the Réunion (Hopp and Trieloff, 2005)). Chondrite, Earth atmosphere and Sun abundances are taken from the data compiled by Mart (2012) (namely Mazor et al. (1970) and Bogard et al. (1971) for chondrite, Ozima and Podosek (2002) for Earth atmosphere which includes air, water and sediments and Anders and Grevesse (1989) for the Sun). Mars atmosphere from Hunten et al. (1987) (as only $^{20}$Ne is given in this paper we use $^{20}$Ne/$^{22}$Ne ~ 10 as given by Swindle et al. (2002) for Mars' atmosphere to determine $^{22}$Ne).*

Solar noble gases abundances (proxy for the solar nebula) differ from chondritic and atmospheric abundances proving that if the primordial atmosphere has been inherited from the solar nebula, either it has been lost or an elemental fractionation has taken place. Chondrites and atmospheres have similar patterns, although atmospheres are depleted in noble gases compared to chondrites, and Mars compared to the Earth. Xe is depleted by a factor of 20 in the Mars and Earth's atmospheres compared to the chondritic pattern scaled to other noble gases abundances (Anders and Owen, 1977). This is the so called '**Missing Xenon'** with 90% of Xe missing from the Earth atmosphere (Ozima and Podosek, 1999).

2/ Xe paradox

The 'Missing Xenon' is associated with a particular isotopic signature. Intricate Xenon isotopes have been studied since the 60's under the name of 'Xenology' (Reynolds, 1963). Xe isotopic composition is given for different cosmochemical end-members on figure A5. Xe

[7] Generally geochemists use $cm^3$ STP / (g-bar) = $4.465x10^{-5}$ mole and normalize it to the mass of sample analyzed: 1 $cm^3$ STP/ (g-bar) = $4.465x10^{-5}$ mol/ (g-bar) = 0.5862 wt%/ (bar) for Xe whose atomic mass is 131.293 g/mol). / (bar) stands for the partial pressure of the noble gas during the experiment. If there is a Xe partial pressure of 2 bar we find 1.1724 wt% Xe.

isotopic composition is well known for chondrites[8] (Pepin and Phinney, 1978; Buseman, 2000), and for the Earth Atmosphere (Basford et al., 1973) based on direct measurements. For Mars' atmosphere, Shergottite or SNC (for Shergotty, Nakhla, Chassigny) meteorites are used (Pépin, 1985, 2006; Swindle et al., 2002) as 'gases from Mars atmosphere were trapped in shock-melted phases of these meteorites as they chilled to glass' (Pepin, 2006). Good correlation was indeed obtained when comparing noble gas contents of a shergottite brought back from Viking spacecraft and actual Viking measurement of noble gas content of Mars atmosphere (Pepin, 1985). Solar wind isotopic composition (Meshik et al. (2014) based on Genesis Mission) is usually preferred to comparison with solar isotopic composition to account for the possible isotopic fractionation during transport of gases from the Sun. Cometary isotopic composition has long remained only hypothetical, based on experimental trapping of noble gases in amorphous ice (Owen, 1992; Notesco et al., 1999). Recently, the Rosetta spacecraft measured coma from one comet, 67P/Churyumov-Gerasimenko (Marty et al., 2017), representative of cometary ice reservoir. However $^{124,126}$Xe have not been measured, and measurements on other comets remain needed. Cometary Xe isotopic composition was not added to figure A5 due to large error bars.

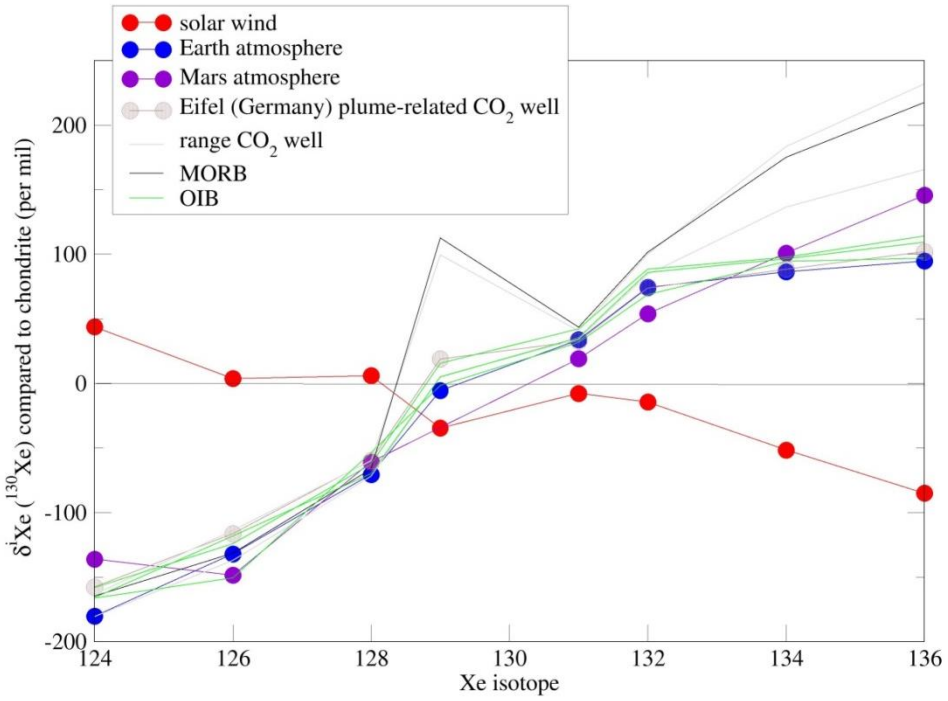


*Figure A5: Xe isotopic composition normalized to AVCC chondrite (Pepin and Phinney, 1978) in solar wind (Meshik et al., 2014), Earth's atmosphere (Basford et al., 1973), Mars' atmosphere (Swindle et al., 2002), MORB (Kunz et al., 1998 summarized by Caffee et al., 1999), OIB (Yokoshi and Marty, 2005), the range of composition for $CO_2$ wells from Colorado, South Australia (Caffee et al., 1999) and New Mexico (Caffee et al., 1999; Holland and Ballentine, 2006). Isotopic composition of the $CO_2$ well in Eifel region (Germany) recently analyzed by Caracausi et al. (2016) is shown.*

[8] AVCC-Xe (Average carbonaceous chondrite) is closed to Xe-Q, which is sited in the surfaces of AVCC-Xe carrier materials (Pépin, 2000)

As already noted for the noble gases abundances, solar wind Xe isotopic composition (close to solar isotopic composition) significantly differs from that of chondrite and planetary atmospheres. Mars and Earth have a similar isotopic composition with a depletion in light Xe isotopes (Krummenacher et al., 1962) compared to chondrite. Terrestrial atmospheric Xe is enriched in its heavy isotopes relatively to chondrite and solar wind by 3-4%.amu$^{-1}$ (Hébrard and Marty, 2014). This is the so-called '**Xenon Paradox'**. Indeed, according to mass dependent fractionation, Krypton (lighter than Xenon) should be less abundant and more fractionated than Xe, whereas the contrary is observed: terrestrial atmospheric Kr is indeed only fractionated by 1%.amu$^{-1}$ (Hébrard and Marty, 2014).
When atmospheric Xe is corrected for mass dependent fractionation, a U-Xe component is obtained (Pépin, 2000), which does not correspond to any known component. U-Xe is similar to solar wind Xe isotopic composition although depleted in $^{134}$Xe and $^{136}$Xe. Indeed U-Xe is calculated to correspond to a primordial atmospheric Xe, further mass dependently fractionated, and with the late addition of degassed radiogenic products from $^{244}$Pu and $^{129}$I decay. It has been proposed that U-Xe could be produced by a mix of chondritic Xe with an addition of 22 ± 5% cometary Xe (Marty et al., 2017).

Intermediate Xe isotopic compositions, between chondritic and atmospheric, have been measured in Archean rocks (Figure A6). Although analyses on such old samples require important corrections (for U and $^{130}$Ba (through multichannel) decays, neutron captures, spallation reactions), this phenomenon has been retrieve for many samples of different ages. Samples displaying fractionation include a hydrothermal quartz dated at 3 ± 0.2 Gy from the 3.5 Gy Dresser formation in Western Australia (Pujol et al., 2011, 2013) (based on $^{128,129,131}$Xe) as well as a barite of 3.5 Gy from the same formation (Srinivasan, 1976; Pujol et al., 2009), fluid inclusions of 3.3 Gy from Barberton quartz, South Africa (Avice et al., 2017), a barite of 0.18 Gy from the Belorechenskoe deposit in North Caucasus, Russia (Meshik et al., 2002), and Karelian shungites, Russia, of 2.8-2.9 Gy (Lokhov et al., 2002). Deep fluids from the Canadian Precambrian Shield isolated since at least 1.5 Gy present the same evidence (based on $^{124,126,128}$Xe) (Holland et al., 2013). No fractionation has been evidenced for other noble gases except from Lokhov et al. (2002) who reported significant Kr fractionation with relative enrichment of lighter isotopes by a factor of 1-1.2 %.amu$^{-1}$ for Kr (and 0.2-0.3 %.amu$^{-1}$ for Xe), although data are not further detailed.

3/ Hypotheses to explain the 'Missing Xenon' and the Xenon paradox

The aforementioned intermediate Xe compositions have been interpreted as a continuous Xe isotopic fractionation throughout the Archean (Pujol et al., 2011, 2013, Avice et al., 2017) (Figure A6). Xe isotope fractionation throughout the Archean could be explained by the combination of high UV flux from the young Sun (Figure A6), and the presence of an organic haze in the early Earth's atmosphere (Hébrard and Marty, 2014). High UV flux enhances Xe photoionization at the altitude of the organic haze, Xe being preferentially ionized compared to other noble gases due to its low ionization potential. Ionization of Xe is significant at the height of the organic haze, whereas ionization of other noble gases will only happen quantitatively at higher altitude. Xe is thus preferentially trapped in the organic haze,

compared to other noble gases, with adsorption process inducing Xe isotopic fractionation, with preferential trapping of heavy Xe isotopes (Marocchi and Marty, 2013). This process however, does not explain why lighter Xe isotopes, not trapped in the organic haze, will be significantly removed from the atmosphere, while other noble gases (such as Kr) will not. Moreover there is so far no clue for the presence of an organic haze in early Mars' history, and it is unclear if the UV flux, decreasing far more rapidly than Xe isotope fractionation (Figure A6) could explain Xe isotope fractionation throughout the entire Archean eon.

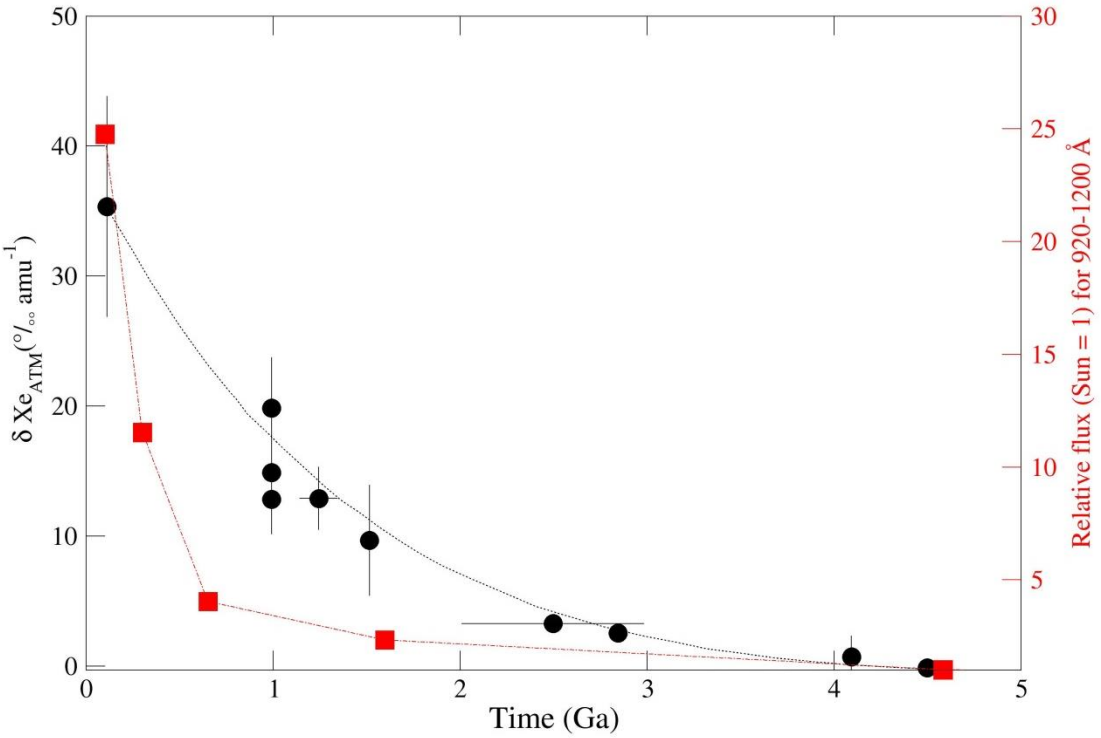


*Figure A6: UV solar flux and intense Xe isotope fractionation throughout the Earth history. Extreme UV solar flux shows rapid decrease compared to progressive Xe isotope fractionation. Plain black circles are data points showing Xe isotope fractionation (references in Hébrard and Marty (2014), recent measurement from Avice et al. (2017) has been added), dashed black line is average Xe isotope fractionation. Plain red squares are solar flux data points from Ribas et al. (2005), dashed red line is a guide for the eyes*.

Alternatively to hydrodynamic escape, Xe could be stored in the solid Earth. High Xe contents have been found in siliceous and calcareous sediments (Matsuda and Nagao, 1986; Matsubara et al., 1988; Matsuda and Matsubara, 1989), meta-anthracite (Lokhov et al., 2002), and shales (Bernatowisz et al., 1984). Indeed adsorption of noble gases increases with its radius, and is therefore maximal for Xe (Ozima and Podosek, 2002). However the volume of sediments on the Earth remains too small to explain the whole 'Missing Xenon'.

Xe becomes a metal at high *P* and has a similar crystallographic structure as Fe (hcp) at core *P*. However, no Xe-Fe(Ni) stable compound have been observed below 200 GPa (Caldwell et al., 1997; Nishio-Hamane et al., 2010; Dewaele et al., 2017; Stavrou et al., 2018), whereas *P* of the Mars' core is 40 GPa, and the *P* of accretion of the Earth's core is thought to be 40-50 GPa (Li and Agee, 1996). Thus Xe storage in the cores is doubtful. Alternatively, Jephcoat (1998) proposed the formation of molten Xe clusters during Earth

differentiation, which will be driven down to the core, although scarcity of Xe makes this assumption rather hypothetical.

Eventually, it has been proposed that Xe could be incorporated in terrestrial mantle and continental crust minerals (Sanloup et al., 2002, 2005, 2011), and this will be the hypothesis explored in this PhD thesis. Indeed martian and terrestrial mantles are relatively similar (Rivoldini et al., 2011), and the early Mars could had a terrestrial-like continental crust (Sautter et al., 2015). Xe retention in crust and mantles could thus be at stake for both planets. Xe incorporation in minerals could also contribute to explain the current xenology. Indeed fractionation of stable isotopes linked with crystallographic structure of the host mineral has already been observed (e.g. for iron: Roskosz et al. (2015)). Moreover, experiments on Ar, Kr, Xe isotopic fractionation in water ice have already shown an enrichment in heavy isotope in water ice (Notesco et al., 1999).

# Chapter B: STATE OF THE ART: XE REACTIVITY AND INCORPORATION IN EARTH'S RELEVANT MATERIALS

## I/ Xe physical properties

Xenon is the heaviest studied of the noble gases, it also has the highest polarizability and consequently the lowest ionization energy as its electrons are farther and as a consequence less bonded to the nucleus (Table B1). Noble gases have long been considered to be inert due to their stable closed-shell electronic configuration. Electronic configuration of Xe is:

$1s^2\ 2s^2\ 2p^6\ 3s^2\ 3p^6\ 4s^2\ 3d^{10}\ 4p^6\ 5s^2\ 4d^{10}\ 5p^6$

However since the 1960's theoretical and experimental chemists have shown that the so-called chemical inertia of Xe was a wrong assumption. Bartlett and coworkers synthesized the first noble-gas compound, $XePtF_6$ (Bartlett et al., 1962). From this landmark, hundreds of Xe compounds have been synthesized (for reviews see Gerber, 2006; Grochala, 2007; Schrobilgen and Brock, 2012; Haner and Shrobilgen, 2015).

| | **He** | **Ne** | **Ar** | **Kr** | **Xe** |
|---|---|---|---|---|---|
| **atomic number** | 2 | 10 | 18 | 36 | 54 |
| **atomic weight (amu)** | 4.0026 | 20.179 | 39.948 | 83.8 | 131.3 |
| **ionization energy (eV)** | 24.48 | 21.56 | 15.76 | 14 | 12.13 |
| **polarizability ($10^{-24}$ $cm^3$)** | 0.201 | 0.39 | 1.62 | 2.46 | 3.99 |

*Table B1: Fundamental properties of noble gases, from Ozima and Podosek (2002), p 31.*

### 1/ Noble gases atomic radii

Atomic Radius of noble gases is not straightforward to define (Table B2). Covalent radii represent the size of an atom within a covalent bond. They are measured by X-ray diffraction on a variety of compounds, ideally involving homonuclear bonds (to preclude polar component) of the element. Van der Waals radii are half of the distance minimizing the potential energy between two atoms, i.e. the sphere actually occupied by one atom in gaseous state. However to study noble gases in minerals and melts, other evaluations are required, as noble gas bonding may be within covalent and van der Waals radii. Cook (1961) published for instance atomic radii of low *T* noble gas crystals and Zhang and Xu (1995) reviewed different existing atomic radii and proposed new atomic radii to study more accurately noble gases in condensed phases in a similar way as other ions. They extrapolate ionic radius of isoelectronic atoms as a function of oxidation state based on previous data and assume a zero oxidation of state for noble gases, which may not be always true as discussed throughout this work.

| | CN | He | Ne | Ar | Kr | Xe |
|---|---|---|---|---|---|---|
| **covalent radius**[a] | - | 0.28 | 0.58 | 1.06 ± (0.10) | 1.16 ± (0.04) | 1.40 ± (0.09) |
| **van der Waals radius**[b] | - | - | 1.55 | 1.88 | 2.00 | 2.18 |
| **radius in crystals (low *T*)**[c] | 12 | 1.78 | 1.60 | 1.92 | 1.98 | 2.18 |
| **ionic type radius**[d] | 4 | 0.90 (0.06) | 1.18 (0.02) | - | - | - |
| **ionic type radius**[d] | 6 | 1.08 (0.06) | 1.21(0.02) | 1.64(0.03) | 1.78(0.03) | 1.96(0.02) |
| **ionic type radius**[d] | 8 | - | 1.32(0.03) | (1.77 (0.06)) | (1.87(0.06)) | (2.03(0.06)) |

*Table B2: Atomic radii of noble gases in Å from [a]Cambridge structural database, [b] Pyykkö (1997), [c] Cook (1961) and [d] Zhang and Xu (1995). Error bars in brackets. When the whole value is in bracket it means that there is a large error bars. CN= coordination number.*

2/ Diffusion and adsorption properties

Atomic radii play a significant role in diffusivity and solubility in melts, glasses and crystals. Diffusion coefficients decrease with increasing radius for a given family of elements. Noble gas diffusion coefficients have been compiled by Baxter (2010). Very few diffusion coefficients are available so far for diffusion of Xe in minerals (see Baxter, 2010): Melcher et al. (1983) implanted Xe in olivine at 1400°C and evaluated a diffusion coefficient greater than $7.10^{-15}$ cm²/s. However, this result may be linked to implantation mechanisms, as it is surprising in regards to our experiments in piston cylinder, in which Xe is clearly seen to diffuse throughout the few mm sample in few hours, i.e. much faster. Noble gases diffusion coefficients in a tholeiitic melt at 1350°C show a decrease with increasing atomic radius (Lux, 1987, Figure B1). Diffusion coefficients in the melt (Figure B1) are around 7 orders of magnitude higher than in crystalline olivine, using result from Melcher et al. (1985) and Lux (1987).

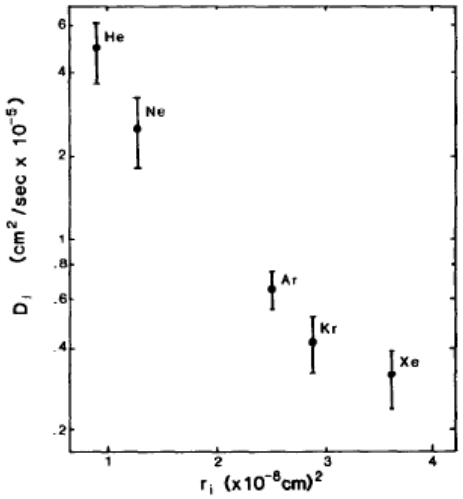


*Figure B1: Diffusion coefficients of noble gases at 1350°C in a tholeiitic melt in function of radius of the atom in a gas. Figure from Lux (1987).*

Another important property is physisorption and chemisorption at the surface of materials. Although these phenomena are preponderant only at low *T* they need to be taken into account as an efficient way of trapping noble gases. Physical adsorption implies relatively weak and reversible interactions (mostly van der Waals) whereas chemical adsorption, less relevant for noble gases, implies sharing electron and is generally not easily reversible (Ozima and Podosek, 2002, p 33). Recently, metal-organic framework (MOF) have been synthesized in order to separate Xe from other noble gases such as Kr or Ar as they are all used for a wide range of industrial applications. Preferential adsorption of Xe is reached using size difference and higher polarizability of Xe compared to other noble gases (Bae et al., 2013; Chen et al., 2015).

3/ Xe phase diagram

Solid xenon exists under two different crystalline structures: fcc (cubic close-packed) and hcp (hexagonal close-packed). The fcc structure is stable at lower *P* and the hcp structure is stable to at least 137 GPa (Jephcoat et al., 1987) (Table B3 and Figures B2 and B3). A martensitic transition between the fcc and hcp structure takes place from 3 GPa to 70 GPa (Cynn et al., 2001). Thermal equations of state for solid xenon have been calculated, although from experimental data below room *T* (Packard and Swenson, 1963; Syassen and Holzapfel, 1978). Isothermal variations of cell parameters as a function of *P* are available although mostly at very high *P* (for example Howie et al., 2016). Xe melting curve (Boelher et al., 2001; Ross et al., 2005; Ferreira and Lobo, 2008) is displayed on figure B2.

| Structure | Space group | Cell parameter | Atomic position | Reference |
|---|---|---|---|---|
| **fcc** | *Fm3m* | $a$ = 6.1317Å | Xe 0 0 0 | Sears and Klug (1962) |
| **hcp** | *P6_3/mmc* | $a$ = 4.34Å<br>$c$ = 7.09Å | Xe 1/3 2/3 1/4 | Sonnenblick et al. (1977) |

*Table B3: Crystallographic structure of pure solid Xe phases.*

At ambient conditions Xe is an insulator. A metallic transition is observed between 121 GPa and 138 GPa (Goettel et al., 1989, Eremets et al., 2000) with a purely metallic behaviour at 155 GPa. Metallization *P* for noble gases increases with decreasing atomic number: for comparison, an insulator-metal transition is expected at 310 GPa for Kr, and at 510 GPa for Ar from first-principles calculations (Kwon et al., 1995).

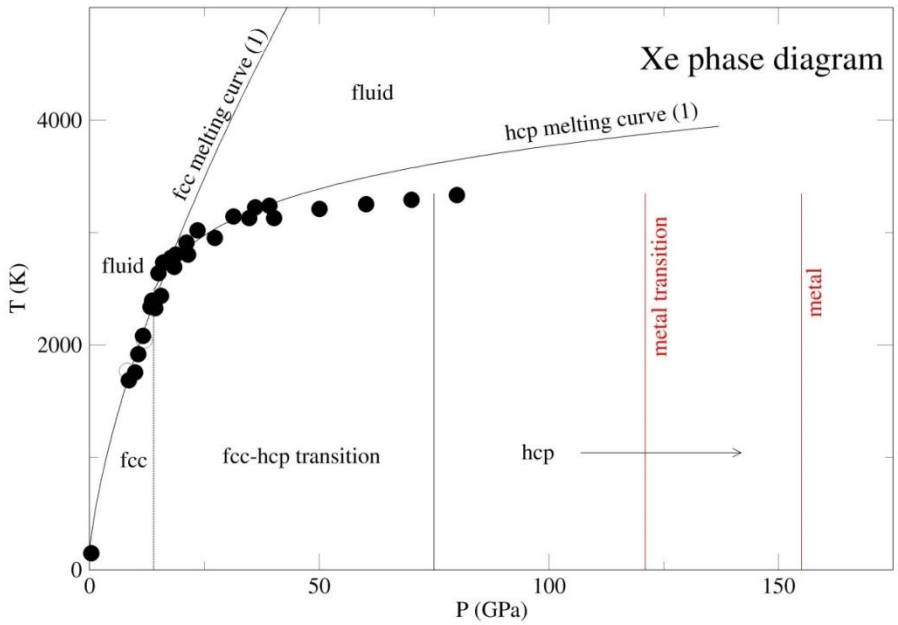


*Figure B2: Xe phase diagram: (1) is melting curve from Ferreira and Lobo (2008), filled circles are experimental data from Boelher et al. (2001) and Ross et al. (2005), and empty circles are experimental data from Jephcoat and Besedin (1998). Xe fluid is mostly a supercritical fluid as its critical point is 289.7 K (Ozima and Podosek, 2002).*

4/ Xe in metallic phases at high *P*

Discovery of metallic Xe at high *P* launched the search for Xe metallic compounds, especially in link with potential Xe storage in the core (A/III/3). Theoretical calculations investigated the solubility of Xe at core conditions: Lee and Steinle-Neuman (2006) found that Xe could be stable at 0.8 mol % in an iron core and Zhu et al. (2014) found Xe/Fe-Ni intermetallic compound stables at *P-T* conditions of the core. However $XeNi_3$ has been synthesized only at ~ 150 GPa and 1500 K (Dewaele et al., 2017; Stavrou et al., 2018) and $XeFe_3$ only above 200 GPa and 2000 K (Stavrou et al., 2018).

Other high-P Xe compounds have been synthesized, such as van der Waals compounds $Xe(N_2)_2$, becoming metallic above 100 GPa (Howie et al., 2016), and $Xe(H_2)_n$ (Somayozulu et al., 2010, 2015). $XeF_2$ was shown to transform into semiconducting $XeF_4$ at 50 GPa and into metallic $XeF_8$ above 70 GPa (Kim et al., 2010). Eventually, $O_2$ impurities (0.6 mol % $O_2$) decrease solid Xe metallization *P* from 130 GPa to 49 GPa (Dewaele et al., 2012).

## II/ Xe in oxides and silicates

Various Xe (and to a less extent Kr and Ar) compounds have been synthesized (Grochala, 2007) as Xe is the most reactive amongst the noble gases. However, high Xe abundances in natural samples are unlikely as Xe is highly volatile at ambient conditions and is likely to escape from the mineral structure. However, wavellite (an hydroxylated aluminophosphate) from the Okhlo natural nuclear plant (in Gabon) has the highest Xe

content retrieved in a natural sample with up to $10^{-2}$ $cm^3$ STP/g Xe (i.e. 60 ppm Xe) (Meshik et al., 2000), followed by a shungite (Lokhov et al., 2002) with $10^{-8}$ $cm^3$ STP/g $^{130}Xe$, and siliceous microfossils (Matsuda and Matsubara, 1989) with up to $7.9.10^{-9}$ $cm^3$ STP/g $^{132}Xe$. Eventually granite from the Sudbury structure (originating from a meteoritic impact), Ontario, Canada presents a high Xe content ($1.3.10^{-8}$ $cm^3$ STP/g) (Kuroda et al., 1977).

1/ Xe in clathrates (van der Waals bonds)

A well-known, geologically relevant type of clathrate is ice clathrate, naturally present in the permafrost, in south and north poles, with $CO_2$ and $CH_4$ as guest molecules. There are different clathrate hydrate structures, the most commons (sI, sII (cubic structure I and II) and sH (hexagonal structure)) consist of combination of 12 pentagons of assembled water molecules. They have been extensively studied (Sloan and Koh, 2007) among other due to the risk of potential greenhouse gases release from ice polar clathrates in case of intensive ice melting linked with global warming. Xe is also among the gases that stabilizes clathrate hydrate structures through van Der Waals interactions. Xe ice clathrates were shown to be stable under two phases up to 2.5 GPa before breaking down (Dyadin et al., 1997; Sanloup et al., 2002). Though natural clathrates in polar ice contain very few Xe, stability of Xe-bearing ice clathrate above 50 GPa and 1500 K proves the possibility of their presence at depth in giant planets or in comets (Iro et al., 2003).

Zeolites are microporous, aluminosilicate minerals (more than 200 different types identified so far), characterized by their cage-like structure. They are strictly speaking part of the clathrate group. Their particular structure is the origin of their adsorbent and catalytic properties frequently used in the industry. Xenon is one of the guest molecules which can enter cages of zeolite (Ito 1984; Heo, 1999; Seoung et al, 2014). Seoung et al. (2014) studied incorporation of Xe in Ag natrolite (Ag-NAT) at 1.7 GPa and 250°C. Xe enters the structure of Ag-NAT while nanoparticles of metal Ag are deposited at the crystal surface. In presence of Xe in the structure $Ag^+$ converts to $Ag^{2+}$ inside the zeolite, linked to an oxidation of water or of lattice oxygen. $Ag^{2+}$ is very unstable and is normally reduced to $Ag^+$, it is possible that high polarizability of Xe stabilizes $Ag^{2+}$ (as proposed by Walker et al. (1999)) potentially acting as an adduct, as for Au(I)F (Kurzydłowski and Grochala, 2008). At ambient *P* Xe is not released and remains inside the Ag-NAT; heating is needed to trigger desorption. Similar experiences with Kr prove that Kr is released, although Seoung et al. (2014) did not report if $Ag^{2+}$ is also produced with Kr.

2/ Xe in stoichiometric oxides

The Earth is generally-speaking an oxidised environment and bonding with oxygen is predominant in the majority of Earth's minerals. $XeO_3$ (Smith, 1963; Templeton et al., 1963) and $XeO_4$ with Xe-O bond length of 1.736 Å (Selig et al., 1964; Gundersen, 1970) have been synthesized from Xe-F compounds (Figure B3), although reactions of formation are endothermic and the Xe compounds are highly unstable. A stable xenon dioxide ($XeO_2$) has been synthetized at 273 K by hydrolysis of $XeF_4$ in acid water (Brock and Schrobilgen, 2011).

Though the structure has not been fully resolved, the authors proposed a planar oxygen environment around Xe (Figure B3) based on Raman analysis.
Theoretical calculations have been performed to investigate possible structures of xenon oxides at high *P*. Based on density functional theory (DFT) and within the generalized gradient approximation (GGA), Zhu (2012) predicted stability of XeO, $XeO_2$ and $XeO_3$ respectively above 83 GPa, 102 GPa, and 114 GPa linked with an increasing oxidation state of Xe with *P* ($Xe^0$, $Xe^{2+}$, $Xe^{4+}$, $Xe^{6+}$) whereas Hermann and Schwerdtfeger (2014) predicted stability of $Xe_3O_2$ above 75 GPa.
Recently Dewaele et al. (2016) observed two Xe oxides, at 83 GPa and 97 GPa and 2000 K in diamond anvil cell using *in situ* X-ray diffraction, Raman and X-ray absorption spectroscopies. $Xe_2O_5$, an insulator, is stable under rich O conditions (metastable till 30 GPa) and composed of $Xe^{4+}$ and $Xe^{6+}$. $Xe_3O_2$, a semimetallic compound, is stable under poor O condition (metastable till 38 GPa) and composed of $Xe^0$ and $Xe^{4+}$ (Figure B3).

Regarding Xe/$H_2O$ phases, above 50 GPa and 1500 K, a stable Xe compound with covalent Xe-O bonds: $Xe_4O_{12}H_{12}$ was found (Sanloup et al., 2013). $Xe_4O_{12}H_{12}$ has a hexagonal structure with 2 $Xe_2O_6H_6$ units (as shown on figure B3) per unit cell. Existence of stable Xe-$H_2O$ phase at these *P-T* conditions could be relevant for giant planets such as Uranus and Neptune but eventually also for cold slabs subducting into the deep mantle.

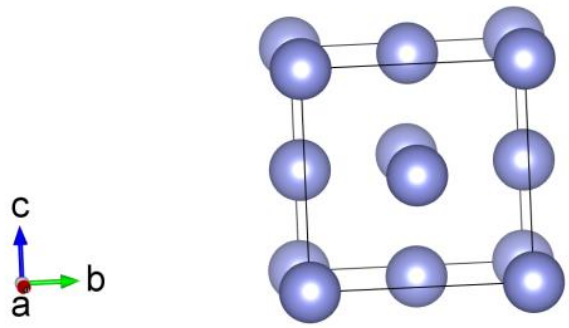


pure Xe: fcc structure

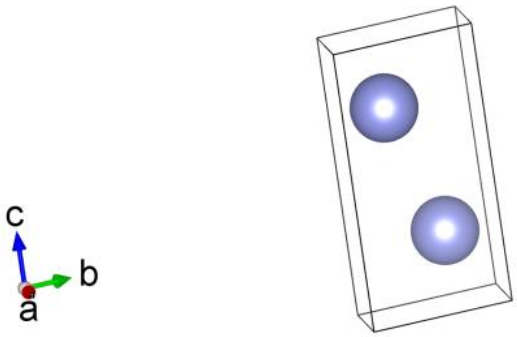


pure Xe: hcp structure

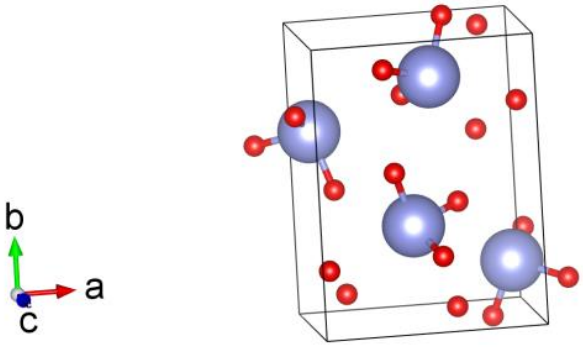


Unstable $XeO_3$ (Templeton et al., 1963)

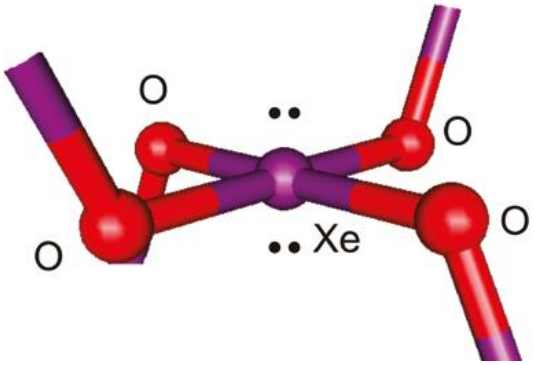


$XeO_2$ (from Brock and Shrobilgen (2011)

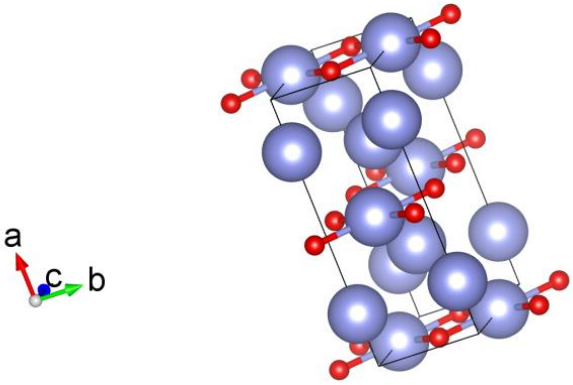


$Xe_3O_2$ (Dewaele et al., 2016)

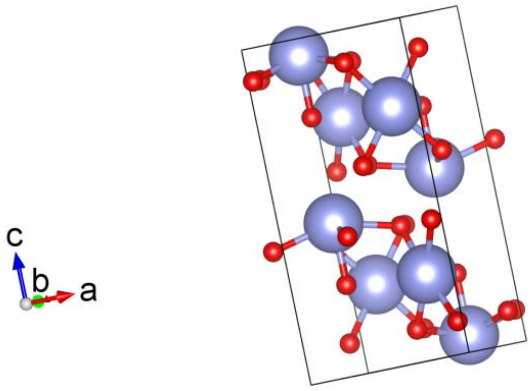


$Xe_2O_5$ (Dewaele et al., 2016)

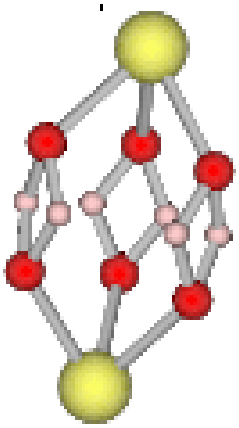

$Xe_2O_6H_6$ figure from Sanloup et al. (2013) (Xe, O, and H, respectively as yellow, red, and white balls).

*Figure B3: Structure of xenon oxides, and pure xenon, which have been synthesized, drawn with VESTA software (Momma and Izumi, 2011).*

Perovskite structure, whose most representative in Earth's sciences is bridgmanite ($(Mg,Fe)SiO_3$) is able to incorporate a large range of elements including Xe. $KM(XeNaO_6)$ (with M= Ca, Sr, Ba) has been synthetized 'under soft hydrothermal conditions, [with] thermal stability limited to the temperature margins of 360–380°C' (Britvin et al., 2015). In this structure Xe is octavalent, in a $XeO_6$ polyhedral environment with Xe-O bond lengths from 1.75 Å to 1.86 Å (Figure B4, left). $K_4Xe_3O_{12}$, a layered-perovskite was also observed (Britvin et al., 2016): one layer is composed of ($XeO_3$) and one layer of $(XeO_6)^{4-}$, with Xe-O bond lengths of 1.8 Å, and Xe charge of + 6 or + 8 (Figure B4, right).

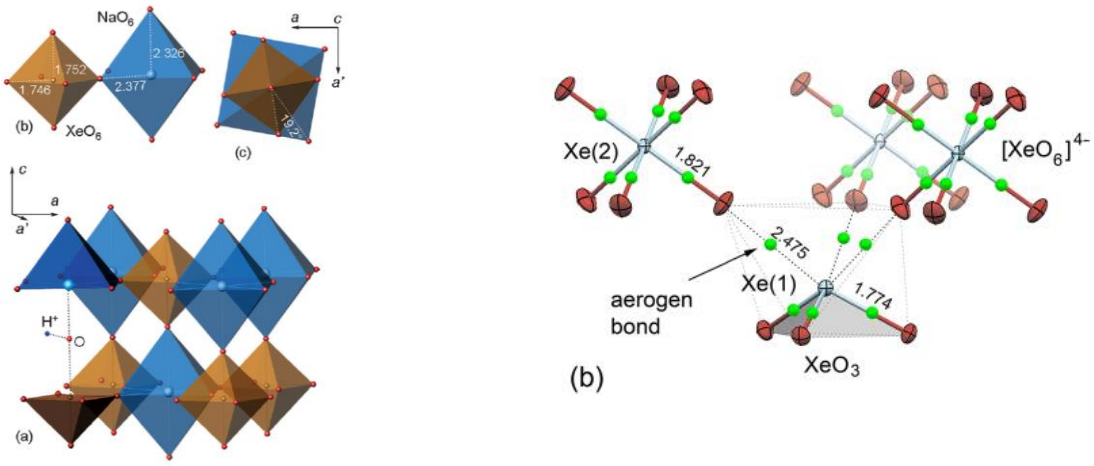


*Figure B4: (left) Structure of Xe-bearing perovskite from Britvin et al. (2015). $K^+$ and $Ca^{2+}$ have been omitted for clarity (right) $K_4Xe_3O_{12}$ structure (Britvin et al., 2016). Xe-O covalent bonds are present for both perovskite, within $XeO_6$ polyhedra. For $K_4Xe_3O_{12}$, aerogens bond involving weak interactions, although stronger than van der Waals interactions are also involved.Figures from Britvin et al. (2015, 2016).*

3/ Xe as a minor or trace element in silicates

Shcheka and Keppler (2012) studied Ar and Xe solubilities in bridgmanite ($MgSiO_3$) at 25 GPa and 1600-1800°C for one hour (after one hour at 10 GPa and 1200°C) from $MgSiO_3$ glass loaded in Pt capsule with Ar or Xe gas. Xe contents were very low (up to 300 ppm) compared to Ar content (up to 1 wt%). However, these very low Xe contents were measured in bubble-free zones and the very large number of Xe bubbles in perovskite (Figure B5) remains to be explained.

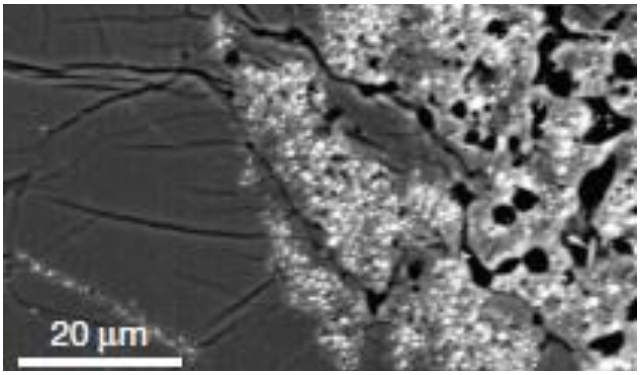


*Figure B5: SEM image from recovered perovskite crystallized in presence of Xe excess. We can see Xe bubbles (bright spots). Figure from Shcheka and Keppler (2012).*

Sanloup et al. (2002) studied Xe-$SiO_2$ system up to 5 GPa and 1750°C in laser-heating diamond anvil cells. At 0.7-1.5 GPa and 1500-1750°C in addition to the Raman signal of α-quartz, three new Raman modes were *in situ* observed immediately after *T*-quenching and disappeared within 20 minutes. Quenching of the phase leads to a new phase stable at room *T* and up to 2.14 GPa. X-ray diffraction pattern at ambient condition on the recovered sample revealed 5 to 6 new peaks which were attributed to a Xe-rich $SiO_2$ phase. Electron microprobe analysis on recovered samples revealed a surprisingly high Xe content: up to 4 wt%.

Sanloup et al. (2005) studied Xe-$SiO_2$ system up to 10 GPa and 2300 K in Paris Edinburgh and multi anvil presses. X-ray diffraction data evidenced an extension of the stability field of quartz. $Pt_3Si$ was observed within the recovered Pt capsule, attesting the release of Si from quartz. These observations led to the hypothesis that Si reduction had been triggered by Xe, through Xe for Si substitution.

Probert (2010) theoretically investigated incorporation mechanisms of Xe in α-quartz guided by these experimental results, in the framework of the Density Functional Theory. He tried different configurations of Xe substitutions on Si or O site and interstitial Xe. If relative energy can help to define the likeliest configuration within one type of substitution, it is not possible to identify a unique incorporation mechanism in absence of confrontation with experimental data.

Kalinowski et al. (2014) theoretically investigated possible Xe incorporation in fibrous silica which can be found in moganite or chalcedoine (Hopkinson et al., 1999). They performed *ab initio* calculations using a robust approach to correctly model chemical-bonding[9]. The choice of fibrous silica was motivated by the fact that Xe has been observed in planar, linear and octahedral environment but never in tetrahedral position. Due to heavy calculations, a chain of 5 Si is considered with OH terminations on both sides with little interaction with the chain, and with one Xe substituted to one Si in the middle of the chain (Figure B6). Xe has a local planar environment surrounded by 4 O at 2.17 Å, and an oxidation state of + 4.

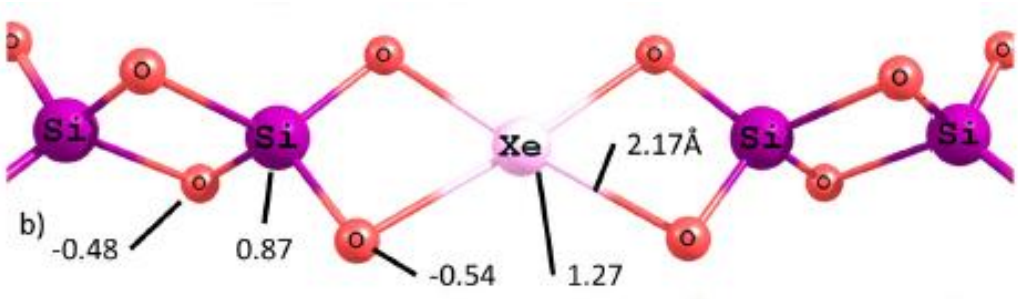


*Figure B6: Fibrous chain of silica with Xe substituted to Si. Xe-O bond length is 2.17Å, numbers are partial charges. Figure from Kalinowski et al. (2014).*

[9] Namely couple cluster with full treatment of single and double excitation associated with many perturbation theory to model triple excitation (CCSD(T))

Sanloup et al. (2011) studied incorporation of Ar and Xe in San Carlos olivine up to 7 GPa and 2000 K. A 1:1 correlation is observed on recovered sample analyzed by electron microprobe between Xe and Si contents with up to 1 at% of Xe whereas there is no correlation between Mg+Fe and Xe and with Ar. Furthermore *in situ* X-ray diffraction on Xe-olivine system revealed a shift in lattice parameters, especially an increase of cell parameter *a*, above Xe melting point. A new Raman mode was seen at 0.9 GPa and 1800 K, disappearing at low *T*. These three evidences were interpreted as a Xe for Si substitution at moderate *P-T* conditions in olivine, and are further investigated in section D/ of this work.

4/ Xe in silicate melts

The structure of polymerized silicate melts or glasses present similarity with local disordered crystal structure (Keen and Dove, 2000) and could be useful to better understand Xe incorporation mechanisms in minerals. Moreover understanding of Xe behavior in melts is crucial to better constrain degassing and recycling processes (more details can be found in Leroy, PhD thesis, 2016). Xe, as all heavy noble gases, is assumed to be extremely incompatible, although available experimental partition coefficients ($K_D$, eq. (1)) span 5 orders of magnitude (Table B4). Xe solubility in melts has been investigated experimentally at very low Xe partial pressure, i.e. below 1 bar (Jambon et al., 1986; Shibata et al., 1986; Lux, 1987; Caroll and Stolper, 1993). In these experiments Xe solubility does not go beyond a few tens of ppb. At high Xe partial pressure (~ 5 GPa), Schmidt and Keppler (2002) measured up to 0.8 wt% Xe in tholeiitic melt, and Leroy et al. (2018) 4.0(0.8) wt% Xe in a haplogranite hydrous melt (with 5.1 wt% $H_2O$) at 3.5 GPa. Schmidt and Keppler (2002) showed that Xe solubility increases with *P* up to 6 GPa, then reaching a plateau potentially linked with changes in the melt structure (Figure B7).

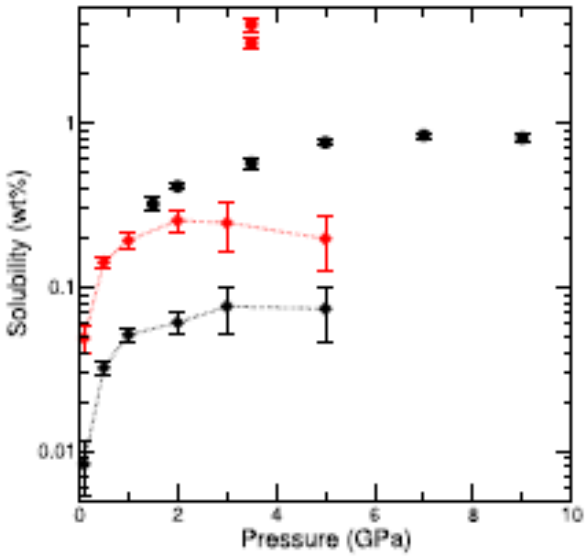


*Figure B7: Xe experimental solubilities in tholeitic melt from Schmidt and Keppler (2002) (black circles) and hydrous haplogranite melt from Leroy et al. (2018) (red circles), and theoretical calculation from Guillot and Sator (2012) for tholeiitic (black diamonds) and haplogranite melt (red diamonds). Figure from Leroy et al. (2018).*

Noble gases solubility in melts are based on *ex situ* analyses of recovered glassy samples, apart from Leroy et al. (2018), and did not directly investigate the noble gas structural environment in the silicate network, as noble gases can escape from the silicate structure at ambient conditions. These studies showed that noble gas solubility decreases with increasing radius (from He to Xe) (Caroll and Stolper, 1993; Lux, 1987; Shibata et al., 1998), and that this solubility strongly depends on the chemical composition of the melt. Noble gas solubility was first related to ionic porosity, i.e. the absolute volume of voids (Caroll and Stolper, 1993), whereas Shibata et al. (1998) showed that it was better inversely correlated to the number of non-bridging oxygen per silicon, even if the presence of Al may modify this trend (Bouhifd and Jephcoat, 2006). Based on these findings and noble gas relative chemical inertia, noble gases were supposed to passively fill the voids of the silicate network.
One recent *in situ* study evidenced bonding of Xe to O in compressed haplogranitic magmas with Xe-O = 2.05 ± 0.05 Å using *in situ* X-ray diffraction (Leroy et al., 2018). Reactivity of Xe with the silicate melt refute a simple passive filling of the voids spaces, and points out the need for more *in situ* study to understand noble gases behaviour in silicate melt. So far no similar study has been performed for other noble gases, and it remains unclear whether Xe behaviour in silicate melt is unique among noble gases.

Xe crystal/melt partition coefficients have been evaluated for a range of minerals and melt compositions. Crystal/melt partition coefficient ($K_D$) refers to the solubility ratio of an element in solid (crystal) ($C_s$) and in melt ($C_l$):

$$K_D = C_s/C_l \qquad (1)$$

Partition coefficients define the compatibility of an element, i.e. its capacity to enter the crystal's structure during crystallization from a melt. We previously mentioned that noble gases are widely used to study degassing of the mantle, based on the assumption of an 'infinite' incompatibility', although experimental values are rather scattered (Table B4).

Hiyagon and Ozima (1986) grew olivine from basaltic and harzburgitic melts (including trace elements) with a flowing noble gas mixture. Broadhurst et al. (1992) investigated anorthite, diopside, spinel, forsterite and synthetic basaltic melt with nearly Fe-free minerals. Experiments were run on minerals and synthetic glass powders: in this study minerals are not grown from the melt. These two studies observe an increasing partition coefficient with increasing atomic number. Broadhurst et al. (1992) proposed an incorporation of noble gases at point defects and at extrinsic defects but they reject similarity of incorporation mechanisms between noble gases and ionic atoms.
Brooker et al. (2003) grew clinopyroxene from a synthetic glass ($Ab_{80}Di_{20}$) enriched in trace elements. Heber et al. (2007) grew clinopyroxene from synthetic glass ($Ab_{40}Di_{60}$) enriched in trace elements and olivine from $Na_2Si_2O_5 + Mg_2SiO_4$. These two last studies used UV Laser Ablation Microprobe which can select zones without bubbles or melt inclusions in contrast to previous studies. As a result, their partition coefficients observed are lower by 3 or 4 orders of magnitude than estimates from Hiyagon and Ozima (1986) and Broadhurst et al. (1992). Brooker et al. (2003) and Heber et al. (2007) explain discrepancy by contamination from gas bubbles and melt inclusions in minerals and / or by adsorption of noble gases on powdered

samples for Broadhurst et al. (1992).

Hiyagon and Ozima (1986), and Broadhurst et al. (1992) performed experiments with Xe partial pressure below 1 bar, and Héber et al. (2007) with 54.6 bar Xe. Low Xe partial pressure explains low Xe solubility values. Indeed following Henry's law, $f_i = X_i H_i$ (where $f_i$ is the gas fugacity in the gas phase, $X_i$ the concentration at the equilibrium in the melts or minerals and $H_i$ the Henry's constant). Henry's law has been shown to work for noble gases' solubility in silicate melts at low $P$ (Lux, 1987; Jambon et al., 1986; Carroll and Stolper, 1993).

| **Mineral** | ***P* (GPa)** | ***T* (K)** | **duration** | **Xe content** | **$K_D$** | **Reference** | **Remarks** |
|---|---|---|---|---|---|---|---|
| Perovskite | 25 | 1873-2073 | 1 hour | 300 ppm | - | Shcheka and Keppler (2012) | Experiment |
| Olivine | 2 to 7 | 1573-2073 | 1-4 hours | 0- 600 ppm | - | Sanloup et al. (2011) | Experiment |
| $SiO_2$ Xe-rich phase | 0-2.14 | after quench | - | 40,000 ppm | - | Sanloup et al. (2002) | Experiment |
| Olivine | 0-1.5 | ~1573* | 1 hour - 2 days* | 0.668- 21.6ppt | <~0.3 | Hiyagon and Ozima (1986) | crystal/melt partitioning experiment |
| Anorthite | 0 | 1573 | 7-18 days | 0.088-5.3 ppb | - | Broadhurst et al. (1992) | crystal/melt partitioning (crystals are not grown from the melt) |
| Diopside | 0 | 1573 | 7-18 days | 0.11-0.43 ppb | 3.2-47 | Broadhurst et al. (1992) | crystal/melt partitioning (crystals are not grown from the melt) |
| Forsterite | 0 | 1573 | 7-18 days | 1.5-6.5 ppb | 90 | Broadhurst et al. (1992) | crystal/melt partitioning (crystals are not grown from the melt) |
| Spinel | 0 | 1573 | 7-18 days | 0.16-0.58 ppb | 0.61-1.8 | Broadhurst et al. (1992) | crystal/melt partitioning (crystals are not grown from the melt) |
| Cpx | 1-3 and 5.6-8.1 | ~1573* | ~6 hours* | - | $10^{-3}$-$10^{-4}$ | Brooker et al. (2003) | crystal/melt partitioning experiment |
| Olivine | 0.1 | ~1300* | ~10 hours* | 0.61 ppb | $6.10^{-4}$ | Heber et al. (2007) | crystal/melt partitioning experiment |
| Cpx | 0.1 | ~1300* | ~16 hours* | 0.45 ppb | $2.10^{-4}$ | Heber et al. (2007) | crystal/melt partitioning experiment |

*Table B4: Xe contents retrieved on minerals grown by experiments. *for crystal/melt partitioning experiments aiming at finding $K_D$ (see eq. (1)) there are two steps during the experiment: heating and slow cooling of ~50°C to grow crystals with variation in time duration and* T. *cpx is clinopyroxene. We emphasize that data from Sanloup et al. (2002 and 2011) are not solubility value, but highest Xe content retrieved on one point of the recovered sample.*

## III/ Prospects

Previous studies dedicated to Xe oxides, Xe solubility and incorporation in minerals emphasize the following points:

1/***In situ* data** must be privileged to evaluate Xe incorporation mechanisms as Xe would escape from the silicate network at ambient conditions due to its high volatility as witnessed for instance by Raman modes which disappear rapidly upon cooling (Sanloup et al., 2002, 2011). Analyses of recovered samples may thus be misleading: are free-bubbles area the best place to evaluate of Xe content if some Xe will degasses upon quenching ?
*In situ* X-ray diffraction (Sanloup et al., 2005, 2011; Leroy et al., 2018), Raman (Sanloup et al., 2002, 2011) or Infra-red spectroscopy, and X-ray absorption spectroscopy (Dewaele et al., 2016) at synchrotron facilities could be a way to observe Xe incorporation in minerals.

2/Xe can be incorporated in cage-like structures (e.g. clathrate, zeolite), although when short Xe-O bonds are involved (around 2 Å) Xe is often found in planar environment surrounded by oxygen atoms (e.g Xe oxides (Brock and Schrobilgen, 2011; Dewaele et al., 2016), fibrous silica (Kalinowski et al., 2014)) or in oxygen hexahedra (Britvin et al., 2015, 2016). Thus is there a **preferential environment** for Xe?
Is Xe incorporated via nanobubbles, or at extrinsic or intrinsic defects?
Is the incorporation of Xe in mineral structure relevant at the Earth's scale?
Can Xe incorporation in minerals generate Xe isotopic fractionation?

3/The **influence of *P* and *T*** on Xe incorporation in minerals is poorly constrained whereas a significant effect of *P* is observed for Xe solubility in melts (Schmidt and Keppler, 2002). Moreover Xe incorporation appears above Xe melting curve for olivine (Sanloup et al., 2011): is it systematic for all minerals?

4/The **oxidation state** of Xe:
Brooker et al. (2003) assumed that noble gases are incorporated in minerals similarly to other (isoelectronic) cations based on theoretical calculations using atomic radii from Zhang and Xu (1995). They conclude that noble gases behave as neutral cations, we should however keep in mind that atomic radius from Zhang and Xu (1995) are coming from the same assumption, e.g. noble gases are considered as neutral ions. However oxidation state of Xe does vary in the following Xe compounds, all involving Xe-O bond lengths ranging from 1.7 Å to 2.2 Å (at ambient *P*): + 4 in $XeO_4$ (Selig et al., 1964; Gundersen et al., 1970) and in $XeO_2$ (Brock and Schrobilgen, 2011), + 4 in fibrous silica (Kalinowski et al., 2014), and + 6 or + 8 in Xe-perovskite (Britvin et al., 2015, 2016). Additionally, Xe may participate to **redox reactions** as implied by Seoung et al. (2014).

## Chapter C: EXPERIMENTAL METHODS

During this PhD thesis, a variety of experimental methods was used to generate high *P-T* conditions (piston cylinder press, diamond anvil cell and Paris Edinburgh Press). Heavy noble gases incorporation was investigated with a range of techniques including X-ray absorption spectroscopy, X-ray diffraction and Infrared spectroscopies using synchrotron beam. Recovered samples were analyzed by scanning electron microscopy, transmission electron microscopy, electron microprobe, and Raman spectroscopy.
*Ab initio* calculations were performed in the framework of the density functional theory, to help interpreting our experimental findings.

### I/ High *P-T* generation

Piston cylinder press was used to dope silicate with noble gases under high *P-T* conditions. In our work new synthesized samples, as well as samples obtained from the previous study of Alexander Griffith, Master student supervised by Chrystèle Sanloup, are presented (noted as 'previous' in experimental tables). To perform *in situ* studies diamond anvil cells and Paris Edinburgh press were used at synchrotron sources.

#### 1/ Piston cylinder press and gas loading devices

The piston cylinder press is a solid medium apparatus used to compress large volume samples (> 1 $mm^3$), it can generally reach *P* up to 5 GPa and *T* close to 2000°C (Figures C1, C2). A comprehensive historical evolution of piston cylinder devices can be found in Hall (1980). Sir Charles Parsons developed the first piston cylinder type apparatus motivated by the disappointed aim of diamond synthesis (1880-1928). Further development by Coes (1962) was marked by the synthesis of coesite (the high *P* polymorph of silica). Piston cylinder presses are now routinely used in Earth's sciences and are nearly fully described by Boyd and England (1960).
The piston cylinder press is based on a Bridgman-type system: a piston slides into an end-loaded cylinder (both generally made of Tungsten Carbide (WC)). The upper plate remains fixed whereas a hydraulic ram applies strength on the bottom plate due to injection of pressurized oil into a chamber: *P* is generated through compression of the sample. Resistive-heating is achieved through a graphite furnace which enables to get high and rather homogeneous *T* through the whole capsule. *T* is read with a thermocouple placed near the top of the capsule.

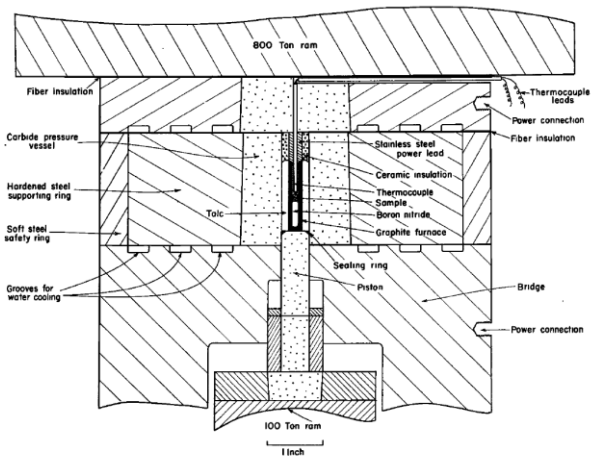


*Figure C1: Piston cylinder scheme from Boyd and England (1960).*

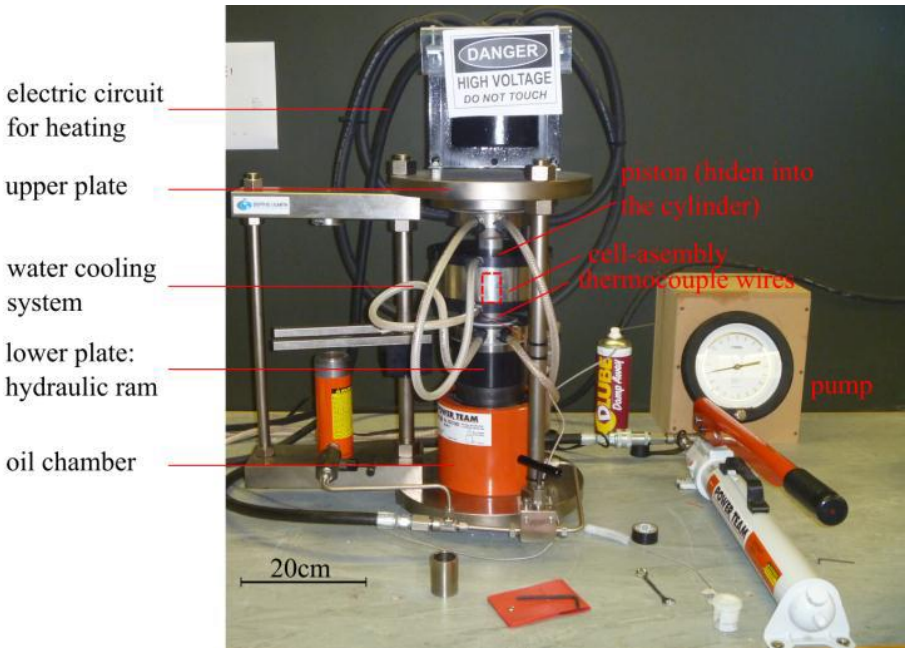


*Figure C2: Photo of the piston cylinder press used in our experiments, basic set-up.*

Noble gases (Xe, and 1:1 (atomic and volume) Xe/Kr, and Xe/Ar gaseous mixes) were loaded with a special device, firstly described by Boettcher et al. (1989) and used in some previous experimental studies on incorporation of Xe in silicate melts (Montana et al., 1993; Schmidt and Keppler, 2002) and minerals (Sanloup et al., 2005 and 2011). This device makes possible to load gases in one-end welded capsule partially filled with packed material avoiding air contamination. The capsule (D) (Figure C3) is inserted in E with the welded-end at the bottom before inserting B and tightly screwing A at the top to seal the open-end of the capsule into C. The capsule is then connected to the vacuum before connection to the bottle of pressurized gases. Eventually E is removed. The capsule and B are placed on a vise and the capsule is crimped. At this point, connection with the bottle of pressurized gases is cut. The capsule is then cut along the top edge and welded shut.

Xe content was measured by weighing the capsule before and after loading. Recovered capsules after piston cylinder runs were weighed before and after being pierced. Weight measurements are however only approximate, and must be considered with caution. Gas-loading process remains difficult, with a success rate of ~ 30%.

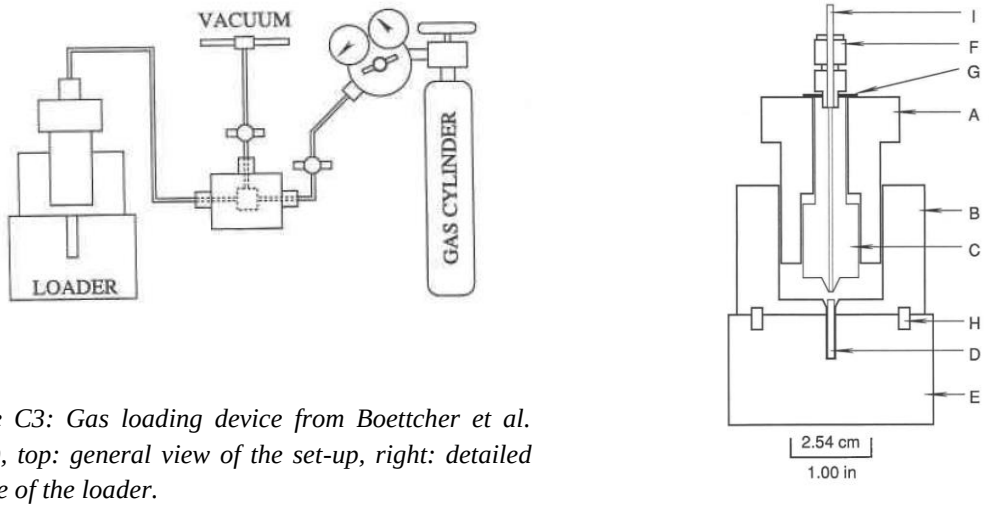


*Figure C3: Gas loading device from Boettcher et al. (1989), top: general view of the set-up, right: detailed scheme of the loader.*

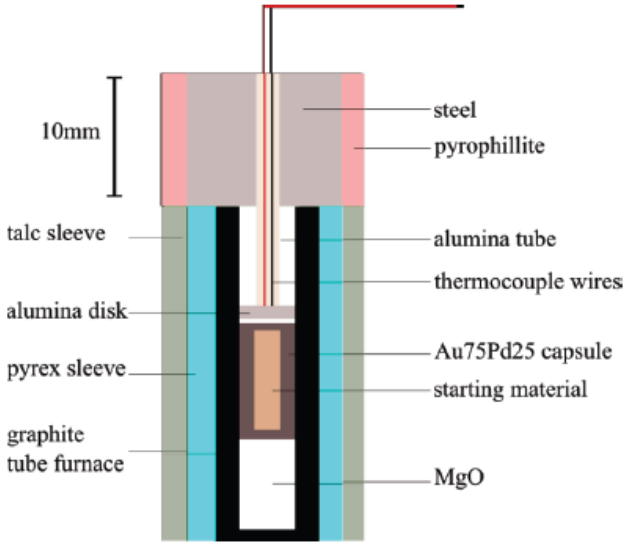


*Figure C4: Scheme of the cell assembly (in our case there are two capsules of Pt separated by an alumina disk).*

Syntheses were done on an end-loaded piston cylinder at the IMPMC. We use a ½ inch cell-assembly (Figure C4) composed of a graphite heater surrounded by pyrex and talc sleeves, with either one or two Pt capsules (3 mm outer diameter, 2.7 mm inner diameter, 5 mm height), with or without gas, separated by an alumina disk (Figure C4). MgO was disposed around the capsule(s) to act as a pressure transmitter. *T* was controlled using a type C thermocouple ($W_{74}Re_{26}$-$W_{95}Re_5$). Bottom-welded and deformed Pt capsules were filled up to one third height with material powder for gas enriched capsules, and up to half height for the gas free capsules. Capsules are then deformed into 'perfect' cylinders to support increase of *P* without opening. When two capsules are run at the same time, graphite furnace can

undergo important deformation due to the fact that Pt capsules and $Al_2O_3$ disks have a very different resistance to deformation stress. If a capsule happens to be shorter than 5 mm after deformation, we fill the space with MgO rods.
*P* was increased slowly before increasing *T* at around 100°C/min. Experiments were run for different duration and terminated by quenching i.e. by turning off the power of the furnace, which implies dropping *T* instantaneously, before slow decompression (to avoid breaking of the capsule).
In recovered samples, Pt inclusions are often observed, either as melt or as crystals indicating that micrometric portions of the capsule are dissolving and melting in the sample. They are generally associated with metallic elements present in the starting material, as discussed for Fe (see D/II/1)

2/ Diamond anvil cell (DAC)

DAC is a high-*P* device making use of the diamond's hardness and of its transparency to X-rays (C being a light element). DACs appeared in 1950 but were developed as a common high-*P* tool in 1960-1980 (Mao and Bell, 1978). Present overview is inspired from Besson (1997).
DAC is composed of two opposed diamond anvils. Each diamond table (i.e. the large flat end) is resting on a hard seat (generally made of tungsten carbide). The other tip of each diamond anvil is a small and flat culet. In-between these two small culets a metal gasket is inserted (Figure C5). The gasket, previously indented is pierced to enclose the sample. *P* increase is done by forcing the two small diamond culets toward each other (the smaller are the culets, the higher is the pressure reached). To increase *P* there is a variety of design that will not be detailed here (an example is given in figure C6). To optimize X-ray diffraction patterns, large opening is needed, therefore we used symmetric large-opening DACs (70°) equipped with Boelher-Almax seats (Boehler et al., 2004). DAC can commonly reach 100 GPa and may be pushed to above 500 GPa with a record of 1 TPa (Dubrovinskaia et al., 2016). To ensure hydrostatic and homogeneous *P* conditions a pressure media is often added around the sample[10]. *P* at ambient *T* is measured by ruby ($Al_2O_3$: $Cr^{3+}$) fluorescence. Cr ions are excited via laser emission. Excited ions further relax via an electronic transition accompanied by a fluorescence emission. Fluorescence emissions are the R1 and R2 ruby lines. With increasing *P*, R1 and R2 lines are shifted toward lower energies.

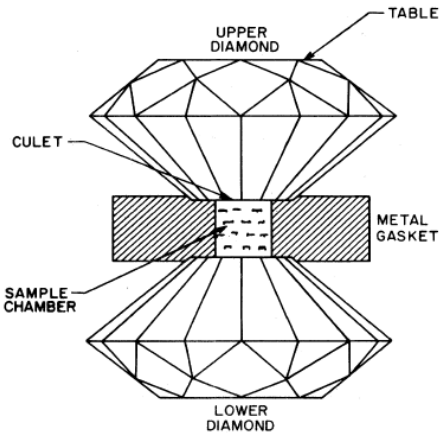


*Figure C5: Schematic view of the main DAC part. Figure from Jarayaman (1983).*

[10] We did not use it in our experiments because we used resistive-heating DACs: homogeneous high *T* diminishes stress and increase hydrostaticity.

This shift has been calibrated (Syassen, 2008) and ruby fluorescence is nowadays commonly used to determine *P* in DAC.

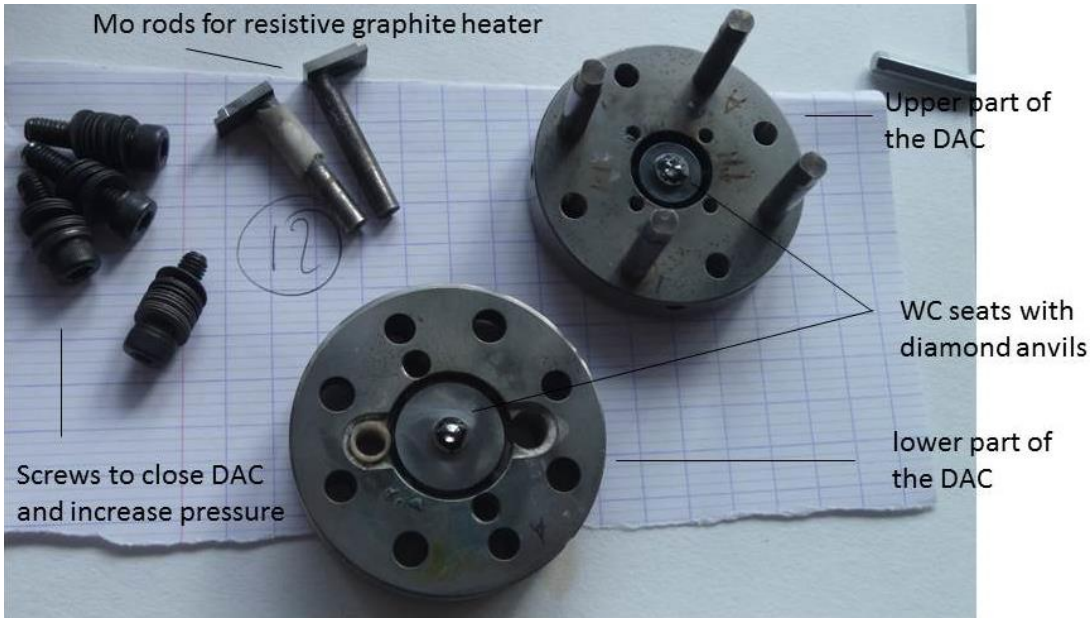


*Figure C6: Example of DAC from P02.2 team, DESY, Hamburg. Design with two symmetric parts, each having a WC seat with a diamond anvil.* P *is increased by closing the cell and screwing the two parts toward each other.*

There are three ways of reaching high *T* in DAC:

1- via an external furnace, i.e. by heating the whole cell. *T* can reach up to 570 K.

2- via an internal heater, i.e. a resistive heater surrounding the diamonds. *T* can reach up to 1700 K under vacuum.

3- via laser heating (YAG or $CO_2$ lasers). *T* can reach up to 5000 K.

The two first methods make it possible to heat homogeneously the whole sample, however they present the inconvenient to oxidize diamonds and seats (oxidization of diamonds starts at 900 K in the air). To reach higher *T* only laser heating can be used, although it implies small heating spots with large *P*-*T* gradients and tricky evaluation of *T*. We will detail here the two types of resistive heaters that we used.

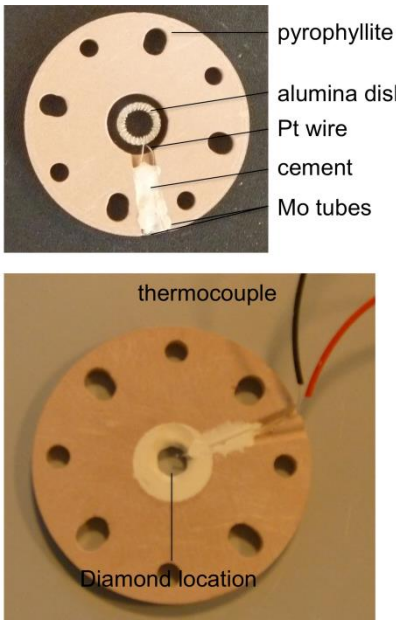


*Figure C7: Heater during fabrication. Top: Pt-wire before recovering by cement, bottom: thermocouple location is shown. Pyrophillite element is 5 cm diameter.*

**Pt-wire heater** has been designed by Y. Fei (Geophysical Lab) and adapted to symmetric cell by C. Sanloup. Resistive-heating is achieved through a Pt wire surrounding the diamond anvils. Pt wire is coiled around an alumina ring (Figure C7, top) and connected to Mo tubes. All pieces are covered by heat-proof cement within a piece of pyrophyllite (insulator). Two Mo needles, connected to high current are inserted into the heater's Mo tubes to supply power to Pt-wire. H/Ar flux prevents rapid oxidation of Mo pieces (Figure C9). *T* is recorded by a K-type thermocouple (Ni+Cr/Ni+Al+Si) placed on the very edge of the gasket indent as close to the sample chamber as possible (Figure C7, bottom). Error is estimated about ± 50 K (De Grouchy et al., 2017). In addition to this internal heater, an external heater may be used to heat the whole cell up to 250°C.

**Graphite heater** was used during experiments at P02.02 (high-*P* X-ray diffraction beamline at Petra III, Hambourg, Germany, Lierman et al. (2009)). Two Mo rods supply power to graphite pieces disposed under and above the gasket (Figure C8). Graphite pieces are cut in the centre so that diamond culets and indentation of the gasket remain uncovered by graphite. An alumina piece is disposed around the diamond anvil on each seat and covered, as well as the seats by heat-proof cement to avoid electrical short-cuts. *T* is recorded by two R-type thermocouples (Pt+Rh/Pt) localized on the diamond facets of each anvil. Error is estimated to ± 60 K (Lierman et al., 2009). The whole set-up is inserted in a vacuum vessel, which prevents oxidation of Mo rods, WC seats and diamonds (Figure C10).

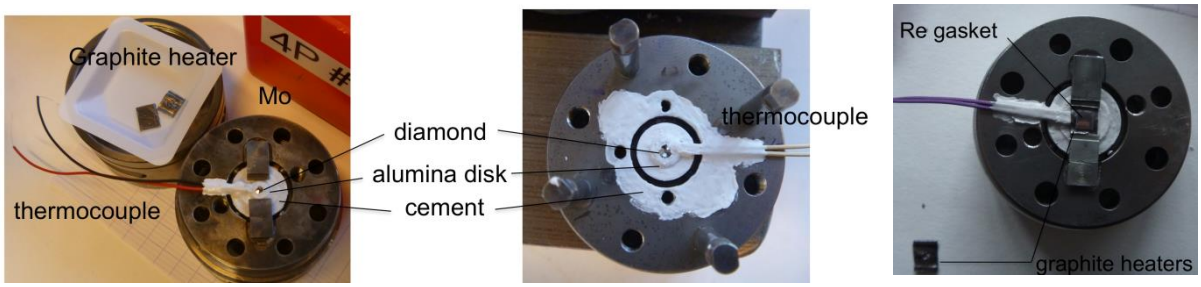


*Figure C8: Graphite heater during fabrication. Centre: heat-proof cement covers directly the seat, right: thermocouples, and graphite pieces surrounding the Re gasket.*

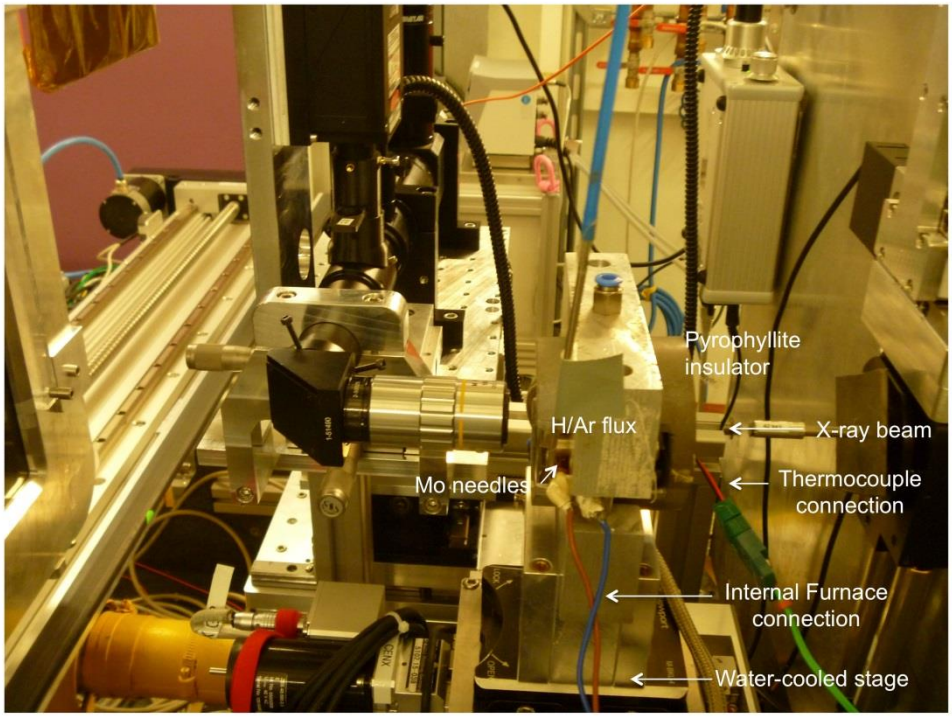


*Figure C9: Experimental set-up on P02.2 (beamline at DESY, Petra III, Hambourg, Germany) for Pt-wire heated DAC. DAC is surrounded by an external heater, itself surrounded by a pyrophyllite holder. Maximal $T$ is 1300 K.*

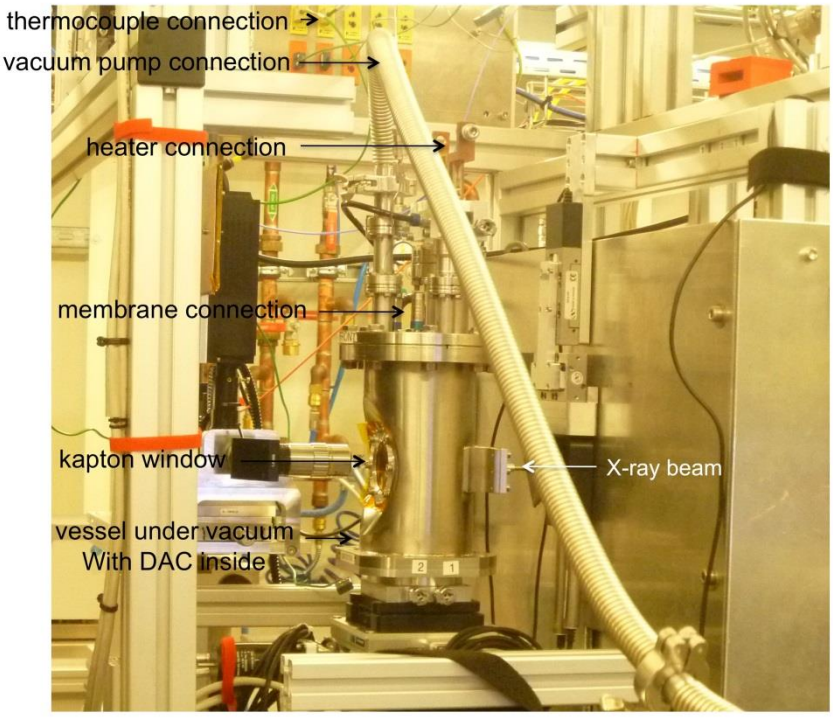


*Figure C10: Experimental set-up on P02.2 (beamline at DESY, Petra III, Hambourg, Germany) for graphite heater. DAC is disposed inside a vacuum vessel to prevent oxidation of Mo rods, WC seats and diamonds. Maximal $T$ is 1700 K.*

3/ Paris Edinburgh press (PEP)

PEP (Figure C11) has been developed in 1992 (Besson et al., 1992) to initially carry out *in situ* neutron measurements at high *P-T* conditions. It was next adapted for X-ray measurements. It is a small solid medium apparatus, which can reach quasi-hydrostatic *P* up to 17 GPa (at HT, Morard et al., 2011) and 3000 K with WC anvils. PEP allows large volume samples (> 1 $mm^3$) like multi-anvil presses (MAP). But in contrast to MAP, it has a very large X-ray/neutron access to the sample which makes angle-dispersive diffraction possible: 60° horizontally and 15° vertically can be investigated (Morard, 2006). PEP has also a smaller size and weight (50 kg) and is easily removable. It can easily be moved on *x*, *y*, *z* axes in order to align the sample with the X-rays. This press is based on the injection of pressurized oil into a chamber that acts on a piston. A Bridgman system is used. A 10 bar oil *P* generates strength of one ton (Morard, 2006). Strength acts on a bottom toroidal WC anvil which faces a similar upper anvil, fixed with a nut. Between anvils there is the gasket with the cell-assembly. A graphite resistive furnace is used to reach homogenous and high *T* (up to 2600 K) via connection to high current.


*Figure C11: Experimental set-up with PEP on beamline BM23, ESRF (European Synchrotron Radiation Facilities). Black cables are furnace connections and grey transparent tube is water cooling system. On the left side: MAR image plate (area detector to record X-ray diffraction pattern).*

4/ *P-T* calibration

*T* can be evaluated either by the use of a thermocouple or by using available power/*T* calibrations (for PEP (Kono et al., 2014) and for RH-DAC (de Grouchy, PhD thesis, 2016)). At high *P-T* conditions for DAC and PEP, *P* is generally determined by the use of internal calibrants: in our case either a Pt grain added at the border of the sample chamber in DACs, or

hBN (and possibly Pt) from the cell assembly in PEP. Equations of state of these calibrants are well-known (Fei et al. (2004) for Pt and Le Godec et al. (2000) for hBN). Cross calibrations can be used to determine both *P* and *T* if two internal calibrants are present.

## II/ *In situ* synchrotron-based probes at high *P-T* conditions

### 1/ Synchrotron source

*In situ* experiments were performed at synchrotron sources during five beamtimes: indeed a highly focused and highly brilliant beam was needed to obtain high-quality X-ray diffraction, X-ray absorption, and Infrared data, on small samples under extreme conditions.
For X-ray absorption spectroscopy at the Kr and Xe *K*-edges (14.3 keV and 34.6 keV respectively) a high energy, high brilliance X-ray beam was needed in combination with a scanning in energy and a high beam stability due to long data-collection. Experiments were performed at beamline BM23 (a bending magnet beamline) at the ESRF, Grenoble, France.
For X-ray diffraction, experiments were performed at beamline P02.2 (an undulator beamline) at PETRA III, Hamburg, Germany and at beamline I15 (a wiggler beamline) at Diamond Light Source, Oxfordshire, United Kingdom.
For Infrared spectroscopy, experiments were performed on SMIS beamline (edge and bending magnet beamline) at SOLEIL Synchrotron, Gif-sur-Yvette, France.

Synchrotron beam is obtained through injection in a storage ring of electrons at near light speed. These electrons are accelerated in a magnetic field in curved sections by bending magnets or in straight sections via arrays of magnets called insertion devices. A broad X-ray spectrum is created. X-rays are emitted in the direction of the electron beam and are polarised in the plane of the ring. Quality of synchrotron beam is defined by **the brilliance** (in photon/s/mrad²/mm²/0.1%BW), which is the intensity (photon per second) divided by the angular divergence (mrad²), the beam size (mm²) and the spectra distribution (the bandwidth expressed in 0.1%). Insertion devices, wigglers and undulators, impose beam brilliance. Use of wigglers, magnets of opposite polarity in a row making electrons wiggling back and forth, multiply brilliance by two, whereas undulators, magnets of opposite polarity create small deflection inducing constructive interference between electrons, multiply brilliance by four[11].
In addition to brilliance, stability of the beam is also a crucial parameter.
Three generations of synchrotron source are generally defined. The first generation made use of a storage ring initially built for particle physics purposes. The second generation was initially built to produce X-rays. The third generation implemented insertion devices.

In a synchrotron source there are various beamlines (49 at the ESRF for instance), depending on their location, they use X-rays created by bending magnets or insertion devices. Each beamline is dedicated to specific techniques and experiments.
On a beamline, optical devices focus the beam via slits and mirrors in the optical hutch. The desired energy is selected using a monochromator based on Bragg's law. Tuned beam is then

[11] Which is not always better if samples are sensitive to high energy beam.

delivered in the experimental hutch, where various techniques depending on the user needs are available. Example of a XAS beamline BM23 (ESRF) is shown in figure C12.

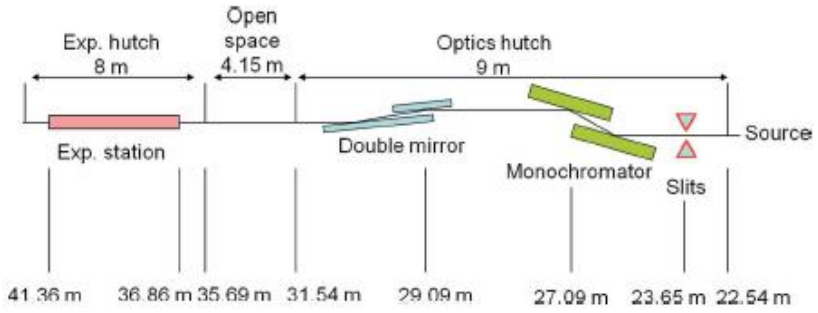


*Figure C12: Layout of BM23, figure from Mathon et al. (2015).*

2/ X-ray absorption spectroscopy (XAS)

Presentation of XAS theory is based on Newville (2004), Calvin (2013) and presentation of Sakura Pascarelli (ESRF user meeting, 2016). XAS consists in bombarding a sample with X-rays of fixed energy $E$ and measuring absorption coefficient of the sample $\mu(E)$. Energy range surrounds the required energy to excite electrons of the investigated atom. The 'edge' qualifies the steep increase in absorption which occurs at this energy, due to electron excitation. Electron of different orbitals can be excited: *K*-edge corresponds to excitation of electrons from the 1st orbital, *L*-edge from the 2nd orbital and *M*-edge from the 3rd orbital.

When X-rays enter the region occupied by an atom several cases can happen: no interaction, an absorption, a scattering, or a photoelectron ejection. According to quantum mechanics, when a system is disturbed, a superposition of possible states exists at the same time. Following Fermi's Golden Rule the probability of each possibility depends on the similarity between the related final state and the initial state (the more similar the more probable). In our case **the likeliest state is when a photoelectron ejected from the absorbing atom is scattered off by a nearby atom and then returns to the original atom from which it has been ejected**. Extended X-ray absorption spectroscopy is **linked to the interference of a photoelectron with itself** (Figure C13). If a nearby atom is located at $R$ from the absorbing atom, there will be constructive interference if

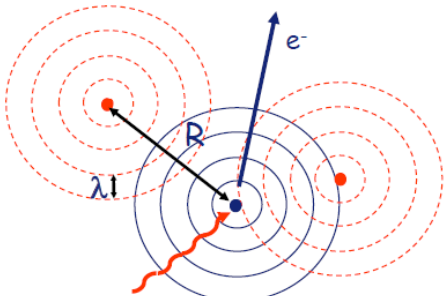


*Figure C13: (from S. Pascarelli, presentation at the ESRF user meeting, 2016). Interference of a photoelectron with itself by backscattering from a neighbour atom.*

$$2R = n\lambda \qquad (2)$$

With $n$, an integer.

Interference, destructive and constructive, of the outgoing and backscattered waves of the ejected and

scattered photoelectron results in a sinusoidal variation of $\mu(E)$. The EXAFS fine structure function $\chi(E)$ is defined as follow:

$$\chi(E) = \frac{\mu(E)-\mu_0(E)}{\Delta\mu_0(E)} \quad (3)$$

It is the normalized variation of absorption coefficient subtracted of a "background" function $\mu_0(E)$ representing the absorption of an atom embedded in the electronic environment of the condensed system but without backscattering from near neighbors. The EXAFS equation (6) is generally expressed as a function of the wavenumber *k*:

$$k = \frac{2\pi}{\lambda} = \frac{p}{\hbar} = \sqrt{\frac{2m(E-E_0)}{\hbar^2}} \quad (4)$$

using non relativistic approximation for a wave in a solid matter with $p$ the momentum of the photoelectron and *m* the mass of the electron. The photoelectron, is described as a spherical wave function $(k, r)$ :

$$\varphi(k,r) = \frac{e^{ikr}}{kr} \quad (5)$$

The wave will travel a distance *R* to the nearby atom and then travel back a distance *R* to the absorbing original atom. We need to take into account the probability of elastic scattering of one atom in the good direction to go back to the absorbing atom, this probability, function of the atom and of $k$ is noted $fa(k)$. Indeed scattering in other direction or inelastic scattering could occur for instance. There is also a shift in the phase *δa(k)*, induced by the scattering atom. Amplitude $fa(k)$ and phase shift *δa(k)* depend on the atomic number and make it possible to determine the nature of nearby atoms. We can write the EXAFS equation, describing the amplitude of the variation of the absorption coefficient at the scattering atom as follows:

$$\chi(k) \sim \frac{e^{ikR}}{kR} fa(k) e^{i\delta a(k)} \frac{e^{ikR}}{kR} \quad (6)$$

There is the outgoing spherical wave and the backscattered wave, both described by a spherical wave function, which are multiplied by the probability of backscattering occurrence $fa(k)$, and the potential phase shift *δa(k)*.

We keep the real part:

$$\chi(k) \sim \frac{fa(k)}{k^2R^2} \cos(2kR + \delta a(k)) \quad (7)$$

That can be rewritten more conventionally as:

$$\chi(k) \sim \frac{f(k)}{kR^2} \sin(2kR + \delta(k)) \quad (8)$$

With $f(k) = kfa(k)$ and $\delta(k) = \delta a(k) + \frac{\pi}{2}$

In our treatment, we focus on a pair of absorber-scatterer. However for an absorber there may be a sum of possibilities related to each nearby atom of different species and distance to the absorber:

$$\chi(k) \sim \sum_i \frac{f_i(k)}{kR_i^2} \sin(2kR_i + \delta_i(k)) \quad (9)$$

There might also be a degeneracy $N_i$ for a given atom species at a given distance from the absorber:

$$\chi(k) \sim \sum_i N_i \frac{f_i(k)}{kR_i^2} \sin(2kR_i + \delta_i(k)) \quad (10)$$

Eventually, there is an effect due to the core-hole lifetime (around $10^{-15}$ s). Indeed the farther the scattering atom the less probable it is to find a hole when the photoelectron is coming back due to filling from an electron of a higher orbital (resulting in fluorescence or ejection of another electron). $\lambda(k)$ is called the mean free path of the photoelectron. It ensures that EXAFS is a local phenomenon (nothing is seen beyond 10 Å).

$$\chi(k) \sim \sum_i N_i \frac{f_i(k)}{kR_i^2} e^{\frac{-2R_i}{\lambda(k)}} \sin(2kR_i + \delta_i(k)) \quad (11)$$

There is an incomplete overlap between final and initial states due to rearrangement of the orbitals. This incomplete overlap is called the amplitude reduction factor, generally noted $S_0^2$, and is ranging between 0.7 and 1.0. This is an empirical factor.

$$\chi(k) \sim S_0^2 \sum_i N_i \frac{f_i(k)}{kR_i^2} e^{\frac{-2R_i}{\lambda(k)}} \sin(2kR_i + \delta_i(k)) \quad (12)$$

The EXAFS function is an average over millions of atoms. Therefore there might be some variation regarding scatterer-absorber distances due to thermal disorder (vibration of chemical bonds at frequency of $10^{13}$ Hz at room *T*) as well as static disorder linked to difference in local environment due to defects of the crystals or amorphous state. $\sigma_i^2$ is the variance of $R_i$ due to static and thermal disorder.

$$\chi(k) = S_0^2 \sum_i N_i \frac{f_i(k)}{kR_i^2} e^{\frac{-2R_i}{\lambda(k)}} e^{-2k^2\sigma_i^2} \sin(2kR_i + \delta_i(k)) \quad (13)$$

Eq. (13) is generally referred as the EXAFS equation.

For data treatment, we take the example of data obtained in the course of beamtime ES442 at BM23, ESRF. Data were obtained in transmission mode, at 500°C and 2 GPa on a Xe/Kr-bearing glass (~ 0.51 wt% Kr). With this example we will go through the entire XAS data processing, using ATHENA and ARTEMIS packages based on the IFEFFIT program (Ravel and Newville, 2005).

*XAS data acquisition*

X-ray absorption can be measured in transmission, in fluorescence mode or by electron yield measurement. Fluorescence measurement is more sensitive and is generally used when the jump of the absorption coefficient at the edge is less than 0.1 which can be the case for thin or diluted sample. The jump at the edge at a given energy E depends on the concentration of the investigated element, the density of the sample ($\rho$), the atomic number Z, the atomic mass A, and the thickness of the sample.

**In transmission mode**: intensity is measured before and after the sample (Figure C14). $\mu(E)$ is related to the incident $I_0$ and to the transmitted intensity $I$ by the Beer Lambert's law :

$$I = I_0 \exp(-\mu(E)L) \text{ i.e. } \mu(E)L = \ln\left(\frac{I_0}{I}\right) \quad (14)$$

with $L$ the thickness of the sample. Jump at the edge can be calculated as:

$$\mu(E)L = \rho\sigma_a(E)\frac{Na}{M} \quad (15)$$

With $\sigma_a(E)$ the atomic cross section of Xe, varying with energy, $\rho$ the density of the sample, $Na$ the Avogadro number and $M$ the atomic mass of investigated atoms:

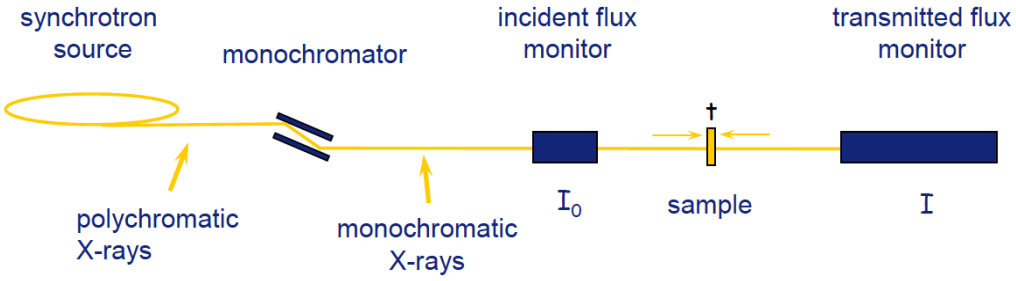


*Figure C14: XAS measurement at the synchrotron in transmission mode. (from S. Pascarelli, presentation at the ESRF user meeting, 2016).*

**In fluorescence mode**, when an atom absorbs an X-ray, a vacancy is created at the core level, which is then filled by an electron from an orbital of higher level accompanied by emission of photon X-ray of lower energy. These lower energies X-rays are released in random directions. A detector located perpendicularly to the beam can record some of them and discriminate emission linked to the investigated atom. However the exact relation between fluorescent intensity $I_F$ and absorption coefficient $\mu(E)$ is not known:

$$\mu(E) \sim I_F/I_0 \quad (16)$$

By **electron yield measurement** (for low Z elements generally), similarly as for fluorescence mode, the created vacancy is filled by an electron from an orbital of higher level. Instead of emitting a photon this process can be accompanied by emission of a high-energy electron (an Auger electron), which can be detected and counted.

*XAS data*

Different features are seen in a XAS spectrum (Figure C15). First of all there is a constant decay of the absorption toward high energy as the probability of absorption of photons by atoms decreases as the energy of the photons increase. Features just before the edge are the X-ray absorption near-edge structure (XANES), this part is characterized by multiple scattering, and cannot be modelled by the EXAFS equation (eq. (13)). XANES part is function of oxidation state as well as environment of the atom and is often used to identify minerals by fingerprinting. At slightly higher energies, the EXAFS: extended X-ray absorption fine structure, composed of gradual oscillations above the edge, which will be modelled by eq. (13).
In data presented in figure C15, oscillations are rather weak and no signal is detected beyond 6.5 $Å^{-1}$: this is due to the fact that our sample is very diluted, and that we study a glass (configurational disorder), at high *T* (thermal vibration). Particularity of XAS on glasses and melts has been reviewed recently in Wilke (2017).

*Data processing (Figure C15: each panel corresponds to a step below except for steps 2 and 3 which are gathered in one panel).*

1- Absorption coefficient is extracted as *ln(I0/I)* for transmission measurements, and as *I*/*I0* for fluorescence (with I the sum of the intensity recorded on the detectors of the fluorescence detector).
2- Correction of pre-edge and post-edge to normalize each EXAFS spectrum to the absorption edge height, the intensity of the jump is normalized to one. Position of the edge is determined by the position of the first derivative of the absorption coefficient.
3- Normalized spectra are merged (5 spectra of 2 s or 4 s).
4- Merged data are corrected using a background function representing the absorption of an atom embedded in the electronic environment of the condensed system but without backscattering from near neighbours. We use an automated background subtraction method (AUTOBKG) developed by Newville (Newville, 2001) and implemented in the ATHENA software. This method minimizes the *R*-space features at distance that are well below the first atom-atom contact distance. We fix $R_{bkg}$ at 1.2 Å in our data treatment. The background needs to pass through all visible oscillations. What happens at energy very close from the edge is not crucial as this signal will not be taken into account as this is the XANES part.

5- By subtraction of the background we obtain the EXAFS function, generally *k* weighted (i.e. multiplied by $k^n$).

6- By taking the Fourier transform of the EXAFS function on a limited *k*-range, which excludes very low wave number (below ~ 2 $Å^{-1}$) related to XANES contribution and high wavenumber related to very noisy oscillations (in our case we choose 2.3-6.5 $Å^{-1}$), we obtain a function in *R*-space, which is referred as the magnitude of the Fourier Transform. **This function is not a radial distribution function**, indeed peaks are not at the right distance, do not have the right intensity and neither the right shape.

7- If we perform a backward-Fourier transform of the obtained Fourier Transform, in a limited *R*-range, excluding oscillations linked to noise contributions (in our case 1.0-3.8 Å), we obtain again *a new EXAFS function*, comparable to the one obtained in 4, although any contribution from noisy oscillation or from XANES features has been removed. This is this backward Fourier Transform that will be fitted in ARTEMIS.

For steps 5 and 6 we use a Hanning window function with a *dk* (or *dR*) of 1.

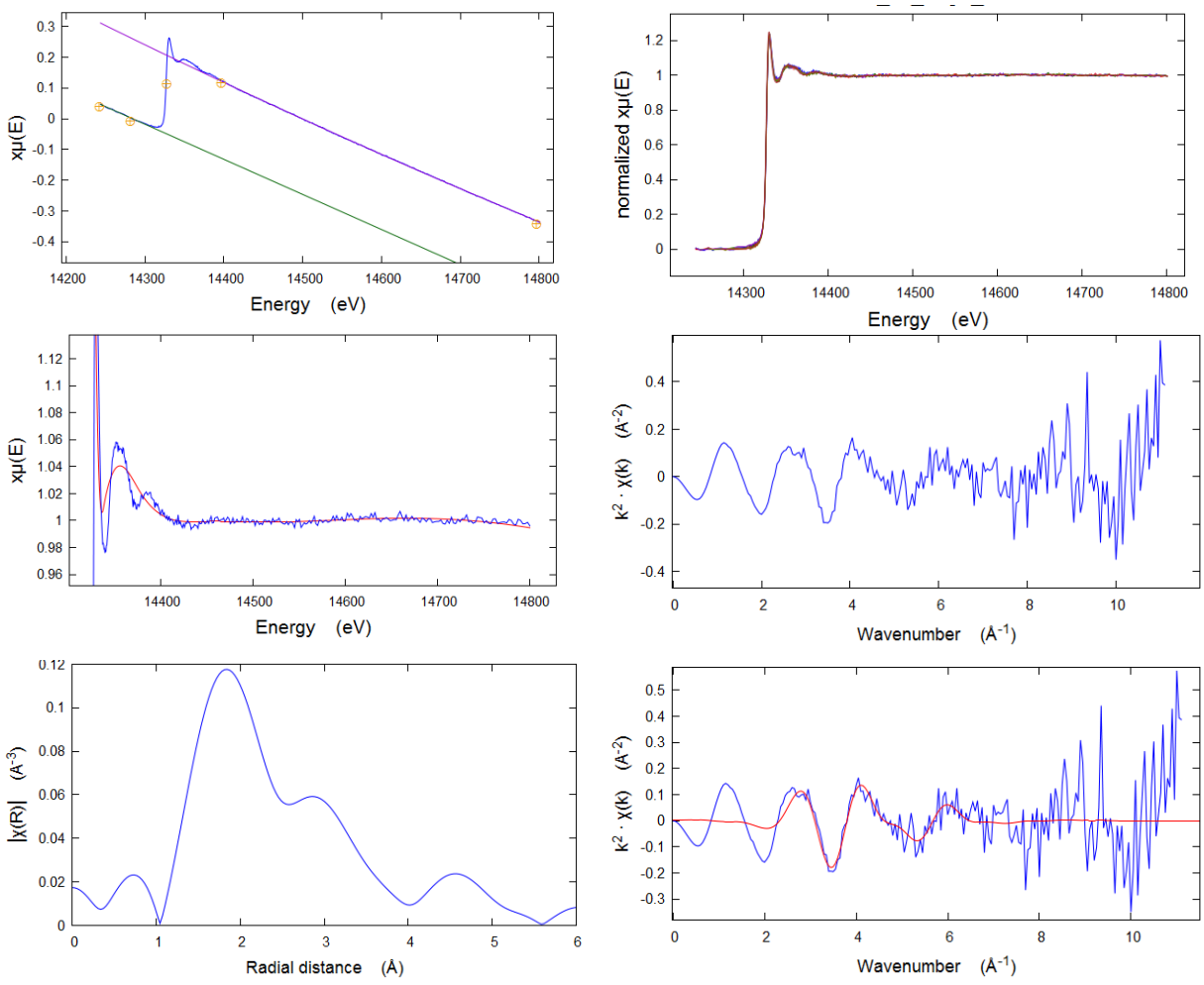


*Figure C15: The different steps of data processing with ATHENA software: from top to bottom and left to right: raw data with correction of pre and post-edge, normalized scans to be merged, background in red,* k²*-weighted EXAFS function, the magnitude of the Fourier transform,* k²*-weighted backward Fourier transform (in red) compared to the previous obtained EXAFS function (in blue). XAS data have been acquired at the Kr* K*-edge (14326 eV), at ambient conditions, on a Xe/Kr-bearing feldspathic glass with 0.52 wt% Kr (PC69, G/II).*

*Fitting of the data*

The backward Fourier transform is then exported to ARTEMIS package and fit to the EXAFS equation (Newville, 2001). A standard model of the crystal or atomic environment is entered to simulate potential paths of a photoelectron contributing to the EXAFS signal. In our case we generate a krypton atom inside a cube of oxygen atoms located at a given distance of the Kr central atom. Indeed in a glass, long-range structure order is not expected and complex paths are unlikely, in contrast to crystal. The program calculates the probability and the phase shift ($fa(k)$ and $\delta a(k)$) associated to a path. Following this step, a number of potential paths are selected. Fit parameters include: the empirical amplitude reduction factor, average distance to the central atom, the Debye Waller factor $\sigma^2$, the difference between the initial energy of the edge and the fitted value, and the coordination number. Furthermore, in case of anharmonicity, which is an asymmetry of the signal due to disorder (caused by glassy or molten state, high *P-T* conditions) the third order anharmonic cumulant expansion (Stern et al., 1991; Farges et al., 1994) is needed to partially compensate this disorder.
Finally, the number of parameters $N$, which can be fit from an EXAFS spectrum can be determined as the number of independent parameters available from a periodic signal (Teo, 1986):

$$N \approx \frac{2\Delta k \Delta R}{\pi} \quad (17)$$

with $\Delta k$and $\Delta R$ the usable *k* and *R* range.

3/X-ray diffraction on crystalline material

Here the principles of X-ray diffraction on crystalline material are briefly presented before focusing on powder X-ray diffraction and its treatment (Rietveld refinement). This overview of a more than 100 year-old technique is based on review by Lavina et al. (2014) and the work of Hunter and Howard (1998) for Rietveld refinement.

X-ray diffraction is an elastic (Thomson) scattering method i.e. incident and diffracted X-rays have the same wavelength comprised between 0.1 nm and 10 nm for X-rays. X-rays are scattered by electrons implying that scattering power of an atom is function of its atomic number (atomic scattering factors can be found in Brown et al., 2006b). Interference between scattered waves coming from the electronic cloud explains why scattered intensity decreases at large angle. Distribution of the electrons is supposed to be spherical around the nucleus, although thermal vibrations as well as static disorder (substitution on an atomic site for instance) can affect this distribution.

X-rays are diffracted if there is a periodicity in the electron distribution, i.e. the material is ordered enough. Furthermore, the periodic structure needs to have a length comparable to X-ray wavelength, which is normally the case for lattice parameters of a crystal. Diffraction phenomenon can be described within the Bragg's representation, which

defines diffraction as the reflection of X-rays by a family of crystallographic planes noted (hkl), separated from each other by a distance $d_{hkl}$. $d_{hkl}$ can be calculated for each family of crystallographic plane in a given crystallographic system. X-rays are reflected by a family of crystallographic planes if their wavelength $\lambda$ and the angle $\theta$ of the incident beam respond to Bragg's law (Bragg, 1913):

$$n\lambda = 2d_{hkl}sin(\theta) \quad (18)$$

where $n$ is an integer. Bragg's law is represented in figure C16. Diffraction from a family of crystallographic planes (hkl) is only possible if $\lambda$ is close to $d_{hkl}$. By combining the Braggs law and the scattering power of an atom, we can define the scattering power of a crystal in the direction of a diffraction peak corresponding to the lattice plane (hkl):

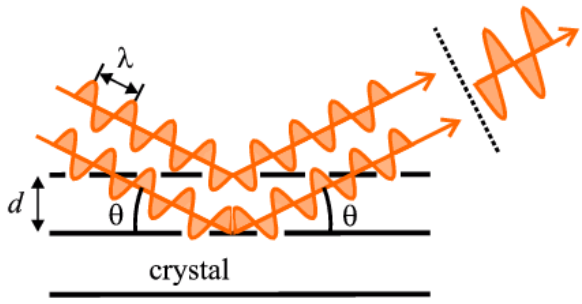


*Figure C16: Bragg's law (figure from Birkbeck College, University of London). Incident light of wavelength λ is scattered by a family of crystallographic planes with interplanar distance d.*

$$F_{hkl} = \sum_{j=1}^{N} f_j e^{-2\pi i(hx_j+ky_j+lz_j)} \quad (19)$$

Where $j$ is the atom, $f_j$ is the scattering factor of the atom $j$, $h,k,l$ are the reflection indices (also called Miler indexes of the plane) and $x_j, y_j, z_j$ are the atomic coordinate of atom $j$ in the crystal. $F_{hkl}$ is called the crystalline structure factor.

Different diffraction methods exist: single crystal diffraction or Laue diffraction, which investigate one or few crystals and powder diffraction. In our work we use exclusively powder diffraction and will only detail this method in the followings.

X-ray diffraction on powder samples requires a good particle statistics, i.e. illumination of around $10^6$ micrograins, randomly oriented. If particle statistic is respected, diffraction from all crystallographic planes families is observed simultaneously on one pattern. Measurement can be done with a polychromatic beam in energy dispersive mode (XEDS), often included in SEM to roughly determine the chemical composition of a phase, although XEDS does not have a good energy resolution. High-resolution measurements are done with a monochromatic beam in angle dispersive mode and recorded by an area detector, which will be integrated using software such as Fit 2D (Hammersley, 1997) or Dioptas (Prescher and Prakapenka, 2015). In powder diffraction, contribution of phase $p$ to intensity of a peak $c$ can be calculated as follow:

$$I_p^c = S_F \frac{\lambda^3 f_p}{V_p^2} \sum_{hkl} (m_{hkl} L_{hkl} P_{hkl} A_{hkl} G_{hkl}^c(\theta) |F_{hkl}|^2)_p + bkg^c \quad (20)$$

Where $S_F$ is the scale factor (depending on experimental conditions), $f_p$ is the volume fraction of phase $p$, $V_p$ is the unit-cell volume of phase $p$, $bkg^c$ is the background at peak $c$, $L_{hkl}$ is the polarization and Lorentz correction, $P_{hkl}$ is the correction for preferred orientation, $A_{hkl}$ is the absorption correction, $G^c_{hkl}(\theta)$ is the peak profile function for peak $c$, and $F_{hkl}$ the previously described scattering power of the crystal in the direction of a diffraction peak corresponding to the lattice plane (hkl). $m_{hkl}$ is the peak multiplicity: if different families of crystallographic planes has a similar $d_{hkl}$, intensities will sum. $A_{hkl}$, $L_{hkl}$ and $P_{hkl}$ need to be fixed prior to structure analysis.

In order to determine the structure of a phase from a powder diffraction pattern, the most reliable treatment is a Rietveld refinement (Rietveld, 1967, 1969). This method has been implemented in a number of programs such as GSAS (Larson and Von Dreele, 2000) or Rietica (Hunter and Howard, 1998). During a Rietveld refinement, total calculated intensity $I_i^{tot,calc}$ is compared to observed intensity at each data point $i$:

$$I_i^{tot,calc} = bkg_i + \sum_{c,p} I_i^{calc,c} \quad (21)$$

$I_i^{calc,c}$ is the calculated intensity for peak $c$ at data point $i$. To calculate the total intensity in $i$ contribution from all phases $p$ and from all peaks $c$ must be taken into account, as well as the background at point $i$: $bkg_i$. The difference between the observed and the total calculated intensity for each data point is minimized using a weighted least square algorithm. Refined parameters include phase proportion and phase structure, i.e. lattice parameters and atomic positions, and more rarely thermal parameters (describing static and dynamic disorder of the electron clouds). Peak profile functions are also fitted, generally modelled as pseudo-Voigt functions (a mix of Lorentzian and Gaussian functions). Background can be refined, or can be fixed by entering manually a set of data points corresponding to the baseline. Parameters depending on the experimental set up can also be refined (the wavelength, the zero position, the polarization, … ).

4/ Infrared (IR) spectroscopy

Our overview is inspired from the book by Stuart (2004). IR spectroscopy is based on changes in electric dipole momentum, i.e. in the system's polarity, during particular vibrations (namely 'IR active') of the sample. We note that selection rules are different for Raman and IR spectroscopies. For a solid with *N* atoms, there are 3*N* degrees of freedom for vibrational modes, 3 being translational (acoustic modes) and 3*N*-3 vibrational (optical modes). Variety of vibrational modes is described in figure C17. The sample absorbs incoming IR radiations, when they have exactly the same frequency as vibrational modes. Vibrational modes generally have frequency within IR range (i.e. < 400 $cm^{-1}$ for Far-IR, 400 $cm^{-1}$ to 4000 $cm^{-1}$ for Mid-IR, and 4000 $cm^{-1}$ to 13000 $cm^{-1}$ for Near-IR). The stronger a bond is, the higher energy is needed to make it vibrate, i.e. that stronger bonds will have lower vibrational mode frequencies (physical description is available in section C/IV/2).

Harmonics are multiples of fundamental frequency corresponding to a vibrational mode. They are producing overtones, with the energy required for the first overtone being twice the energy of the fundamental frequency. The first overtone will thus appear at twice higher wavelength than the fundamental frequency. Combination bands occur when two fundamental frequencies absorb energies simultaneously. Overtone and combination bands are frequent artifacts in IR spectroscopy, in contrast to Raman spectroscopy, for which they are very rare.

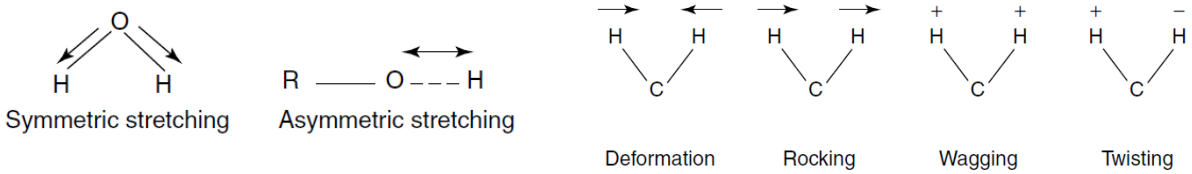


*Figure C17: Description of the different vibration modes: stretching (left) and bending (right). + indicates that the atom is moving toward us, and – the contrary. Figures from Stuart (2004).*

There are different types of instrument to perform IR measurements. Fourier Transform Infrared Spectrometer (Figure C18) was used for our study, and will thus be described here. A polychromatic IR source is used, frequently a Globar source (i.e. heating at ~ 1100° of a SiC rod), while synchrotron source was used in this work. Beam focus is achieved via cassegrain reflectors, as they increase focal length in a small system.

A Fourier transform interferometer, variant of the Michelson interferometer with a moving mirror, divides the incoming beam in two, via a KBr beamsplitter. 50% of the beam goes into a fixed mirror at 90° of the beam, and 50% in a moving mirror, parallel to the source. Changes in optical path lengths will result in change in phase difference. Split beams, with similar frequency, but phase difference, are reflected to the beamsplitter, recombined by superposition of waves, and transmitted at 90° of the source. Optical path length is recorded, and then Fourier transformed to obtain a signal in function of wavenumbers. Interferogram of the direct beam is recorded, and Fourier transformed. The same is consequently done for the sample and the background, before dividing the sample signal by the background one. IR spectra can be presented either in absorbance i.e. showing which frequencies the sample is absorbing, or in transmittance i.e. showing which frequencies the sample is not interacting with. The use of an interferometer makes it possible to reach an exceptional dispersion, far more precise than gratings.

Choice of detector depends on the IR investigated region: the most common is a MCT (Mercury Cadmium Telluria) detector, i.e. a photodetector converting light photons into current. MCT detector is working in a wide frequency range. Bolometers can be alternatively used, and for Far-IR a Germanium photodetector is needed cooled by liquid He.

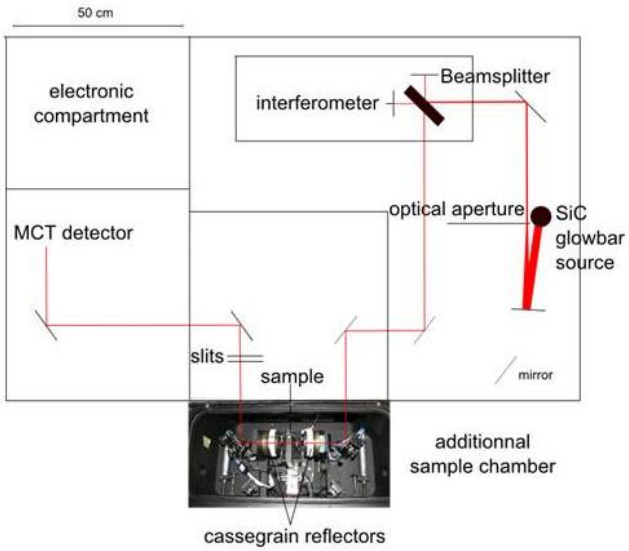


*Figure C18: Simple FTIR scheme.*

In our work, IR measurements were done at SMIS beamline, Soleil synchrotron. IR spectra were recorded in the air in transmission mode (Figure C19) from 650 $cm^{-1}$ to 6000 $cm^{-1}$ with a resolution of 0.5 $cm^{-1}$ and a scan accumulation of 100, repeated 4 times, using a MCT detector frequently cooled by liquid nitrogen. Absorbance was obtained after subtraction of the background (measured after each analysis in the same conditions as the sample) with the help of the OPUS/IR software. No further data treatment was done.

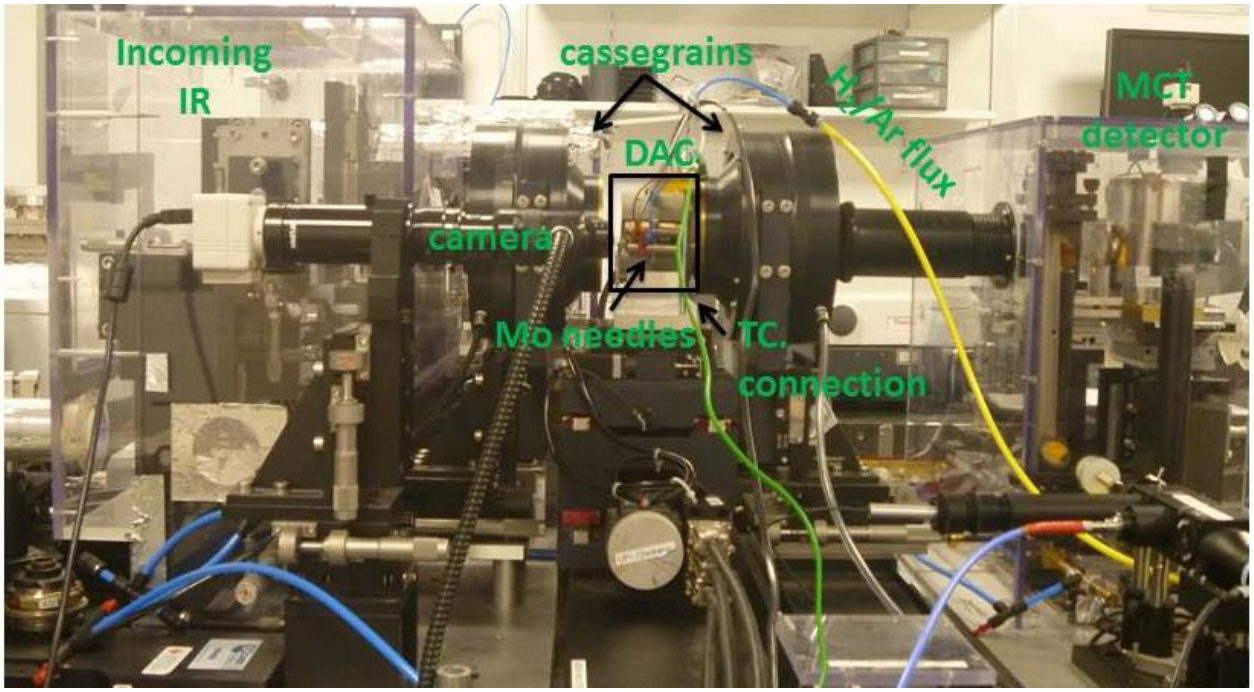


*Figure C19: Experimental set-up on SMIS beamline, Soleil synchrotron. Fourier-transform interferometer is used, with synchrotron source and MCT detector. T.C. = thermocouple, Mo needles are internal furnace connection for Pt-wire heater (described in C/I/2).*

## III/ Analytical methods

To characterize recovered samples, we used the following analytical techniques: Scanning Electron Microscopy, Transmission Electron Microscopy, Electron Microprobe analysis, and Raman spectroscopy.

### 1/ Scanning Electron Microscopy (SEM)

SEM is used for sample imaging, with a usual resolution around 20 nm for the most recent machines. SEM uses a 1-40 kV focused electron beam. The electron beam can be produced either by a W filament via resistive-heating, or by a $LaB_6$ or $CeB_6$ crystals, or a Field Emission Gun (wire of W with a sharp tip < 100 nm). The electron beam is focused in the optical column by condenser lenses, and deflected by scan coils to scan sample area. Samples need thus to be conductive so that electrons will flow at its surface. This is generally achieved by coating for insulator specimens. Electron beam interacts with the sample within few micrometers (Figure C20). Three types of signals are analyzed by SEM:

1/ Backscattered electrons (elastic incoherent scattering[12]) produced by backscattering of the incident electron beam. Backscattered electrons are high energy electrons scattered nearly perpendicularly to the incident beam. They are probing few micrometers of the sample, and are sensitive to chemical composition: high-Z atoms backscattered electrons more efficiently.

2/ Secondary electrons (SEs) (inelastic incoherent scattering) are valence electrons ejected from the sample during interaction with the incident electron beam. Due to low energies, only SEs produced at the surface of the sample are detected. SEs are emitted at large angle, and are useful to study topography of a sample.

3/ Characteristic X-rays (inelastic incoherent scattering). Electron beam can excite inner-shell electrons, triggering their ejection. The electron hole created is then filled by an outer-shell electron with the emission of a characteristic X-ray (or an Auger electron). Energy difference between the outer shell and the inner shell is characteristic of an element. Energy dispersive X-ray spectrometry (XEDS) identifies sample elemental composition although analyses are usually not quantitative. Chemical mapping can be performed by scanning an area. To probe heavy elements a high energy beam is required to excite inner-shell electrons (e.g. 20-25 keV for Xe). A common artifact of XEDS measurements is the presence of 'sum peaks': it happens when two photons enter the detector at exactly the same time. Sum peaks are likelier for major elements (Figure C21).

[12] To describe electron interaction with matter, we used the dual wave-particle nature of the electron. Elastic scattering means that the scattered and incident beams have the same energy, and coherent scattering means that scattered and incident beams have the same frequency and waveform, i.e. that incident and scattered electrons have the same direction.

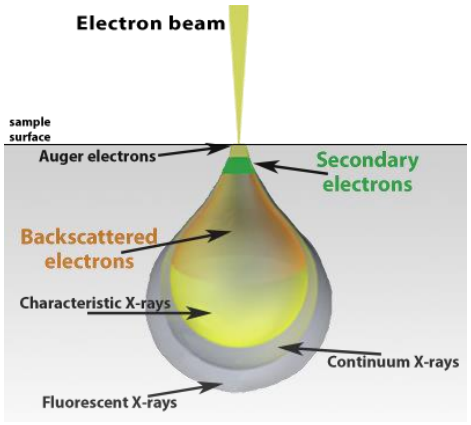


*Figure C20: Different electron-sample interactions are shown, depth is few µm[13]. For SEM, only secondary and backscattered electrons, and characteristics X-rays are used.*

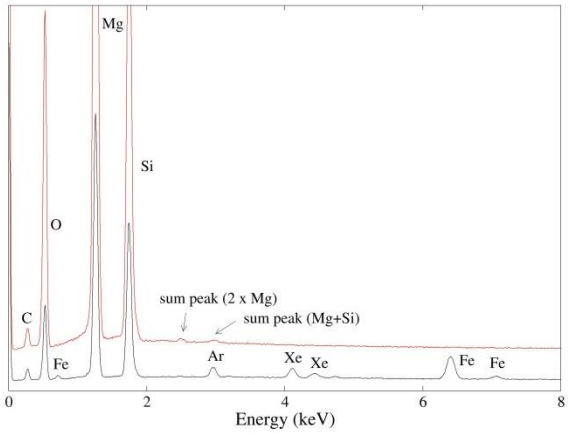


*Figure C21: XEDS spectra of olivine (plain in red, and Xe/Ar-bearing in black). Different contributions are shown.*

In this PhD thesis, samples were mounted in epoxy, polished, and carbon coated. Samples were observed with a Zeiss Supra 55 equipped with a field emission gun at ISTeP, Sorbonne Université with Omar Boudouma. Detection of Xe is optimized with an acceleration voltage of 20-25 keV and a working distance of 7.0 mm in backscattered mode. Indeed Xe is way heavier than Si, Mg and O and will backscatter electrons far more intensely than the surrounding silicate material, appearing brighter. Detection limit for Xe by SEM is around 0.15 wt% Xe based on our work: however it also depends on the presence of bubbles, easier to identify than presence of Xe in the bulk.

2/ Transmission Electron Microscopy (TEM)

Present TEM overview is based on the classes from Nicolas Menguy (IMPMC), and the book from William and Carter (2009) on TEM basics. TEM has usually a higher energy electron beam than SEM (100-300 kV). Wavelength of the incident beam is thus very small: 0.0251 Å for 200 kV electron beam, making it possible to image very fine details at the nanoscale. On the contrary of SEM, TEM observations are mostly linked with electrons transmitted through the sample, so that the sample needs to be very thin (~ 20 nm). TEM resolution should be equal to electron wavelength, however, due to lenses aberration; resolution is generally limited to 0.15-0.19 nm. Electrons can be transmitted though the sample via elastic scattering or inelastic scattering. Here we will focus on diffracted electrons, as this is the signal we used the most. We will then briefly describe other modes of observation.

Incident electrons are diffracted by the sample, following the law and principles of X-ray diffraction developed in C/II/3. However unlike X-rays which are only diffracted by electron clouds, electrons are diffracted both by electrons clouds and nuclei. They are also more diffracted as electrons are charged particles. Their scattering angles are very low (few

[13] https://www.nanoscience.com/technology/sem-technology/ (open on the 8th of april 2018)

degrees) due to their small wavelengths. Diffraction patterns can give information on the crystallographic structure of the sample, by evaluating the different d-spacing ($d_{hkl}$), as detailed in figures C22 and C23. To restrict analysis to a small part of the sample, an aperture placed in the first image plane allows the so-called Selected Area Electron Diffraction (SAED or SAD) mode.

Diffracted electrons can also be recorded for imaging purpose, as high-mass (high-Z and density) and high thickness area diffract more than others. Two imaging modes are available: bright field, i.e. that direct beam is analyzed, with high-mass/thickness zones appearing in dark, or in dark field, i.e. that only the diffracted beam is analyzed, with high-mass/thickness zones appearing this time with a brighter contrast (Figure C23, left). An objective aperture is used to block the direct beam in dark field imaging.

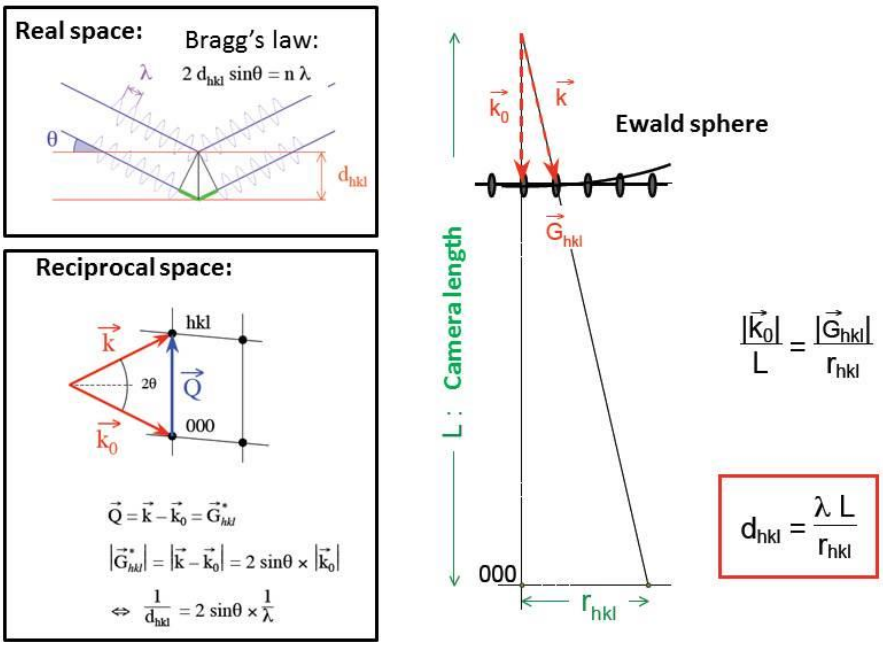


*Figure C22: Diffraction conditions for electron diffraction in TEM. Ewald sphere can cross several nodes simultaneously, due to small electrons' wavelength. Resolution is defined by camera length. Figure adapted from classes from Nicolas Menguy.*

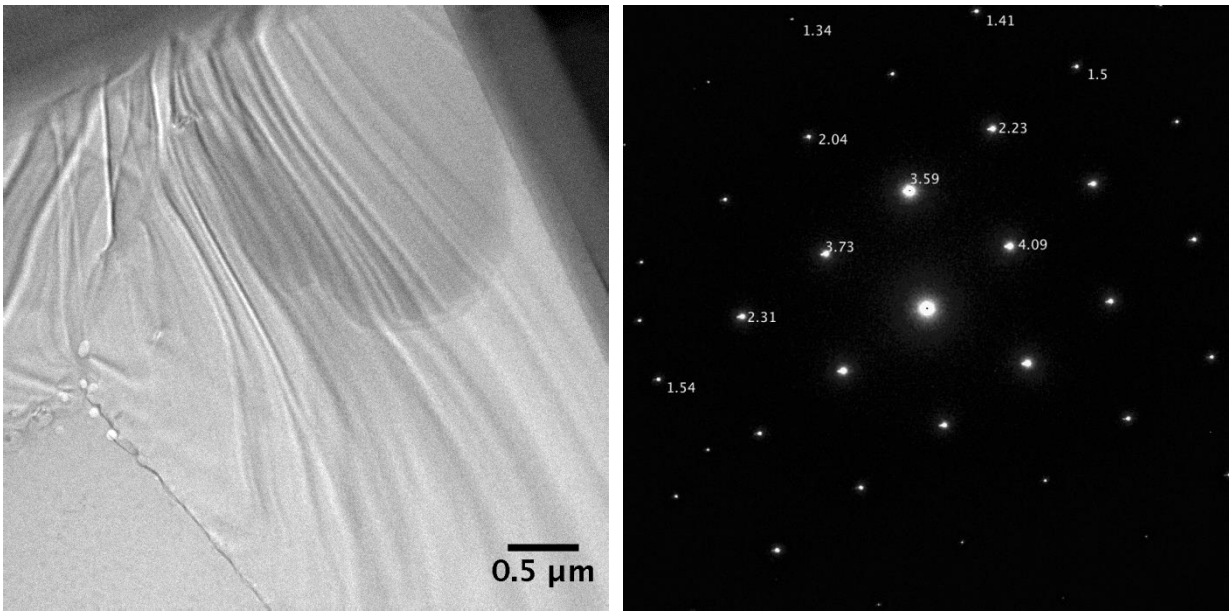


*Figure C23: (left) TEM image of Xe/Ar-bearing sanidine PC63 (Table F1, and details in F/I/2, Figure F4) in dark field mode. (right) Diffraction pattern (corresponding to the dark crystal at the top of the image) with calculated d-spacings ($d_{hkl}$) (right). In this case* $\lambda$ *= 0.0251 Å and* L *= 100 cm (=22450 pixels).* $r_{hkl}$ *are measured (in pixel) on the image (beginning from the bright direct beam at the center), to calculate consequently* $d_{hkl.}$

Similarly as in SEM, electron beam can scan the sample using scan coils in a TEM. Scanning TEM (STEM) can be combined with bright field (STEM-BF) and high angle annular dark field (STEM-HAADF) modes using an annular detector located below the sample. In STEM-HAADF mode, the detector thus collects incoherently scattered electrons at high angle (> 70 mrad). The scattered intensity is proportional to the sample density and thickness and also very sensitive to the atomic number of atoms within the sample (Z-contrast). This STEM-HAADF imaging mode is particularly efficient to visualize Xe atoms in a light elements bearing matrix.

X-ray Energy Dispersive Spectrometry (XEDS) can also be performed similarly to SEM. By combining STEM mode with XEDS, elemental mapping is possible.

Although TEM analyses are very powerful, beam damage can occur (Figure C24) due to the use of a high-energy, highly-focused beam, mainly through heating of the sample. Damage can also occur during sample preparation using focused ion beam (FIB). Analyses of highly volatile elements such as Xe can be very tricky, as we do observe destabilization under the beam for some of our sample. For volatile elements, observations under very low *T* using a cooled stage are sometimes preferred.

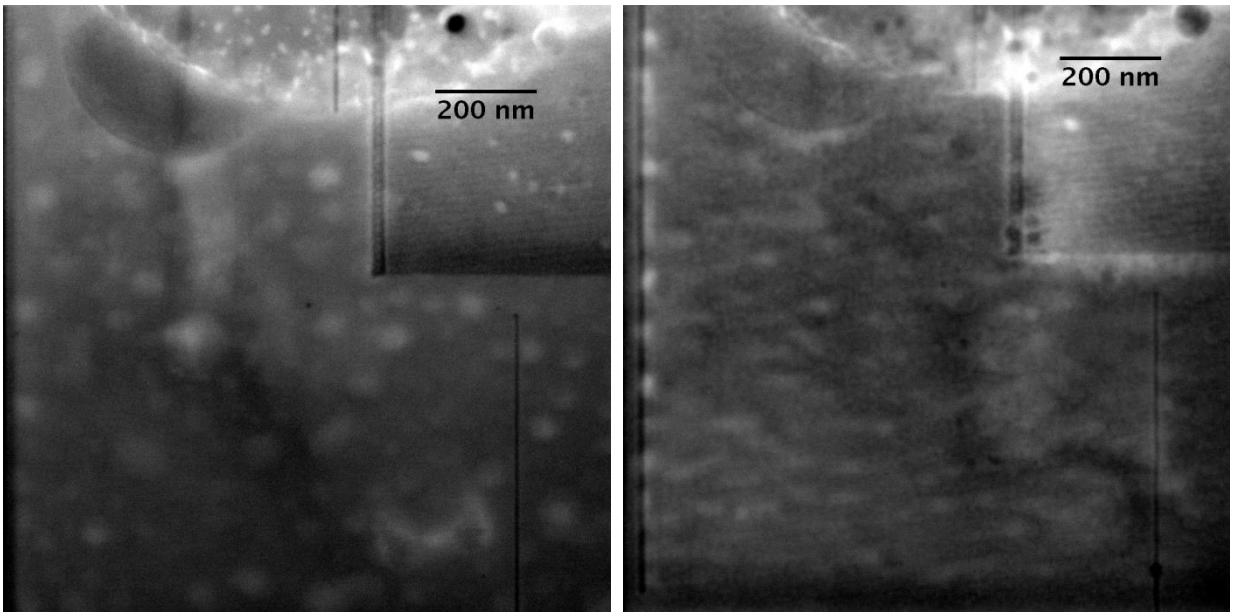


*Figure C24: STEM-HAADF image of Xe/Ar-bearing sanidine (PC63, Table F1) showing sample before (left) and after (right) elemental mapping (10 min), bright Xe(Fe)-rich zones are clearly modified under the beam.*

For this PhD thesis, ultra-thin sections were realized by David Troadec by FIB with a $Ga^+$ beam, and deposited on a Cu grid using a focused ion-beam at the IEMN (Institut d'Electronique, de Microélectronique et de Nanotechnologie, Lille). TEM analyses were performed at the IMPMC with Nicolas Menguy using a JEOL 2100 F with emission gun, a high resolution (UHR) pole piece, a JEOL detector with an ultrathin window allowing detection of light elements, and a STEM device which allowed Z-contrast imaging in the STEM-HAADF mode. Chemical analyses were performed by XEDS elemental mapping in the STEM-XEDS mode. SAED patterns were recorded at a camera length of 50 cm or 100 cm.

3/ Electron microprobe analyses (EMPA)

Electron Microprobe is used in Earth's Sciences to perform quantitative elemental analyses. EMP works similarly to the SEM, with an electron beam inducing electron sample interaction, triggering characteristic X-ray emissions. However, instead of an energy dispersive X-ray spectrometry, wavelength dispersive spectrometry is used, to reach lower detection limits. Based on Bragg's law, crystals are used to select characteristic X-ray emission energies of a given element. For calibration purposes, a set of well-known standards is always analyzed previously to analysis. EMP analyses are however limited for low-Z elements (such as H), and relatively volatile elements such as Na, or K, as they usually escape during analyses, under the electron beam.

EMPA have been performed on a CAMECA SX5, at CAMPARIS centre at Sorbonne Université and on a CAMECA SX100 at the School of Geosciences, University of Edinburgh. Operating conditions were 15 kV accelerating voltage, 10 nA beam current, and a focused beam for point analysis. We used method from Montana et al. (1993): calibration for Ar, Xe

and Kr was done by measuring the counts on neighboring elements (i.e. on Cl, I and Rb respectively). Xe-bearing sanidine Nat. glass (PC53, Table G1), previously analyzed by Particle Induced X-ray Emission (PIXE) (Leroy et al., 2018) was analyzed to calibrate our measurements. Details of calibration are given in Appendix C1 and C2.

4/ Raman spectroscopy

Raman scattering is an inelastic process. Whereas most of the incoming light is elastically scattered, a small portion (1/10000) is inelastically scattered, due to photon interaction with vibration modes of the sample. The frequency of the incident light is shifted by plus (Anti-Stokes shift) or minus (Stokes shift) the frequency of a vibration mode (Figure C25). Raman active modes involve changes in the electronic polarizability, defined as the ratio of the dipole momentum by the electric field which created the dipole momentum. Electronic polarization in solids only depends on atomic displacements, and modulation of atomic positions leads to weak contribution to the scattered light.

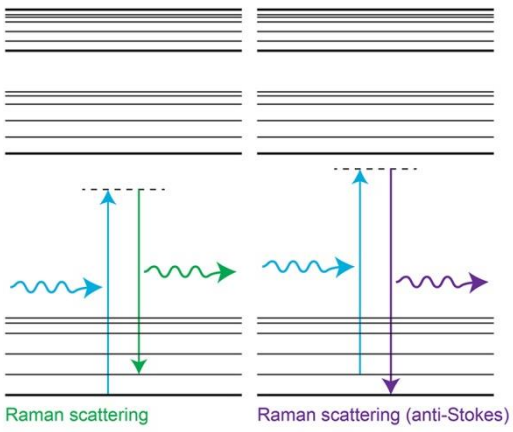


*Figure C25: Raman scattering, with Stokes (left), and anti-Stokes (right) contributions. Stokes contribution involves transition from lower to higher-energy vibration levels and are thus more intense than anti-Stokes contribution.* [14]

Raman spectrometers are equipped with a monochromatic visible, near UV or near IR light source (laser). Scattered light is usually measured at right angle from the incident beam, and separated into different wavelengths either with the use of gratings (dispersive Raman) or with an interferometer for near-IR light (as developed for IR spectroscopy C/II/3). Stokes contributions, more intense than anti-Stokes ones, are generally detected.

Most of Raman analyses have been performed in the Raman lab at IMPMC with the help of Olivier Beyssac on a Renishaw InVia dispersive Raman microspectrometer at 532 nm (green laser). Laser power at the surface of the sample ranges from 1 mW to 50 mW,

[14] From the Renishaw website (http://www.renishaw.com/en/raman-spectroscopy-in-more-detail--25806 visited the 15th of April 2018).

depending on the sample. Spectra were acquired from 80 $cm^{-1}$ to 1380 $cm^{-1}$. They were averaged from 5 accumulations, each with a counting time of 5 s.

## IV/ Theoretical modelling of Xe incorporation in minerals

### 1/ Density functional theory (DFT) in condensed matter

This part is largely based on Finocchi (2011), Baroni et al. (2001), and Gonze and Lee (1997). For a better understanding we define here the main notations:

| | | | | | |
|---|---|---|---|---|---|
| $e$ | : | Charge of the electron | $r$ | : | Electronic position |
| $R_\tau$ | : | Atomic position $R_\tau(R_{\tau,i}, R_{\tau,j}, R_{\tau,k})$ | $\hbar$ | : | Planck constant divided by $2\pi$ |
| $\varphi_k$ | : | Monoelectronic wave-function | $u_{\tau,i}$ | : | Atomic displacement of the atom $\tau$ along i |
| $f_p$ | : | Occupation factor (from 0 to 2) | $m$ | : | Mass of the electron |
| $n(r)$ | : | Electronic density | $\tau / \tau'$ | : | Atom (nucleus) |
| $E$ | : | Total energy | $i / j / k$ | : | Cartesian coordinate |
| $M_\tau$ | : | Atomic mass | $\vec{q}$ | : | Wave vector of the Brillouin zone (reciprocal space) |
| $\vec{R}$ | : | Lattice vector (real space) | | | |

DFT has become an increasingly sophisticated tool to study properties of condensed matter since 1970's. *Ab initio* or first-principles calculations enable to study properties of matter with no hypothesis regarding inter-atomic potentials (as it is the case for non-quantum molecular dynamics or Monte-Carlo calculations).

The Schrödinger equation within the Born Oppenheimer (BO) approximation[15] can be rewritten as a function of the electronic density leading to the Kohn and Sham equations (eq. (22) and eq. (23)). Kohn and Sham equations transform a complex many-body problem of $N_e$ interacting electrons into $N_e$ problems of non-interacting electrons moving in an effective potential. Use of the electronic density makes it possible to transform a $3N_e$ dimensions problem into a 3 dimensions problem. Furthermore all properties of a system are uniquely defined by the ground state electronic density.

$$\left[ -\frac{\hbar^2 \nabla_2}{2\mathrm{m}} + V_{ext}(\vec{r}) + e^2 \int d^3r' \frac{n(\vec{r'})}{|\vec{r} - \vec{r'}|} + V_{XC}\left(\vec{r};[n]\right) \right] \varphi_p(\vec{r}) = \mu_p \varphi_p(\vec{r}) \quad (22)$$

[15] Decoupling of motions of atomic nuclei and electrons

$$n(\vec{r}) = \sum_p f_p \left(\varphi_p(\vec{r})\right)^2 \quad (23)$$

Eq. (22) is a monoelectronic equation in an external potential ($V_{ext}$) with $V_{XC}(\vec{r};[n])$ the exchange-correlation potential. Eq. (22) can be written for each electron of the system. $\mu_p$ are the eigenvalues of the whole system. Kohn and Sham equations lead to the exact solution if and only if $V_{XC}(\vec{r};[n])$ is the exact exchange-correlation potential. Unfortunately this potential is unknown: as a consequence the exchange-correlation potential needs to be approximated (e.g. Local Density Approximation, Generalized Gradient Approximation, etc) and solutions remain approximate. Practically, Kohn and Sham equations are solved using self-consistent field (scf) variational approach (Hohemberg and Kohn theorems) to find the electronic ground state density. For condensed matter, wave functions $\varphi_p(\vec{r})$ are expanded in a combination of plane waves. Periodic boundary conditions are used and inner-core electrons are described with non-local pseudo-potential (Trouiller and Martins, 1991).

Relaxation of a structure (i.e. determination of the equilibrium atomic positions) can be achieved within the framework of the DFT. Indeed within the BO approximation, positions of nuclei are external parameters (which do not directly affect electronic structure but modify ground state density) and their equilibrium positions are achieved by minimization of the residual stress $F_\tau$ on each individual atom $\tau$.

$$F_\tau = -\frac{\partial E(R_\tau)}{\partial R_\tau} \quad (24)$$

Electronic density and total energy of the system can be expanded as a function of nucleus coordinates (on a similar basis as perturbation theorem in quantum mechanics).

$$E_{pot}(R_\tau) = E_{pot}(R_\tau) + \sum_{\tau,i}\left[\frac{\partial E_{pot}}{\partial R_{\tau,i}}\right]_0 u_{\tau,i} + \sum_{\tau,i,\tau',j}\left[\frac{\partial^2 E_{pot}}{\partial R_{\tau,i}\partial R_{\tau',j}}\right]_0 u_{\tau,i}u_{\tau',j} + \ldots \quad (25)$$

At equilibrium, the first order contribution is null. Within the harmonic approximation we neglect any term higher than the second order in the atomic displacements, and we can express the atomic force $F_{\tau,i}$ exerted on the atom $\tau$, in the direction $i$ as follows:

$$F_{\tau,i} = -\sum_{\tau',j} C_{\tau,i;\tau',j} u_{\tau',j} \quad (26)$$

With $C_{\tau,i,\tau',j}$ the interatomic force constant matrix, corresponding to the force constants between each pair of atom (τ, τ'), in the three directions, i.e. *N*x3x*N*x3 components. $C_{\tau,i,\tau',j}$ can be calculated as follows:

$$C_{\tau,i;\tau',j} = \left[ \frac{\partial^2 E_{pot}}{\partial R_{\tau,i} \partial R_{\tau',j}} \right]_0 \quad (27)$$

As periodic boundary conditions and plane wave functions are used for condensed matter it is easier to work in the reciprocal space. A dynamical matrix $D_{\tau,i;\tau',j}(\vec{q})$ is defined as the Fourier transform of the Interatomic force constant matrix (*N*x3x*N*x3 components):

$$D_{\tau,i;\tau',j}(\vec{q}) = \sum_{\vec{L}} C_{\tau,i;\tau',j} e^{i\vec{R}.\vec{q}} / \sqrt{M_\tau M_{\tau'}} \quad (28)$$

($\vec{q} = 0$ if we calculate phonon/vibration at the center of the Brillouin zone)

The 3N squared phonon frequencies (modes) $\omega_m{}^2$ at a particular $\vec{q}$ are eigenvalues of the dynamical matrix. Eigenvectors $U_m(\tau,i')$ are the associated displacement for the vibrational mode $m$ defined for each atom $\tau$ along the three Cartesian directions (*N*x3 matrix). They form an orthonormal set.

2/ Infrared and Raman spectra modeling

IR and Raman spectroscopies investigate phonons only at the center of the Brillouin zone due to the range of wave numbers of incident light: far bigger than the size of the first Brillouin zone. This part is largely based on Farmer (1974), Balan et al. (2001) and Madejova et al. (2011). For a better understanding we define here basic notations used in the following theoretical part.

| | | | | | |
|---|---|---|---|---|---|
| $\omega_m$ | : | Frequency of the *m* vibrational mode | $\lambda$ | : | Wavelength |
| $\omega_0$ | : | Frequency of the incident light | | | |
| $m$ | : | vibrational mode | $K_{\text{int}}$ | : | Integrated molar absorption coefficient |
| $U_m(\tau,i) = r_m$ | : | Displacement of the atom $\tau$ along $i$ | $A_{\text{int}}$ | : | Integrated absorption |
| $r_{\tau,i}$ | : | in the $m$ vibrational mode<br>Displacement of the atom $\tau$ along $i$ | | | |
| $\varepsilon_{ij}(\infty)$ | : | Dielectric tensor at infinite frequency | $A(\omega)$ | : | Absorbance |
| $N_m$ | : | Number of mode | $\Omega_0$ | : | Volume of the primitive unit-cell |
| i/j | : | Cartesian coordinates | $\varepsilon_{ij}(\omega)$ | : | Low frequency dielectric tensor |
| $\Gamma = g_m / 2$ | : | Damping coefficient (correct for the divergence at $\omega_m$ ) | $k_b$ | : | Boltzmann constant |
| | | | $T$ | : | Temperature |

IR and Raman are related to vibrations between atoms. These vibrations can be approximated as a harmonic oscillator (non-quantum consideration). A crystal can thus be modeled as a collection of harmonic oscillators and expression of the dielectric tensor components can be determined from the Lorentz theory.

The equation of motion can be written for each oscillator (an oscillator corresponds to a vibrational mode):

$$M_m \frac{d^2 r_m}{dt^2} + M_m g_m \frac{dr_m}{dt} + M_m \omega_m^2 r_m = Q_m E \quad (29)$$

Where $M_m g_m \frac{dr_m}{dt}$ is the friction component, $M_m$ is the effective mass of the oscillator i.e. $M_m = \sum_\tau M_\tau^2 r_m^2$ and $Q_m$ is the charge of the harmonic oscillator.

By solving eq. (29) we can find the expression of the displacement associated with one mode:

$$r_m = E \frac{Q_m(\omega_m^2 - \omega^2 - i\omega g_m)}{M_m\left[(\omega_m^2 - \omega^2)^2 + \omega^2 g_m^2\right]} = E \frac{Q_m}{M_m(\omega_m^2 - \omega^2 + i\omega g_m)} \quad (30)$$

And then deduce *P* the polarization of the system through:

$$P = \sum_\tau Q_\tau r_\tau = E \frac{N_m Q_m^2}{M_m(\omega_m^2 - \omega^2 + i\omega g_m)} \quad (31)$$

From Maxwell's theory of polarization, $P(\omega)$ inside matter can be linked to the macroscopic electromagnetic field, $E(\omega)$, existing in the material, via the low-frequency dielectric tensor $\varepsilon(\omega)$:

$$4\pi P(\omega) = (\varepsilon(\omega) - 1)E(\omega) \quad (32)$$

$$\varepsilon_{ij}(\omega) = 1 + 4\pi \frac{P}{E} = 1 + 4\pi \sum_m \frac{N_m Q_m^2}{M_m(\omega_m^2 - \omega^2 + i\Gamma)} \quad (33)$$

$$N_m Q_m^2 / M_m = S_{m,ij} = \left[\sum_{\tau,i'} Z^*_{ii',\tau} U_m(\tau, i')\right]\left[\sum_{\tau',j'} Z^*_{jj',\tau'} U_m(\tau', j')\right] \quad (34)$$

$S_{m,ij}$ is the mode-oscillator strength of the mode *m* and $Z^*_{ii',\tau}$ the Born effective charge describing the linear relation between the polarization per unit cell along $i$ and the displacement of the atom $\tau$ along the direction $i'$. It is in practice calculated as the mixed second order derivative of the potential energy of a given atom with respect to atomic displacement along $i'$ and macroscopic electric field along $i$ (3x3x*N* components).

**Infrared spectroscopy**

If we put $\Gamma' = g_m = 2\Gamma$ and neglect the term $-\Gamma^2$, Eq. (33) becomes as follows, which is the equation implemented in our code calculating IR spectra:

$$\varepsilon_{ij}(\omega) = \varepsilon_{ij}(\infty) + \frac{4\pi}{\Omega_0}\sum_m \frac{S_{m,ij}}{\omega_m^2 - (\omega + i\Gamma')^2} \quad (35)$$

Transmission IR analyses record $A(\omega)$, the Absorbance i.e.:

$$A(\omega) = \log\left(\frac{I_0(\omega)}{I_t(\omega)}\right) \quad (36)$$

$$A(\omega) = \frac{4\pi k}{\lambda} \quad (37)$$

$$\varepsilon(\omega) = \varepsilon_1 + i\varepsilon_2 = N^2 = (n + ik)^2 \quad (38)$$

with $N$ the complex refraction index, thus

$$k = \sqrt{\frac{\varepsilon_i}{2}\left(\sqrt{\frac{\varepsilon_r^2}{\varepsilon_i^2} + 1} - \frac{\varepsilon_r}{\varepsilon_i}\right)} \quad (39)$$

By combining eq. (38) and eq. (39) we can deduce the absorbance (along the three directions): this is the infrared spectrum.

**Raman spectroscopy**

Intensity $I_m$ of the Stokes contribution in an insulating crystal for vibration mode $m$ can be written as follows and was calculated using the implementation made by Lazzeri and Mauri (2003):

$$I_m \propto \frac{(\omega_0 - \omega_m)^4}{c}\left|\vec{P_l}\cdot\overleftrightarrow{T_m}\cdot\vec{P_s}\right|^2 \frac{\hbar}{2\omega_m}\left(\exp\left(\frac{\hbar\,\omega_m}{k_b T} - 1\right) + 1\right) \quad (40)$$

With $\vec{P_l}$ polarization of the incident light, $\vec{P_s}$ polarization of the scattered light and $\overleftrightarrow{T_m}$ the Raman tensor defined as follows:

$$T_{m,kj} = \sum_{\tau,i} \frac{\partial^3 E}{\partial E_k \partial E_j \partial r_{\tau,i}} \frac{U_m(\tau,i)}{\sqrt{M_\tau}} \quad (41)$$

Where $E_k$ is the $k^{\text{th}}$ cartesian component of a uniform electric field.

The Raman tensor is computed by the code following eq. (41) (Baroni and Resta, 1986). The Raman tensor gives frequency shifts of scattered light keeping in mind that only modes inducing a change in polarization of the crystals are Raman active.

3/ Computational details

Atomic relaxations were performed by using Density Functional Theory (DFT) and the generalized gradient approximation (GGA) for the exchange-correlation functional as proposed by Perdew, Burke, and Ernzerhof (PBE) (Perdew et al., 1996) with the PWscf code of the Quantum espresso 5.0.2 package http://www.quantum-espresso.org/; Gianozzi et al., 2009).We use norm-conserving pseudo-potential to describe inner core electrons (Trouiller and Martins, 1991). Forces on the atom were minimized to less than $10^{-4}$Ry/au. Convergence for scf calculation was set to $10^{-10}$ Ry.

Second order derivatives were computed using the PHonon code of the Quantum espresso 5.0.2 package. http://www.quantum-espresso.org/; Gianozzi et al., 2009). Output of the PHonon code includes Born effective charges $Z^*_{ii',\tau}$ eigenvalues (frequency of vibration mode) and eigenvectors (atomic displacements in the vibrational mode) of the dynamical matrix and the electronic dielectric tensor. With the help of these ingredients we can generate polarized IR and Raman spectra as previously detailed.

Calculations were performed using the IBM iDataPlex cluster and the MeSU servers of the Sorbonne Université.

4/ Previous modelling of Xe within the DFT framework

There are few calculations based on DFT involving Xe in minerals relevant for the Earth (see Gerber, 2006 and Grochala, 2007 for Xe-bearing molecules of chemical interest). Most of them are dedicated to high-*P* xenon oxides (Zhu et al., 2012; Hermann and Schwerdtfeger, 2014; Dewaele et al., 2016) or try to evaluate the presence of Xe in the core (Zhu et al. (2014) for Xe-Ni-Fe system). Only two theoretical studies focused on Xe incorporation in silicate minerals, namely in α-quartz (Probert, 2010) and fibrous silica (Kalinowski et al., 2014).

In the treatment of noble gases, DFT provides reasonable description of structures and properties, although van der Waals corrections need sometimes to be implemented (as developed for calculations regarding Xe incorporation in olivine, D/II). However, it has been shown that DFT cannot perfectly describe bond energies of molecules containing noble gases, Post Hartree-Fock methods are required (Lai et al., 2011) as used by Kalinowski et al. (2014), but become quickly prohibitive in computational resources. Furthermore at very high *P* (around 100 GPa), Dewaele et al. (2016) point out that a pseudo-potential cannot be used to describe Xe *4d* orbitals due to a spatial overlap of *4d* orbitals with *5s* and *5p* orbitals. However for our *P* range (less than 10 GPa) this phenomenon is unlikely to happen.

## Chapter D: XE INCORPORATION IN OLIVINE

Olivine is the major mineral of the terrestrial upper mantle, and as such, Xe incorporation in olivine could be crucial at the Earth's scale. In this work we synthesized Xe-bearing olivine, and studied the effect of water and iron on *ex situ* recovered samples.
Previous experimental results based on *in situ* X-ray diffraction on Xe-bearing San Carlos olivine (Sanloup et al., 2011) at high *P-T* conditions are reinvestigated to solve Xe incorporation mechanisms (using DFT) in olivine: this work was published in *Geochimica et Cosmochimica Acta* (Crépisson et al., 2018). Eventually new *in situ* IR spectroscopy and X-ray diffraction data on Xe-bearing olivine at high *P-T* conditions are presented.

### I/ *Ex situ* analyses

#### 1/ Sample synthesis

Different heavy noble gases-bearing olivine samples were synthesized (Table D1). For $(Mg_{0.9}Fe_{0.1})_2SiO_4$ and $(Mg_{0.5}Fe_{0.5})_2SiO_4$, starting material was prepared by homogenizing mixture of high purity oxides (reagent grade): MgO (free from sulfate 40.32 $g.mol^{-1}$), $SiO_2$ and FeO (99.9% purity). MgO and $SiO_2$ powders were dehydrated at 1000°C and brucite at 70°C (to get rid of water adsorbed at the surface). Powders were then grounded in an agate mortar to obtain a homogeneous powder. For fayalite ($Fe_2SiO_4$), starting material consists in powder of natural fayalite. For hydrated samples, $H_2O$ content is around 5 wt%, added either as liquid water in the capsule or under the form of brucite ($Mg(OH)_2$).

#### 2/ SEM and EMP analyses

Noble gases are observed only as bubbles (~ μm) (Figure D1) and were not detected in the mass of the crystal (Table D2) for Xe/Kr (PC99B) and Xe/Ar (PC128B) -bearing **dry** synthetic olivines ($(Mg_{0.9}Fe_{0.1})_2SiO_4$).

| Name | Starting material | gas mix | *P* (GPa) | *T* (°C) | Duration (hours) | powder (mg) | gas (mg) | weight loss after piercing (mg) | comment |
|---|---|---|---|---|---|---|---|---|---|
| **PC99A** | $(Mg_{0.9}Fe_{0.1})_2SiO_4$ + water liq. | - | 2 | 1300 | 30 | 19.8 | - | 1.2 | - |
| **PC99B** | $(Mg_{0.9}Fe_{0.1})_2SiO_4$ | Xe/Kr | 2 | 1300 | 30 | 14.4 | - | 0.7 | Xe/Kr bubbles |
| **PC125A** | Fayalite + water liq. | Xe/Ar | 2 | 1300 | 5 | 22.7 | - | 0.5 | NO XE |
| **PC126** | $(Mg_{0.9}Fe_{0.1})_2SiO_4$ + water liq. | Xe/Ar | 2 | 1300 | 5 | 29.9 | 1 | 1.4 | Bubbles fizzing at the opening NO XE |
| **PC128A** | Fayalite | Xe/Ar | 1.5 - 2 | 1100 | 5* | 26.1 | - | 3 | NO XE |
| **PC128B** | $(Mg_{0.9}Fe_{0.1})_2SiO_4$ | Xe/Ar | 1.5 - 2 | 1100 | 5* | 13.4 | - | 3 | Xe/Kr bubbles |
| **PC133-1** | $(Mg_{0.5}Fe_{0.5})_2SiO_4$ + water (brucite) | Xe | 2 | 1200 | 48 | 26.1 | 0.6 | 12.4 | Big hole NO XE |
| **PC135-1** | $(Mg_{0.5}Fe_{0.5})_2SiO_4$ + water (brucite) | Xe | 2 | 1200 | 48 | 23.3 | 0.4 | 17.5 | Big hole NO XE |

*Table D1: Synthesis conditions and compositions. All samples have been synthesized during this work. *interrupted and continued after 1 hour.*

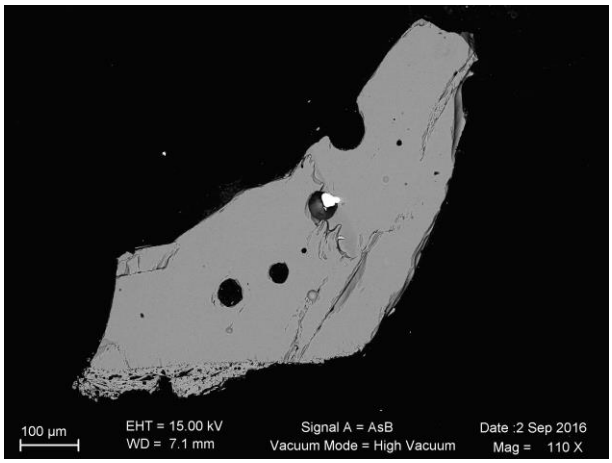


*a/ PC99A :noble gas-free olivine : presence of large holes due to water oversaturation.*

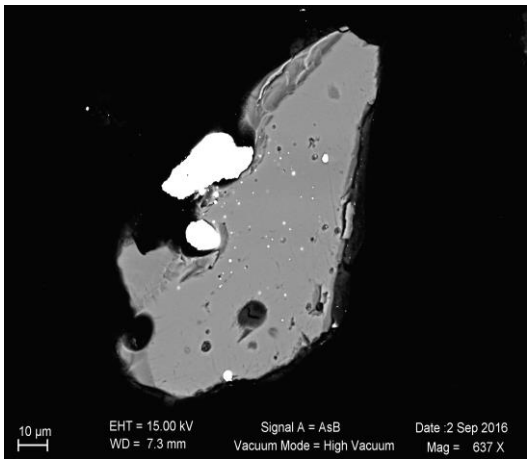


*b/ PC99B:Xe/Kr-bearing olivine (PC99B2). Bright dots within the crystal: Xe/Kr bubbles. Bright blocks on the left: Pt from the capsule.*

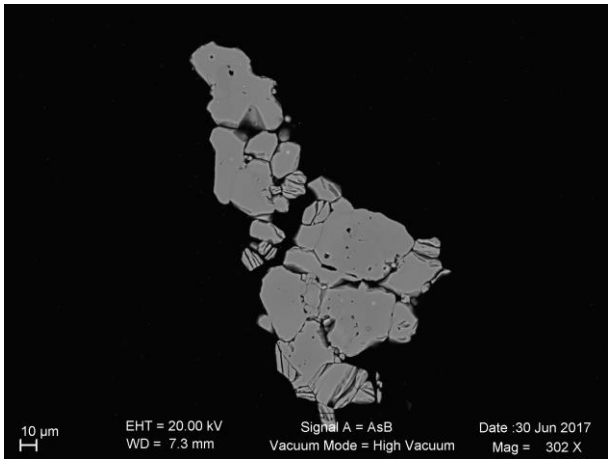


*c/ PC128B: Xe/Ar bearing olivine. Bright blurry dots within the crystal: Xe/Ar bubbles.*

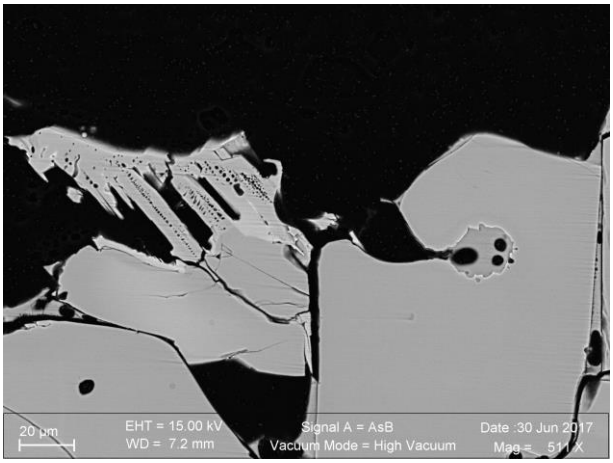


*d/ PC126: $(Mg_{0.9}Fe_{0.1})_2SiO_4$ olivine. Olivine is the main phase, although pyroxene is seen around lines of empty bubbles (top left) and residual glass is seen in the round structure with three holes inside (right). No noble gas observed.*

*Figure D1: SEM images in backscattered mode of olivine samples.*

In presence of water, no noble gases were retained inside the olivine crystals (Table D1). Indeed, in the course of run PC126 (Mg#96), while opening the recovered Pt capsule, a water bubble was clearly seen fizzing out of the capsule, implying that the capsule was correctly closed. Moreover, an increase of weight was measured after loading (Table D1). The fact that no noble gas was retrieved inside the recovered sample indicates that Xe preferentially goes into the free aqueous gas phase, and not in the olivine mineral. Although water was not directly measured, low oxide total for PC126 indicates that water content could reach 2.8 wt%. For synthesis using brucite as a primary source of water (PC133-1, Mg#73 and PC135-1, Mg#92) a large hole was observed inside both recovered capsules (Figures D2, D3), indicating that a massive degassing happened, confirmed by a large weight loss at

opening of the capsule. In Crépisson et al. (2014) hydrated forsterite (Fe-free) were grown from brucite without massive degassing, however experiments are needed to test the effect of Fe.

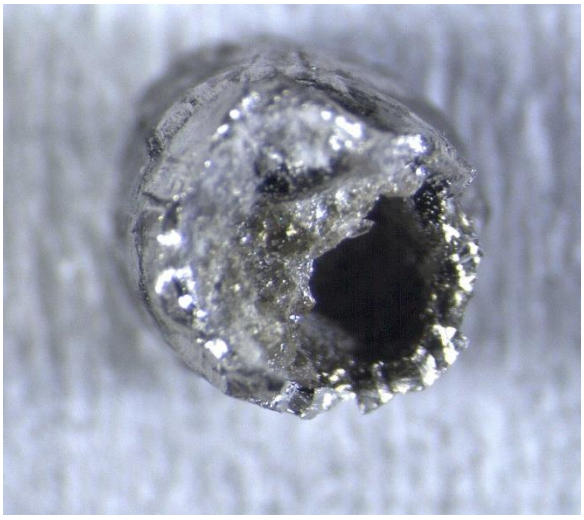

*Figure D2: Recovered Pt capsules for PC133-1 at the opening big holes indicating massive degassing. Capsule diameter is 3 mm.*

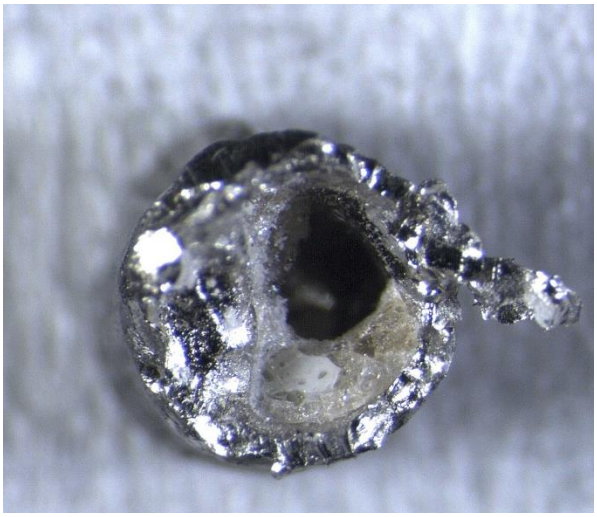

*Figure D3: Recovered Pt capsules for PC135-1 at the opening big holes indicating massive degassing. Capsule diameter is 3 mm.*

During piston cylinder press experiments on silicate using a Pt capsule, Fe presents as a starting material tends to form a metallic alloy with the Pt capsule. For olivine, this phenomenon is to be linked to the phase transformation of olivine into pyroxene with presence of residual glass observed in all recovered samples (Figure D1). As reminded by Sanloup et al. (2011), this destabilization of San Carlos type olivine in Pt capsule is well known as 'early partial melting' (Jaoul et al., 1987; Kohlsted and Maxwell, 1987) occurring at a restricted $fO_2$ for *T* below 1350°C (Jaoul et al., 1987). It is linked to uptake of Fe by the Pt capsule and is driven by the following equations:

$$Fe_2SiO_4 \rightarrow FeSiO_3 + FeO \quad \text{or} \quad Fe_2SiO_4 \rightarrow SiO_2 + 2FeO$$
$$4FeO \rightarrow Fe_{Pt} + Fe_3O_4$$

In our case we observe pyroxene and $SiO_2$-rich residual glass, Fe-Pt alloys were also found within the samples and at the border of the Pt capsule. Some samples present a large proportion of pyroxene, such as PC135-1[16] and to a less extent PC128B. This may be due to slight differences in experimental parameters (*P* / *T* / water and / or noble gases fugacities).

Fe was not retrieved in recovered olivine, synthesized at 2 GPa, without Xe (PC99A, Mg#100), whereas it was retrieved on Xe-bearing olivine (and pyroxene) (PC99B, Mg#98) synthesized in the same conditions. Higher Fe content was retrieved on Xe-bearing olivine, PC128B, synthesized at lower *T* (Mg#92).

[16] This is to be linked to lower Fe content in PC135-1, where pyroxene are mainly observed, than in PC133-1, where only olivine are observed.

| sample | mineral | MgO | $SiO_2$ | $Al_2O_3$ | CaO | FeO | Total | Mg# |
|---|---|---|---|---|---|---|---|---|
| **PC99B** | **olivine** | 56 (1) | 42.8 (8) | 0.03 (2) | 0.02 (1) | 2 (1) | 100.8 (4) | 98 (1) |
| **PC99B** | **pyroxene** | 39.4 (8) | 60 (1) | 0.17 (5) | 0.13 (4) | 0.6 (6) | 100 (1) | 99.2 (8) |
| **PC128B** | **olivine** | 50.7(9) | 41.0(8) | 0.00 (2) | 0.03 (3) | 8.0 (8) | 100 (1) | 91.8 (9) |
| **PC99A** | **olivine** | 57.1 (4) | 43.2 (7) | - | - | 0.1 (1) | 100.5 (8) | 99.9 (1) |
| **PC126** | **olivine** | 53.5 (7) | 41.1 (5) | 0.01 (2) | 0.01(2) | 2.4 (7) | 97.2 (7) | 97.5 (7) |
| **PC133-1** | **olivine** | 36 (1) | 38.1 (9) | 0.01 (2) | 0.03 (3) | 23 (2) | 98.1 (9) | 73 (2) |
| **PC135-1** | **pyroxene** | 35.3 (6) | 59 (1) | 0.03 (3) | 0.03 (3) | 5.5 (9) | 100 (1) | 92 (1) |

*Table D2: Average chemical composition. Xe/Kr and Xe/Ar are present in PC99B and PC128B respectively. Full EMPA are given in Appendix D1 is shown here. Mg# correspond to the atomic ratio 100Mg/(Fe+Mg). Noble gases contents are not shown here as noble gases are only present inside nanobubbles and below detection limit in the bulk. Distinction between olivine and pyroxene is made on the basis of atomic formula unit.*

Experiments on hydrated fayalite (PC125A) and dry fayalite (PC128A) show a more advanced early partial melting (Figure D4): fayalite only represents a minor component in the recovered samples whereas pyroxene is the major component (similarly as for PC135-1). Fe-rich glass or iron oxides (hard to tell by SEM analyses) were also observed in both samples (Figure D4). There is a clear problem of buffering and it seems that we cannot synthesize Xe-bearing fayalite using our experimental set-up: controlled $fO_2$ atmosphere is needed (we ran PC128A in-between Pyrex powder, but it does not seem to help). Interestingly, large irregularly shaped holes (Figure D4) are observed in both recovered samples although no noble gas was identified. The irregular shape and large number of holes indicate that some unknown crystalline phase got destabilized upon opening of the capsules.

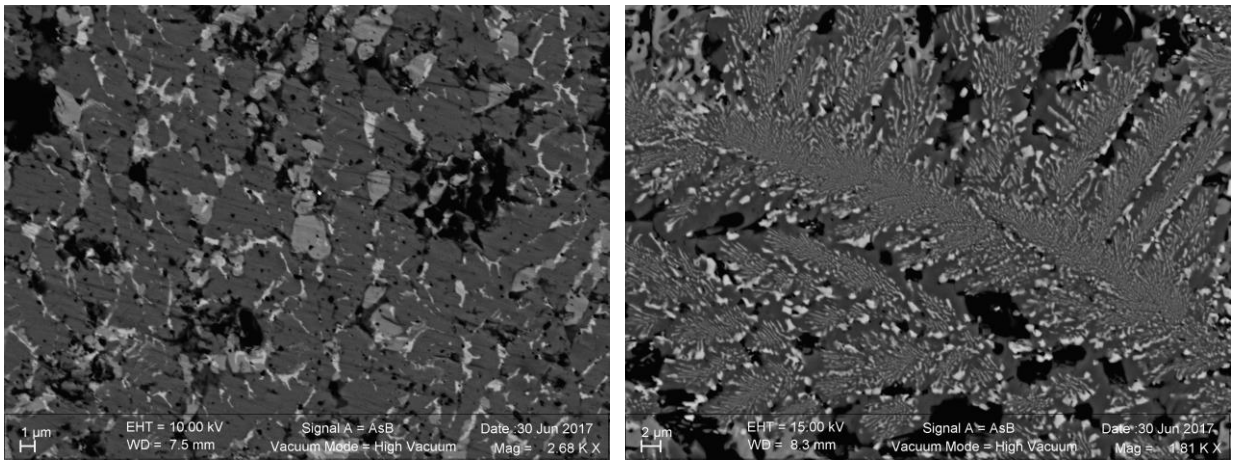


*a/ PC125A: hydrated fayalite $Fe_2SiO_4$ (intermediate grey with round shape). Pyroxene (dark grey constituting the matrix) and Fe-rich glass or iron oxide in bright. Black zones: empty irregularly shaped holes. No noble gas observed.*

*b/ PC128A: dry fayalite (intermediate grey on the right side). Dark grey: Px., bright zones: iron oxides, black zones: empty irregularly shaped holes. No noble gas observed.*

*Figure D4: SEM images in backscattered mode of fayalite samples.*

## II/ New constraints on Xe incorporation in olivine from First-principles calculations (Crépisson et al., 2018)

*Abstract*

Storage of Xe at depth in silicate minerals has recently been proposed to explain the low Xe abundance in the Earth's and Mars' atmospheres compared to other noble gases (the so-called 'Missing Xenon' issue). Evidences for incorporation, and thus reactivity of Xe in olivine at high pressure and high temperature are based on variations in cell parameters and the appearance of a new Raman band. To constrain the, so far only hypothetical, Xe incorporation mechanism in olivine, we theoretically investigated models of Xe-bearing olivine using density functional theory. Three types of incorporation mechanisms are tested: Xe for Si and Xe for Mg substitutions, and interstitial Xe. Xe for Si substitution, implying an oxidation of Xe, is found to be the only mechanism consistent with experimental observations, leading to an increase of cell parameter *a* and the appearance of a new Raman band around 720-750 $cm^{-1}$ associated with Xe-O stretching vibrations. Raman spectroscopy makes it possible to identify Xe incorporation site, even at low Xe content, due to high Xe polarizability. An estimation of Xe content in olivine, based on present work and previous *in situ* experimental results, shows that up to 0.4 at % Xe could be stored in olivine at depth.

### 1/ Introduction

Noble gases, highly volatile and poorly reactive elements, are of particular interest in Earth and planetary sciences to study and date the formation of the atmosphere (Avice and Marty, 2014) or to trace magmatic sources and degassing processes. Xenon, the heaviest of the noble gases, with nine stable isotopes ($^{124,126,128,129,130,131,132,134,136}Xe$), is at the heart of a long-standing question, the so-called 'Missing Xenon' issue. Elemental Xe, compared to other noble gases, is missing in the atmospheres of the Earth and Mars relative to chondritic abundances (Anders and Owen, 1977). According to Ozima and Podosek (1999), around 90% of Earth's primordial Xe is missing from the atmosphere. In addition, the atmospheres of Earth and Mars present a strong deficit in Xe light isotopes ($^{124,126,128}Xe$) (Krumennacher, 1962). Some Archean rocks present a Xe isotopic composition falling in between primitive chondritic and present-Earth atmospheric values, with an enrichment of the light non-radiogenic Xe isotopes relative to the present-Earth atmosphere of 2.1 (±0.3) % $amu^{-1}$ for a 3.5 Gy barite (Pujol et al., 2009), and 1 (±0.5) % $amu^{-1}$ for a 3.0 (±0.2) Gy quartz (Pujol et al., 2011). These findings indicate a storage and fractionation of Xe throughout the Archean (Avice and Marty, 2014) which could continue nowadays through subduction processes (Holland and Ballentine, 2006). Recently, a number of studies have supported storage of Xe in silicates at depth. Xe oxides have been synthesized: $XeO_2$ at ambient pressure and temperature (Brock and Schrobilgen, 2010), and $Xe_3O_2$ and $Xe_2O_5$ at respectively 97 GPa and 83 GPa, and at around 2000 K (Dewaele et al., 2016); as well as a Xe-bearing perovskite (Britvin et al., 2015) at ambient pressure. Furthermore, experiments brought evidence of Xe-incorporation in $SiO_2$ phases (Sanloup et al., 2002, 2005) and olivine (Sanloup et al., 2011) at crustal and upper mantle P-T conditions. If the presence of pure Xe oxides in the Earth is

unlikely, storage in silicates as a trace element may be a significant phenomenon in Xe retention at depth. Furthermore, a granite from the Sudbury impact structure (Kuroda et al., 1977) as well as siliceous sediments (Matsubara et al., 1988; Matsuda and Matsubara, 1989) have been found to be enriched in Xe by 2 to 3 orders of magnitude.

A detailed understanding of incorporation mechanisms of Xe, and reliable values of Xe solubility in minerals are presently needed to quantify the role of Xe incorporation in minerals in the context of the 'Missing Xenon' issue at the Earth's scale. Reliable partition coefficients are also needed to understand the fate of Xe in melting and crystallizing processes (from the magma ocean era to the current day magmatic processes). All available data on Xe-solubility in minerals are based on *ex situ* analyses of Xe-saturated samples, synthesized at high temperatures and, in some cases, at high pressures. Measured Xe solubility in olivine varies from 6.5 ppb down to 0.67 ppt (Broadhurst et al., 1992; Heber et al., 2007; Hiyagon and Ozima, 1986). Similarly, olivine melt partition coefficient varies from 90 to $6.10^{-4}$ (Broadhurst et al., 1992; Hiyagon and Ozima, 1986; Heber et al., 2007) and the compatibility (or not) of Xe in minerals remains controversial. In samples recovered from high pressure and temperature experiments, Xe is at least partly located in gas bubbles, and inconsistencies in Xe solubility and partition coefficient mainly stem from whether or not bubbles are analyzed, keeping in mind that their sizes range from the nm to the mm scale, and that part or all of these bubbles may form upon quenching to room conditions. Consequently, the evaluation of Xe content should be preferentially based on *in situ* measurements as proposed in the present study.

Recent experiments have focused on the incorporation mechanism of Xe in olivine, one of the most widespread terrestrial minerals. Sanloup et al. (2011) studied Xe-bearing San Carlos olivine up to 7 GPa and 2000 K by *in situ* x-ray diffraction and Raman spectroscopy reporting shifts of lattice parameters in presence of Xe at high pressure and for temperatures above Xe melting point. Cell parameter *a* increases, *c* decreases (although *c* is strongly temperature dependent) while *b* is not affected (Figure D5). This lattice distortion was interpreted as potentially due to Xe incorporation on Si sites, as Si release from olivine was observed. A new Raman mode, in presence of Xe, (disappearing within few minutes after quench) was also observed at 786 $cm^{-1}$ in presence of Xe at 0.9 GPa after heating at 1800 K. This new Raman band is close to the stretching of $XeO_4$ at 776 $cm^{-1}$ (Gerken and Schrobilgen, 2002), and is in the Si-O stretching region of olivine (Noël et al., 2006). As for other heavy rare gases, Ar was not observed to substitute to Si in olivine up to 7 GPa-2000 K (Sanloup et al., 2011). In the absence of studies devoted to the incorporation of Kr in minerals at depth, we can temporarily conclude that this mechanism is specific to Xe and of major relevance to the 'Missing Xe' issue.

First-principles calculations represent a powerful complementary approach to identify incorporation sites of trace elements in minerals. Regarding Xe in silicates only two theoretical studies are so far available. Probert (2010) investigated different incorporation mechanisms of Xe in $\alpha$-quartz, but the lack of related measurements prevents definitive conclusion. Kalinowski et al. (2014) investigated Xe incorporation in fibrous silica, which can be found on Earth in moganite or chalcedoine (Hopkinson et al., 1999). Computed Raman spectra of Xe-bearing fibrous silica possibly reproduce observations for Xe-rich quartz

(Sanloup et al., 2002) and $XeO_2$ (Brock and Schrobilgen, 2011).

In the present work, we study the structure, stability and vibrational properties of different incorporation sites of Xe in olivine, by means of first-principles calculations based on density functional theory (DFT). These theoretical results are then compared to the experimental data of Sanloup et al. (2011) to infer potential mechanisms of Xe storage in Earth's interior.

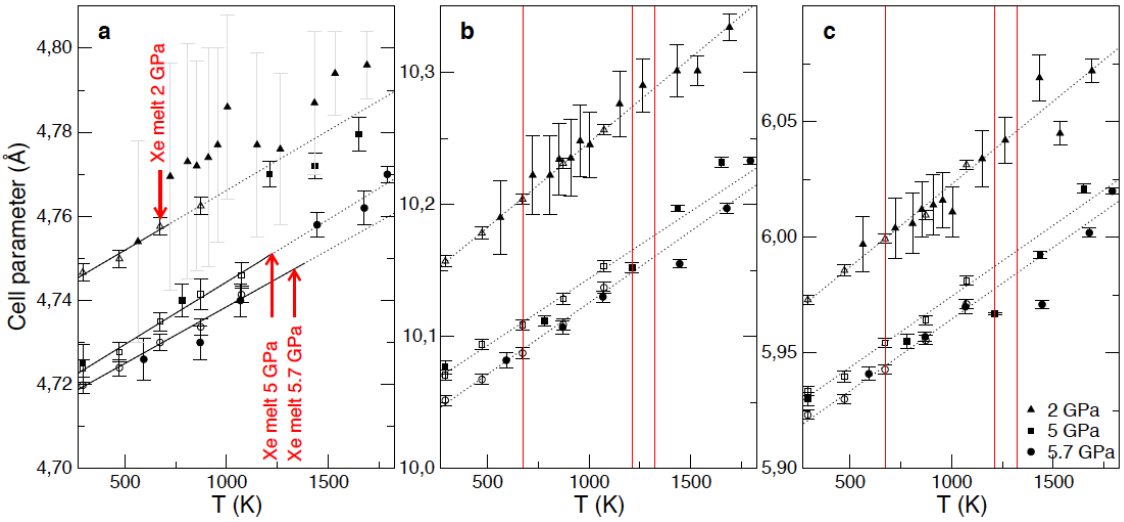


*Figure D5: Filled symbols are results for Xe-enriched olivine and empty symbols are data for San Carlos olivine Xe-free olivine, dotted line is thermal equation of state of forsterite. Figure from Sanloup et al. (2011).*

## 2/ Methods

Various systems are investigated: two reference compounds ($XeO_4$ molecule, $Xe_3O_2$ condensed phase); pure forsterite ($Mg_2SiO_4$, the Mg-rich end member of the olivine series,); Xe-bearing forsterite in which one Xe atom substitutes one Si (or Mg) atom or in which one Xe atom is added at an interstitial position. In all cases, the charge of the simulation cell is neutral. Xe-bearing forsterite is simulated using supercells of various sizes: 2x1x2, 4x1x2, 3x1x3, 4x2x4 (with respect to the forsterite unit cell containing 28 atoms) corresponding to a concentration of approximately 0.89, 0.45, 0.40, 0.11 at % Xe (or 5.5, 2.8, 2.5, 0.72 wt % Xe), respectively.

All calculations are done within density functional theory (DFT) and the generalized gradient approximation (GGA-PBE) of Perdew et al. (1996), by using the PWscf code of the Quantum ESPRESSO package http://www.quantum-espresso.org/; Gianozzi et al., 2009). Norm-conserving pseudopotentials (Troullier and Martins, 1991) are used. Electronic wave-functions (charge-density) are expanded up to an energy cut-off of 80 (480) Ry. Equilibrium structures are obtained after full relaxation of atomic positions and cell parameters (total energy is converged within 1 mRy/atom and forces to less than $10^{-4}$ Ry/au). Electronic k-point sampling of $Xe_3O_2$ and pure forsterite uses 6x16x10 and 2x1x2 shifted grids, while that of the Xe-bearing larger cells uses one shifted k-point. Spin polarized calculations were tested, obtaining zero magnetic moments for all the systems. Vibrational properties (dynamical matrices, dielectric constants, Born effective charges, and Raman tensor) are obtained within the approach of Baroni et al. (2001) and Lazzeri and Mauri (2003). For Raman tensors and

effective charges calculations a finer k-point sampling is used (4x2x4 grid for pure forsterite and a 2x2x2 one for Xe-bearing forsterites).
For the Xe-bearing forsterites, actual DFT calculations of the dynamical matrices (and, thus, of the interatomic force constants, IFCs) have been done only for the 2x1x2 cell. To simulate larger cells, we have used a force-matching approach similar to that of Lazzeri and Thibaudeau (2006). One considers a forsterite cell (larger than the 2x1x2 cell) containing one Xe atom: the IFCs among the atoms in the neighborhood of the Xe atom (a sphere centred on the Xe atom with a 6.35 Å radius i.e. containing ~ 80 atoms) are taken from the DFT calculations done on the 2x1x2 cell, the other IFCs (for atoms located further than 6.35 Å from the Xe atom) are taken from pure forsterite bulk calculations.
In the following, calculated Raman spectra are done in a back-scattering geometry and, unless otherwise stated, the spectra are obtained after averaging polarizations and sample orientation. We note that for the kind of systems presently studied, vibrational frequencies are generally underestimated by DFT-GGA calculations. To make the comparison with measurements easier, all theoretical frequencies are multiplied by a factor 1.05 (in order to match the most intense theoretical Raman bands of pure forsterite with the measured ones, Appendix D2) as in Lazzeri and Mauri (2003).

## 3/ Results

### a/ Reference compounds and pure forsterite

As a test, we calculated the structure of the $XeO_4$ tetrahedral molecule and $Xe_3O_2$ condensed phase (Table D3). For $XeO_4$, Xe-O bond length is 2.0% larger than the experimental value (Gundersen et al., 1970) whereas the one from Probert (2010) is 4.8% larger (Table D3). $Xe_3O_2$ was simulated at 97 GPa using the orthorhombic *Immm* space group as predicted by Herman and Schwerdtfeger (2014) and synthesized by Dewaele et al. (2016). Bond lengths are well reproduced (within 0.5%) whereas cell parameters are slightly different (within 1.5%) (Table D3).

| **$XeO_4$** | **This study** | **Calc.[a]** | **Exp.[b]** |
|---|---|---|---|
| Xe - O (Å) | 1.77 | 1.82 | 1.736 |
| **$Xe_3O_2$** | **This study** | **Calc.[c]** | **Exp.[c]** |
| *a* (Å) | 8.377 | 8.388 | 8.457 |
| *b* (Å) | 3.206 | 3.195 | 3.166 |
| *c* (Å) | 4.881 | 4.881 | 4.904 |
| $Xe^{4+}$- O (Å) | 2.01 | 2.01 | 1.99 |
| $Xe^{0}$-$Xe^{0}$ (Å) | 3.05 | 3.05 | 3.06 |
| $Xe^{4+}$-$Xe^{0}$ (Å) | 2.95-3.00 | 2.95-3.00 | 2.96-3.01 |
| $Xe^{4+}$- $Xe^{4+}$ (Å) | 3.21 | 3.19 | 3.17 |

*Table D3: Bond lengths and cell parameters of Xe reference compounds: $XeO_4$ molecule and $Xe_3O_2$ at 97 GPa. [a]Probert (2010), [b] Gundersen et al.(1970) and [c] Dewaele et al. (2016).*

Forsterite ($Mg_2SiO_4$) has an orthorhombic structure with three distinct oxygen sites (O1, O2 and O3), two distinct magnesium sites (Mg1 and Mg2) and one silicon site. Our calculated cell parameters for pure forsterite ($a$ = 4.78 Å, $b$ = 10.25 Å, $c$ = 5.99 Å) are in good agreement with single crystal X-ray diffraction measurements recorded on pure forsterite at ambient conditions, i.e. $a$ = 4.752(3) Å, $b$ = 10.193(8) Å, $c$ = 5.977(5) Å (Hazen et al., 1976). Similar values were obtained by previous studies using also GGA (which tends to increase cell parameters) and similar computational parameters (Balan et al., 2011). Born effective charges (Appendix D3) and calculated Raman frequencies of pure forsterite (Appendix D2) are in good agreement with the ones calculated by Noël et al. (2006). Computed polarized Raman spectra are in agreement with McKeown et al. (2011) (Appendix D5). The average Raman spectrum compares well with the experimental spectrum of San Carlos olivine (Sanloup et al., 2011). Presence of Fe in San Carlos olivine ($(Mg_{0.9}Fe_{0.1})_2SiO_4$) does not significantly change the average Raman spectrum compared to pure forsterite (Figure D10).

**b/ Xe incorporation models**

Three main types of Xe incorporation mechanisms are investigated: Xe for Si substitutions ($Xe_{Si}$), Xe for Mg substitutions (in Mg1 and Mg2 sites) ($Xe_{Mg1}$, $Xe_{Mg2}$), and Xe in interstitial site ($Xe_i$). We relaxed atomic positions at constant volume for these four mechanisms for 0.89 at % Xe. No significant change was observed in the configurations of Xe incorporation sites for more diluted defects (0.45 at % Xe or 0.40 at % Xe, depending on the supercell) or for simultaneous relaxation of atomic positions and cell parameters. The configurations and selected parameters of the four main Xe incorporation sites ($Xe_{Si}$, $Xe_{Mg1}$, $Xe_{Mg2}$ and $Xe_i$) are reported (Figures D6, D7, D8) following simultaneous relaxation of atomic positions and cell parameters at 0 GPa for 0.89 at % Xe. *.CIF* files for all configurations can be found in supplementary materials. One third of the trace of the Born effective charge tensor ($Z^{eff}$) is used to evaluate atomic charges, as discussed by Ghosez et al. (1998).

Xe incorporation sites can be described in terms of the closest surrounding oxygens. Indeed only oxygens are located within the sum of covalent radii that Xe forms with other elements (i.e. ~ 2 Å for oxygen). These oxygens appear to be strongly affected by the presence of Xe in term of variations of $Z^{eff}$ (Figures D6, D7, D8) compared to pure forsterite (Appendix D3). For the atoms located beyond the sum of covalent radii no significant variations of $Z^{eff}$ are observed.

*Most stable configurations of Xe incorporation sites*

For the most stable Xe for Si substitutions, Xe is located on the face of the oxygen tetrahedron (Figure D6). Xe is surrounded by one O1 and two O3 at a distance of ~ 2 Å forming a plane including Xe, with dihedral angles inferior to 2°. $Z^{eff}$ for Xe is slightly more positive than that for Si in pure forsterite (+ 2.85; Appendix D3). These charges significantly differ from the formal ones (+ 4). This indicates a covalent character of Xe-O bonds involving the closest oxygens (O1 and O3).

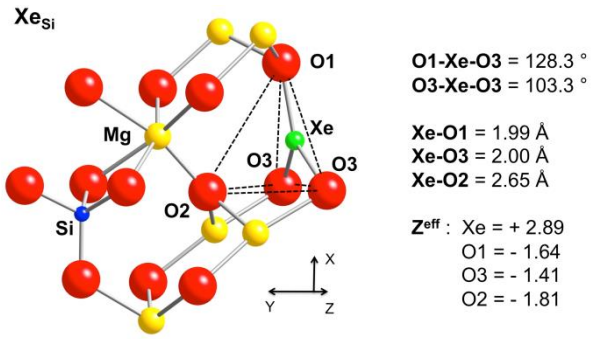


*Figure D6: Calculated structure of the $Xe_{Si}$ incorporation site in forsterite. Note the localization of the Xe on the face of the oxygen tetrahedron. Relevant O-Xe-O angles, Xe-O bond length, and one third of the trace of the Born effective charge tensor ($Z^{eff}$) are indicated. a, b, and c forsterite lattice parameters are along x, y, and z axes, respectively.*

Regarding Xe for Mg substitutions, $Xe_{Mg2}$ incorporation site was found more stable than $Xe_{Mg1}$ by 1.05 eV. For both configurations, Xe is located in the former oxygen octahedron. Nevertheless, two oxygen atoms are located close to the sum of covalent radii of Xe and O with Xe-O bond lengths ~ 2 Å whereas others O atoms are located significantly further (Figure D7). The geometry is nearly linear with angle O3*-Xe-O3* close to 180° for $Xe_{Mg2}$ and O2-Xe-O2 equal to 180° for $Xe_{Mg1}$. $Z^{eff}$ for Xe in $Xe_{Mg1}$ and $Xe_{Mg2}$ are slightly higher than that for Mg1 (+ 1.95) and Mg2 (+ 2.10) in pure forsterite (Appendix D3). The small excess of $Z^{eff}$ of Xe in these configurations, compared to charge of Mg in pure forsterite, is counterbalanced by more negative $Z^{eff}$ for the two closest oxygens (Figure D7) compared to pure forsterite (Appendix D3). These results suggest a covalent character of Xe-O bonds involving these oxygens.

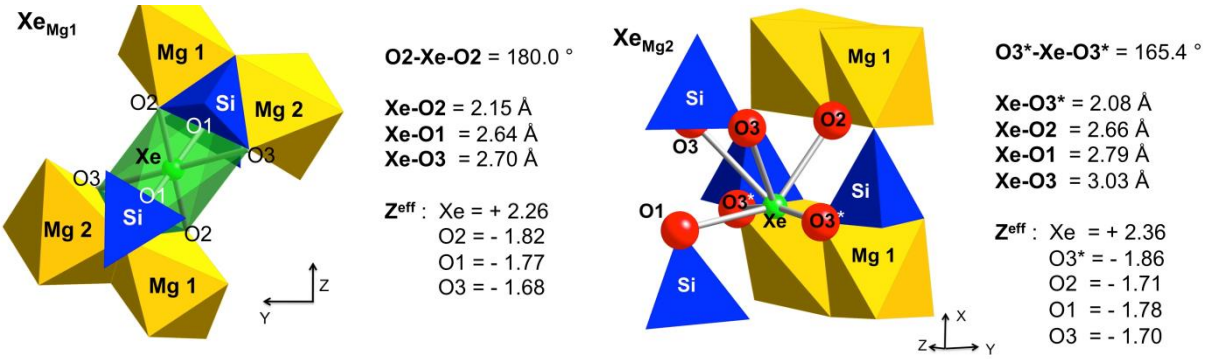


*Figure D7: Calculated structures of the $Xe_{Mg1}$ and $Xe_{Mg2}$ incorporation sites (see also figure D6 caption). O3 and O3* atoms are equivalent in pure forsterite.*

For $Xe_i$, no oxygen atoms are located within the sum of covalent radii of Xe and O (Figure D8). $Z^{eff}$ for Xe is close to 0 indicating that Xe is nearly neutral in this configuration. Small positive $Z^{eff}$ for Xe, is counterbalanced by slightly more negative $Z^{eff}$ for surrounding oxygens (Figure D8) compared to pure forsterite (Appendix D3). However, large Xe-O distances discard the possibility of covalency for Xe-O bond.

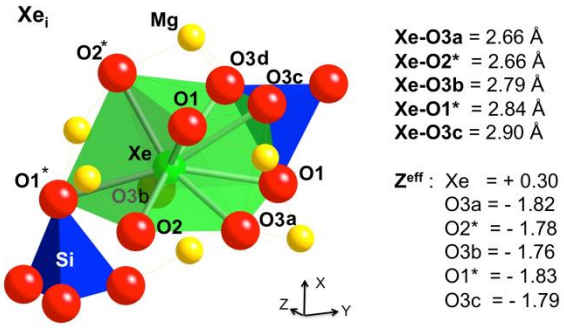


*Figure D8: Calculated structure of the $Xe_i$ incorporation site (see also figure D6 caption). O3a/O3b/O3c/O3d atoms (as O2/O2* and O1/O1*) are equivalent in pure forsterite. For clarity, only details for O within 3.05 Å around Xe are given.*

*Less stable configurations of Xe incorporation sites*

For Xe for Si substitution (which was found to best reproduce the experimental observations as further detailed), we investigated possible configurations by slightly moving Xe within the oxygen tetrahedron visible in figure D6. We identified another configuration: $Xe_{Si}$(b), less stable than $Xe_{Si}$ by 0.54 eV, where Xe is quasi aligned with O1 and O2 (O1-Xe-O2 = 157 °) though Xe remains inside the tetrahedron. For both $Xe_{Si}$ and $Xe_{Si}$(b) there exist *non symmetric variant* (respectively $Xe_{Si}$' and $Xe_{Si}$(b)') with Xe slightly shifted toward one of the two O3 of the oxygen tetrahedron so that symmetry of the Xe incorporation sites is broken. These *non symmetric variants* are slightly more stable than the corresponding symmetric variants by 55 meV (for $Xe_{Si}$ and $Xe_{Si}$') and 54 meV (for $Xe_{Si}$(b) and $Xe_{Si}$(b)'). We checked that these results are not due to incomplete convergence or artefacts of calculations. A major concern was Van der Waals interactions, which may be crucial for calculations involving noble gases. We therefore repeated our calculations after adding a correction for Van der Waals interactions via a pairwise atomic potential proportional to $R^{-6}$ (with R the distance between the atoms of a pair) as implemented by Barone et al. (2009) for DFT, based on results from Grimme (2006). We obtained similar geometries for the four configurations and similar relative stabilities as previously found. We only observe a small variation in differences of energies between configurations: from 0.54 eV to 0.68 eV between $Xe_{Si}$ and $Xe_{Si}$(b) and from 55 meV to 35 meV and from 54 meV to 46 meV, between respectively $Xe_{Si}$ and $Xe_{Si}$' and $Xe_{Si}$(b) and $Xe_{Si}$(b)'.

*Comparison with other systems*

In our calculation, the most stable Xe for Si substitutions (i.e. $Xe_{Si}$ and $Xe_{Si}$') present a planar geometry with Xe located on the face of the oxygen tetrahedron, surrounded by one O1 and two O3 (Figure D6). As emphasized by Kalinowski et al. (2014), a planar structure is common for Xe compounds: in particular under the form of $XeO_4$ units or chains present in $XeO_2$ (Brock and Schrobilgen, 2011), $Xe_3O_2$ and $Xe_2O_5$ (Dewaele et al., 2016). This planar geometry was also proposed for Xe incorporation in fibrous silica (Kalinowski et al., 2014) and in $\alpha$-quartz via Xe for Si substitution (Probert, 2010). Other examples of incorporations

associated with planar geometries have been reported on boron incorporation in olivine (Ingrin et al., 2014) and carbonate incorporation in fluor-apatite (Yi et al., 2013). In both cases, the carbon and boron atoms share significantly covalent bonds with surrounding oxygens.

Less stable configurations for Xe for Si substitution (i.e. $Xe_{Si}$(b) and $Xe_{Si}$(b)'), as well as Xe for Mg substitutions, present nearly linear geometries as in common compounds such as $XeF_2$ or noble gas hydrides.

For Xe for Si and Xe for Mg substitutions the nearest oxygen atoms have Xe-O bond lengths within the sum of the covalent radii of Xe and O (~ 2 Å) (Figures D6, D7). Also, the values of $Z^{eff}$ indicate a certain degree of covalency of Xe-O bonds. Xe-O bonds are thus likely to be at least partially covalent for the closest oxygen atoms. This result implies that Xe can react with olivine by oxidation processes.

*Energetics of the Xe-bearing models*

Let us define:

$\Delta E(Xe_{Si})=E(Xe_{Si})-E_{Xe}-E_{Fs\text{-}Si}$
$\Delta E(Xe_{Mg})=E(Xe_{Mg})-E_{Xe}-E_{Fs\text{-}Mg}$
$\Delta E(Xe_i)=E(Xe_i)-E_{Xe}-E_{Fs}$

where $E(Xe_{Si})$, $E(Xe_{Mg})$, $E(Xe_i)$ are the calculated energies for the cell used to simulate the different type of incorporation mechanisms ($Xe_{Si}$, $Xe_{Mg}$ and $Xe_i$). $E_{Xe}$ is the energy of an isolated Xe atom. $E_{Fs\text{-}Si}$ and $E_{Fs\text{-}Mg}$ are the energies of the forsterite cell with one neutral Si or Mg vacancy (the atomic structure was fully relaxed) and $E_{Fs}$ is the energy of a pure forsterite cell. The calculated ΔE values are reported in table D4 and represent the energy of the various incorporations in a forsterite presenting Si and Mg vacancies. Occurrence of Si and Mg vacancies in synthetic forsterite samples is suggested by the observation of related hydroxylated point defects (e.g. Lemaire et al. 2004, Balan et al. 2011, Ingrin et al. 2013, Balan et al. 2017, Blanchard et al. 2017). How the present ΔE values can be compared to measurements is questionable. Indeed, besides the fact that the vacancies in the calculations are neutral, temperature effects are not included. Both effects are expected to be relevant (Verna and Karki, 2009). That said, according to table D4, Xe incorporation in the Si vacancy site ($Xe_{Si}$) is more stable than Mg-vacancy ($Xe_{Mg}$) and interstitial ($Xe_i$) incorporations. A different conclusion would be reached if considering forsterite without vacancies. In this case the relative stability would be dominated by the formation energy of the vacancy itself, which is higher for Si than for Mg (Béjina et al., 2000, Stashans and Flores, 2013), as can be seen in Table D4 by comparing:

$\Delta E_v(Si) = E_{Fs\text{-}Si} - E_{Fs} + E_{Si}$
$\Delta E_v(Mg) = E_{Fs\text{-}Mg} - E_{Fs} + E_{Mg}$,

where $E_{Si}$ and $E_{Mg}$ are the energies of one atom of Si and Mg in the equilibrium diamond and *hcp* bulk, respectively.

The relative stability of the three different incorporation mechanisms (Table D4), $\Delta E(Xe_{Si}) < \Delta E(Xe_{Mg}) < \Delta E\ (Xe_i)$, results from an interplay of oxidation state and strain induced on the host structure. Although we cannot unambiguously disentangle these effects and determine which one dominates, we note that there is a correlation between the value of $\Delta E$ and the Xe oxidation estimated in Figures D5, D6, D7, D8: the more stable structures having the highest Xe oxidation (as it would be expected if oxidation was the only stabilization mechanism at play). On the other hand, the $\Delta E$ ordering can simply reflect the fact that different inclusions correspond to different volume increase of the host forsterite: the more stable structures corresponding to the smaller volume increase (bottom panel of Figure D9), as will be discussed in the next section.

| | **ΔE (eV)** | | **ΔEv (eV)** |
|---|---|---|---|
| **$Xe_{Si}$** | -0.12 | **Si** | 15.2 |
| **$Xe_{Mg1}$** | 2.75 | **$Mg_1$** | 8.9 |
| **$Xe_{Mg2}$** | 1.48 | **$Mg_2$** | 10.0 |
| **$Xe_i$** | 8.21 | | |

*Table D4: Formation energies for the different Xe incorporation mechanisms. $\Delta E$ and $\Delta E_v$ are defined in the text*.

### c /Cell parameters vs. Xe concentration

For each configuration, relaxation was done at 0, 2, 5 and 5.7 GPa for 0.89 at% Xe, 0.45 at% Xe and 0.40 at% Xe. Cell parameters are only shown at 0 GPa and 5.7 GPa (Figure D9), but the overall trend is similar at 2 GPa and 5 GPa (Appendix D4). We observe an increase of volume with increasing Xe content (+ 1.6% for Xe for Si substitutions, of + 2.3% for Xe for Mg substitutions, and + 4% for Xe in interstitial site at 0 GPa from 0 at% Xe to 0.89 at% Xe). However, variations of each cell parameters are strongly dependent on the Xe incorporation site (figure D9), and this can help to determine the likeliest incorporation site.

Variations of cell parameters for $Xe_{Si}$ incorporation site reproduce the experimentally observed increase of cell parameter *a* associated with very small variations of cell parameter *b* (Sanloup et al., 2011) compared to the thermal equation of state of olivine (Liu and Li, 2006). Other incorporation mechanisms do not reproduce this concomitant evolution of *a* and *b*. Experimental variations of cell parameter *c* are strongly *T*-dependent (Sanloup et al., 2011), therefore they are not used for comparison with calculations, as they are unlikely to be reproduced quantitatively by our calculations at 0 K. In contrast, the relative variations of *a* and *b*, between the pure and the Xe-bearing systems can be used to assess the concentration of Xe in olivine. For $Xe_{Si}$, calculated increase of cell parameter *a* from 0 at% Xe to 0.40 at% Xe, is about 0.4% at all investigated *P*. This increase is close to the experimentally observed one (i.e. + 0.2% at 2 GPa, + 0.4% at 5 GPa and + 0.2% at 5.7 GPa). Consequently the Xe content in olivine at high *P*-*T*, studied by Sanloup et al. (2011), can be estimated to be equal or

slightly less than 0.40 at% Xe. We note that the Xe content thus determined does not significantly vary with *P* between 2 GPa and 5.7 GPa.

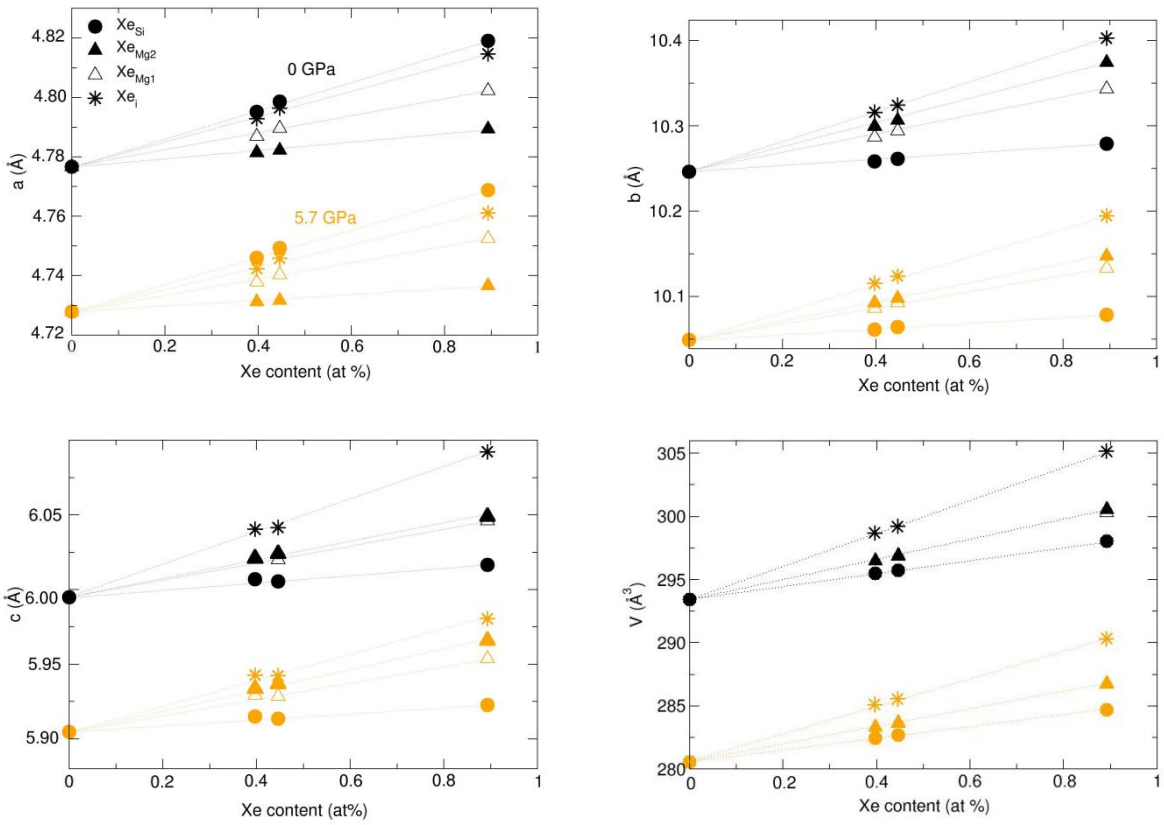


*Figure D9: Calculated evolution of cell parameters a, b, c and volume as a function of Xe content at 0 GPa (black symbols) and 5.7 GPa (orange symbols). Dotted lines are guides for the eyes.*

### d/ Raman spectra

Raman spectra were computed for 0.89 at% Xe (figure D10). The two most intense Raman bands of olivine at 822 $cm^{-1}$ and 855 $cm^{-1}$ are clearly visible for $Xe_{Si}$ and $Xe_{Mg2}$ incorporation sites. For $Xe_i$ and $Xe_{Mg1}$ these two olivine bands are mixed with other contributions linked to the presence of Xe. New well-resolved and intense Raman bands appear in the 650-800 $cm^{-1}$ region for $Xe_{Si}$ and, although less intense, for $Xe_{Mg1}$ (Figure D10). All these new Xe-related Raman bands involve the nearest oxygens around Xe (described and indexed in figures D6, D7, D8). For $Xe_{Si}$, the 720 $cm^{-1}$ band is linked to strong Xe-O1 stretching along the *a* axis (and weak stretching of a $SiO_4$ tetrahedron close to Xe also along *a* axis), whereas the weak 685 $cm^{-1}$ band is linked to Xe-O2 bending. For $Xe_{Mg1}$ the 739 $cm^{-1}$ band is linked to the two Xe-O2 twisting. A new well-resolved intense band is also visible for $Xe_{Mg2}$ at 900 $cm^{-1}$ linked to the two Xe-O3* symmetrical stretching with a wagging component. The bands are visible in parallel polarization along axis or planes corresponding to the maximal direction of the associated vibrational modes (Figure D10). For $Xe_i$ (which closest oxygen is only located at 2.66 Å), no new intense bands is observed.

For $Xe_{Si}$ and $Xe_{Mg}$, lots of poorly resolved bands are visible below 650 $cm^{-1}$ and above 800 $cm^{-1}$. These weak bands are linked to the high Xe polarizability, which implies that Xe presence will be felt by all atoms of the cell. In order to test this hypothesis, we calculate Raman spectra for lower Xe contents. Results for 0.11 at % Xe are shown in figure D11. Weak non-resolved bands below 650 $cm^{-1}$ and above 800 $cm^{-1}$ visible for 0.89 at % Xe (Fig. D10) disappear with decreasing Xe content. Furthermore, for all Xe incorporation sites, pure forsterite bands are well identified for 0.11 at % Xe not only at 822 $cm^{-1}$ and 855 $cm^{-1}$ but also at 340 $cm^{-1}$, 611 $cm^{-1}$, 882 $cm^{-1}$, 923 $cm^{-1}$, 964 $cm^{-1}$ (Fig. D11) implying that the presence of Xe is just felt locally as expected for a diluted defect.

For 0.11 at % Xe, Raman bands induced by Xe are still visible for $Xe_{Si}$ (at 720 $cm^{-1}$), $Xe_{Mg2}$ (at 900 $cm^{-1}$), and $Xe_{Mg1}$ (at 710 $cm^{-1}$). In contrast, spectra calculated for $Xe_i$ only present minor variations compared to pure forsterite. Presence of Xe in interstitial site can therefore not be evidenced by Raman spectroscopy.

We also computed Raman spectra for $Xe_{Si}$', $Xe_{Si}$(b) and $Xe_{Si}$(b)' for 0.89 at% Xe. Spectra show well-defined Xe-related bands at 745 $cm^{-1}$ for $Xe_{Si}$', 748 $cm^{-1}$ for $Xe_{Si}$ (b) and 750 $cm^{-1}$ for $Xe_{Si}$(b)' (Appendix D6) similar to the Xe-related band at 720 $cm^{-1}$ in Raman spectrum computed for $Xe_{Si}$ (Figure D10).

The bands observed between 720 $cm^{-1}$ and 750 $cm^{-1}$ for Xe for Si substitutions and at 710 $cm^{-1}$ for $Xe_{Mg1}$ are good candidates to explain the new Raman band observed by Sanloup et al. (2011) (Figure D11), keeping in mind that only $Xe_{Si}$ reproduces observed variations of cell parameters. Broadness of the experimental Raman band may be caused firstly by the coexistence of $Xe_{Si}$ , $Xe_{Si}$', $Xe_{Si}$(b) and $Xe_{Si}$(b)' at high *T*. It may also be caused by the chemical complexity of San Carlos olivine (see for instance trace and major element analyses of San Carlos olivine in Spandler and O'Neill, 2010). Indeed there exist a variety of Si vacancies, which slightly differs in terms of structural configuration and electronic properties due to Fe and trace elements. Distribution of Xe in these Si vacancies will lead to a range of slightly different vibration modes and consequently to a broad Raman signal as compared to the present ideal model. Eventually, the high *T* of measurement (1800 K) induces broadening of the bands (Kolesov and Geiger, 2004). In cases of band ascribed to chemical defects, this broadening can highly depends on the interaction of the trace element with its crystalline host (e.g. Balan et al., 2017).. High *T* may also induce a shift in Raman frequency, as observed for characteristic bands of forsterite (decrease of 15 $cm^{-1}$ from 273 K to 1473 K, Kolesov and Geiger, 2004).

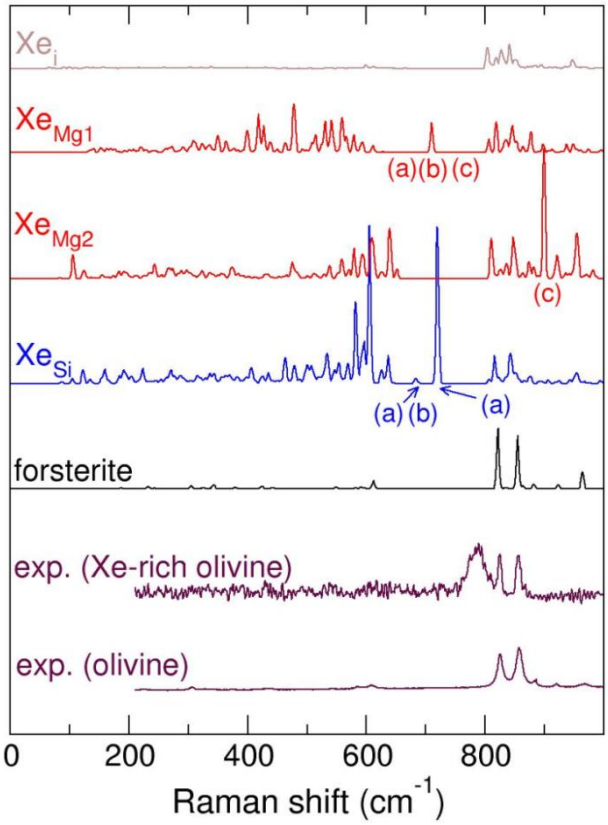


*Figure D10: Calculated Raman spectra of the different stable configurations of Xe incorporation in forsterite (0.89 at% Xe) and pure forsterite vs. measurements (exp.) from Sanloup et al. (2011). The spectrum on Xe-rich olivine was recorded at 0.9 GPa after quenching* T *from 1800K. The spectrum on Xe-free olivine was recorded at 0.9 GPa and 300 K before heating (i.e. before reaction of Xe with olivine). The labels associated with some calculated Xe-related bands indicate strong polarization: the bands are visible only in parallel polarization along specific axes (corresponding to the a, b, c lattice parameters).*

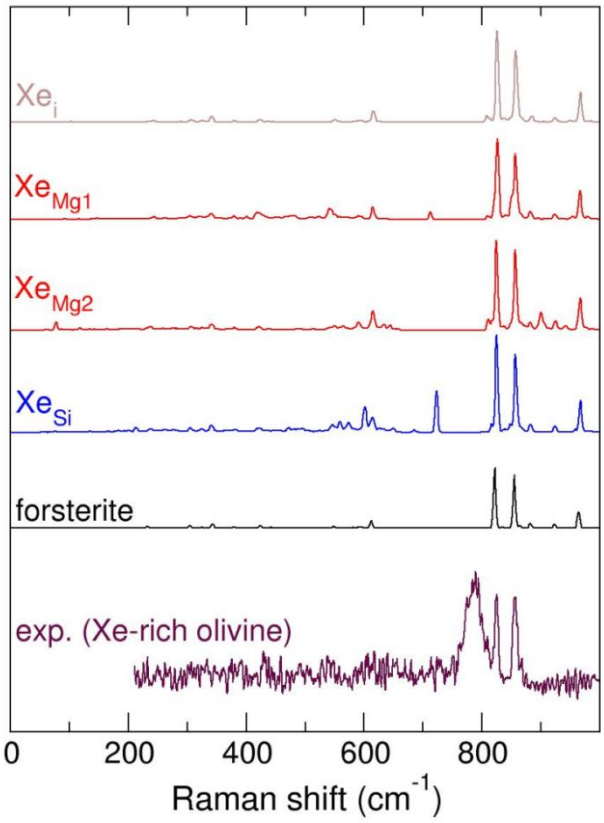


*Figure D11: Calculated Raman spectra of the different stable configurations of Xe incorporation in forsterite (0.11 at% Xe) and pure forsterite vs. measurements (exp.) from Sanloup et al. (2011).*

*Xe concentration from Raman spectra*

Our calculated Raman spectra can be used to constrain the experimental Xe content in olivine. Raman spectrum was computed for 0.45 at% Xe for $Xe_{Si}$ (Figure D12). The intensity of the Raman spectrum calculated for $Xe_{Si}$ was integrated within the four energy windows shown in figure D12. The intensity was, first, normalized to the integrated intensity in window "3" (corresponding to the characteristic olivine bands) and, then, the contribution from pure forsterite was subtracted. The normalized integrated intensity of Xe-related bands is linearly related to the Xe content (Figure D13). The corresponding value extracted from the measured Raman spectrum of Xe-rich olivine (Sanloup et al., 2011) is 2.3, which corresponds to ~ 0.2 at% Xe in figure D13. This evaluation must be considered as a first approximation and only represents a lower limit due to the significant signal to noise ratio in the

experimental spectrum. Comparing Raman spectroscopy and X-ray diffraction, the evaluation of Xe content based on XRD-determined cell-parameters variation (D/II/3/c) should be more reliable.

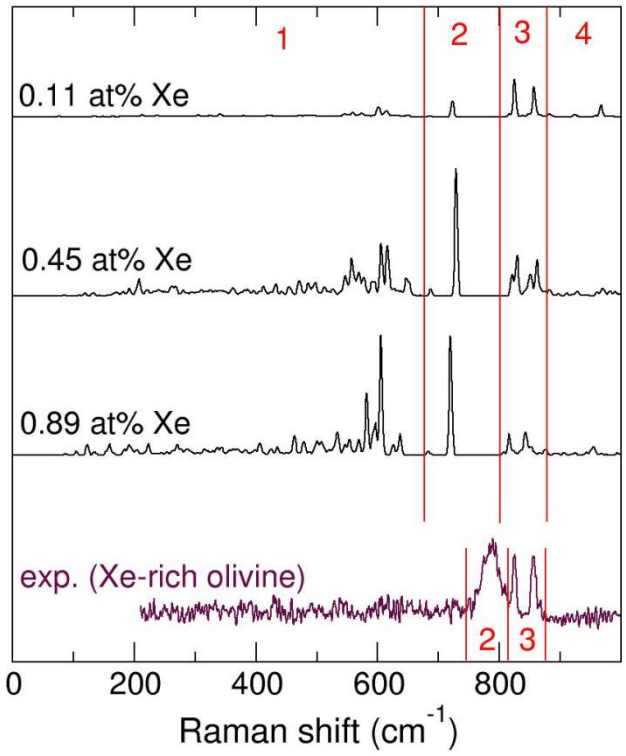


*Figure D12: Calculated Raman spectra for $Xe_{Si}$ for various Xe content. Measurements (exp.) from Sanloup et al. (2011). The four energy windows (1, 2, 3 and 4) used to integrate the intensity of Raman bands (see text) are shown.*

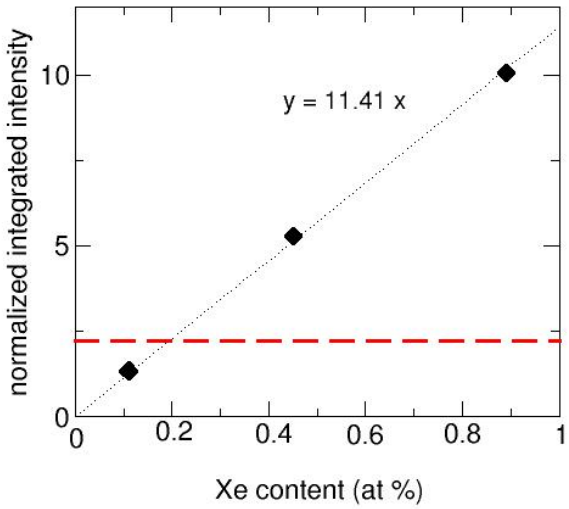


*Figure D13: Normalized integrated intensity of Xe-related Raman bands for $Xe_{Si}$ incorporation site as a function of Xe content from the present calculations. The dotted line is a linear fit. The horizontal dashed line indicates value for experimental Raman spectrum of Xe-rich olivine from Sanloup et al. (2011).*

## 4/ Conclusion

This work brings new insights on Xe storage at depth, attesting the possibility of Xe incorporation in olivine. We tested here three types of incorporation mechanisms: Xe for Mg and Xe for Si substitutions, and interstitial Xe. Only Xe for Si substitutions can reproduce the observed evolution of the cell parameters induced by Xe at different pressures (Sanloup et al., 2011): the increase of *a* is substantially more important than the increase of *b* (variations of *c*, which are strongly temperature dependent, are unlikely to be reproduced by zero temperature calculations). Furthermore, Xe for Si substitutions induce new Raman bands between 720 $cm^{-1}$ and 750 $cm^{-1}$ comparable with the broad band centred at 786 $cm^{-1}$ observed on Xe-rich San Carlos olivine (Sanloup et al., 2011). Besides these two main results, calculations reported in Table D4 also indicate that Xe for Si substitution might be the most stable from the energetic point of view. The results of table D4 are, however, to be taken only as a temptative estimation of the energetics, since calculations do not include temperature effects and consider vacancies as neutrally charged. Consequently, reactivity of Xe with the olivine is explained by substitution of Xe with silicon inducing Xe oxidation via formation of Xe-O bonds with an important degree of covalency. Presence of Fe and other redox sensitive trace elements may modulate the reactivity of Xe. Incorporation sites may also slightly change their geometries compared to pure forsterite as studied here.

Raman spectroscopy turns out to be a valuable tool for the study of Xe incorporation in minerals. According to our findings, the high Xe polarizability makes it possible to retrieve a Xe signature for 0.11 at % Xe, and likely below. Moreover, the strong polarization of the Xe-related bands could, in principle, allow to discriminate experimentally among different incorporation mechanisms.

As detailed in the introduction, evaluation of Xe content based on *in situ* measurements is strongly needed. The present calculations can be used to estimate the Xe content in olivine from the *in situ* measurements (Sanloup et al., 2011). This has been done in two independent ways: i) by comparing the calculated and the X-ray diffraction measured values of cell parameters; ii) by comparing the Xe-related Raman-band intensities. According to i) or ii), the Xe concentration is ~ 0.40 at % Xe or ~ 0.20 at % Xe, respectively. We judge 0.40 at % Xe to be more reliable and 0.20 at % Xe should be simply used as a lower boundary. However, the qualitative agreement between the two values is very encouraging, suggesting that future improvements of the present simplified structural model (based on a simple model of iron-free olivine) could provide a theoretical calibration to determine Xe-content from Raman measurements.

Using previously determined Xe solubility value of 0.2 - 0.4 at % for olivine, at 0.9 GPa and 1800 K, and a value of 0.08 mol% Xe for a tholeitic melt at 1.5 GPa and 1773 K (Schmidt and Keppler, 2002), we found a partition coefficient for olivine/tholeitic melt ($^{ol./melt}D_{Xe}$) of 2.5 - 5. A value of $^{ol./melt}D_{Xe}$ close to, or higher than 1, in agreement with Hiyagon and Ozima (1986) and Broadhurst et al. (1992), challenges the supposedly incompatible behaviour of Xe in olivine. However, our value of $^{ol./melt}D_{Xe}$ significantly differs from Heber et al. (2007) ($^{ol./melt}D_{Xe} = 6.10^{-4}$). Heber et al. (2007) evaluated the Xe content of

olivine exclusively on regions free of bubbles and melt inclusions, on the basis that they might have formed upon quenching at ambient conditions, and if so, did not reflect the equilibrium at high pressure and temperature. In contrast Hiyagon and Ozima (1986) and Broadhurst et al. (1992) extracted Xe by heating the whole sample. Our result thus questions the actual quest for free-bubble analysis of recovered samples as a guaranty of reliable estimates of Xe content at high pressure and temperature in corresponding melt or minerals.

Sanloup et al. (2011) observed Xe incorporation in olivine approximately throughout the entire range of lithospheric mantle P/T conditions. Assuming that olivine represents 60% of the mantle volume (Bina, 1998), and that 90% of the Earth's primordial Xe is missing from the atmosphere (Ozima and Podosek, 1999), storing the entire amount of the 'Missing Xe' in the olivine of the upper mantle requires a Xe content in olivine of 0.012 ppb. This estimate is much lower than the solubility value of 0.4 at % (i.e. 2.5 wt % Xe) found here, hence the entire amount of the 'Missing Xe' could be stored in the upper mantle.

Although more data are needed on the dependence of Xe solubility in olivine on olivine chemical composition (e.g. Fe and other trivalent cations), pressures and temperatures, but also in other minerals, these preliminary results prove that storage of Xe at depth can no longer be discarded in the 'Missing Xenon' issue.

To our knowledge, there is currently no data available on the potential isotopic fractionation of Xe during incorporation in minerals. However, it could be a key to explain particular terrestrial Xe isotopic compositions, such as the observed $^{136}$Xe enrichment in mantle xenoliths of Mt Quincan (North Queensland, Australia), Victoria (Southeastern Australia) and Reunion Island, which cannot be explained by mass dependent fractionation (Czuppon et al., 2009).

## III/ *In situ* IR spectroscopy on Xe-bearing olivine

### 1/ Methods

*In situ* IR spectra were collected on Xe/Ar-bearing olivine PC128B (Mg#92, Table D1), at 2.0 ± 0.3 GPa and up to 773 K. High *P-T* conditions were generated by a resistive-heating DAC. A Re gasket was pierced with two holes, one was loaded with KCl used as a transparent background, and one with a thin compressed platelet of the sample and further filled with KCl. Experiments were conducted on beamline SMIS at SOLEIL synchrotron (Figure C19). *P* was determined using fluorescence of a ruby sphere located in the sample chamber, and *T* was read from a type-K thermocouple located near the diamond tip. IR spectra were retrieved from 650 $cm^{-1}$ to 4000 $cm^{-1}$ with a resolution of 0.5 $cm^{-1}$ and accumulation of 100 scans, repeated 4 times. A MCT detector, frequently cooled by liquid nitrogen, was used. The background used for subtraction was measured through KCl after each sample measurement.

2/ Results and discussion

Above Xe melting curve i.e. ≥ 673 K at 2 GPa (Ferreira and Lobo, 2008), a new peak appears at 718 ± 3 $cm^{-1}$, in addition to olivine IR signal (Figure D14). This new peak is attributed to Xe incorporation in olivine, as Ar is unlikely to react with olivine as shown by Sanloup et al. (2011). Moreover, Ar is classically used as a *P*-transmitting medium. We calculated at 0 GPa IR spectra for pure forsterite and for Xe for Si substitution ($Xe_{Si}$) in forsterite (Figure D6) for 0.89 at% Xe, using similar *ab initio* computational parameters as described in D/II/2/. Theoretical forsterite IR signal compares well with experimental signal recorded at room-*T* on Xe/Ar-bearing olivine. IR signal of $Xe_{Si}$ presents two small peaks at 690 $cm^{-1}$ and at 730 $cm^{-1}$ which could correspond to the new observed peak. Similarly as mentioned for Raman spectra, presence of Fe in the experimentally investigated olivine is likely to modify signal compared to theoretical spectra for Xe incorporation in pure forsterite. However this new IR data are supporting results from Crépisson et al. (2018) (D/II).

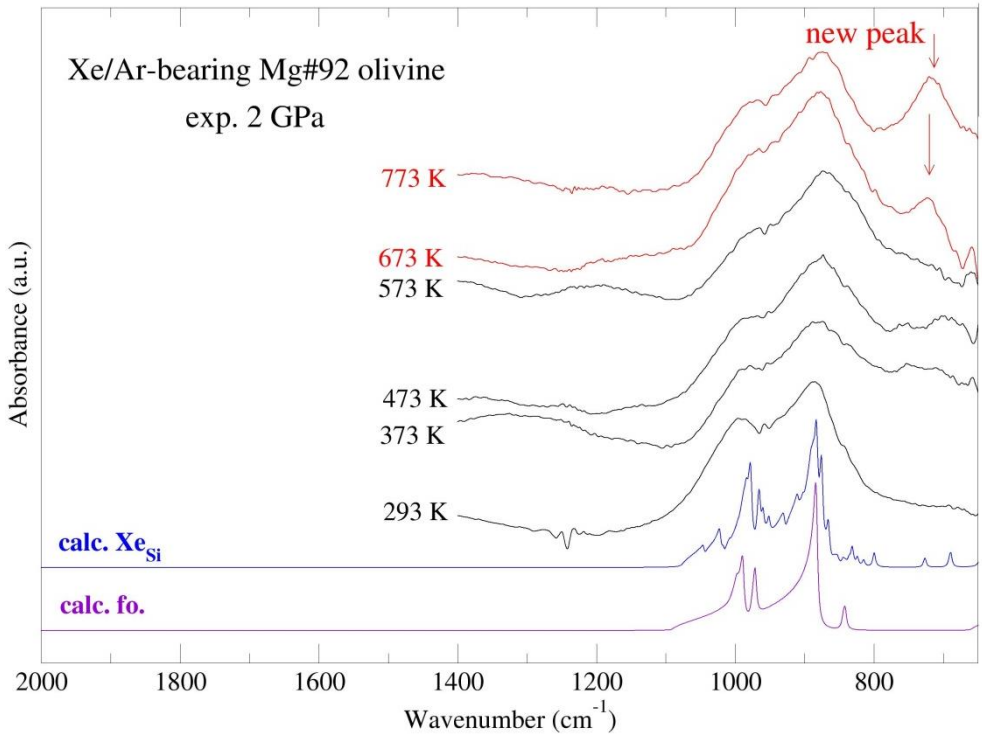


*Figure D14: IR spectra for Xe/Ar-bearing olivine (PC128B). Experimental (exp.) IR spectra recorded at high* P-T *conditions below (black) and above (red) Xe melting curve. Calculated (calc.) spectra for pure forsterite (fo.) and for Xe for Si substitution in pure forsterite ($Xe_{Si}$), calculated spectra were shifted to easily compare with the experiment.*

## IV/ New *in situ* X-ray diffraction on synthetic olivine

In order to better understand the role of Fe and of trivalent elements on Xe incorporation in olivine, we performed new *in situ* X-ray diffraction. Sanloup et al. (2011) acquired data on natural San Carlos olivine ($(Mg_{0.9}Fe_{0.1})_2SiO_4$ + trivalent elements) and we acquired in this work new data on synthetic olivine $(Mg_{0.9}Fe_{0.1})_2SiO_4$. The initial aim was to

investigate Xe incorporation in olivine with various Fe contents, although it was only possible to investigate one Fe content within this PhD thesis.

1/ Methods and samples

*In situ* X-ray diffraction data were collected on a Xe/Ar-bearing olivine (PC128B, Mg#92) and on plain olivine (PC99A, Mg#100) up to 6.9 GPa and 1339 K. High *P-T* conditions were generated by resistive-heating DAC. Experiments were conducted on beamline I15 at Diamond Light Source in July 2017 using a round 70 micron-radius beam at 29.2 keV. Xe/Ar-bearing and plain olivine samples were loaded in two holes of 150 micron pierced in a single Re gasket to simultaneously investigate both compositions. *T* was determined from power / *T* calibration from De Grouchy (PhD thesis, 2016). *P* was determined by fluorescence of a ruby sphere at ambient *T*, and upon heating from unit-cell volume of a Pt grain inserted on the verge of the sample chamber using equation of state from Fei et al. (2004). During each measurement the cell was oscillated from -5° to +5° to avoid intensity artifacts from potential preferential orientation. Four runs were performed, namely HT2-1, HT2-2, HT2-4, RT1-2 (Table D5) (HT2-1 and HT2-2 have the same gasket). RT1-2 plain sample has likely underwent significant Re contaminated due to diffusion from Re gasket at the very high *T* reached and is not presented here.
Image plates were integrated with DIOPTAS (Prescher and Prakapenka, 2015). Le Bail refinements of crystal cell parameters were performed with GSAS software (Larson and Von Dreele, 2000).

Recovered samples (within Re gaskets) were coated without other sample preparation, and analyzed by SEM and EMP (Table D5). Neither Xe nor Ar was retrieved in recovered samples. In addition to olivine, pyroxenes were also identified (they only appear as minor contribution in X-ray diffraction spectra). Recovered samples from run HT2-1 and HT2-2 (both plain and Xe/Ar-bearing samples) are homogeneous, with olivine and few pyroxenes identified by SEM. Xe/Ar bearing samples HT2-4-Xe/Ar and RT1-2-Xe/Ar present a phase separation, between a Fe-poor olivine with a slight proportion of pyroxene (Mg#99.8 (1) for HT2-4-Xe/Ar and Mg#96.0 (9) for RT1-2-Xe/Ar), and a $Mg_{1.8}Fe_{0.2}SiO_4$ phase (similar to the starting material) are observed (Figure D15).

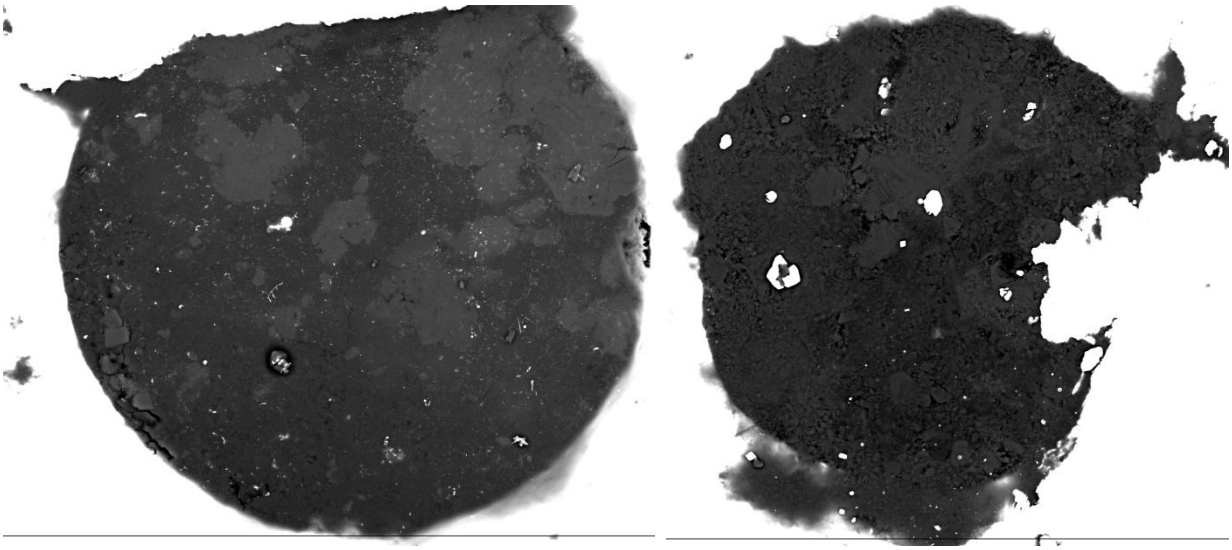

*Figure D15: SEM images in backscattered mode, showing phase separation between Fe-poor olivine, Mg#96-100 (dark zones), and Fe-rich olivine, Mg#91-92 (light zones) for HT2-4-Xe/Ar (left), and RT1-2-Xe/Ar (right). Diameter of the holes is 150 µm.*

| Sample | minerals | MgO | $SiO_2$ | $Al_2O_3$ | CaO | FeO | NiO | $Re_2O_7$ | Total | Mg# |
|---|---|---|---|---|---|---|---|---|---|---|
| **HT2-1-plain** | ol. + px. | 51.3 (3) | 41 (2) | 0.1 (2) | 0.05 (2) | 6 (4) | 0.07 (5) | 0.3 (4) | 99 (1) | 94 (4) |
| **HT2-1-Xe/Ar** | * | 46 (2) | 41 (1) | 0 (1) | 0.09 (2) | 8.3 (5) | 1.3 (5) | 3.3 (7) | 100 (2) | 90.8 (5) |
| **HT2-4-plain** | ol. | 49.8 (6) | 41.3 (6) | 0.00 (2) | 0.05 (3) | 9.2 (4) | 0.00 (3) | 0.03 (8) | 100.5 (5) | 90.6 (4) |
| **HT2-4-Xe/Ar dark zone** | ol. + px. | 54.8 (9) | 42.5 (6) | 0.00 (1) | 0.03 (3) | 0.2 (1) | - | 0.9 (4) | 98.6 (9) | 99.8 (1) |
| **HT2-4-Xe/Ar light zone** | ol. | 48 (1) | 40.7 (9) | 0.01 (2) | 0.06 (1) | 8.5 (8) | 0.01 (3) | 1.1 (4) | 98 (1) | 90.9 (9) |
| **RT1-2Xe/Ar dark zone** | ol. + px. | 51.7 (8) | 43.0 (7) | 0.00 (2) | 0.08 (3) | 4.0 (9) | 0.00 (2) | - | 98.8 (6) | 96 (1) |
| **RT1-2- Xe/Ar-light zone** | ol. | 50 (1) | 40.5 (7) | 0.1 (1) | 0.07 (5) | 8.2 (7) | - | 0.2 (7) | 99 (2) | 91.5 (5) |

*Table D5: Average chemical composition in oxide wt%, and Mg# of the recovered samples (from Appendix D7). HT2-2 and HT2-1 have same gasket. Standard deviation on the last digit is given in bracket. Minerals are determined from calculation of atomic formula unit. * Presence of Re from the gasket precludes this treatment for HT2-1-Xe/Ar. Starting material composition (PC99A and PC128B) is given in Table D2. ol. = olivine and px. = pyroxene.*

## 2/ Results and discussion

### a/ X-ray diffraction

As already reported for olivine (Sanloup et al., 2011), the unit-cell volume of olivine in presence of Xe is systematically larger up to 2.6%, at all investigated *P*, than the volume predicted by the equation of state from Liu and Li (2006) for Mg#90 olivine, i.e. similar to Xe-bearing sample (Table D6). For HT2-1-plain and HT2-2-plain, volume is smaller than predicted by the equation of state (Table D6), as starting material was Fe-free (PC99A, Mg#100), whereas the equation of state used considers olivine with Mg#90. For HT2-4-plain volumes fall in between those of plain sample and Xe/Ar-bearing samples, thus HT2-4-plain

is likely a mix of plain and Xe/Ar-bearing olivine starting materials, which occured during loading. For HT2-1-plain and HT2-2-plain the presence of a little amount of Xe/Ar-bearing starting material cannot be discarded as recovered samples present a small amount of Fe (Table D5).

Cell parameters were corrected from *P* (Appendix D8), using third-order isothermal Birch Murnaghan equation of state, with 'bulk modulii' for cell parameters and their first derivatives with *P* from Abramson et al. (1997). Error bars due to the correction were evaluated by comparing corrected data from Liu and Li (2006) at a given *T* and at different *P*, by taking the largest differences as a conservative error bar estimate (i.e. ± 0.008 Å for cell parameter *a*, ± 0.01 Å for *b*, and ± 0.007 Å for *c*). An increase of all cell parameters in presence of Xe is observed compared to plain samples (Figure D16).

This result differs from Sanloup et al. (2011), who only observed an increase of cell parameter *a* above Xe melting point, whereas our data points, at the exception of two data points, are all below Xe melting curve (Table D6). The fact that Sanloup et al. (2011) did not observe any variation of cell parameters below Xe melting point could indicate that Xe incorporation is potentially controlled by diffusion of Xe which was initially loaded as a pure phase surrounding silica in experiments from Sanloup et al. (2011), in contrast to our experiment where the starting material was already Xe-doped. Moreover, Xe incorporation mechanisms could differ below and above Xe melting point, as observed for quartz in chapter E. Interstitial Xe and / or Xe for Mg substitutions in olivine below Xe melting point could explain the increase of all cell parameters observed here, following theoretical results previously presented for forsterite (Figures D7, D8, D9).

| Sample | *T* (K) | *P* (GPa) | *a* (Å) | | *b* (Å) | | *c* (Å) | | V (Å$^3$) | | $V_{th}$ (Å$^3$) | excess V (%) |
|---|---|---|---|---|---|---|---|---|---|---|---|---|
| **HT2-1-Xe/Ar** | | | | | | | | | | | | |
| 229453 | 298 | 4.3 | 4.7604 | (3) | 10.1882 | (8) | 5.9789 | (3) | 289.98 | (2) | 283.20 | 2.3 |
| 229460 | 372 | 3.6 | 4.7625 | (3) | 10.1978 | (9) | 5.9853 | (3) | 290.69 | (3) | 285.13 | 1.9 |
| 229474 | 520 | 1.7 | 4.7683 | (2) | 10.2251 | (7) | 5.9979 | (3) | 292.43 | (2) | 290.50 | 0.7 |
| *229486 | 647 | 1.6 | 4.7702 | (3) | 10.2415 | (7) | 6.0057 | (3) | 293.41 | (2) | 292.06 | 0.5 |
| 229497 | 795 | 2.6 | 4.7721 | (3) | 10.2470 | (7) | 6.0089 | (3) | 293.83 | (2) | 291.30 | 0.9 |
| *229508 | 947 | 3.0 | 4.7740 | (3) | 10.2542 | (7) | 6.0134 | (3) | 294.38 | (2) | 292.03 | 0.8 |
| 229520 | 1123 | 4.6 | 4.7767 | (2) | 10.2593 | (7) | 6.0171 | (3) | 294.87 | (2) | 290.04 | 1.6 |
| 229540 | 298 | 3.8 | 4.7581 | (3) | 10.2094 | (7) | 5.988 | (3) | 290.88 | (2) | 284.16 | 2.3 |
| **HT2-1-plain** | | | | | | | | | | | | |
| 229465 | 372 | 0.9 | 4.7521 | (2) | 10.1932 | (3) | 6.0014 | (3) | 290.7 | (2) | 290.830 | 0.0 |
| 229480 | 520 | 0.0 | 4.7594 | (2) | 10.2221 | (3) | 6.0122 | (3) | 292.51 | (1) | 294.490 | -0.7 |
| 229491 | 647 | 0.0 | 4.7638 | (2) | 10.2352 | (3) | 6.0166 | (3) | 293.36 | (1) | 296.000 | -0.9 |
| 229502 | 795 | 0.4 | 4.7660 | (2) | 10.2404 | (2) | 6.01756 | (3) | 293.69 | (1) | 296.840 | -1.1 |
| 229513 | 947 | 1.0 | 4.7567 | (2) | 10.2237 | (4) | 6.0096 | (4) | 292.25 | (2) | 297.230 | -1.7 |
| 229529 | 1123 | 2.1 | 4.7700 | (3) | 10.2376 | (5) | 6.0162 | (5) | 293.79 | (2) | 296.550 | -0.9 |
| 229545 | 298 | 0.0 | 4.7534 | (2) | 10.1832 | (3) | 5.9865 | (2) | 289.77 | (1) | 292.130 | -0.8 |
| **HT2-2-Xe/Ar** | | | | | | | | | | | | |
| 229643 | 298 | 4.1 | 4.7561 | (2) | 10.2036 | (7) | 5.9826 | (3) | 290.34 | (2) | 283.580 | 2.3 |

| | | | | | | | | | | | | |
|---|---|---|---|---|---|---|---|---|---|---|---|---|
| 229659 | 373 | 4.1 | 4.7594 | (3) | 10.2093 | (9) | 5.9848 | (3) | 290.8 | (2) | 284.140 | 2.3 |
| 229672 | 523 | 3.4 | 4.7650 | (2) | 10.2223 | (9) | 5.9939 | (3) | 291.96 | (2) | 286.810 | 1.8 |
| 229685 | 674 | 3.6 | 4.7662 | (3) | 10.2329 | (7) | 6.0029 | (3) | 292.77 | (2) | 287.770 | 1.7 |
| 229695 | 802 | 4.5 | 4.7681 | (2) | 10.2408 | (8) | 6.0072 | (3) | 293.32 | (2) | 287.010 | 2.2 |
| 229707 | 960 | 5.2 | 4.7709 | (2) | 10.2476 | (8) | 6.0118 | (3) | 293.92 | (2) | 286.970 | 2.4 |
| 229717 | 1133 | 5.9 | 4.7737 | (3) | 10.2535 | (9) | 6.016 | (3) | 294.47 | (3) | 287.050 | 2.5 |
| 229727 | 1160 | 5.7 | 4.7741 | (2) | 10.2594 | (8) | 6.0178 | (3) | 294.75 | (2) | 287.780 | 2.4 |
| 229740 | 298 | 3.5 | 4.7603 | (3) | 10.2218 | (8) | 5.9931 | (3) | 291.62 | (2) | 284.750 | 2.4 |
| **HT2-2-plain** | | | | | | | | | | | | |
| 229649 | 298 | 0.06 | 4.7519 | (1) | 10.1813 | (2) | 5.9896 | (2) | 289.78 | (1) | 291.990 | -0.8 |
| 229664 | 373 | 0 | 4.7554 | (2) | 10.1925 | (3) | 5.9943 | (2) | 290.54 | (1) | 292.890 | -0.8 |
| 229677 | 523 | 0 | 4.7617 | (1) | 10.2139 | (3) | 6.007 | (2) | 292.15 | (1) | 294.530 | -0.8 |
| 229690 | 674 | 0.09 | 4.7639 | (1) | 10.2270 | (2) | 6.012 | (2) | 292.91 | (1) | 296.100 | -1.1 |
| 229700 | 802 | 0.79 | 4.7659 | (2) | 10.2326 | (3) | 6.0171 | (3) | 293.44 | (1) | 295.900 | -0.8 |
| 229712 | 960 | 1.49 | 4.7680 | (2) | 10.2402 | (2) | 6.0207 | (2) | 293.97 | (1) | 296.070 | -0.7 |
| 229722 | 1133 | 2.36 | 4.7721 | (1) | 10.2475 | (2) | 6.0254 | (3) | 294.66 | (1) | 295.970 | -0.4 |
| 229732 | 1160 | 2.3 | 4.7745 | (2) | 10.2528 | (3) | 6.0292 | (3) | 295.15 | (1) | 296.480 | -0.5 |
| 229745 | 298 | - | 4.7522 | (2) | 10.1851 | (2) | 5.9893 | (2) | 289.90 | (1) | - | - |
| **HT2-4-Xe/Ar** | | | | | | | | | | | | |
| 229953 | 298 | 6.9 | 4.7377 | (4) | 10.1350 | (1) | 5.9504 | (3) | 285.71 | (3) | 278.460 | 2.5 |
| 229964 | 523 | 4.0 | 4.7597 | (3) | 10.2118 | (6) | 5.9892 | (3) | 291.10 | (2) | 285.560 | 1.9 |
| 229974 | 609 | 3.2 | 4.763 | (3) | 10.2241 | (6) | 5.9971 | (2) | 292.07 | (2) | 288.020 | 1.4 |
| 229982 | 722 | 4.3 | 4.766 | (3) | 10.2279 | (6) | 6.0006 | (2) | 292.48 | (2) | 286.700 | 2.0 |
| 229992 | 914 | 4.7 | 4.769 | (3) | 10.2308 | (6) | 6.0086 | (3) | 293.16 | (2) | 287.650 | 1.9 |
| 230000 | 1052 | 5.9 | 4.772 | (3) | 10.2479 | (6) | 6.0081 | (2) | 293.83 | (2) | 286.270 | 2.6 |
| 2300013 | 298 | 3.9 | 4.761 | (3) | 10.2019 | (7) | 5.9887 | (2) | 290.86 | (2) | 283.970 | 2.4 |
| **HT2-4-plain** | | | | | | | | | | | | |
| 229948 | 298 | 8.1 | 4.7399 | (5) | 10.0350 | (9) | 5.9141 | (6) | 281.30 | (4) | 276.420 | 1.7 |
| 229960 | 523 | 4.0 | 4.7557 | (4) | 10.1543 | (5) | 5.9544 | (3) | 287.54 | (2) | 285.560 | 0.7 |
| 229970 | 609 | 3.2 | 4.7647 | (5) | 10.1616 | (5) | 5.9630 | (3) | 288.71 | (3) | 288.030 | 0.2 |
| 229978 | 722 | 3.6 | 4.7624 | (4) | 10.1714 | (4) | 5.9673 | (3) | 289.06 | (3) | 288.240 | 0.3 |
| 229988 | 914 | 5.5 | 4.7620 | (4) | 10.1840 | (4) | 5.9751 | (2) | 289.77 | (2) | 285.870 | 1.3 |
| 229997 | 1052 | 5.7 | 4.7690 | (4) | 10.1926 | (4) | 5.9807 | (2) | 290.72 | (2) | 286.720 | 1.4 |
| 230007 | 298 | - | 4.7535 | (3) | 10.1700 | (4) | 5.968 | (3) | 288.51 | (4) | - | - |
| **RT1-2-Xe/Ar** | | | | | | | | | | | | |
| 229756 | 298 | 3.6 | 4.7441 | (3) | 10.1794 | (7) | 5.972 | (7) | 288.4 | (2) | 284.550 | 1.3 |
| 229777 | 373 | 3.4 | 4.7465 | (3) | 10.1831 | (5) | 5.9729 | (3) | 288.7 | (2) | 285.540 | 1.1 |
| 229791 | 523 | 2.6 | 4.7531 | (3) | 10.1994 | (5) | 5.9895 | (3) | 290.37 | (2) | 288.530 | 0.6 |
| 229805 | 600 | 2.6 | 4.7545 | (3) | 10.2047 | (5) | 5.9905 | (3) | 290.65 | (2) | 289.270 | 0.5 |
| 229820 | 657 | 3.1 | 4.7578 | (3) | 10.2117 | (5) | 5.9910 | (3) | 291.08 | (2) | 288.720 | 0.8 |
| 229830 | 780 | 3.6 | 4.7604 | (3) | 10.224 | (5) | 5.9971 | (3) | 291.88 | (2) | 288.810 | 1.1 |
| 229856 | 793 | 4.0 | 4.7596 | (3) | 10.2217 | (5) | 5.9969 | (4) | 291.76 | (2) | 288.030 | 1.3 |
| 229864 | 875 | 4.2 | 4.7562 | (3) | 10.2261 | (6) | 6.0006 | (3) | 291.86 | (2) | 288.400 | 1.2 |
| 229881 | 993 | 4.6 | 4.7575 | (3) | 10.2306 | (6) | 6.0028 | (3) | 292.17 | (2) | 288.680 | 1.2 |
| 229888 | 1052 | 4.9 | 4.7556 | (3) | 10.2315 | (5) | 6.0060 | (3) | 292.23 | (2) | 288.580 | 1.2 |
| 229902 | 1150 | 5.4 | 4.7635 | (3) | 10.2377 | (6) | 6.0047 | (4) | 292.83 | (2) | 288.390 | 1.5 |
| 229912 | 1241 | 5.9 | 4.7645 | (3) | 10.2414 | (6) | 6.0068 | (4) | 293.11 | (2) | 288.110 | 1.7 |
| 229920 | 1339 | 6.4 | 4.7650 | (3) | 10.2479 | (6) | 6.0096 | (4) | 293.45 | (2) | 287.870 | 1.9 |
| 229933 | 298 | 3.2 | 4.7574 | (3) | 10.2135 | (5) | 5.9878 | (3) | 290.94 | (2) | 285.340 | 1.9 |

*Table D6: Cell parameters, volumes (V) and predicted volumes ($V_{th}$) of Xe/Ar-bearing and plain olivines for this work. Errors on* P *and* T *are ± 0.3 GPa and ± 50 K. error on predicted volume is ± 0.6 Å$^3$. * indicates data points above Xe melting point. Numbers on the left are numbers of the acquired spectra.*

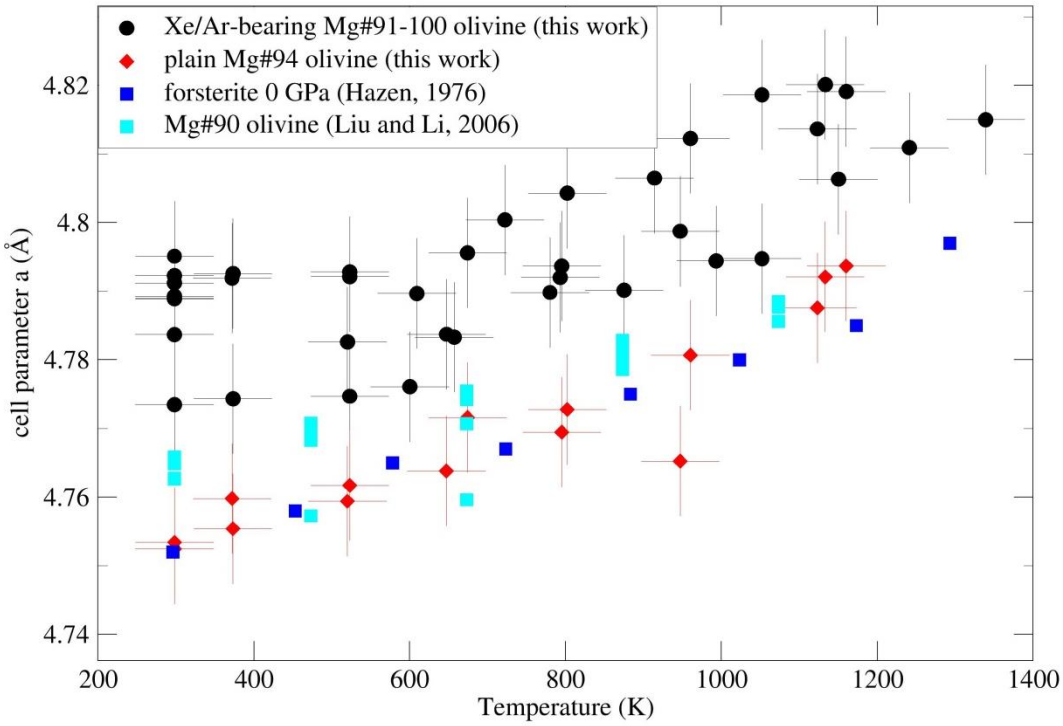


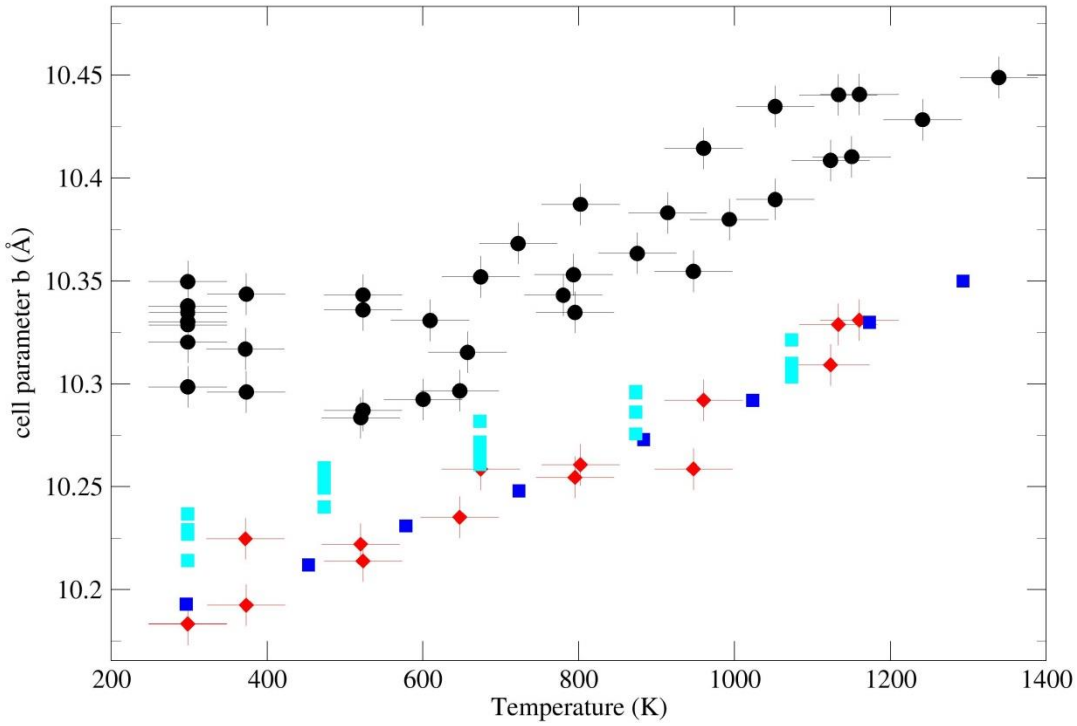

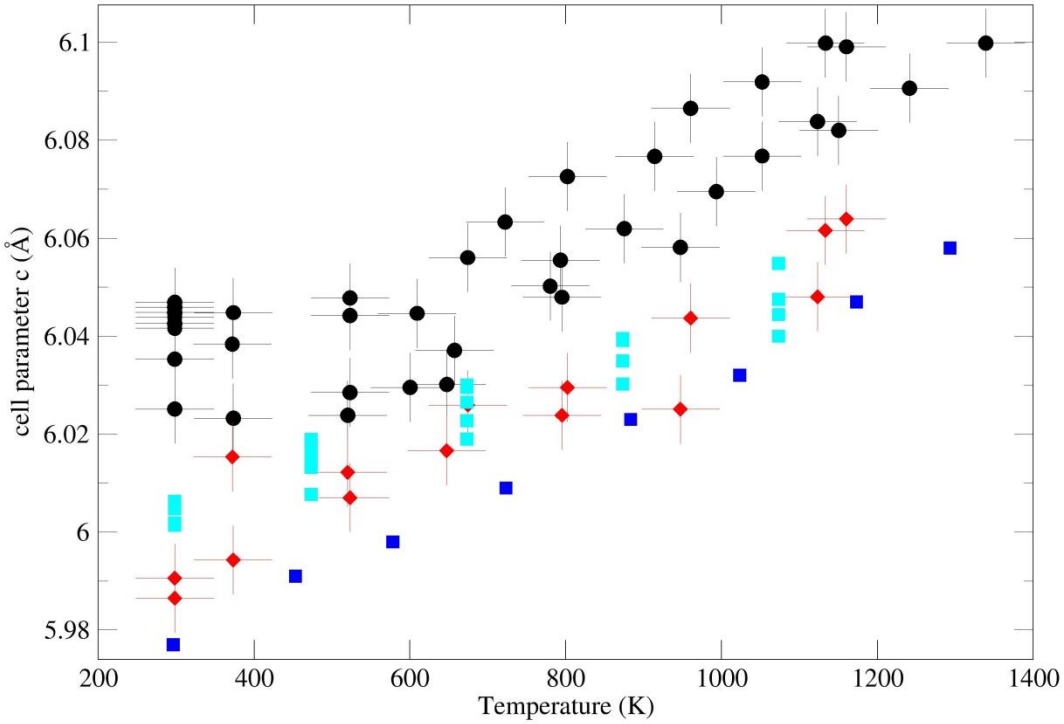


*Figure D16: Evolution of olivine cell parameters, after correction from* P *effect as described in the text for San Carlos olivine (Liu and Li, 2006), and for this work: Xe/Ar-bearing olivine ( HT2-1-Xe/Ar, HT2-2-Xe/Ar, HT2-4-Xe/Ar, and RT1-2-Xe/Ar) and plain olivine (HT2-1-plain and HT2-2-plain). Pure forsterite (Hazen, 1976) is also shown.*

## V/ Conclusion

In this chapter Xe incorporation in olivine at *P-T* conditions relevant for upper mantle conditions was elucidated: Xe incorporation occurs via a Xe for Si substitution, with the creation of short, at least partially covalent Xe-O bonds (~ 2 Å) above Xe melting point (Crépisson et al., 2018; D/II). New *in situ* X-ray diffraction data acquired below Xe melting point could indicate that Xe could be incorporated via another mechanism at lower *T* (D/IV).

In dry piston cylinder press experiments using Pt capsule, Fe is retained in the olivine mineral only in presence of Xe. Moreover, a phase separation is observed between a Fe-rich olivine and a Fe-poor olivine in presence of Xe which echoes the phase separation observed in sanidine between a Fe-rich (and Xe-rich) sanidine and a Fe-poor sanidine (F/I). Preliminary results on fayalite could indicate the formation of volatile phases (possibly Xe-rich) under high *P-T* conditions, destabilizing upon quenching. Fe and Xe are thus likely to stabilize each other, although more experiments are needed.

Eventually, presence of a water fluid phase in the Pt capsule during piston cylinder press synthesis prevents Xe incorporation in olivine, indicating that Xe is entirely going into the fluid phase, on the contrary of what is observed for feldspathic melt (G/I).

## Chapter E: XE INCORPORATION IN QUARTZ

Quartz is a widespread continental crust mineral present under two forms: a low-*T* phase (α-quartz) and a high-*T* phase (β-quartz); α-quartz transforming into β-quartz at 848 K at ambient *P* (Kihara, 1990; Carpenter et al., 1998). Previous X-ray study of the Xe-$SiO_2$ system (Sanloup et al., 2005) showed an extension of the quartz stability field and the formation of platinum silicides inside the Pt capsule attesting the release of Si from quartz. These observations led to the hypothesis that Si reduction had been triggered by Xe through Xe for Si substitution reaction. We performed here new experiments and reinvestigated previous experimental data from Sanloup et al. (2005). The Xe-$SiO_2$ system was investigated at *P-T* conditions ranging from 0.7 GPa to 2.7 GPa and up to 1900 K, by *in situ* X-ray powder diffraction and *in situ* IR spectroscopy. *P-T* conditions are relevant for the continental crust, with highest *P-T* conditions relevant for orogenic contexts, where continental crust can reach 80 km depth (~2.2 GPa) and 1473 K under the Tibetan plateau (Jimenez-Munt et al., 2008). Experimental data were complemented by *ab initio* calculations to solve Xe incorporation mechanisms. This work is to be submitted at *Geochemistry, Geophysics, Geosystems* as **The Xe-$SiO_2$ system at moderate pressure and high temperature**.

.

### I/ Sample synthesis

Noble gases-bearing quartz samples were synthesized in previous work at 3.5 GPa and 1100°C for 24 hours using a piston cylinder press from $SiO_2$ powder + Xe/Ar gaseous mix (PC64 Qz.) or $SiO_2$ glass + Xe/Kr gaseous mix (PC66). In recovered samples, noble gases are seen at grain boundaries and in extrinsic defects present in the crystals (Figure E1).

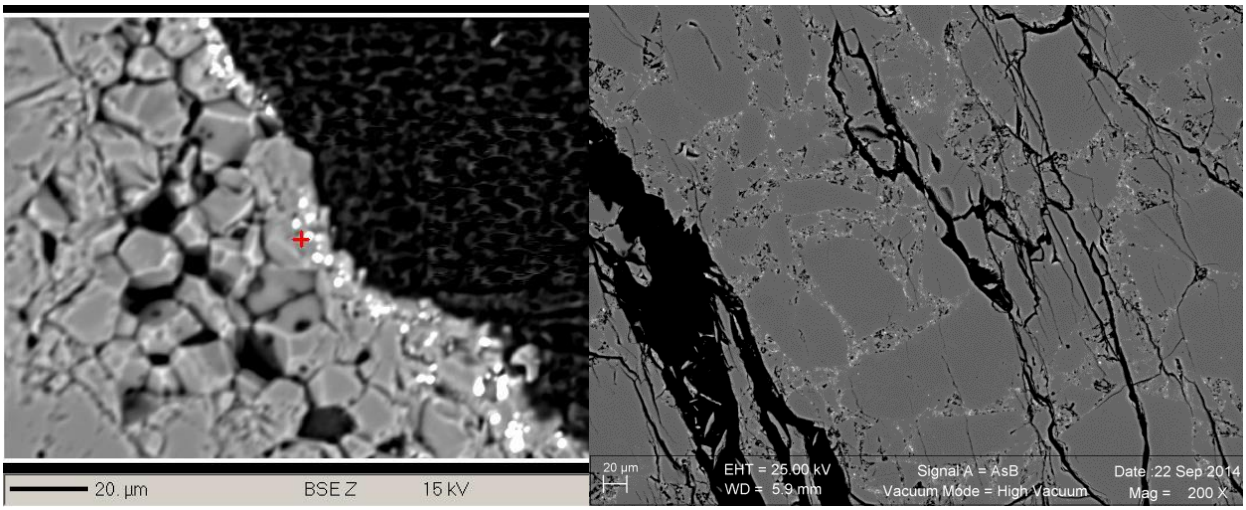


*Figure E1: SEM image of PC64 Qz. (left) and PC66 (right) in backscattered mode.*

## II/ The Xe-$SiO_2$ system at moderate *P* and high *T* (submitted to $G^3$)

### 1/ Methods

#### a/ X-ray diffraction

Two sets of *in situ* X-ray diffraction experiments are used here. The first set (XRD1) was collected on $SiO_2$ ($SiO_2$ as cristoballite or as Herasil glass) plus Xe gas loaded in a Pt capsule using a Paris Edinburgh cell up to 1 GPa and 1900 K at 71.68 keV on beamline ID27 at the European Synchrotron Radiation Facility (Sanloup et al., 2005). Second set (XRD2) was collected on Xe/Ar-bearing quartz (PC64 Qz, Figure E1). *In situ* X-ray diffraction data were collected up to 2.7 GPa and 900 K using resistive-heating DAC. Experiments were conducted on beamline P02.2 at Petra III synchrotron source using a 3x8 $\mu m^2$ beam at 42.7 keV. *P* was determined using unit-cell volume of a Pt grain inserted on the verge of the sample chamber, and *T* was read from a type-K thermocouple located near the diamond tip. During each measurement, the cell was oscillated from -3° to +3° to avoid intensity artefacts from potential preferential orientation. Image plates were integrated with Fit2D (Hammersley, 1997) or DIOPTAS (Prescher and Prakapenka, 2015). Le Bail refinements of crystal cell parameters were performed with GSAS software (Larson and Von Dreele, 2000).

#### b/ Infrared spectroscopy

*In situ* IR spectra were collected on the same Xe/Ar-bearing quartz as used for XRD2 (i.e. PC64 Qz), at 1.0(3) GPa and up to 773 K using resistive-heating DACs. Two chambers were drilled in a Re gasket, one was loaded with KCl used as a transparent background, and the other with a thin compressed platelet of the sample and further filled with KCl. Experiments were conducted on beamline SMIS at SOLEIL synchrotron (Figure C19). *P* was determined using fluorescence of a ruby sphere located in the sample chamber, and *T* was read from a type-K thermocouple located near the diamond tip. IR spectra were retrieved from 650 $cm^{-1}$ to 4000 $cm^{-1}$ with a resolution of 0.5 $cm^{-1}$ and accumulation of 100 scans, repeated 4 times. A MCT detector, frequently cooled by liquid nitrogen, was used. The background used for subtraction was measured through KCl after each sample measurement. IR spectra were smoothed using Savitzki-Golay filter.

#### c/ *Ab initio* calculations

All calculations were done within the density functional theory (DFT) and using the generalized gradient approximation (GGA-PBE) of Perdew et al. (1996), with the PWscf code of the Quantum espresso package http://www.quantum-espresso.org/; Gianozzi et al., 2009). The same norm-conserving pseudopotentials (Trouiller and Martins, 1991) as in Crépisson et al. (2018) are used. Electronic wave-functions (charge-density) are expanded up to an energy cut-off of 80 (480) Ry. For the new (Xe,Si)$O_2$ phase, electronic k-points sampling use a 2x4x4 centred grid for the unit-cell, and a 2x1x1 centred grid for the 1x3x3 supercell. For α-quartz unit-cell, electronic k-points sampling uses a 2x2x2-centred grid, while for the 2x2x2

and 3x3x3 supercells, calculations are restricted to the center of the Brillouin zone. These computational parameters allow the total energy to be converged within 1mRy/atom. For all investigated systems, the charge of the simulation cell is neutral, and spin-polarized calculations were tested, obtaining zero magnetic moments. Equilibrium structures are obtained after full relaxation of atomic positions and cell parameters until convergence of forces on atoms to less than $10^{-4}$ Ry/au. Born effective charges are obtained within the approach of Baroni et al. (2001). Born effective charges ($Z^{eff}$) are used to evaluate atomic charges as discussed by Ghosez et al. (1998). Following the same procedure as Balan et al. (2011), vibrational modes and corresponding IR absorption spectra were calculated from the dynamical matrix.

2/ Results and discussion

**a/ Increase of unit-cell volume of quartz in presence of Xe**

As reported for olivine (Sanloup et al., 2011; Crépisson et al., 2018), the unit-cell volume of quartz is systematically larger by up to 4.2%, in presence of Xe, than the volume predicted by the equations of state of plain quartz (Table E1). Presence of Ar is unlikely to affect the unit-cell volume of quartz as Ar is classically used as a *P*-transmitting medium. For α-quartz, the excess volume presents a minimum at 468-565 K, which is the Xe melting point at the *P* of the experiment, possibly indicating a different Xe environment in α-quartz below and above Xe melting point. For β-quartz, data were all collected above Xe melting point. It is not possible to evaluate cell distortions as there is no available thermal equation of state for cell parameters of quartz at our *P*-*T* conditions. For α-quartz, predicted volumes are calculated with second-order Birch Murnaghan equation of state using parameters from Wang et al. (2015), and for β-quartz, from first-order thermal Birch Murnaghan equation of state, with $K_T$ obtained from linear interpolation of data from Dorogokupets (1995), thermal expansion from Bourova et al. (1998), and volume at 0 GPa and 848 K from Kihara (1990).

To theoretically determine Xe incorporation mechanism in quartz, two supercells were built: 2x2x2 and 3x3x3 (relative to the unit-cell of α-quartz, i.e. 9 atoms), and corresponding respectively to 1.4 at% Xe and 0.41 at% Xe. Xe for Si, Xe for O substitutions ($Xe_{Si}$, $Xe_O$), and interstitial Xe ($Xe_I$) were investigated. Structures were fully relaxed at 0 GPa, 1.2 GPa and 2.65 GPa. Relaxed configurations are similar at all *P* and Xe contents, and comparable to results from Probert (2010).
In $Xe_{Si}$ configuration, Xe is located in a quasi-linear environment, surrounded by two O atoms at 1.98-2.00 Å (i.e. within the sum of covalent radii that Xe forms with O, ~ 2 Å) while the next two O atoms, not located in the same plane as the two closest ones, are at 2.27-2.28 Å (Figure E2). $Z^{eff}$ for Xe in $Xe_{Si}$ (+ 2.8) is smaller than for Si (+ 3.4) in pure α-quartz (Appendix E1), which is counterbalanced by slightly less negative $Z^{eff}$ for the four closest O atoms (Figure E2, Appendix E1). In $Xe_O$ configuration, the closest Xe neighbor is Si atom at 2.5(1) Å (i.e. within the sum of covalent radii that Xe forms with Si, ~ 2.5 Å). $Z^{eff}$ for Xe in $Xe_O$ (+ 0.54) significantly differs from that for O (- 1.7) in pure α-quartz (Appendix E1), which is counterbalanced by smaller $Z^{eff}$ for the two closest Si, and more negative $Z^{eff}$ for the

three surrounding O compared to that for Si and O in pure α-quartz (Figure E2, Appendix E1). In $Xe_I$ configuration, we find no atoms within the sum of covalent radii that Xe forms with O or Si. Xe introduces a slight $Z^{eff}$ excess (+ 0.13), counterbalanced by less negative $Z^{eff}$ for the four closest O compared to pure α-quartz (Figure E2, Appendix E1). It must be noted that $Z^{eff}$ for Xe dramatically varies as a function of the incorporation mechanism.

An increase of unit-cell volume is observed in presence of Xe for all incorporation mechanisms, *P*, and Xe contents, (Table E2 and Appendix E2) in contrast to Probert (2010) who observed a decrease of volume at 0 GPa for $Xe_{Si}$ followed by an increase at higher *P*. The significantly smallest excess volume is obtained in the case of Xe for Si substitution. This suggests that Xe for Si substitution is the likeliest Xe incorporation mechanism in quartz, as shown by our previous study on Xe-bearing olivine (Crépisson et al., 2018).

α- and β-quartz structures are both hexagonal with same site multiplicities, and only differ by minor variations of bond lengths and angles (Kihara, 1990). Due to structural similarity, results from *ab initio* calculations on Xe incorporation at 0 K are thus expected to be similar for both phases, with Xe for Si substitution being the likeliest Xe incorporation mechanism.

| ***P* (GPa)** | ***T* (K)** | **cell parameters *a*, *c* (Å)** | **observed V(Å$^3$)** | **predicted V (Å$^3$)** | **excess V (%)** | **Phase** |
|---|---|---|---|---|---|---|
| 2.65 | 298 | 4.860(1)<br>5.378(3) | 110.00(4) | 106.56 | 3.1 | α-quartz |
| 2.05 | 371 | 4.873(1)<br>5.378(3) | 110.58(4) | 108.03 | 2.3 | α-quartz |
| 1.26 | 468 | 4.893(1)<br>5.378(3) | 111.51(3) | 110.23 | 1.1 | α-quartz |
| 1.2 | 565 | 4.900(1)<br>5.392(2) | 112.12(3) | 110.72 | 1.2 | α-quartz |
| 1.62 | 685 | 4.910(1)<br>5.390(2) | 112.51(3) | 109.97 | 2.3 | α-quartz |
| 1.93 | 771 | 4.912(1)<br>5.394(2) | 112.73(3) | 109.39 | 3 | α-quartz |
| 2.55 | 873 | 4.918(1)<br>5.384(3) | 112.80(3) | 108.04 | 4.2 | α-quartz |
| 1.01 | 1591 | 4.976(2)<br>5.459(4) | 117.06(4) | 115.94 | 0.97 | β-quartz |
| 1.03 | 1581 | 4.977(2)<br>5.434(3) | 116.44(3) | 115.95 | 0.42 | β-quartz |
| 0.96 | 1651 | 4.977(2)<br>5.435(4) | 116.59(4) | 115.74 | 0.73 | β-quartz |
| 0.95 | 1429 | 4.9741(9)<br>5.517(2) | 118.22(3) | 116.46 | 1.51 | β-quartz |
| 0.85 | 1520 | 4.9806(4)<br>5.4252(7) | 116.55(1) | 116.41 | 0.12 | β-quartz |

*Table E1: Experimental quartz cell parameters and volume compared to predicted volume for plain quartz. For data on α-quartz, errors on* P *and* T *are 0.2 GPa and 50 K, and error on predicted volume is ± 0.5 Å$^3$. For β-quartz, errors on* P *and T are 0.3 GPa and 50 K, and error on predicted volume is ± 0.4 Å$^3$. Uncertainty on the last digit is given in brackets.*

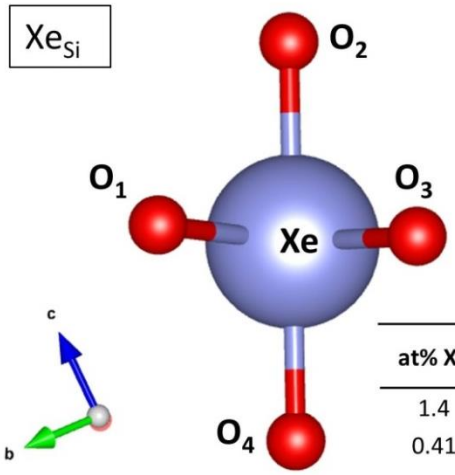


$Z^{eff}$

**Xe = + 2.8**

**$O_1 = O_3 = -1.4$**

**$O_2 = O_4 = -1.6$**

| at% Xe | Xe-$O_1$ = Xe-$O_3$ (Å) | Xe-$O_2$ = Xe-$O_4$ (Å) | $O_2$-Xe-$O_4$ (°) | $O_1$-Xe-$O_3$ (°) |
|---|---|---|---|---|
| 1.4 | 2.28 | 1.98 | 175.5 | 71.0 |
| 0.41 | 2.27 | 2.00 | 178.2 | 69.6 |

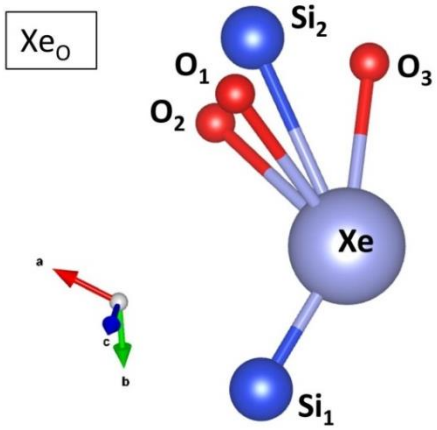


$Z^{eff}$

**Xe = + 0.54**

**$Si_2$ = + 2.1**

**$Si_1$ = + 3.3**

**$O_2 = O_3 = -1.8$**

**$O_1 = -1.7$**

| at% Xe | Xe-$Si_1$ (Å) | Xe-$Si_2$ (Å) | Xe-$O_1$ (Å) | Xe-$O_2$ (Å) | Xe-$O_3$ (Å) |
|---|---|---|---|---|---|
| 1.4 | 2.49 | 3.38 | 3.03 | 3.02 | 2.74 |
| 0.41 | 2.51 | 3.41 | 3.03 | 3 | 2.78 |

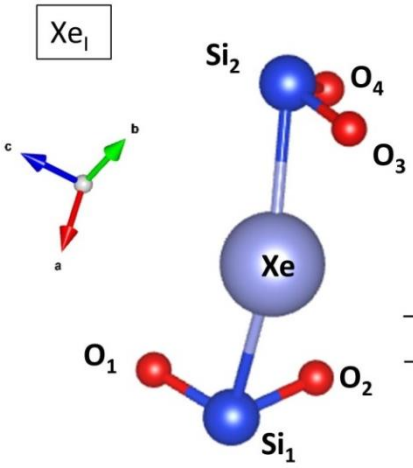


$Z^{eff}$

**Xe = + 0.13**

**$Si_1 = Si_2$ = +3.5**

**$O_1 = O_2 = O_3 = O_4$ = -1.8**

| at% Xe | Xe-$Si_1$ (Å) | Xe-$Si_2$ (Å) | $Si_1$-$O_1$ (Å) | $Si_1$-$O_2$ (Å) | $Si_2$-$O_3$ (Å) | $Si_2$-$O_4$ (Å) |
|---|---|---|---|---|---|---|
| 1.4 | 3 | 3 | 1.63 | 1.66 | 1.65 | 1.63 |
| 0.41 | 3 | 3 | 1.63 | 1.66 | 1.66 | 1.63 |

*Figure E2: Local structural and electronic environment of Xe for the three investigated incorporation mechanisms. Configurations are similar for all investigated Xe contents and* P. *Atomic charges ($Z^{eff}$) were evaluated at 0 GPa for 1.38 at% Xe while bond lengths are given for both Xe contents. Si, O and Xe are blue, red and light blue ball, respectively.*

| ***P* (GPa)** | 0 | 0 | 1.2 | 1.2 | 2.65 | 2.65 |
|---|---|---|---|---|---|---|
| **Xe content (at%)** | 1.4 | 0.41 | 1.4 | 0.41 | 1.4 | 0.41 |
| **$Xe_{Si}$ excess V (%)** | 1.6 | 0.4 | 1.8 | 0.6 | 1.9 | 0.6 |
| **$Xe_{O}$ excess V (%)** | 4.2 | 1.5 | 4.1 | 1.5 | 4.2 | 1.4 |
| **$Xe_{I}$ excess V (%)** | 2.4 | 2 | 4 | 2 | 4.9 | 2.2 |

*Table E2: Calculated excess volume (V) for Xe-doped quartz, for the three investigated Xe incorporation mechanisms, compared to pure α-quartz.*

### b/ A new (Xe,Si)$O_2$ phase at high temperature

*X-ray diffraction data*

In addition to β-quartz diffraction peaks, four new peaks appeared above 1700 K at 0.8(3) GPa for XRD1 dataset for both cristobalite and $SiO_2$ glass used as starting material, at interplanar distances of 2.86 Å, 2.59 Å, 2.53 Å, and 2.40 Å (Figure E3). These four new peaks correspond to continuous rings on the image plate (Figure E3), and cannot be attributed to any potential contamination. Appearance of these four new peaks, in a very narrow interval of interplanar distances (0.5 Å), therefore attests the modification of the β-quartz structure in presence of Xe, leading to the formation of a new phase. To maximize the signal to noise ratio in the area of the new peaks, six X-ray diffraction patterns recorded at similar *P*-*T* conditions were summed.

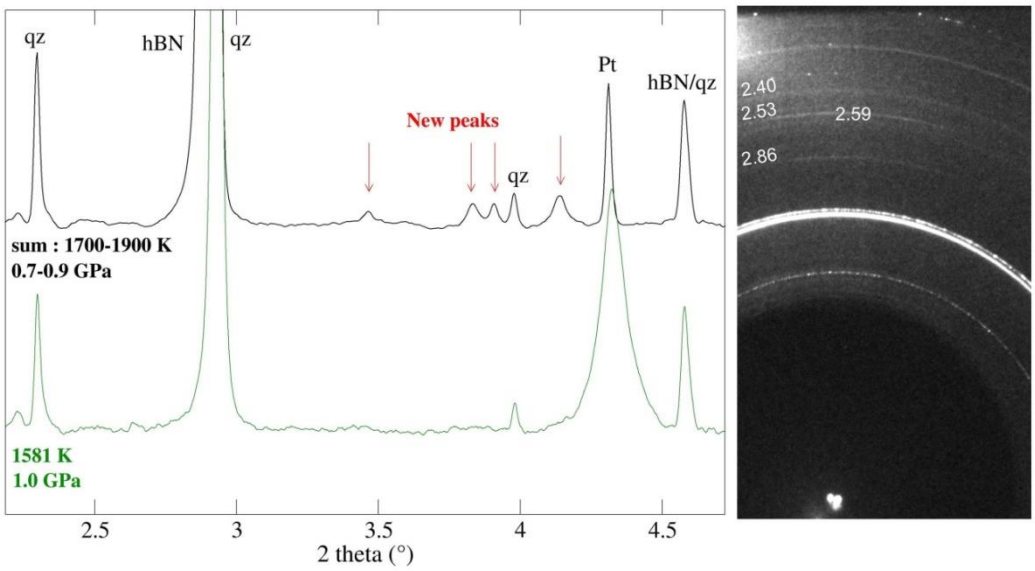


*Figure E3: (left) X-ray diffraction pattern on $SiO_2$ + Xe at high* T *(≥ 1700 K, XRD1). Summed X-ray diffraction pattern (black thick line) with four new peaks (red arrows) in addition to other β-quartz peaks, and hBN or platinum (Pt.) peaks from the cell assembly, also visible at low* T*, (green line). (right) Image plate on $SiO_2$ + Xe at 0.8 GPa and 1814 K with new interplanar distances. Numbers (in Å) are interplanar distances corresponding to the four new continuous rings. The very bright ring corresponds to the (002) hBN peak.*

The peaks observed in the summed pattern were indexed using DICVOL, a powder diffraction indexing software (Boultif and Louër, 1991) (Table E3). The solution of highest symmetry is an orthorhombic cell with $a$ = 8.66(1) Å, $b$ = 5.45(1) Å, $c$ = 5.06(1) Å. This orthorhombic structure can be obtained by elongating β-quartz hexagonal unit-cell ($a \approx 4.98$ Å and $c \approx 5.45$ Å) along the $b$ axis and by defining new axes $a'$, $b'$, $c'$ (Figure E4) so that:

$$a' = a + 2b$$
$$b' = c$$
$$c' = a$$

These relations give $a'$ = 8.64 Å, $b'$ = 5.43 Å and $c'$ = 5.00 Å i.e. very close to the cell parameters obtained with DICVOL. The orthorhombic structure is thus considered as the likeliest based on its highest symmetry (other solutions are monoclinic), and the possibility to convert the β-quartz hexagonal structure into the orthorhombic structure by elongation. Based on extinction rules, four possible orthorhombic space groups were identified: P 2 2 2, P 2 2 $2_1$, Pmm2, Pmmm. For P 2 2 $2_1$, only one Wyckoff position is possible, hence discarding this space group.

| **hkl** | **$d_{hkl}$calc (Å)** | **$d_{hkl}$obs (Å)** |
|---|---|---|
| 101 | 4.32 | 4.31 |
| 200 | 4.28 | |
| 111 | 3.38 | 3.38 |
| 210 | 3.36 | |
| 300 | 2.87 | 2.86* |
| 120 | 2.58 | 2.59* |
| 310 | 2.53 | 2.53* |
| 301 | 2.49 | 2.49 |
| 021 | 2.39 | 2.40* |
| 102 | 2.41 | |
| 202 | 2.17 | 2.17 |
| 212 | 2.02 | 2.01 |
| 410 | 2.00 | |
| 022 | 1.85 | 1.84 |
| 321 | 1.84 | |
| 312 | 1.79 | 1.79 |
| 203, 511 | 1.56 | 1.56 |
| 600 | 1.44 | 1.44 |
| 313, 422, 521 | 1.4 | 1.4 |
| 232, 430, 610 | 1.39 | 1.39 |
| 620 | 1.27 | 1.27 |
| 104, 530, 602 | 1.25 | 1.25 |
| 204, 531 | 1.21 | 1.21 |
| 423 | 1.19 | 1.19 |
| 711 | 1.17 | 1.17 |

*Table E3: List of observed interplanar distances ($d_{hkl}$obs) for the new (Xe,Si)$O_2$ phase, compared to interplanar distances calculated ($d_{hkl}$calc) from DICVOL. * notes the four new peaks. The average 2θ difference for indexed lines is 0.0018°.*

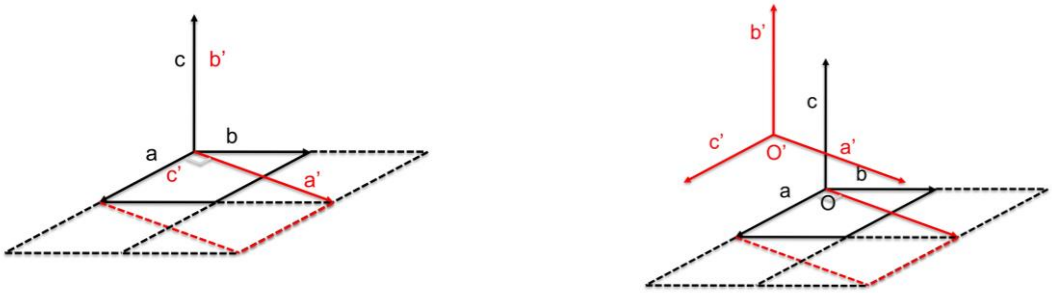


*Figure E4: Operations to pass from hexagonal β-quartz structure (in black) to orthorhombic structure (in red).*

There are 3 Si and 6 O atoms in one unit-cell of β-quartz, and consequently 6 Si and 12 O atoms are expected in the new orthorhombic cell. Based on the multiplicity of Wyckoff positions, atomic positions can only be described in the P 2 2 2 space group (Table E4).

| **$SiO_2$** | **atom** | **x** | **y** | **z** | **Wyckoff position** |
|---|---|---|---|---|---|
| P 2 2 2 | Si | 0 | ½ | 0 | 1c |
| orthorhombic | Si | 1/4 | 1/6 | 1/4 | 4u |
| a = 8.66(1) Å | Si | ½ | ½ | ½ | 1h |
| b = 5.45(1) Å | O | 0.10 | 2/3 | 0.81 | 4u |
| c = 5.06(1) Å | O | 0.60 | 1/3 | 0.69 | 4u |
| | O | 0.71 | 0 | 0 | 2i |
| | O | 0.79 | 0 | ½ | 2j |

*Table E4: Crystallographic structure found by elongation of β-quartz in the P 2 2 2 space group.*

Xe incorporation occurs through Xe for Si substitution in olivine (Sanloup et al., 2011; Crépisson et al., 2018), and Xe retention in quartz was shown to release Si. Furthermore, the present *ab initio* calculations show that Xe for Si substitution is the likeliest Xe incorporation mechanism in quartz (E/II/2/a). Therefore, we assume that Xe substitutes for Si in the new orthorhombic phase, Si being present on 1c, 1h, and 4u Wyckoff positions for the new orthorhombic phase (Table E4).

The new $(Xe,Si)O_2$ phase results from the elongation of the β-quartz, similar to the formation of wadsleyite-II ($Mg_{1.71}Fe_{0.177}Al_{0.01}Si_{0.967}H_{0.332}O_4$) from wadsleyite (β-$Mg_2SiO_4$) in presence of water at 17.5 GPa and 1673 K (Smyth and Kawamoto, 1997). Wadsleyite-II has the same orthorhombic space group and the same *a* and *c* axes as wadsleyite, whereas its *b* axis is 2.5 times longer. X-ray diffraction patterns of both minerals are very similar, apart from some slight differences in peak intensities and appearance of 5 new peaks for wadsleyite II (Smyth et al., 2005).

Ab initio *calculations*

Xe location and occupancy in the new $(Xe,Si)O_2$ phase cannot be refined by Rietveld refinement due to the use of Sollers slits that affects peak intensity versus 2θ. Instead, *ab-initio* calculations were performed using elongated β-quartz as the starting structure (Table

E4). Xe was substituted for Si on 1h, 1c, or 4u Wyckoff positions ($Xe_{Si(1h)}$, $Xe_{Si(1c)}$ or $Xe_{Si(4u)}$ respectively). Structures were fully relaxed at 0 GPa for one Xe atom per unit-cell (i.e. 5.56 at% Xe or 28.32 wt% Xe) and for a 1x3x3 supercell (i.e. 0.62 at% Xe or 5.92 wt% Xe). Indeed 36.6 wt% Xe to 38.1 wt% Xe were initially loaded in these experiments, thus we test circa maximal Xe content and a lower Xe content. It was shown that only 0.4 at% Xe can be incorporated in the olivine structure (Crépisson et al., 2018), and thus only a part of the available Xe may have been incorporated in the new $(Xe,Si)O_2$ phase.

$Xe_{Si(1h)}$, $Xe_{Si(1c)}$ lead to similar structures; 1h and 1c positions being equivalent by translation of the unit-cell. For the three sites, final total energies are similar within 0.4 eV, and the most stable configuration depends on Xe content (Table E5). Calculated volume for Xe in 1h or 1c sites is larger than for Xe in 4u site, and both are larger than experimentally determined volume. Keeping the same reasoning as before, we note that the volume increase related to the presence of Xe is smaller in the case of $Xe_{Si(4u),}$ which suggests that the crystallographic site 4u is the likeliest location.

| | **$Xe_{Si(4u)}$** | **$Xe_{Si(1h)/(1c)}$** | **$Xe_{Si(4u)}$** | **$Xe_{Si(1h)/(1c)}$** | **DICVOL** |
|---|---|---|---|---|---|
| **at% Xe** | 5.56 | 5.56 | 0.62 | 0.62 | - |
| ***a* (Å)** | 8.75 | 9.41 | 8.74 | 8.93 | 8.66 (1) |
| ***b* (Å)** | 6.03 | 6.07 | 5.58 | 5.49 | 5.45 (1) |
| ***c* (Å)** | 4.80 | 4.77 | 5.00 | 5.12 | 5.06 (1) |
| **V (Å$^3$)** | 252.94 | 271.92 | 243.84 | 251.01 | 239 (1) |
| **excess V (%)** | 6.07 | 14.03 | 2.25 | 5.26 | - |
| **final energy (eV)** | -6189.43 | -6189.00 | -53280.20 | -53280.64 | - |

*Table E5: Theoretical cell parameters, volumes and energies for Xe for Si substitutions at 0 GPa, for the 3 possible Wyckoff positions (1h, 1c, and 4u; see Table 4) compared with experimental observations (exp.).*

Relaxed structures are shown in figure E5. Xe is surrounded by four O atoms in a quasi-planar configuration, for both $Xe_{Si(1h)}$ and $Xe_{Si(4u)}$, with Xe-O bond lengths equal to 2.02-2.09 Å, i.e. close to the sum of covalent radii of Xe and O (~ 2 Å). This result is similar to predicted mechanism of Xe incorporation in fibrous silica, where Xe substituted for Si with a planar local environment formed by four oxygen atoms, and Xe-O bond lengths of 2.17 Å (Kalinowski et al., 2014). However, this result differs from Xe incorporation in olivine: although Xe also substituted for Si with a quasi-planar local environment and Xe-O bonds lengths circa 2 Å, Xe was surrounded only by three O atoms in olivine (Crépisson et al., 2018).

For $Xe_{Si(1h)}$ or $Xe_{Si(1c)}$ $Z^{eff}$ for Xe is larger than average for Si atoms located far from Xe. $Z^{eff}$ for the four surrounding O are also less negative than for O located far from Xe (Figure E5). The general excess $Z^{eff}$ is likely counterbalanced by the whole electric field of surrounding atoms. For $Xe_{Si(4u)}$ $Z^{eff}$ for Xe is smaller than for Si atoms located far from Xe, which is counterbalanced by slightly less negative $Z^{eff}$ for the four surrounding O, compared to that for O atoms located far from Xe (Figure E5), similarly to what is observed for Xe for Si substitution in α-quartz (Figure E2).

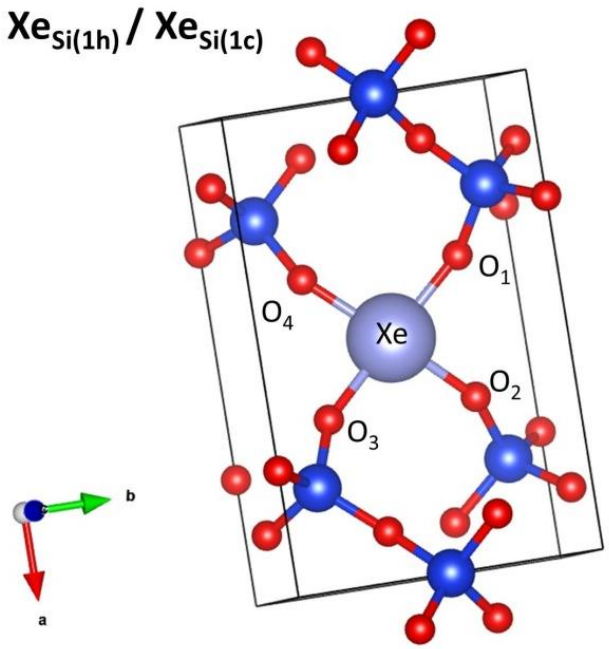


**$Z^{eff}$**
**Xe = + 3.84 (+3.47)**
**$O_1 = O_2 = O_3 = O_4$ = -1.85 to -1.84 (-1.61)**
**Si = + 3.72 to + 3.78 (+ 3.31 to + 3.48)**
**other O = -1.93 to -1.86 (-1.76 to -1.68)**

**Xe-O** = 2.06 Å (2.08 Å)
**$O_1$-Xe-$O_2$ = $O_3$-Xe-$O_4$** = 95.6° (94.7°)
**$O_4$-Xe-$O_1$ = $O_2$-Xe-$O_3$** = 86.0° (84.4°)
**$O_1$-Xe-$O_3$ = $O_4$-Xe-$O_2$** = 166.7° (164.4°)

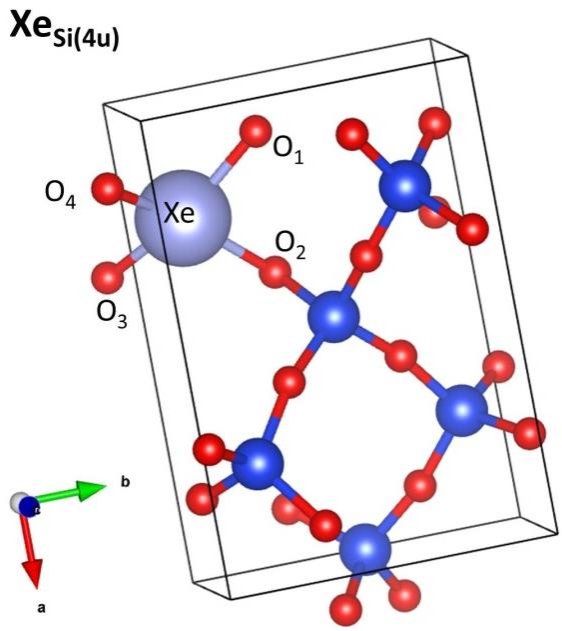


**$Z^{eff}$**
**Xe = + 3.45 (+ 3.21)**
**$O_1 = O_2 = O_3 = O_4$ = -1.68 (-1.50 to -1.48)**
**Si = + 3.64 to + 3.75 (+ 3.28 to + 3.66)**
**other O = -1.99 to -1.75 (-1.91 to -1.64)**

**Xe-$O_1$ = Xe-$O_2$** = 2.07 Å (2.09 Å )
**Xe-$O_3$** = 2.03 Å (2.08 Å)
**Xe-$O_4$** = 2.03 Å (2.09 Å )
**$O_4$-Xe-$O_1$** = 94.8° (96.6°)
**$O_3$-Xe-$O_2$** = 94.8° (94.3°)
**$O_1$-Xe-$O_2$** = 85.8° (89.1°)
**$O_3$-Xe-$O_4$** = 93.3° (91.2°)
**$O_1$-Xe-$O_3$** = 157.2° (154.7°)
**$O_2$-Xe-$O_4$** = 157.2° (154.3°)

*Figure E5: Relaxed structures of the new (Xe,Si)$O_2$ phase at 0 GPa with Xe in either 1h, 1c sites (top) or 4u site (bottom). Bond lengths angles and atomic charges ($Z^{eff}$) are given for 5.56 at% Xe, and in brackets for 0.62 at% Xe. Si, O and Xe are blue, red and light blue ball, respectively..*

*IR data*

*In situ* IR spectrum recorded at 1.0 ± 0.3 GPa and at ambient *T* compares well with that of α-quartz at ambient conditions (Figure E6) (Williams et al., 1993). Upon increasing *T*,

above 473 K, a progressive splitting of the 1085 $cm^{-1}$ band related to asymmetric stretching vibrations of $SiO_4$ tetrahedra (Williams et al., 1993), is observed (Figure E6). This is not expected for pure quartz, as IR quartz signal at 1273 K (Shoval et al., 1997) is similar to the one recorded at ambient conditions, except for slight shift in frequency (Figure E6, Table E6). Splitting must thus be related to Xe incorporation in quartz at $T$ = 473 K, i.e. just above Xe melting point (Ferreira and Lobo, 2008).

*Ab initio* calculations for pure α-quartz at 0 GPa are in agreement with experimental data from Williams et al. (1993) and Shoval et al. (1997) (Table E6) apart from a global shift in frequency, common to DFT calculations. Our results also agree with theoretical calculations from Méheut (2008), who used similar computational techniques (Table E6).

IR signal was calculated for Xe for Si substitution in α-quartz ($Xe_{Si}$) for 1.38 at% Xe (Figures E2 and E6). $Xe_{Si}$ in α-quartz cannot explain the observed splitting of the main 1085 $cm^{-1}$ band despite the calculated new contributions at 30 $cm^{-1}$ below and at 50-150 $cm^{-1}$ above the main band, as those are too weak.

Instead, a phase transition could be at stake, as observed by X-ray diffraction (Figures E3 and E5). To test this hypothesis, we calculated IR signal of the new $(Xe,Si)O_2$ phase for 5.56 at% Xe, for $Xe_{Si(1h)}$ and $Xe_{Si(4u)}$ configurations (Figures E5 and E6). For both configurations a splitting of the main 1085 $cm^{-1}$ band is observed: for $Xe_{Si(1h)}$ significant contributions appear at 50 $cm^{-1}$ below and 120 $cm^{-1}$ above the main band, and for $Xe_{Si(4u)}$ at 150 $cm^{-1}$ above the main band (Figure E6). IR signal of $Xe_{Si(4u)}$ compares significantly better to the experimental IR spectra than that of $Xe_{Si(1h)}$ (Figure E6), and $Xe_{Si(4u)}$ leads to a smaller volume increase than $Xe_{Si(1h)}$ (Table E5), thus $Xe_{Si(4u)}$ is the likeliest configuration for the new $(Xe,Si)O_2$ phase. Transition to the new $(Xe,Si)O_2$ phase from α-quartz is not surprising due to the similarity of α- and β-quartz structures. We note that phase transition observed by X-ray diffraction based on XRD1 occurred at much higher $T$ (figure E3) potentially controlled by diffusion of Xe which was initially loaded as a pure phase surrounding silica, in contrast to IR data experiment where the starting material was already Xe-doped.

| **Shoval et al. (1997) 1273 K exp.** | **Williams et al. (1993), exp.** | **this work calc.** | **Méheut PhD, (2008) calc.** | **Symmetry** |
|---|---|---|---|---|
| 1166 | 1170 | 1127 | 1128 | E |
| 1084 | 1080 | 1031 | 1033 | $A_2$ |
| - | - | 1026 | 1028 | E |
| 797 | 800 | 753 | 754 | E |
| 778 | 780 | 742 | 745 | $A_2$ |
| 694 | 696 | 656 | 657 | E |

*Table E6: IR active frequencies for α-quartz from experiments (exp.) and calculations (calc.)*

.

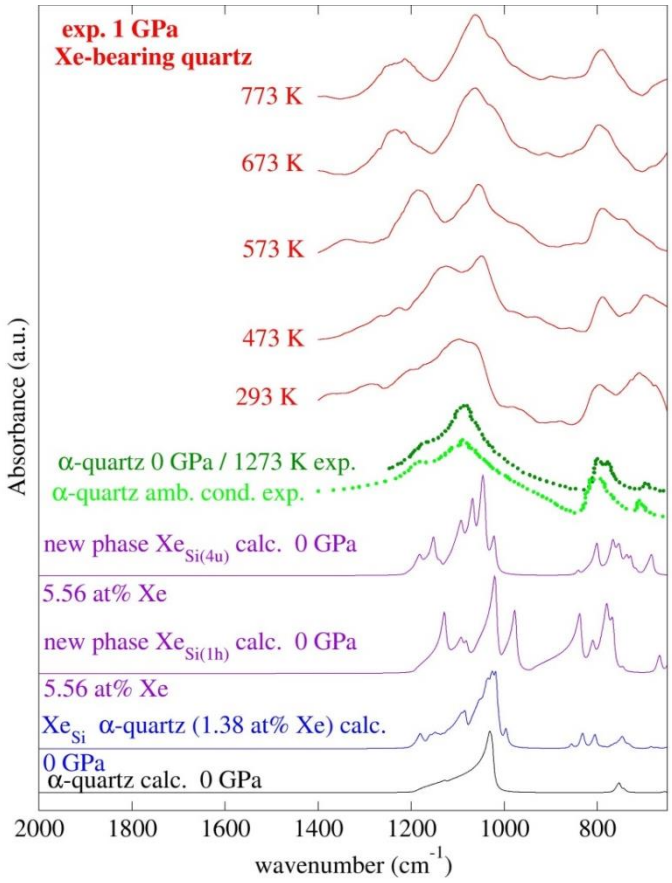


*Figure E6: IR spectra for the Xe-$SiO_2$ system. Experimental (exp.) IR spectra (red) recorded at high* P-T *conditions compared with experimental spectra for α-quartz (at 0 GPa - 1273 K from Shoval et al. (1997) and at ambient conditions from Williams et al. (1993)), calculated (calc.) spectra for α-quartz and the new (Xe,Si)$O_2$ phase.*

## III/ Conclusion

Xe retention in $SiO_2$ at the conditions of the deep continental crust is elucidated. Xe substitutes to Si in quartz, as in olivine (Crépisson et al., 2018). In addition to Xe incorporation as point defects in quartz, for the first time a phase transition is observed in presence of Xe at higher *T*. Occurrence of a phase transition indicates that Xe for Si substitution is increasingly enhanced above Xe melting curve, breaking the quartz symmetry at a macroscopic scale, thus suggesting high Xe content in the new (Xe,Si)$O_2$ phase.

Xe is incorporated in quartz at point defects bonding closely to two oxygens in a linear configuration, while in the new (Xe,Si)$O_2$ phase Xe is bonded to four oxygens in a quasi-planar environment. In both cases Xe-O bond lengths range from 1.98 Å to 2.09 Å, proving that Xe-O bonds are at least partly covalent.

Xe reactivity is thus widespread in lithospheric minerals, affecting at least quartz and olivine; quartz, the silicic end-member, being representative of the continental crust, while olivine, the magnesian end-member, is representative of the lithospheric mantle. Xe reactivity is therefore expected to be ubiquitous in the lithosphere and potentially at greater depths which remains to be investigated.

## Chapter F: XE INCORPORATION IN HIGH-TEMPERATURE FELDSPAR (SANIDINE)

With quartz, feldspar is a widespread continental crust mineral with a more complex chemical composition. Sanidine ($KAlSi_3O_8$) is a high-*T* feldspar, of atomic composition $(K_xNa_{1-x})AlSi_3O_8$ with $x > 0.32$ (Bendel and Schmidt, 2008). Xe-bearing sanidine minerals were synthesized and Fe-rich and Xe-rich sanidine phases were identified on recovered samples. Crystalline Xe-bearing and plain sanidines were investigated *in situ* by X-ray diffraction up to 6.8 GPa. Xe-bearing and plain sanidine glasses were also recrystallized at high water fugacity into sanidine and K-cymrite (sanidine hydrate: $KAlSi_3O_8.H_2O$), and observed *in situ* by X-ray diffraction up to 9.7 GPa.

### I/ *Ex situ* analyses

#### 1/ Sample synthesis

Different heavy noble gases-bearing samples were synthesized (Table F1) from three natural sanidines. Sanidine Nat.[17] and sanidine Itrongahi[18] were obtained from the mineralogical collection of Sorbonne Université and sanidine Volkesfeld was given by B. Schmidt (University of Göttingen). Minerals were inspected to remove visible contamination before being cleaned in ultrasound bath of ethanol and grounded in agate mortar. To confirm their nature, X-ray diffraction data were recorded at IMPMC (Appendix F1), and EMPA were performed (Table F2). For hydrated samples, liquid water was added to the starting material in the capsule ($H_2O$ content is around 5 wt%).

| Name | Starting material | gas mix | *P* (GPa) | *T* (°C) | Duration (hours) | powder (mg) | gas (mg) | weight loss after piercing (mg) | Exp. |
|---|---|---|---|---|---|---|---|---|---|
| PC58-plain | San. Nat. | - | 3.5 | 1100 | 24 | - | - | - | Previous |
| PC58-Xe | San. Nat. | Xe | 3.5 | 1100 | 24 | - | - | - | Previous |
| PC63 | San. Nat. | Xe/Ar | 3.5 | 1100 | 24 | - | - | - | Previous |
| PC66 | San. Nat. | Xe/Kr | 3.5 | 1100 | 24 | - | - | - | Previous |
| PC67 | San. Nat. | Xe/Kr | 3.5 | 1100 | 24 | - | - | - | Previous |
| PC129 | San. It. | - | 3.5 | 1100 | 5 | - | - | - | This work |
| PC103 | San. It. | Xe/Kr | 3.5 | 1100 | 24 | 24.5 | - | 5.1 | This work |

*Table F1: Sample synthesis: experimental conditions and compositions. San. Nat. = sanidine Nat., and San. It. = sanidine Itrongahi. In red are samples used for* in situ *X-ray diffraction (F/II).*

[17] Arbitrarily named

[18] Sanidine Itrongahi was chosen as a Fe-rich sanidine (Coombs, 1954), nevertheless we noticed afterward that sanidine Nat. has a higher Fe content than our crystal of sanidine Itrongahi (Table F2).

2/ SEM / TEM / EMP / Raman analysis

Plain samples (PC58-plain and PC129) are homogeneous with similar chemical composition as starting sanidine, except for a slight depletion in Al, and a slight enrichment in Si (Table F2).

In presence of Xe, a phase separation is observed between a Fe-poor sanidine phase and a Fe-rich sanidine phase (Figures F1 and F2), the latter being enriched in noble gases, depleted in Al (TEM elemental mapping is shown in figure F3), and significantly enriched in Si for sanidine Itrongahi (Table F2). Fe-poor zones have similar composition as plain samples (PC58-plain and PC129). Bubbles of noble gases, ranging from nm to µm in size are present mostly in Fe-poor zones (Figure F1). Presence of large bubbles means that saturation was reached, while small bubbles may indicate exsolution upon quenching due to the fact that Xe escaped the silicate network. The fact that no bubbles are seen in Fe-rich zones, suggests that Xe is located in the silicate network (Figure F3). Diffraction performed by TEM indicates that Fe-rich areas are amorphous on the recovered sample (Figure F4), although this may have happened upon quenching, during FIB preparation or TEM observation. Indeed, formula unit of Fe-rich phase is very close to sanidine formula, and is enriched in Si for sanidine Itrongahi, which is unlikely in case of partial melting (Table F2).

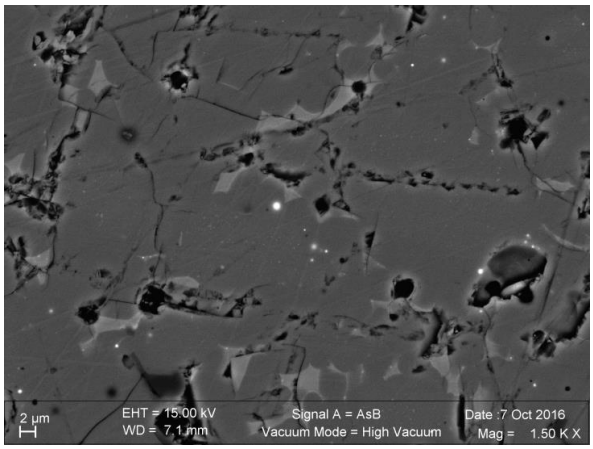


*Figure F1: Xe/Kr-bearing Sanidine Itrongahi (PC103) Lighter grey: Fe-rich zones, bright spots: Xe/Kr bubbles.*

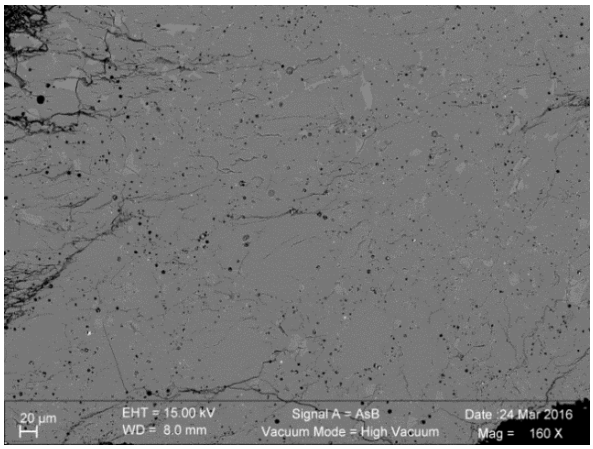


*Figure F2: Xe/Ar-bearing sanidine Nat. (PC63) Lighter grey: Fe-rich zones, bright spots: Xe/Ar bubbles.*

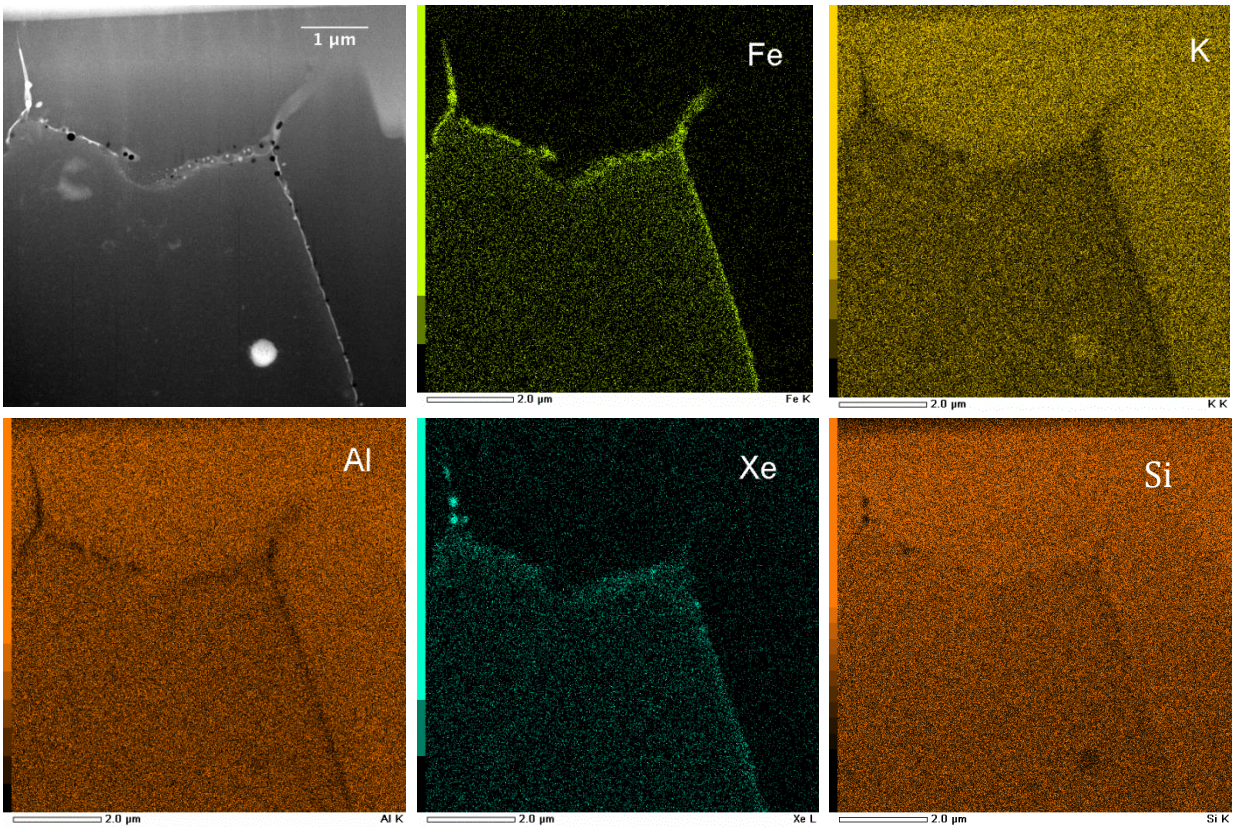


*Figure F3: STEM (-HAADF and XEDS) observation of Xe/Ar bearing-sanidine Nat. (PC63), showing a Fe-rich zone. Big bright circle on the STEM-HAADF image is NaCl contamination. No variation was observed for Na.*

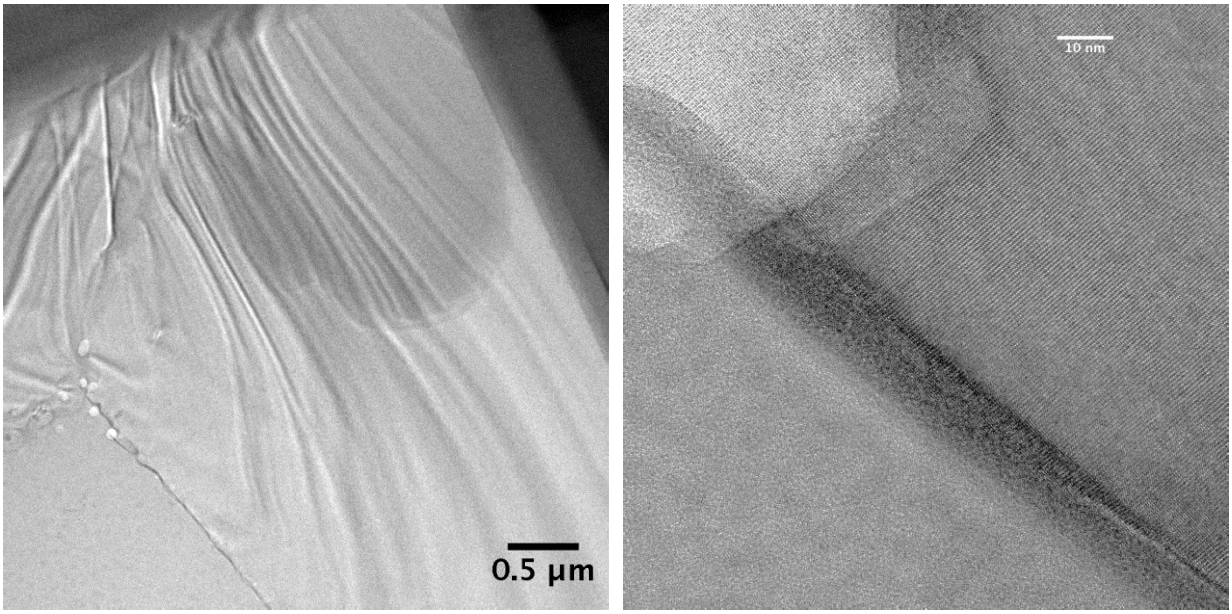


*Figure F4: TEM images on Xe/Ar-bearing sanidine Nat. (PC63): observed part is the same where chemical mapping was performed (Figure F3). Image on right is a zoom of image on the left. Difference between crystalline Fe-poor zone (right) and amorphous Fe-rich zone (left) is visible on both TEM images.*

| Sample | Starting material | Data points | Na | K | Al | Fe | Si | O | Xe | Kr | Ar |
|---|---|---|---|---|---|---|---|---|---|---|---|
| **PC66 (Fe-rich)** | San Nat. (Xe/Kr) | 3 | 0.49 | 0.36 | 0.85 | 0.20 | 3.00 | 8 | 0.03 | 0.02 | - |
| **PC66 (Fe-poor)** | San Nat. (Xe/Kr) | 23 | 0.42 | 0.52 | 1.03 | 0.01 | 2.97 | 8 | - | - | - |
| **PC103 (Fe-rich)** | San It. (Xe/Kr) | 10 | 0.14 | 0.78 | 0.79 | 0.10 | 3.11 | 8 | 0.005 | 0.003 | - |
| **PC103 (Fe-poor)** | San It. (Xe/Kr) | 24 | 0.07 | 0.91 | 0.99 | 0.02 | 3.00 | 8 | - | - | - |
| **PC67 (Fe-poor)** | San Nat. (Xe/Kr) | 5 | 0.40 | 0.53 | 1.03 | 0.007 | 2.98 | 8 | - | - | - |
| **PC63 (Fe-poor)** | San Nat. (Xe/Ar) | 8 | 0.42 | 0.55 | 1.03 | 0.00 | 2.97 | 8 | 0.004 | - | 0.01 |
| **PC58-Xe (Fe-poor)** | San Nat. (Xe) | 8 | 0.43 | 0.54 | 1.02 | 0.00 | 2.97 | 8 | 0.01 | - | - |
| **PC58-plain (Fe-poor)** | San Nat. | 23 | 0.45 | 0.52 | 1.03 | 0.01 | 2.96 | 8 | - | - | - |
| **PC129 (Fe-poor)** | San. It. | 20 | 0.06 | 0.89 | 1.01 | 0.02 | 3.00 | 8 | - | - | - |
| **San Nat.** | San Nat. | 14 | 0.45 | 0.53 | 1.04 | 0.01 | 2.95 | 8 | - | - | - |
| **San It.** | San It. | 15 | 0.16 | 0.82 | 1.03 | 0.01 | 2.97 | 8 | - | - | - |
| **PC116A (Glass)** | San It. (Xe/Ar) + water liq. | 15 | 0.06 | 0.76 | 1.02 | 0.00 | 3.03 | 8 | 0.01 | - | 0.02 |
| **PC70 (Glass)** | San Nat. (Xe) | 20 | 0.46 | 0.52 | 1.05 | 0.00 | 2.94 | 8 | 0.001 | - | 0.001 |
| **PC139 (Glass)** | San It. + water liq. | * | 0.07 | 0.80 | 0.98 | 0.01 | 3.02 | 8 | - | - | - |

*Table F2: Atomic composition for one formula unit of starting sanidine and synthesized samples (Appendix F2, F3). San = sanidine and It. = Itrongahi. * indicates that composition is based on XEDS by SEM, and is less reliable than EMPA. In red are samples used for* in situ *X-ray diffraction (F/II). Sanidine glasses presented in chapter G (Table G1) are shown here as they are used for X-ray diffraction experiments (F/II).*

We analyzed by EMP noble gas bubbles in Fe-poor zones i.e. < 0.4 at% Fe for Xe/(Kr or Ar)-bearing sanidine Nat. (PC63, PC66, PC67). These analyses of the gas bubbles and the surrounding sanidine made it possible to retrieve potential trend(s) which would have been preserved after quenching, assuming that nanometric bubbles analyzed correspond to an exsolution of the noble gases present in the sanidine crystalline structure upon quenching. After correction of the analyses for the volume of the gas bubbles (using gas content as a first approximation) a negative trend between Xe (and Kr) and Si is observed, whereas trend remains poor between Ar and Si (Figure F5). It must also be noted that Xe is twice more abundant than Kr, whereas gas mixes used in the experiments are 1:1 mixes. No special trend is observed between noble gases and other elements such as Al, Na, or K (Appendix F4). As O content is calculated from other elements' contents, it is not possible to conclude regarding possible trends between O and noble gases.

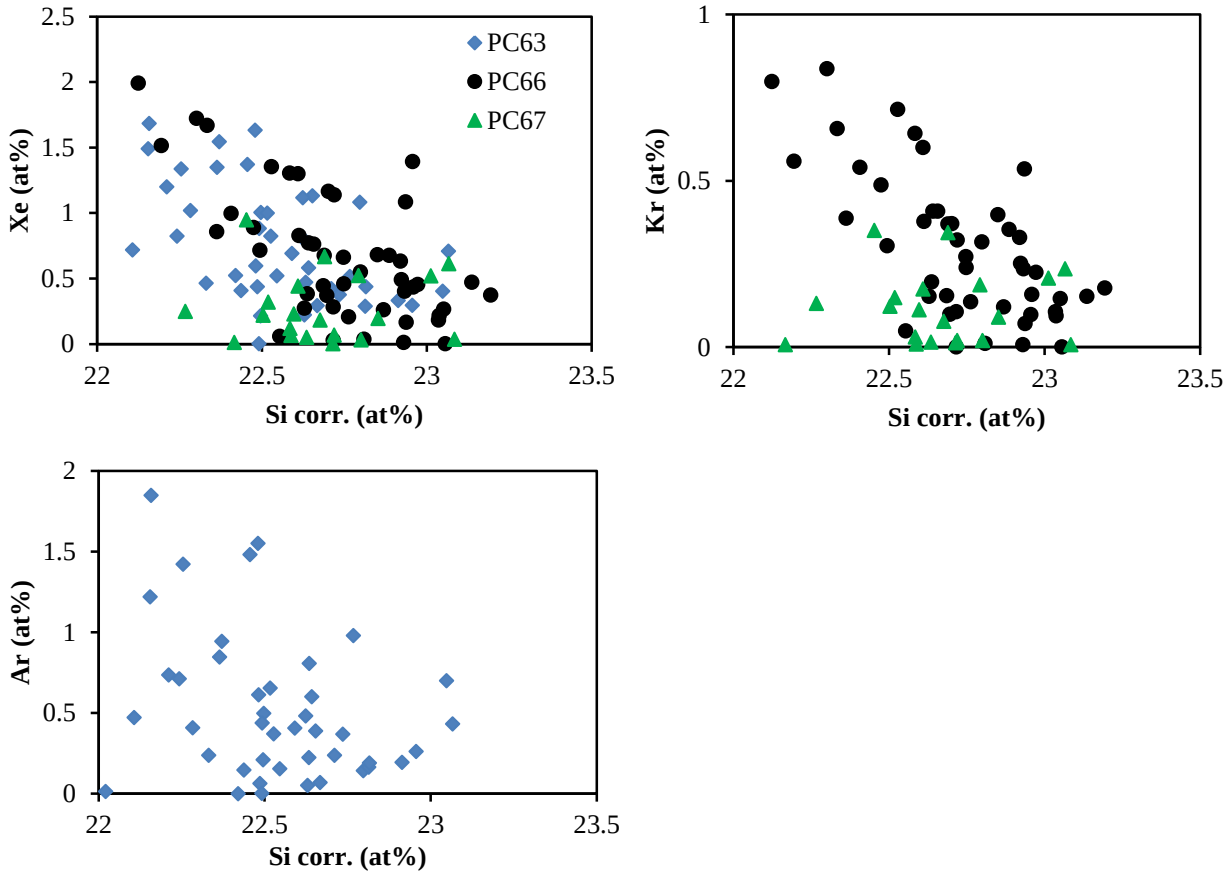


*Figure F5: Observed trends from EMPA of noble gases bubbles and surrounding sanidine on Fe-poor zones for Xe/(Kr or Ar)-bearing sanidine Nat.: PC63, PC66, PC67 (Table F1). Si contents have been corrected from the volume of the noble gas bubble using noble gas contents as a first approximation.*

Raman signals of Xe/Kr-bearing sanidine Itrongahi (PC103) and plain sanidine Itrongahi (PC129) are similar (Figure F6). Some analyses recorded on bright dots present in Xe/Kr-bearing sample, show bands characteristic of the quartz Raman signal at 463.6 - 464.8 $cm^{-1}$, at 354.8 $cm^{-1}$, and 199.6 $cm^{-1}$ (Figure F6). Although no quartz was observed on the recovered samples throughout SEM observations and EMPA, its presence cannot be totally ruled out. X-ray diffraction retrieved on samples (F/II) can neither discard the possibility of quartz presence, as the main quartz peak is overlapping a sanidine peak. However presence of quartz, only on the Xe/Kr-bearing sanidine (PC103) remains difficult to explain.

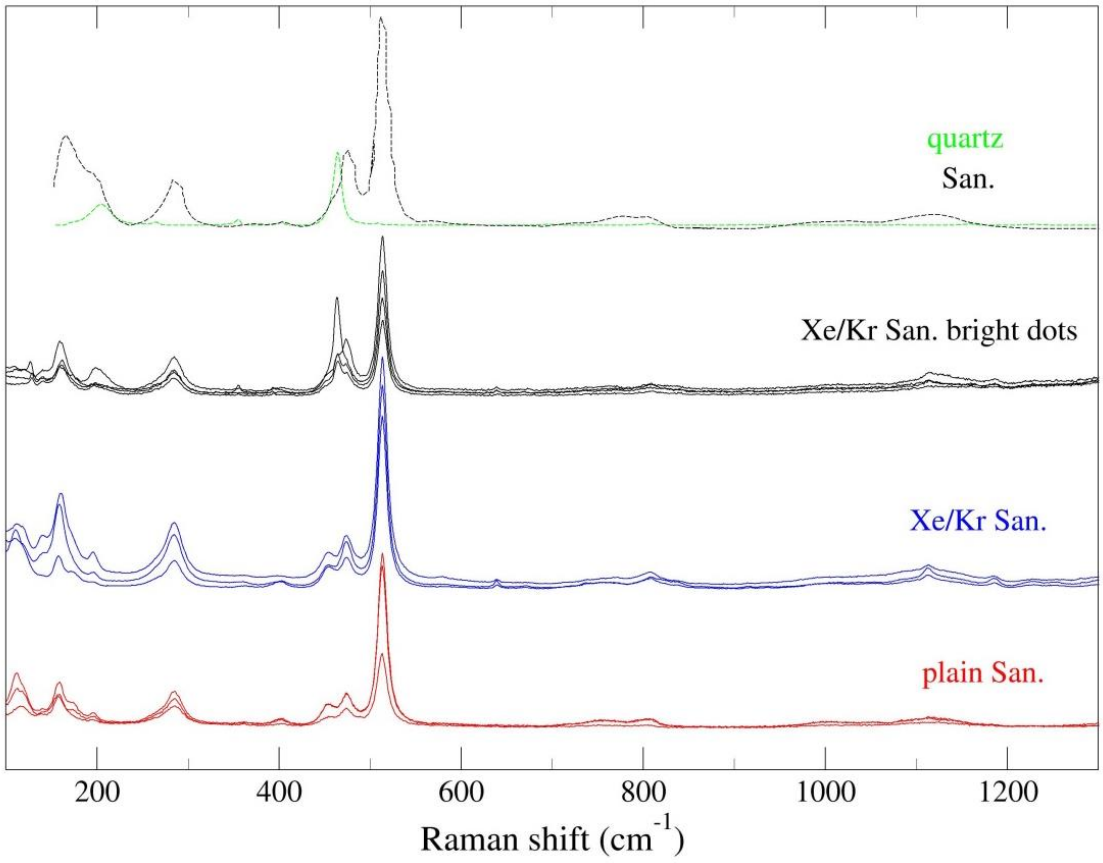


*Figure F6: Raman spectra recorded on Xe/Kr-bearing sanidine (San.) Itrongahi (PC103), and plain sanidine Itrongahi (PC129). 'ref.' stands for reference spectra (from the RRUFF database).*

## II/ *In situ* X-ray diffraction

### 1/ Methods and samples

Three sets of data were used in this work (Tables F3, F4):

High *P-T* conditions were generated by resistive-heating DAC. Experiments were conducted: 1) on beamline P02.2 at Petra III synchrotron source using a 3x8 $\mu m^2$ beam at 42.7 keV. 2) on beamline I15 at Diamond light Source in July 2017, using a 70 µm diameter beam at 29.2 keV. 3) on beamline I15 at Diamond light Source in April 2018, using a 50 µm diameter beam at 29.2 keV. *P* was determined using unit-cell volume of a Pt grain inserted on the verge of the sample chamber, and *T* was read from a type-K thermocouple located near the diamond tip (for 1) and 3)) or using calibration from De Grouchy (PhD thesis, 2016) (for 2)). During measurement the cell was oscillated from -3° to +3° (for 1)) or from -5° to +5° (for 2) and 3)), when possible, to avoid intensity artefacts from potential preferential orientation.

Image plates were integrated with DIOPTAS (Prescher and Prakapenka, 2015). Rietveld and Le Bail refinements were performed with GSAS software (Larson and Von Dreele, 2000), starting from sanidine structure described by Keefer and Brown (1978) and

from K-cymrite structure described by Fasshauer et al. (1997). Image plates are shown in Appendix F5.

| | **P-cell2-Xe/Kr** | **P-cell6-plain** | **P-cell4-Xe** | **P-cell4-plain** | **D-RT1-1-Xe/Kr** |
|---|---|---|---|---|---|
| **Beamline** | Petra III P02.2 | Petra III P02.2 | Petra III P02.2 | Petra III P02.2 | Diamond I15 (july 2017) |
| ***P* range (GPa)** | 0.8-2.5 | 0.2-5.3 | 1.8-6.8 | 2.5-6.8 | 1.5-3.4 |
| ***T* max (K)** | 873 | 1168 | 1473 | 1473 | 852 |
| **Composition** | Xe/Kr dry sanidine Itrongahi (PC103) | dry sanidine Itrongahi | Xe dry sanidine Nat. **glass** (PC53) | dry sanidine Nat. | Xe/Kr dry sanidine Itrongahi (PC103) |
| **State** | crystalline | crystalline | **glass** recrystallized[19] at 5.3 GPa and 1073 K | Crystalline | crystalline |
| **Gasket analysis** | lost | SEM / Raman / EMP | SEM / Raman / EMP / TEM | SEM / Raman / EMP / TEM | lost |

*Table F3: Summary of* in situ *X-ray diffraction data recorded on dry sanidine. Synthesis conditions and composition of PC103 and PC53 can be found in Tables F1 and F2.*

| | **P-cell3-Xe/Ar** | **P-cell6-Xe/Ar** | **D-HT2-1-plain** | **D-RT1-1-plain** |
|---|---|---|---|---|
| **Beamline** | Petra III P02.2 | Petra III P02.2 | Diamond I15 (april 2018) | Diamond I15 (april 2018) |
| ***P* range (GPa)** | 0.4-9.7 | 0.2-5.3 | 1.7-6.4 | 0.6-5.7 |
| ***T* max (K)** | 1347 | 1168 | 1158 | 1359 |
| **Composition** | Xe/Ar hydrated sanidine Itrongahi glass (PC116A) | Xe/Ar hydrated sanidine Itrongahi glass (PC116A) | hydrated sanidine Itrongahi glass (PC139) | hydrated sanidine Itrongahi glass (PC139) |
| **State** | glass recrystallized at 9.7 GPa and 1254 K | glass recrystallized at 4.8 GPa and 1073 K | glass recrystallized at 6.4 GPa and 1093-1158 K | glass recrystallized at 5.7 GPa and 1244 K |
| **Gasket analysis** | SEM / TEM / EMP | SEM / Raman / EMP | SEM | SEM |

*Table F4: Summary of* in situ *data X-ray diffraction recorded on recrystallized glasses of hydrated sanidine at high* P-T *conditions. Synthesis conditions and composition of PC116A and PC139 can be found in Tables G1 and F2.*

When available, recovered samples (within Re gaskets) were coated without other sample preparation, and analyzed by SEM, TEM, Raman and EMP (Table F5):
For P-cell4-plain and P-cell6-plain, both recovered samples are homogeneous with presence of only sanidine in the recovered sample (Table F5 and Raman in Appendix F6).
For P-cell4-Xe, Xe bubbles are observed throughout the recovered sample. EMPA and Raman analyses confirm the presence of sanidine, with no significant difference between plain and Xe-bearing sample (Table F5, Raman in Appendix F6).
For D-HT2-1-plain and D-RT1-1-plain, both recovered samples are similar, with the presence of two phases differing from their textures (Figure F7), whereas no obvious colour contrasts (difference in atomic number) are visible. Although quantitative composition could not be

[19] Glass recrystallization was used in order to obtain very fine grain and very good statistics. Image plates displayed in Appendix F5 confirm that statistics is better than when already crystalline sample are investigated.

measured on an unpolished sample using XEDS, it was seen that composition is corresponding to feldspar for the two phases (Table F5), with only variation in O content, interpreted as a variation in water content, confirming presence of both sanidine ($KAlSi_3O_8$) and K-cymrite ($KAlSi_3O_8.H_2O$).

For P-cell6-Xe/Ar, recovered sample shows a separation between dark and light areas (Figure F8); difference in atomic number mostly relying on K content. Light areas are likely pure sanidine (with formula unit similar to plain sanidine Itrongahi), whereas dark areas are likely composed of sanidine and coesite explaining why Si+Al ≠ 4 in the formula unit obtained from EMPA (Table F5). Raman analyses show a pure sanidine spectrum (Appendix F6).

For P-cell3-Xe/Ar, recovered sample presents 10-20 nm crystals (Figure F9 and TEM observations). Xe and Ar contents are similar to those of the starting Xe/Ar-bearing sanidine Itrongahi glass (PC116A), with 0.62 wt% Xe and 0.30 wt% Ar in the recovered sample, compared to 0.57 wt% Xe and 0.31 wt% Ar in the starting glass (Table F5). Moreover no gas bubbles are seen, even at the nanoscale (from TEM observations), which tends to indicate that Xe is retained within the silicate network. An attempt was made to observe this sample by TEM, but sample was seen to be damaged under the electron beam. Bright, Xe-rich, zones with crystalline shape were observed (Figure F10), TEM observation tends to indicate that they are amorphous, although beam damage is likely.

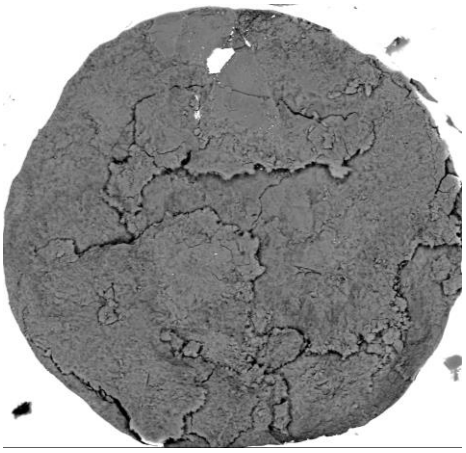

*Figure F7: SEM image in backscattered mode for recovered sample of D-HT2-1-plain (hole is 150 µm) diameter). Bright part at the top is Pt contamination.*

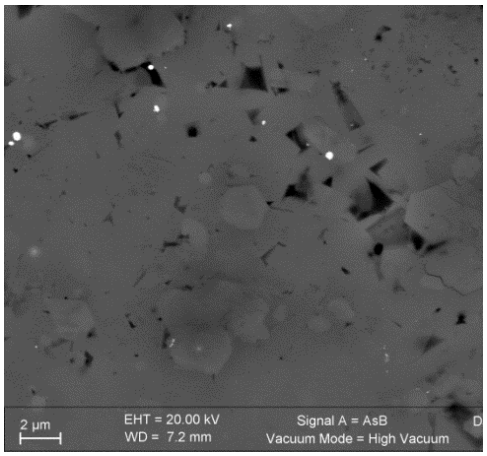


*Figure F8: SEM image in backscattered mode for recovered sample of P-cell6-Xe/Ar showing dark and light zones. Bright dots are Re from Re gasket.*

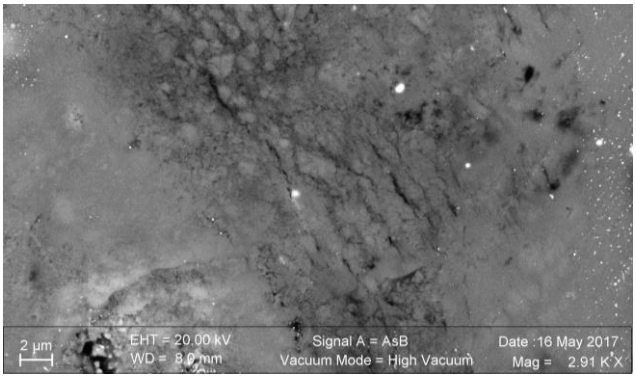


*Figure F9: SEM image in backscattered mode for recovered sample of P-cell3-Xe/Ar. Bright dots are Re from Re gasket.*

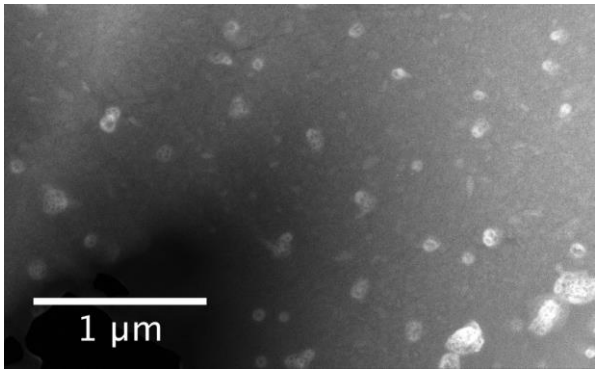


*Figure F10: TEM image of P-cell3-Xe/Ar in dark field, showing bright Xe-rich zones. Large damage under the beam prevented chemical mapping.*

| Sample | Data points | Na | K | Al | Si | Fe | Xe | Ar | oxide total |
|---|---|---|---|---|---|---|---|---|---|
| **P-cell4-Xe** | 10 | 0.41 | 0.47 | 1.07 | 2.95 | 0 | 0.01 | - | 100 (1) |
| **P-cell4-plain** | 11 | 0.45 | 0.54 | 1.05 | 2.94 | 0.01 | - | - | 100.8 (8) |
| **P-cell6-plain** | 3 | 0.04 | 0.88 | 1.01 | 2.99 | 0.03 | - | - | 101.3 (9) |
| **P-cell6-Xe/Ar dark zone** | 9 | 0.03 | 0.81 | 1.16 | 2.91 | 0 | - | - | 100.6 (7) |
| **P-cell6-Xe/Ar light zone** | 11 | 0.03 | 0.93 | 1.04 | 2.97 | 0 | - | - | 101 (1) |
| **P-cell3-Xe/Ar** | 6 | 0.07 | 0.78 | 1.03 | 3.01 | 0 | 0.01 | 0.02 | 97.4 (2) |

*Table F5: Average formula unit for 8 oxygen atoms for recovered samples based on EMPA given in Appendix F7. The total for wt% oxide retrieved by EMPA is given to estimate water content.*

2/ Results for dry sanidine

Measured unit-cell volumes for plain sanidine Itrongahi (P-cell6-plain) compare well with theoretical volumes calculated by using first order thermal Birch Murnaghan equation of state with parameters recommended by Chang et al. (2013) (Table F6). Measured volumes are in agreement with predicted volumes within ± 0.6 % proving that this equation of state is valid for sanidine Itrongahi in this *P-T* range (Table F6).

On the contrary, for plain sanidine Nat. (P-cell4-plain), the equation of state does not satisfactorily reproduce the observed volume for sanidine, with deviation ranging from -2.5 % to +1.3 % [20] (Table F6). Coesite cell parameters are poorly fitted by the equation of state (parameters from Chang et al., 2013); moreover coesite peak (at 5.4°, figure F11, c)) disappears after quenching although coesite is normally quenchable. It remains unclear if this peak could correspond to another unidentified phase.

In presence of Xe/Kr, for sanidine Itrongahi, for both P-cell2-Xe/Kr and D-RT1-1-Xe/Kr, a systematic excess volume up to 3.4% is observed (Table F6), linked with Xe (and possibly Kr) incorporation in sanidine. For both Xe/Kr-bearing sanidine, shape of the two main peaks at 5° and 5.1° differs from the one of the plain sample (Figure F11, a) and b)), although comparison is uneasy for D-RT1-1-Xe/Kr due to worse resolution coming from measurement at higher wavelength (Figure F11, b)). Examples of Rietveld refinements are given for P-cell2-Xe/Kr (Figure F12), D-RT1-1-Xe/Kr (Figure F13), and P-cell6-plain (Appendix F8). It must be noted that refinements are not perfect for the plain sample.

For P-cell2-Xe/Kr, Xe is present as a cubic phase up to Xe melting point, i.e. above 473 K for our *P* (Figure F11, a)). This solid Xe may come from an inclusion present in the starting material (PC103). Another phase is present with the most intense contribution at $d_{hkl}$ = 5.2 Å, corresponding to a continuous ring on the image plate. Other contributions are also visible after quenching, with the list of interplanar distances displayed in table F7. This phase disappears, possibly melts, above 753 K and reappears, more intense upon quenching (Figure F11, a)). Indexing with DICVOL software gives a tetragonal (with $a$ = 6.679(2) Å and $c$ = 23.848(9) Å) or an orthorhombic solution ($a$ = 9.151(3) Å; $b$ = 5.1283(8) Å, and $c$ = 3.349(2)

[20] Initial volume obtained from X-ray diffraction at ambient conditions on powders of starting sanidine (Appendix F1) gives a volume of 701.53 $Å^3$ for sanidine Nat. (against 720.55 $Å^3$ for sanidine Itrongahi), far smaller than initial volume used in the present equation of state (i.e. 720.3 $Å^3$). However a mere change of the initial volume does not significantly improve the fit.

Å), that we could not identify so far. The fact that this unknown phase is not seen on Xe/Kr-bearing sanidine Itrongahi without initial Xe/Kr excess (D-RT1-1-Xe/Kr) could mean that this phase is linked to this initial excess, and if so could affect results on sanidine regarding Xe incorporation.

For Xe-bearing sanidine Nat. (P-cell4-Xe), due to poor fitting of the equation of state for the plain sample (P-cell4-plain, Table F6) nothing can be concluded regarding the effect of Xe incorporation on unit-cell volume. In presence of Xe, relative peak intensities systematically differ, with again a different shape of the two main peaks at 5° and 5.1°. Moreover the peak at 4° is systematically smaller and the peak at 4.8° systematically higher (except at 1373 K) in presence of Xe. Example of Rietveld refinement is given in Appendix F9.

| Sample | *P* (GPa) | *T* (K) | phase | *a* (Å) | *b* (Å) | *c* (Å) | beta (°) | observed V(Å$^3$) | predicted V (Å$^3$) | excess V(%) |
|---|---|---|---|---|---|---|---|---|---|---|
| **P-cell6-plain** | 0.4 | 298 | San. | 8.5720(5) | 12.9844(8) | 7.2019(4) | 116.010(6) | 720.39(5) | 719.0 | **0.2** |
| **P-cell6-plain** | 0.2 | 361 | San. | 8.5948(8) | 12.983(2) | 7.2079(6) | 116.103(7) | 722.3(1) | 722.5 | **0.0** |
| **P-cell6-plain** | 0.2 | 466 | San. | 8.5972(6) | 12.9850(9) | 7.2000(5) | 115.959(6) | 722.69(6) | 723.3 | **-0.1** |
| **P-cell6-plain** | 0.3 | 579 | San. | 8.6027(6) | 12.9770(9) | 7.2005(4) | 115.940(6) | 722.86(6) | 724.2 | **-0.2** |
| **P-cell6-plain** | 0.5 | 676 | San. | 8.6161(5) | 12.9741(7) | 7.2027(5) | 115.904(5) | 724.27(5) | 723.5 | **0.1** |
| **P-cell6-plain** | 0.4 | 773 | San. | 8.619(1) | 12.957(1) | 7.1950(7) | 115.894(9) | 722.84(9) | 725.4 | **-0.4** |
| **P-cell6-plain** | 0.7 | 873 | San. | 8.599(1) | 12.943(2) | 7.181(1) | 115.72(2) | 720.1(1) | 724.3 | **-0.6** |
| **P-cell6-plain** | 3.5 | 976 | San. | 8.504(4) | 12.865(5) | 7.126(2) | 115.64(3) | 702.9(3) | 699.1 | **0.5** |
| **P-cell6-plain** | 4.5 | 1073 | San. | 8.428(1) | 12.931(2) | 7.105(1) | 116.44(2) | 693.3(1) | 691.8 | **0.2** |
| **P-cell6-plain** | 6.7 | 1168 | San. | 8.376(1) | 12.894(2) | 7.057(1) | 116.80(2) | 680.2(1) | 676.3 | **0.6** |
| **P-cell6-plain** | 4.9 | quench | San. | 8.377(2) | 12.912(3) | 7.065(2) | 116.91(3) | 681.4(1) | 678.6 | **0.4** |
| **P-cell4-plain** | 3.2 | 300 | San. | 8.482 (6) | 12.96 (1) | 7.114 (2) | 116.63 (3) | 699.1 (3) | 696.64 | **0.4** |
| **P-cell4-plain** | 6.0 | 378 | San. | 8.367 (4) | 12.792 (9) | 7.049 (2) | 115.85 (3) | 678.9 (3) | 671.35 | **1.1** |
| **P-cell4-plain** | 6.3 | 494 | San. | 8.390 (8) | 12.82 (1) | 6.986 (3) | 115.38 (7) | 679.0 (2) | 670.50 | **1.3** |
| **P-cell4-plain** | 6.3 | 646 | San. | 8.324 (5) | 12.849 (9) | 7.012 (2) | 115.93 (4) | 674.6 (3) | 672.26 | **0.3** |
| **P-cell4-plain** | 6.2 | 791 | San. | 8.262 (4) | 12.861 (8) | 7.042 (2) | 116.32 (4) | 670.7 (2) | 674.50 | **-0.6** |
| **P-cell4-plain** | 6.4 | 866 | San. | 8.219 (3) | 12.923 (6) | 7.019 (2) | 115.75 (4) | 671.5 (2) | 674.41 | **-0.4** |
| **P-cell4-plain** | 6.2 | 892 | San. | 8.214 (2) | 12.967 (6) | 7.008 (1) | 115.88 (3) | 671.5 (3) | 675.74 | **-0.6** |
| **P-cell4-plain** | 6.2 | 965 | San. | 8.197 (2) | 12.962 (6) | 6.995 (2) | 115.70(4) | 669.8 (2) | 676.78 | **-1.0** |
| **P-cell4-plain** | 6.8 | 1073 | San. | 8.203 (2) | 12.858 (3) | 7.034 (2) | 116.62 (2) | 663.3 (2) | 674.40 | **-1.7** |
| **P-cell4-plain** | 6.3 | 1172 | San. | 8.3090 (9) | 12.894 (2) | 7.0798 (9) | 117.055 (9) | 675.5 (1) | 679.08 | **-0.5** |
| | | | co. | 7.266 (2) | 12.068 (3) | 6.992 (1) | 119.15 (2) | 535.4 (1) | 521.23 | **2.6** |
| **P-cell4-plain** | 6.5 | 1272 | San. | 8.305 (2) | 12.878 (3) | 7.043 (2) | 117.30 (2) | 669.4 (2) | 679.35 | **-1.5** |
| | | | co. | 7.8 (1) | 12.4 (1) | 6.82 (4) | 116.9 (6) | 588 (5) | 521.28 | **11.3** |
| **P-cell4-plain** | 5.1 | 1373 | San. | 8.408 (2) | 12.934 (3) | 7.090 (2) | 117.01 (2) | 686.9 (2) | 691.93 | **-0.7** |
| | | | co. | 7.126 (8) | 12.151 (8) | 7.096 (7) | 12.21 (5) | 531.0 (3) | 528.36 | **0.5** |
| **P-cell4-plain** | 2.5 | 1473 | San. | 8.425 (1) | 12.941 (3) | 7.137 (2) | 116.16 (2) | 698.3 (1) | 716.02 | **-2.5** |
| | | | co. | 7.11 (2) | 12.21 (2) | 7.21 (2) | 121.2 (1) | 535.6 (7) | 541.63 | **-1.1** |
| **P-cell4-plain** | 4.1 | quench | San. | 8.352 (1) | 12.916 (2) | 7.1140 (8) | 116.04 (1) | 689.53 (7) | 685.08 | **0.6** |
| **D-RT1-1-Xe/Kr** | 3.4 | 298 | | 8.582(3) | 12.924(4) | 7.166(2) | 115.84(4) | 715.4(2) | 691.0 | 3.4 |
| **D-RT1-1-Xe/Kr** | 2.7 | 373 | San. | 8.558(2) | 12.992(3) | 7.156(2) | 116.19(2) | 714.0(2) | 697.9 | 2.3 |
| **D-RT1-1-Xe/Kr** | 1.5 | 523 | San. | 8.613(2) | 13.003(3) | 7.198(1) | 116.04(2) | 724.2(1) | 711.0 | 1.8 |
| ***D-RT1-1-Xe/Kr** | 2.5 | 852 | San. | 8.598(1) | 13.007(2) | 7.181(1) | 116.20(1) | 720.5(1) | 705.9 | 2.0 |
| **D-RT1-1-Xe/Kr** | 2.9 | quench | San. | 8.572(1) | 12.999(2) | 7.170(1) | 116.14(1) | 717.2(1) | 695.3 | 3.1 |

| | | | | | | | | | | |
|---|---|---|---|---|---|---|---|---|---|---|
| **P-cell2-Xe/Kr** | 0.8 | 373 | San. | 8.639(2) | 13.001(3) | 7.193(2) | 115.87(2) | 726.9(2) | 716.0 | 1.5 |
| **P-cell2-Xe/Kr** | 1.6 | 413 | San. | 8.635(2) | 12.980(3) | 7.192(2) | 116.05(2) | 724.1(2) | 709.0 | 2.1 |
| ***P-cell2-Xe/Kr** | 1.0 | 473 | San. | 8.637(3) | 12.988(3) | 7.177(2) | 115.70(2) | 725.5(3) | 714.9 | 1.5 |
| ***P-cell2-Xe/Kr** | 1.4 | 573 | San. | 8.650(2) | 12.969(3) | 7.180(1) | 115.82(2) | 725.1(2) | 712.8 | 1.7 |
| ***P-cell2-Xe/Kr** | 1.6 | 653 | San. | 8.650(2) | 12.972(2) | 7.188(1) | 115.84(2) | 725.9(2) | 712.2 | 1.9 |
| ***P-cell2-Xe/Kr** | 1.2 | 753 | San. | 8.652(2) | 12.974(2) | 7.195(1) | 115.88(2) | 726.7(2) | 716.9 | 1.3 |
| ***P-cell2-Xe/Kr** | 2.5 | 873 | San. | 8.660(1) | 12.977(2) | 7.204(1) | 115.90(1) | 728.3(1) | 706.7 | 3.0 |
| **P-cell2-Xe/Kr** | 1.0 | quench | San. | 8.650(5) | 12.97(1) | 7.195(4) | 115.42(6) | 728.8(7) | 713.8 | 2.1 |
| **P-cell4-Xe** | 5.3 | 1073 | San. | 8.190 (2) | 12.854 (6) | 7.012 (3) | 116.49 (3) | 660.7 (3) | 685.79 | **-3.8** |
| **P-cell4-Xe** | 6.2 | 1171 | San. | 8.265 (3) | 12.876 (6) | 7.066 (2) | 117.44 (2) | 667.3 (3) | 679.81 | **-1.9** |
| | | | co. | 7.080 (6) | 12.02 (1) | 7.114 (6) | 120.33 (4) | 522.6 (6) | 521.65 | **0.2** |
| **P-cell4-Xe** | 6.8 | 1272 | San. | 8.285 (3) | 12.900 (5) | 7.068 (3) | 117.46 (2) | 670.3 (2) | 677.08 | **-1.0** |
| | | | co. | 7.001 (4) | 12.189 (3) | 7.126 (3) | 120.24 (3) | 525.3 (3) | 519.97 | **1.0** |
| **P-cell4-Xe** | 6.7 | 1373 | San. | 8.366 (3) | 12.739 (8) | 7.085 (3) | 116.98 (3) | 672.9 (3) | 680.00 | **-1.1** |
| | | | co. | 7.015 (3) | 12.217 (5) | 7.148 (5) | 120.37 (4) | 528.5 (3) | 521.55 | **1.3** |
| ***P-cell4-Xe** | 3.1 | 1473 | San. | 8.529 (3) | 13.002 (6) | 7.165 (3) | 116.42 (4) | 711.6 (4) | 710.27 | **0.2** |
| | | | co. | 6.901 (6) | 12.416 (9) | 7.093 (8) | 119.83 (8) | 527.2 (5) | 538.49 | **-2.1** |
| **P-cell4-Xe** | 1.8 | quench | San. | 8.347 (2) | 12.951 (4) | 7.105 (1) | 115.72 (3) | 696.0 (2) | 705.17 | **-1.3** |

*Table F6: Cell parameters and volume for plain sanidine Itrongahi (P-cell6-plain), plain sanidine Nat. (P-cell4-plain), and Xe/Kr-bearing sanidine Itrongahi (D-RT1-1-Xe/Kr and P-cell2-Xe/Kr) and Xe-bearing sanidine Nat. (P-cell4-Xe). * indicates data points above Xe melting point (for Xe-bearing samples). Uncertainties on the last digit are given in brackets. For P-cell6-plain, P-cell4-plain, and P-cell2-Xe/Kr errors on* P *and* T *are 0.2 GPa and 50 K, and error on predicted volume is ± 2 Å$^3$. For D-RT1-1-Xe/Kr errors on* P *and* T *are 50 K and 0.3 GPa. Error on predicted volume is ± 3 Å$^3$.*

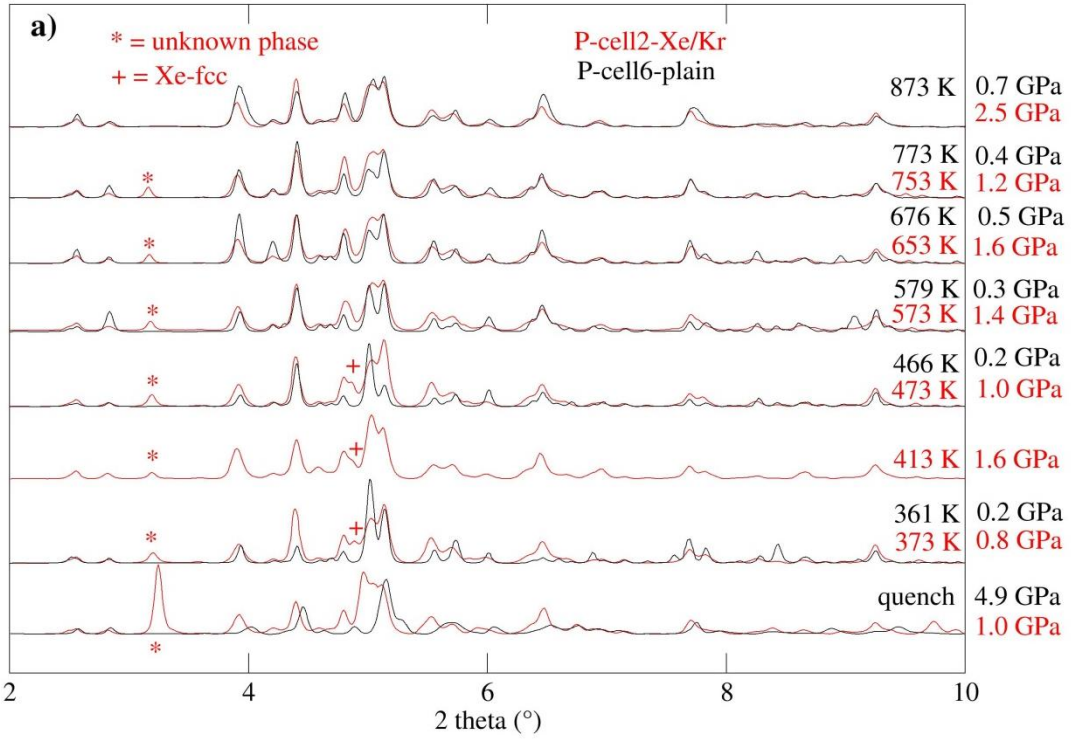

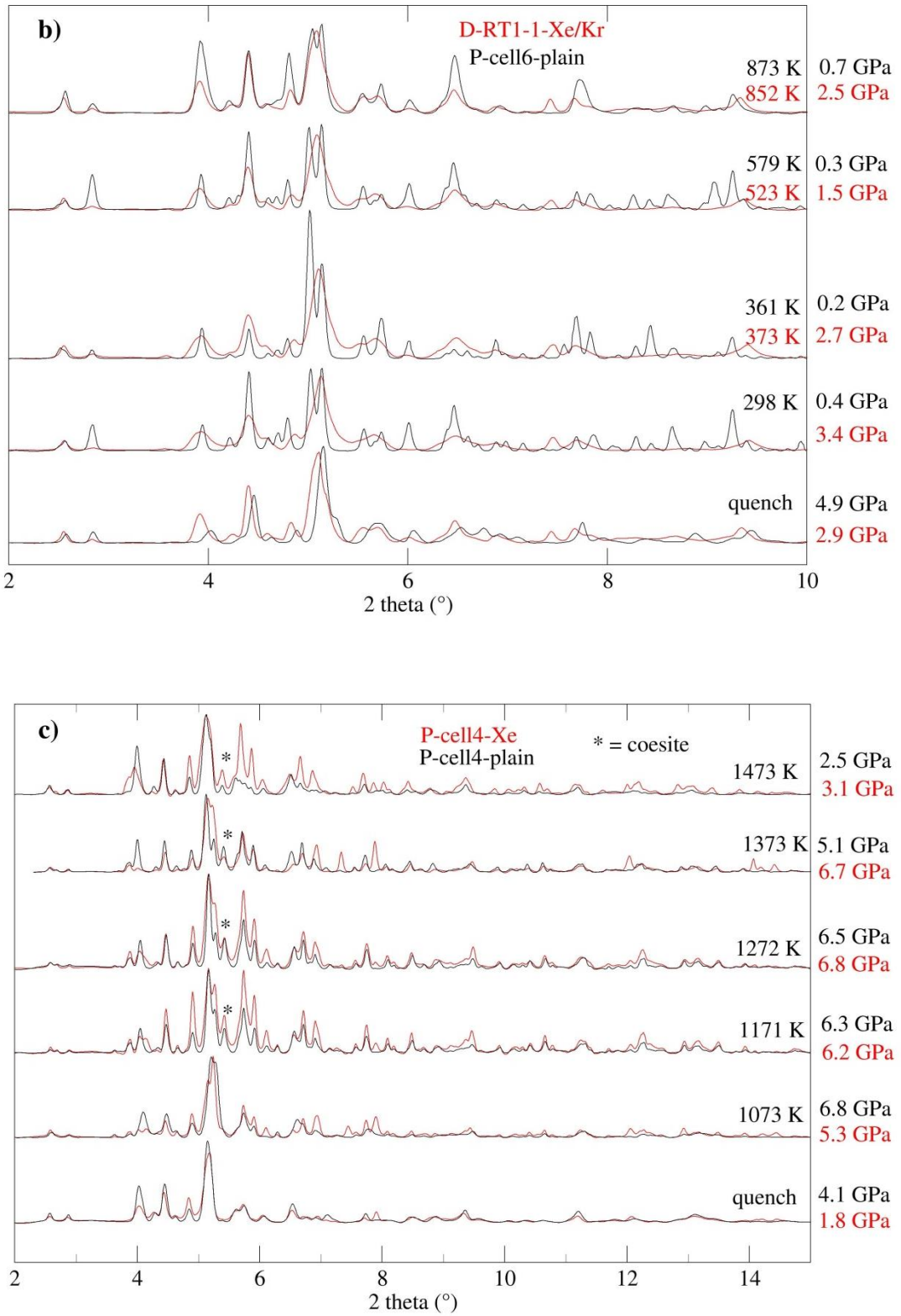


*Figure F11: Comparison of X-ray diffraction patterns with and without Xe for sanidine Itrongahi: a) P-cell6-plain compared to P-cell2-Xe/Kr, b) P-cell6-plain compared to D-RT1-1-Xe/Kr, and for sanidine Nat.: c) P-cell4-plain compared to P-cell4-Xe. λ (wavelength) = 0.2902Å.*

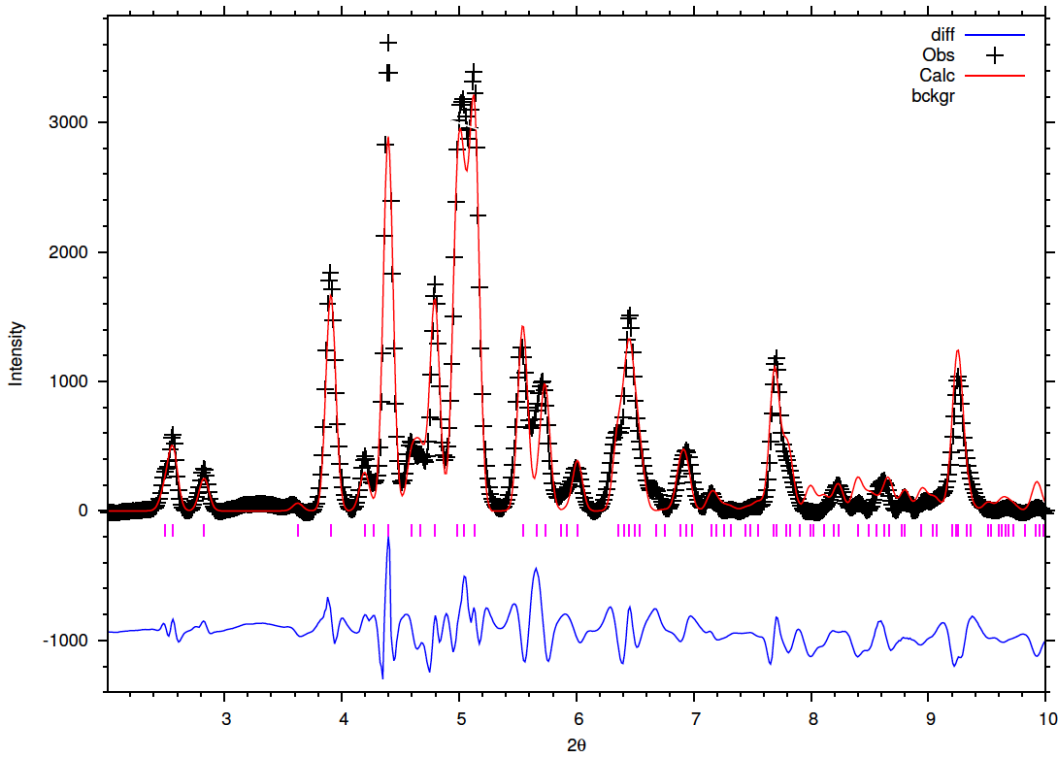


*Figure F12: Rietveld refinement for Xe/Kr-bearing sanidine Itrongahi (P-cell2-Xe/Kr) at 2.5 GPa and 873 K. λ = 0.2902 Å.*

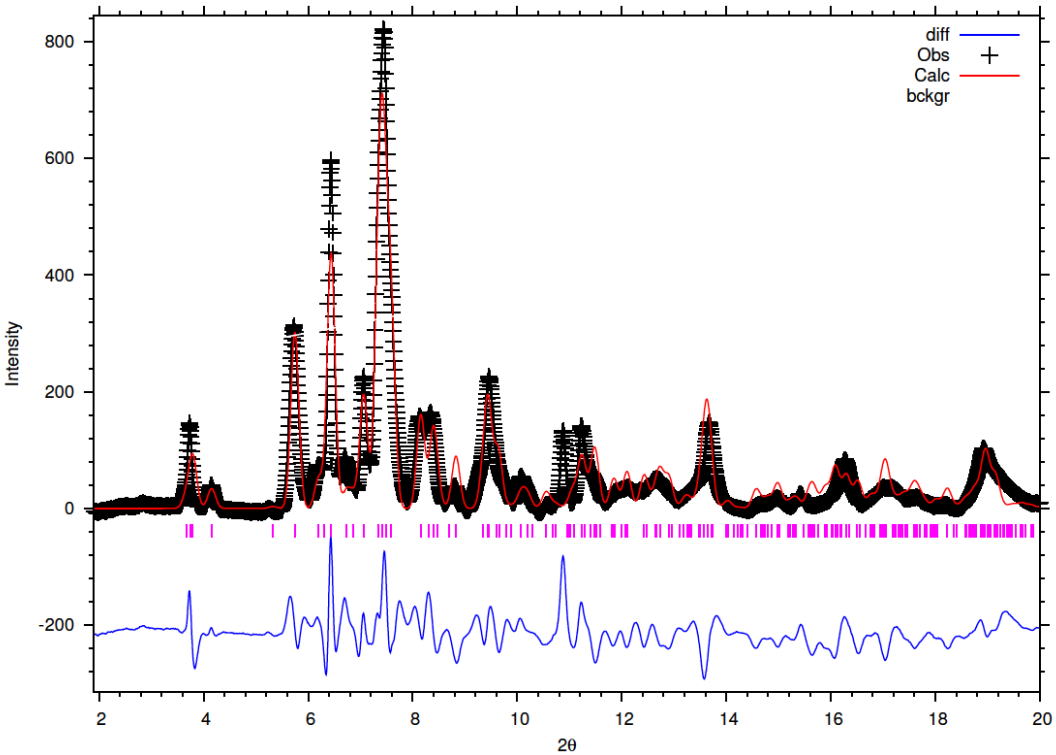


*Figure F13: Rietveld refinement for Xe/Kr-bearing sanidine Itrongahi (D-RT1-1-Xe/Kr) at 2.5 GPa and 852 K. λ = 0.4246 Å.*

| $d_{hkl}$ (Å) |
|---|
| 5.13 |
| 3.35 |
| 3.054 |
| 2.47 |
| 2.1 |
| 1.71 |
| 1.68 |

*Table F7: List of interplanar distances ($d_{hkl}$) for the unknown phase present in P-cell2-Xe/Kr.*

3/ Results for K-cymrite and sanidine at high water fugacity

Sanidine transforms into K-cymrite at high water fugacity and at high *P-T* conditions (Seki and Kennedy, 1964; Fasshauer et al., 1997; Thomson et al., 1998; Yong et al., 2006; Romanenko et al., 2017). K-cymrite is composed of double tetrahedral sheets with $H_2O$ molecules inside their cavities, K is acting as an interlayer cation (Figures F14). K-cymrite also exists as an anhydrous form: hexasanidine as named by Thomson et al. (1998) or kokchetavite, which can be obtained by dehydration of K-cymrite. Kokchetavite was identified in Kokchetav high-pressure terrane (Hwang et al., 2004), proving that K-cymrite or kokchetavite can be present at depth in the Earth. However, there is no published study dedicated to K-cymrite or its anhydrous form (kokchetavite) above 4 GPa, and stability field of K-cymrite is strongly dependent on water activity (Figure F15). K-cymrite is expected to break down into hollandite[21] + water above 9 GPa (Yong et al., 2006), however Romanenko et al. (2017) mentioned that an unknown phase was observed at 9 GPa, which is not hollandite. Romanenko et al. (2017) also observed presence of coesite coexisting with K-cymrite above 4 GPa.

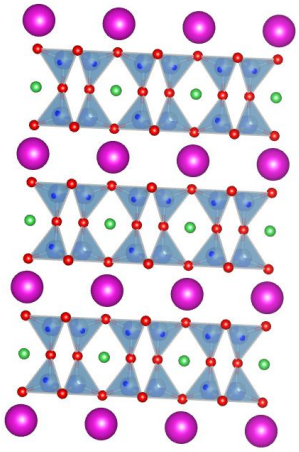

*Figure F14: K-cymrite in the (*bc*) plane showing the layered structure with molecular water in cavities. O, $H_2O$, and K are red, green and magenta ball respectively, and Si/Al tetrahedra are blue tetrahedra.*

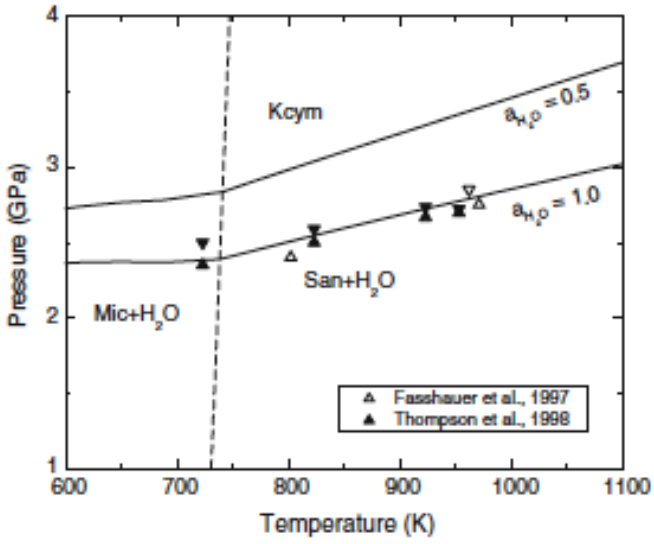


*Figure F15: K-cymrite (Kcym) stability field, from Yong et al. (2006). San = sanidine, Mic = microcline, $a_{H2O}$ = water activity.*

[21] High-*P* form of feldspars (Ringwood et al., 1967).

Plain hydrated sanidine glasses (D-HT2-1-plain and D-RT1-1-plain) recrystallized into K-cymrite ($KAlSi_3O_8.H_2O$) and sanidine (Table F8). For D-HT2-1-plain, it was observed that first K-cymrite coexists with a residual glass (at 1093 K and 6.4 GPa), which further recrystallized into sanidine (at 1158 K and 5.6 GPa) (Figure F16).
Xe/Ar-bearing hydrated sanidine Itrongahi glasses (P-cell6-Xe/Ar and P-cell3-Xe/Ar) recrystallized into K-cymrite and coesite. At 4.8 GPa sanidine is also present (P-cell-Xe/Ar), whereas above 9 GPa (P-cell3-Xe/Ar) another phase is present (Figure F16).

Yong et al. (2006) derived a second order thermal equation of state from a set of experimental data from Fasshauer et al. (1997). However, this equation of state is not fitting data from Thomson et al. (1998), with predicted volumes being an average of 4.2 % smaller than the observed ones, and is neither fitting our data for plain samples (D-HT2-1-plain and D-RT1-1-plain) at high *P-T* conditions, with predicted volumes being an average of 5.7 % smaller than the observed ones (Table F8). Misfits from the equation of state of Yong et al. (2006) may be due to the fact that experimental data from Fasshauer et al. (1997) are room-*P* data up to 648 K to determine thermal expansion and room-*T* data up to 5.99 GPa to determine bulk modulus and its derivative. Thus, this equation of state may not be relevant for data at higher *P-T* range such as ours. Moreover K-cymrite has variable water contents: data from Fasshauer et al. (1997) having 6.07 wt% water and data from Thomson et al. (1998) 4.42-4.85 wt% water.
K-cymrite synthesized at high *P-T*, which further undergoes increase of *T* at low *P*, is better fitted by the equation of state from Yong et al. (2006) within 1.2 % (Table F8), although these samples could have undergone dehydration (Thomson et al., 1998).
For plain sample (D-HT2-1-plain and D-RT1-1-plain), the observed volume of sanidine coexisting with K-cymrite is 2.6 % larger than the predicted one (Table F8), although the equation of state well fits the data for dry plain sanidine Itrongahi within 0.6 % (Table F6). This excess volume for sanidine may be due to water incorporation (Beran, 1986).

It is difficult to identify any excess volume for K-cymrite and sanidine in presence of Xe (at high water fugacity) due to the absence of reliable equation of state. For P-cell6-Xe/Ar, K-cymrite peak intensities are wrong, with very low intensity for peak at 8.3° which is likely due to poor statistics from poor recrystallization (image plate in Appendix F5). However, for P-cell3-Xe/Ar, peak intensities for K-cymrite systematically differ compared to plain sample (Figure F16). Indeed, in presence of Xe, the relative intensities for the two main peaks at 8.3° and 9.1° are modified, while the doublet at 6.2° and 6.7° is smaller in presence of Xe. Rietveld refinements are given for the plain sample (D-HT2-1-plain) on figure F17 and for Xe/Ar-bearing sample (P-cell3-Xe/Ar) on figure F18.
It is to be noted that coesite is only present for Xe/Ar-bearing samples in our experiment (Table F8), although Romanenko et al. (2017) systematically observed coesite in presence of K-cymrite above 4 GPa. Eventually the unknown phase, appearing for Xe-bearing sample at 9.2-9.7 GPa (P-cell3-Xe/Ar) remains unexplained (Figure F16). It does not correspond to any of the possible expected phases (stishovite, jadeite, hollandite, diopside, wadeite, sanidine). Interplanar distances of the unknown phase at high *P-T* are given in table F9. DICVOL

software (Boultif and Louër, 1991) gives an orthorhombic solution (solution of highest symmetry), with cell parameters $a$ = 17.686(6) Å, $b$ = 4.504(4) Å and $c$ = 3.639(3) Å. This phase could correspond to the phase observed by Romanenko et al. (2017). As it does not appear at lower $P$ (4.8-5.3 GPa) for Xe/Ar bearing samples (P-cell6-Xe/Ar), its appearance may thus only be linked to high $P$ and not to presence of Xe.

| NAME | *P* (GPa) | *T* (K) | phase | *a* (Å) | *b* (Å) | *c* (Å) | beta (°) | observed V(Å$^3$) | predicted V (Å$^3$) | excess V(%) |
|---|---|---|---|---|---|---|---|---|---|---|
| **D-HT2-1-plain** | 6.4 | 1093 | Kcym | 5.3065 (2) | 5.3065 (2) | 7.4596 (4) | 120 | 181.92 (1) | 170.902 | **6.1** |
| | | | glass | - | - | - | - | - | - | - |
| **D-HT2-1-plain** | 5.6 | 1158 | Kcym | 5.3137 (3) | 5.3137 (3) | 7.4996 (9) | 120 | 183.38 (2) | 174.188 | **5.0** |
| | | | San. | 8.552 (1) | 12.898 (2) | 7.085 (1) | 116.30 (1) | 700.6 (1) | 684.469 | **2.3** |
| **D-HT2-1-plain** | 1.6 | 418 | Kcym | 5.3120 (1) | 5.3120 (1) | 7.5062 (4) | 120 | 183.425 (9) | 184.393 | **-0.5** |
| | | | San. | 8.546 (1) | 12.883 (1) | 7.076 (1) | 116.289 (9) | 698.4 (1) | 708.739 | **-1.5** |
| **D-HT2-1-plain** | 1.6 | 313 | Kcym | 5.3075 (1) | 5.3075 (1) | 7.4913 (5) | 120 | 182..75 (1) | 183.892 | **-0.6** |
| | | | San. | 8.5463 (8) | 12.875 (1) | 7.1279 (9) | 116.447 (8) | 702.21 (9) | 707.538 | **-0.8** |
| **D-HT2-1-plain** | 2 | 368 | Kcym | 5.3075 (1) | 5.3075 (1) | 7.4867 (5) | 120 | 182.64 (1) | 182.593 | **0.0** |
| | | | San. | 8.5203 (9) | 12.837 (1) | 7.1634 (7) | 115.995 (6) | 704.85 (8) | 704.347 | **0.1** |
| **D-HT2-1-plain** | 2.6 | 478 | Kcym | 5.3073 (1) | 5.3073 (1) | 7.5027 (4) | 120 | 183.02 (1) | 180.844 | **1.2** |
| | | | San. | 8.5173 (9) | 12.874 (1) | 7.0797 (9) | 116.198 (9) | 696.5 (1) | 700.092 | **-0.5** |
| **D-HT2-1-plain** | 1.7 | 308 | Kcym | 5.3060 (2) | 5.3060 (2) | 7.5042 (4) | 120 | 182.97 (1) | 183.478 | **-0.3** |
| | | | San. | 8.510 (1) | 12.869 (1) | 7.086 (1) | 116.109 (9) | 696.8 (1) | 706.521 | **-1.4** |
| **D-RT1-1-plain** | 5.7 | 1244 | Kcym | 5.3156 (2) | 5.3156 (2) | 7.4925 (9) | 120 | 183.34 (2) | 174.489 | **5.1** |
| | | | San. | 8.4994 (9) | 12.939 (2) | 7.0934 (9) | 116.329 (8) | 699.2 (1) | 685.076 | **2.1** |
| **D-RT1-1-plain** | 5.7 | 1359 | Kcym | 5.3182 (3) | 5.3182 (3) | 7.6227 (7) | 120 | 186.71 (2) | 175.412 | **6.4** |
| | | | San. | 8.5548 (8) | 12.978 (1) | 7.1244 (9) | 116.122 (8) | 710.2 (1) | 686.991 | **3.4** |
| **D-RT1-1-plain** | 0.6 | 313 | Kcym | 5.3144 (7) | 5.3144 (7) | 7.676 (2) | 120 | 187.76 (4) | 187.898 | **-0.1** |
| | | | San. | 8.5083 (7) | 12.9748 (9) | 7.1184 (5) | 116.044 (6) | 706.03 (7) | 717.525 | **-1.6** |
| | | | glass | - | - | - | - | - | - | - |
| **P-cell6-Xe/Ar** | 4.8 | 1073 | San. | 8.409(3) | 12.922(5) | 7.102(1) | 115.97(2) | 693.8(3) | 689.4 | **0.6** |
| | | | Kcym | 5.2992(1) | 5.2992(1) | 7.582(3) | 120 | 184.38(8) | 176.5 | **4.3** |
| | | | Co. | 6.986(2) | 12.28(4) | 7.13(1) | 120.3(1) | 528(2) | 527.2 | **0.2** |
| **P-cell6-Xe/Ar** | 5.3* | 1168 | San. | 8.4530(8) | 12.911(1) | 7.0829(8) | 116.291(9) | 692.95(8) | 687.0 | **0.9** |
| | | | Kcym | 5.3040(4) | 5.3040(4) | 7.693(3) | 120 | 187.01(8) | 175.5 | **6.1** |
| | | | Co | 6.951(2) | 12.250(3) | 7.174(2) | 120.70(1) | 525.8(1) | - | - |
| **P-cell6-Xe/Ar** | 2.5 | quench | San. | 8.483(2) | 12.960(3) | 7.117(1) | 116.32(1) | 701.4(2) | 698.9 | **0.4** |
| | | | Co. | 7.098(2) | 12.376(2) | 7.125(2) | 121.15(3) | 535.7(2) | 533.6 | **0.4** |
| **P-cell3-Xe/Ar** | 9.7 | 1254 | Kcym (co.) u.p. | 5.240(2) - | 5.240(2) - | 7.248(4) - | 120 - | 172.4(1) - | 160.7 - | **6.8** - |
| **P-cell3-Xe/Ar** | 9.2 | 1347 | Kcym (co.) u.p. | 5.2459(6) - | 5.2459(6) - | 7.255(2) - | 120 - | 172.90(4) - | 163.1 - | **5.7** - |
| **P-cell3-Xe/Ar** | 5.2 | quench | Kcym (co.) u.p. | 5.2556(7) - | 5.2556(7) - | 7.314(2) - | 120 - | 174.97(5) - | 170.6 - | **2.5** - |
| **P-cell3-Xe/Ar** | 1.4 | 298 | Kcym (co.) u.p. | 5.344(1) - | 5.344(1) - | 7.568(3) - | 120 - | 187.16(7) - | 184.6 - | **1.4** - |

| | | | | | | | | | | |
|---|---|---|---|---|---|---|---|---|---|---|
| **P-cell3-Xe/Ar** | 1 | 369 | Kcym (co.) u.p. | 5.334(1) - | 5.334(1) - | 7.568(3) - | 120 - | 186.44(8) - | 186.5 - | **0.0 -** |
| **P-cell3-Xe/Ar** | 1 | 373 | Kcym (co.) u.p. | 5.337(1) - | 5.337(1) - | 7.578(3) - | 120 - | 186.90(8) - | 186.6 - | **0.2 -** |
| **P-cell3-Xe/Ar** | 0.6 | 467 | Kcym (co.) u.p. | 5.318(1) - | 5.318(1) - | 7.585(4) - | 120 - | 185.76(9) - | 188.8 - | **-1.6 -** |
| **P-cell3-Xe/Ar** | 0.4 | 570 | Kcym (co.) u.p. | 5.301(1) - | 5.301(1) - | 7.641(3) - | 120 - | 185.98(7) - | 190.1 - | **-2.2 -** |
| **P-cell3-Xe/Ar** | 1.1 | 669 | Kcym (co.) u.p. | 5.2943(8) - | 5.2943(8) - | 7.701(2) - | 120 - | 186.93(5) - | 187.9 - | **-0.5 -** |
| **P-cell3-Xe/Ar** | 1.1 | 727 | Kcym (co.) u.p. | 5.2954(8) - | 5.2954(8) - | 7.726(2) - | 120 - | 187.61(6) - | 188.3 - | **-0.4 -** |
| **P-cell3-Xe/Ar** | 1.0 | 483 | Kcym (co.) u.p. | 5.2888(7) - | 5.2888(7) - | 7.713(2) - | 120 - | 186.85(5) - | 187.2 - | **-0.2 -** |
| **P-cell3-Xe/Ar** | 1.6 | quench | Kcym (co.) u.p. | 5.2812(8) - | 5.2812(8) - | 7.697(2) - | 120 - | 185.92(6) - | 184.0 - | **1.1 -** |

*Table F8: Cell parameters of K-cymrite (Kcym), sanidine (san.), and coesite (co.) for recrystallized plain hydrated sanidine glass (D-HT2-1-plain and D-RT1-1-plain), and for recrystallized Xe/Ar-bearing hydrated sanidine glass (P-cell3-Xe/Ar and P-cell6-Xe/Ar). 'u.p.' stands for unknown phase, and '(co.)' means that coesite peaks are very small.* * P *was calculated from coesite's cell parameters as no Pt calibrant was available. Errors on* P *and* T *are 0.2 GPa and 50 K. Uncertainties on the last digit is given in brackets. Error on predicted volume is ± 2 Å$^3$ for sanidine, ± 0.7 Å$^3$ for K-cymrite, and ± 1 Å$^3$ for coesite. Cell parameters were not determined for coesite when the amount is too small to get any reliable evaluation.*

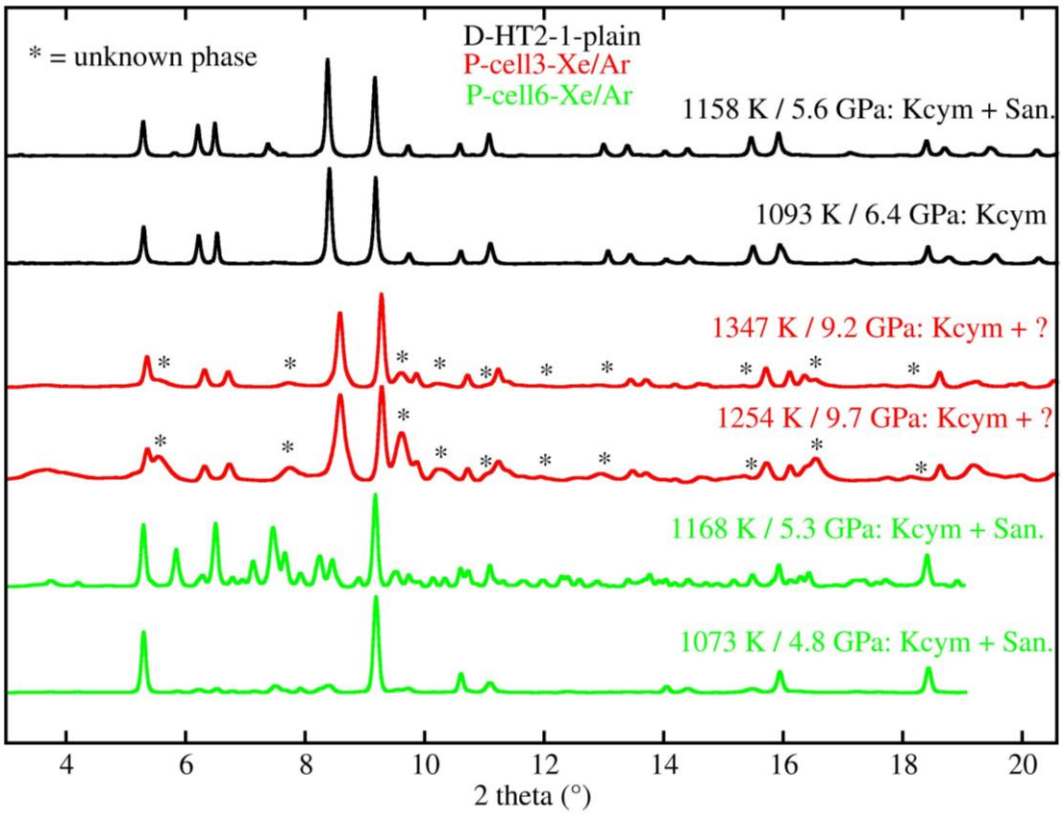


*Figure F16: X-ray diffraction patterns for plain hydrated sanidine glass after recrystallization into K-cymrite (Kcym) and sanidine (san.) for D-HT2-1-plain: black line, and for Xe/Ar hydrated sanidine glass after recrystallization into K-cymrite and sanidine for P-cell6-Xe/Ar: green line, and into K-cymrite and another unknown phase (whose $d_{hkl}$ are listed in table F8) for P-cell3-Xe/Ar: red line. λ = 0.4246 Å.*

| $d_{hkl}$ (Å) |
|---|
| 4.37 (1) |
| 3.15 |
| 2.53 |
| 2.38 (1) |
| 2.21 |
| 2.05 (1) |
| 1.89 (1) |
| 1.59 |
| 1.47 |
| 1.35 |

*Table F9: List of $d_{hkl}$ for the unknown phase evaluated for P-cell3-Xe/Ar from patterns recorded at 9.7 GPa and 1254 K and at 9.2 GPa and 1347 K.*

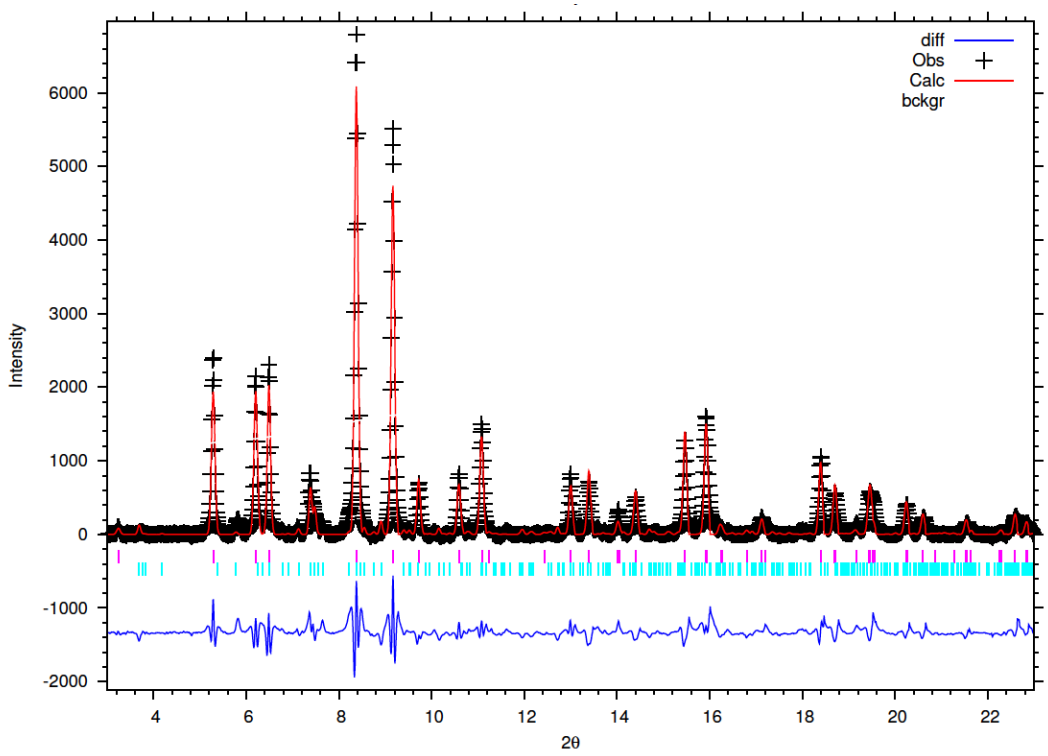


*Figure F17: Rietveld refinement for D-HT2-1-plain at 5.6 GPa and 1158 K. Pattern is fitted with K-cymrite (magenta tickmarks) and sanidine (cyan tickmarks). λ = 0.4246 Å.*

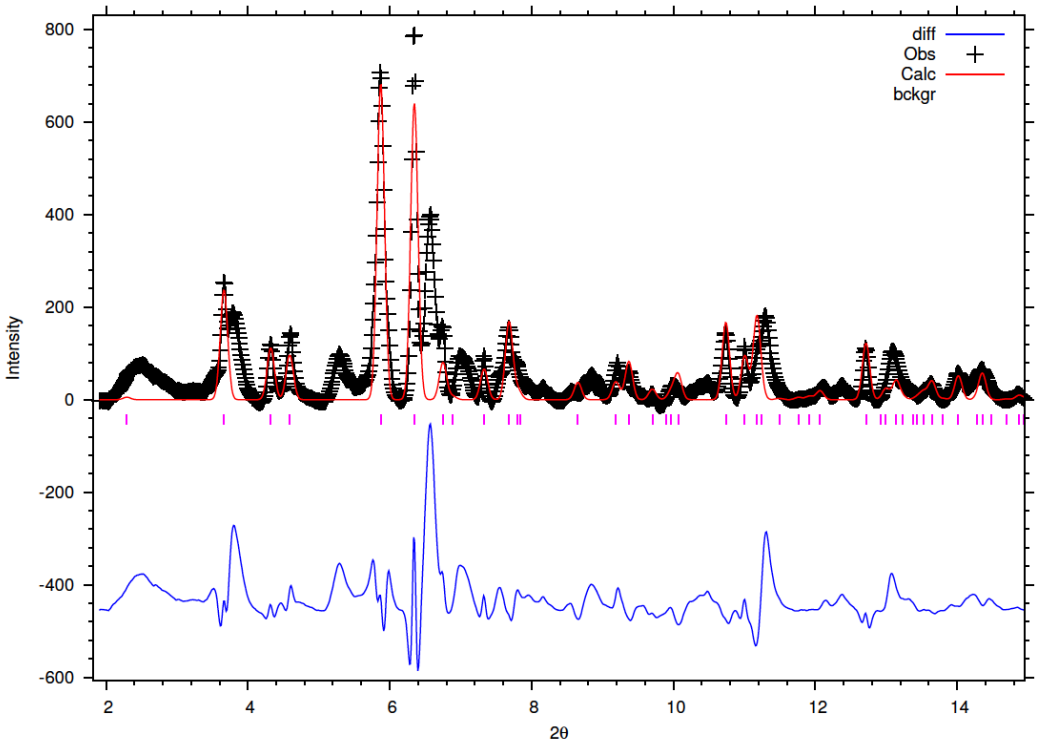


*Figure F18: Rietveld refinement for P-cell3-Xe/Ar at 9.7 GPa and 1254 K. Pattern is fitted with K-cymrite (magenta tickmarks), peaks not fitted are corresponding to the unknown phase. Coesite peak is not seen in this view. By comparing with figure F14 it is observed that sanidine could explain unknown phase, although peak intensities will be wrong. λ = 0.2902 Å.*

## III/ Conclusion

There are two tetrahedral sites in sanidine. Ackermann et al. (2004) combining X-ray and neutron diffraction on sanidine Itrongahi showed that Fe substitutes in tetrahedral site T1, which is occupied preferentially by Al (whereas tetrahedral site T2 is mostly occupied by Si), with 65% Si, 33% Al and 2% Fe (in at %) on T1 site and 88% Si and 12% Al (in at %) on T2 site. Ordering of the cations increases with ionic size, explaining why Fe is more ordered than Al. Xe, due to its large radius is expected to be located uniquely on the T1 site in case of substitution with cation.

The observed separation of sanidine in Fe-rich and Fe-poor zones on recovered samples reminds separation between a Fe-rich and a Fe-poor olivine in presence of Xe (D/IV/1).

In Fe-rich sanidine phase, Xe may substitute to Al on T1 site, which will explain systematic Al depletion, although higher Si content remains to explain. The presence of Xe on the T1 site could trigger a stabilization of $Fe^{3+}$ on this site, by preventing Fe reduction to the Pt capsule (as detailed for olivine in D/I/2). Indeed, Xe was already shown to stabilize $Ag^{2+}$ (normally reducing to $Ag^{+}$) in a Ag-natrolite (zeolite) (Seoung et al., 2004). Such stabilization may be due to high Xe polarizability (Walker et al., 1999), with Xe acting as an adduct, as previously shown for Au(I)F (Kurzydłowski and Grochala, 2008).

In Fe-poor zones, Xe is likely to have escaped the silicate network upon quenching, explaining that it is only found as bubbles. Based on observed Xe:Si and Kr:Si trend retrieved by EMPA of noble gases bubbles and surrounding sanidine on Fe-poor zones, Xe and Kr may have been incorporated through Xe (Kr) for Si substitution in sanidine.

*In situ* X-ray diffraction confirms Xe incorporation in sanidine with an observed excess volume up to 3.4 % and change in peak intensities. *In situ* X-ray diffraction data are likely to probe Xe incorporation mechanisms in Fe-poor zones, as these zones represent the major part of the sample (Figure F1). However, it has not been possible so far to determine Xe location based on Rietveld refinements although difference on peak intensities are observed in presence of Xe.

So far, potential Xe incorporation in K-cymrite remains unclear, due to poor knowledge of the behavior of K-cymrite at high *P-T* conditions, although differences in peak intensities are observed in presence of Xe for K-cymrite. Moreover recovered sample for P-cell3-Xe/Ar seems to indicate that Xe is retained within the silicate network in presence of K-cymrite above 9 GPa.

## Chapter G: XE AND KR INCORPORATIONS IN FELDSPATHIC GLASS AND MELT

Little is known about noble gases solubility mechanisms in silicate melts or glasses, whereas it is fundamental to constrain degassing of the Earth. Moreover, as previously mentioned, $^{131,133,135}$Xe and $^{85}$Kr are common radioactive fission products, and as such, their release in $UO_2$ fuels, as well as in silicate glasses; nuclear waste confinement by vitrification in $SiO_2$-rich glasses being used for many years (Ojovan and Lee, 2011), needs to be understood. To model release of fission gases in $UO_2$, implanted Xe (and Kr) is observed in $UO_2$ at high *T* (to simulate irradiation). Xe is mostly located in nanobubbles following implantation. Nanobubbles are shown to grow bigger with increasing *T* (e.g. TEM studies from Michel et al., 2012), and Martin et al. (2008) showed that they are pressurized up to 2.8 GPa at 1073 K. No Xe-U or Xe-O bonds were identified by XAS (Martin et al., 2008), although it may be due to their very low proportions compared to Xe-Xe bonds found in nanobubbles. Kr has a similar behaviour as Xe in $UO_2$ (Michel et al., 2012, Martin et al., 2015).

In this work we synthesized different heavy noble gases-bearing feldspathic glasses and investigated them *in situ* at high *P-T* conditions, to resolve incorporation mechanisms of Xe and Kr in silicate melts. We report here the first *in situ* XAS measurements at the Kr *K*-edges on a feldspathic Xe/Kr-bearing glass and melt (2.2 wt% Xe, and 0.5 wt % Kr) up to 2.7 GPa. The results have been submitted to *Chemical Geology*, reviews have been received and a corrected version is being reviewed. We also report first *in situ* XAS measurements at the Xe *K*-edges on the same sample up to 3 GPa.

.

### I/ Sample synthesis

Different Xe/(Ar,Kr)-bearing glasses have been synthesized (Table G1), from three natural sanidines (Appendix F1). Average chemical composition is given in Appendix G1 (and full EMPA in Appendix G2). Xe contents measured in the bulk, away from microbubbles, range from 0.05 wt% Xe to 2.39 wt% Xe (Table G1). Leroy et al. (2018) retrieved 4.0 (0.8) wt% Xe in a haplogranite glass. Very low Xe contents retrieved here do not reflect Xe solubility but are due to low amounts of Xe initially loaded in the capsules. Xe was observed as microbubbles, in addition to its presence in the bulk for PC53, PC69, and in a less extent for PC116A, and PC116B indicating that saturation was reached for these samples.

For experiments in presence of water (PC116A and PC116B), Xe is still retrieved in the recovered glass (Table G1), which is different from what is observed for olivine (section D/I/2/) for which no Xe was detected in the crystal in presence of water. PC116A and PC116B samples contain 2.9 wt% and 7.9 wt% water based on oxide totals (Table G1). Many large holes are observed on recovered PC116B (Figure G1), indicating water saturation.

Xe and Ar melt/fluid partition coefficients can be calculated for PC116A, as loaded Xe/Ar content, and Xe/Ar content in the melt are known. We found a Xe melt/fluid partition coefficient of 2.9 $10^{-2}$ for sanidine melt at 2 GPa and 1400°C. Result is similar for Ar melt / fluid partition coefficient.

| Sample | Starting material | gas mix | *P* (GPa) | *T* (°C) | Duration (hours) | powder (mg) | gas (mg) | weight loss after piercing (mg) | Exp. | wt% Xe recovered glass |
|---|---|---|---|---|---|---|---|---|---|---|
| **PC53** | San. Nat. | Xe | 3.5 | 1400 | 4 | - | - | - | Previous | 1.91 |
| **PC69** | San. Nat. | Xe/Kr | 3.5 | 1400 | 4 | - | - | - | Previous | 2.18 (4) |
| **PC70** | San. Nat. | Xe/Ar | 3.5 | 1400 | 4 | - | - | - | Previous | 0.05–0.09 |
| **PC112A** | San. It. | Xe/Kr | 3.5 | 1400 | 2.5 | 13.2 | 1 | - | This work | 0.09–0.11 |
| **PC112B** | San. Volk. | Xe/Kr | 3.5 | 1400 | 2.5 | 12.9 | 1 | - | This work | 0.06-0.07 |
| **PC116A** | San. It. + $H_2O$ | Xe/Ar | 2 | 1400 | 1 | 8.4 | 5 | 2 | This work | 0.55 (4) |
| **PC116B** | San. Nat. + $H_2O$ | Xe/Ar | 2 | 1400 | 1 | 11.1 | - | 2 | This work | 0.15-0.17 |
| **PC139** | San. It. | - | 2 | 1400 | 1 | 41 | - | - | This work | - |

*Table G1: Experimental conditions and compositions. San. It. = sanidine Itrongahi and San. Volk. = sanidine Volkesfeld. In red sample used for* in situ *XAS measurements in G/II and G/III. Average chemical composition is given in Appendix G1 and EMPA in Appendix G2.*

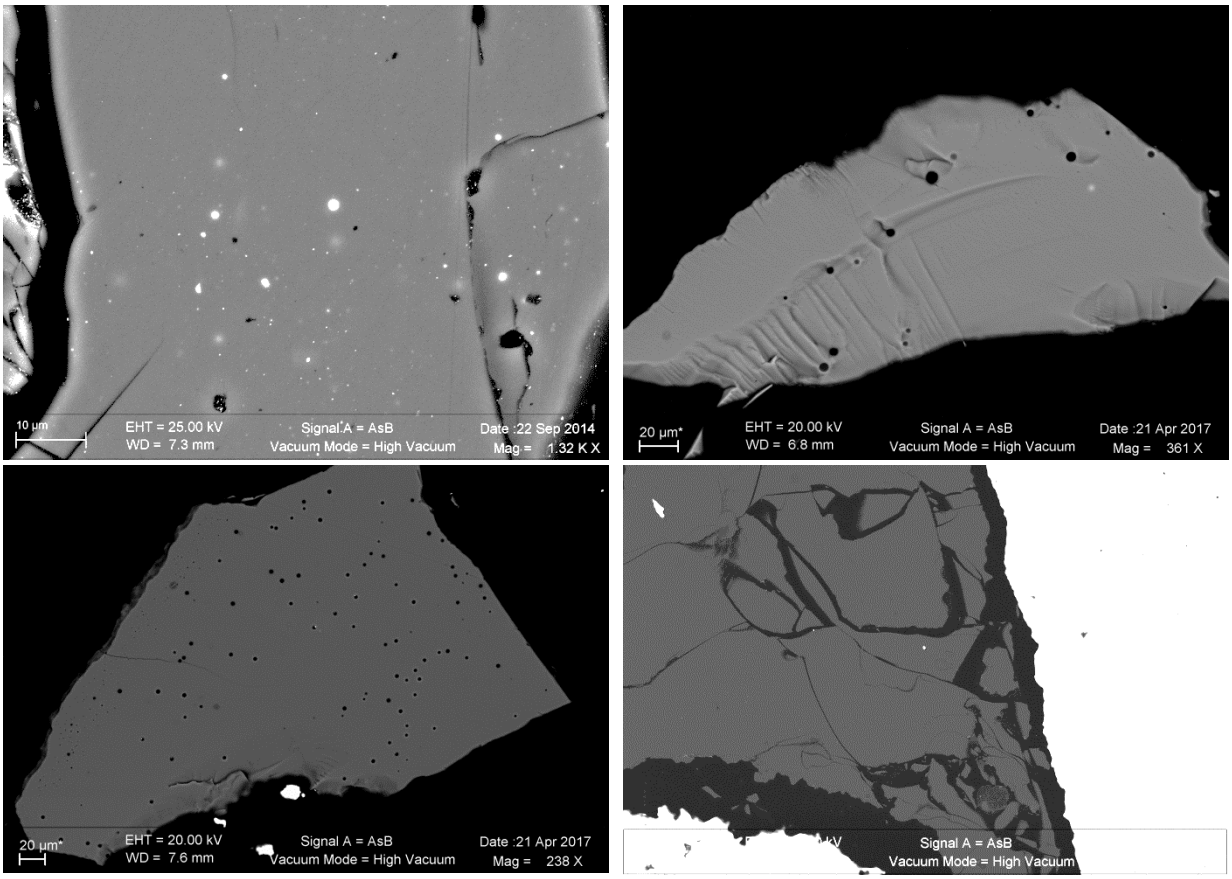


*Figure G1: SEM images in backscattered mode. Top left: PC69, Xe/Kr bright bubbles are visible. Top right: PC116A showing one bright Xe/Ar bubble. Bottom left: PC116B showing many large holes. Bottom right: PC70 showing no gaseous bubbles (bright inclusions are Pt), same scale bar as PC116B.*

## II/ Kr environment in a feldspathic glass and melt: a high *P-T* XAS study (published in *Chem. Geol.*)

### 1/ Introduction

*In situ* structural data on the environment of heavy noble gases in silicate melts and glasses are scarce. Wulf et al. (1999) performed an X-ray absorption study at the Kr *K*-edge in a $SiO_2$ glass (1.97 wt % Kr). They identified a Kr-O distance of 3.45 ± 0.1 Å, interpreted as corresponding to a local rearrangement of the silicate network into a local clathrasil-type environment around the Kr atom. Bonding of Xe to O in compressed haplogranitic magmas had also been evidenced by *in situ* X-ray diffraction (Leroy et al. 2018).

In the present study, we perform *in situ* X-ray absorption spectroscopy (XAS) at the Kr *K*-edge, to specifically access Kr structural environments in a feldspathic (sanidine) glass. Starting $(Na,K)AlSi_3O_8$ glass composition is representative of the chemistry of a major mineral of the continental crust, and proxy of silica-rich melts that can be generated at *P* reaching 2 GPa in orogenic contexts (Jimenez-Munt et al., 2008), and in subduction contexts from melting of hydrous basalt (Prouteau et al., 2001), or silica-rich sediments (Turner et al., 2012). Experiments were conducted at *P* and *T* up to 3 GPa and 1415°C, relevant for both continental crust melting and subduction zone contexts.

### 2/ Methods

#### a/ Sample: synthesis and characterization

The synthesized starting glass (PC69, Tables G1, G2) is chemically homogeneous with presence of Xe/Kr gas bubbles indicating that saturation was reached. Contents of 2.2 wt % Xe (0.36 at %) and 0.5 wt % Kr (0.13 at %) were measured by EMPA (Table G2). Recovered sample was quenched from 1040°C and 2.7 GPa, where it reequilibrated as partial melt and feldspar crystals (Figure G2), following cooling from fully molten state (1415°C and 3 GPa) which was reached with the initial purpose to collect XAS data at the Xe *K*-edge. Kr and Xe are only observed in the glass, with striking alignments of Xe/Kr gas nanobubbles (Figure G2). Average analyses of the recovered sample are given in Table G2, although degassing upon quenching prevents Xe and Kr contents to be determined by EMP analysis.

| sample | $Na_2O$ | $SiO_2$ | $Al_2O_3$ | $K_2O$ | CaO | Xe | Kr | Total |
|---|---|---|---|---|---|---|---|---|
| PC69 | 4.8 (2) | 63.6 (4) | 19.2 (1) | 8.7 (2) | 0.78 (5) | 2.18 (4) | 0.52 (5) | 99.7 (5) |
| Recovered sample | 2.9 (6) | 65 (1) | 19.8 (6) | 11 (1) | 0.3 (2) | [0-1.2]* | [0-0.5]* | 100(1) |

*Table G2: Average composition of the starting glass and recovered sample (20 data points both in the glassy and crystalline parts, full EMPA in Appendix G2 and Appendix G3) in oxide wt %, in brackets: standard deviation.* due to degassing upon quenching Kr and Xe contents cannot be properly evaluated by EMPA. Ranges of analyzed contents are given as an indication.*

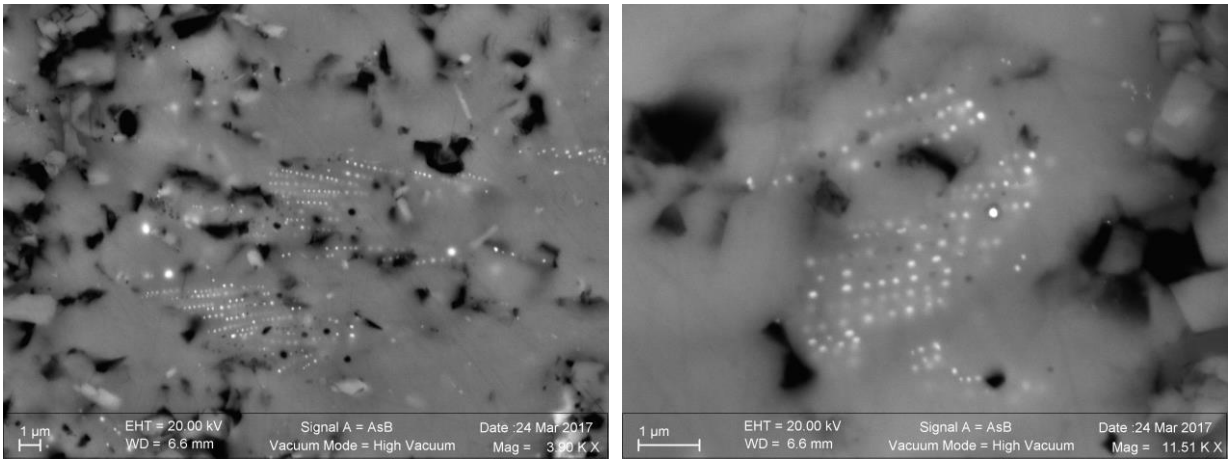


*Figure G2: SEM images in backscattered mode of recovered sample after XAS measurements. Feldspars recrystallized upon cooling to 1040°C at 2.7 GPa, coexisting with partial melt recovered as a glass upon quenching. Xe/Kr-nanobubbles (bright dots) are visible.*

### b/ Experimental set-up

*In situ* XAS was performed on beamline BM23 at the ESRF, dedicated to general purpose XAS (Mathon et al., 2015) shown in Figure C11. High *P-T* conditions up to 2.7 GPa and 1086°C (Table G3) were generated in a PEP (Besson et al., 1992). We used a cell assembly developed by Kono et al. (2014) and adapted from Yamada et al. (2011). More details on the cell-assembly and experimental set-up can be found in Rosa et al. (2016). The sample (0.75 mm diameter and 1.5 mm height) was encapsulated in a synthetic nanopolycrystalline diamond (NPD) cylinder caped with Pt-Rh caps. The use of NPD prevents glitches from a single or polycrystalline diamond capsule, which deteriorate the XAS signal. *T* was determined using calibration from Kono et al. (2014), and *P* using unit-cell volume of hBN from the cell assembly (based on X-ray diffraction measurements) and equation of state from Le Godec et al. (2000). Error bars are ± 50°C for *T* and ± 0.2 GPa for *P*.

| ***P* (GPa)** | ***T* (°C)** | **state** | **n.s.** | **count. time** |
|---|---|---|---|---|
| 0 | 20 | glass | 7 | 2 s |
| 2.6 | 920 | melt | 4 | 3 s |
| 2.7 | 1086 | melt | 5 | 4 s |
| 2 | 706 | glass | 5 | 5 s |
| 2 | 505 | glass | 5 | 6 s |
| 1.4 | 20 | quench | 4 | 7 s |

*Table G3:* P-T *conditions and state of the sample for each XAS measurement at Xe* K*-edge. n.s = number of scans, count. time = counting time per point analysis (451 point analysis).*

### c/ X-ray diffraction and XAS measurements

Angle-resolved X-ray diffraction data were recorded on a MAR165 CCD at 15 keV. Image plates were integrated using Fit 2D software (Hammersley, 1997). Cell parameters of hBN were determined using POWDER CELL software (Kraus and Nolze, 1996).
XAS transmission measurements were performed first at the Kr *K*-edge (14326 eV) up to 2.7 GPa, upon increase of *T* up to 1086°C, and upon decrease of *T* down to 505°C, before quenching to room *T* (Table G3). Xe *K*-edge spectra were recorded following measurement at the Kr *K*-edge. Xe *K*-edge spectra are however not of sufficient quality to allow fitting, given the very small absorption jump (0.09 compared to 0.25 at the Kr *K*-edge), and are shown in a separate section (G/III). Energy calibration of the edge position was made by frequent analyses of Kr gaseous standards. The beam size on the sample was 300 x 80 µm². Transmitted X-ray intensity was recorded by ionization chambers filled with gaseous Ar-He mixed gas. Signal was collected from 14244 eV to 14971 eV at the Kr *K*-edge (451 points analysis). Counting times, number of scans and *P*-*T* conditions are given in Table G3. Energy steps were adapted as a function of the edge position. Each scan takes about 1 hour.

### d/ Processing of XAS data

The edge of the standard was fixed to 14326 eV, and the edge of each sample was recalibrated using the averaged edge value of two gaseous Kr standards taken before and after the sample measurement. For Kr standard, no significant shift of the Kr *K*-edge was noted (0.4 eV at the largest). After correction of edge position, data were cut at 14800 eV for better normalization.
Data processing was performed using ATHENA and ARTEMIS packages, based on the IFEFFIT programs (Ravel and Newville, 2005). Each scan was corrected with a pre-edge and a post-edge baseline. Position of the edge was determined by the position of the first derivative of the absorption. The intensity of the jump at the edge was then normalized to one. After merging of the scans collected at a given *P*-*T* condition, data were corrected using a background function. We used an automated background subtraction method (AUTOBKG) developed by Newville (Newville, 2001) and implemented in the ATHENA software. This correction minimizes the features below the first atom-atom distance in the *R*-space. $R_{bkg}$ was fixed to 1.2 Å.
To fit the data at the Kr *K*-edge, we used a *k*-range of ~ 2.2-6.5 $Å^{-1}$ (Table G4), due to low signal to noise ratio at higher *k* values. A small *k*-range ensures that all the different contributions to the Fourier transform are not artifacts but really arise from neighboring atoms. Real part of backward Fourier transform was exported to ARTEMIS software to be fitted using *R*-range ~ 1.1-3.8 Å (Table G4). Fitting made on real part of backward Fourier transform ensures that all XANES and noise contributions are removed from the EXAFS signal. Fit parameters include: amplitude reduction factor (*S0*), average distances of the neighboring atom to the central Kr atom, Debye Waller factor ($\sigma^2$), and difference of edge position compared to standard value ($\Delta E_0$). $\Delta E_0$ values remain smaller than 7 eV, attesting consistency of the fits. It was necessary to add a third order anharmonic cumulant expansion fitting parameter (*C3*) for high *P* or high *T* measurements (Stern et al, 1991; Farges et al.,

1994). *C3* is a measure of the asymmetry of the signal disorder, which arises in glasses from configurational disorder associated to thermal vibration at high *P* and/or high *T* conditions. The absolute value of *C3* remains smaller than 0.009 $Å^3$, similar to values found by Cochain et al. (2015) on silicate glasses and melts at high *P-T* conditions. As no Kr standard was analyzed in the course of the experiment besides Kr gas, it is not possible to determine coordination numbers (CN). We therefore fixed *S0* at a common value of 0.79, and fixed the value of CN. In total, seven parameters must be fitted (first interatomic distance, $\sigma^2$ and *C3* for the two contributions and $\Delta E_0$) whereas $N$, the number of variables to fit, cannot exceed (Teo, 1986):

$$N = \frac{2\Delta R \Delta k}{\pi} \qquad (1)$$

In our case $\Delta k \approx 4.3$ $Å^{-1}$ and $\Delta R \approx 2.8$ Å. Therefore maximum number of parameters $N$, which can be fitted is ~ 7.7, indicating that we can theoretically fit our data as exposed above.

## 3/ Results and Discussion

### a/ XAS data at the Kr *K*-edge

XAS data were recorded at ambient conditions, at high *P-T*, and after quenching (Table G3). Glass transition temperature (*Tg*) of felspathic glass at 1 atm was found in-between 907-948°C based on viscosity measurements (Petermann et al., 2008; Richet and Bottinga, 1984). Therefore our measurements at 1086°C (and potentially at 920°C) were recorded above *Tg* and before recrystallization, i.e. on the supercooled liquid, behaving like a melt. Well-defined oscillations are visible in the X-ray absorption signal, and clearly differ from the signature of Kr gas and Kr liquid under *P* (Di Cicco et al., 1996) (Figures G3 and G4).

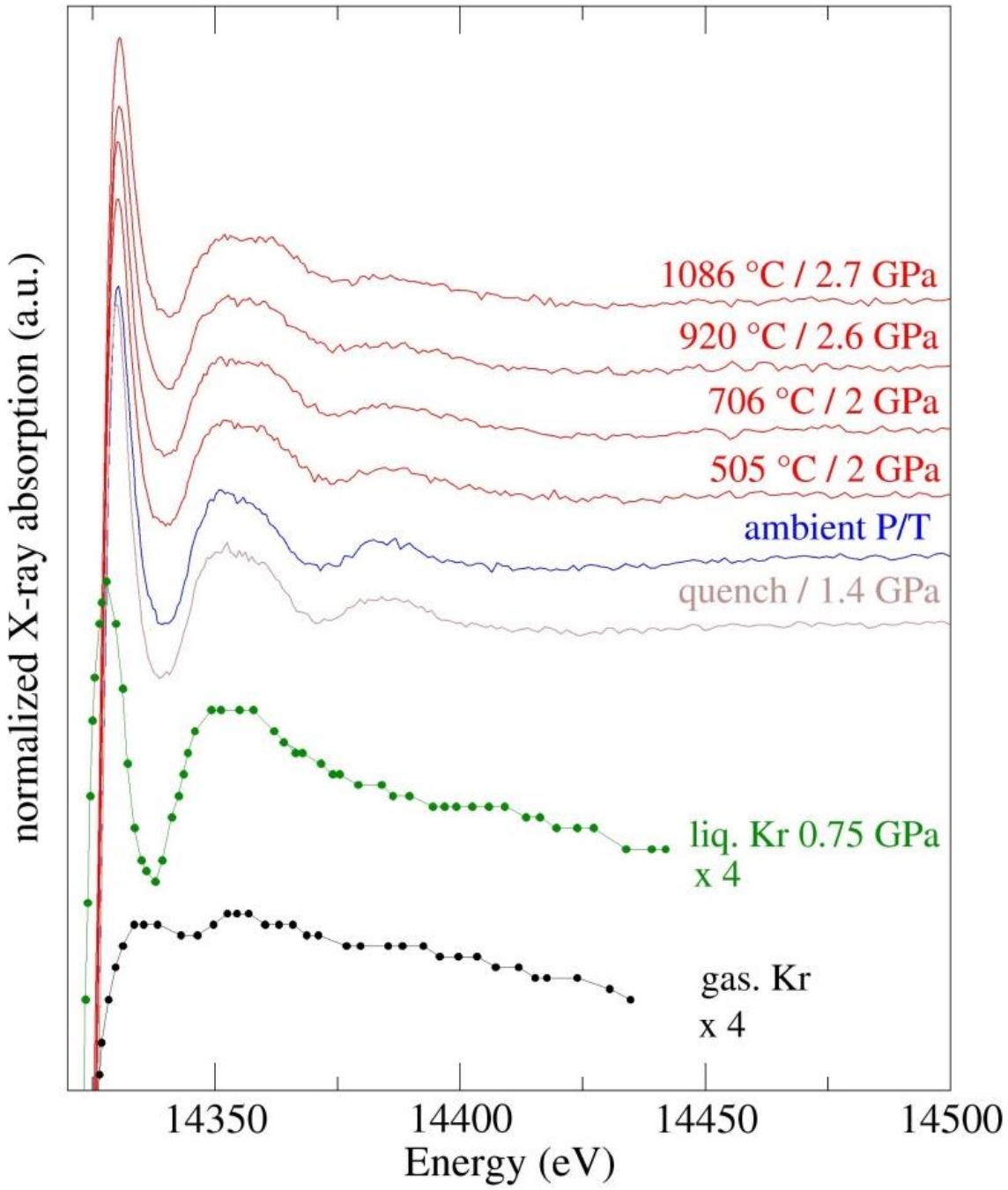


*Figure G3: Normalized X-ray absorption spectra for sanidine glass and supercooled liquid this study), gaseous Kr at ambient conditions, and liquid Kr at 0.75 GPa (Di Cicco et al., 1996).*

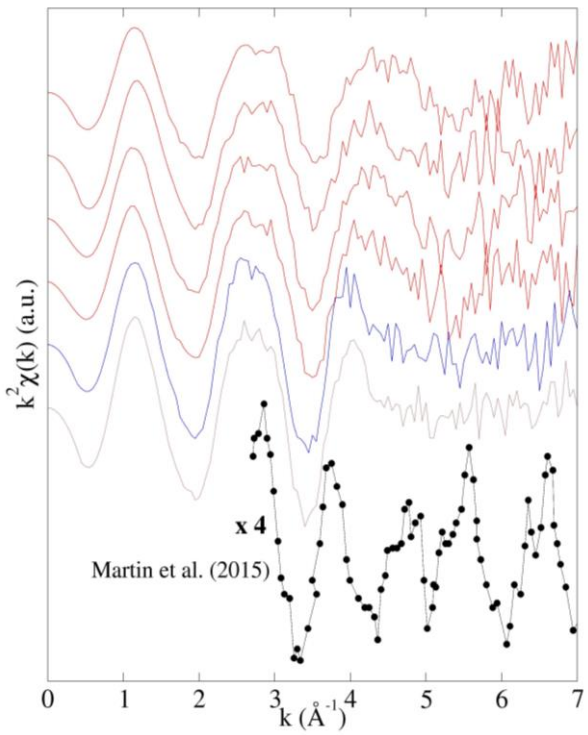


*Figure G4:* $k^2$*-weighted EXAFS function for sanidine glass and supercooled liquid (same color legend as in Figure G5), and for* $UO_2$ *at room conditions (Martin et al., 2015).*

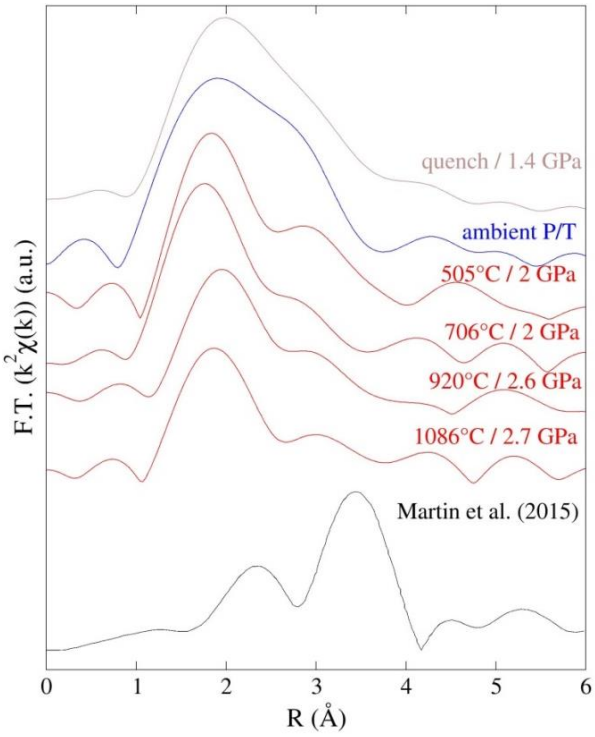


*Figure G5: Magnitude of the Fourier transform of the* $k^2$*-weighted Kr EXAFS function without phase correction (same samples as Figure G4). The peak observed at ~1.9 Å corresponds to Kr-O = 2.49 Å, and the peak at ~2.9 Å corresponds to Kr-O = 3.32 Å. A general decrease of the amplitude is observed with increasing* T *(as noticed by Stern et al., 1991).*

Rapid damping of the EXAFS signal indicates disorder beyond the first shell. We compare in Figure G4 our data with the $k^2$-weighted EXAFS function recorded at 27°C on $UO_2$ (8 at % Kr) previously implanted with Kr ions (Martin et al., 2015). Oscillations observed after 4 $Å^{-1}$ clearly differ from our data sets. The magnitude of the Fourier transform (*k*-range used is displayed in Table G4) clearly shows two peaks at all measurement conditions (Figure G5), indicating that two distances contribute to the signal, with the main distance at ~ 1.9 Å, while Martin et al. (2015) reports a main distance at 3.44 Å. Kr environment in sanidine glass is therefore different from that observed by Martin et al. (2015) in $UO_2$, i.e. Kr nanoclusters. There is no noticeable change in the room *T* glass with *P*: data at ambient *P* and after quenching at 1.4 GPa being similar (Figures G3, G4, G5). The relative intensity of the two peaks however varies with *T*, the magnitude of the Fourier transform (Figure G5) being different at ambient *T*, at 505°C and 706°C, and especially in the melt at 920°C and 1086°C.

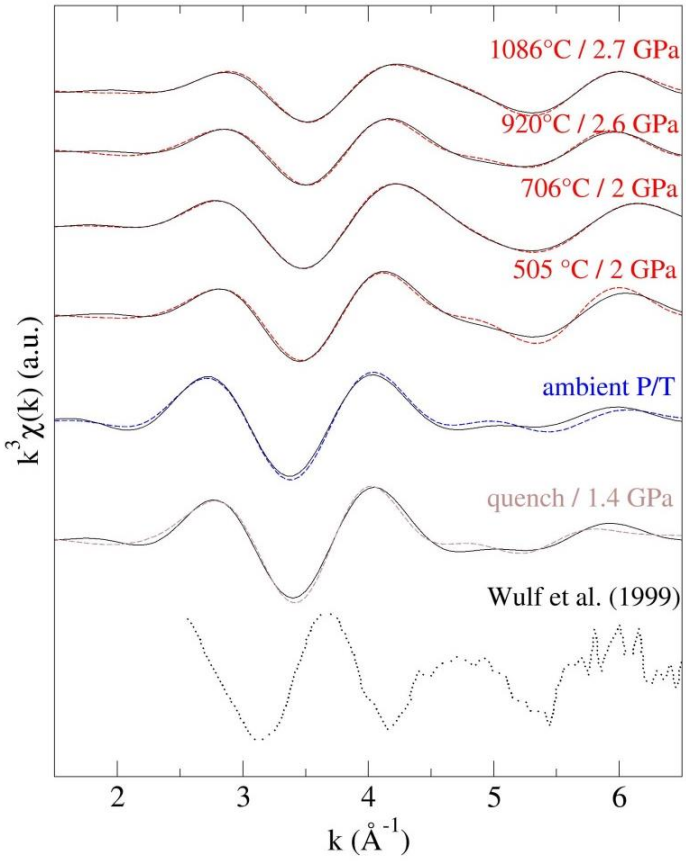


*Figure G6: Real-part of backward Fourier transform (in dashed lines) and fit to the data (plain black line) for sanidine glass and supercooled liquid, and Kr-bearing $SiO_2$ glass (Wulf et al., 1999).*

| ***P* (GPa)** | ***T* (°C)** | ***k*-range (Å$^{-1}$)** | ***R*-range (Å)** | **$\Delta E_0$ (eV)** |
|---|---|---|---|---|
| 0 | 20 | 2.2 - 6.5 | 1.1 - 3.5 | 3.32 |
| 2.6 | 920 | 2.3 - 6.5 | 1.2 - 4.0 | 6.09 |
| 2.7 | 1086 | 2.3 - 6.5 | 1.1 - 3.8 | 7.00 |
| 2 | 706 | 2.3 - 6.5 | 1.1 - 3.5 | 6.45 |
| 2 | 505 | 2.3 - 6.5 | 1.1 - 3.8 | 5.84 |
| 1.4 | 20 | 2.2 - 6.5 | 1.1 - 4.0 | 3.50 |
| ***P* (GPa)** | ***T* (°C)** | **Kr-O1 (Å)** | **$\sigma^2$1 (Å$^2$)** | **$C3_1$ (Å$^3$)** |
| 0 | 20 | 2.42 | 0.025 | - |
| 2.6 | 920 | 2.45 | 0.009 | 0.0021 |
| 2.7 | 1086 | 2.51 | 0.014 | 0.0078 |
| 2 | 706 | 2.53 | 0.009 | 0.0085 |
| 2 | 505 | 2.53 | 0.012 | 0.0076 |
| 1.4 | 20 | 2.49 | 0.021 | 0.0035 |

| ***P* (GPa)** | ***T* (°C)** | **Kr-O2 (Å)** | $\sigma^2$**2 (Å$^2$)** | ***C3*$_2$ (Å$^3$)** |
|---|---|---|---|---|
| 0 | 20 | 3.38 | 0.048 | - |
| 2.6 | 920 | 3.27 | 0.040 | -0.0090 |
| 2.7 | 1086 | 3.37 | 0.042 | 0.0090 |
| 2 | 706 | 3.34 | 0.064 | -0.0034 |
| 2 | 505 | 3.29 | 0.045 | -0.0090 |
| 1.4 | 20 | 3.30 | 0.049 | -0.0057 |

*Table G4:* P-T *conditions and EXAFS-derived structural parameters. Conservative error bars are ± 0.05 eV for* $\Delta E_0$, *± 0.1 Å for Kr-O distances and ± 0.05 Å² for* $\sigma^2$.

### b/ Resolving Kr environment in sanidine glass and melt

Variations of fitted Kr-O distances over our experimental *P-T* range are within error (i.e. ± 0.1 Å). We thus evaluate averaged Kr-O distances for the whole *P-T* range. Two Kr-O distances are identified at 2.49 ± 0.1 Å and 3.32 ± 0.1 Å (Table G4, Fig. G6). No other neighboring atom than oxygen could fit the observed XAS signal, although we considered other atomic pairs such as Kr-Kr, Kr-Si, Kr-Na, or Kr-K. Identified distances confirm the absence of Kr neighbors. Indeed Kr-Kr distance in solid cubic Kr is 3.68 Å at 2 GPa and room *T* (Di Cicco et al., 1996). We can interpret these results either as one Kr population, with Kr surrounded by two shells of O atoms located at 2.49 ± 0.1 Å and 3.32 ± 0.1 Å, or as two distinct populations of Kr located in two different sites of the silicate network. Results clearly differ from Wulf et al. (1999), who only reported a Kr-O distance at 3.45 Å, as shown in Figure G6.

At ambient condition, there is no non-bridging oxygen in sanidine glass ($KAlSi_3O_8$), and Al coordination number is four for all Al atoms (Thompson et al., 2011). Study of an albite glass ($NaAlSi_3O_8$) quenched from the melt at 2.6 GPa showed that less than 3% of Al atoms present a coordination number of five, whereas all remaining Al atoms have a coordination number of 4 (Gaudio et al., 2015). Sanidine glass is thus fully polymerized, with all $Na^+/K^+$ compensating the charge deficit created by the presence of $Al^{3+}$ in tetrahedral position. Molecular dynamic simulations showed that in soda aluminosilicate glass, for Na/Si = 1, distribution of the aluminosilicate rings at ambient *P* varies from 2 to 13-membered-rings, with 6 or 7-membered-rings being the most present ring population (Xiang et al., 2013). Similarly, at ambient *P*, a ring size distribution from 2 to 12-membered rings is predicted for silica glass with 6 to 7 membered-rings being the dominant ring population (Kohara et al. 2011; Guerette et al., 2015). To our knowledge, no pore size distribution data is available for our glass composition. Based on the similarity of ring size distribution between aluminosilicate and silica glass, we assume that size of cages within aluminosilicate rings range from 0.9 Å to 5.9 Å in diameter, like in silica glass (Guerette et al., 2015). This size distribution indicates the presence of 5.0-5.9 Å-diameter voids, inside the largest (i.e. ~ 12-membered) aluminosilicate rings. The Kr-O distance of 2.49 ± 0.1 Å is therefore compatible with a Kr atom located inside the largest observed rings of the silicate network. This Kr-O

distance falls in-between the sum of covalent radii of Kr and O (1.16 Å and 0.66 Å respectively (Cordero et al., 2008)) and the sum of ionic radii of $Kr^0$ and $O^{2-}$ (respectively 1.78 Å for a coordination number of 6 (Zhang and Xue, 1995) and 1.4 Å (Shannon, 1976)). This result indicates that Kr is interacting closely with the neighboring oxygen atoms, suggesting an oxidation of Kr. Under *P*, the edge position shifts by + 0.6 eV (Figure G7). Shift of the edge can be related to change in the oxidation state as observed for Cu, Co, Fe, Mn (e.g. Klysubun et al., 2015). This observation further supports a change in Kr oxidation due to Kr-O bonding. Kr is in the oxidation state II in most of Kr compounds synthesized, such as $KrF_2$, $KrF^+$ or $Kr_2F_3^+$ (Grosse et al., 1963, Burbank et al., 1972, Lehmann et al., 2001). Kr oxidation number is expected to increase compared to gaseous Kr, if Kr is surrounded by several O atoms.

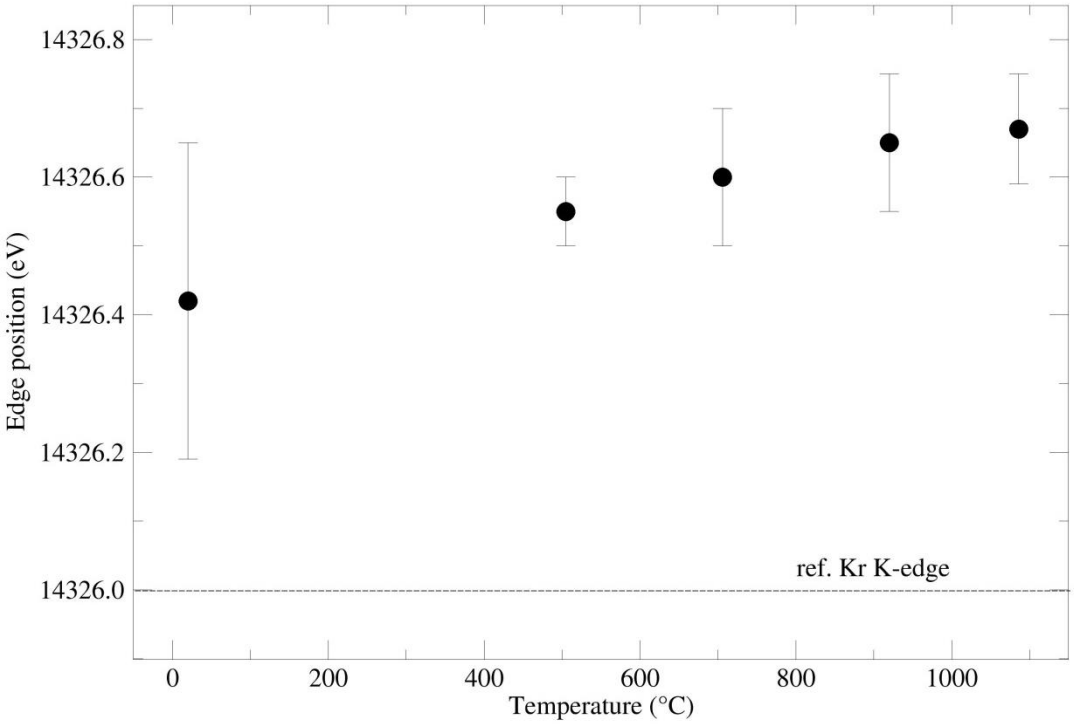


*Figure G7: Shift of the Kr* K*-edge from 1.4 GPa to 2.7 GPa (cf Table G3) compared to the standard reference value (14326 eV).*

The Kr-O distance of 3.32 ± 0.1 Å cannot correspond to the presence of Kr atoms inside aluminosilicate rings, as the size distribution is limited to 5.9 Å in diameter. This larger Kr-O distance is similar to the 3.45 ± 0.1 Å distance reported in $SiO_2$ glass at ambient *P* and 5 K (Wulf et al., 1999), and close to predictions from first-principles molecular dynamics. Zhang et al. (2009) indeed found Kr-O = 3.5 Å in liquid silica, with Kr coordination number varying from 10 to 15 depending on *P*. Similar result was found by Guillot and Sator (2012) using molecular dynamics with Kr-O = 3.45 Å in silica melt and 3.31 Å in rhyolite melt. This large distance is explained by the formation of large cavities in the melt where noble gases are accommodated, in agreement with a passive filling of the void space.

Disappearance of the larger Kr-O distance at higher *T* (Figure G5) indicates that smaller Kr-O distance is more favorable, possibly with the increase of Kr reactivity. Moreover, the Debye Waller factor associated with the smallest Kr-O distance ($\sigma^2 1$) is twice

larger at room *T* than at high *T* (Table G4), suggesting that ordering of the smaller Kr-O environment is higher. Measurements at high *P-T* conditions are all above Kr melting point, whereas measurement after quenching at 1.4 GPa is below Kr melting point (Ferreira and Lobo, 2008). Kr reactivity therefore seems enhanced above Kr melting curve, suggesting that it is *P*-induced, i.e. it favors smaller volume, as observed for Xe incorporation in olivine (Sanloup et al., 2011). Besides, the larger Kr-O distance vanishes in the melt, i.e. at 920°C and 1086°C (Figure G5), indicating structural changes between the melt and the glass.

Current knowledge of glass and silicate melt structures therefore supports the hypothesis of two Kr populations, with one population of Kr, oxidized and possibly located in the largest aluminosilicate rings, and one population filling the large cavities available in the silicate network.

## 4/ Conclusion

Kr fitting of the EXAFS signal shows that Kr is surrounded by oxygen atoms. Two Kr-O distances are identified: 2.49 ± 0.1 Å and 3.32 ± 0.1 Å. Results can be interpreted as two Kr populations. Kr surrounded by O atoms at 3.32 ± 0.1 Å suggests a filling of the large cavities available in the silicate network, in agreement with previous studies. On the contrary, Kr surrounded by O atoms at 2.49 ± 0.1 Å, and the observed + 0.6 eV shift of the edge position at high *P*, suggest Kr bonding to O atoms and Kr oxidation inside cages formed by the largest aluminosilicate rings (i.e. ~ 12-membered-rings). Present results show that heavy noble gases incorporation in silicate melts can no longer be considered as a passive filling of the voids.

The present work provides evidence for the reactivity of Kr with silicate that adds up to the previously reported evidences of Kr reactivity (Grochala, 2007). Kr oxidizes in feldspathic glass and melt at high *P-T* conditions as shown by formation of short Kr-O bonds (2.49 ± 0.1 Å) and shift of the edge position. Kr behavior in compressed magmas thus appears to be intermediate between that of an inert noble gas (He, Ne, Ar) and that of the heavier Xe. Indeed Xe is shown to fully oxidize in compressed haplogranitic melts with Xe in the most abundant 6-membered rings containing 12 nearest O, Xe-O distance of 2.05 ± 0.05 Å is similar to distance reported for covalent Xe-O bond in crystalline silicates (Probert, 2010; Kalinowski et al., 2014; Crépisson et al., 2018). Both results question the supposed passive filling of the void spaces by heavy noble gases (Caroll and Stolper, 1993; Shibata et al., 1998), and the assumption that all noble gases can be considered as zero-charge cation (e.g. Brooker et al., 2003).

Formation of short Kr-O bonds in sanidine melt at depth, supports the role of Kr recycling at subduction zones, proposed by Holland and Ballentine (2006), as Kr will efficiently dissolve in the melt. Hydrated melts will now need to be studied to test the influence of water, which is thought to dramatically increase noble gases solubility (Nuccio and Paonita, 2000).

The Earth's atmosphere is depleted in heavy Kr isotopes compared to chondrites (Holland et al., 2009). Observation of short Kr-O bonds in silicate melt, implying Kr reactivity, suggests potential isotopic fractionation during partial-melting and melt percolation, as shown for instance for Cu (Huang et al., 2017), and/or during recrystallization of the melt, which could have contributed to enrichment of the deep mantle gases in heavy Kr isotopes.

## III/ *In situ* XAS study of Xe incorporation in a feldspathis glassy and crystalline sample

### 1/ Methods

The same sample investigated at the Kr *K*-edge by XAS (PC69, Tables G1, G2), was studied at the Xe *K*-edge (34561 eV) up to 3 GPa, upon increase of *T* up to 1415°C, and upon decrease of *T* down to 1040°C, before quenching to room *T* (Table G5). Set-up was entirely similar to Kr *K*-edge measurements, and we only detailed here specificity of measurements at the Xe *K*-edge.

Angle-resolved X-ray diffraction data were recorded in this case at 34 keV, and ionization chambers used to collect XAS signal were filled with gaseous Kr-He mixed gas.

Signal was collected from 34219 eV to 35311 eV at the Xe *K*-edge (649 points analysis). The edge of the standard was fixed to 34561 eV and the edge of each sample was recalibrated using the averaged edge value of two gaseous Xe standards taken before and after the sample measurement. For Xe standard, large shifts of the edge were recorded throughout the experiments (up to 4 eV). After correction of edge position, data were cut at 35000 eV for better normalization.

| ***P* (GPa)** | ***T* (°C)** | **state** | **n.s** | **count. time** |
|---|---|---|---|---|
| 1.6 | 20 | quench | 3 | 2 s |
| 1.7 | 200 | Glass | 4 | 2 s |
| 1.8 | 305 | Glass | 4 | 2 s |
| 1.9 | 390 | Glass | 4 | 2 s |
| 2 | 500 | Glass | 5 | 2 s /4 s |
| 2.1 | 585 | Glass | 3 | 4 s |
| 2.3 | 765 | Glass | 2 | 4 s |
| 2.5 | 985 | Glass | 2 | 4 s |
| 2.7 | 1165 | Glass | 1 | 1 s |
| 2.9 | 1330 | cr. | 2 | 4 s |
| 3 | 1415 | cr./melt | 2 | 4 s |
| 2.8 | 1310 | cr./melt | 4 | 4 s |
| 2.7 | 1195 | cr./melt | 2 | 1 s/ 4 s |
| n.m. | 1040 | cr./melt | 1 | 4 s |
| n.m. | 20 | quench | 1 | 1 s |

*Table G5:* P-T *conditions and state of the sample for each XAS measurement at the Xe* K*-edge, following measurements at the Kr* K*-edge (Table G3). n.s = number of scans, count. time = counting time per point analysis (649 point analysis). cr. = crystalline, n.m. = not measured.*

### 2/ XAS data at the Xe *K*-edge in sanidine (glass and crystal)

Position of the edge varied from 34560 eV to 34562.2 eV after correction using Xe gaseous standards. The large error bar on the edge position up to 2 eV prevents any quantitative analysis of these shifts in terms of oxidation processes. In the glass, XAS signal was recorded from 20°C to 1165°C and from 1.6 GPa to 2.7 GPa. Oscillations are visible, and

clearly differ from Xe gas signal, which does not display any EXAFS features (Figures G8 and G9). The EXAFS function shows a rapid damping indicating disorder beyond the first coordination shell. Oscillations get flatter with increasing *T* due to increase in Debye-Waller factor linked to increase in thermal vibrations, however no other significant changes are observed with *P-T*. EXAFS signal observed in the glass could not be fitted. Indeed the combination of limited *k*-range (5 $Å^{-1}$ max) and noisy oscillations prevents any quantitative assessment of Xe local environment (nature and distance of first neighboring atom(s)). Therefore only qualitative interpretation will be done below, in comparison with previous results from the literature.

Martin et al. (2008) performed a XAS study at the Xe *K*-edge (at -261°C) on $UO_2$ (8 at % Xe) previously implanted with Xe ions. They interpreted their results by the presence of pressurized (2.8 ± 0.3 GPa) Xe nanoclusters in $UO_2$, still present after annealing of the sample up to 1500°C. We compare our data with results from Martin et al. (2008) in figures G8 and G9. Normalized signal and the EXAFS function of Martin et al. (2008) are shifted in energy compared to our data. This shift could be linked to calibration, experimental conditions, data treatment or difference in matrix compositions. We arbitrarily shifted data from Martin et al. (2008), by - 6 eV for the normalized X-ray absorption signal and by - 0.75 $Å^{-1}$ for the $k^2$-weighted EXAFS function, to compare them with our own data. XANES and EXAFS structures recorded on the Xe/Kr bearing sanidine radically differ from results from Martin et al. (2008), thus excluding the presence of Xe nanoclusters in the sanidine glass.

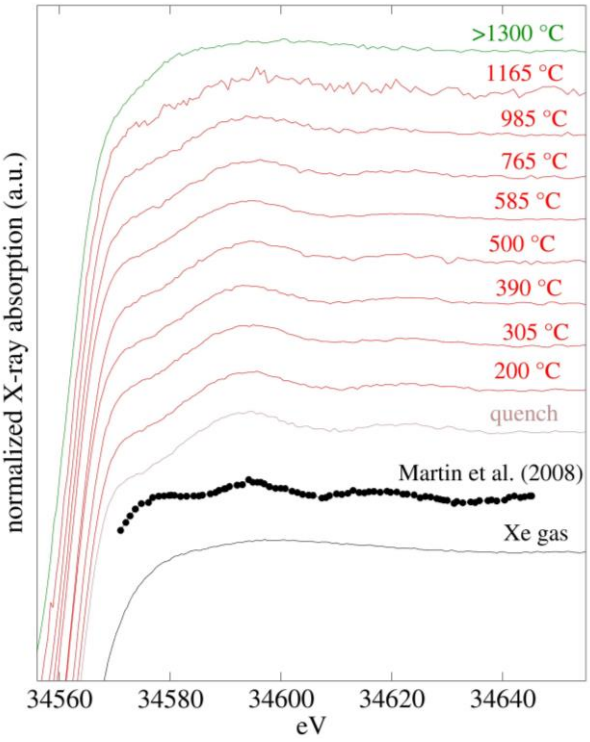


*Figure G8: Normalized X-ray absorption for Xe/Kr-bearing sanidine at the Xe* K*-edge. Data from Martin et al. (2008) have been shifted by - 6 eV.*

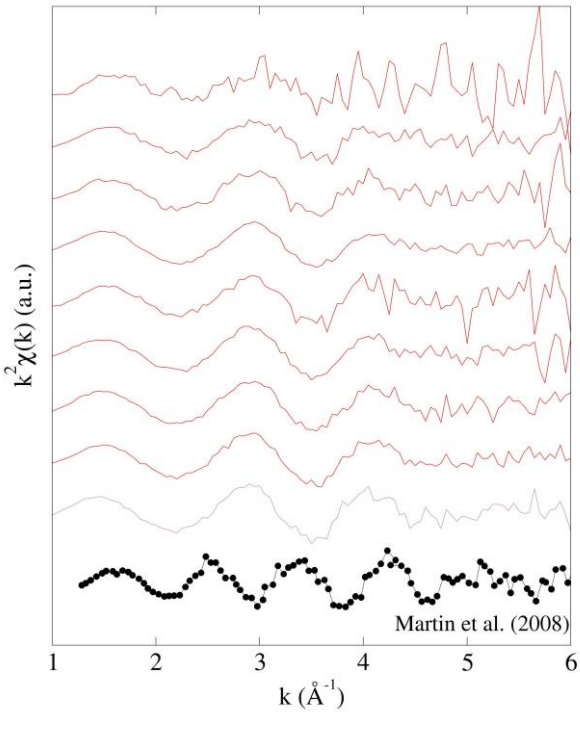


*Figure G9:* k²*-weighted EXAFS function for Xe/Kr-bearing sanidine glass at the Xe K-edge. Same color legend as Figure G8. Data from Martin et al. (2008) have been shifted by -0.75* $Å^{-1}$.

3/ Conclusion

On the present sanidine glass sample with 2.18 wt% Xe, the absorption jump at the edge is only 0.1 in transmission mode, with very weak oscillations and limited *k*-range of maximum 5 $Å^{-1}$. The higher signal to noise ratio observed at the Kr *K*-edge than at the Xe *K*-edge whereas Kr is 4 times more diluted than Xe in our sample, is due to the much higher synchrotron flux at the Kr *K*-edge energy.

Two others samples were tested:

a Xe-bearing haplogranite (PC57 with an average of 0.3 wt% Xe, Appendix I) in free-standing had an absorption jump of 0.03 in transmission mode. Very long fluorescence measurements (10 hours) on the same haplogranite composition, although recrystallized, give no oscillation at all.

An attempt was made to perform XAS measurement on free-standing Xe/Kr-bearing crystalline sanidine (PC103, Tables F1, F2) with locally up to 0.22 wt% Xe in Fe-rich zones which represent minor component of the sample, whereas Fe-poor zones representing most of the volume are Xe/Kr-free (SEM image in Figure F1). However absorption jump at the edge was only 0.001 in transmission mode, which is way too small for any analysis even in fluorescence mode.

Therefore, in the current state of the art it is very difficult to get reliable XAS data on Xe environment in glasses and even more in crystals, a higher flux at the Xe *K*-edge being needed to fully resolve the Xe structural environment in silicate glass using XAS.

## Chapter H: GENERAL CONCLUSIONS AND PERSPECTIVES

In the course of this PhD thesis, Xe incorporation has been tested in three major minerals of the continental crust and the upper mantle, namely olivine, quartz, and feldspars (sanidine).

Throughout this work it has been shown that *in situ* studies need to be favored to investigate Xe incorporation: indeed most Xe escapes from the silicate network upon quenching, gathering in bubbles of various sizes. Only in Fe-rich zones of sanidine, and for K-cymrite, Xe is preserved inside the silicate network, and further TEM observations using a cooling stage should bring more reliable information on the crystallographic structure. *In situ* techniques turned out to be successful:
X-ray diffraction (especially from recrystallization of glass, leading to very good statistics) made it possible to retrieve increase of unit-cell volume in presence of Xe, although Rietveld refinement was hardly useful to determine location of small Xe content at a specific site.
X-ray absorption spectroscopy made it possible to observe Kr oxidation and Kr-O bond lengths albeit only for Kr content higher than 0.5 wt%, while measurements at the Xe *K*-edge cannot be used for Xe incorporation in silicate, Xe content needing to be much higher than 2 wt% Xe for XAS signal to be detected, which is far higher than expected in minerals. Eventually *in situ* IR spectroscopy appears as a promising method to identify changes in vibration modes linked to Xe incorporation in the silicate network, and possibly phase transition triggered by Xe.
Our study has also emphasized the need of a collaborative approach based on theory and experiments.

Xe incorporation mechanisms involve Xe for Si substitution for both quartz and olivine (and possibly sanidine following primary *ex situ* EMPA). Xe environment is linear in quartz at point defects, and planar in olivine at point defects and in the new $(Xe,Si)O_2$ phase. Planar and linear environments are not surprising for Xe, as nearly all known Xe-compounds have these geometries (Grochala et al., 2007). Short Xe-O bonds are formed (~ 2 Å), indicating that Xe-O bonds are at least partially covalent.

Fe could play a role in Xe incorporation in both olivine and sanidine: indeed Fe is retained in recovered olivine only in presence of Xe in the capsule if using Pt capsule. In addition, a phase separation is observed between a Fe-rich phase and a Fe-poor phase for both olivine and sanidine, with in the case of sanidine up to 0.22 wt% Xe retrieved on Fe-rich phases. This could indicate that Xe prevents Fe reduction and stabilizes $Fe^{2+}$ (for olivine) and $Fe^{3+}$ (for sanidine) in the mineral. Similarly Seoung et al. (2014) have shown that Xe stabilized $Ag^{2+}$ in zeolite. However a more systematic investigation is needed, as well as *in situ* data on Xe-bearing minerals with different Fe contents, starting with olivine and sanidine.

Water also plays a role in Xe incorporation in silicates. Xe preferentially goes into the fluid phase, when present. Our preliminary evaluation shows that a large part of Xe remains in the feldspathic glass, with Xe melt/fluid partition coefficient of $10^{-2}$. This phenomenon needs to

be further understood especially to constrain Xe recycling at subduction zones, as Xe will be found in water-rich environments. Fluid composition may modify melt/fluid partition coefficient, as a significant deviation was observed between noble gases solubility in water and in supercritical $CO_2$ - water system (Warr et al., 2015).

Xe and Kr reactivity with olivine, quartz and feldspathic glass are also significantly enhanced above Xe melting curve.

Incorporation of Xe appears as a ubiquitous phenomenon, with Xe significantly present in both silica and magnesian end-members (pure silica and olivine), and also in alkali minerals. Contribution of Xe incorporation in minerals in the framework of the 'missing xenon' appears thus as a viable mechanism, although isotope fractionation needs to be tested.

We also proved that Kr significantly reacts with silicate glass and melt under *P*, thus investigation is now needed to quantify Kr incorporation in minerals. Primary results on Xe/Kr-doped sanidine also show a remnant Kr:Si trend after quenching, although twice less Kr is present than Xe. Potential related isotopic fractionation needs to be investigated, as it could explain Kr isotope fractionation observed at depth (Holland et al., 2009). This could be achieved either on recovered samples, or *in situ* using nuclear resonant inelastic X-ray scattering (NRIXS) for Kr, as it is a nuclear resonant isotope.

Xe and Kr incorporations in silicate melts may also be more complicated than previously thought, as our study for Kr in a feldspathic melt and study from Leroy et al. (2018) for Xe in a haplogranite melt proved a Kr and Xe oxidation, with the incorporation of heavy noble gases in the silicate network. Nevertheless Xe is shown to be fully oxidized, whereas behavior of Kr might be intermediate between Xe and chemically inert lighter noble gases. Further work is needed, based on *in situ* X-ray diffraction or X-ray absorption spectroscopy, although the latter remains challenging and currently limited to relatively high Kr contents (> 0.5 wt% Kr).

## REFERENCES


Abramson E.H., Brown M., Slutsky L.J., Zaug J. 1997. The elastic constants of San Carlos olivine to 17 GPa. *Journal of Geophysical Research*, 102 (B6), 12253-12263.

Ackermann S., Kunz M., Armbruster T., Schefer J., Hänni H. 2004. Cation distribution in a Fe-bearing K-feldspar from Itrongay, Madagascar. A combined neutron and X-ray single crystal diffraction study. *Schweizerische Mineralogische und Petrographische Mitteilungen*, 84, 345-354.

Allègre C.J., Staudacher T., Sarda P. 1986/1987. Rare gas systematics" formation of the atmosphere, evolution and structure of the Earth's mantle. *Earth and Planetary Science Letters*, 81, 127-150.

Anders E., Owen T. 1977. Mars and Earth : Origin and Abundance of volatiles. *Science*, 198, 4316, 453-465.

Anders E., Grevesse N. 1989. Abundances of the elements: Meteoritic and solar. *Geochimica et Cosmochimica Acta*, 53, 197-214.

Avice G., Marty B. 2014. The iodine–plutonium–xenon age of the Moon–Earth system revisited. *Physical Transactions of the Royal Society*, A372.

Avice G., Marty B., Burgess R., 2017. The origin and degassing history of the Earth's atmosphere revealed by Archean xenon. *Nature Communications*, 8, 15455.

Bae Y-S., Hauser B.G., Colón Y.J., Hupp J.T., Farha O.K., Snurr R.Q. 2013. High xenon / krypton selectivity in a metal-organic framework with small pores and strong adsorption sites. *Microporous and Mesoporous Materials*, 169, 176-179.

Balan E., Saitta A.M., Mauri F., Calas G. 2001. First-principles modeling of the infrared spectrum of kaolinite. *American Mineralogist*, 86, 1321-1330.

Balan E. Ingrin J., Delattre S., Kovács I., Blanchard M. 2011. Theoretical infrared spectrum of OH-defects in forsterite. *European Journal of Mineralogy*, 23, 285–292.

Balan E., Blanchard M., Lazzeri M., Ingrin J. 2017. Theoretical Raman spectrum and anharmonicity of tetrahedral OH defects in hydrous forsterite. *European Journal of Mineralogy*. 29, 201-212.

Baldwin S.L., Das J.P. 2015. Atmospheric Ar and Ne returned from mantle depths to the Earth's surface by forearc recycling. *Proceedings of the National Academy of Sciences*, 112, 46, 14174-14179.

Barone V., Casarin M., Forrer D., Pavone M., Sambi M., Vittadini A. 2009. Role and Effective Treatment of Dispersive Forces in Materials: Polyethylene and Graphite Crystals as Test Cases. *Journal of Computational Chemistry*, 30, 934-939.

Baroni S., Resta R. 1986. Ab initio calculation of the low-frequency Raman cross section in silicon. *Physical Review B*, 35, 5969.

Baroni, S., de Gironcoli, S., Dal Corso, A., Giannozzi, P., 2001. Phonons and related crystal properties from density-functional perturbation theory. *Reviews of Modern Physics*, 73, 515-562.

Bartlett N. 1962. Xenon Hexafluoroplatinate(v) Xe+[PtF,]-. *Proceedings of the chemical society*, 218.

Basford J. R., Dragon J. C., Pepin R. O., Coscio M. R., Murthy V. R. 1973. Krypton and Xenon in lunar fines. *Lunar Science Conference, 4th, Houston, Texas, March 5-8, 1973, Proceeding*s. Volume 2. (A74-22805 09-30),1915-1955.

Batygin K., Laughlin G. 2015. Jupiter's decisive role in the inner Solar System's early evolution. *Proceedings of the National Academy of Sciences*, 112 (14), 4214-4217.

Baxter E.F. 2010. Diffusion of Noble Gases in Minerals. *Reviews in Mineralogy and Geochemistry*, 72, 509-557.

Becker T.W., Kellogg J.B., O'Connell R.J. 1999. Thermal constraints on the survival of primitive blobs in the lower mantle. *Earth and Planetary Science Letters*, 171(3), 351-365

Béjina F., Blanchard M., Wright K. and Price G.D. 2009. A computer simulation of the effect of pressure on Mg diffusion in forsterite. *Physics of the Earth and Planetary Interiors*, 172, 13-19.

Bendel V., Schmidt B.C. 2008. Raman spectroscopic characterisation of disordered alkali feldspars along the join KAlSi3O8–NaAlSi3O8: applicationto natural sanidine and anorthoclase. *European Journal of Mineralogy*, 20, 1055–1065.

Beran A. 1986. A Model of Water Allocation in Alkali Feldspar, derived from Infrared-Spectroscopic Investigations. *Physics and Chemistry of Minerals*, 13, 306-310.

Bernatowicz T.J., Podosek F.A., Honda M., Kramer F.E. 1984. The atmospheric inventory of xenon and noble gases in shales: The plastic bag experiment. *Journal of Geophysical Research*, 89 (B6), 4597-4611.

Besson J.M., Hamel G., Grima T., Nelmes R.J., Loveday J.S., Hull S., Häusermann D. 1992. A large volume pressure cell for high temperature. *High Pressure Research*, 8, 625-630.

Besson J.M. 1997. The Generation of High Pressures. in *High Pressure Techniques in Chemistry and Physics a practical approach*, 23-41.

Blanchard M., Ingrin J., Balan E., Kovacs I., Withers A.C. 2017. Effect of iron and trivalent cations on OH-defects in olivine. *American Mineralogist*, 102, 302-311.

Bina C. R. 1998. Olivine emerges from isolation. *Nature*, 392, 650-653

Black D.C. 1971. Trapped neon-argon isotopic correlations in gas rich meteorites and carbonaceous chondrites. *Geochimica et Cosmochimica Acta*, 35(2), 230-235.

Blanchard M., Ingrin J., Balan E., Kovacs I., Withers A.C. 2017. Effect of iron and trivalent cations on OH-defects in olivine. *American Mineralogist*, 102, 302-311.

Boehler R., de Handsetters K. 2004. New anvil designs in diamond-cells. *High Pressure Research*, 24 (3), 391-396.

Boehler R., Ross M., Söderlind P., Boercker DB. 2001. High-pressure melting curves of argon, krypton, and xenon: deviation from corresponding states theory. *Physical Review Letters*, 86 (25), 5731-5734.

Boettcher S.L., Guo Q., Montana A. 1989. A simple device for loading gases in high-pressure experiments. *American Mineralogist*, 74, 1383-1384.

Bogard D.D., Clark R.S., Keith J.E., Reynolds M.A. 1971. Noble Gases and Radionuclides in Lost City and other recently fallen meteorites. *Journal of Geophysical Research*, 76 (17), 4076-4083.

Böhlke J.K., Irwin J.J. 1992. Brine history indicated by argon, krypton, chlorine, bromine, and iodine analyses of fluid inclusions from the Mississippi Valley type lead-fluorite-barite deposits at Hansonburg, New Mexico. *Earth and Planetary Science Letters*, 110, 51-66.

Bouhifd A., Jephcoat A.P. 2006. Aluminium control of Argon solubility in silicate melts under pressure. *Nature*, 439, 961-964.

Boultif, A., Louër, D., 1991. Indexing of Powder Diffraction Patterns for Low-Symmetry Lattices by the Successive Dichotomy Method. *Journal of Applied Crystallography*, 24 (6), 987-993.

Bourova, E., Richet, P., 1998. Quartz and Cristobalite: high-temperature cell parameters and volumes of fusion. *Geophysical Research Letters*, 25, 2333-2336.

Bowyer T.W., Schlosser C., Abel K.H., Auer M., Hayes J.C., Heimbigner T.R., McIntyre J.I., Panisko M.E., Reeder P.L., Satorius H., Schulze J., Weiss W. 2002. Detection and analysis of xenon isotopes for the comprehensive nuclear-test-ban treaty international monitoring system. *Journal of Environmental Radioactivity*, 59, 139–151.

Boyd F.R., England J.L. 1960. Apparatus for Phase-Equilibrium Measurements at Pressures up to 50 Kilobars and Temperatures up to 1750°C. *Journal of Geophysical Research*, 65 (2), 741-748.

Bragg W.L. 1913. The diffraction of short electromagnetic waves by a crystal. *Proceedings of the Cambridge philosophical society*, 17, 43-57.

Britvin S., Kashtanov A., Krzhizhanovskaya M.G., Gurinov A.A., Glumov O.V., Strekopytov S., Kretser Y.L., Zaitsev A.N., Chukanov N.V., Krivovichev S.V. 2015. Perovskites with the Framework-Forming Xenon. *Angewandte Chemie International Edition*, 54, 14340-14344.

Britvin S.N., Kashtanov S.A., Krivovichev S.V., Chukanov N.V. 2016. Xenon in rigid oxide frameworks: structure, bonding and explosive properties of layered perovskite $K_4Xe_3O_{12}$. *The Journal of American Chemical Society*, 138 (42), 13838–13841.

Broadhurst C.L., Drake I.M.J., Hagee B.E., Bernatowicz T.J. 1992. Solubility and partitioning of Ne, Ar, Kr, and Xe in minerals and synthetic basaltic melts. *Geochimica et Cosmochimica Acta*, 56, 709-723.

Brock D.S., Schrobilgen G.J. 2011. Synthesis of the Missing Oxide of Xenon, $XeO_2$, and its Implications for Earth's Missing Xenon. *Journal of the American Chemical Society*, 133, 6265–6269.

Brooker R.A., Du Z., Blundy J.D., Kelley S.P., Allan N.L., Wood B.J., Chamorro E.M., Wartho J-A., Purtonk J.A.. 2003. The 'zero charge' partitioning behaviour of noble gases during mantle melting. *Nature*, 423, 738-741.

Brown PJ., Fox A.G., Maslen E.N., O'Keefe M.A., Willis B.T.M. 2006b. Intensity of diffracted intensities. *International Tables for Crystallography*, 554-595.

Burbank R.D., Falconer W.E., Sunder W.A. 1972. Crystal Structure of Krypton Difluoride at - 80°C. *Science*, 178, 1285-1286.

Busemann H., Baur H., Willer R. 2000. Primordial noble gases in "phase Q" in carbonaceous and ordinary chondrites studied by closed-system stepped etching. *Meteoritics and Planetary Science*, 35, 949-973.

Caffee M.W., Hudson G.B., Velsko C., Huss G.R., Alexander E.C. Jr, Chivas A.R. 1999. Primordial noble gases from Earth's mantle: identification of a primitive volatile component. *Science*, 285, 2115-2118.

Caldwell W.A., Nguyen J.H., Pfrommer B.G., Mauri F., Louie S.G., Jeanloz R. 1997. Structure, Bonding, and Geochemistry of Xenon at High Pressures. *Science*, 277, 930-933.

Calvin S. 2013. XAFS for everyone. NW: CRC Press (Taylor and Francis Group)

Caracausi A., Avice G., Burnard P.G., Füri E., Marty B. 2016. Chondritic xenon in the Earth's mantle. *Nature*, 533, 82-85.

Carpenter M.A., Salje E.K.H., Graeme-Barber A., Wruck B., Dove M.T., Knight K.S. 1998. Calibration of excess thermodynamic properties and elastic constant variations associated with the alpha < -- > beta phase transition in quartz. *American Mineralogist*, 83, 2-22.

Carroll M.R., Stolper E.M. 1993. Noble gas solubilities in silicate melts and glasses: New experimental results for argon and the relationship between solubility and ionic porosity. *Geochimica et Cosmochimica Acta*, 57, 5039-5051.

Chambers J.E. 2004. Planetary accretion in the inner Solar System. *Earth and Planetary Science Letters*, 223, 241–252.

Chang L., Chen Z., Liu X., Wang H. 2013. Expansivity and compressibility of wadeite-type $K_2Si_4O_9$ determined by *in situ* high T/P experiments, and their implication. *Physics and Chemistry of Minerals*, 40 (1), 29-40.

Chen X., Plonka A.M., Banerjee D., Krishna R., Schaef H.T., Ghose S., Thallapally P.K., Parise J.B. 2015. Direct Observation of Xe and Kr Adsorption in a Xe selective Microporous Metal Organic Framework. *Journal of the American Chemical Society*, 137 (22), 7007-7010.

Chopelas A. 1991. Single crystal Raman spectra of forsterite, fayalite, and monticellite. *American Mineralogist*, 76, 1101-1109.

Clarke W.B., Beg M.A., Craig H. 1969. Excess 3He in the sea : evidence for terrestrial primordial Helium. *Earth and Planetary Science Letters*, 6 (3), 213-220.

Cochain B., Sanloup C., De Grouchy C., Crépisson C., Bureau H., Leroy C., Kantor I., Irifune T. 2015. Bromine speciation in hydrous silicate melts at high pressure. *Chemical Geology*, 404, 18-26.

Coes L. 1962. Synthesis of minerals at high pressures. in *Modern very high pressure techniques*, Chapter 7.

Cook G.A. 1961. Introduction and general survey. In *Argon, helium, and the rare gases: I. History, occurrence and properties, Interscience New York.*

Coombs D.S. 1954. Ferriferous orthoclase from Madagascar. *Journal of the Mineralogical Society*, 30 (226), 409-427.

Cordero B., Gomez V., Cremades E., Alvarez S. 2008. Covalent radii revisited. *Dalton Transactions*, 2832-2838.

Crépisson C., Blanchard M., Bureau H., Sanloup C., Withers A.C., Khodja H., Surblé S., Raepsaet C., Béneut K., Leroy C., Giura P., Balan E. 2014. Clumped fluoride-hydroxyl defects in forsterite: Implications for the upper-mantle. *Earth and Planetary Science Letters*, 390, 287–295.

Crépisson C., Blanchard M., Lazzeri M., Balan E., Sanloup C. 2018. New constraints on Xe incorporation mechanisms in olivine from first-principles calculations. *Geochimica et Cosmochimica Acta*, 222, 146-155.

Crépisson C., Sanloup C., Cormier L., Blanchard M., Hudspeth J., Rosa A., Irifune T., Mathon O. 2018. Kr environment in a feldspathic glass and melt: a high pressure, high temperature X-ray absorption study. *Chemical Geology*, 493, 525-531

Cynn H., Yoo C.S., Baer B., Iota-Herbei V., McMahan A.K., Nicol M., Carlson S. 2001. Martensitic fcc-to-hcp Transformation Observed in Xenon at High Pressure. *Physics Review Letters*, 86, 2001.

Czuppon G., Matsumoto T., Handler M. R., Matsuda J.-I. 2009. Noble gases in spinel peridotite xenoliths from Mt Quincan, North Queensland, Australia: undisturbed morb-type noble gases in the subcontinental lithospheric mantle. *Chemical Geology*, 266, 19–28.

Dai L-Q., Zheng Y-F., He H-Y., Zhao Z-F. 2016. Postcollisional mafic igneous rocks record recycling of noble gases by deep subduction of the continental crust. *Lithos*, 252-253, 135-144.

Damen T.C., Porto S.P.S., Tel B. 1966. Raman Effect in Zinc Oxide. *Physical Review*, 142 (2), 571-574.

Dauphas N. 2003. The Dual Origin of the Terrestrial Atmosphere. *Icarus*, 165, 326–339.

De Grouchy C.J.L. 2016. The influence of trace element incorporation on the structure of silicate melts and glasses at high pressure. PhD thesis. University of Edinburgh.

De Grouchy C., Sanloup C., Cochain B., Drewitt JWE., Kono Y., Crépisson C. 2017. Lutetium incorporation in magmas at depth: Changes in melt local environment and the influence on partitioning behaviour. *Earth and Planetary Science Letters*, 464, 155-165.

Dewaele A., Loubeyre P., Dumas P., Mezouar M. 2012. Oxygen impurities reduce the metallization pressure of xenon. *Physical Review B*, 86, 014103.

Dewaele A., Worth N., Pickard C.J., Needs R.J., Pascarelli S., Mathon O., Mezouar M., Irifune T., 2016. Synthesis and stability of xenon oxides $Xe_2O_5$ and $Xe_3O_2$ under pressure. *Nature Chemistry*, 8 (8), 784–790.

Dewaele A., Pépin C.M., Geneste G., Garbarino G. 2017. Reaction between nickel or iron and xenon under high pressure. *High Pressure Research*, 37 (2), 137-146.

Di Cicco A., Filipponi A., Itié J-P., Polian A. 1996. High-pressure EXAFS measurements of solid and liquid Kr. *Physical Review B*, 54, 9086-9098.

Dorogokupets P.I., 1995. Equation of state for lambda transition in quartz. *Journal of Geophysical Research*, 100 (B5), 8489-8499.

Drüppel K., Hösch A., Franz G. 2007. The system $Al_2O_3$-$P_2O_5$-$H_2O$ at temperatures below 200 °C: Experimental data on the stability of variscite and metavariscite $AlPO_4 \cdot 2H_2O$. *American Mineralogist*, 82, 1695-1703.

Dubrovinskaia N., Dubrovinsky L., Solopova N.A., Abakumov A., Turner S., Michael Hanfland, Bykova E., Bykov M., Prescher C., Prakapenka V.B., Petitgirard S., Chuvashova I., Gasharova B., Mathis Y-L., Ershov P., Snigireva I., Snigirev A. 2016. Terapascal static pressure generation with ultrahigh yield strength nanodiamond. *Science Advances*, 2 (7), 16000341.

Dyadin Y.A., Larionov E.G., Mirinskij D.S., Mikina T.V. 1997. Phase Diagram of the Xe–$H_2O$ System up to 15 kbar. *Journal of Inclusion Phenomena and Molecular Recognition in Chemistry*, 28, 271–285.

Elkins-Tanton, Linda T. 2012. Magma Oceans in the Inner Solar System. *Annual Review of Earth and Planetary Sciences*, 40, 113-139.

Eremets M.I., Eugene A.G., Victor V.S., Mao H., Hemley R.J., Mulders N., Zimmerman N.M. 2000. Electrical Conductivity of Xenon at Megabar Pressures. *Physical Review Letters*, 85 (13), 2797-2800.

Farges F., Brown G.E., Calas G., Galoisy L., Waychuna G.A. 1994. Structural transformation in Ni-bearing Na2Si2O5 glass and melt. *Geophysical Research Letters*, 21, 1931-1934.

Farmer V.C. 1974. The infrared spectra of Minerals. ed. London: Mineralogical society.

Fasshauer D.W., Chatterjee N.D., Marler B. 1997. Synthesis, structure, thermodynamic properties, and stability relations of K-cymrite, $K[AlSi_3O_8]\cdot H_2O$. *Physics and Chemistry of Minerals*, 24 (6), 455-462.

Fei Y., van Orman J., Li J., van Westrenen W., Sanloup C., Minarik W., Hirose K., Komabayashi T., Walter M., Funakoshi K., 2004. Experimentally determined postspinel transformation boundary in $Mg_2SiO_4$ using MgO as an internal pressure standard and its geophysical implications. *Journal of Geophysical Research: Solid Earth*, 109, B02305.

Ferreira A.G.M., Lobo L.Q. 2008. The fusion curves of xenon, krypton, and argon. *The Journal of Chemical Thermodynamics*, 40, 618-624.

Finocchi F. 2011. DFT for beginners. 2011.

French S.W., Romanowicz B. 2015. Broad plumes rooted at the base of the Earth's mantle beneath major hot spots. *Nature*, 525, 95-99.
Gaudio S.J., Lesher C.E., Maekawa H., Sen S. 2015. Linking high-pressure structure and density of albite liquid near the glass transition. *Geochimica et Cosmochimica Acta*, 157, 28–38.

Gautheron C., Cartigny P., Moreira M., Harris J.W., Allègre C.J. 2005. Evidence for a mantle component shown by rare gases, C and N isotopes in polycrystalline diamonds from Orapa (Botswana). *Earth and Planetary Science Letters*, 240, 559– 572.

Gerber R.B. 2006. New Chemistry of the Noble Gas Elements: Novel Molecules, Polymers and Clusters. *ChemInform*, 37 (29), 7-14.

Gerken M., Schrobilgen G.J. 2002. Solution Multi-NMR and Raman Spectroscopic Studies of Thermodynamically Unstable $XeO_4$. The First $^{131}Xe$ NMR Study of a Chemically Bound Xenon Species. *Inorganic Chemistry*, 41 (2), 198–204.

Ghosez Ph., Michenaud J.-P., Gonze X. 1998. Dynamical atomic charges: the case of $ABO_3$ compounds. *Physical Review B*, 58, 6224-6240.

Giannozzi, P., Baroni, S., Bonini, N., Calandra, M., Car, R., Cavazzoni, C., Ceresoli, D., Chiarotti, G.L., Cococcioni, M., Dabo, I., Dal Corso, A., de Gironcoli, S., Fabris, S., Fratesi, G., Gebauer, R., Gerstmann, U., Gougoussis, C., Kokalj, A., Lazzeri, M., Martin-Samos, L. 2009. Quantum Espresso: a modular and open-source software project for quantum simulations of materials. *Journal of Physics: Condensed Matter*, 21, 395502-395521.

Giskow R., Lind J., Schmidt E. 2004. The Variety of Phosphates for Refractory and Technical Applications by the Example of Aluminium Phosphates. *cfi/Berichte der DKG*, 81 (5).

Goettel K.A., Eggert J.H., Silvera I.F., Moss W.C. 1989. Optical Evidence for the Metallization of Xenon at 132(5) GPa. *Physical Review Letters*, 62 (6), 665-668.

Gomes R., Levison H.F., Tsiganis K., Morbidelli A. 2005. Origin of the cataclysmic Late Heavy Bombardment period of the terrestrial planets. *Nature*, 435, 466-469.

Gonze X., Lee C. 1997. Dynamical matrices, Born effective charges, dielectric permittivity tensors, and interatomic force constants from density-functional perturbation theory. *Physical Review B*, 55 (16), 10355-10368.

Graham D.W. 2002. Noble Gas Isotope Geochemistry of Mid-Ocean Ridge and Ocean Island Basalts: Characterization of Mantle Source Reservoirs. in *Geochemistry and Cosmochemistry D. Porcelli, C. J. Ballentine and R. Wieler (editors) Reviews in Mineralogy and Geochemistry, 47, 247-319.*

Grimberg A, Baur H., Bochsler P., Bühler F., Burnett D.S., Hays C.C., Heber V.S., Jurewicz A.J., Wieler R. 2006. Solar Wind Neon from Genesis: Implications for the Lunar Noble gas record. *Science*, 314, 1133-1135.

Grimme S. 2006. Semiempirical GGA-Type Density Functional Constructed with a Long-Range Dispersion Correction. *Journal of Computational Chemistry*, 27, 1787-1799.

Grochala W., 2007. Atypical compounds of gases, which have been called 'noble'. *Chemical Society Reviews*, 36, 1632-1655.

Grosse A.V., Kirshenbaum A.D., Streng A.G, Streng L.V. 1963. Krypton Tetrafluoride: Preparation and Some Properties. *Science*, 139, 1047-1048.

Guerette M., Ackerson M.R., Thomas J., Yuan F., Watson E.B., Walker D., Huang L. 2015. Structure and Properties of Silica Glass Densified in Cold Compression and Hot Compression. *Nature Scientific Reports*, 5.

Guillot B., Sator N. 2012. Noble gases in high-pressure silicate liquids: A computer simulation study. *Geochimica et Cosmochimica Acta*, 80, 51-69.

Gundersen G., Hedberg K., Huston J. L. 1970. Molecular Structure of Xenon Tetroxide, $XeO_4$. *The Journal of Chemical Physics*, 52, 812-813.

Hall T.H. 1980. High-pressure techniques. in *Chemical Experimentation Under Extreme Conditions, Techinques of Chemistry*, IX, 9-72.

Halliday A.N. 213. The origins of volatiles in the terrestrial planets. *Geochimica et Cosmochimica Acta*, 105, 146-171.

Hammersley A. 1997. FIT2D: An Introduction and Overview. *Technical Report No.ESRF97HA02*, ESRF.

Haner J., Schrobilgen G.J. 2015. The Chemistry of Xenon(IV). *Chemical Reviews*, 115, 1255−1295.

Hazen R. M. 1976. Effects of temperature and pressure on the crystal structure of forsterite. *American Mineralogist*, 61, 1280-1293.

Heber V. S., Brooker R. A., Kelley S. P., Wood B. J. 2007. Crystal-melt partitioning of noble gases (helium, neon, argon, krypton, and xenon) for olivine and clinopyroxene. *Geochimica et Cosmochimica Acta*, 71, 1041-1061.

Hébrard E., Marty B. 2014. Coupled noble gas-hydrocarbon evolution of the early Earth atmosphere upon solar UV irradiation. *Earth and Planetary Science Letters*, 385, 40-48.

Heo N.H., Lim W.T., Kim B.J., Lee S.Y., Kim M.C., Seff K.. 1999. Crystal Structures of Encapsulates within Zeolites. 3. Xenon in Zeolite A. *The Journal of Physical Chemistry B*,103, 1881-1889.

Hermann A., Schwerdtfeger P. 2014. Xenon Suboxides Stable under Pressure. *The Journal of Physical Chemistry Letters*, 5 (24), 4336-4342.

Hiyagon H., Ozima M. 1986. Partition of noble gases between olivine and basalt melt. *Geochimica et Cosmochimica Acta*, 50, 2045-2057.

Holland G., Ballentine C.J. 2006. Seawater subduction controls the heavy noble gas composition of the mantle. *Nature*, 441, 186–191.

Holland G., Cassidy M., Ballentine C.J.. 2009. Meteorite Kr in Earth's Mantle Suggests a Late Accretionary Source for the Atmosphere. *Science*, 326, 1522-1525.

Holland G., Lollar B.S., Li L., Lacrampe-Couloume G., Slater G.F., Ballentine C.J. 2013. Deep fracture fluids isolated in the crust since the Precambrian era. *Nature*, 497, 357-362.

Honda M., McDougall I., Patterson D.B., Doulgeris A., Clague D.A. 1991. Possible solar noble-gas component in Hawaiian basalts. *Nature*, 349, 149-151.

Hopkinson L., Roberts S., Herrington R., Wilkinson J. 1999. The nature of crystalline silica from the TAG submarine hydrothermal mound, 26°N Mid Atlantic Ridge. *Contributions to Mineralogy and Petrology*, 137, 342-350.

Hopp J., Trieloff M. 2005. Refining the noble gas record of the Réunion mantle plume source: Implications on mantle geochemistry. *Earth and Planetary Science Letters*, 240, 573– 588.

Hourdin F., Issartel J.P. 2000. Sub-surface nuclear tests monitoring through the CTBT xenon network. *Geophysical Research Letters*, 27 (15), 2245-2248.

Howie R.T., Turnbull R., Binns J., Frost M., Dalladay-Simpson P., Gregoryanz E. 2016 Formation of xenon-nitrogen compounds at high pressure. *Scientific Reports*, 6, 34896.

Huang J., Huang F., Wang Z., Zhang X., Yu H. 2017. Copper isotope fractionation during partial melting and melt percolation in the upper mantle: Evidence from massif peridotites in Ivrea-Verbano Zone, Italian Alps. *Geochimica et Cosmochimica Acta*, 211, 48-63.

Hunten D.M., Pepin R.O., Walker J.C.G. 1987. Mass Fractionation in Hydrodynamic Escape. *Icarus*, 69, 532-549.
Hunter B.A., Howard C.J. 1998. LHPM, A computer program for Rietveld analysis of X-ray and neutron powder diffraction patterns. *Australian Nuclear Science and technology organization*.

Hwang S-L., Shen P., Chu H-T., Yui T-F., Liou J.G., Sobolev N.V., Zhang R-Y., Shatsky V.S., Zayachkovsky A.A. 2004. Kokchetavite: a new potassium-feldspar polymorph from the Kokchetav ultrahigh-pressure terrane. Contribution to Mineralogy and Petrology, 148, 380-389.

Iishi K. 1978. Lattice dynamics of forsterite. *American Mineralogist*, 63, 1198-1208.

Ingrin J., Kovacs I., Deloule E., Balan E., Blanchard M., Kohn S.C., Hermann J. 2014. Identification of hydrogen defects linked to boron substitution in synthetic forsterite and natural olivine. *American Mineralogist*, 99, 2138-2141.

Ingrin J., Liu J., Depecker C., Kohn S.C., Balan E., Grant K.J. 2013. Low-temperature evolution of OH bands in synthetic forsterite, implication for the nature of H defects at high pressure. *Physics and Chemistry of Minerals*, 40, 499-510.

Iro N., Gautier D., Hersant F., Bockelée-Morvan D., Lunine J.I. 2003. An interpretation of the nitrogen deficiency in comets. *Icarus*, 161, 511–532.

Ito T. 1984. NMR study of $^{129}$Xe adsorbed on L, Z and ZSM zeolites. *Chemical Physics Letters*, 111 (3), 271-274.

Jackson M.G., Kurz M.D., Hart S.R., Workman R.K. 2007. New Samoan lavas from Ofu Island reveal a hemispherically heterogeneous high $^{3}$He/$^{4}$He mantle. *Earth and Planetary Science Letters*, 264, 360–374.

Jackson C.R.M., Parman S.W., Kelley S.P., Cooper R.F. 2013. Noble gas transport into the mantle facilitated by high solubility in amphibole. *Nature Geoscience*, 6, 562-565.

Jambon A., Weber H., Braun O. 1986. Solubility of He, Ne, Ar, Kr and Xe in a basalt melt in the range 1250–1600°C. Geochemical implications. *Geochimica et Cosmochimica Acta*, 50, 401-408.

Jaoul O., Houlier B., Cheraghmakani M., Pichon R. Liebermann R.C. 1987. Surface destabilization and laboratory induced non-stoichiometry in San Carlos olivine. *Physics and Chemistry of Minerals*, 15, 15-41.

Jayaraman A. 1983. Diamond anvil cell and high-pressure physical investigations. *Reviews of Modern Physics*, 55 (1), 65-108.

Jephcoat A. P., Mao H.K., Finger L.W., Cox D.E., Hemley R.J., Zha C.S. 1987. Pressure-Induced Structural Phase Transitions in Solid Xenon. *Physical Review Letters*, 59 (23), 2670-2673.

Jephcoat A.P., Besedin S.P. 1998. Melting of Rare Gas Solids Ar, Kr, Xe at High Pressures and Fixed Points in the P-T Plane. in *Properties of Earth and Planetary Materials at High Pressure and Temperature edited by Manghnami M.H. and Yag*i T., 287-296.

Jephcoat, A.P., 1998. Rare-gas solids in the Earth's deep interior. *Nature*, 393, 355-358.

Jiménez-Munt, I., Fernandez, M., Vergés, J., Platt, J.P. 2008. Lithosphere structure underneath the Tibetan Plateau inferred from elevation, gravity, and geoid anomalies. *Earth and Planetary Science Letters*, 267, 276-289.

Kalinowski J., Rasanen M., Gerber R.B. 2014. Chemically-bound xenon in fibrous silica. *Physical Chemistry Chemical Physics*, 16, 11658–11661.

Kalinowski M., Axelsson A., Bean M., Blanchard X., Bowyer T.W., Brachet G., Hebel S., McIntyre J., Peters J., Pistner C., Raith M., Ringbom A., Saey P.J.R., Schlosser C., Stocki T., Taffary T., Ungar K. 2011. Discrimination of Nuclear Explosions against Civilian Sources Based on Atmospheric Xenon Isotopic Activity Ratios. *Pure Applied Geophysics*, 167, 517–539.

Keefer K.D., Brown G.E. 1978. Crystal structures and composition of sanidine and high albite in cryptoperthitic intergrowth. *American Mineralogist*, 63, 1264-1273.

Keen D. A., Dove M.T. 2000. Total scattering studies of silica polymorphs: similarities in glass and disordered crystalline local structure. *Mineralogical Magazine*, 64(3), 447-457.

Kendrick M.A., Scambelluri M., Honda M., Phillips D. 2011. High abundances of noble gas and chlorine delivered to the mantle by serpentinite subduction. *Nature Geoscience*, 4, 807-812.

Kendrick M.A., Honda M., Pettke T., Scambelluri M., Phillips D., Giuliani A. 2013. Subduction zone fluxes of halogens and noble gases in seafloor and forearc serpentinites. *Earth and Planetary Science Letters*, 365, 86-96.

Kihara K., 1990. An X-ray study of the temperature dependence of the quartz structure. *European Journal of Mineralogy*, 2 (1), 63-77.

Kim M., Debessai M., Yoo C.S. 2010. Two- and three-dimensional extended solids and metallization of compressed $XeF_2$. *Nature Chemistry*, 2 (9), 784-788.

Klysubun W., Hauzenberger C.A., Ravel B., Klysubun P., Huang Y., Wongtepa W., Sombunchoo P. 2014. Understanding the blue color in antique mosaic mirrored glass from the Temple of the Emerald Buddha, Thailand. *X-ray spectrometry*, 44, 116-123.

Kohara S., Akola J., Morita H. , Suzuya K., Weber J.K.R., Wilding M.C., Benmore C.J. 2011. Relationship between topological order and glass forming ability in densely packed enstatite and forsterite composition glasses. *Proceedings of the National Academy of Sciences*, 108, 14780-14785.

Kohlstedt D. L., Maxwell S.J. 1987. High-temperature stability of San Carlos olivine. *Contribution to Mineralogy and Petrology*, 95, 226-230.

Kolesov A., Geiger C. A. 2004. A Raman spectroscopic study of Fe–Mg olivines. *Physics and Chemistry of Minerals*, 31, 142-154.

Kono Y., Park C., Kenney-Benson C., Shen G., Wang Y. 2014. Toward comprehensive studies of liquids at high pressures and high temperatures: Combined structure, elastic wave velocity, and viscosity measurements in the Paris–Edinburgh cell. *Physics of the Earth and Planetary Interiors*, 228, 269-280.

Kraus W., Nolze G. 1996. POWDER CELL - a program for the representation and manipulation of crystal structures and calculation of the resulting X-ray powder patterns. *Journal of Applied Crystallography*, 29, 301-303.

Krummenacher D., Merrihue C.M., Pepin R.O., Reynolds J.H. 1962. Meteoritic krypton and barium versus the general isotopic anomalies in xenon. *Geochimica et Cosmochimica Acta*, 26, 231–249.

Kunz J., Staudacher T., Allègre C.J. 1998. Plutonium-Fission Xenon Found in Earth's Mantle. *Science*, 280 (5365), 877-880.

Kuroda P.K., Sherrill R.D, Jackson K.C. 1977. Abundances and isotopic compositions of rare gases in granites. *Geochemical Journal*, 11, 75-90.

Kurzydłowski D., Grochala W. 2008. Xenon as a Mediator of Chemical Reactions? Case of Elusive Gold Monofluoride, AuF, and its Adduct with Xenon, XeAuF. *Zeitschrift für anorganische und allgemeine Chemie*, 634 (6-7),1082-1086.

Kwon I., Collins L.A., Kress J.D. 1995. First-principles study of solid Ar and Kr under compression. *Physical Review B*, 52 (21), 15165-15169.

Lai T-Y., Yang C-Y., Lin H-J., Yang C-Y., Hu W-P. 2011. Benchmark of density functional theory methods on the prediction of bond energies and bond distances of noble-gas containing molecules. *The Journal of Chemical Physics*, 134, 244110.

Larson A.C., Von Dreele,R.B. 2000. General Structure Analysis System (GSAS). *Los Alamos National Report*, 86-748.

Lavina B., Dera P., Downs R.T. 2014. Modern X-ray diffraction methods in mineralogy and geosciences . *Reviews in Mineralogy and Geochemistry*, 78 (1), 1-31.

Lazzeri M., Mauri F. 2003. First-Principles Calculation of Vibrational Raman Spectra in Large Systems: Signature of Small Rings in Crystalline $SiO_2$. *Physical Review Letters*, 90, 036401-036405.

Lazzeri M., Thibaudeau P. 2006. *Ab initio* Raman spectrum of the normal and disordered $MgA_{l2}O_4$ spinel. *Physical Review B*, 74, 140301-140305.

Le Godec Y., Solozhenko V.L., Mezouar M., Besson J-M., Syfosse G. 2000. In situ X-ray diffraction studies of formation of cubic and hexagonal graphite-like boron nitride by the reaction of elemental boron with supercritical hydrazine. *Science and Technology of High Pressure*, 2, 1031-1034.

Lee K.M., Steinle-Neumann G. 2006. High-pressure alloying of iron and xenon: 'Missing' Xe in the Earth's core ? *Journal of Geophysical Research*, 111, B02202.

Lehmann J.F., Dixon D.A., Schrobilgen G. 2001. X-ray Crystal Structures of alpha-KrF2, [KrF][$MF_6$] (M=As, Sb, Bi), $Kr_2F_3$][$SbF_6$].KrF2, [$Kr_2F_3$]$_2$[$SbF_6$]$_2$.$KrF_2$, and $Kr_2F_3$][$AsF_6$] .[KrF][AsF6]; Synthesis and Characterization of [$Kr_2F_3$][$PF_6$].n$KrF_2$; and Theoretical Studies of $KrF_2$, KrF+, $Kr_2F_3$+, and the [KrF][$MF_6$](M = P, As, Sb, Bi) Ion Pairs. *Inorganic Chemistry*, 40, 3002-3017.

Lemaire C., Kohn S.C., Brooker R.A. 2004. The effect of silica activity on the incorporation mechanism of water in synthetic forsterite: a polarised infrared spectroscopic study. *Contribution to Mineralogy and Petrology*, 147, 48-57.

Leroy C. 2016. I and Xe in melts: two distinct behaviours. PhD thesis. Sorbonne Université

Leroy C., Sanloup C., Bureau H., Schmidt B.C., Konopkova Z., Raepsaet C. 2018. Bonding of xenon to oxygen in magmas at depth. *Earth and Planetary Science Letters*, 484, 103–110.

Li J., Agee C.B. 1996. Geochemistry of mantle-core differentiation at high pressure. *Nature,* 381, 686-689.

Liermann H-P., Merkel S., Miyagi L., Wenk H-F., Shen G., Cynn H., Evans W. J. 2009. Experimental method for in situ determination of material textures at simultaneous high pressure and high temperature by means of radial diffraction in the diamond anvil cell. *Review of Scientific Instrument*s, 80, 104501.

Liu W., Li B. 2006. Thermal equation of state of $(Mg_{0.9}Fe_{0.1})_2SiO_4$ olivine. *Physics of the Earth and Planetary Interiors*, 157, 188-195.

Lokhov K., Levsky K., Begemann F. 2002. Volatile components in Karelian shungites as indicators of composition of Protherozoic atmosphere, in: *Astrobiology Expeditions*.

Lux G. 1987. The behavior of noble gases in silicate liquids: Solution, diffusion, bubbles and surface effects, with applications to natural samples. *Geochimica et Cosmochimica Acta*, 31, 1549-1560.

Mao H-K., Bell P.M. 1978. Design and varieties of the megabar cells. *Carnegie Institution of Washington Year Book*, 77, 904.

Madejova J., Balan E., Petit S. 2011. Application of vibrational spectroscopy to the characterization of phyllosilicates and otherindustrial minerals. *European Mineralogical Union Notes in Mineralogy*, 9, 171-226.

Marrocchi Y., Marty B., Reinhardt P., Robert F. 2011. Adsorption of xenon ions onto defects in organic surfaces: Implications for the origin and the nature of organics in primitive meteorites. *Geochimica et Cosmochimica Acta*, 75 (20), 6255-6266.

Marrocchi Y., Marty B. 2013. Experimental determination of the xenon isotopic fractionation during adsorption. *Geophysical Research Letters*, 40, 4165–4170.

Martin P.M., Garcia P., Carlot G., Sabathier C., Valot C., Nassif V., Proux O., Hazemann J-L. 2008. XAS characterisation of xenon bubbles in uranium dioxide. *Nuclear Instruments and Methods in Physics Research B*, 266, 2887–2891.

Martin P.M., Vathonne E., Carlot G., Delorme R., Sabathier C., Freyss M., Garcia P., Bertolus M., Glatzel P., Proux O. 2015. Behavior of fission gases in nuclear fuel: XAS characterization of Kr in $UO_2$. *Journal of Nuclear Materials*, 466, 379-392.

Marty B. 1989. Neon and xenon isotopes in MORB: implications for the earth-atmosphere evolution. *Earth and Planetary Science Letters*, 94, 45-56.

Marty B. 2012. The origins and concentrations of water, carbon, nitrogen and noble gases on Earth. *Earth and Planetary Science Letters*, 313–314, 56-66.

Marty B., Avice G. 2014. The iondine-plutonium-xenon age of the formation of the Earth-Moon system revisited. *Philosophical Transactions A*, 372.

Marty B., Avice G., Sano Y., Altwegg K., Balsiger H., Hässig M., Morbidelli A., Mousis O., Rubin M. 2016. Origins of volatile elements (H, C, N, noble gases) on Earth and Mars in light of recent results from the ROSETTA cometary mission. *Earth and Planetary Science Letters*, 441, 91-102.

Marty B., Altwegg K., Balsiger H., Bar-Nun A., Bekaert D.V., Berthelier J.J., Bieler A., Briois C., Calmonte U., Combi M., De Keyser J., Fiethe B., Fuselier S.A., Gasc S., Gombosi T.I., Hansen K.C., Hässig M., Jäckel A., Kopp E., Korth A., Le Roy L., Mall U., Mousis O., Owen T., Rème H., Rubin M., Sémon T., Tzou C.Y., Waite J.H., Wurz P. 2017. Xenon isotopes in 67P/Churyumov-Gerasimenko show that comets contributed to Earth's atmosphere. *Science*, 356(6342), 1069-1072

Mathew K. J., Marti K. 2001. Early evolution of Martian volatiles: Nitrogen and noble gas components in ALH 84001 and Chassigny. *Journal of Geophysical Research*, 106, 1401–1422.

Mathon O., Beteva A., Borrel J., Bugnazet D., Gatla S., Hino R., Kantor I., Mairs T., Munoz M., Pasternak S., Perrina F., Pascarelli S. 2015. The time-resolved and extreme conditions XAS (TEXAS) facility at the European Synchrotron Radiation Facility: the general-purpose EXAFS bending-magnet beamline BM23. *Journal of synchrotron radiation*, 22, 1548-1554.

Matsubara K., Matsuda J., Nagao K., Kita I., Taguchi S. 1988. Xe in amorphous silica: a new thermometer in geothermal systems. *Geophysical Research Letters*, 15(7), 657-660.

Matsuda J.-I., Matsubara K. 1989. Noble gases in silica and their implication for the terrestrial 'missing' Xe. *Geophysical Research Letters*, 16, 81–84.

Matsuda J.-I., Nagao K. 1986. Noble gas abundances in a deep-sea sediment core from eastern equatorial Pacific. *Geochemical Journal*, 20, 1-80.

Mazor E., Heymann D., Anders E. 1970. Noble gases in carbonaceous chondrites. *Geochimica et Cosmochimica Acta*, 34, 781–824.

McKeown D., Bell M.I., Caracas R. 2011. Theoretical determination of the Raman spectra of single-crystal forsterite ($Mg_2SiO_4$). *American Mineralogist*, 95, 980–986.

Meheut, M. 2008. Theoretical prediction of isotope fractionation factor between minerals in the framework of the density functional theory. PhD thesis. Sorbonne Université.

Melcher C.L., Tombrello T.A., Burnett D.S. 1983. Retention of ion-implanted-xenon in olivine: Dependence on implantation dose. *Geochimica et Cosmochimica Acta*, 47, 1707-1712.

Meshik A.P., Kehm K., Hohenberg C.M. 2000. Anomalous xenon in zone 13 Okelobondo. *Geochimica et Cosmochimica Acta*, 64, 9, 1651-1661.

Meshik A., Hohenberg C., Pravdivtseva O., Burnett D. 2014. Heavy noble gases in solar wind delivered by Genesis mission. *Geochimica et Cosmochimica Acta*, 127, 326–347.

Michel A., Sabathier C., Carlot G., Cabié M., Bouffard S., Garcia P. 2012. A TEM Study of Bubbles Growth with Temperature in Xenon and Krypton Implanted Uranium Dioxide. *Defect and Diffusion Forum*, 323-325, 191-196.

Momma K., Izumi F. 2011. VESTA 3 for three-dimensional visualization of crystal, volumetric and morphology data. *Journal of Applied Crystallography*, 44, 1272-1276.

Montana A., Guo Q., Boettcher S., White B.S., Brearley M. 1993. Xe and Ar in high-pressure silicate liquids. *American Mineralogist*, 78, 1135-1142.

Morard G., Mezouar M., Bauchau S., Alvarez-Murga M., Hodeau J-L., Garbarino G. 2011. High efficiency multichannel collimator for structural studies of liquids and low-Z materials at high pressures and temperatures. *Review of Scientific Instruments*, 82 (2), 023904.

Morard G. 2006. Fe-FeS and Fe-S-Si systems at high pressures and temperatures: Implication for the cores of planetary bodies. PhD thesis. Sorbonne Université.

Moreira M., Raquin A. 2007. The origin of rare gases on Earth: The noble gas 'subduction barrier' revisited. *Comptes Rendus Geoscience*, 339, 937–945.

Moreira M., Kunz J., Allègre J.C. 1998. Rare gas systematics in popping rock: Isotopic and elemental compositions in the upper mantle. *Science*, 279, 1178-1181.

Moreira M. 2013. Discusssion of the Origin of Noble Gases on Earth and the Evolution of The Mantle/Atmosphere System. *Geochemical Perspectives*, 2 (2), 352-373.

Mukhopadhyay S. 2012. Early differentiation and volatile accretion recorded in deep-mantle neon and xenon. *Nature*, 486, 101-104.

Newville M. 2001. EXAFS analysis using FEFF and FEFFIT. *Journal of Synchrotron Radiation*, 8, 96-100.

Newville M. 2004. Fundamentals of XAFS. *Reviews in Mineralogy and Geochemistry*, 78 (1), 33-74.

Nishio-Hamane D., Yagi T., Sata N., Fujita T., Okada T. 2010. No reactions observed in Xe-Fe system even at Earth even at Earth core pressure. *Geophysical Research Letters*, 37, 2010.

Noël Y., Catti M., d'Arco P., Dovesi R. 2006. The vibrational frequencies of forsterite $Mg_2SiO_4$: an all-electron *ab initio* study with the CRYSTAL code. *Physics and Chemistry of Minerals*, 33, 383-393.

Notesco G., Laufer D., Bar-Nun A. 1999. An experimental study of the isotopic enrichment in Ar, Kr,and Xe when trapped in water ice. *Icarus*, 142, 298-300.

Nuccio P.M., Paonita A. 2000. Investigation of the noble gas solubility in $H_2O$-$CO_2$ bearing silicate liquids at moderate pressure II: the extended ionic porosity (EIP) model. *Earth and Planetary Science Letters*, 183, 499-512.

Ojovan M.I., Lee W. E. 2010. Glassy wasteforms for nuclear waste immobilization. *Metallurgical and Materials Transactions A*, 42 (4), 837-851.

Owen T., Bar-Nun A., Kleinfeld I. 1992. Possible cometary origin of heavy noble gases in the atmospheres of Venus,Earth and Mars. *Nature*, 358, 43-45.

Ozima M., Podosek F. A. 1999. Formation age of Earth from $^{129}I/^{127}I$ and $^{244}Pu/^{238}U$ systematics and the missing Xe. *Journal of Geophysical Research*, 104 (B11), 25493-25499.

Ozima M., Zashu S. 1991. Noble gas state of the ancient mantle as deduced from noble gases in coated diamonds. *Earth and Planetary Science Letters*, 105, 13-27.

Ozima M., Podosek F.A. 2002 (1983). Noble gas geochemistry second edition. Cambridge University Press.

Ozima M., Igarashi G. 2000. The primordial noble gases in the Earth: a key constraint on Earth evolution models. *Earth and Planetary Science Letters*, 176, 219-232.

Packard J.R., Swenson C.A. 1963. An experimental equation of state for solid xenon. *Journal of Physics and Chemistry of Solids*, 24 (12), 1405-1418.

Parai R., Mukhopadhyay S., Standish J.J. 2012. Heterogeneous upper mantle Ne, Ar and Xe isotopic compositions and a possible Dupal noble gas signature recorded in basalts from the Southwest Indian Ridge. *Earth and Planetary Science Letters*, 359-360, 227-239.

Parai R., Mukhopadhyay S. 2015. The evolution of MORB and plume mantle volatile budgets: Constraints from fission Xe isotopes in Southwest Indian Ridge basalts. *Geochemistry, Geophysics, Geosystems*, 719-735.

Pepin R. O., Phinney D. 1976. The Formation Interval of the Earth. *Lunar and Planetary Science Conference, 7th*, 682-684.

Pepin R. O., Phinney D. 1978. Components of xenon in the Solar System. *Unpublished preprint, University of Minnesota*.

Pepin R.O. 1985. Evidence of Martian Origins. *Nature,* 317, 473-475.

Pepin R.O. 1991. On the Origin and Early Evolution of Terrestrial Planet Atmospheres and Meteoritic Volatiles. *Icarus*, 92, 2-79.

Pepin R.O. 2000. On the isotopic composition of primordial xenon in terrestrial planet atmospheres. *Space Science Reviews*, 92, 371–395.

Pepin R.O. 2006. Atmospheres on the terrestrial planets: Clues to origin and evolution. *Earth and Planetary Science Letters*, 252, 1-14.

Perdew, J.P., Burke, K., Ernzerhof, M., 1996. Generalized gradient approximation made simple, *Physical Review Letters*, 77, 3865-3868.

Petö M., Mukhopadhyay S., Kelley K. 2013. Heterogeneities from the first 100 million years recorded in deep mantle noble gases from the Northern Lau Back-arc Basin. *Earth and Planetary Science Letters*, 369-370, 13-23.

Petermann M., Whittington A.G., Hofmeister A.M., Spera F.J., Zayak J. 2008. Transport properties of low-sanidine single-crystals, glasses and melts at high temperature. *Contributions to Mineralogy and Petrology,* 155, 689-702.

Podosek F.A., Cassen P. 1994. Theoretical, observational, and isotopic estimates of the lifetime of the solar nebula. *Meteoritics*, 29, 6-25.

Porcelli D., Ballentine C.J. 2002. Models for distribution of terrestrial noble gases and evolution of the atmosphere. *Reviews in Mineralogy and Geochemistry,* 47, 1-19.

Prescher, C., Prakapenka, V.B. 2015. DIOPTAS: a program for reduction of two-dimensional X-ray diffraction data and data exploration. *High Pressure Research,* 35 (3), 223-230.

Probert M.I.J. 2010. An *ab initio* study of xenon retention in α-quartz. *Journal of Physics: Condensed Matter*, 22, 025501.

Prouteau, G., Scaillet, B., Pichavant, M., Maury, R. 2001. Evidence for mantle metasomatism by hydrous silicic melts derived from subducted oceanic crust. *Nature*, 410, 6825, 197–200.

Pujol M., Marty B., Burnard P., Philippot P. 2009. Xenon in Archean barite: Weak decay of $^{130}$Ba, mass-dependent isotopic fractionation and implication for barite formation. *Geochimica et Cosmochimica Acta*, 73, 6834–6846.

Pujol, M., Marty, B., Burgess, R. 2011. Chondritic-like xenon trapped in Archean rocks: A possible signature of the ancient atmosphere. *Earth and Planetary Science Letters*, 308, 298–306.

Pujol, M., Marty, B. and Burgess R. 2013. Reply to comment on "Chondritic-like xenon trapped in Archean rocks: A possible signature of the ancient atmosphere" by Pujol, M., Marty, B., Burgess, R. by Pepin, R.O., *Earth and Planetary Science Letters*, 308 (2011) 298-306. *Earth and Planetary Science Letters*, 371, 296-298.

Pyykkö P. 1997. Strong closed-shell interactions in organic chemistry. *Chemical Reviews*, 97, 597-636.

Ravel B., Newville M. 2005. ATHENA, ARTEMIS, HEPHAESTUS: data analysis for X-ray absorption spectroscopy using IFEFFIT. *Journal of Synchrotron Radiation*, 12, 537–541.

Reynolds J.H. 1963. Xenology. *Journal of Geophysical Research*, 68 (10), 2939-2956.

Ribas, I., Guinan, E.F., Güdel, M., Audard, M. 2005. Evolution of the Solar Activity over Time and Effects on Planetary Atmospheres. I. High-Energy Irradiances (1–1700 Å). *Astrophysical Journal*, 622 (1), 680-694.

Richet P., Bottinga Y. 1984. Glass transitions and thermodynamic properties of amorphous $SiO_2$, $NaAlSi_nO_{2n+2}$ and $KAlSi_3O_8$. *Geochimica et Cosmochimica Acta*, 48 (3), 453-470.

Rietveld H.M. 1967. Line profile of neutron powder-diffraction peaks for structure refinement. *Acta Crystallographica*, 22, 151-152.

Rietveld H.M. 1969. A profile refinement method for nuclear and magnetic structures.» *Journal of Applied Crystallography*, 2, 65-71.

Ringwood A.E. 1967. High-Pressure $KAlSi_3O_8$, an Aluminosilicate with Sixfold Coordination. *Acta Crystallographica*, 23, 1093-1095.

Rivoldini A, Van Hoolst T., Verhoeven O, Mocquet A., Dehant V. 2011. Geodesy constraints on the interior structure and composition of Mars. *Icarus*, 213 (2), 451-472.

Romanenko A.V., Rashchenko S.V., Goryainov S.V., Likhacheva A.Y. 2017. Phase relations in $KAlSi_3O_8$-$H_2O$ system at high pressure and temperature. *Conference 11th International School of Earth Sciences ISES-2017, at Miass, Russia.*

Rosa A.D., Pohlenz J., de Grouchy C., Cochain B., Kono Y., Pasternak S., Mathon O., Irifune T., Wilke M. 2016. *In situ* characterization of liquid network structures at high pressure and temperature using X-ray Absorption Spectroscopy coupled with the Paris-Edinburgh press. *High Pressure Research*, 36, 332-347.

Roskosz M., Siob C.K.I., Dauphas N., Bi W., Tissot F.L.H., Hu M.Y., Zhao J., Alp E.E. 2015. Spinel–olivine–pyroxene equilibrium iron isotopic fractionation and applications to natural peridotites. *Geochimica et Cosmochimica Acta*, 169, 184–199.

Ross M., Boelher R., Söderlind P. 2005. Xenon melting curve to 80 GPa and 5 *p-d* hybridization. *Physical Review Letters*, 95, 257801

Saal A.E., Hauri E.H., Langmuir C.H., Perfit M.R. 2002. Vapour undersaturation in primitive mid-ocean-ridge basalt and the volatile content of Earth's upper mantle. *Nature*, 419, 451-455.

Saito K., Alexander E.C., Dragon J.C. 1984. Rare Gases in Cyclosilicates and Cogenetic Minerals. *Journal of Geophysical Research*, 89, 7891-7901.

Sanloup C., Hemley R.J., Mao H.K., 2002. Evidence for xenon silicates at high pressure and temperature. *Geophysical Research Letters*, 29, 1883-1886.

Sanloup C., Schmidt B.C., Perez E.C., Jambon A., Gregoryanz E., Mezouar M., 2005. Retention of xenon in quartz and Earth's missing xenon. *Science*, 310, 1174–1177.

Sanloup C., Schmidt B.C., Gudfinnsson G., Dewaele A., Mezouar M. 2011. Xenon and argon: a contrasting behavior in olivine at depth. *Geochimica et Cosmochimica Acta*, 75, 6271–6284.

Sanloup C., Bonev S.A., Hochlaf M., Maynard-Casely H.E. 2013. Reactivity of Xenon with Ice at Planetary Conditions. *Physical Review Letters*, 110, 265501.

Sasaki S. 1991. Off-Disk Penetration of Ancient Solar Wind. *Icarus*, 91, 29-38

Sautter V., Toplis M.J., Wiens R.C., Cousin A., Fabre C., Gasnault O., Maurice S., Forni O., Lasue J., Ollila O., Bridges J.C., Mangold N., Le Mouélic S., Fisk M., Meslin P.Y., Beck P., Pinet P., Le Deit L., Rapin W., Stolper E.M., Newsom H., Dyar D., Lanza N., Vaniman D., Clegg S., Wray J.J. 2015. *In situ* evidence for continental crust on early Mars. *Nature Geoscience*, 8, 605-609.

Schmidt B.C., Keppler H. 2002. Experimental evidence for high noble gas solubilities in silicate melts under mantle pressures, *Earth and Planetary Science Letters*, 195, 277-290.

Schrobilgen G.J., Brock D.S. 2012. Noble gases. *Annual Report on the Progress of Chemistry Section A: Inorganic Chemistry*, 108, 138–145.

Sears D.R., Klug H.P. 1962. Density and Expansivity of Solid Xenon. *The Journal of Chemical Physics*, 37 (12), 3002-3006.

Seki Y., Kennedy G.C. 1964. The breakdown of potassium feldspar, KAlSi3O8, at high temperatures and high pressures. *American Mineralogist*, 49, 1688-1706.

Selig H., Malm J.G., Claassen H.H., Chernick C.L., Huston J.L. 1964. Xenon tetroxide: Preparation and some Properties. *Science*, 143, 1322-1323.

Seoung D., Lee Y., Cynn H., Park C., Choi K-Y., Blom D.A., Evans W.J., Kao C-C., Vogt T., Lee Y. 2014. Irreversible xenon insertion into a small-pore zeolite at moderate pressures and temperatures. *Nature Chemistry*, 6, 835-839.

Servoin J.L., B. Piriou. 1973. Infrared Reflectivity and Raman Scattering of $Mg_2SiO_4$ Single Crystal. *Physica Status Solidi (b)*, 56, 677-686.

Shannon R.D. 1976. Revised effective ionic radii and systematic studies of interatomic distances in halides and chalcogenides. *Acta Crystallographica*, A32, 751-767.

Shcheka S.S., Keppler H. 2012. The origin of the terrestrial noble-gas signature. *Nature*, 490, 531-534.

Shibata T., Takahashi E., Matsuda J.I. 1998. Solubility of neon, argon, krypton, and xenon in binary and ternary silicate systems: A new view on noble gas solubility. *Geochimica et Cosmochimica Acta*, 62, 1241-1253.

Shoval S., Champagnon B., Panczer G. 1997. The quartz-cristobalite transformation in heated chert rock composed of micro and crypto-quartz by Micro-Raman and FTIR spectroscopy methods. *Journal of Thermal Analysis*, 50 (1-2), 203–213.

Sloan E.D., Koh C. 2007. Clathrate Hydrates of Natural Gases, Third Edition. CRC Press.

Smith D.F. 1963. Xenon Trioxide. *The Journal of American Chemical Society*, 85 (6) , 816-817.

Smye A.J., Jackson C.R.M., Konrad-Schmolke M., Hesse M.A., Parman S.W., Shuster D.L., Ballentine C.J. 2017. Noble gases recycled into the mantle through cold subduction zones. *Earth and Planetary Science Letters*, 471, 65-73.

Smyth J.R., Kawamoto T. 1997. Wadsleyite II: a new high pressure hydrous phase in the peridotite-H2O system. *Earth and Planetary Science Letters*, 146, E9-E16.

Smyth J.R., Holl C.M., Langenhorst F., Laustsen H.M.S., Rossman G.R., Kleppe A., McCammon C.A., Kawamoto T., Van Aken P.A., 2005. Crystal chemistry of wadsleyite II and water in the Earth's interior. *Physics and Chemistry of Minerals*, 31, 691–705.

Somayazulu M., Dera P., Goncharov A.F., Gramsch S.A., Liermann P., Yang W., Liu Z., Mao H.K., Hemley R.J. 2010. Pressure-induced bonding and compound formation in xenon–hydrogen solids. *Nature Chemistry*, 2, 50-53.

Somayozulu M., Dera P., Smith J., Hemley R.J. 2015. Structure and stability of solid Xe-$(H_2)_n$. *The Journal of chemical physics*, 142, 104503.

Sonnenblick Y., Alexander E., Kalman Z-H., Steinberger L.T. 1977. Hexagonal close packed krypton and xenon. Chemical Physics Letters, 52 (2), 276-278.

Spandler C., O'Neill H. St.C. 2010. Diffusion and partition coefficients of minor and trace elements in San Carlos olivine at 1,300°C with some geochemical implications. *Contributions to Mineralogy and Petrology*, 159, 791-818.

Srinivasan B. 1976. Barites: anomalous xenon from spallation and neutron induced reactions. *Earth and Planetary Science Letters*, 31, 129-141.

Stashans A., Flores Y. 2013. Modelling of neutral vacancies in forsterite mineral. *International Journal of Modern Physics B*, 27, 1350141.

Staudacher T., Allègre C.J. 1982. Terrestrial xenology. *Earth and Planetary Science Letters*, 60, 389-406.

Stavrou E., Yao Y., Goncharov A.F., Lobanov S.S., Zaug J.M., Liu H., Greenberg E., Prakapenka V.B. 2018. Synthesis of Xenon and Iron-Nickel Intermetallic Compounds at Earth's Core Thermodynamic Conditions. *Physical Review Letters*, 120, 096001

Stern E.A., Livins P., Zhang Z. 1991. Thermal vibration and melting from a local perspective. *Physical review B*, 43, 8850-8860.

Stuart B. 2004. Infrared spectroscopy: Fundamentals and applications. ed. John Wiley & Sons, Ltd.

Sumino H., Burgess R., Mizukami T., Wallis S.R., Holland G., Ballentine C.J. 2010. Seawater-derived noble gases and halogens preserved in exhumed mantle wedge peridotite. *Earth and Planetary Science Letters*, 294, 163–172.

Sun Y., Carrigan C.R., Hao Y. 2015. Radioxenon Production and Transport from an Underground Nuclear Detonation to Ground Surface. *Pure an Applied Geophysics*, 172, 243–265.

Swindle T.D. 2002. Martian Noble Gases. *Reviews in Mineralogy and Geochemistry*, 47 (1), 171-190.

Syassen K., Holzapfel W.D. 1978. High-pressure equation of state for solid xenon. *Physical Review B*, 18, 5826.

Syassen K. 2008. Ruby under pressure. *High pressure Research*, 28 (2), 75-126.

Templeton D.H., Zalkin A., Forrester J.D., Williamson S.M. 1963. Crystal and molecular structure of xenon trioxide, *Journal of the American Chemical Society*, 85 (6), 817.

Teo B.K. 1986. EXAFS: Basic Principles and data analysis. *Inorganic Chemistry Concepts*, 9.

Thompson P., Parsons I., Graham C.M., Jackson B. 1998. The breakdown of potassium feldspar at high water pressures. *Contribution to Mineralogy and Petrology*, 130 (2), 176-186.

Thompson L.M., Stebbins J.F. 2011. Non-bridging oxygen and high-coordinated aluminum in metaluminous and peraluminous calcium and potassium aluminosilicate glasses: High-resolution $^{17}$O and $^{27}$Al MAS NMR results. *American Mineralogist*, 96, 841–853.

Trieloff M., Kunz J., Clague D., Harrison D., Allègre J.C. 2000. The nature of pristine noble gases in mantle plumes. *Science*, 288, 5468, 1036-1038.

Trieloff M., Kunz J. 2005. Isotope systematics of noble gases in the Earth's mantle: possible sources of primordial isotopes and implications for mantle structure. *Physics of the Earth and Planetary Interiors*, 4 (148), 13-38.

Troullier, N., Martins, J. L., 1991. Efficient pseudopotentials for plane-wave calculations. *Physical Review B*, 43, 1993-2006.

Tucker J.M., Mukhopadhyay S., Schilling J-G. 2012. The heavy noble gas composition of the depleted MORB mantle (DMM) and its implications for the preservation of heterogeneities in the mantle. *Earth and Planetary Science Letters*, 355–356, 244–254.

Turner G., Harrison T.M., Holland G., Mojzsis S.J., Gilmour J. 2004. Extinct 244Pu in Ancient Zircons. *Science*, 306, 89-91.

Turner S., Caulfield J., Turner M., vanKeken P., Maury R., Sandiford M., Prouteau G. 2012. Recent contribution of sediments and fluids to the mantle's volatile budget. *Nature Geoscience*, 5 (1), 50–54.

Van der Hilst R.D., Widiyantoro S., Engdahl E.R. 1997. Evidence for deep mantle circulation from global tomography. *Nature*, 386, 578-584.
Verma A. K. and Karki B. B. 2009. Ab initio investigations of native protonic point defects in $Mg_2SiO_4$ polymorphs under high pressure. *Earth and Planetary Science Letters,* 285, 140-149.

Walker N. R., Wright R.R., Stace A.J. 1999. Stable Ag(II) Coordination Complexes in the Gas Phase. *Journal of the American Chemical Society*, 121, 4837-4844.

Walsh K.J., Morbidelli A., Raymond S.N., O'Brien D.P., Mandell A.M. 2011. A low mass for Mars from Jupiter's early gas-driven migration. *Nature*, 475, 206-209.

Wang J., Mao Z., Jiang F., Duffy T.S. 2015. Elasticity of single-crystal quartz to 10 GPa. *Physics and Chemistry of Minerals*, 45, 203–212.

Warr O., Rochelle C.A., Masters A., Ballentine C.J. 2015. Determining noble gas partitioning within a $CO_2$–$H_2O$ system at elevated temperatures and pressures. *Geochimica et Cosmochimica Acta*, 159, 112-125.

Watrous M.G., Delmore J.E., Hague R.K., Houghton T.P., Jenson D.D., Mann N.R. 2015. Radioxenon spiked air. *Journal of Environmental Radioactivity*, 150, 126-131.

Wetherill G.W. 1985. Occurrence of Giant Impacts During the Growth of the Terrestrial Planets. *Science*, 228 (4701), 877-879.

Widder W., Wondratschek H., Fehlmann M., Klapper H. 1994. X-ray topographie study of Eifel sanidine (Volkesfeld). *Zeitschrift für Kristallographie*, 209, 206-209.

Williams, Q., Hemley, R.J., Kruger, M.B., Jeanloz, R. 1993. High-pressure infrared sepctra of α-quartz, coesite, stishovite and silica glass. *Journal of Geophysical Research*, 98 (B12), 22157-22170.

Williams D.B., Carter C.B. 2009 (1996). Transmission Electron Microscopy: a textbook for material science. Second ed., Springer.

Wulf R., Calas G., Ramos A., Büttner H., Roselib K., Rosenhauer M. 1999. Structural environment of krypton dissolved in vitreous silica. American Mineralogist, 84, 1461–1463.

Xiang Y., Du J., Smedskjaer M.M., Mauro J.C. 2013. Structure and properties of sodium aluminosilicate glasses from molecular dynamics simulations. *The Journal of Chemical Physics*, 139.

Yamada A., Wang Y., Inoue T., Yang W., Park C., Yu T., Shen G. 2011. High-pressure x-ray diffraction studies on the structure of liquid silicate using a Paris–Edinburgh type large volume press. *Review of Scientific Instruments*, 82, 015103.

Yi H., Balan E., Gervais C., Segalen L., Fayon F., Riche D., Person A., Morin G., Guillaumet M., Blanchard M., Lazzeri M., Babonneau F. 2013. A carbonate-fluoride defect model for carbonate-rich fluorapatite. *American Mineralogist*, 98, 1066-1069.

Yokochi R., Marty B. 2004. A determination of the neon isotopic composition of the deep mantle. *Earth and Planetary Science Letters*, 225, 77– 88.

Yokochi R., Marty B. 2005. Geochemical constraints on mantle dynamics in the Hadean. *Earth and Planetary Science Letters*, 238, 17– 30.

Yong W., Dachs E., Withers A.C., Essene E.J. 2006. Heat capacity and phase equilibria of hollandite polymorph of $KAlSi_3O_8$. *Physics and Chemistry of Minerals*, 33 (3), 167-177.

Zahnle K., Kastling J.F. 1986. Mass fractionation during transonic escape and implications for loss of water from Mars and Venus. *Icarus*, 68, 462-480.

Zahnle K., Kastling J.F., Pollack J.B. 1990. Mass fractionation of noble gases in diffusion-limited hydrodynamic hydrogen escape. *Icarus*, 84 (2), 502-527.

Zhang Y., Xue Z. 1995. Atomic radii of noble gas elements in condensed phases, *American Mineralogist*, 80, 670-675.

Zhu Q., Jung D.Y., Oganov A.R., Glass C.W., Gatti C., Lyakhov A.O. 2012. Stability of xenon oxides at high pressures. *Nature Chemistry*, 61-65.

Zhu L., Liu H., Pickard C.J., Zou G., Ma Y. 2014. Reactions of xenon with iron and nickel are predicted in the Earth's inner core. *Nature Chemistry*, 6, 644-648.

## APPENDIX

## APPENDIX C/ (i.e. related to chapter C)

### Appendix C1/ EMPA calibrations for Xe

For our study, EMP analyses have been performed on CAMECA SX5, at CAMPARIS centre at Sorbonne Université during four sessions. Throughout the four sessions, Xe-bearing sanidine Nat. glass (PC53) was analyzed to calibrate our measurements. Average measured Xe contents from the different sessions are given in Table 1. We calculated the weighted (by number of data points) average mean and corrected Xe content for all analyses.
We also used previous EMPA acquired on the same Electron Microprobe (CAMECA SX5), noted 'Previous EMPA (CAMECA SX5)': no calibration was possible for Xe due to the absence of analyzed standard.
We eventually used previous EMPA acquired at the School of GeoSciences at the University of Edinburgh (on a CAMECA SX100), noted 'Previous EMPA University of Edinburgh': for these data standard PC53 was analyzed and we recalibrate these analyses for Xe content compared to our new analyses of the standard (Table 1).

Except for Appendix C2, all EMPA data presented have been calibrated for Xe as explained here.

| Sessions | data points | $Na_2O$ | MgO | $SiO_2$ | $Al_2O_3$ | $K_2O$ | CaO | FeO | MnO | $TiO_2$ | Xe (wt%) | Xe (at%) | BaO | $Cr_2O_3$ | NiO | Total |
|---|---|---|---|---|---|---|---|---|---|---|---|---|---|---|---|---|
| **This work : 2017-05-19** | 7 | 3.6 (9) | 0.02(2) | 63.7 (8) | 19.6 (1) | 8 (1) | 0.80 (3) | 0.76 (6) | 0.01 (1) | 0.14 (3) | 1.83 (5) | 0.31 (1) | 0.28 (8) | - | - | 99 (1) |
| **This work : 2017-05-29** | 4 | 3.2 (5) | 0.01 (1) | 63.1 (3) | 20.1 (2) | 8.0 (4) | 0.82 (3) | 0.8 (2) | 0.01 (2) | 0.11 (2) | 2.39 (7) | 0.41 (1) | 0.28 (5) | - | - | 99 (1) |
| **This work : 2017-11-16** | 8 | 2.5 (7) | 0.01 (1) | 67 (1) | 20.4 (5) | 7 (1) | 0.80 (3) | 0.5 (3) | 0.01 (2) | 0.16 (3) | 1.96 (8) | 0.33 (4) | 0.3 (1) | 0.2 (1) | 0.00 (2) | 100 (1) |
| **This work : 2018-03-15** | 36 | 4.0 (3) | 0.01 (1) | 63 (1) | 19.1 (4) | 8.5 (2) | 0.82 (9) | 0.3 (3) | 0.02 (3) | 0.13 (7) | 1.86 (9) | 0.32 (2) | 0.3 (2) | 0.1 (1) | - | 98.3 (9) |
| **Weighted average mean** | 55 | **3.7** | **0.01** | **63.7** | **19.4** | **8.2** | **0.81** | **0.42** | **0.02** | **0.13** | **1.91** | **0.33** | **0.3** | **-** | **-** | **98.7** |
| **Previous EMPA University of Edinburgh** | 4 | 4.68 (4) | 0.008 (2) | 63.9 (3) | 19.2 (2) | 7.88 (8) | 0.78 (1) | 0.3 (2) | 0.02 (1) | 0.097 (3) | 2.57 (3) | 0.419 (4) | -. | -. | - | 99.4 (6) |

*Table 1: Comparison of average EMPA for standard PC53 (Xe-bearing sanidine Nat. glass, Table G1) throughout EMPA sessions for these work. The average mean, weighted by the number of data point is given in bold, it will be used to recalibrate Xe content during the session: for instance to recalibrate Xe content for session on 2017-05-19, Xe content (in wt%) is multiplied by 0.33/0.31.Previous analyzed performed on CAMECA SX100 at the School of GeoSciences at the university of Edinburgh are recalibrated for Xe content: Xe content (in wt%) is multiplied by 1.91/2.57.*

## Appendix C2/ EMPA of PC53 standard (Xe-bearing sanidine Nat. glass)

| 2017-05-29 n° of analysis | sample | $Na_2O$ | MgO | $SiO_2$ | $Al_2O3$ | Ar | $K_2O$ | CaO | FeO | MnO | $TiO_2$ | Kr | Xe | BaO | $Cr_2O_3$ | NiO | $Re_2O_7$ | Total |
|---|---|---|---|---|---|---|---|---|---|---|---|---|---|---|---|---|---|---|
| 1 / 1 . | PC53 | 2.85 | 0.01 | 64.53 | 19.89 | 0.02 | 7.46 | 0.80 | 0.71 | 0.02 | 0.11 | -0.51 | -0.01 | 0.36 | | | | 96.76 |
| 2 / 1 . | PC53 | 3.00 | 0.01 | 63.24 | 19.91 | 0.01 | 7.62 | 0.81 | 0.67 | 0.03 | 0.12 | -0.01 | 2.44 | 0.24 | | | | 98.09 |
| 3 / 1 . | PC53 | 3.39 | 0.01 | 63.42 | 20.19 | 0.00 | 8.22 | 0.78 | 0.67 | 0.01 | 0.12 | -0.01 | 2.32 | 0.23 | | | | 99.36 |
| 67 / 1 . | PC53 | 3.52 | 0.00 | 66.75 | 21.06 | 0.01 | 7.77 | 0.80 | 0.71 | 0.00 | 0.11 | 0.00 | 2.34 | 0.28 | | | | 103.36 |
| 68 / 1 . | PC53 | 3.91 | 0.01 | 65.17 | 20.86 | 0.01 | 8.43 | 0.87 | 0.74 | 0.00 | 0.07 | 0.01 | 2.38 | 0.33 | | | | 102.80 |
| 69 / 1 . | PC53 | 3.76 | 0.02 | 62.81 | 20.32 | 0.00 | 8.44 | 0.83 | 1.03 | 0.03 | 0.08 | -0.01 | 2.35 | 0.30 | | | | 99.99 |
| 70 / 1 . | PC53 | 3.04 | 0.03 | 60.52 | 19.22 | -0.01 | 7.86 | 0.81 | 0.89 | 0.01 | 0.11 | -0.01 | 2.26 | 0.40 | | | | 95.16 |
| 71 / 1 . | PC53 | 2.64 | 0.01 | 63.08 | 20.09 | -0.01 | 7.67 | 0.84 | 0.70 | -0.01 | 0.10 | -0.01 | 2.45 | 0.34 | | | | 97.92 |
| 72 / 1 . | PC53 | 3.94 | 0.01 | 65.39 | 20.96 | -0.01 | 8.30 | 0.79 | 0.67 | 0.02 | 0.13 | 0.02 | 2.38 | 0.40 | | | | 103.01 |
| 73 / 1 . | PC53 | 3.55 | 0.01 | 66.03 | 20.97 | -0.01 | 8.23 | 0.84 | 0.66 | 0.01 | 0.12 | -0.03 | 2.37 | 0.33 | | | | 103.12 |
| 74 / 1 . | PC53 | 4.26 | 0.01 | 56.62 | 17.47 | -0.02 | 8.12 | 0.81 | 0.55 | 0.01 | 0.09 | 0.01 | 2.27 | 0.30 | | | | 90.52 |

| 2017-05-19<br>n° of analysis | sample | $Na_2O$ | MgO | $SiO_2$ | $Al_2O3$ | Ar | $K_2O$ | CaO | FeO | MnO | $TiO_2$ | Kr | Xe | BaO | $Cr_2O_3$ | NiO | $Re_2O_7$ | Total |
|---|---|---|---|---|---|---|---|---|---|---|---|---|---|---|---|---|---|---|
| 160 / 1 . | PC53 | 2.67 | 0.01 | 62.59 | 19.01 | 0.00 | 7.33 | 0.81 | 0.70 | 0.03 | 0.13 | -0.01 | 1.86 | 0.23 | | | | 95.37 |
| 161 / 1 . | PC53 | 4.20 | 0.01 | 66.42 | 20.40 | 0.00 | 8.35 | 0.75 | 0.77 | -0.02 | 0.15 | -0.01 | 1.90 | 0.17 | | | | 103.11 |
| 162 / 1 . | PC53 | 3.91 | 0.02 | 66.28 | 20.96 | 0.01 | 8.19 | 0.80 | 1.11 | 0.00 | 0.11 | 0.00 | 1.76 | 0.28 | | | | 103.41 |
| 163 / 1 . | PC53 | 0.09 | 0.01 | 1.16 | 0.29 | -0.01 | 0.11 | 0.02 | 0.03 | -0.01 | 0.02 | 0.00 | 0.03 | 0.10 | | | | 1.84 |
| 164 / 1 . | PC53 | 4.16 | 0.03 | 63.33 | 19.72 | 0.00 | 8.39 | 0.79 | 0.68 | 0.00 | 0.14 | -0.02 | 1.80 | 0.28 | | | | 99.31 |
| 165 / 1 . | PC53 | 3.51 | 0.02 | 62.82 | 19.56 | 0.01 | 8.18 | 0.81 | 0.70 | 0.00 | 0.12 | 0.01 | 1.83 | 0.31 | | | | 97.91 |
| 166 / 1 . | PC53 | 3.76 | 0.01 | 65.52 | 20.34 | 0.00 | 8.47 | 0.78 | 0.82 | -0.04 | 0.17 | -0.01 | 1.90 | 0.29 | | | | 102.04 |
| 167 / 1 . | PC53 | 3.14 | 0.01 | 63.64 | 19.33 | 0.00 | 8.07 | 0.75 | 0.81 | -0.01 | 0.17 | 0.00 | 1.90 | 0.15 | | | | 97.97 |
| 168 / 1 . | PC53 | 4.19 | 0.01 | 63.69 | 19.79 | 0.01 | 8.35 | 0.79 | 0.78 | 0.02 | 0.14 | 0.01 | 1.82 | 0.21 | | | | 99.81 |
| 169 / 1 . | PC53 | 4.02 | 0.01 | 64.08 | 19.57 | 0.00 | 8.30 | 0.77 | 0.74 | 0.02 | 0.15 | -0.02 | 1.85 | 0.39 | | | | 99.91 |
| 170 / 1 . | PC53 | 4.12 | 0.01 | 63.03 | 19.61 | 0.00 | 8.47 | 0.81 | 0.83 | -0.01 | 0.13 | -0.01 | 1.84 | 0.36 | | | | 99.21 |
| 171 / 1 . | PC53 | 1.84 | 0.06 | 65.36 | 19.55 | -0.01 | 5.47 | 0.84 | 0.81 | 0.02 | 0.09 | 0.00 | 1.74 | 0.27 | | | | 96.05 |

| 2017-11-16<br>n° of analysis | sample | $Na_2O$ | MgO | $SiO_2$ | $Al_2O3$ | Ar | $K_2O$ | CaO | FeO | MnO | $TiO_2$ | Kr | Xe | BaO | $Cr_2O_3$ | NiO | $Re_2O_7$ | Total |
|---|---|---|---|---|---|---|---|---|---|---|---|---|---|---|---|---|---|---|
| 1 / 1 . | PC53 | 4.07 | 0.01 | 65.17 | 19.50 | 0.00 | 8.48 | 0.76 | 0.25 | -0.02 | 0.12 | 0.00 | 1.90 | 0.15 | 0.11 | 0.03 | -0.15 | 100.54 |
| 70 / 1 . | PC53 | 2.66 | 0.01 | 66.72 | 20.36 | 0.00 | 7.48 | 0.82 | 0.05 | -0.03 | 0.18 | -0.01 | 2.05 | 0.37 | 0.02 | -0.02 | -0.11 | 100.72 |
| 71 / 1 . | PC53 | 2.63 | 0.00 | 66.07 | 20.22 | 0.01 | 6.99 | 0.80 | 0.10 | 0.01 | 0.19 | 0.00 | 2.09 | 0.21 | 0.03 | 0.02 | -0.13 | 99.38 |
| 72 / 1 . | PC53 | 1.32 | 0.01 | 71.56 | 22.01 | 0.01 | 5.65 | 0.71 | 0.27 | 0.01 | 0.15 | 0.01 | 2.02 | 0.16 | 0.09 | 0.01 | -0.06 | 103.99 |
| 231 / 1 . | PC53 | 2.33 | 0.02 | 67.84 | 20.89 | -0.01 | 6.31 | 0.78 | 0.77 | 0.03 | 0.19 | 0.00 | 1.95 | 0.23 | 0.29 | -0.03 | -0.15 | 101.62 |
| 232 / 1 . | PC53 | 2.67 | 0.01 | 64.53 | 19.81 | 0.01 | 6.77 | 0.84 | 0.69 | 0.00 | 0.17 | -0.01 | 1.97 | 0.34 | 0.23 | 0.02 | -0.19 | 98.06 |
| 233 / 1 . | PC53 | 2.05 | 0.01 | 66.99 | 20.55 | 0.00 | 5.89 | 0.82 | 0.74 | 0.03 | 0.10 | 0.00 | 1.96 | 0.31 | 0.28 | -0.03 | -0.10 | 99.75 |
| 234 / 1 . | PC53 | 2.69 | 0.01 | 63.97 | 19.48 | 0.00 | 7.32 | 0.81 | 0.80 | 0.01 | 0.11 | 0.00 | 1.95 | 0.37 | 0.29 | -0.01 | -0.10 | 97.81 |
| 235 / 1 . | PC53 | 1.60 | 0.02 | 69.18 | 21.04 | -0.01 | 5.01 | 0.78 | 0.89 | 0.01 | 0.14 | 0.00 | 1.97 | 0.34 | 0.27 | 0.00 | -0.09 | 101.27 |
| 236 / 1 . | PC53 | 1.73 | 0.03 | 69.63 | 21.05 | 0.01 | 5.73 | 0.75 | 0.95 | 0.00 | 0.18 | 0.01 | 1.94 | 0.27 | 0.29 | -0.02 | -0.12 | 102.57 |
| 237 / 1 . | PC53 | 1.67 | 0.01 | 66.03 | 19.99 | 0.00 | 5.89 | 0.81 | 0.65 | 0.00 | 0.17 | 0.02 | 2.04 | 0.27 | 0.24 | 0.02 | -0.15 | 97.82 |
| 238 / 1 . | PC53 | 2.71 | 0.01 | 56.46 | 17.20 | 0.00 | 6.51 | 0.86 | 0.47 | 0.02 | 0.13 | 0.00 | 1.99 | 0.49 | 0.19 | -0.02 | -0.08 | 87.03 |

| | | | | | | | | | | | | | | | | | | |
|---|---|---|---|---|---|---|---|---|---|---|---|---|---|---|---|---|---|---|
| 239 / 1 . | PC53 | 2.55 | 0.00 | 64.33 | 19.82 | 0.00 | 6.27 | 0.80 | 0.41 | -0.01 | 0.14 | 0.01 | 1.99 | 0.17 | 0.19 | 0.04 | -0.09 | 96.73 |
| 240 / 1 . | PC53 | 3.27 | 0.04 | 39.85 | 11.73 | -0.02 | 6.76 | 0.77 | 0.31 | 0.00 | 0.14 | -0.01 | 1.90 | 0.33 | 0.15 | 0.02 | -0.21 | 65.26 |
| 241 / 1 . | PC53 | 1.79 | 0.00 | 70.19 | 21.78 | 0.01 | 6.26 | 0.71 | 0.15 | 0.00 | 0.10 | -0.01 | 2.02 | 0.31 | 0.06 | -0.01 | -0.07 | 103.40 |
| 242 / 1 . | PC53 | 2.33 | 0.00 | 66.41 | 20.83 | 0.00 | 5.90 | 0.78 | 0.78 | 0.01 | 0.15 | -0.01 | 1.82 | 0.10 | 0.27 | 0.00 | -0.03 | 99.37 |
| 243 / 1 . | PC53 | 2.79 | 0.02 | 26.49 | 8.10 | -0.02 | 6.12 | 0.89 | 0.97 | 0.04 | 0.07 | 0.01 | 1.83 | 0.10 | 0.32 | 0.05 | -0.01 | 47.79 |

| 2018-03-15 | | | | | | | | | | | | | | | | | | |
|---|---|---|---|---|---|---|---|---|---|---|---|---|---|---|---|---|---|---|
| **n° of analysis** | **sample** | **$Na_2O$** | **MgO** | **$SiO_2$** | **$Al_2O3$** | **Ar** | **$K_2O$** | **CaO** | **FeO** | **MnO** | **$TiO_2$** | **Kr** | **Xe** | **BaO** | **$Cr_2O_3$** | **NiO** | **$Re_2O_7$** | **Total** |
| 239 / 1 . | PC53 | 3.82 | 0.02 | 63.48 | 18.95 | 0.00 | 8.61 | 0.84 | 0.10 | 0.00 | 0.25 | 0.02 | 1.99 | 0.38 | 0.00 | | | 98.47 |
| 240 / 1 . | PC53 | 4.00 | 0.03 | 63.79 | 18.81 | 0.00 | 8.65 | 0.71 | 0.08 | 0.01 | 0.12 | 0.00 | 1.91 | 0.20 | 0.00 | | | 98.30 |
| 241 / 1 . | PC53 | 4.01 | 0.01 | 63.34 | 19.17 | 0.00 | 8.66 | 0.89 | 0.03 | 0.01 | 0.10 | 0.03 | 1.98 | 0.12 | 0.00 | | | 98.36 |
| 242 / 1 . | PC53 | 3.81 | 0.05 | 64.36 | 18.77 | 0.02 | 8.44 | 0.85 | 0.04 | 0.00 | 0.10 | 0.00 | 1.73 | 0.26 | 0.00 | | | 98.42 |
| 243 / 1 . | PC53 | 3.75 | 0.04 | 63.44 | 18.81 | 0.01 | 8.23 | 1.03 | 0.01 | 0.11 | 0.06 | 0.00 | 2.07 | 0.49 | 0.00 | | | 98.04 |
| 244 / 1 . | PC53 | 3.56 | 0.00 | 63.37 | 18.65 | 0.00 | 8.45 | 0.92 | 0.00 | 0.07 | 0.10 | 0.00 | 1.82 | 0.30 | 0.00 | | | 97.24 |
| 245 / 1 . | PC53 | 3.92 | 0.01 | 63.93 | 18.78 | 0.00 | 8.92 | 0.88 | 0.02 | 0.00 | 0.05 | 0.00 | 1.92 | 0.46 | 0.00 | | | 98.89 |
| 246 / 1 . | PC53 | 3.68 | 0.00 | 63.29 | 19.33 | 0.02 | 9.03 | 0.69 | 0.04 | 0.03 | 0.04 | 0.01 | 1.78 | 0.07 | 0.01 | | | 98.01 |
| 247 / 1 . | PC53 | 3.95 | 0.03 | 63.80 | 19.07 | 0.00 | 8.63 | 0.83 | 0.00 | 0.00 | 0.16 | 0.00 | 1.88 | 0.23 | 0.00 | | | 98.57 |
| 248 / 1 . | PC53 | 2.97 | 0.03 | 59.35 | 18.02 | 0.00 | 7.29 | 1.10 | 0.11 | 0.01 | 0.22 | 0.00 | 1.72 | 0.37 | 0.04 | | | 91.20 |
| 249 / 1 . | PC53 | 3.74 | 0.01 | 63.34 | 18.92 | 0.00 | 8.52 | 0.80 | 0.05 | 0.00 | 0.10 | 0.00 | 1.85 | 0.46 | 0.00 | | | 97.79 |
| 250 / 1 . | PC53 | 3.95 | 0.00 | 64.92 | 19.93 | 0.00 | 8.45 | 0.66 | 0.00 | 0.00 | 0.09 | 0.02 | 1.91 | 0.51 | 0.00 | | | 100.44 |
| 251 / 1 . | PC53 | 3.89 | 0.00 | 62.79 | 19.04 | 0.00 | 8.73 | 0.84 | 0.00 | 0.00 | 0.15 | 0.01 | 1.93 | 0.35 | 0.00 | | | 97.74 |
| 252 / 1 . | PC53 | 4.12 | 0.03 | 62.37 | 18.64 | 0.02 | 8.66 | 0.81 | 0.40 | 0.00 | 0.27 | 0.00 | 1.84 | 0.11 | 0.12 | | | 97.41 |
| 253 / 1 . | PC53 | 4.01 | 0.01 | 64.56 | 19.17 | 0.00 | 8.49 | 0.71 | 0.16 | 0.00 | 0.17 | 0.00 | 1.93 | 0.42 | 0.01 | | | 99.64 |
| 254 / 1 . | PC53 | 4.15 | 0.02 | 63.38 | 18.66 | 0.01 | 8.57 | 0.88 | 0.28 | 0.00 | 0.23 | 0.01 | 1.80 | 0.30 | 0.11 | | | 98.38 |
| 255 / 1 . | PC53 | 3.77 | 0.02 | 64.19 | 19.39 | 0.01 | 8.18 | 0.83 | 0.41 | 0.00 | 0.07 | 0.02 | 1.84 | 0.50 | 0.14 | | | 99.36 |
| 256 / 1 . | PC53 | 3.93 | 0.04 | 63.50 | 18.90 | 0.03 | 8.38 | 0.88 | 0.70 | 0.00 | 0.24 | 0.00 | 1.64 | 0.34 | 0.24 | | | 98.83 |
| 257 / 1 . | PC53 | 3.83 | 0.01 | 63.39 | 18.54 | 0.01 | 8.37 | 0.65 | 0.72 | 0.00 | 0.12 | 0.00 | 1.91 | 0.18 | 0.28 | | | 98.00 |
| 258 / 1 . | PC53 | 4.10 | 0.01 | 63.86 | 18.94 | 0.00 | 8.24 | 0.88 | 0.70 | 0.04 | 0.06 | 0.01 | 1.79 | 0.43 | 0.21 | | | 99.28 |
| 259 / 1 . | PC53 | 3.89 | 0.00 | 62.84 | 19.48 | 0.01 | 8.42 | 0.87 | 0.68 | 0.00 | 0.15 | 0.00 | 1.88 | 0.00 | 0.28 | | | 98.51 |

| | | | | | | | | | | | | | | | | | |
|---|---|---|---|---|---|---|---|---|---|---|---|---|---|---|---|---|---|
| 260 / 1 . | PC53 | 3.81 | 0.00 | 62.12 | 18.62 | 0.00 | 8.14 | 0.87 | 0.54 | 0.08 | 0.17 | 0.00 | 1.77 | 0.11 | 0.22 | | 96.46 |
| 261 / 1 . | PC53 | 3.93 | 0.02 | 60.92 | 18.49 | 0.00 | 8.72 | 0.71 | 0.77 | 0.00 | 0.12 | 0.00 | 1.74 | 0.26 | 0.25 | | 95.91 |
| 262 / 1 . | PC53 | 0.47 | 0.03 | 13.87 | 5.09 | 0.00 | 1.64 | 0.68 | 0.05 | 0.03 | 0.00 | 0.00 | 0.36 | 0.00 | 0.03 | | 22.24 |
| 263 / 1 . | PC53 | 3.63 | 0.00 | 63.43 | 19.12 | 0.01 | 8.68 | 0.98 | 0.39 | 0.00 | 0.11 | 0.00 | 1.97 | 0.15 | 0.15 | | 98.62 |
| 264 / 1 . | PC53 | 3.81 | 0.01 | 64.62 | 18.79 | 0.01 | 8.15 | 0.80 | 0.48 | 0.03 | 0.00 | 0.05 | 1.83 | 0.51 | 0.08 | | 99.18 |
| 265 / 1 . | PC53 | 3.77 | 0.02 | 64.40 | 18.98 | 0.01 | 8.32 | 0.58 | 0.73 | 0.00 | 0.22 | 0.02 | 2.05 | 0.19 | 0.20 | | 99.50 |
| 266 / 1 . | PC53 | 3.82 | 0.01 | 63.31 | 18.84 | 0.00 | 8.78 | 0.82 | 0.32 | 0.00 | 0.12 | 0.00 | 1.88 | 0.09 | 0.09 | | 98.08 |
| 267 / 1 . | PC53 | 3.83 | 0.00 | 64.54 | 19.73 | 0.00 | 8.67 | 0.71 | 0.19 | 0.00 | 0.07 | 0.02 | 1.82 | 0.00 | 0.10 | | 99.67 |
| 122 / 1 . | PC53 | 4.08 | 0.00 | 61.98 | 19.30 | 0.00 | 8.72 | 0.80 | 0.00 | 0.03 | 0.02 | 0.04 | 1.81 | 0.36 | 0.00 | | 97.16 |
| 123 / 1 . | PC53 | 4.46 | 0.02 | 61.95 | 19.04 | 0.00 | 8.40 | 0.83 | 0.00 | 0.00 | 0.11 | 0.00 | 1.70 | 0.18 | 0.01 | | 96.69 |
| 124 / 1 . | PC53 | 4.30 | 0.00 | 62.71 | 18.75 | 0.00 | 8.57 | 0.85 | 0.02 | 0.03 | 0.24 | 0.01 | 1.73 | 0.21 | 0.02 | | 97.42 |
| 125 / 1 . | PC53 | 4.31 | 0.00 | 62.12 | 18.54 | 0.00 | 8.67 | 0.72 | 0.00 | 0.03 | 0.26 | 0.00 | 1.78 | 0.19 | 0.00 | | 96.62 |
| 1 / 1 . | PC53 | 4.60 | 0.00 | 61.88 | 19.49 | 0.00 | 8.42 | 0.88 | 0.21 | 0.00 | 0.08 | 0.00 | 1.92 | 0.42 | 0.08 | | 97.98 |
| 2 / 1 . | PC53 | 3.86 | 0.00 | 63.59 | 19.61 | 0.00 | 8.49 | 0.77 | 0.08 | 0.02 | 0.13 | 0.00 | 1.93 | 0.49 | 0.01 | | 98.99 |
| 3 / 1 . | PC53 | 3.83 | 0.01 | 62.72 | 19.51 | 0.00 | 8.16 | 0.79 | 0.61 | 0.06 | 0.10 | 0.00 | 1.87 | 0.25 | 0.23 | | 98.15 |
| 4 / 1 . | PC53 | 3.85 | 0.01 | 62.21 | 19.22 | 0.00 | 8.21 | 0.84 | 0.77 | 0.02 | 0.12 | 0.00 | 1.88 | 0.35 | 0.26 | | 97.76 |
| 5 / 1 . | PC53 | 4.14 | 0.01 | 60.32 | 18.92 | 0.00 | 8.18 | 0.93 | 1.12 | 0.05 | 0.09 | 0.00 | 1.67 | 0.18 | 0.33 | | 95.94 |
| 6 / 1 . | PC53 | 4.72 | 0.01 | 59.69 | 19.07 | 0.00 | 8.13 | 0.92 | 1.30 | 0.02 | 0.15 | 0.00 | 1.75 | 0.44 | 0.34 | | 96.53 |
| 7 / 1 . | PC53 | 4.28 | 0.01 | 63.11 | 19.36 | 0.00 | 8.55 | 0.76 | 0.08 | 0.00 | 0.13 | 0.01 | 1.89 | 0.37 | 0.01 | | 98.57 |

| **Previous EMPA University of Edinburgh n° of analysis** | **sample** | **$Na_2O$** | **MgO** | **$SiO_2$** | **$Al_2O3$** | **Ar** | **$K_2O$** | **CaO** | **FeO** | **MnO** | **$TiO_2$** | **Kr** | **Xe** | **BaO** | **$Cr_2O_3$** | **NiO** | **$Re_2O_7$** | **Total** |
|---|---|---|---|---|---|---|---|---|---|---|---|---|---|---|---|---|---|---|
| 1 / 1 . | PC53 | 4.73 | 0.01 | 64.37 | 19.38 | 0.00 | 7.94 | 0.78 | 0.29 | 0.03 | 0.10 | | 2.59 | | | | | 100.21 |
| 2 / 1 . | PC53 | 4.66 | 0.01 | 63.61 | 18.99 | 0.00 | 7.85 | 0.77 | 0.28 | 0.02 | 0.10 | | 2.58 | | | | | 98.86 |
| 3 / 1 . | PC53 | 4.64 | 0.01 | 63.81 | 19.31 | 0.00 | 7.95 | 0.78 | 0.16 | 0.01 | 0.10 | | 2.59 | | | | | 99.36 |
| 4 / 1 . | PC53 | 4.71 | 0.01 | 63.71 | 19.02 | 0.00 | 7.79 | 0.80 | 0.52 | 0.00 | 0.09 | | 2.54 | | | | | 99.20 |

*EMPA in wt% oxide of Xe-bearing sanidine Nat. glass standard (PC53) throughout the sessions, no correction is applied for Xe content (in orange wt% oxide total lower than 96% or higher than 102%). Blank means that element has not been analyzed.*

## APPENDIX D/

## Appendix D1/ EMPA of synthesized olivine

| 2017-11-16 | | | | | | | | | | | | | | | | | | |
|---|---|---|---|---|---|---|---|---|---|---|---|---|---|---|---|---|---|---|
| **n° of analysis** | **Sample** | **$Na_2O$** | **MgO** | **$SiO_2$** | **$Al_2O_3$** | **Ar** | **$K_2O$** | **CaO** | **FeO** | **MnO** | **$TiO_2$** | **Kr** | **Xe** | **BaO** | **$Cr_2O_3$** | **NiO** | **$Re_2O_7$** | **Total** |
| **olivine** | | | | | | | | | | | | | | | | | | |
| 5 / 1 . | PC128B | 0.02 | 50.46 | 42.34 | 0.02 | 0.00 | -0.01 | 0.05 | 9.02 | 0.00 | -0.01 | -0.03 | -0.02 | -0.04 | -0.01 | -0.01 | -0.14 | 101.92 |
| 6 / 1 . | PC128B | -0.01 | 49.60 | 40.91 | -0.02 | 0.00 | -0.01 | 0.00 | 9.16 | -0.01 | 0.02 | -0.05 | 0.01 | -0.09 | 0.02 | 0.04 | -0.11 | 99.75 |
| 7 / 1 . | PC128B | -0.04 | 48.91 | 40.99 | -0.02 | -0.01 | 0.01 | 0.02 | 9.31 | 0.00 | 0.00 | -0.07 | 0.01 | 0.10 | -0.01 | 0.04 | -0.12 | 99.39 |
| 8 / 1 . | PC128B | -0.02 | 48.59 | 40.64 | 0.02 | 0.00 | 0.03 | 0.04 | 9.11 | -0.02 | 0.00 | -0.03 | -0.01 | 0.08 | -0.02 | 0.02 | -0.14 | 98.51 |
| 9 / 1 . | PC128B | -0.06 | 47.43 | 38.85 | 0.00 | 0.02 | 0.01 | 0.01 | 10.40 | 0.00 | -0.06 | -0.10 | -0.01 | -0.12 | -0.01 | -0.04 | -0.10 | 96.71 |
| 10 / 1 . | PC128B | -0.06 | 47.02 | 37.88 | 0.02 | -0.01 | -0.01 | 0.03 | 11.11 | -0.02 | -0.01 | -0.13 | -0.02 | 0.12 | 0.01 | 0.09 | -0.12 | 96.28 |
| 11 / 1 . | PC128B | 0.01 | 55.17 | 41.96 | 0.04 | 0.00 | -0.01 | 0.08 | 9.53 | -0.03 | 0.01 | -0.04 | -0.02 | 0.14 | 0.01 | 0.08 | -0.08 | 107.04 |
| 16 / 1 . | PC128B | 0.01 | 51.16 | 42.35 | -0.03 | 0.00 | 0.00 | -0.02 | 7.94 | -0.02 | -0.01 | -0.03 | -0.02 | -0.01 | -0.01 | -0.03 | -0.03 | 101.46 |
| 19 / 1 . | PC128B | 0.01 | 50.56 | 40.37 | 0.01 | 0.01 | -0.01 | 0.07 | 8.40 | 0.00 | 0.03 | -0.03 | 0.00 | -0.05 | 0.00 | -0.06 | 0.00 | 99.46 |
| 20 / 1 . | PC128B | 0.00 | 50.02 | 39.66 | 0.02 | 0.00 | 0.02 | 0.03 | 8.94 | 0.01 | 0.02 | -0.02 | 0.01 | -0.12 | 0.01 | 0.01 | -0.06 | 98.75 |
| 21 / 1 . | PC128B | 0.00 | 49.96 | 41.56 | 0.01 | 0.01 | -0.02 | 0.13 | 8.19 | -0.04 | 0.02 | -0.03 | 0.02 | -0.01 | 0.00 | -0.01 | -0.01 | 99.89 |
| 25 / 1 . | PC128B | -0.06 | 48.25 | 38.97 | 0.03 | -0.01 | -0.01 | 0.00 | 8.77 | -0.06 | -0.06 | -0.09 | 0.05 | -0.07 | 0.03 | -0.01 | -0.10 | 96.10 |
| 27 / 1 . | PC128B | 0.00 | 50.66 | 41.59 | -0.02 | 0.01 | 0.02 | 0.01 | 8.24 | -0.04 | -0.01 | -0.02 | -0.02 | -0.06 | 0.00 | 0.03 | -0.11 | 100.55 |
| 28 / 1 . | PC128B | 0.01 | 50.47 | 41.53 | -0.02 | 0.01 | 0.04 | 0.04 | 8.30 | 0.02 | 0.04 | -0.03 | 0.00 | 0.00 | 0.01 | 0.06 | -0.15 | 100.53 |
| 29 / 1 . | PC128B | 0.00 | 51.59 | 41.10 | 0.01 | 0.00 | 0.01 | 0.02 | 8.04 | 0.00 | 0.00 | -0.02 | 0.03 | -0.01 | 0.01 | -0.02 | -0.07 | 100.82 |
| 30 / 1 . | PC128B | 0.01 | 51.65 | 40.87 | 0.02 | -0.01 | 0.00 | 0.04 | 7.14 | -0.02 | -0.05 | -0.03 | 0.00 | -0.01 | -0.01 | 0.02 | -0.17 | 99.75 |
| 31 / 1 . | PC128B | -0.01 | 51.14 | 42.23 | -0.02 | 0.00 | 0.00 | 0.03 | 7.70 | 0.00 | 0.02 | -0.04 | 0.01 | -0.06 | -0.01 | 0.02 | -0.07 | 101.18 |
| 32 / 1 . | PC128B | 0.01 | 51.15 | 41.90 | 0.05 | 0.00 | -0.02 | 0.03 | 7.92 | -0.02 | 0.02 | -0.03 | -0.01 | 0.02 | 0.02 | 0.04 | -0.10 | 101.15 |
| 33 / 1 . | PC128B | 0.01 | 50.58 | 41.03 | 0.02 | 0.00 | -0.01 | 0.06 | 8.04 | 0.03 | 0.03 | -0.03 | -0.02 | 0.03 | -0.02 | -0.02 | -0.09 | 99.83 |
| 34 / 1 . | PC128B | 0.00 | 51.56 | 40.72 | -0.03 | 0.01 | 0.01 | 0.02 | 8.03 | 0.01 | 0.03 | -0.02 | 0.00 | -0.06 | 0.00 | -0.01 | -0.13 | 100.39 |
| 35 / 1 . | PC128B | -0.01 | 51.74 | 40.95 | 0.02 | 0.01 | -0.02 | -0.01 | 7.10 | -0.03 | 0.00 | -0.05 | 0.00 | 0.05 | 0.01 | -0.01 | -0.11 | 99.89 |
| 36 / 1 . | PC128B | 0.02 | 51.55 | 40.69 | 0.00 | 0.00 | -0.01 | 0.02 | 7.31 | -0.06 | 0.04 | -0.03 | -0.02 | -0.05 | -0.01 | 0.06 | -0.07 | 99.68 |
| 38 / 1 . | PC128B | 0.00 | 51.04 | 40.04 | 0.02 | 0.00 | 0.00 | 0.00 | 7.84 | 0.02 | 0.00 | -0.03 | 0.02 | 0.00 | 0.00 | 0.00 | -0.08 | 98.99 |

| | | | | | | | | | | | | | | | | | | |
|---|---|---|---|---|---|---|---|---|---|---|---|---|---|---|---|---|---|---|
| 40 / 1 . | PC128B | 0.00 | 50.08 | 39.47 | 0.02 | 0.00 | -0.01 | 0.04 | 8.14 | -0.04 | 0.05 | -0.04 | 0.02 | 0.13 | -0.02 | -0.06 | -0.06 | 97.96 |
| 43 / 1 . | PC128B | -0.12 | 46.44 | 35.87 | 0.01 | -0.01 | 0.00 | 0.00 | 8.66 | 0.03 | -0.05 | -0.17 | 0.01 | 0.05 | 0.03 | -0.02 | -0.01 | 91.10 |
| 44 / 1 . | PC128B | -0.01 | 50.25 | 40.71 | 0.01 | 0.01 | 0.01 | 0.03 | 8.30 | -0.01 | -0.02 | -0.05 | 0.02 | 0.05 | -0.03 | -0.03 | -0.07 | 99.39 |
| 45 / 1 . | PC128B | -0.04 | 48.89 | 38.30 | 0.05 | 0.00 | -0.02 | 0.05 | 6.35 | 0.04 | -0.04 | -0.10 | -0.04 | -0.17 | 0.01 | -0.03 | -0.10 | 93.69 |
| 46 / 1 . | PC128B | -0.01 | 52.21 | 41.12 | 0.01 | 0.01 | -0.01 | 0.01 | 5.99 | -0.01 | -0.03 | -0.04 | -0.01 | -0.04 | 0.00 | -0.05 | -0.11 | 99.35 |
| 47 / 1 . | PC128B | -0.02 | 51.27 | 39.71 | 0.01 | 0.02 | 0.02 | 0.02 | 6.54 | 0.04 | -0.02 | -0.05 | -0.02 | 0.08 | 0.03 | 0.03 | -0.11 | 97.75 |

**olivine**

| | | | | | | | | | | | | | | | | | | |
|---|---|---|---|---|---|---|---|---|---|---|---|---|---|---|---|---|---|---|
| 12 / 1 . | PC128B- high Xe | 0.01 | 16.61 | 10.25 | 0.04 | 0.13 | -0.02 | 0.01 | 5.40 | 0.02 | 0.02 | 0.00 | 0.26 | -0.23 | 0.00 | -0.01 | -0.46 | 32.76 |
| 13 / 1 . | PC128B- high Xe | 0.00 | 16.70 | 10.70 | -0.04 | 0.10 | 0.01 | -0.02 | 4.85 | 0.02 | 0.06 | -0.02 | 0.28 | 0.08 | 0.02 | 0.02 | -0.44 | 32.84 |
| 14 / 1 . | PC128B- high Xe | 0.01 | 50.79 | 41.64 | -0.02 | 0.06 | 0.00 | 0.03 | 8.17 | 0.02 | -0.01 | -0.04 | 0.19 | -0.02 | -0.02 | 0.00 | -0.09 | 100.92 |
| 17 / 1 . | PC128B- high Xe | 0.01 | 47.35 | 37.79 | 0.02 | 0.12 | 0.01 | 0.02 | 8.63 | 0.02 | 0.01 | -0.02 | 0.23 | -0.14 | -0.01 | 0.05 | -0.13 | 94.26 |
| 18 / 1 . | PC128B- high Xe | 0.00 | 49.06 | 39.23 | 0.03 | 0.40 | 0.00 | 0.02 | 8.82 | 0.07 | 0.02 | -0.01 | 1.33 | -0.09 | 0.02 | 0.02 | -0.01 | 99.06 |
| 22 / 1 . | PC128B- high Xe | 0.01 | 47.18 | 38.72 | 0.04 | 0.80 | 0.02 | 0.01 | 7.05 | 0.00 | 0.02 | -0.03 | 0.59 | 0.13 | -0.03 | -0.02 | -0.16 | 94.58 |
| 23 / 1 . | PC128B- high Xe | 0.02 | 50.15 | 40.43 | -0.01 | 0.32 | -0.01 | -0.02 | 7.49 | 0.02 | 0.01 | -0.01 | 0.96 | 0.08 | -0.01 | -0.02 | -0.11 | 99.50 |
| 24 / 1 . | PC128B- high Xe | 0.00 | 50.16 | 40.46 | -0.01 | 0.35 | 0.01 | 0.00 | 8.10 | -0.02 | 0.03 | -0.01 | 1.17 | -0.16 | -0.01 | 0.04 | -0.11 | 100.34 |
| 26 / 1 . | PC128B- high Xe | 0.02 | 49.63 | 39.56 | 0.02 | 0.17 | 0.00 | 0.05 | 8.57 | -0.01 | 0.04 | -0.03 | 0.40 | 0.00 | -0.01 | 0.04 | -0.11 | 98.49 |
| 37 / 1 . | PC128B- high Xe | -0.02 | 49.08 | 37.70 | 0.03 | 0.62 | 0.00 | -0.02 | 8.04 | -0.01 | 0.09 | -0.02 | 1.88 | -0.09 | -0.02 | 0.00 | -0.05 | 97.50 |
| 39 / 1 . | PC128B- high Xe | 0.03 | 49.72 | 38.90 | 0.02 | 0.18 | 0.00 | 0.04 | 7.75 | -0.01 | 0.03 | -0.01 | 0.63 | 0.06 | -0.02 | -0.01 | -0.11 | 97.36 |
| 41 / 1 . | PC128B- high Xe | 0.00 | 47.67 | 37.01 | 0.04 | 1.26 | 0.02 | 0.01 | 6.99 | -0.01 | 0.24 | 0.00 | 4.05 | -0.38 | -0.03 | 0.00 | -0.01 | 97.40 |
| 42 / 1 . | PC128B- high Xe | 0.01 | 48.83 | 38.12 | 0.02 | 0.62 | 0.00 | 0.02 | 7.89 | 0.00 | 0.13 | -0.01 | 1.69 | -0.08 | -0.03 | 0.00 | -0.02 | 97.37 |

**olivine**

| | | | | | | | | | | | | | | | | | | |
|---|---|---|---|---|---|---|---|---|---|---|---|---|---|---|---|---|---|---|
| 133 / 1 . | PC99A | 0.00 | 57.02 | 44.45 | 0.01 | 0.00 | 0.02 | -0.01 | 0.09 | 0.02 | 0.00 | -0.02 | 0.01 | -0.12 | 0.01 | -0.01 | -0.22 | 101.63 |
| 244 / 1 . | PC99A | 0.01 | 56.80 | 44.15 | 0.02 | 0.01 | 0.00 | -0.01 | 0.08 | 0.03 | 0.07 | -0.02 | 0.00 | -0.03 | 0.00 | -0.05 | -0.13 | 101.17 |
| 245 / 1 . | PC99A | 0.00 | 56.98 | 44.32 | -0.03 | 0.00 | 0.00 | -0.01 | 0.12 | 0.01 | 0.01 | -0.01 | 0.00 | -0.07 | -0.01 | -0.05 | -0.17 | 101.45 |
| 246 / 1 . | PC99A | 0.00 | 57.25 | 44.50 | 0.03 | 0.01 | 0.00 | 0.03 | 0.02 | -0.05 | -0.03 | -0.02 | 0.04 | 0.02 | 0.00 | 0.04 | -0.16 | 101.95 |
| 247 / 1 . | PC99A | 0.00 | 57.28 | 44.85 | 0.01 | 0.00 | 0.03 | 0.02 | 0.08 | 0.01 | 0.01 | -0.01 | -0.02 | 0.02 | -0.01 | -0.05 | -0.15 | 102.31 |
| 248 / 1 . | PC99A | 0.01 | 57.08 | 43.82 | -0.05 | 0.00 | 0.01 | 0.00 | 0.06 | -0.02 | 0.03 | -0.01 | 0.00 | -0.09 | -0.01 | 0.00 | -0.19 | 101.00 |
| 249 / 1 . | PC99A | 0.00 | 57.21 | 44.03 | 0.02 | 0.00 | -0.01 | 0.01 | 0.07 | 0.00 | 0.00 | -0.03 | 0.02 | 0.02 | -0.01 | 0.01 | -0.20 | 101.40 |

| | | | | | | | | | | | | | | | | | | |
|---|---|---|---|---|---|---|---|---|---|---|---|---|---|---|---|---|---|---|
| 250 / 1 . | PC99A | 0.02 | 57.27 | 42.28 | -0.01 | 0.00 | 0.02 | 0.00 | 0.04 | -0.01 | -0.02 | -0.01 | 0.04 | 0.01 | -0.01 | -0.01 | -0.07 | 99.67 |
| 251 / 1 . | PC99A | 0.00 | 56.89 | 42.53 | 0.00 | 0.00 | 0.01 | 0.02 | 0.04 | 0.01 | 0.00 | -0.01 | 0.00 | 0.06 | 0.01 | 0.04 | -0.09 | 99.60 |
| 252 / 1 . | PC99A | 0.01 | 56.46 | 42.66 | -0.03 | -0.01 | 0.03 | 0.00 | 0.03 | -0.04 | -0.04 | -0.03 | 0.00 | 0.02 | 0.00 | 0.01 | -0.09 | 99.22 |
| 253 / 1 . | PC99A | 0.00 | 56.74 | 43.21 | -0.01 | 0.01 | 0.00 | 0.01 | 0.05 | 0.02 | 0.02 | 0.00 | -0.02 | -0.09 | -0.02 | -0.02 | -0.03 | 100.06 |
| 254 / 1 . | PC99A | 0.01 | 56.90 | 42.90 | 0.01 | 0.00 | 0.00 | 0.01 | 0.06 | -0.01 | -0.01 | -0.01 | 0.00 | -0.05 | 0.02 | -0.06 | -0.07 | 99.90 |
| 255 / 1 . | PC99A | 0.00 | 57.42 | 42.71 | -0.01 | 0.00 | 0.00 | 0.00 | 0.04 | 0.04 | 0.02 | -0.01 | 0.00 | 0.04 | -0.01 | 0.04 | -0.05 | 100.32 |
| 256 / 1 . | PC99A | 0.00 | 57.09 | 42.77 | -0.01 | 0.01 | 0.01 | 0.00 | 0.06 | 0.00 | -0.01 | -0.02 | 0.01 | -0.03 | 0.00 | 0.05 | -0.03 | 100.00 |
| 257 / 1 . | PC99A | -0.01 | 57.49 | 42.79 | 0.01 | -0.01 | 0.01 | 0.00 | 0.10 | 0.05 | 0.02 | 0.00 | 0.00 | -0.03 | 0.00 | -0.02 | -0.07 | 100.47 |
| 258 / 1 . | PC99A | -0.01 | 57.76 | 42.48 | -0.01 | 0.01 | 0.00 | 0.00 | 0.04 | 0.03 | -0.05 | -0.02 | 0.00 | -0.08 | 0.00 | 0.00 | -0.06 | 100.32 |
| 259 / 1 . | PC99A | 0.01 | 57.11 | 43.11 | 0.02 | 0.01 | -0.01 | 0.02 | 0.07 | 0.05 | 0.02 | 0.00 | 0.01 | 0.08 | -0.01 | 0.01 | -0.10 | 100.50 |
| 260 / 1 . | PC99A | 0.00 | 57.19 | 42.91 | 0.01 | 0.00 | 0.02 | 0.00 | 0.02 | 0.02 | 0.05 | 0.00 | -0.03 | -0.02 | -0.01 | -0.02 | -0.15 | 100.23 |
| 261 / 1 . | PC99A | 0.00 | 56.11 | 43.15 | 0.04 | 0.00 | 0.01 | -0.01 | -0.01 | -0.03 | -0.02 | -0.01 | 0.00 | -0.15 | 0.00 | 0.03 | -0.09 | 99.36 |
| 262 / 1 . | PC99A | -0.01 | 56.82 | 43.12 | 0.03 | 0.00 | -0.02 | -0.01 | 0.00 | -0.01 | -0.01 | -0.02 | -0.02 | -0.07 | 0.00 | -0.02 | -0.11 | 99.97 |
| 263 / 1 . | PC99A | 0.00 | 56.91 | 43.44 | 0.03 | 0.00 | 0.00 | 0.01 | 0.01 | -0.04 | 0.02 | -0.01 | 0.01 | -0.02 | -0.02 | 0.00 | -0.14 | 100.44 |
| | | | | | | | | | | | | | | | | | | |
| **olivine** | | | | | | | | | | | | | | | | | | |
| 137 / 1 . | PC126 | 0.00 | 54.03 | 41.95 | 0.02 | 0.00 | 0.00 | 0.04 | 2.12 | -0.03 | 0.00 | -0.01 | 0.01 | -0.08 | 0.00 | 0.02 | -0.16 | 98.20 |
| 138 / 1 . | PC126 | 0.01 | 54.47 | 42.27 | 0.02 | 0.00 | -0.01 | -0.02 | 1.96 | 0.02 | -0.04 | -0.02 | 0.00 | -0.06 | 0.03 | 0.00 | -0.09 | 98.79 |
| 139 / 1 . | PC126 | 0.01 | 54.20 | 41.58 | -0.01 | 0.00 | 0.04 | 0.04 | 2.20 | 0.02 | 0.03 | -0.01 | 0.04 | 0.02 | 0.01 | 0.02 | -0.17 | 98.19 |
| 140 / 1 . | PC126 | 0.01 | 53.54 | 41.05 | 0.02 | 0.00 | 0.02 | 0.00 | 2.78 | -0.04 | 0.02 | -0.02 | 0.01 | 0.09 | 0.01 | 0.01 | -0.14 | 97.58 |
| 141 / 1 . | PC126 | 0.02 | 53.17 | 40.93 | 0.01 | 0.00 | -0.01 | 0.01 | 3.14 | -0.04 | 0.02 | -0.02 | 0.03 | -0.03 | 0.00 | 0.03 | -0.19 | 97.36 |
| 142 / 1 . | PC126 | 0.01 | 53.50 | 40.65 | 0.01 | 0.00 | -0.02 | 0.00 | 1.89 | -0.02 | -0.03 | -0.01 | -0.02 | -0.05 | 0.01 | 0.00 | -0.18 | 96.08 |
| 143 / 1 . | PC126 | 0.00 | 52.17 | 41.05 | -0.01 | 0.00 | -0.01 | 0.02 | 4.28 | 0.03 | -0.01 | -0.01 | -0.02 | -0.01 | -0.01 | 0.03 | -0.16 | 97.58 |
| 144 / 1 . | PC126 | 0.01 | 53.78 | 41.19 | 0.01 | -0.01 | 0.02 | 0.03 | 2.15 | -0.04 | 0.00 | -0.04 | -0.02 | -0.05 | 0.00 | -0.03 | -0.21 | 97.20 |
| 145 / 1 . | PC126 | 0.01 | 53.17 | 41.00 | -0.02 | 0.00 | -0.01 | 0.00 | 3.04 | -0.01 | -0.01 | -0.03 | -0.01 | 0.07 | 0.02 | -0.02 | -0.21 | 97.32 |
| 146 / 1 . | PC126 | 0.01 | 52.82 | 41.05 | -0.01 | -0.01 | 0.00 | -0.02 | 3.27 | 0.01 | 0.00 | -0.03 | 0.01 | -0.01 | 0.00 | 0.03 | -0.15 | 97.21 |
| 147 / 1 . | PC126 | 0.00 | 52.96 | 40.95 | 0.03 | 0.00 | 0.00 | 0.04 | 2.75 | 0.00 | -0.01 | -0.03 | 0.01 | 0.03 | -0.01 | 0.04 | -0.16 | 96.82 |
| 148 / 1 . | PC126 | 0.00 | 53.84 | 41.84 | -0.03 | -0.01 | 0.00 | 0.01 | 1.99 | 0.04 | 0.04 | -0.01 | 0.00 | -0.16 | 0.02 | 0.01 | -0.17 | 97.78 |
| 149 / 1 . | PC126 | 0.01 | 53.20 | 41.71 | 0.02 | 0.00 | 0.01 | 0.00 | 1.78 | 0.00 | -0.01 | -0.02 | 0.01 | -0.06 | 0.01 | -0.03 | -0.16 | 96.75 |
| 150 / 1 . | PC126 | -0.01 | 52.39 | 40.81 | 0.02 | 0.01 | -0.01 | 0.01 | 2.89 | -0.01 | 0.00 | -0.01 | 0.00 | 0.13 | 0.00 | 0.00 | -0.19 | 96.27 |

| | | | | | | | | | | | | | | | | | |
|---|---|---|---|---|---|---|---|---|---|---|---|---|---|---|---|---|---|
| 151 / 1 . | PC126 | 0.02 | 53.57 | 41.07 | 0.00 | 0.01 | -0.01 | 0.03 | 1.86 | 0.01 | 0.03 | 0.00 | 0.00 | -0.08 | 0.01 | -0.08 | -0.17 | 96.60 |
| 152 / 1 . | PC126 | 0.00 | 53.24 | 40.56 | 0.01 | -0.01 | 0.01 | 0.00 | 2.82 | 0.02 | -0.01 | -0.01 | 0.01 | 0.18 | 0.03 | -0.07 | -0.14 | 96.88 |
| 153 / 1 . | PC126 | 0.01 | 54.39 | 40.94 | 0.03 | 0.00 | -0.01 | 0.02 | 1.30 | -0.01 | 0.02 | -0.02 | -0.02 | 0.09 | 0.03 | 0.04 | -0.12 | 96.87 |
| 154 / 1 . | PC126 | 0.02 | 54.18 | 40.28 | 0.00 | 0.01 | 0.03 | 0.00 | 1.92 | 0.02 | 0.06 | -0.01 | 0.00 | -0.04 | 0.01 | -0.01 | -0.14 | 96.53 |
| 155 / 1 . | PC126 | 0.00 | 54.76 | 40.51 | -0.03 | 0.01 | 0.00 | 0.02 | 1.61 | -0.02 | -0.02 | -0.03 | 0.01 | -0.08 | 0.00 | 0.03 | -0.15 | 96.95 |
| 156 / 1 . | PC126 | 0.02 | 53.70 | 40.45 | -0.02 | 0.00 | 0.01 | 0.01 | 2.51 | 0.01 | 0.02 | 0.00 | 0.02 | -0.09 | -0.01 | 0.00 | -0.15 | 96.75 |
| 157 / 1 . | PC126 | 0.02 | 52.94 | 40.27 | 0.04 | 0.00 | -0.02 | 0.02 | 3.15 | -0.01 | 0.05 | 0.00 | -0.02 | 0.01 | -0.01 | -0.01 | -0.12 | 96.50 |

| **2018-03-15** | | | | | | | | | | | | | | | | | |
|---|---|---|---|---|---|---|---|---|---|---|---|---|---|---|---|---|---|
| **n° of analysis** | **sample** | **$Na_2O$** | **MgO** | **$SiO_2$** | **$Al_2O_3$** | **Ar** | **$K_2O$** | **CaO** | **FeO** | **MnO** | **$TiO_2$** | **Kr** | **Xe** | **BaO** | **$Cr_2O_3$** | **NiO** | **$Re_2O_7$** | **Total** |
| **olivine** | | | | | | | | | | | | | | | | | |
| 137 / 1 . | PC133-1 | 0.01 | 36.06 | 38.24 | 0.02 | 0.00 | 0.02 | 0.00 | 24.02 | 0.04 | 0.00 | 0.00 | 0.09 | 0.11 | 0.02 | | | 98.63 |
| 138 / 1 . | PC133-1 | 0.01 | 35.92 | 37.69 | 0.00 | 0.00 | 0.05 | 0.04 | 24.71 | 0.04 | 0.02 | 0.00 | 0.00 | 0.00 | 0.01 | | | 98.50 |
| 139 / 1 . | PC133-1 | 0.00 | 41.04 | 39.58 | 0.01 | 0.00 | 0.00 | 0.00 | 17.94 | 0.10 | 0.01 | 0.00 | 0.03 | 0.00 | 0.00 | | | 98.71 |
| 140 / 1 . | PC133-1 | 0.01 | 37.00 | 39.08 | 0.00 | 0.02 | 0.02 | 0.06 | 21.77 | 0.04 | 0.05 | 0.00 | 0.00 | 0.00 | 0.01 | | | 98.05 |
| 141 / 1 . | PC133-1 | 0.02 | 39.25 | 39.66 | 0.05 | 0.05 | 0.00 | 0.09 | 19.52 | 0.01 | 0.00 | 0.00 | 0.00 | 0.00 | 0.03 | | | 98.67 |
| 142 / 1 . | PC133-1 | 0.03 | 36.73 | 37.88 | 0.02 | 0.04 | 0.01 | 0.06 | 23.32 | 0.04 | 0.00 | 0.00 | 0.00 | 0.00 | 0.04 | | | 98.16 |
| 143 / 1 . | PC133-1 | 0.02 | 36.72 | 38.51 | 0.00 | 0.00 | 0.00 | 0.06 | 23.41 | 0.06 | 0.03 | 0.00 | 0.05 | 0.08 | 0.02 | | | 98.95 |
| 144 / 1 . | PC133-1 | 0.01 | 36.84 | 38.35 | 0.00 | 0.01 | 0.00 | 0.00 | 24.18 | 0.02 | 0.00 | 0.00 | 0.05 | 0.13 | 0.01 | | | 99.60 |
| 145 / 1 . | PC133-1 | 0.00 | 36.80 | 37.22 | 0.00 | 0.01 | 0.03 | 0.01 | 22.87 | 0.10 | 0.00 | 0.00 | 0.00 | 0.00 | 0.03 | | | 97.07 |
| 146 / 1 . | PC133-1 | 0.00 | 36.06 | 38.64 | 0.02 | 0.04 | 0.00 | 0.04 | 23.47 | 0.10 | 0.00 | 0.00 | 0.00 | 0.06 | 0.02 | | | 98.46 |
| 147 / 1 . | PC133-1 | 0.00 | 37.10 | 38.15 | 0.00 | 0.01 | 0.00 | 0.00 | 23.41 | 0.13 | 0.00 | 0.00 | 0.00 | 0.14 | 0.00 | | | 98.94 |
| 148 / 1 . | PC133-1 | 0.00 | 36.46 | 38.74 | 0.00 | 0.01 | 0.03 | 0.05 | 23.67 | 0.07 | 0.00 | 0.00 | 0.00 | 0.00 | 0.00 | | | 99.03 |
| 149 / 1 . | PC133-1 | 0.02 | 36.47 | 38.73 | 0.00 | 0.00 | 0.00 | 0.02 | 22.88 | 0.22 | 0.01 | 0.00 | 0.00 | 0.00 | 0.00 | | | 98.35 |
| 150 / 1 . | PC133-1 | 0.00 | 33.63 | 39.30 | 0.02 | 0.00 | 0.02 | 0.02 | 22.97 | 0.04 | 0.01 | 0.00 | 0.02 | 0.00 | 0.00 | | | 96.02 |
| 151 / 1 . | PC133-1 | 0.00 | 36.46 | 36.76 | 0.00 | 0.01 | 0.02 | 0.00 | 23.64 | 0.10 | 0.01 | 0.00 | 0.05 | 0.08 | 0.01 | | | 97.15 |
| 152 / 1 . | PC133-1 | 0.00 | 35.95 | 37.30 | 0.00 | 0.01 | 0.00 | 0.00 | 23.50 | 0.18 | 0.03 | 0.00 | 0.09 | 0.19 | 0.01 | | | 97.26 |
| 153 / 1 . | PC133-1 | 0.02 | 35.89 | 37.60 | 0.04 | 0.03 | 0.05 | 0.00 | 24.54 | 0.03 | 0.02 | 0.00 | 0.00 | 0.09 | 0.06 | | | 98.36 |
| 154 / 1 . | PC133-1 | 0.00 | 35.95 | 38.14 | 0.05 | 0.00 | 0.01 | 0.00 | 24.57 | 0.00 | 0.07 | 0.00 | 0.00 | 0.00 | 0.00 | | | 98.79 |
| 155 / 1 . | PC133-1 | 0.00 | 35.82 | 37.78 | 0.02 | 0.00 | 0.01 | 0.00 | 24.56 | 0.10 | 0.00 | 0.00 | 0.00 | 0.09 | 0.03 | | | 98.43 |

| | | | | | | | | | | | | | | | | |
|---|---|---|---|---|---|---|---|---|---|---|---|---|---|---|---|---|
| 157 / 1 . | PC133-1 | 0.01 | 35.61 | 36.93 | 0.00 | 0.00 | 0.02 | 0.02 | 20.65 | 0.10 | 0.02 | 0.00 | 0.00 | 0.34 | 0.00 | 93.72 |
| 159 / 1 . | PC133-1 | 0.04 | 36.00 | 37.43 | 0.02 | 0.02 | 0.04 | 0.00 | 24.27 | 0.10 | 0.00 | 0.00 | 0.08 | 0.20 | 0.00 | 98.21 |
| 160 / 1 . | PC133-1 | 0.01 | 35.31 | 37.17 | 0.00 | 0.01 | 0.06 | 0.06 | 24.88 | 0.05 | 0.00 | 0.00 | 0.04 | 0.19 | 0.02 | 97.81 |
| 161 / 1 . | PC133-1 | 0.01 | 35.40 | 37.22 | 0.00 | 0.05 | 0.05 | 0.07 | 24.39 | 0.11 | 0.07 | 0.00 | 0.00 | 0.00 | 0.01 | 97.38 |
| 162 / 1 . | PC133-1 | 0.01 | 34.10 | 36.71 | 0.00 | 0.02 | 0.02 | 0.05 | 25.08 | 0.03 | 0.00 | 0.00 | 0.05 | 0.03 | 0.02 | 96.11 |
| 163 / 1 . | PC133-1 | 0.01 | 26.49 | 21.64 | 0.02 | 0.00 | 0.04 | 0.01 | 13.22 | 0.08 | 0.00 | 0.00 | 0.02 | 0.00 | 0.02 | 61.56 |
| 164 / 1 . | PC133-1 | 0.00 | 0.00 | 0.00 | 0.02 | 0.00 | 0.00 | 0.04 | 0.15 | 0.03 | 0.00 | 0.00 | 0.02 | 0.00 | 0.01 | 0.26 |
| 165 / 1 . | PC133-1 | 0.04 | 33.67 | 37.21 | 0.00 | 0.00 | 0.00 | 0.00 | 24.72 | 0.04 | 0.00 | 0.00 | 0.05 | 0.00 | 0.01 | 95.74 |
| 166 / 1 . | PC135-1 | 0.02 | 35.59 | 58.00 | 0.09 | 0.00 | 0.00 | 0.00 | 6.56 | 0.23 | 0.06 | 0.00 | 0.00 | 0.24 | 0.00 | 100.79 |
| 167 / 1 . | PC135-1 | 0.01 | 34.71 | 58.93 | 0.00 | 0.00 | 0.04 | 0.07 | 6.52 | 0.19 | 0.00 | 0.00 | 0.01 | 0.00 | 0.00 | 100.47 |
| 168 / 1 . | PC135-1 | 0.00 | 34.72 | 59.56 | 0.01 | 0.00 | 0.05 | 0.00 | 5.78 | 0.08 | 0.00 | 0.03 | 0.00 | 0.00 | 0.03 | 100.25 |
| 170 / 1 . | PC135-1 | 0.03 | 35.33 | 59.07 | 0.02 | 0.02 | 0.03 | 0.01 | 4.58 | 0.23 | 0.05 | 0.01 | 0.03 | 0.00 | 0.01 | 99.41 |
| 171 / 1 . | PC135-1 | 0.03 | 35.06 | 59.30 | 0.00 | 0.02 | 0.01 | 0.05 | 5.04 | 0.06 | 0.10 | 0.00 | 0.00 | 0.00 | 0.04 | 99.70 |
| 172 / 1 . | PC135-1 | 0.02 | 35.26 | 57.32 | 0.03 | 0.00 | 0.04 | 0.05 | 5.21 | 0.20 | 0.00 | 0.01 | 0.00 | 0.08 | 0.02 | 98.24 |
| 173 / 1 . | PC135-1 | 0.04 | 34.82 | 57.66 | 0.04 | 0.00 | 0.00 | 0.04 | 5.48 | 0.23 | 0.05 | 0.00 | 0.02 | 0.00 | 0.03 | 98.41 |
| 174 / 1 . | PC135-1 | 0.00 | 35.73 | 57.20 | 0.01 | 0.00 | 0.01 | 0.04 | 4.96 | 0.34 | 0.01 | 0.00 | 0.07 | 0.05 | 0.03 | 98.45 |
| 175 / 1 . | PC135-1 | 0.00 | 36.92 | 58.41 | 0.00 | 0.00 | 0.02 | 0.14 | 4.05 | 0.24 | 0.00 | 0.00 | 0.00 | 0.00 | 0.03 | 99.79 |
| 176 / 1 . | PC135-1 | 0.01 | 35.96 | 57.58 | 0.03 | 0.00 | 0.00 | 0.03 | 5.08 | 0.13 | 0.00 | 0.00 | 0.00 | 0.13 | 0.04 | 98.99 |
| 177 / 1 . | PC135-1 | 0.00 | 35.05 | 59.04 | 0.00 | 0.00 | 0.00 | 0.02 | 6.71 | 0.22 | 0.06 | 0.00 | 0.00 | 0.08 | 0.02 | 101.21 |
| 178 / 1 . | PC135-1 | 0.00 | 35.35 | 58.63 | 0.00 | 0.01 | 0.01 | 0.00 | 5.68 | 0.25 | 0.00 | 0.00 | 0.00 | 0.07 | 0.02 | 100.01 |
| 179 / 1 . | PC135-1 | 0.01 | 35.51 | 59.52 | 0.00 | 0.00 | 0.02 | 0.06 | 5.19 | 0.31 | 0.00 | 0.00 | 0.00 | 0.00 | 0.00 | 100.61 |
| 180 / 1 . | PC135-1 | 0.00 | 35.14 | 59.74 | 0.04 | 0.00 | 0.04 | 0.06 | 4.85 | 0.25 | 0.07 | 0.00 | 0.03 | 0.00 | 0.00 | 100.22 |
| 182 / 1 . | PC135-1 | 0.01 | 35.31 | 59.60 | 0.01 | 0.01 | 0.00 | 0.06 | 4.76 | 0.29 | 0.00 | 0.00 | 0.04 | 0.00 | 0.06 | 100.15 |
| 183 / 1 . | PC135-1 | 0.02 | 33.98 | 54.10 | 0.02 | 0.00 | 0.00 | 0.07 | 4.67 | 0.25 | 0.01 | 0.00 | 0.03 | 0.04 | 0.00 | 93.21 |
| 184 / 1 . | PC135-1 | 0.00 | 34.38 | 55.20 | 0.08 | 0.00 | 0.00 | 0.01 | 6.97 | 0.21 | 0.08 | 0.00 | 0.00 | 0.00 | 0.02 | 96.96 |
| 186 / 1 . | PC135-1 | 0.00 | 35.44 | 59.48 | 0.00 | 0.03 | 0.00 | 0.01 | 4.71 | 0.28 | 0.00 | 0.00 | 0.00 | 0.16 | 0.04 | 100.16 |
| 134 / 1 . | PC135-1 | 0.00 | 35.60 | 59.44 | 0.00 | 0.00 | 0.00 | 0.01 | 5.10 | 0.24 | 0.04 | 0.00 | 0.00 | 0.00 | 0.02 | 100.46 |
| 135 / 1 . | PC135-1 | 0.01 | 35.47 | 58.76 | 0.10 | 0.00 | 0.01 | 0.00 | 4.56 | 0.20 | 0.00 | 0.00 | 0.00 | 0.04 | 0.05 | 99.20 |

| | | | | | | | | | | | | | | | | | |
|---|---|---|---|---|---|---|---|---|---|---|---|---|---|---|---|---|---|
| 136 / 1 . | PC135-1 | 0.02 | 34.22 | 58.71 | 0.07 | 0.03 | 0.03 | 0.03 | 7.26 | 0.25 | 0.00 | 0.00 | 0.00 | 0.01 | 0.04 | | 100.66 |

| **2017-05-29** | | | | | | | | | | | | | | | | | |
|---|---|---|---|---|---|---|---|---|---|---|---|---|---|---|---|---|---|
| **n° of analysis** | **Sample** | **$Na_2O$** | **MgO** | **$SiO_2$** | **$Al_2O_3$** | **Ar** | **$K_2O$** | **CaO** | **FeO** | **MnO** | **$TiO_2$** | **Kr** | **Xe** | **BaO** | **$Cr_2O_3$** | **NiO** | **$Re_2O_7$** | **Total** |
| **olivine** | | | | | | | | | | | | | | | | | |
| 42 / 1 . | PC99B1 bubble | 0.01 | 54.57 | 41.89 | 0.05 | 0.01 | 0.01 | 0.01 | 3.60 | -0.01 | 0.01 | 0.07 | 0.33 | -0.13 | | | | 100.63 |
| 113 / 1 . | PC99B1 bubble | 0.01 | 53.08 | 37.79 | 0.04 | 0.22 | 0.01 | -0.03 | 0.14 | 0.02 | 0.26 | 2.09 | 6.79 | -0.27 | | | | 102.16 |
| 43 / 1 . | PC99B1 | 0.01 | 54.61 | 41.93 | 0.01 | 0.00 | 0.01 | 0.03 | 3.76 | 0.00 | 0.01 | -0.02 | 0.00 | 0.04 | | | | 100.42 |
| 44 / 1 . | PC99B1 | 0.01 | 54.79 | 41.98 | 0.02 | 0.01 | 0.02 | 0.03 | 3.46 | 0.00 | -0.01 | -0.01 | 0.01 | 0.11 | | | | 100.44 |
| 45 / 1 . | PC99B1 | 0.01 | 57.51 | 43.50 | 0.07 | 0.00 | 0.02 | 0.02 | 0.16 | 0.00 | 0.03 | -0.01 | 0.01 | -0.09 | | | | 101.33 |
| 112 / 1 . | PC99B1 | 0.01 | 54.02 | 39.16 | 0.07 | 0.13 | 0.00 | 0.05 | 0.16 | 0.01 | 0.01 | 0.01 | 0.13 | -0.08 | | | | 93.79 |
| 119 / 1 . | PC99B1 | 0.01 | 54.97 | 43.69 | 0.03 | 0.00 | 0.00 | 0.01 | 2.05 | -0.02 | -0.03 | -0.02 | -0.01 | -0.02 | | | | 100.77 |
| 120 / 1 . | PC99B1 | 0.01 | 56.24 | 42.79 | 0.05 | 0.00 | 0.02 | 0.00 | 1.94 | 0.00 | -0.02 | -0.01 | 0.01 | -0.05 | | | | 101.06 |
| **pyroxene** | | | | | | | | | | | | | | | | | |
| 46 / 1 . | PC99B1 | 0.04 | 40.23 | 60.17 | 0.22 | 0.00 | 0.01 | 0.08 | 0.09 | 0.05 | 0.00 | -0.02 | 0.00 | 0.01 | | | | 100.91 |
| 48 / 1 . | PC99B1 | 0.04 | 40.09 | 60.63 | 0.21 | 0.00 | 0.00 | 0.09 | 0.08 | -0.02 | 0.03 | 0.00 | 0.00 | -0.06 | | | | 101.18 |
| 49 / 1 . | PC99B1 | 0.02 | 39.95 | 60.65 | 0.13 | 0.00 | -0.03 | 0.12 | 0.26 | 0.00 | 0.00 | -0.01 | -0.04 | -0.15 | | | | 101.13 |
| 50 / 1 . | PC99B1 | 0.06 | 39.06 | 60.49 | 0.23 | 0.00 | 0.02 | 0.09 | 0.24 | 0.02 | 0.01 | -0.01 | 0.01 | 0.10 | | | | 100.32 |
| 51 / 1 . | PC99B1 | 0.03 | 39.75 | 60.08 | 0.09 | 0.00 | 0.00 | 0.11 | 0.82 | 0.01 | -0.02 | -0.02 | -0.01 | -0.05 | | | | 100.90 |
| 52 / 1 . | PC99B1 | -0.02 | 37.86 | 57.71 | 0.13 | -0.01 | 0.01 | 0.15 | 1.86 | -0.02 | 0.02 | -0.04 | -0.02 | 0.01 | | | | 97.75 |
| 53 / 1 . | PC99B1 bubble | 0.02 | 37.72 | 55.93 | 0.42 | 0.05 | -0.01 | 0.13 | 1.29 | 0.00 | 0.06 | 0.59 | 1.69 | 0.02 | | | | 98.34 |
| 54 / 1 . | PC99B1 | 0.04 | 38.28 | 58.20 | 0.20 | 0.03 | 0.00 | 0.18 | 1.13 | -0.01 | 0.00 | 0.01 | 0.02 | 0.12 | | | | 98.21 |
| 110 / 1 . | PC99B1 | 0.03 | 39.72 | 59.79 | 0.12 | 0.01 | 0.00 | 0.23 | 0.84 | 0.01 | 0.02 | -0.03 | 0.00 | 0.03 | | | | 100.81 |
| 116 / 1 . | PC99B1 | 0.03 | 40.01 | 61.05 | 0.19 | 0.00 | -0.01 | 0.14 | 0.21 | -0.03 | 0.01 | 0.00 | 0.01 | 0.03 | | | | 101.69 |
| 117 / 1 . | PC99B1 | 0.03 | 38.78 | 61.49 | 0.20 | 0.00 | 0.01 | 0.10 | 0.22 | 0.02 | 0.03 | -0.02 | -0.01 | 0.07 | | | | 100.95 |
| 118 / 1 . | PC99B1 | 0.03 | 39.56 | 60.10 | 0.10 | 0.00 | 0.00 | 0.13 | 0.71 | -0.01 | -0.02 | -0.02 | 0.00 | 0.13 | | | | 100.77 |
| **olivine** | | | | | | | | | | | | | | | | | |
| 26 / 1 . | PC99A2 | 0.00 | 57.10 | 43.15 | -0.01 | | 0.01 | 0.01 | 0.06 | 0.00 | -0.01 | | | -0.01 | | | | 100.33 |

| | | | | | | | | | | | | |
|---|---|---|---|---|---|---|---|---|---|---|---|---|
| 27 / 1 . | PC99A2 | 0.01 | 57.10 | 43.12 | 0.01 | 0.00 | 0.00 | 0.29 | -0.01 | -0.01 | -0.05 | 100.55 |
| 28 / 1 . | PC99A2 | 0.00 | 57.05 | 43.02 | -0.01 | -0.01 | 0.01 | 0.19 | 0.01 | 0.00 | -0.01 | 100.29 |
| 29 / 1 . | PC99A2 | 0.01 | 57.14 | 43.39 | -0.03 | 0.02 | 0.00 | 0.08 | 0.00 | 0.00 | 0.01 | 100.65 |
| 30 / 1 . | PC99A2 | -0.01 | 56.73 | 43.28 | 0.00 | 0.02 | 0.01 | 0.28 | 0.03 | -0.04 | -0.01 | 100.35 |
| 31 / 1 . | PC99A2 | 0.01 | 57.00 | 43.25 | 0.01 | 0.02 | -0.01 | 0.37 | 0.00 | 0.01 | -0.19 | 100.69 |
| 32 / 1 . | PC99A2 | 0.01 | 56.92 | 43.19 | 0.02 | 0.01 | 0.01 | 0.35 | 0.01 | -0.02 | -0.05 | 100.54 |
| 33 / 1 . | PC99A2 | 0.00 | 57.24 | 43.35 | -0.01 | 0.01 | 0.02 | 0.16 | 0.02 | 0.01 | 0.01 | 100.82 |
| 34 / 1 . | PC99A2 | 0.00 | 57.19 | 43.23 | 0.00 | 0.00 | 0.00 | 0.05 | -0.01 | -0.03 | 0.02 | 100.49 |
| 35 / 1 . | PC99A2 | 0.01 | 57.31 | 43.17 | -0.01 | 0.00 | -0.01 | 0.04 | 0.00 | 0.04 | 0.19 | 100.76 |
| 36 / 1 . | PC99A2 | 0.02 | 57.48 | 42.87 | 0.01 | 0.01 | 0.00 | 0.07 | 0.01 | 0.00 | -0.06 | 100.48 |
| 37 / 1 . | PC99A2 | 0.00 | 57.54 | 43.27 | 0.01 | 0.03 | 0.00 | 0.08 | 0.00 | -0.02 | 0.14 | 101.09 |

*EMPA of synthesized olivine (in orange wt% oxide total lower than 96% or higher than 102%). PC99A2 is the same as PC99A although other samples coming from the same capsule. Blanks mean that element has not been analyzed.*

## Appendix D2/ Calculated Raman frequencies of pure forsterite

| Symmetry group | this work | McKeown et al., 2010 (calc.) | Noël et al., 2006 (calc.) | McKeown et al., 2010 (meas.) | Kolesov and Geiger, 2004 (meas.) | Chopelas, 1991 (meas.) | Lishi K, 1978 (meas.) | Servoin and Piriou, 1973 (meas.) |
|---|---|---|---|---|---|---|---|---|
| Ag | 187 | 190 | 188 | 183 | 184 | 183 | 183 | 183 |
| | 231 | 227 | 234 | 227 | 227 | 226 | 227 | 227 |
| | 302 | 318 | 307 | 305 | 304 | 304 | 305 | 305 |
| | 323 | 337 | 329 | 329 | 329 | 329 | 329 | 329 |
| | 340 | 357 | 345 | 340 | 339 | 332 | 340 | 340 |
| | 420 | 436 | 425 | 423 | 421 | 422 | 424 | 424 |
| | 548 | 540 | 560 | 546 | 544 | 545 | 546 | 545 |
| | 611 | 606 | 618 | 609 | 608 | 608 | 609 | 609 |
| | 822 | 819 | 819 | 826 | 824 | 824 | 826 | 826 |
| | 855 | 849 | 856 | 856 | 856 | 856 | 856 | 856 |
| | 964 | 962 | 967 | 966 | 966 | 965 | 966 | 966 |
| B1g | 221 | 225 | 225 | 227 | – | 220 | 224 | 197 |
| | 256 | 259 | 260 | (275) | – | 274 | 260 | 265 |
| | 317 | 329 | 317 | 318 | 316 | 318 | 318 | 317 |
| | 354 | 365 | 367 | (374) | – | 351 | – | – |
| | 389 | 387 | 391 | 384 | – | 383 | 418 | 418 |
| | 437 | 447 | 442 | 434 | 434 | 434 | 434 | 434 |
| | 581 | 578 | 596 | 583 | 588 | 582 | 585 | 583 |
| | 633 | 629 | 645 | 632 | – | 632 | 632 | 632 |
| | 835 | 832 | 835 | 839 | 838 | 838 | 839 | 839 |
| | 864 | 859 | 866 | 866 | 866 | 866 | 866 | 866 |
| | 975 | 972 | 979 | 976 | – | 975 | 976 | 976 |
| B2g | 182 | 178 | 183 | (175) | – | 175 | (142) | – |
| | 240 | 250 | 253 | 244 | 243 | 242 | 244 | 244 |
| | 323 | 332 | 324 | 324 | – | 323 | 324 | 324 |
| | 370 | 374 | 373 | 368 | – | 365 | 368 | 365 |
| | - | - | – | - | – | – | – | 407 |
| | 445 | 452 | 451 | 441 | 434 | 439 | 441 | 438 |
| | 590 | 580 | 608 | 588 | 588 | 586 | 588 | 585 |
| | 882 | 875 | 883 | 882 | 882 | 881 | 884 | 881 |
| B3g | 183 | 197 | 190 | (203) | (243) | – | (226) | – |
| | 292 | 289 | 303 | 272 | – | 286 | 272 | – |
| | 319 | 323 | 322 | 318 | 316 | 315 | 318 | 314 |
| | 379 | 387 | 381 | 376 | 373 | 374 | 376 | 374 |
| | 416 | 421 | 421 | 411 | 409 | 410 | 412 | 406 |
| | - | - | – | - | – | 435 | – | 466 |
| | - | - | – | - | – | – | – | 484 |
| | 595 | 587 | 609 | 595 | 588 | 592 | 595 | 591 |
| | 923 | 914 | 927 | 922 | 920 | 920 | 922 | 920 |

*Calculated Raman frequencies of pure forsterite (using frequency scaling factor of 1.05) compared to experimental (meas.) and theoretical (calc.) values. Non-reliable frequencies are shown into brackets. Table is adapted from Noël et al. (2006), see references therein.*

## Appendix D3/ Calculated diagonal elements of Born effective charge tensor of pure forsterite

| | Mg1 | | | Mg2 | | | Si | | | O1 | | | O2 | | | O3 | | |
|---|---|---|---|---|---|---|---|---|---|---|---|---|---|---|---|---|---|---|
| **This work** | 2.19 | 1.71 | 1.95 | 1.95 | 2.29 | 2.05 | 3.04 | 2.6 | 2.9 | -2.38 | -1.40 | -1.49 | -1.63 | -2.00 | -1.54 | -1.60 | -1.61 | -1.95 |
| **Noël et al. (2006)** | 2.25 | 1.75 | 2.02 | 2.00 | 2.33 | 2.10 | 3.13 | 2.69 | 2.96 | -2.37 | -1.46 | -1.55 | -1.69 | -2.01 | -1.58 | -1.66 | -1.65 | -1.97 |

*Calculated diagonal elements of Born effective charge tensor of pure forsterite. Results compare well with previous calculations from Noël et al. (2006).*

## Appendix D4/ Calculated cell parameters and volumes of the different Xe incorporation sites

| $Xe_{Si}$ | | | | | | | | | | | | | | | | | | | |
|---|---|---|---|---|---|---|---|---|---|---|---|---|---|---|---|---|---|---|---|
| **0 GPa** | | | | | **2 GPa** | | | | | **5 GPa** | | | | | **5.7 GPa** | | | | |
| **Xe content** | ***a*** | ***b*** | ***c*** | **V** | **Xe content** | ***a*** | ***b*** | ***c*** | **V** | **Xe content** | ***a*** | ***b*** | ***c*** | **V** | **Xe content** | **a** | **b** | **c** | **V** |
| **0.00** | 4.777 | 10.246 | 5.995 | 293.400 | **0.00** | 4.758 | 10.172 | 5.961 | 288.538 | **0.00** | 4.733 | 10.071 | 5.915 | 281.955 | **0.00** | 4.728 | 10.049 | 5.905 | 280.527 |
| **0.40** | 4.795 | 10.258 | 6.007 | 295.482 | **0.40** | 4.777 | 10.184 | 5.973 | 290.539 | **0.40** | 4.751 | 10.083 | 5.925 | 283.887 | **0.40** | 4.746 | 10.061 | 5.915 | 282.446 |
| **0.45** | 4.799 | 10.261 | 6.005 | 295.710 | **0.45** | 4.780 | 10.187 | 5.971 | 290.758 | **0.45** | 4.755 | 10.086 | 5.924 | 284.088 | **0.45** | 4.749 | 10.064 | 5.913 | 282.645 |
| **0.89** | 4.819 | 10.279 | 6.016 | 298.025 | **0.89** | 4.800 | 10.203 | 5.981 | 292.946 | **0.89** | 4.774 | 10.101 | 5.933 | 286.129 | **0.89** | 4.769 | 10.079 | 5.923 | 284.655 |
| $Xe_{Mg2}$ | | | | | | | | | | | | | | | | | | | |
| **0 GPa** | | | | | **2 GPa** | | | | | **5 GPa** | | | | | **5.7 GPa** | | | | |
| **Xe content** | ***a*** | ***b*** | ***c*** | **V** | **Xe content** | ***a*** | ***b*** | ***c*** | **V** | **Xe content** | ***a*** | ***b*** | ***c*** | **V** | **Xe content** | **a** | **b** | **c** | **V** |
| **0.00** | 4.777 | 10.246 | 5.995 | 293.400 | **0.00** | 4.758 | 10.172 | 5.961 | 288.538 | **0.00** | 4.733 | 10.071 | 5.915 | 281.955 | **0.00** | 4.728 | 10.049 | 5.905 | 280.527 |
| **0.40** | 4.781 | 10.299 | 6.021 | 296.501 | **0.40** | 4.762 | 10.221 | 5.988 | 291.497 | **0.40** | 4.737 | 10.115 | 5.943 | 284.772 | **0.40** | 4.731 | 10.093 | 5.933 | 283.317 |
| **0.45** | 4.782 | 10.307 | 6.024 | 296.913 | **0.45** | 4.763 | 10.228 | 5.992 | 291.890 | **0.45** | 4.737 | 10.121 | 5.947 | 285.135 | **0.45** | 4.732 | 10.098 | 5.937 | 283.668 |
| **0.89** | 4.789 | 10.374 | 6.049 | 300.534 | **0.89** | 4.769 | 10.287 | 6.018 | 295.277 | **0.89** | 4.742 | 10.172 | 5.975 | 288.259 | **0.89** | 4.737 | 10.148 | 5.966 | 286.746 |
| $Xe_{Mg1}$ | | | | | | | | | | | | | | | | | | | |
| **0 GPa** | | | | | **2 GPa** | | | | | **5 GPa** | | | | | **5.7 GPa** | | | | |
| **Xe content** | ***a*** | ***b*** | ***c*** | **V** | **Xe content** | ***a*** | ***b*** | ***c*** | **V** | **Xe content** | ***a*** | ***b*** | ***c*** | **V** | **Xe content** | **a** | **b** | **c** | **V** |
| **0.00** | 4.777 | 10.246 | 5.995 | 293.400 | **0.00** | 4.758 | 10.172 | 5.961 | 288.538 | **0.00** | 4.733 | 10.071 | 5.915 | 281.955 | **0.00** | 4.728 | 10.049 | 5.905 | 280.527 |
| **0.40** | 4.787 | 10.287 | 6.021 | 296.459 | **0.40** | 4.768 | 10.211 | 5.987 | 291.483 | **0.40** | 4.743 | 10.109 | 5.939 | 284.784 | **0.40** | 4.738 | 10.086 | 5.929 | 283.336 |
| **0.45** | 4.790 | 10.294 | 6.020 | 296.815 | **0.45** | 4.771 | 10.218 | 5.986 | 291.824 | **0.45** | 4.746 | 10.115 | 5.939 | 285.107 | **0.45** | 4.740 | 10.093 | 5.928 | 283.638 |
| **0.89** | 4.802 | 10.343 | 6.046 | 300.306 | **0.89** | 4.784 | 10.263 | 6.012 | 295.141 | **0.89** | 4.758 | 10.156 | 5.964 | 288.217 | **0.89** | 4.752 | 10.133 | 5.954 | 286.721 |

| $Xe_i$ | | | | | | | | | | | | | | | | | | | |
|---|---|---|---|---|---|---|---|---|---|---|---|---|---|---|---|---|---|---|---|
| **0 GPa** | | | | | **2 GPa** | | | | | **5 GPa** | | | | | **5.7 GPa** | | | | |
| **Xe content** | ***a*** | ***b*** | ***c*** | **V** | **Xe content** | ***a*** | ***b*** | ***c*** | **V** | **Xe content** | ***a*** | ***b*** | ***c*** | **V** | **Xe content** | **a** | **b** | **c** | **V** |
| **0.00** | 4.777 | 10.246 | 5.995 | 293.400 | **0.00** | 4.758 | 10.172 | 5.961 | 288.538 | **0.00** | 4.733 | 10.071 | 5.915 | 281.955 | **0.00** | 4.728 | 10.049 | 5.905 | 280.527 |
| **0.40** | 4.793 | 10.316 | 6.040 | 298.651 | **0.40** | 4.773 | 10.239 | 6.003 | 293.435 | **0.40** | 4.748 | 10.137 | 5.953 | 286.515 | **0.40** | 4.742 | 10.116 | 5.943 | 285.072 |
| **0.45** | 4.796 | 10.324 | 6.042 | 299.173 | **0.45** | 4.777 | 10.248 | 6.004 | 293.928 | **0.45** | 4.751 | 10.146 | 5.953 | 286.957 | **0.45** | 4.746 | 10.124 | 5.942 | 285.505 |
| **0.89** | 4.815 | 10.403 | 6.092 | 305.135 | **0.89** | 4.794 | 10.323 | 6.050 | 299.414 | **0.89** | 4.767 | 10.217 | 5.993 | 291.892 | **0.89** | 4.761 | 10.195 | 5.980 | 290.278 |

*Calculated cell parameters (in Å) and volumes (in $Å^3$) of the different Xe incorporation sites, following simultaneous relaxation of atomic positions and cell parameters, for various Xe contents (in at% Xe) and pressures.*

## Appendix D5/ Calculated polarized Raman spectra of pure forsterite

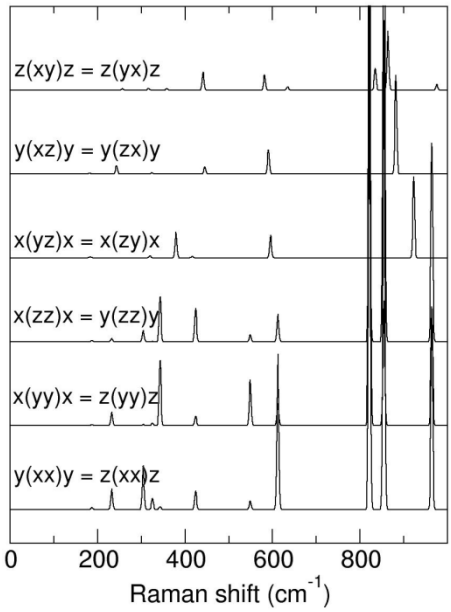


*Calculated polarized Raman spectra of pure forsterite (using frequency scaling factor of 1.05). Porto notation (Damen, 1966) is used: x(yz)y indicates that the incident beam (polarized along the y direction) is coming along the x axis of the crystal and the scattered light (polarized along the z direction) is detected along the y axis. Due to symmetry of the olivine there are only six different polarized Raman spectra.*

## Appendix D6/ Calculated Raman spectra of the different configurations for Xe for Si substitution

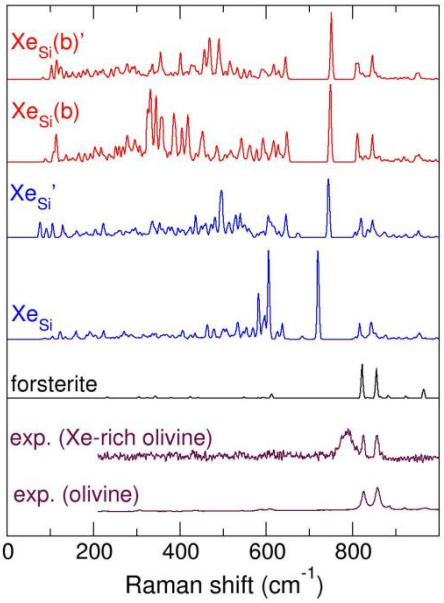


*Calculated Raman spectra of the different configurations for Xe for Si substitution sites in forsterite (0.89 at% Xe) and pure forsterite vs. measurements (exp.) from Sanloup et al. (2011). The spectrum on Xe-rich olivine was recorded at 0.9 GPa after quenching T from 1800 K. The spectrum on Xe-free olivine was recorded at 0.9 GPa and 300 K before heating (i.e. before reaction of Xe with olivine). Bands below 650 $cm^{-1}$ are linked to unrealistically high Xe content as discussed in the text.*

## Appendix D7/ EMPA on recovered gaskets after *in situ* X-ray diffraction in DAC

| 2017-11-16<br>n° of analysis | Sample | $Na_2O$ | MgO | $SiO_2$ | $Al_2O_3$ | Ar | $K_2O$ | CaO | FeO | MnO | $TiO_2$ | Kr | Xe | BaO | $Cr_2O_3$ | NiO | $Re_2O_7$ | Total |
|---|---|---|---|---|---|---|---|---|---|---|---|---|---|---|---|---|---|---|
| **olivine + pyroxene ?** | | | | | | | | | | | | | | | | | | |
| 73 / 1 . | HT2-1-plain | -0.03 | 29.32 | 25.49 | 0.11 | 0.02 | 0.00 | 0.34 | 1.14 | 0.05 | -0.02 | -0.08 | -0.02 | -0.21 | -0.01 | 5.35 | 16.39 | 78.20 |
| 74 / 1 . | HT2-1-plain | 0.02 | 46.50 | 38.63 | 0.09 | 0.01 | 0.03 | 0.17 | 0.26 | 0.03 | 0.00 | -0.01 | -0.02 | -0.08 | -0.01 | 2.08 | 7.07 | 94.89 |
| 75 / 1 . | HT2-1-plain | 0.03 | 22.77 | 33.90 | 0.01 | -0.01 | 0.00 | 0.28 | 6.23 | 0.03 | 0.01 | -0.03 | -0.02 | -0.06 | 0.02 | 1.43 | 3.21 | 67.91 |
| 76 / 1 . | HT2-1-plain | 0.04 | 50.75 | 41.07 | 0.00 | 0.00 | 0.00 | 0.09 | 8.11 | 0.01 | 0.02 | -0.02 | 0.00 | -0.03 | 0.81 | 0.36 | 1.33 | 102.59 |
| 77 / 1 . | HT2-1-plain | 0.03 | 47.03 | 32.72 | 0.01 | 0.00 | 0.00 | 0.11 | 7.67 | 0.06 | 0.36 | -0.02 | 0.01 | -0.10 | 0.02 | 1.18 | 2.07 | 91.26 |
| 78 / 1 . | HT2-1-plain | 0.03 | 45.86 | 39.64 | 0.02 | 0.00 | 0.01 | 0.12 | 8.64 | 0.02 | 0.03 | -0.03 | 0.00 | -0.01 | 0.02 | 1.72 | 6.56 | 102.67 |
| 79 / 1 . | HT2-1-plain | 0.10 | 35.03 | 37.61 | 0.09 | 0.01 | 0.01 | 0.46 | 4.20 | 0.05 | -0.04 | -0.01 | -0.01 | -0.06 | 0.02 | 5.42 | 15.65 | 98.65 |
| 80 / 1 . | HT2-1-plain | 0.03 | 36.39 | 45.84 | 0.07 | -0.01 | 0.00 | 0.60 | 1.11 | 0.02 | 0.05 | -0.01 | 0.03 | -0.13 | 0.03 | 3.75 | 10.66 | 98.58 |
| 81 / 1 . | HT2-1-plain | 0.05 | 51.03 | 36.04 | 0.04 | 0.00 | 0.00 | 0.13 | 8.71 | -0.02 | -0.01 | -0.04 | -0.01 | 0.07 | 0.64 | 0.75 | 2.57 | 100.03 |
| 82 / 1 . | HT2-1-plain | 0.01 | 43.88 | 38.67 | 0.03 | 0.01 | 0.00 | 0.10 | 8.20 | 0.00 | -0.02 | -0.02 | -0.01 | -0.12 | 0.01 | 1.34 | 3.06 | 95.29 |
| 83 / 1 . | HT2-1-plain | 0.03 | 43.09 | 36.76 | 0.02 | -0.01 | 0.00 | 0.16 | 7.83 | 0.08 | 0.00 | -0.02 | -0.03 | -0.06 | -0.02 | 3.16 | 12.94 | 104.05 |
| 84 / 1 . | HT2-1-plain | 0.01 | 53.95 | 39.90 | 0.03 | -0.01 | 0.01 | 0.03 | 8.47 | 0.03 | -0.04 | -0.03 | -0.02 | -0.03 | 0.03 | 0.26 | 0.59 | 103.33 |
| 85 / 1 . | HT2-1-plain | 0.02 | 49.54 | 40.36 | 0.02 | 0.00 | 0.01 | 0.08 | 8.50 | 0.01 | 0.01 | -0.02 | 0.01 | 0.01 | 0.00 | 0.16 | 0.24 | 98.98 |
| 86 / 1 . | HT2-1-plain | 0.00 | 46.81 | 42.25 | 0.03 | 0.00 | 0.00 | 0.05 | 9.29 | 0.01 | 0.03 | -0.03 | 0.02 | 0.02 | -0.01 | 0.11 | 0.07 | 98.68 |
| 87 / 1 . | HT2-1-plain | 0.01 | 46.69 | 41.58 | -0.03 | 0.00 | 0.02 | 0.02 | 9.38 | -0.01 | 0.02 | -0.03 | 0.01 | -0.14 | 0.01 | 0.06 | 0.18 | 97.99 |
| 88 / 1 . | HT2-1-plain | 0.00 | 6.03 | 7.18 | 0.01 | 0.01 | 0.00 | 0.12 | 0.26 | 0.04 | 0.02 | -0.01 | 0.00 | 0.07 | 0.02 | 2.14 | 1.97 | 17.88 |
| 89 / 1 . | HT2-1-plain | 0.07 | 59.05 | 45.25 | 0.37 | 0.00 | 0.16 | 0.03 | 0.10 | 0.01 | 0.04 | -0.01 | 0.01 | 0.09 | 0.02 | 0.07 | 0.53 | 105.80 |
| 90 / 1 . | HT2-1-plain | 0.02 | 40.34 | 45.03 | 0.01 | 0.00 | 0.04 | 0.03 | 8.32 | 0.01 | 0.08 | -0.02 | 0.00 | -0.04 | 0.02 | 0.03 | 0.24 | 94.15 |
| 91 / 1 . | HT2-1-plain | 0.03 | 42.24 | 41.99 | 0.08 | 0.00 | -0.01 | 0.08 | 7.72 | 0.05 | 0.02 | -0.02 | 0.02 | -0.04 | 0.02 | 0.61 | 1.55 | 94.41 |
| 92 / 1 . | HT2-1-plain | 0.08 | 54.79 | 44.30 | 0.39 | 0.00 | 0.15 | 0.07 | 0.10 | -0.03 | -0.03 | -0.02 | 0.01 | -0.09 | 0.00 | 0.05 | 0.81 | 100.75 |
| 93 / 1 . | HT2-1-plain | 0.05 | 52.58 | 43.13 | 0.24 | -0.01 | 0.11 | 0.06 | 0.08 | 0.04 | -0.04 | 0.00 | 0.01 | 0.02 | -0.01 | 0.07 | 0.88 | 97.26 |
| 94 / 1 . | HT2-1-plain | 0.05 | 60.40 | 44.79 | 0.22 | -0.01 | 0.07 | 0.02 | 0.08 | -0.01 | 0.00 | -0.03 | 0.01 | -0.14 | -0.01 | 0.03 | 0.37 | 106.04 |
| 95 / 1 . | HT2-1-plain | 0.03 | 41.33 | 39.62 | 0.25 | -0.01 | 0.11 | 0.03 | 0.26 | 0.02 | -0.02 | -0.02 | -0.02 | -0.16 | 0.00 | 0.04 | 4.23 | 85.92 |
| 96 / 1 . | HT2-1-plain | 0.02 | 53.71 | 38.36 | 0.04 | 0.01 | 0.01 | 0.03 | 6.56 | 0.04 | -0.02 | -0.02 | 0.02 | -0.02 | 0.04 | 0.04 | 0.02 | 98.88 |
| 97 / 1 . | HT2-1-plain | 0.01 | 51.68 | 38.67 | 0.09 | -0.01 | -0.01 | 0.03 | 6.65 | -0.01 | -0.01 | -0.02 | 0.00 | -0.02 | 0.01 | 0.03 | 0.00 | 97.16 |

| | | | | | | | | | | | | | | | | | | |
|---|---|---|---|---|---|---|---|---|---|---|---|---|---|---|---|---|---|---|
| 98 / 1 . | HT2-1-plain | 0.00 | 49.11 | 37.43 | 0.05 | 0.01 | -0.02 | 0.05 | 5.06 | -0.03 | -0.01 | -0.03 | 0.01 | 0.05 | 0.02 | 0.30 | 0.79 | 92.89 |
| 99 / 1 . | HT2-1-plain | 0.02 | 54.95 | 43.04 | 0.00 | 0.00 | 0.00 | 0.04 | 4.26 | 0.00 | -0.01 | -0.04 | -0.02 | -0.03 | -0.01 | 0.22 | 0.25 | 102.78 |
| 100 / 1 . | HT2-1-plain | 0.02 | 26.56 | 43.73 | 0.03 | 0.00 | 0.02 | 0.05 | 7.11 | 0.03 | 0.01 | -0.02 | 0.00 | 0.09 | 0.01 | 0.26 | 1.04 | 78.98 |
| 101 / 1 . | HT2-1-plain | 0.01 | 50.28 | 37.29 | 0.02 | 0.00 | 0.01 | 0.02 | 0.17 | -0.03 | 0.01 | -0.01 | 0.00 | 0.02 | -0.01 | 0.88 | 3.02 | 91.72 |
| 102 / 1 . | HT2-1-plain | 0.02 | 39.72 | 35.76 | -0.01 | 0.01 | -0.03 | 0.09 | 6.32 | 0.01 | -0.01 | -0.01 | -0.02 | -0.03 | -0.03 | 0.90 | 5.01 | 87.82 |
| 103 / 1 . | HT2-1-plain | 0.04 | 48.32 | 37.02 | 0.12 | 0.00 | 0.01 | 0.19 | 0.10 | 0.02 | 0.01 | -0.01 | -0.02 | -0.03 | 0.02 | 2.49 | 10.52 | 98.85 |
| 104 / 1 . | HT2-1-plain | 0.00 | 11.07 | 26.46 | 0.01 | 0.01 | 0.00 | 0.13 | 6.06 | 0.06 | 0.00 | -0.01 | 0.00 | -0.10 | 0.02 | 2.63 | 2.15 | 48.61 |
| | | | | | | | | | | | | | | | | | | |
| 105 / 1 . | HT2-1-Xe/Ar | 0.02 | 47.02 | 40.57 | -0.03 | 0.00 | 0.00 | 0.12 | 8.49 | 0.08 | -0.01 | -0.03 | | 0.10 | 0.00 | 1.19 | 2.98 | 100.60 |
| 106 / 1 . | HT2-1-Xe/Ar | 0.02 | 45.25 | 41.94 | 0.27 | 0.00 | -0.01 | 0.12 | 8.66 | 0.02 | 0.00 | -0.03 | -0.01 | 0.04 | 0.02 | 1.56 | 3.37 | 101.28 |
| 107 / 1 . | HT2-1-Xe/Ar | 0.02 | 44.21 | 39.34 | 4.44 | 0.00 | 0.01 | 0.08 | 8.20 | 0.06 | -0.06 | -0.03 | 0.01 | 0.01 | 0.04 | 1.30 | 4.28 | 102.01 |
| 108 / 1 . | HT2-1-Xe/Ar | 0.02 | 48.29 | 41.28 | 0.03 | -0.02 | 0.00 | 0.07 | 8.76 | -0.02 | -0.04 | -0.01 | 0.01 | 0.05 | -0.02 | 1.07 | 2.21 | 101.79 |
| 109 / 1 . | HT2-1-Xe/Ar | 0.01 | 47.17 | 40.57 | -0.01 | 0.01 | 0.01 | 0.09 | 8.16 | -0.01 | -0.04 | -0.02 | -0.02 | -0.08 | 0.00 | 1.40 | 3.56 | 100.99 |
| 110 / 1 . | HT2-1-Xe/Ar | 0.02 | 47.92 | 41.31 | 0.05 | 0.00 | -0.01 | 0.11 | 8.71 | 0.05 | -0.04 | -0.04 | -0.02 | -0.06 | -0.01 | 1.00 | 2.63 | 101.79 |
| 111 / 1 . | HT2-1-Xe/Ar | 0.03 | 47.34 | 42.55 | 0.02 | 0.00 | 0.02 | 0.08 | 8.87 | -0.04 | -0.05 | -0.03 | -0.03 | -0.19 | 0.00 | 0.74 | 3.19 | 102.85 |
| 112 / 1 . | HT2-1-Xe/Ar | 0.02 | 46.89 | 41.89 | 0.03 | 0.00 | -0.01 | 0.12 | 7.70 | 0.02 | -0.04 | -0.03 | -0.03 | 0.05 | 0.00 | 1.12 | 3.58 | 101.43 |
| 114 / 1 . | HT2-1-Xe/Ar | 0.01 | 45.19 | 40.45 | 0.02 | -0.01 | 0.02 | 0.08 | 7.74 | 0.03 | 0.04 | -0.03 | 0.02 | -0.08 | -0.01 | 1.29 | 3.93 | 98.84 |
| 115 / 1 . | HT2-1-Xe/Ar | 0.03 | 46.15 | 40.23 | 0.01 | 0.00 | 0.01 | 0.13 | 7.54 | 0.01 | -0.01 | -0.03 | 0.02 | 0.00 | 0.01 | 1.12 | 2.88 | 98.13 |
| 158 / 1 . | HT2-1-Xe/Ar | 0.03 | 42.63 | 36.92 | -0.01 | 0.00 | -0.01 | 0.12 | 7.04 | 0.02 | 0.04 | -0.01 | 0.02 | -0.01 | 0.00 | 3.03 | 6.09 | 95.95 |
| 159 / 1 . | HT2-1-Xe/Ar | 0.02 | 44.03 | 37.80 | -0.01 | 0.00 | 0.01 | 0.09 | 7.58 | 0.02 | 0.01 | -0.01 | 0.01 | 0.19 | 0.00 | 2.25 | 5.15 | 97.16 |
| 160 / 1 . | HT2-1-Xe/Ar | 0.03 | 44.49 | 38.59 | 0.00 | 0.00 | -0.01 | 0.09 | 8.14 | 0.05 | 0.01 | -0.02 | 0.00 | 0.02 | 0.00 | 2.33 | 4.28 | 98.05 |
| 161 / 1 . | HT2-1-Xe/Ar | 0.03 | 46.98 | 40.19 | 0.00 | 0.01 | -0.01 | 0.05 | 8.75 | 0.00 | 0.03 | -0.03 | 0.00 | -0.08 | 0.03 | 1.01 | 3.23 | 100.30 |
| 162 / 1 . | HT2-1-Xe/Ar | 0.04 | 42.93 | 41.87 | 0.00 | 0.01 | -0.02 | 0.11 | 8.71 | 0.01 | 0.00 | -0.03 | 0.03 | -0.16 | -0.03 | 1.92 | 2.75 | 98.38 |
| 163 / 1 . | HT2-1-Xe/Ar | 0.01 | 48.54 | 39.84 | 0.03 | 0.00 | 0.00 | 0.07 | 8.24 | 0.03 | 0.01 | -0.03 | 0.02 | 0.04 | 0.00 | 1.23 | 2.89 | 100.95 |
| 164 / 1 . | HT2-1-Xe/Ar | 0.03 | 47.72 | 40.33 | 0.04 | 0.01 | 0.00 | 0.08 | 8.66 | 0.00 | 0.04 | -0.02 | -0.03 | -0.12 | 0.02 | 1.13 | 3.10 | 101.17 |
| 165 / 1 . | HT2-1-Xe/Ar | 0.03 | 47.30 | 41.45 | 1.40 | 0.00 | -0.02 | 0.08 | 8.88 | 0.00 | -0.01 | -0.03 | 0.01 | -0.01 | 0.02 | 0.87 | 2.07 | 102.09 |
| 166 / 1 . | HT2-1-Xe/Ar | 0.04 | 46.73 | 41.76 | 0.01 | 0.01 | -0.02 | 0.07 | 8.62 | 0.06 | -0.01 | -0.02 | 0.02 | 0.07 | 0.01 | 0.94 | 2.81 | 101.17 |
| 167 / 1 . | HT2-1-Xe/Ar | 0.01 | 44.57 | 38.98 | 0.01 | 0.01 | 0.00 | 0.05 | 8.29 | -0.01 | 0.04 | -0.02 | -0.03 | -0.13 | 0.02 | 1.02 | 11.45 | 104.46 |
| 168 / 1 . | HT2-1-Xe/Ar | 0.03 | 46.59 | 41.46 | 0.11 | 0.00 | 0.00 | 0.08 | 8.95 | 0.00 | -0.01 | -0.04 | -0.01 | -0.10 | -0.01 | 2.32 | 2.67 | 102.21 |

| | | | | | | | | | | | | | | | | | | |
|---|---|---|---|---|---|---|---|---|---|---|---|---|---|---|---|---|---|---|
| **Olivine** | | | | | | | | | | | | | | | | | | |
| 122 / 1 . | HT2-4-plain | 0.03 | 49.43 | 41.91 | 0.00 | 0.01 | 0.02 | 0.09 | 9.17 | 0.02 | 0.00 | -0.02 | 0.02 | 0.09 | 0.00 | 0.02 | -0.02 | 100.81 |
| 123 / 1 . | HT2-4-plain | 0.02 | 49.19 | 41.25 | 0.05 | 0.00 | 0.00 | 0.06 | 9.23 | 0.02 | -0.01 | -0.04 | -0.01 | 0.14 | 0.00 | 0.05 | 0.03 | 100.05 |
| 124 / 1 . | HT2-4-plain | -0.01 | 49.81 | 41.26 | 0.00 | 0.01 | 0.01 | 0.05 | 9.24 | 0.02 | -0.04 | -0.02 | 0.00 | -0.08 | -0.01 | 0.03 | -0.02 | 100.44 |
| 125 / 1 . | HT2-4-plain | 0.02 | 50.03 | 41.52 | 0.01 | 0.00 | 0.00 | 0.06 | 8.90 | 0.02 | -0.03 | -0.02 | 0.01 | -0.06 | 0.03 | -0.03 | 0.02 | 100.64 |
| 126 / 1 . | HT2-4-plain | 0.02 | 50.74 | 41.45 | 0.01 | 0.00 | 0.00 | 0.00 | 8.77 | 0.00 | 0.04 | -0.03 | -0.02 | -0.07 | -0.01 | 0.01 | -0.07 | 101.05 |
| 185 / 1 . | HT2-4-plain | 0.04 | 49.49 | 40.74 | 0.02 | 0.00 | 0.03 | 0.03 | 9.55 | 0.00 | 0.03 | -0.03 | 0.01 | -0.02 | 0.01 | 0.01 | 0.02 | 99.97 |
| 186 / 1 . | HT2-4-plain | 0.01 | 50.07 | 41.62 | 0.01 | 0.00 | 0.03 | 0.07 | 9.66 | 0.03 | -0.02 | -0.04 | 0.02 | 0.12 | -0.02 | -0.01 | -0.05 | 101.64 |
| 187 / 1 . | HT2-4-plain | -0.01 | 49.01 | 41.37 | -0.01 | 0.00 | -0.01 | 0.06 | 9.73 | 0.02 | -0.04 | -0.01 | 0.02 | -0.05 | -0.01 | -0.02 | -0.03 | 100.21 |
| 188 / 1 . | HT2-4-plain | 0.01 | 50.30 | 41.63 | 0.02 | -0.01 | 0.00 | 0.08 | 9.39 | -0.02 | 0.00 | -0.04 | -0.01 | 0.07 | 0.00 | -0.04 | -0.03 | 101.52 |
| 189 / 1 . | HT2-4-plain | 0.01 | 49.75 | 41.71 | -0.01 | -0.01 | 0.01 | 0.02 | 8.24 | -0.01 | 0.01 | -0.02 | 0.00 | -0.09 | -0.02 | -0.02 | 0.00 | 99.75 |
| 190 / 1 . | HT2-4-plain | 0.03 | 49.46 | 41.20 | 0.02 | -0.01 | -0.01 | 0.09 | 9.40 | 0.00 | -0.01 | -0.03 | 0.00 | -0.06 | -0.01 | -0.04 | -0.02 | 100.20 |
| 191 / 1 . | HT2-4-plain | 0.01 | 49.71 | 41.09 | 0.02 | 0.01 | 0.02 | 0.02 | 9.52 | -0.02 | -0.04 | -0.03 | -0.01 | -0.01 | -0.01 | -0.03 | 0.08 | 100.49 |
| 192 / 1 . | HT2-4-plain | 0.03 | 50.61 | 40.08 | 0.00 | 0.00 | 0.01 | 0.07 | 9.54 | 0.00 | 0.09 | -0.03 | -0.02 | 0.11 | -0.01 | -0.01 | 0.00 | 100.53 |
| 193 / 1 . | HT2-4-plain | 0.02 | 50.93 | 40.28 | 0.04 | 0.01 | 0.00 | 0.03 | 9.01 | 0.00 | -0.05 | -0.02 | -0.01 | 0.00 | 0.00 | -0.02 | 0.02 | 100.33 |
| 194 / 1 . | HT2-4-plain | 0.02 | 50.34 | 40.66 | -0.03 | 0.01 | 0.03 | 0.04 | 9.48 | 0.00 | 0.01 | -0.03 | 0.00 | -0.08 | 0.00 | 0.05 | 0.29 | 100.93 |
| 195 / 1 . | HT2-4-plain | 0.03 | 50.32 | 41.07 | -0.01 | 0.00 | 0.01 | 0.05 | 8.60 | 0.03 | -0.02 | -0.03 | 0.00 | -0.10 | -0.01 | -0.03 | 0.05 | 100.16 |
| 196 / 1 . | HT2-4-plain | 0.02 | 48.89 | 41.62 | -0.03 | 0.00 | 0.01 | 0.08 | 9.76 | 0.01 | -0.01 | -0.02 | 0.00 | -0.10 | -0.01 | -0.04 | -0.01 | 100.40 |
| 197 / 1 . | HT2-4-plain | 0.01 | 48.95 | 41.20 | -0.02 | -0.01 | 0.03 | 0.05 | 9.21 | 0.00 | 0.01 | -0.03 | 0.00 | -0.04 | 0.02 | 0.04 | 0.14 | 99.66 |
| 198 / 1 . | HT2-4-plain | 0.01 | 48.95 | 42.49 | -0.01 | 0.00 | 0.02 | 0.02 | 8.68 | 0.03 | -0.03 | -0.03 | 0.01 | -0.10 | 0.01 | 0.01 | 0.10 | 100.32 |
| 199 / 1 . | HT2-4-plain | 0.03 | 49.95 | 41.46 | 0.00 | 0.01 | 0.01 | 0.04 | 9.11 | 0.00 | 0.03 | -0.02 | -0.02 | 0.07 | 0.00 | 0.04 | 0.07 | 100.83 |
| **olivine + pyroxene** | | | | | | | | | | | | | | | | | | |
| 119 / 1 . | HT2-4-Xe/Ar dark zone | 0.03 | 54.92 | 42.86 | -0.01 | 0.00 | 0.00 | -0.01 | 0.13 | -0.01 | -0.04 | -0.01 | -0.03 | -0.07 | 0.02 | 0.00 | 0.49 | 98.46 |
| 120 / 1 . | HT2-4-Xe/Ar dark zone | 0.02 | 54.91 | 42.25 | 0.01 | 0.00 | 0.00 | 0.01 | 0.37 | 0.02 | -0.04 | -0.02 | 0.00 | 0.12 | 0.00 | -0.04 | 1.42 | 99.13 |
| 121 / 1 . | HT2-4-Xe/Ar dark zone | 0.02 | 54.81 | 42.33 | 0.00 | -0.01 | 0.01 | 0.03 | 0.26 | -0.01 | 0.01 | 0.00 | -0.01 | 0.11 | -0.01 | -0.01 | 0.78 | 98.36 |
| 169 / 1 . | HT2-4-Xe/Ar dark zone | 0.02 | 54.88 | 42.27 | 0.00 | -0.01 | 0.02 | 0.01 | 0.09 | -0.03 | -0.02 | -0.01 | 0.02 | 0.02 | -0.01 | 0.01 | 1.32 | 98.68 |
| 170 / 1 . | HT2-4-Xe/Ar dark zone | 0.02 | 55.50 | 42.26 | 0.01 | 0.00 | 0.02 | 0.03 | 0.16 | -0.01 | 0.03 | -0.02 | 0.00 | -0.01 | 0.00 | -0.03 | 1.13 | 99.16 |
| 171 / 1 . | HT2-4-Xe/Ar dark zone | 0.01 | 55.25 | 41.64 | -0.01 | 0.00 | 0.02 | 0.04 | 0.15 | -0.02 | 0.03 | -0.02 | 0.03 | -0.02 | 0.02 | 0.00 | 1.20 | 98.40 |
| 172 / 1 . | HT2-4-Xe/Ar dark zone | 0.02 | 55.01 | 42.31 | -0.02 | 0.01 | 0.04 | 0.05 | 0.17 | 0.01 | 0.02 | -0.02 | 0.02 | 0.03 | -0.02 | 0.03 | 0.96 | 98.68 |

| | | | | | | | | | | | | | | | | | | |
|---|---|---|---|---|---|---|---|---|---|---|---|---|---|---|---|---|---|---|
| 173 / 1 . | HT2-4-Xe/Ar dark zone | 0.03 | 52.83 | 42.11 | 0.00 | 0.00 | -0.01 | 0.09 | 0.29 | -0.03 | -0.02 | -0.01 | -0.02 | 0.05 | 0.01 | -0.04 | 0.99 | 96.41 |
| 174 / 1 . | HT2-4-Xe/Ar dark zone | 0.02 | 54.85 | 42.55 | -0.01 | 0.00 | 0.00 | 0.00 | 0.34 | 0.02 | -0.02 | -0.02 | 0.01 | -0.05 | -0.01 | -0.04 | 0.83 | 98.60 |
| 175 / 1 . | HT2-4-Xe/Ar dark zone | 0.02 | 53.73 | 43.40 | 0.00 | 0.01 | 0.02 | 0.03 | 0.35 | -0.04 | 0.04 | 0.00 | -0.01 | 0.03 | 0.00 | 0.02 | 0.37 | 98.02 |
| 176 / 1 . | HT2-4-Xe/Ar dark zone | 0.02 | 54.15 | 40.60 | 0.02 | 0.00 | 0.00 | 0.01 | 0.41 | 0.04 | -0.01 | -0.01 | -0.01 | -0.06 | -0.02 | 0.04 | 0.36 | 95.66 |
| 177 / 1 . | HT2-4-Xe/Ar dark zone | 0.03 | 56.16 | 43.55 | 0.02 | 0.00 | -0.02 | 0.02 | 0.06 | -0.03 | -0.07 | -0.01 | -0.01 | 0.00 | 0.00 | 0.04 | 0.33 | 100.21 |
| **olivine** | | | | | | | | | | | | | | | | | | |
| 116 / 1 . | HT2-4-Xe/Ar light zone | 0.03 | 47.64 | 41.09 | 0.01 | -0.01 | 0.01 | 0.04 | 9.07 | -0.01 | -0.02 | -0.03 | 0.02 | -0.12 | -0.01 | 0.00 | 1.20 | 99.11 |
| 117 / 1 . | HT2-4-Xe/Ar light zone | 0.02 | 46.98 | 41.42 | 0.00 | 0.01 | -0.01 | 0.06 | 8.77 | -0.01 | 0.01 | -0.05 | 0.01 | 0.05 | 0.02 | -0.05 | 1.21 | 98.54 |
| 118 / 1 . | HT2-4-Xe/Ar light zone | 0.01 | 47.92 | 40.45 | 0.02 | 0.00 | 0.01 | 0.06 | 8.74 | 0.01 | 0.00 | -0.03 | -0.01 | -0.03 | 0.03 | 0.02 | 1.17 | 98.46 |
| 178 / 1 . | HT2-4-Xe/Ar light zone | 0.02 | 49.21 | 41.40 | -0.01 | 0.00 | 0.01 | 0.09 | 8.88 | -0.02 | 0.00 | -0.03 | 0.01 | -0.04 | 0.00 | 0.01 | 0.39 | 100.04 |
| 179 / 1 . | HT2-4-Xe/Ar light zone | 0.01 | 48.09 | 40.62 | 0.01 | 0.00 | -0.03 | 0.05 | 8.36 | 0.00 | 0.03 | -0.01 | -0.01 | -0.01 | 0.01 | -0.02 | 1.37 | 98.54 |
| 180 / 1 . | HT2-4-Xe/Ar light zone | 0.01 | 47.60 | 39.43 | 0.00 | 0.00 | -0.01 | 0.07 | 8.46 | -0.01 | 0.00 | -0.03 | -0.01 | 0.02 | 0.01 | 0.05 | 1.27 | 96.91 |
| 181 / 1 . | HT2-4-Xe/Ar light zone | 0.03 | 47.18 | 39.19 | -0.02 | -0.02 | 0.01 | 0.04 | 9.02 | 0.04 | 0.03 | -0.04 | -0.01 | -0.02 | -0.03 | 0.02 | 1.55 | 97.11 |
| 182 / 1 . | HT2-4-Xe/Ar light zone | 0.03 | 47.25 | 39.92 | 0.00 | 0.01 | 0.00 | 0.06 | 9.17 | 0.02 | 0.01 | -0.01 | -0.02 | -0.04 | -0.01 | 0.04 | 1.14 | 97.66 |
| 183 / 1 . | HT2-4-Xe/Ar light zone | 0.02 | 47.99 | 41.53 | 0.03 | 0.00 | 0.01 | 0.06 | 8.61 | -0.03 | 0.03 | -0.02 | -0.01 | 0.08 | 0.02 | -0.01 | 0.63 | 99.00 |
| 184 / 1 . | HT2-4-Xe/Ar light zone | 0.03 | 50.55 | 41.66 | 0.05 | 0.01 | 0.02 | 0.05 | 6.28 | -0.02 | -0.05 | -0.01 | 0.01 | 0.01 | 0.00 | 0.03 | 0.85 | 99.54 |
| **olivine** | | | | | | | | | | | | | | | | | | |
| 127 / 1 . | RT1-2-Xe/Ar light zone | 0.02 | 49.14 | 40.26 | 0.29 | 0.00 | 0.00 | 0.02 | 7.80 | -0.04 | -0.01 | -0.03 | 0.00 | 0.03 | 0.00 | 0.03 | 0.02 | 97.61 |
| 128 / 1 . | RT1-2-Xe/Ar light zone | 0.03 | 48.56 | 41.36 | 0.01 | -0.01 | 0.01 | 0.04 | 7.82 | 0.00 | 0.01 | -0.03 | 0.00 | -0.01 | 0.00 | -0.08 | 0.01 | 97.84 |
| 129 / 1 . | RT1-2-Xe/Ar light zone | 0.05 | 48.99 | 39.91 | 0.02 | -0.01 | -0.01 | 0.10 | 7.71 | -0.01 | -0.02 | -0.02 | 0.01 | -0.04 | -0.01 | 0.02 | 0.15 | 96.94 |
| 208 / 1 . | RT1-2-Xe/Ar light zone | 0.02 | 50.79 | 41.14 | 0.00 | 0.00 | 0.01 | 0.04 | 8.99 | 0.00 | 0.01 | -0.02 | -0.01 | 0.03 | 0.00 | -0.01 | -0.12 | 101.03 |
| 209 / 1 . | RT1-2-Xe/Ar light zone | 0.00 | 50.91 | 40.92 | 0.02 | 0.00 | -0.01 | 0.11 | 8.77 | 0.01 | 0.05 | -0.02 | 0.01 | 0.01 | 0.00 | -0.01 | -0.09 | 100.81 |
| 210 / 1 . | RT1-2-Xe/Ar light zone | 0.01 | 51.04 | 40.53 | 0.02 | 0.00 | -0.01 | 0.04 | 9.39 | -0.03 | -0.01 | -0.03 | -0.02 | 0.00 | -0.01 | -0.02 | -0.08 | 101.03 |
| 211 / 1 . | RT1-2-Xe/Ar light zone | 0.06 | 48.78 | 40.48 | 0.03 | -0.01 | 0.04 | 0.16 | 7.59 | 0.00 | 0.04 | -0.02 | -0.01 | 0.02 | 0.04 | 0.02 | 0.01 | 97.28 |
| 213 / 1 . | RT1-2-Xe/Ar light zone | 0.02 | 50.09 | 39.40 | 0.00 | 0.00 | 0.02 | 0.02 | 7.78 | -0.01 | 0.03 | -0.04 | -0.01 | -0.07 | -0.01 | -0.03 | 2.03 | 99.39 |
| **olivine + pyroxene** | | | | | | | | | | | | | | | | | | |
| 130 / 1 . | RT1-2-Xe/Ar light zone | 0.02 | 52.04 | 42.52 | -0.01 | -0.01 | 0.00 | 0.02 | 3.76 | 0.00 | -0.05 | -0.01 | -0.01 | -0.07 | 0.00 | 0.00 | -0.05 | 98.37 |

| | | | | | | | | | | | | | | | | | | |
|---|---|---|---|---|---|---|---|---|---|---|---|---|---|---|---|---|---|---|
| 131 / 1 . | RT1-2-Xe/Ar light zone | 0.00 | 52.36 | 42.67 | 0.00 | 0.00 | 0.01 | 0.10 | 3.84 | -0.01 | -0.02 | -0.03 | 0.02 | 0.15 | 0.02 | 0.00 | -0.07 | 99.17 |
| 200 / 1 . | RT1-2-Xe/Ar light zone | 0.02 | 50.59 | 43.17 | 0.00 | 0.00 | -0.01 | 0.12 | 4.71 | 0.00 | -0.02 | -0.01 | -0.02 | -0.05 | 0.02 | -0.03 | -0.03 | 98.64 |
| 201 / 1 . | RT1-2-Xe/Ar light zone | 0.02 | 51.14 | 42.96 | -0.01 | 0.01 | 0.01 | 0.06 | 4.31 | 0.01 | -0.02 | -0.03 | -0.03 | -0.05 | 0.02 | 0.00 | -0.04 | 98.55 |
| 202 / 1 . | RT1-2-Xe/Ar light zone | 0.02 | 52.30 | 41.90 | 0.03 | 0.01 | 0.00 | 0.08 | 5.42 | 0.00 | -0.03 | -0.02 | 0.00 | 0.00 | 0.03 | 0.03 | -0.06 | 99.85 |
| 205 / 1 . | RT1-2-Xe/Ar light zone | 0.03 | 51.94 | 43.35 | -0.02 | 0.00 | 0.02 | 0.08 | 3.13 | 0.00 | -0.01 | -0.02 | 0.01 | -0.18 | 0.00 | -0.02 | -0.08 | 98.56 |
| 206 / 1 . | RT1-2-Xe/Ar light zone | 0.01 | 50.69 | 42.99 | 0.02 | -0.01 | -0.01 | 0.08 | 4.32 | 0.02 | 0.03 | -0.02 | -0.01 | -0.14 | 0.00 | 0.00 | -0.03 | 98.16 |
| 207 / 1 . | RT1-2-Xe/Ar light zone | 0.03 | 52.38 | 44.20 | 0.01 | 0.00 | 0.01 | 0.08 | 2.44 | 0.02 | 0.02 | -0.02 | 0.04 | 0.04 | -0.01 | 0.01 | -0.07 | 99.27 |

*EMPA on recovered gasket after experiments (in orange wt% oxide total lower than 96% or higher than 102%).*

## Appendix D7/ Olivine cell parameters corrected from pressure effect

| HT2-1 Xe/Ar | *T* (K) | *P* (GPa) | *a* (Å) | corr. *a* (Å) | *b* (Å) | corr. *b* (Å) | *c* (Å) | corr. *c* (Å) |
|---|---|---|---|---|---|---|---|---|
| 29453 | 298 | 4.3 | 4.7604 | 4.7951 | 10.1882 | 10.3286 | 5.9789 | 6.0416 |
| 229460 | 372 | 3.6 | 4.7625 | 4.7919 | 10.1978 | 10.3169 | 5.9853 | 6.0384 |
| 229474 | 520 | 1.7 | 4.7683 | 4.7826 | 10.2251 | 10.2836 | 5.9979 | 6.0238 |
| 229486 | 647 | 1.6 | 4.7702 | 4.7837 | 10.2415 | 10.2967 | 6.0057 | 6.0302 |
| 229497 | 795 | 2.6 | 4.7721 | 4.7937 | 10.2470 | 10.3348 | 6.0089 | 6.0479 |
| 229508 | 947 | 3.0 | 4.7740 | 4.7987 | 10.2542 | 10.3547 | 6.0134 | 6.0581 |
| 229520 | 1123 | 4.6 | 4.7767 | 4.8136 | 10.2593 | 10.4086 | 6.0171 | 6.0838 |
| 229540 | 298 | 3.8 | 4.7581 | 4.7890 | 10.2094 | 10.3347 | 5.9880 | 6.0439 |
| **HT2-1 no gas** | | | | | | | | |
| 229465 | 372 | 0.9 | 4.7521 | 4.7598 | 10.1932 | 10.2247 | 6.0014 | 6.0153 |
| 229480 | 520 | 0.0 | 4.7594 | 4.7594 | 10.2221 | 10.2221 | 6.0122 | 6.0122 |
| 229491 | 647 | 0.0 | 4.7638 | 4.7638 | 10.2352 | 10.2352 | 6.0166 | 6.0166 |
| 229502 | 795 | 0.4 | 4.7660 | 4.7695 | 10.2404 | 10.2546 | 6.0176 | 6.0238 |
| 229513 | 947 | 1.0 | 4.7567 | 4.7652 | 10.2237 | 10.2587 | 6.0096 | 6.0251 |
| 229529 | 1123 | 2.1 | 4.7700 | 4.7876 | 10.2376 | 10.3093 | 6.0162 | 6.0480 |
| 229545 | 298 | 0.0 | 4.7534 | 4.7534 | 10.1832 | 10.1832 | 5.9865 | 5.9865 |
| **HT2-2 Xe/Ar** | | | | | | | | |
| 229643 | 298 | 4.1 | 4.7561 | 4.7893 | 10.2036 | 10.3380 | 5.9826 | 6.0426 |
| 229659 | 373 | 4.1 | 4.7594 | 4.7926 | 10.2093 | 10.3437 | 5.9848 | 6.0448 |
| 229672 | 523 | 3.4 | 4.7650 | 4.7928 | 10.2230 | 10.3360 | 5.9939 | 6.0442 |
| 229685 | 674 | 3.6 | 4.7662 | 4.7956 | 10.2329 | 10.3520 | 6.0029 | 6.0560 |
| 229695 | 802 | 4.5 | 4.7681 | 4.8043 | 10.2408 | 10.3872 | 6.0072 | 6.0726 |
| 229707 | 960 | 5.2 | 4.7709 | 4.8123 | 10.2476 | 10.4145 | 6.0118 | 6.0865 |
| 229717 | 1133 | 5.9 | 4.7737 | 4.8201 | 10.2535 | 10.4405 | 6.0160 | 6.0998 |
| 229727 | 1160 | 5.7 | 4.7741 | 4.8191 | 10.2594 | 10.4407 | 6.0178 | 6.0990 |
| 229740 | 298 | 3.5 | 4.7603 | 4.7889 | 10.2218 | 10.3379 | 5.9931 | 6.0448 |
| **HT2-2 no gas** | | | | | | | | |
| 229649 | 298 | 0.1 | 4.7519 | 4.7524 | 10.1813 | 10.1835 | 5.9896 | 5.9906 |
| 229664 | 373 | 0.0 | 4.7554 | 4.7554 | 10.1925 | 10.1925 | 5.9943 | 5.9943 |
| 229677 | 523 | 0.0 | 4.7617 | 4.7617 | 10.2139 | 10.2139 | 6.0070 | 6.0070 |
| 229690 | 674 | 0.1 | 4.7639 | 4.7716 | 10.2270 | 10.2585 | 6.0120 | 6.0259 |
| 229700 | 802 | 0.8 | 4.7659 | 4.7728 | 10.2326 | 10.2607 | 6.0171 | 6.0295 |
| 229712 | 960 | 1.5 | 4.7680 | 4.7807 | 10.2402 | 10.2920 | 6.0207 | 6.0437 |
| 229722 | 1133 | 2.4 | 4.7721 | 4.7921 | 10.2475 | 10.3289 | 6.0254 | 6.0616 |
| 229732 | 1160 | 2.3 | 4.7745 | 4.7937 | 10.2528 | 10.3309 | 6.0292 | 6.0639 |
| 229745 | 298 | - | 4.7522 | - | 10.1851 | - | 5.9893 | - |
| **HT2-4 Xe/Ar** | | | | | | | | |
| 229953 | 298 | 6.9 | 4.7377 | 4.7912 | 10.1350 | 10.3498 | 5.9504 | 6.0469 |
| 229964 | 523 | 4.0 | 4.7597 | 4.7921 | 10.2118 | 10.3432 | 5.9892 | 6.0478 |
| 229974 | 609 | 3.2 | 4.7634 | 4.7897 | 10.2241 | 10.3308 | 5.9971 | 6.0446 |
| 229982 | 722 | 4.3 | 4.7657 | 4.8004 | 10.2279 | 10.3683 | 6.0006 | 6.0633 |
| 229992 | 914 | 4.7 | 4.7688 | 4.8065 | 10.2308 | 10.3831 | 6.0086 | 6.0767 |
| 230000 | 1052 | 5.9 | 4.7722 | 4.8186 | 10.2479 | 10.4349 | 6.0081 | 6.0919 |
| 2300013 | 298 | 3.9 | 4.7606 | 4.7923 | 10.2019 | 10.3302 | 5.9887 | 6.0459 |
| **RT1-2 Xe/Ar** | | | | | | | | |
| 229756 | 298 | 3.6 | 4.7441 | 4.7735 | 10.1794 | 10.2985 | 5.9720 | 6.0251 |
| 229777 | 373 | 3.4 | 4.7465 | 4.7743 | 10.1831 | 10.2961 | 5.9729 | 6.0232 |
| 229791 | 523 | 2.6 | 4.7531 | 4.7747 | 10.1994 | 10.2872 | 5.9895 | 6.0285 |
| 229805 | 600 | 2.6 | 4.7545 | 4.7761 | 10.2047 | 10.2925 | 5.9905 | 6.0295 |
| 229820 | 657 | 3.1 | 4.7578 | 4.7833 | 10.2117 | 10.3154 | 5.9910 | 6.0371 |

| | | | | | | | | |
|---|---|---|---|---|---|---|---|---|
| 229830 | 780 | 3.6 | 4.7604 | 4.7898 | 10.2240 | 10.3431 | 5.9971 | 6.0502 |
| 229856 | 793 | 4.0 | 4.7596 | 4.7920 | 10.2217 | 10.3531 | 5.9969 | 6.0555 |
| 229864 | 875 | 4.2 | 4.7562 | 4.7901 | 10.2261 | 10.3635 | 6.0006 | 6.0619 |
| 229881 | 993 | 4.6 | 4.7575 | 4.7944 | 10.2306 | 10.3799 | 6.0028 | 6.0695 |
| 229888 | 1052 | 4.9 | 4.7556 | 4.7948 | 10.2315 | 10.3897 | 6.0060 | 6.0767 |
| 229902 | 1150 | 5.4 | 4.7635 | 4.8063 | 10.2377 | 10.4104 | 6.0047 | 6.0820 |
| 229912 | 1241 | 5.9 | 4.7645 | 4.8109 | 10.2414 | 10.4284 | 6.0068 | 6.0906 |
| 229920 | 1339 | 6.4 | 4.7650 | 4.8150 | 10.2479 | 10.4489 | 6.0096 | 6.0998 |
| 229933 | 298 | 3.2 | 4.7574 | 4.7837 | 10.2135 | 10.3202 | 5.9878 | 6.0353 |
| **Liu and Li (2006)** | | | | | | | | |
| | 1073 | 8.2 | 4.7253 | 4.7877 | 10.0537 | 10.3033 | 5.9275 | 6.0400 |
| | 1073 | 6.7 | 4.7364 | 4.7885 | 10.0997 | 10.3090 | 5.9504 | 6.0444 |
| | 1073 | 6.4 | 4.7385 | 4.7885 | 10.1091 | 10.3101 | 5.9573 | 6.0475 |
| | 1073 | 5.4 | 4.7428 | 4.7856 | 10.1487 | 10.3214 | 5.9775 | 6.0548 |
| | 873 | 7.7 | 4.7223 | 4.7813 | 10.0393 | 10.2757 | 5.9238 | 6.0302 |
| | 873 | 5.9 | 4.7322 | 4.7786 | 10.0994 | 10.2864 | 5.9511 | 6.0349 |
| | 873 | 4.8 | 4.7415 | 4.7799 | 10.1405 | 10.2957 | 5.9697 | 6.0391 |
| | 873 | 4 | 4.7504 | 4.7828 | 10.1649 | 10.2963 | 5.9809 | 6.0395 |
| | 673 | 7.3 | 4.7192 | 4.7755 | 10.0351 | 10.2608 | 5.9175 | 6.0190 |
| | 673 | 5.4 | 4.7314 | 4.7742 | 10.0924 | 10.2651 | 5.9454 | 6.0227 |
| | 673 | 4.3 | 4.7360 | 4.7707 | 10.1294 | 10.2698 | 5.9638 | 6.0265 |
| | 673 | 3.5 | 4.7310 | 4.7596 | 10.1658 | 10.2819 | 5.9783 | 6.0300 |
| | 673 | 2.7 | 4.7530 | 4.7754 | 10.1808 | 10.2718 | 5.9891 | 6.0296 |
| | 473 | 6.8 | 4.7164 | 4.7692 | 10.0282 | 10.2402 | 5.9124 | 6.0077 |
| | 473 | 5.1 | 4.7277 | 4.7683 | 10.0854 | 10.2494 | 5.9398 | 6.0132 |
| | 473 | 3.9 | 4.7256 | 4.7573 | 10.1309 | 10.2592 | 5.9584 | 6.0156 |
| | 473 | 3.2 | 4.7445 | 4.7708 | 10.1480 | 10.2547 | 5.9690 | 6.0165 |
| | 473 | 2.2 | 4.7499 | 4.7683 | 10.1783 | 10.2532 | 5.9857 | 6.0190 |
| | 298 | 6.5 | 4.7142 | 4.7649 | 10.0233 | 10.2271 | 5.9104 | 6.0019 |
| | 298 | 4.7 | 4.7251 | 4.7628 | 10.0769 | 10.2292 | 5.9367 | 6.0048 |
| | 298 | 3.6 | 4.7332 | 4.7626 | 10.1177 | 10.2368 | 5.9528 | 6.0059 |
| | 298 | 2.8 | 4.7427 | 4.7659 | 10.1426 | 10.2368 | 5.9644 | 6.0063 |
| | 298 | 0 | 4.7656 | 4.7656 | 10.2142 | 10.2142 | 6.0014 | 6.0014 |

*Cell parameters corrected (corr.) from pressure using a third-order isothermal Birch Murnaghan equation of state with bulk modulus and its derivative from Abramson et al. (1997). Error bar estimates are ± 0.008 Å for cell parameter* a, *± 0.01 Å for* b, *and ± 0.007 Å for* c.

## APPENDIX E/

### Appendix E1/ Calculated diagonal elements of Born effective charge tensor for pure α-quartz

| | $Si_1$ | $Si_2$ | $O_1$ | $O_2$ | $O_3$ |
|---|---|---|---|---|---|
| **X** | 3.005 | 3.526 | -1.330 | -1.409 | -2.317 |
| **Y** | 3.699 | 3.178 | -2.041 | -1.961 | -1.054 |
| **Z** | 3.462 | 3.462 | -1.735 | -1.735 | -1.735 |
| **Average** | 3.389 | 3.389 | -1.702 | -1.702 | -1.702 |

*Calculated diagonal elements of Born effective charge tensor of pure α-quartz.*

## Appendix E2/ Calculated evolution of cell parameters for Xe-bearing α-quartz

| 0 GPa | Xe (at%) | *a* (Å) | *b* (Å) | *c* (Å) | gamma (°) | alpha (°) | beta (°) | V (Å$^3$) | excess V (%) |
|---|---|---|---|---|---|---|---|---|---|
| **2x2x2 no Xe** | 0 | 5.029 | | 5.522 | 120.000 | 90.000 | 90.000 | 120.959 | - |
| **3x3x3 no Xe** | 0 | 5.031 | | 5.520 | 120.000 | 90.000 | 90.000 | 121.011 | - |
| **$Xe_{Si}$** | 1.4 | 5.026 | 5.043 | 5.593 | 119.888 | 91.132 | 90.000 | 122.859 | 1.6 |
| **$Xe_{I}$** | 1.4 | 5.084 | 5.084 | 5.532 | 119.939 | 89.446 | 90.559 | 123.907 | 2.4 |
| **$Xe_{O}$** | 1.4 | 5.094 | 5.138 | 5.573 | 120.152 | 88.736 | 90.599 | 126.059 | 4.2 |
| **$Xe_{Si}$** | 0.41 | 5.028 | 5.035 | 5.540 | 119.953 | 90.313 | 90.000 | 121.541 | 0.4 |
| **$Xe_{I}$** | 0.41 | 5.069 | 5.069 | 5.546 | 119.969 | 89.876 | 90.124 | 123.456 | 2.0 |
| **$Xe_{O}$** | 0.41 | 5.049 | 5.069 | 5.540 | 120.006 | 89.646 | 90.142 | 122.780 | 1.5 |
| **1.2 GPa** | | | | | | | | | |
| **2x2x2 no Xe** | 0 | 4.968 | | 5.470 | 120.000 | 90.000 | 90.000 | 116.916 | - |
| **3x3x3 no Xe** | 0 | 4.966 | | 5.466 | 120.000 | 90.000 | 90.000 | 116.822 | - |
| **$Xe_{Si}$** | 1.4 | 4.964 | 4.983 | 5.549 | 119.874 | 91.143 | 90.000 | 118.964 | 1.8 |
| **$Xe_{I}$** | 1.4 | 5.049 | 5.050 | 5.500 | 119.835 | 89.661 | 90.385 | 121.646 | 4.0 |
| **$Xe_{O}$** | 1.4 | 5.075 | 5.087 | 5.465 | 120.374 | 89.364 | 90.234 | 121.695 | 4.1 |
| **$Xe_{Si}$** | 0.41 | 4.966 | 4.974 | 5.489 | 119.947 | 90.324 | 90.000 | 117.491 | 0.6 |
| **$Xe_{I}$** | 0.41 | 5.010 | 5.010 | 5.486 | 120.100 | 90.399 | 89.607 | 119.109 | 2.0 |
| **$Xe_{O}$** | 0.41 | 4.985 | 5.007 | 5.485 | 119.983 | 89.702 | 90.067 | 118.590 | 1.5 |
| **2.65 GPa** | | | | | | | | | |
| **2x2x2 no Xe** | 0 | 4.905 | | 5.418 | 120.000 | 90.000 | 90.000 | 112.861 | - |
| **3x3x3 no Xe** | 0 | 4.904 | | 5.414 | 120.000 | 90.000 | 90.000 | 112.751 | - |
| **$Xe_{Si}$** | 1.4 | 4.898 | 4.922 | 5.502 | 119.835 | 91.115 | 90.000 | 115.031 | 1.9 |
| **$Xe_{I}$** | 1.4 | 5.002 | 5.003 | 5.454 | 119.869 | 89.866 | 90.129 | 118.354 | 4.9 |
| **$Xe_{O}$** | 1.4 | 5.016 | 5.018 | 5.413 | 120.278 | 89.473 | 90.146 | 117.656 | 4.2 |
| **$Xe_{Si}$** | 0.41 | 4.901 | 4.911 | 5.438 | 119.934 | 90.322 | 90.000 | 113.424 | 0.6 |
| **$Xe_{I}$** | 0.41 | 4.954 | 4.954 | 5.432 | 120.200 | 90.463 | 89.538 | 115.224 | 2.2 |
| **$Xe_{O}$** | 0.41 | 4.914 | 4.937 | 5.439 | 119.957 | 89.917 | 89.861 | 114.320 | 1.4 |

*Full evolution of cell parameters for the different Xe incorporation mechanisms at different pressures and Xe contents for α-quartz.*

## APPENDIX F/

## Appendix F1/ X-ray diffraction on starting sanidine powders

X-ray diffraction on sanidine powders (starting material) were obtained on diffractometer PANALYTICAL X'pert Pro MPD with Co anode (for sanidine Itrongahi), and Cu anode (for sanidine Nat. and Volkesfeld) at the IMPMC. Rietveld refinements using GSAS software are shown. Misfit for the most intense sanidine peak remains unexplained.

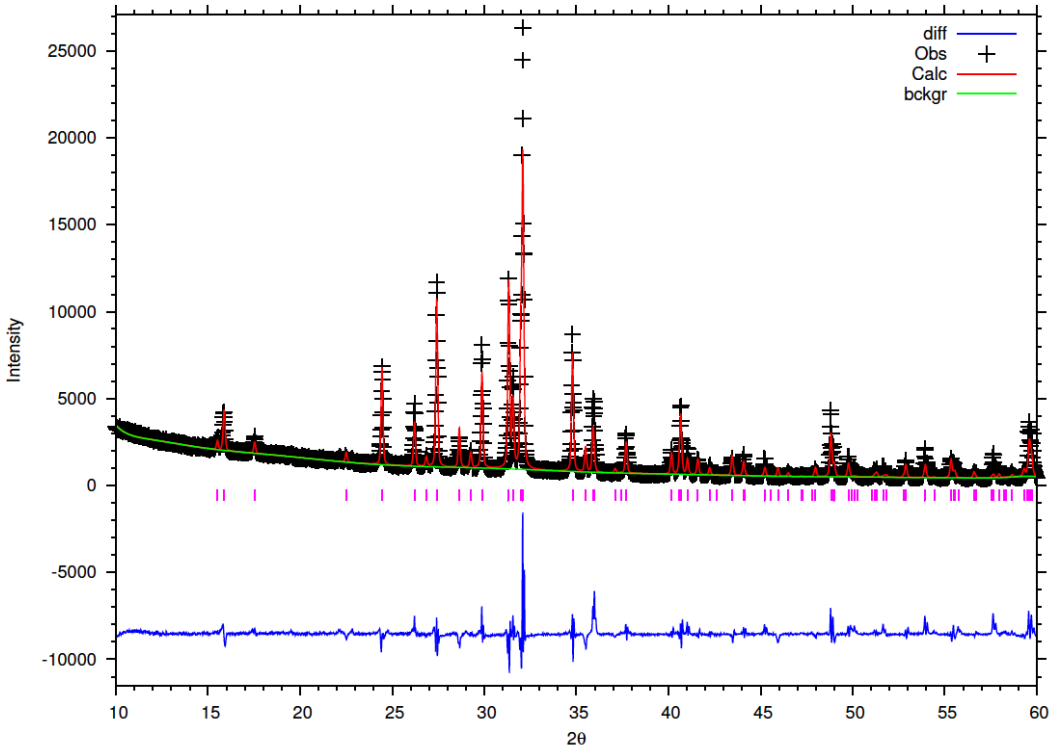


*Rietveld refinement for sanidine Itronghai at the Co K-edge.*

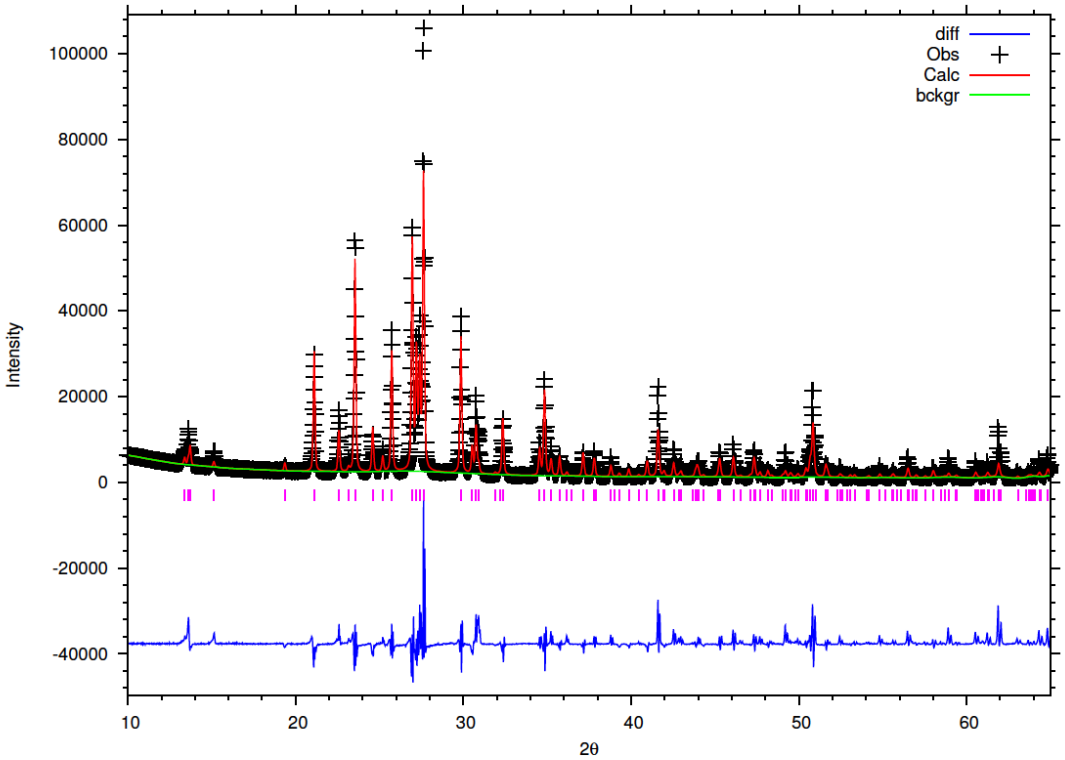


*Rietveld refinement for sanidine Volkesfeld at the Cu K-edge.*

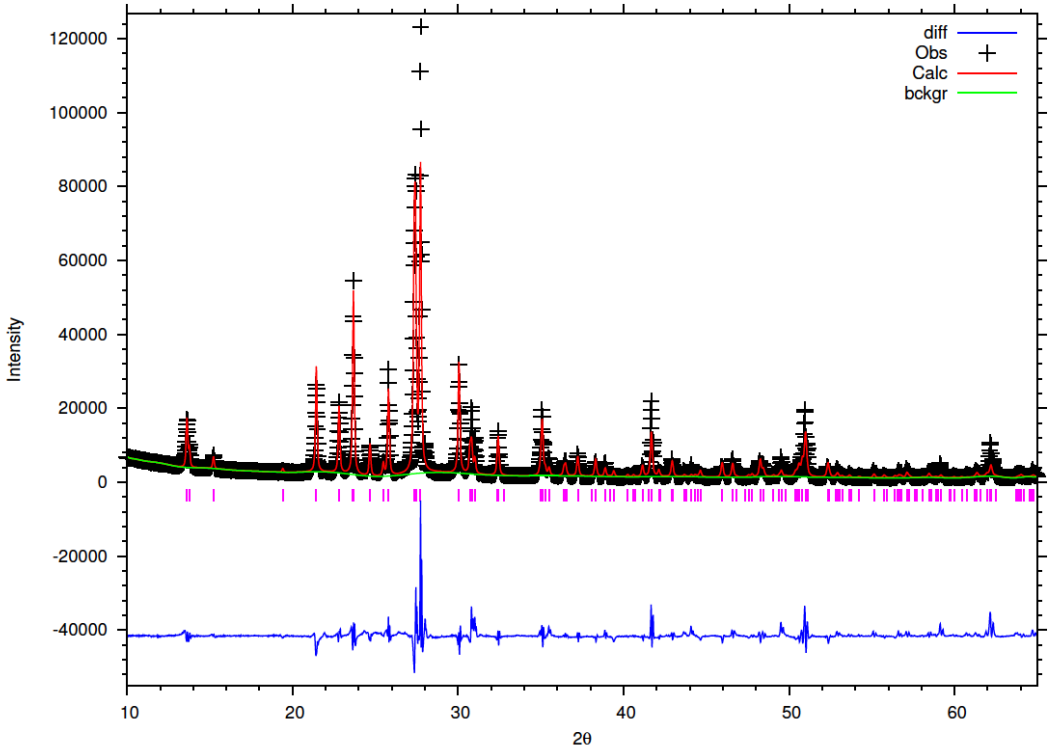


*Rietveld refinement for sanidine Nat. at the Cu K-edge.*

| sanidine | *a* (Å) | *b* (Å) | *c* (Å) | beta (°) | V (Å$^3$) |
|---|---|---|---|---|---|
| **Itrongahi** | 8.5748 (3) | 12.9858 (3) | 7.2026 (2) | 116.050 (3) | 720.55 (3) |
| **Nat.** | 8.3952 (4) | 12.9947 (5) | 7.1616 (3) | 116.113 (3) | 701.53 (3) |
| **Volkesfeld** | 8.5403 (4) | 13.0150 (5) | 7.1805 (2) | 115.989 (3) | 717.42 (3) |

*Cell parameters determined from Rietveld refinements.*

## Appendix F2/ EMPA of starting sanidine

| 2017-05-19 | | | | | | | | | | | | |
|---|---|---|---|---|---|---|---|---|---|---|---|---|
| **n° of analysis** | **Sample** | **$Na_2O$** | **MgO** | **$SiO_2$** | **$Al_2O_3$** | **$K_2O$** | **CaO** | **FeO** | **MnO** | **$TiO_2$** | **BaO** | **Total** |
| 83 / 1 . | San. Volk.. | 0.84 | 0.02 | 66.63 | 18.07 | 15.64 | -0.01 | 0.76 | 0.02 | 0.02 | 0.13 | 102.14 |
| 84 / 1 . | San. Volk. | 0.88 | 0.01 | 65.96 | 18.13 | 15.39 | -0.01 | 0.82 | 0.01 | 0.03 | 0.05 | 101.30 |
| 85 / 1 . | San. Volk. | 0.85 | 0.02 | 66.29 | 17.87 | 15.58 | -0.03 | 0.71 | 0.00 | 0.00 | 0.03 | 101.37 |
| 86 / 1 . | San. Volk. | 0.86 | 0.01 | 65.99 | 18.00 | 15.58 | -0.03 | 0.81 | 0.01 | -0.03 | 0.07 | 101.37 |
| 87 / 1 . | San. Volk. | 0.84 | 0.01 | 66.57 | 18.04 | 15.76 | -0.01 | 0.75 | -0.01 | -0.03 | 0.05 | 102.04 |
| 88 / 1 . | San. Volk. | 0.87 | 0.02 | 66.14 | 18.09 | 15.65 | -0.01 | 0.80 | -0.02 | 0.03 | -0.01 | 101.60 |
| 89 / 1 . | San. Volk. | 0.84 | 0.01 | 66.07 | 18.13 | 15.64 | -0.02 | 0.87 | -0.02 | 0.00 | 0.12 | 101.69 |
| 90 / 1 . | San. Volk. | 0.86 | 0.02 | 66.04 | 17.93 | 15.52 | -0.03 | 0.77 | 0.00 | 0.06 | 0.08 | 101.29 |
| 91 / 1 . | San. Volk. | 0.84 | 0.01 | 66.78 | 18.00 | 15.57 | -0.02 | 0.67 | 0.00 | -0.03 | 0.05 | 101.92 |
| 92 / 1 . | San. Volk. | 0.90 | 0.00 | 66.47 | 18.03 | 15.49 | -0.02 | 0.79 | 0.02 | 0.03 | 0.08 | 101.83 |
| 93 / 1 . | San. Volk. | 0.86 | 0.01 | 66.19 | 17.96 | 15.54 | -0.02 | 0.79 | 0.02 | 0.02 | 0.06 | 101.45 |
| 94 / 1 . | sanidine_Nat | 5.17 | 0.00 | 66.26 | 19.61 | 9.22 | 0.55 | 0.16 | 0.02 | 0.03 | 0.32 | 101.34 |
| 95 / 1 . | San. Nat. | 5.06 | -0.01 | 66.25 | 19.82 | 9.47 | 0.61 | 0.17 | 0.01 | 0.04 | 0.26 | 101.69 |
| 96 / 1 . | San. Nat. | 5.06 | 0.00 | 66.75 | 19.72 | 9.19 | 0.58 | 0.20 | 0.02 | 0.02 | 0.41 | 101.95 |
| 97 / 1 . | San. Nat. | 5.11 | 0.01 | 66.68 | 19.71 | 9.56 | 0.64 | 0.26 | 0.00 | 0.03 | 0.34 | 102.35 |
| 98 / 1 . | San. Nat. | 5.28 | 0.01 | 66.64 | 19.73 | 9.19 | 0.65 | 0.21 | 0.00 | 0.05 | 0.32 | 102.10 |
| 99 / 1 . | San. Nat. | 5.11 | 0.00 | 66.08 | 19.64 | 9.21 | 0.63 | 0.24 | 0.00 | 0.07 | 0.43 | 101.41 |
| 100 / 1 . | San. Nat. | 5.21 | 0.01 | 66.08 | 19.56 | 9.22 | 0.63 | 0.23 | -0.04 | 0.07 | 0.39 | 101.42 |
| 101 / 1 . | San. Nat.t | 5.26 | 0.00 | 66.37 | 19.72 | 9.14 | 0.76 | 0.22 | -0.02 | 0.04 | 0.28 | 101.79 |
| 102 / 1 . | San. Nat. | 5.30 | 0.00 | 66.02 | 19.67 | 9.16 | 0.65 | 0.19 | -0.01 | 0.02 | 0.37 | 101.39 |
| 103 / 1 . | San. Nat. | 5.20 | 0.00 | 65.88 | 19.59 | 9.17 | 0.63 | 0.22 | 0.01 | 0.01 | 0.32 | 101.04 |
| 104 / 1 . | San. Nat. | 5.24 | 0.01 | 65.70 | 19.71 | 9.39 | 0.66 | 0.27 | 0.01 | 0.00 | 0.41 | 101.39 |
| 105 / 1 . | San. Nat. | 8.53 | 0.01 | 63.86 | 23.45 | 1.75 | 4.13 | 0.41 | 0.01 | 0.04 | -0.09 | 102.19 |
| 106 / 1 . | San. Nat. | 5.22 | 0.00 | 65.86 | 19.80 | 9.03 | 0.70 | 0.26 | 0.00 | 0.03 | 0.29 | 101.19 |

| | | | | | | | | | | | | |
|---|---|---|---|---|---|---|---|---|---|---|---|---|
| 107 / 1 . | San. Nat. | 5.21 | 0.00 | 66.05 | 19.74 | 9.24 | 0.61 | 0.25 | -0.01 | 0.02 | 0.25 | 101.37 |
| 108 / 1 . | San. Nat. | 5.34 | -0.01 | 66.16 | 19.68 | 8.96 | 0.69 | 0.22 | 0.01 | 0.01 | 0.33 | 101.42 |
| 109 / 1 . | San. Nat. | 5.33 | -0.01 | 65.28 | 19.61 | 9.12 | 0.68 | 0.22 | -0.05 | 0.01 | 0.38 | 100.65 |
| 110 / 1 . | San. Nat. | 5.27 | 0.00 | 65.41 | 19.71 | 9.30 | 0.70 | 0.23 | -0.01 | 0.02 | 0.20 | 100.85 |
| | | | | | | | | | | | | |
| 111 / 1 . | San. Itrongahi | 1.75 | 0.00 | 65.03 | 19.11 | 13.86 | -0.01 | 0.17 | 0.01 | -0.04 | 1.14 | 101.08 |
| 112 / 1 . | San. Itrongahi | 1.85 | 0.00 | 64.89 | 19.12 | 13.95 | 0.00 | 0.17 | -0.01 | 0.02 | 1.14 | 101.16 |
| 113 / 1 . | San. Itrongahi | 1.80 | -0.01 | 65.11 | 19.09 | 14.18 | -0.01 | 0.14 | -0.04 | -0.01 | 1.12 | 101.45 |
| 114 / 1 . | San. Itrongahi | 1.86 | 0.00 | 64.84 | 18.99 | 13.92 | 0.01 | 0.12 | -0.04 | -0.02 | 0.97 | 100.71 |
| 115 / 1 . | San. Itrongahi | 1.80 | 0.01 | 64.77 | 19.03 | 14.14 | -0.03 | 0.24 | -0.02 | -0.01 | 1.12 | 101.15 |
| 116 / 1 . | San. Itrongahi | 1.83 | 0.01 | 63.99 | 19.03 | 14.00 | 0.00 | 0.20 | 0.03 | -0.03 | 0.90 | 100.00 |
| 117 / 1 . | San. Itrongahi | 1.85 | 0.00 | 63.90 | 19.12 | 14.22 | 0.00 | 0.13 | -0.02 | 0.04 | 0.95 | 100.23 |
| 118 / 1 . | San. Itrongahi | 1.84 | 0.00 | 65.26 | 19.15 | 14.03 | -0.01 | 0.19 | -0.02 | -0.01 | 0.93 | 101.41 |
| 119 / 1 . | San. Itrongahi | 1.91 | -0.01 | 65.63 | 18.99 | 14.05 | 0.00 | 0.12 | -0.01 | -0.01 | 1.12 | 101.82 |
| 120 / 1 . | San. Itrongahi | 1.80 | 0.00 | 65.52 | 19.09 | 13.94 | 0.01 | 0.24 | -0.03 | 0.00 | 1.06 | 101.66 |
| 121 / 1 . | San. Itrongahi | 1.71 | 0.00 | 65.30 | 19.17 | 14.08 | 0.00 | 0.19 | 0.02 | -0.01 | 0.98 | 101.47 |
| 122 / 1 . | San. Itrongahi | 1.85 | 0.01 | 65.33 | 19.15 | 14.06 | 0.00 | 0.15 | -0.02 | -0.02 | 1.04 | 101.60 |
| 123 / 1 . | San. Itrongahi | 1.83 | -0.01 | 64.93 | 19.05 | 14.10 | -0.01 | 0.16 | 0.00 | -0.02 | 0.86 | 100.93 |
| 124 / 1 . | San. Itrongahi | 1.83 | 0.01 | 65.09 | 19.23 | 13.93 | -0.03 | 0.15 | 0.01 | 0.01 | 1.07 | 101.36 |
| 125 / 1 . | San. Itrongahi | 1.82 | -0.01 | 65.05 | 19.05 | 14.09 | -0.01 | 0.15 | -0.01 | -0.02 | 1.01 | 101.18 |

*EMPA recorded on starting sanidine (San.) material Volk. = Volkesfeld (in orange wt% oxide total lower than 96% or higher than 102%).*

## Appendix F3/ EMPA of synthesized sanidine samples

| Previous EMPA (CAMECA SX5) n° of analysis | sample | $Na_2O$ | MgO | $SiO_2$ | $Al_2O_3$ | Ar | $K_2O$ | CaO | FeO | MnO | $TiO_2$ | Kr | Xe | BaO | $Cr_2O_3$ | NiO | $Re_2O_7$ | Total |
|---|---|---|---|---|---|---|---|---|---|---|---|---|---|---|---|---|---|---|
| **Pyroxene** | | | | | | | | | | | | | | | | | | |
| 25 / 1 . | PC63 | 5.35 | | 64.08 | 17.65 | 0.79 | 7.12 | 1.02 | 1.19 | | | | 1.74 | | | | | 98.93 |
| 26 / 1 . | PC63 | 0.83 | | 69.31 | 18.35 | 0.83 | 3.58 | 1.09 | 1.25 | | | | 1.81 | | | | | 97.04 |
| 27 / 1 . | PC63 | 5.08 | | 65.99 | 17.27 | 0.85 | 6.66 | 0.98 | 1.41 | | | | 1.81 | | | | | 100.06 |
| 28 / 1 . | PC63 | 3.84 | | 66.20 | 16.80 | 0.85 | 6.89 | 0.99 | 1.14 | | | | 2.04 | | | | | 98.75 |
| 29 / 1 . | PC63 | 5.07 | | 66.09 | 15.94 | 0.81 | 6.48 | 0.97 | 1.95 | | | | 1.88 | | | | | 99.20 |
| 30 / 1 . | PC63 | 4.59 | | 65.39 | 17.64 | 0.80 | 6.79 | 1.06 | 2.35 | | | | 1.70 | | | | | 100.32 |
| 31 / 1 . | PC63 | 5.27 | | 64.70 | 17.08 | 0.80 | 6.81 | 1.14 | 2.19 | | | | 1.70 | | | | | 99.69 |
| **Glass** | | | | | | | | | | | | | | | | | | |
| 32 / 1 . | PC63 | 4.65 | | 61.57 | 18.09 | 0.66 | 7.25 | 0.88 | 0.08 | | | | 2.30 | | | | | 95.48 |
| 33 / 1 . | PC63 | 4.89 | | 61.57 | 18.45 | 0.66 | 6.99 | 0.67 | 0.13 | | | | 2.42 | | | | | 95.78 |
| 34 / 1 . | PC63 | 4.62 | | 61.40 | 18.33 | 0.65 | 7.33 | 0.71 | -0.14 | | | | 2.45 | | | | | 95.35 |
| **Sanidine** | | | | | | | | | | | | | | | | | | |
| 35 / 1 . | PC63 | 4.24 | | 64.93 | 19.67 | 0.02 | 9.36 | 0.68 | 0.21 | | | | 0.00 | | | | | 99.11 |
| 36 / 1 . | PC63 bubble | 4.72 | | 64.88 | 20.37 | 0.15 | 9.08 | 1.31 | 0.07 | | | | 0.90 | | | | | 101.47 |
| 37 / 1 . | PC63 bubble | 4.45 | | 64.98 | 18.42 | 0.02 | 9.69 | 0.52 | 0.15 | | | | -0.02 | | | | | 98.23 |
| 38 / 1 . | PC63 bubble | 4.31 | | 65.87 | 18.86 | 0.18 | 9.67 | 0.57 | 0.03 | | | | 0.55 | | | | | 100.04 |
| 39 / 1 . | PC63 | 4.11 | | 66.08 | 18.64 | 0.01 | 10.01 | 0.41 | -0.03 | | | | 0.00 | | | | | 99.23 |
| 40 / 1 . | PC63 bubble | 4.51 | | 64.87 | 20.05 | 0.47 | 9.46 | 0.89 | 0.04 | | | | 2.51 | | | | | 102.79 |
| | | | | | | | | | | | | | | | | | | |
| **Pyroxene** | | | | | | | | | | | | | | | | | | |
| 13 / 1 . | PC66 | 0.45 | | 52.54 | 1.09 | -0.02 | 0.07 | 23.19 | 8.77 | | | | -0.03 | | | | | 86.06 |
| 14 / 1 . | PC66 | 0.48 | | 51.36 | 1.16 | -0.01 | 0.08 | 22.76 | 8.36 | | | | 0.00 | | | | | 84.20 |
| 15 / 1 . | PC66 | 0.89 | | 51.12 | 2.28 | 0.00 | 0.11 | 21.44 | 7.99 | | | | -0.03 | | | | | 83.80 |
| **Sanidine** | | | | | | | | | | | | | | | | | | |
| 16 / 1 . | PC66 Fe-rich zone | 5.32 | | 59.87 | 15.21 | 0.47 | 5.60 | 2.33 | 5.07 | | | | 1.23 | | | | | 95.09 |

| | | | | | | | | | | |
|---|---|---|---|---|---|---|---|---|---|---|
| 17 / 1 . | PC66 Fe-rich zone | 5.31 | 63.08 | 16.44 | 0.56 | 6.25 | 1.44 | 2.26 | 1.47 | 96.82 |
| 18 / 1 . | PC66 Fe-rich zone | 4.56 | 63.31 | 16.84 | 0.58 | 6.25 | 1.65 | 2.27 | 1.50 | 96.96 |
| 19 / 1 | PC66 Fe-rich zone | 5.27 | 62.04 | 14.86 | 0.51 | 5.90 | 1.86 | 4.87 | 1.29 | 96.60 |
| 20 / 1 . | PC66 Fe-rich zone | 5.11 | 60.84 | 15.05 | 0.59 | 5.34 | 2.21 | 5.13 | 1.46 | 95.73 |
| 21 / 1 . | PC66 | 4.83 | 66.01 | 19.44 | 0.01 | 8.96 | 0.73 | 0.03 | 0.00 | 100.03 |
| 22 / 1 . | PC66 | 4.66 | 65.41 | 19.38 | 0.02 | 8.83 | 0.65 | 0.04 | 0.01 | 98.98 |
| 23 / 1 . | PC66 | 4.56 | 65.09 | 19.19 | 0.04 | 9.35 | 0.78 | 0.25 | 0.07 | 99.33 |
| 24 / 1 . | PC66 | 5.20 | 66.57 | 19.10 | 0.01 | 9.23 | 0.72 | 0.25 | 0.02 | 101.11 |
| 25 / 1 . | PC66 | 4.72 | 66.73 | 19.31 | 0.02 | 9.20 | 0.72 | 0.21 | -0.02 | 100.89 |
| 26 / 1 . | PC66 | 4.81 | 66.02 | 19.26 | 0.02 | 8.96 | 0.75 | 0.25 | 0.01 | 100.08 |
| 27 / 1 . | PC66 | 4.77 | 66.27 | 19.24 | 0.02 | 9.23 | 0.68 | 0.24 | 0.02 | 100.45 |
| 28 / 1 . | PC66 bubble | 5.64 | 63.78 | 19.77 | 0.67 | 7.04 | 1.39 | 0.00 | 3.89 | 102.18 |
| 29 / 1 . | PC66 bubble | 4.68 | 59.42 | 17.35 | 0.66 | 8.73 | 0.65 | 0.10 | 7.72 | 99.30 |
| 30 / 1 . | PC66 bubble | 4.83 | 61.97 | 19.46 | 1.95 | 8.11 | 0.62 | 0.07 | 10.54 | 107.54 |
| 31 / 1 . | PC66 bubble | 4.36 | 57.47 | 18.23 | 1.23 | 7.80 | 0.65 | -0.12 | 6.61 | 96.22 |
| 32 / 1 . | PC66 | 4.90 | 65.04 | 19.49 | 0.02 | 9.01 | 0.75 | 0.25 | -0.04 | 99.42 |
| 32 / 2 . | PC66 | 4.70 | 66.92 | 19.38 | 0.01 | 8.56 | 0.68 | 0.13 | 0.00 | 100.39 |
| 32 / 3 . | PC66 | 5.00 | 65.62 | 19.68 | 0.04 | 8.95 | 0.69 | 0.08 | 0.13 | 100.19 |
| 32 / 4 . | PC66 | 5.01 | 66.45 | 19.50 | 0.01 | 9.19 | 0.54 | 0.35 | 0.00 | 101.05 |
| 32 / 5 . | PC66 | 5.04 | 66.89 | 19.75 | 0.02 | 9.06 | 0.72 | 0.13 | 0.02 | 101.64 |
| 32 / 6 . | PC66 | 4.92 | 65.33 | 19.02 | 0.22 | 9.36 | 0.69 | -0.04 | 1.06 | 100.56 |
| 32 / 7 . | PC66 | 4.72 | 65.99 | 18.81 | 0.02 | 9.05 | 0.68 | 0.20 | 0.00 | 99.48 |
| 32 / 8 . | PC66 | 4.63 | 65.01 | 19.84 | 0.01 | 9.67 | 0.64 | 0.18 | 0.01 | 100.00 |
| 32 / 9 . | PC66 | 4.50 | 65.11 | 19.44 | 0.06 | 9.11 | 0.67 | 0.17 | 0.33 | 99.38 |
| 32 / 10 . | PC66 | 4.95 | 65.55 | 19.80 | 0.03 | 8.98 | 0.65 | -0.11 | -0.01 | 99.83 |
| 32 / 11 . | PC66 | 4.85 | 66.31 | 19.72 | 0.03 | 9.22 | 0.56 | 0.28 | 0.00 | 100.97 |
| 32 / 12 . | PC66 | 4.74 | 66.18 | 19.03 | 0.03 | 9.60 | 0.64 | 0.15 | 0.01 | 100.39 |
| 32 / 13 . | PC66 | 4.86 | 65.04 | 18.30 | 0.03 | 9.64 | 0.60 | 0.23 | 0.03 | 98.71 |
| 32 / 14 . | PC66 | 5.40 | 65.48 | 17.97 | 0.02 | 7.17 | 1.28 | 1.10 | 0.03 | 98.44 |
| 32 / 15 . | PC66 | 4.95 | 65.35 | 18.64 | 0.02 | 8.66 | 0.64 | 0.00 | 0.05 | 98.30 |

| | | | | | | | | | | | | | | | | | |
|---|---|---|---|---|---|---|---|---|---|---|---|---|---|---|---|---|---|
| 32 / 16 . | PC66 | 4.85 | | 63.13 | 18.90 | 0.01 | 9.43 | 0.77 | -0.01 | | | 0.00 | | | | | 97.06 |
| 32 / 17 . | PC66 | 4.91 | | 66.35 | 19.78 | 0.01 | 9.15 | 0.79 | 0.01 | | | 0.00 | | | | | 101.00 |
| 32 / 18 . | PC66 | 4.91 | | 66.54 | 18.90 | 0.02 | 8.21 | 0.84 | 0.79 | | | 0.02 | | | | | 100.23 |
| 32 / 19 . | PC66 | 4.30 | | 57.70 | 16.53 | 0.02 | 7.76 | 0.69 | 0.13 | | | 0.01 | | | | | 87.13 |
| 32 / 20 . | PC66 | 4.91 | | 67.32 | 19.44 | 0.01 | 8.97 | 0.82 | -0.06 | | | 0.02 | | | | | 101.43 |
| **Sanidine** | | | | | | | | | | | | | | | | | |
| 33 / 1 . | PC67 | 4.41 | | 65.62 | 19.38 | 0.01 | 9.06 | 0.71 | 0.20 | | | -0.02 | | | | | 99.38 |
| 34 / 1 . | PC67 | 4.69 | | 66.65 | 19.73 | 0.01 | 9.67 | 0.59 | 0.06 | | | 0.02 | | | | | 101.42 |
| 35 / 1 . | PC67 | 4.67 | | 66.52 | 19.15 | 0.01 | 9.40 | 0.64 | 0.23 | | | -0.01 | | | | | 100.61 |
| 36 / 1 . | PC67 | 4.42 | | 67.60 | 19.78 | 0.01 | 8.98 | 0.51 | 0.18 | | | 0.00 | | | | | 101.49 |
| 37 / 1 . | PC67 | 4.90 | | 67.24 | 19.40 | 0.01 | 9.18 | 0.62 | 0.28 | | | -0.02 | | | | | 101.62 |
| 39 / 1 . | PC67 | 4.57 | | 67.13 | 20.07 | 0.03 | 9.65 | 0.59 | 0.15 | | | 0.05 | | | | | 102.25 |
| 40 / 1 . | PC67 brigh dot | 5.21 | | 61.78 | 17.26 | 0.02 | 8.62 | 0.64 | 0.18 | | | -0.02 | | | | | 93.68 |
| 41 / 1 . | PC67 light zone | 4.11 | | 63.67 | 15.73 | 0.88 | 5.54 | 1.81 | 1.88 | | | 1.91 | | | | | 95.53 |
| 42 / 1 . | PC67 bubble | 4.53 | | 56.71 | 17.48 | 1.09 | 7.98 | 0.68 | 0.00 | | | 6.51 | | | | | 94.96 |
| 43 / 1 . | PC67 bubble | 4.54 | | 57.49 | 17.10 | 1.47 | 7.64 | 0.66 | -0.11 | | | 9.32 | | | | | 98.10 |
| 44 / 1 . | PC67 bubble | 4.71 | | 62.21 | 18.69 | 0.55 | 8.13 | 0.79 | -0.08 | | | 4.58 | | | | | 99.57 |
| **?** | | | | | | | | | | | | | | | | | |
| 38 / 1 . | PC67 | 6.15 | | 59.64 | 25.73 | 0.03 | 1.56 | 7.66 | 0.20 | | | -0.05 | | | | | 100.93 |

| **2018-03-15** | | | | | | | | | | | | | | | | | |
|---|---|---|---|---|---|---|---|---|---|---|---|---|---|---|---|---|---|
| **n° of analysis** | **sample** | **$Na_2O$** | **MgO** | **$SiO_2$** | **$Al_2O_3$** | **Ar** | **$K_2O$** | **CaO** | **FeO** | **MnO** | **$TiO_2$** | **Kr** | **Xe** | **BaO** | **$Cr_2O_3$** | **NiO** | **$Re_2O_7$** | **Total** |
| **Sanidine** | | | | | | | | | | | | | | | | | |
| 74 / 1 . | PC103 | 0.85 | 0.02 | 62.22 | 17.31 | 0.00 | 15.35 | 0.00 | 0.95 | 0.00 | 0.01 | 0.00 | 0.03 | 0.23 | 0.00 | | | 96.97 |
| 75 / 1 . | PC103 | 0.81 | 0.00 | 62.85 | 18.24 | 0.00 | 15.83 | 0.00 | 0.21 | 0.00 | 0.03 | 0.00 | 0.00 | 0.05 | 0.00 | | | 98.03 |
| 76 / 1 . | PC103 | 0.82 | 0.01 | 63.08 | 17.86 | 0.00 | 15.96 | 0.00 | 0.64 | 0.00 | 0.00 | 0.00 | 0.09 | 0.20 | 0.00 | | | 98.67 |
| 77 / 1 . | PC103 | 0.86 | 0.01 | 63.54 | 17.87 | 0.02 | 15.62 | 0.00 | 0.48 | 0.00 | 0.02 | 0.00 | 0.02 | 0.17 | 0.01 | | | 98.62 |
| 81 / 1 . | PC103 | 0.69 | 0.00 | 60.74 | 18.14 | 0.04 | 14.78 | 0.00 | 0.08 | 0.03 | 0.07 | 0.20 | 1.45 | 0.00 | 0.00 | | | 96.19 |

| | | | | | | | | | | | | | | | | |
|---|---|---|---|---|---|---|---|---|---|---|---|---|---|---|---|---|
| 82 / 1 . | PC103 | 0.68 | 0.00 | 58.53 | 16.89 | 0.08 | 13.90 | 0.00 | 0.39 | 0.03 | 0.20 | 0.30 | 2.42 | 0.26 | 0.00 | 93.63 |
| 84 / 1 . | PC103 | 0.64 | 0.01 | 55.75 | 17.14 | 0.07 | 12.99 | 0.00 | 0.07 | 0.03 | 0.24 | 0.94 | 4.96 | 0.05 | 0.00 | 92.78 |
| 85 / 1 . | PC103 | 0.68 | 0.01 | 56.62 | 16.65 | 0.12 | 13.73 | 0.00 | 0.23 | 0.00 | 0.24 | 0.75 | 3.67 | 0.00 | 0.00 | 92.61 |
| 86 / 1 . | PC103 | 0.78 | 0.05 | 60.03 | 17.19 | 0.06 | 15.02 | 0.00 | 0.75 | 0.00 | 0.05 | 0.15 | 0.59 | 0.40 | 0.01 | 95.05 |
| 88 / 1 . | PC103 | 0.72 | 0.01 | 61.12 | 18.27 | 0.03 | 14.62 | 0.00 | 0.15 | 0.01 | 0.06 | 0.12 | 1.06 | 0.00 | 0.00 | 96.14 |
| 89 / 1 . | PC103 | 1.03 | 0.00 | 56.51 | 16.51 | 0.13 | 13.90 | 0.00 | 0.25 | 0.05 | 0.21 | 0.94 | 3.35 | 0.00 | 0.00 | 92.80 |
| 90 / 1 . | PC103 | 0.78 | 0.00 | 57.59 | 17.12 | 0.06 | 14.28 | 0.00 | 0.19 | 0.00 | 0.05 | 0.55 | 2.05 | 0.22 | 0.00 | 92.84 |
| 92 / 1 . | PC103 | 0.73 | 0.01 | 56.95 | 16.82 | 0.06 | 14.40 | 0.01 | 0.78 | 0.00 | 0.16 | 0.43 | 2.49 | 0.31 | 0.00 | 93.10 |
| 93 / 1 . | PC103 | 0.70 | 0.02 | 57.99 | 17.44 | 0.03 | 14.26 | 0.00 | 0.21 | 0.00 | 0.11 | 0.22 | 1.18 | 0.01 | 0.00 | 92.16 |
| 94 / 1 . | PC103 | 0.76 | 0.00 | 57.58 | 17.14 | 0.03 | 15.20 | 0.00 | 0.37 | 0.00 | 0.09 | 0.18 | 1.34 | 0.00 | 0.00 | 92.66 |
| 95 / 1 . | PC103 | 0.75 | 0.00 | 54.78 | 16.30 | 0.07 | 14.19 | 0.00 | 0.28 | 0.00 | 0.09 | 0.67 | 2.34 | 0.00 | 0.00 | 89.40 |
| **sanidine/Fe-rich zone** | | | | | | | | | | | | | | | | |
| 73 / 1 . | PC103 | 1.39 | 0.09 | 63.16 | 15.24 | 0.00 | 14.27 | 0.02 | 2.61 | 0.00 | 0.07 | 0.06 | 0.13 | 0.15 | 0.00 | 97.20 |
| 83 / 1 . | PC103 | 1.26 | 0.11 | 59.37 | 11.21 | 0.05 | 11.54 | 0.08 | 6.27 | 0.00 | 0.00 | 0.51 | 1.14 | 0.20 | 0.00 | 91.71 |
| 91 / 1 . | PC103 | 1.13 | 0.07 | 59.63 | 15.77 | 0.01 | 14.75 | 0.00 | 2.55 | 0.00 | 0.01 | 0.09 | 0.42 | 0.05 | 0.00 | 94.48 |
| 96 / 1 . | PC103 | 0.82 | 0.02 | 57.15 | 16.69 | 0.00 | 15.03 | 0.00 | 1.24 | 0.00 | 0.00 | 0.00 | 0.02 | 0.37 | 0.02 | 91.35 |
| 97 / 1 . | PC103 | 0.92 | 0.04 | 57.36 | 15.89 | 0.03 | 14.99 | 0.02 | 1.28 | 0.00 | 0.01 | 0.31 | 1.00 | 0.00 | 0.00 | 91.82 |
| **Sanidine** | | | | | | | | | | | | | | | | |
| 98 / 1 . | PC67 | 5.02 | 0.02 | 64.54 | 18.95 | 0.02 | 9.10 | 0.67 | 0.29 | 0.02 | 0.11 | 0.00 | 0.00 | 0.47 | 0.06 | 99.28 |
| 99 / 1 . | PC67 | 5.15 | 0.02 | 67.28 | 19.71 | 0.00 | 9.57 | 0.66 | 0.18 | 0.00 | 0.10 | 0.00 | 0.00 | 0.43 | 0.02 | 103.10 |
| 100 / 1 . | PC67 | 5.18 | 0.02 | 67.24 | 20.16 | 0.02 | 9.06 | 0.65 | 0.13 | 0.00 | 0.02 | 0.00 | 0.04 | 0.28 | 0.00 | 102.80 |
| 101 / 1 . | PC67 | 5.16 | 0.00 | 67.37 | 19.32 | 0.02 | 9.30 | 0.68 | 0.18 | 0.00 | 0.02 | 0.00 | 0.00 | 0.54 | 0.00 | 102.59 |
| 102 / 1 . | PC67 | 4.97 | 0.02 | 66.76 | 19.44 | 0.01 | 9.18 | 0.61 | 0.14 | 0.01 | 0.11 | 0.10 | 0.33 | 0.47 | 0.00 | 102.14 |
| 103 / 1 . | PC67 | 5.25 | 0.00 | 67.90 | 20.12 | 0.00 | 9.57 | 0.63 | 0.24 | 0.00 | 0.00 | 0.00 | 0.03 | 0.40 | 0.00 | 104.14 |
| 104 / 1 . | PC67 | 5.26 | 0.01 | 66.51 | 19.45 | 0.02 | 9.23 | 0.73 | 0.21 | 0.00 | 0.05 | 0.04 | 0.01 | 0.54 | 0.00 | 102.06 |
| 105 / 1 . | PC67 | 5.12 | 0.00 | 66.68 | 19.55 | 0.00 | 9.93 | 0.76 | 0.20 | 0.03 | 0.11 | 0.00 | 0.00 | 0.21 | 0.00 | 102.59 |
| 106 / 1 . | PC67 | 5.03 | 0.01 | 66.70 | 19.28 | 0.02 | 9.26 | 0.64 | 0.22 | 0.03 | 0.04 | 0.00 | 0.07 | 0.67 | 0.00 | 101.98 |
| 107 / 1 . | PC67 | 5.09 | 0.01 | 66.60 | 19.61 | 0.01 | 9.41 | 0.71 | 0.22 | 0.00 | 0.12 | 0.00 | 0.00 | 0.03 | 0.00 | 101.80 |

| | | | | | | | | | | | | | | | | |
|---|---|---|---|---|---|---|---|---|---|---|---|---|---|---|---|---|
| 108 / 1 . | PC67 | 5.31 | 0.01 | 65.36 | 19.83 | 0.00 | 9.00 | 0.86 | 0.01 | 0.00 | 0.04 | 0.00 | 0.00 | 0.29 | 0.00 | 100.71 |
| 109 / 1 . | PC67 | 5.03 | 0.00 | 64.57 | 19.08 | 0.03 | 9.24 | 0.67 | 0.22 | 0.00 | 0.00 | 0.25 | 0.83 | 0.29 | 0.00 | 100.19 |
| 110 / 1 . | PC67 | 5.09 | 0.00 | 64.86 | 19.51 | 0.02 | 8.97 | 0.71 | 0.04 | 0.00 | 0.05 | 0.38 | 1.05 | 0.47 | 0.00 | 101.11 |
| 111 / 1 . | PC67 | 5.24 | 0.00 | 66.35 | 19.15 | 0.01 | 9.24 | 0.67 | 0.19 | 0.09 | 0.02 | 0.10 | 0.36 | 0.22 | 0.00 | 101.63 |
| 112 / 1 . | PC67 | 5.34 | 0.01 | 65.45 | 19.48 | 0.01 | 8.82 | 0.74 | 0.00 | 0.00 | 0.00 | 0.23 | 0.61 | 0.51 | 0.00 | 101.19 |
| 113 / 1 . | PC67 | 5.84 | 0.01 | 68.02 | 20.48 | 0.00 | 8.84 | 0.89 | 0.01 | 0.00 | 0.00 | 0.00 | 0.09 | 0.37 | 0.00 | 104.54 |
| 114 / 1 . | PC67 | 5.37 | 0.00 | 65.79 | 20.03 | 0.01 | 9.15 | 0.82 | 0.00 | 0.08 | 0.09 | 0.11 | 0.18 | 0.29 | 0.00 | 101.90 |
| 115 / 1 . | PC67 | 5.00 | 0.00 | 63.89 | 18.70 | 0.03 | 8.72 | 0.69 | 0.00 | 0.00 | 0.12 | 0.56 | 1.93 | 0.44 | 0.01 | 100.02 |
| 116 / 1 . | PC67 | 5.15 | 0.01 | 62.02 | 19.07 | 0.04 | 8.49 | 0.70 | 0.02 | 0.03 | 0.21 | 1.11 | 3.81 | 0.25 | 0.00 | 100.82 |
| 118 / 1 . | PC67 | 4.54 | 0.01 | 64.37 | 19.01 | 0.04 | 8.46 | 1.15 | 0.92 | 0.00 | 0.15 | 0.33 | 0.92 | 0.22 | 0.00 | 100.10 |
| 119 / 1 . | PC67 | 5.14 | 0.03 | 64.14 | 19.35 | 0.00 | 8.48 | 0.89 | 0.58 | 0.00 | 0.15 | 0.35 | 2.09 | 0.12 | 0.00 | 101.27 |
| 120 / 1 . | PC67 | 5.06 | 0.00 | 65.11 | 18.99 | 0.03 | 8.88 | 0.78 | 0.35 | 0.00 | 0.10 | 0.25 | 0.78 | 0.41 | 0.00 | 100.72 |
| 121 / 1 . | PC67 | 4.98 | 0.00 | 63.82 | 19.33 | 0.03 | 8.67 | 0.74 | 0.12 | 0.07 | 0.11 | 0.51 | 1.38 | 0.18 | 0.01 | 99.93 |

**Sanidine**

| | | | | | | | | | | | | | | | | |
|---|---|---|---|---|---|---|---|---|---|---|---|---|---|---|---|---|
| 217 / 1 . | PC58-plain | 5.17 | 0.01 | 64.98 | 19.67 | 0.03 | 8.87 | 0.84 | 0.10 | 0.00 | 0.10 | 0.00 | 0.01 | 0.41 | 0.00 | 100.19 |
| 218 / 1 . | PC58-plain | 5.25 | 0.01 | 64.36 | 19.16 | 0.00 | 8.80 | 0.68 | 0.15 | 0.00 | 0.00 | 0.00 | 0.00 | 0.31 | 0.01 | 98.73 |
| 219 / 1 . | PC58-plain | 5.15 | 0.03 | 64.74 | 19.71 | 0.00 | 9.16 | 0.74 | 0.02 | 0.04 | 0.00 | 0.00 | 0.00 | 0.45 | 0.00 | 100.05 |
| 220 / 1 . | PC58-plain | 5.37 | 0.02 | 64.02 | 19.94 | 0.00 | 8.71 | 0.81 | 0.00 | 0.03 | 0.00 | 0.00 | 0.00 | 0.57 | 0.00 | 99.47 |
| 221 / 1 . | PC58-plain | 5.32 | 0.01 | 65.45 | 19.35 | 0.00 | 8.85 | 0.89 | 0.09 | 0.00 | 0.00 | 0.00 | 0.00 | 0.26 | 0.00 | 100.22 |
| 222 / 1 . | PC58-plain | 5.15 | 0.03 | 66.28 | 19.48 | 0.01 | 9.19 | 0.51 | 0.11 | 0.00 | 0.09 | 0.00 | 0.06 | 0.53 | 0.00 | 101.41 |
| 223 / 1 . | PC58-plain | 5.37 | 0.09 | 64.65 | 18.40 | 0.01 | 7.87 | 1.06 | 1.00 | 0.00 | 0.18 | 0.06 | 0.00 | 0.16 | 0.00 | 98.86 |
| 224 / 1 . | PC58-plain | 4.96 | 0.12 | 65.02 | 18.14 | 0.03 | 7.73 | 1.12 | 0.82 | 0.00 | 0.30 | 0.08 | 0.09 | 0.14 | 0.02 | 98.58 |
| 225 / 1 . | PC58-plain | 5.18 | 0.00 | 65.98 | 19.45 | 0.00 | 9.13 | 0.63 | 0.09 | 0.08 | 0.13 | 0.00 | 0.05 | 0.30 | 0.01 | 101.03 |
| 226 / 1 . | PC58-plain | 5.22 | 0.00 | 67.29 | 19.68 | 0.00 | 8.91 | 0.73 | 0.04 | 0.00 | 0.04 | 0.00 | 0.01 | 0.33 | 0.04 | 102.29 |
| 227 / 1 . | PC58-plain | 5.16 | 0.02 | 66.96 | 18.84 | 0.05 | 8.89 | 0.85 | 0.04 | 0.00 | 0.06 | 0.00 | 0.00 | 0.04 | 0.01 | 100.91 |
| 228 / 1 . | PC58-plain | 5.68 | 0.05 | 66.64 | 19.13 | 0.03 | 7.96 | 0.77 | 0.25 | 0.06 | 0.12 | 0.02 | 0.00 | 0.03 | 0.00 | 100.75 |
| 229 / 1 . | PC58-plain | 5.04 | 0.00 | 68.03 | 19.40 | 0.00 | 9.07 | 0.64 | 0.14 | 0.00 | 0.06 | 0.00 | 0.01 | 0.67 | 0.00 | 103.07 |
| 230 / 1 . | PC58-plain | 4.91 | 0.01 | 65.48 | 19.78 | 0.01 | 9.19 | 0.62 | 0.04 | 0.01 | 0.00 | 0.00 | 0.00 | 0.48 | 0.01 | 100.51 |
| 231 / 1 . | PC58-plain | 5.06 | 0.00 | 65.84 | 19.43 | 0.00 | 9.17 | 0.63 | 0.00 | 0.00 | 0.09 | 0.03 | 0.00 | 0.24 | 0.01 | 100.50 |

| | | | | | | | | | | | | | | | | | |
|---|---|---|---|---|---|---|---|---|---|---|---|---|---|---|---|---|---|
| 232 / 1 . | PC58-plain | 5.05 | 0.01 | 66.57 | 19.48 | 0.00 | 9.09 | 0.77 | 0.12 | 0.01 | 0.00 | 0.00 | 0.00 | 0.38 | 0.00 | | 101.48 |
| 233 / 1 . | PC58-plain | 4.89 | 0.00 | 66.03 | 19.78 | 0.00 | 9.26 | 0.80 | 0.00 | 0.00 | 0.02 | 0.01 | 0.04 | 0.53 | 0.00 | | 101.36 |
| 234 / 1 . | PC58-plain | 4.88 | 0.02 | 66.23 | 19.21 | 0.01 | 9.04 | 0.79 | 0.00 | 0.00 | 0.00 | 0.00 | 0.00 | 0.44 | 0.00 | | 100.61 |
| 235 / 1 . | PC58-plain | 4.78 | 0.01 | 66.73 | 19.55 | 0.03 | 9.25 | 0.78 | 0.00 | 0.00 | 0.01 | 0.06 | 0.11 | 0.53 | 0.00 | | 101.83 |
| 236 / 1 . | PC58-plain | 4.84 | 0.00 | 66.31 | 19.19 | 0.00 | 10.01 | 0.51 | 0.10 | 0.00 | 0.00 | 0.00 | 0.09 | 0.43 | 0.00 | | 101.48 |
| 237 / 1 . | PC58-plain | 5.09 | 0.02 | 65.39 | 19.48 | 0.01 | 9.22 | 0.67 | 0.08 | 0.00 | 0.09 | 0.00 | 0.00 | 0.35 | 0.01 | | 100.41 |
| 238 / 1 . | PC58-plain | 5.22 | 0.00 | 64.02 | 19.26 | 0.00 | 9.20 | 0.63 | 0.15 | 0.10 | 0.00 | 0.01 | 0.00 | 0.34 | 0.02 | | 98.94 |
| 128 / 1 . | PC58-plain | 5.36 | 0.00 | 63.56 | 19.83 | 0.01 | 8.59 | 0.82 | 0.05 | 0.00 | 0.01 | 0.00 | 0.02 | 0.59 | 0.00 | | 98.85 |
| 129 / 1 . | PC58-plain | 4.94 | 0.00 | 62.82 | 19.19 | 0.01 | 8.92 | 0.77 | 0.21 | 0.01 | 0.00 | 0.01 | 0.02 | 0.38 | 0.00 | | 97.30 |
| 130 / 1 . | PC58-plain | 5.24 | 0.00 | 63.45 | 19.23 | 0.00 | 9.16 | 0.57 | 0.04 | 0.00 | 0.04 | 0.00 | 0.00 | 0.11 | 0.00 | | 97.84 |

**2017-11-16**

| n° of analysis | sample | $Na_2O$ | MgO | $SiO_2$ | $Al_2O_3$ | Ar | $K_2O$ | CaO | FeO | MnO | $TiO_2$ | Kr | Xe | BaO | $Cr_2O_3$ | NiO | $Re_2O_7$ | Total |
|---|---|---|---|---|---|---|---|---|---|---|---|---|---|---|---|---|---|---|
| **Sanidine** | | | | | | | | | | | | | | | | | | |
| 134 / 1 . | PC129 | 0.71 | 0.02 | 65.73 | 17.98 | 0.00 | 15.46 | -0.04 | 0.76 | 0.00 | 0.00 | -0.01 | -0.02 | 0.03 | 0.03 | 0.01 | -0.17 | 100.74 |
| 265 / 1 . | PC129 | 0.61 | 0.00 | 64.99 | 19.12 | 0.00 | 15.15 | -0.02 | 0.17 | -0.01 | 0.00 | -0.03 | -0.01 | 0.04 | -0.01 | 0.00 | -0.11 | 100.10 |
| 266 / 1 . | PC129 | 0.73 | 0.04 | 64.09 | 16.73 | 0.00 | 14.21 | -0.01 | 1.37 | -0.02 | 0.03 | -0.02 | 0.03 | 0.04 | 0.00 | 0.00 | -0.16 | 97.26 |
| 267 / 1 . | PC129 | 0.62 | -0.01 | 64.63 | 19.05 | 0.00 | 15.29 | -0.02 | 0.21 | 0.02 | -0.02 | 0.00 | 0.00 | 0.08 | 0.01 | -0.05 | -0.18 | 99.91 |
| 268 / 1 . | PC129 | 0.72 | 0.00 | 64.70 | 18.76 | 0.00 | 15.19 | 0.00 | 0.21 | 0.00 | 0.01 | -0.02 | -0.02 | -0.04 | 0.01 | 0.01 | -0.21 | 99.63 |
| 269 / 1 . | PC129 | 0.69 | 0.01 | 64.66 | 18.68 | -0.01 | 15.63 | -0.01 | 0.16 | -0.02 | -0.02 | -0.01 | 0.00 | 0.21 | 0.00 | 0.02 | -0.16 | 100.07 |
| 270 / 1 . | PC129 | 0.63 | 0.01 | 64.76 | 18.87 | 0.01 | 15.68 | -0.04 | 0.13 | 0.04 | -0.03 | -0.03 | 0.00 | 0.15 | -0.01 | 0.02 | -0.24 | 100.28 |
| 271 / 1 . | PC129 | 0.66 | 0.01 | 65.76 | 19.06 | 0.01 | 15.31 | 0.01 | 0.13 | 0.00 | 0.00 | -0.01 | 0.00 | -0.06 | -0.02 | 0.00 | -0.14 | 100.95 |
| 272 / 1 . | PC129 | 0.72 | 0.02 | 65.53 | 18.56 | -0.01 | 14.87 | 0.02 | 0.88 | -0.01 | 0.05 | -0.01 | -0.02 | -0.01 | 0.02 | -0.02 | -0.15 | 100.66 |
| 273 / 1 . | PC129 | 0.67 | 0.01 | 65.98 | 18.76 | 0.00 | 15.28 | -0.02 | 0.77 | 0.00 | -0.02 | -0.03 | -0.01 | 0.19 | -0.01 | 0.02 | -0.20 | 101.68 |
| 274 / 1 . | PC129 | 0.67 | 0.00 | 66.00 | 18.81 | 0.02 | 14.64 | -0.02 | 0.70 | 0.03 | 0.03 | 0.00 | 0.00 | -0.03 | 0.00 | -0.07 | -0.24 | 100.90 |
| 275 / 1 . | PC129 | 0.67 | 0.03 | 65.38 | 18.50 | 0.01 | 14.40 | 0.01 | 0.76 | 0.00 | 0.06 | -0.02 | 0.01 | 0.06 | -0.03 | 0.03 | -0.16 | 99.90 |
| 276 / 1 . | PC129 | 0.67 | 0.00 | 64.27 | 18.86 | 0.00 | 15.38 | -0.03 | 0.37 | -0.01 | -0.03 | -0.01 | 0.00 | 0.04 | 0.01 | -0.04 | -0.15 | 99.60 |
| 277 / 1 . | PC129 | 0.67 | 0.01 | 62.66 | 17.88 | 0.01 | 15.66 | -0.01 | 0.41 | -0.04 | -0.04 | -0.01 | -0.01 | -0.05 | 0.01 | 0.01 | -0.10 | 97.31 |
| 278 / 1 . | PC129 | 0.72 | 0.03 | 63.72 | 17.91 | 0.00 | 15.05 | -0.01 | 0.96 | 0.00 | 0.06 | 0.00 | -0.01 | -0.05 | -0.01 | -0.01 | -0.10 | 98.46 |

| | | | | | | | | | | | | | | | | | |
|---|---|---|---|---|---|---|---|---|---|---|---|---|---|---|---|---|---|
| 279 / 1 . | PC129 | 0.68 | 0.00 | 63.70 | 18.59 | 0.01 | 14.53 | 0.00 | 0.61 | 0.02 | 0.01 | -0.01 | -0.01 | -0.08 | 0.01 | 0.02 | -0.17 | 98.19 |
| 280 / 1 . | PC129 | 0.82 | 0.08 | 61.49 | 14.57 | 0.01 | 13.36 | 0.02 | 3.07 | 0.02 | 0.06 | -0.01 | 0.02 | 0.12 | 0.01 | 0.06 | -0.14 | 93.70 |
| 281 / 1 . | PC129 | 0.70 | 0.02 | 63.88 | 18.19 | 0.00 | 14.81 | -0.01 | 0.77 | 0.00 | -0.01 | -0.02 | 0.01 | 0.09 | 0.00 | 0.02 | -0.11 | 98.49 |
| 282 / 1 . | PC129 | 0.66 | 0.00 | 63.42 | 18.59 | 0.00 | 15.71 | 0.00 | 0.17 | -0.01 | 0.01 | -0.02 | 0.01 | 0.10 | 0.00 | 0.01 | -0.14 | 98.68 |
| 283 / 1 . | PC129 | 0.71 | 0.02 | 64.12 | 18.50 | -0.01 | 14.50 | 0.01 | 0.68 | -0.03 | 0.02 | 0.00 | 0.01 | 0.18 | 0.01 | 0.00 | -0.16 | 98.76 |
| 284 / 1 . | PC129 | 0.66 | 0.00 | 64.95 | 18.64 | 0.01 | 14.95 | -0.01 | 0.42 | 0.02 | 0.00 | -0.01 | 0.00 | -0.03 | 0.00 | -0.03 | -0.12 | 99.65 |

| **2017-05-29** | | | | | | | | | | | | | | | | | |
|---|---|---|---|---|---|---|---|---|---|---|---|---|---|---|---|---|---|
| **n° of analysis** | **sample** | **$Na_2O$** | **MgO** | **$SiO_2$** | **$Al_2O_3$** | **Ar** | **$K_2O$** | **CaO** | **FeO** | **MnO** | **$TiO_2$** | **Kr** | **Xe** | **BaO** | **$Cr_2O_3$** | **NiO** | **$Re_2O_7$** | **Total** |
| **Sanidine** | | | | | | | | | | | | | | | | | |
| 4 / 1 . | PC103 | 0.79 | 0.01 | 65.76 | 19.04 | -0.01 | 14.45 | -0.02 | 0.64 | 0.00 | 0.01 | -0.01 | -0.02 | 0.02 | | | | 100.71 |
| 5 / 1 . | PC103 | 0.74 | 0.02 | 65.33 | 18.53 | 0.00 | 15.25 | -0.01 | 0.65 | 0.01 | -0.01 | -0.01 | 0.01 | 0.03 | | | | 100.58 |
| 6 / 1 . | PC103 | 0.75 | 0.01 | 65.80 | 18.07 | 0.00 | 15.52 | -0.02 | 0.17 | 0.00 | -0.02 | -0.01 | 0.00 | 0.05 | | | | 100.35 |
| 7 / 1 . | PC103 | 0.78 | 0.02 | 64.78 | 18.27 | 0.00 | 15.51 | -0.03 | 0.32 | -0.01 | 0.02 | -0.03 | 0.01 | -0.01 | | | | 99.72 |
| 8 / 1 . | PC103 | 0.73 | 0.01 | 64.71 | 18.22 | 0.01 | 15.56 | -0.02 | 0.53 | -0.03 | 0.03 | 0.11 | 0.25 | 0.13 | | | | 100.36 |
| 9 / 1 . | PC103 | 0.80 | 0.03 | 65.29 | 18.47 | 0.00 | 15.97 | 0.00 | 0.19 | 0.00 | -0.01 | -0.01 | -0.01 | 0.11 | | | | 100.87 |
| 10 / 1 . | PC103 | 0.80 | 0.02 | 65.17 | 17.93 | -0.01 | 15.72 | 0.00 | 0.83 | 0.01 | 0.00 | -0.04 | 0.00 | 0.14 | | | | 100.62 |
| 11 / 1 . | PC103 | 0.82 | 0.03 | 65.71 | 18.00 | -0.02 | 15.70 | -0.01 | 0.37 | -0.01 | 0.03 | 0.00 | -0.01 | 0.01 | | | | 100.69 |
| 12 / 1 . | PC103 | 0.78 | 0.02 | 65.39 | 17.87 | 0.00 | 15.54 | -0.02 | 0.89 | 0.01 | 0.02 | 0.00 | -0.02 | 0.16 | | | | 100.69 |
| 13 / 1 . | PC103 | 0.80 | 0.00 | 64.71 | 18.43 | 0.00 | 15.97 | -0.02 | 0.26 | 0.04 | 0.03 | -0.01 | -0.02 | 0.16 | | | | 100.40 |
| 14 / 1 . | PC103 | 0.83 | 0.03 | 64.90 | 18.16 | 0.01 | 15.83 | -0.02 | 0.49 | -0.01 | 0.00 | 0.00 | 0.01 | 0.11 | | | | 100.39 |
| 15 / 1 . | PC103 | 0.78 | 0.00 | 64.94 | 18.71 | 0.01 | 15.68 | -0.01 | 0.27 | -0.02 | -0.02 | 0.01 | -0.01 | 0.07 | | | | 100.48 |
| 16 / 1 . | PC103 | 0.77 | 0.00 | 64.93 | 18.69 | 0.00 | 15.79 | -0.01 | 0.25 | 0.01 | 0.00 | 0.00 | 0.02 | 0.12 | | | | 100.60 |
| 18 / 1 . | PC103 | 0.79 | 0.01 | 65.01 | 18.54 | 0.00 | 15.73 | 0.00 | 0.50 | 0.00 | 0.01 | 0.00 | 0.00 | 0.13 | | | | 100.73 |
| 19 / 1 . | PC103 | 0.80 | 0.01 | 65.07 | 18.15 | 0.00 | 15.54 | -0.02 | 0.84 | -0.01 | -0.02 | 0.00 | 0.02 | 0.11 | | | | 100.54 |
| 20 / 1 . | PC103 | 0.81 | 0.01 | 65.75 | 18.04 | -0.01 | 15.94 | -0.03 | 0.61 | 0.00 | 0.01 | -0.01 | -0.01 | -0.05 | | | | 101.16 |
| 21 / 1 . | PC103 | 0.97 | 0.03 | 65.39 | 18.10 | 0.01 | 15.43 | -0.02 | 0.69 | -0.03 | -0.02 | 0.00 | 0.02 | 0.12 | | | | 100.76 |
| 22 / 1 . | PC103 | 0.92 | 0.02 | 65.70 | 17.68 | 0.00 | 15.36 | 0.00 | 0.87 | -0.01 | 0.02 | 0.00 | 0.03 | -0.01 | | | | 100.61 |
| 23 / 1 . | PC103 | 0.78 | 0.01 | 65.49 | 18.36 | 0.00 | 15.79 | 0.00 | 0.75 | 0.02 | 0.02 | 0.00 | -0.01 | 0.18 | | | | 101.41 |
| 24 / 1 . | PC103 | 0.78 | 0.01 | 65.07 | 18.10 | 0.00 | 15.65 | -0.03 | 0.67 | -0.01 | 0.02 | -0.01 | 0.01 | 0.05 | | | | 100.35 |

| | | | | | | | | | | | | | | | | | | |
|---|---|---|---|---|---|---|---|---|---|---|---|---|---|---|---|---|---|---|
| 26 / 1 . | PC103 | 0.68 | 0.03 | 64.64 | 19.10 | 0.01 | 13.26 | -0.01 | 0.17 | 0.00 | 0.02 | -0.01 | 0.00 | 0.09 | | | | 98.00 |
| 30 / 1 . | PC103 | 0.84 | 0.04 | 65.05 | 18.36 | 0.00 | 14.96 | 0.01 | 0.36 | 0.02 | 0.07 | 0.00 | 0.02 | 0.16 | | | | 99.89 |
| 31 / 1 . | PC103 | 0.76 | 0.03 | 65.25 | 18.65 | 0.00 | 14.79 | 0.00 | 0.34 | 0.00 | -0.02 | 0.00 | -0.02 | 0.09 | | | | 99.92 |
| 37 / 1 . | PC103 | 0.82 | 0.02 | 65.09 | 18.16 | 0.00 | 15.59 | -0.02 | 0.64 | -0.02 | 0.01 | 0.00 | 0.02 | 0.07 | | | | 100.42 |
| 39 / 1 . | PC103 | 1.18 | 0.12 | 64.85 | 16.89 | 0.02 | 14.93 | 0.01 | 1.31 | 0.00 | 0.11 | 0.05 | 0.06 | 0.13 | | | | 99.67 |
| **Sanidine : Fe-rich zone** | | | | | | | | | | | | | | | | | | |
| 27 / 1 . | PC103 | 1.43 | 0.37 | 67.69 | 13.85 | 0.02 | 11.57 | 0.10 | 2.57 | 0.01 | 0.38 | 0.08 | 0.16 | 0.32 | | | | 98.60 |
| 28 / 1 . | PC103 | 1.15 | 0.34 | 66.55 | 14.19 | 0.02 | 11.78 | 0.08 | 2.25 | -0.01 | 0.40 | 0.09 | 0.15 | 0.34 | | | | 97.36 |
| 29 / 1 . | PC103 | 1.01 | 0.23 | 67.09 | 15.92 | 0.01 | 12.76 | 0.07 | 1.55 | -0.02 | 0.29 | 0.06 | 0.12 | 0.11 | | | | 99.25 |
| 32 / 1 . | PC103 | 1.63 | 0.25 | 64.82 | 13.92 | 0.01 | 12.99 | 0.07 | 2.83 | -0.03 | 0.27 | 0.13 | 0.27 | 0.35 | | | | 97.60 |
| 33 / 1 . | PC103 | 1.74 | 0.28 | 65.42 | 13.36 | 0.00 | 12.72 | 0.06 | 3.06 | 0.02 | 0.40 | 0.11 | 0.19 | 0.35 | | | | 97.78 |
| 35 / 1 . | PC103 | 1.61 | 0.22 | 65.63 | 14.23 | 0.01 | 13.45 | 0.06 | 2.50 | -0.02 | 0.34 | 0.10 | 0.21 | 0.15 | | | | 98.55 |
| 36 / 1 . | PC103 | 1.45 | 0.21 | 65.80 | 14.81 | 0.02 | 13.74 | 0.06 | 2.11 | 0.01 | 0.31 | 0.10 | 0.18 | 0.28 | | | | 99.13 |
| 38 / 1 | PC103 | 2.01 | 0.27 | 65.66 | 12.63 | 0.03 | 12.74 | 0.08 | 3.43 | 0.02 | 0.39 | 0.15 | 0.21 | 0.33 | | | | 97.99 |
| 40 / 1 . | PC103 | 1.61 | 0.20 | 65.32 | 14.19 | 0.01 | 13.62 | 0.05 | 2.52 | 0.01 | 0.25 | 0.10 | 0.17 | 0.29 | | | | 98.38 |
| 41 / 1 . | PC103 | 1.24 | 0.20 | 64.92 | 14.64 | 0.01 | 13.92 | 0.06 | 1.76 | 0.02 | 0.21 | 0.07 | 0.12 | 0.21 | | | | 97.40 |
| **Phase ?** | | | | | | | | | | | | | | | | | | |
| 17 / 1 . | PC103 | 0.62 | 0.00 | 70.01 | 15.26 | -0.01 | 13.58 | -0.02 | 0.20 | -0.01 | 0.04 | 0.00 | -0.01 | 0.00 | | | | 99.72 |
| 25 / 1 . | PC103 | 1.94 | 0.76 | 66.20 | 10.56 | 0.04 | 10.07 | 0.23 | 2.96 | 0.01 | 1.15 | 0.15 | 0.27 | 0.36 | | | | 94.77 |
| 34 / 1 . | PC103 | 2.22 | 0.47 | 65.29 | 9.90 | 0.03 | 10.46 | 0.18 | 4.28 | 0.00 | 0.63 | 0.20 | 0.32 | 0.48 | | | | 94.55 |

| **Previous EMPA University of Edinburgh** | | | | | | | | | | | | | | | | | |
|---|---|---|---|---|---|---|---|---|---|---|---|---|---|---|---|---|---|
| **n° of analysis** | **sample** | **$Na_2O$** | **MgO** | **$SiO_2$** | **$Al_2O_3$** | **Ar** | **$K_2O$** | **CaO** | **FeO** | **MnO** | **$TiO_2$** | **Kr** | **Xe** | **BaO** | **$Cr_2O_3$** | **NiO** | **$Re_2O_7$** | **Total** |
| **Sanidine** | | | | | | | | | | | | | | | | | | |
| 2 / 1 . | PC58 Xe | 1.83 | 0.08 | 65.77 | 16.58 | 0.00 | 4.74 | 1.27 | 1.38 | 0.02 | 0.35 | | 0.81 | | | | | 93.12 |
| 4 / 1 . | PC58 Xe | 2.34 | 0.00 | 65.50 | 18.96 | 0.00 | 6.38 | 0.65 | 0.06 | -0.01 | -0.01 | | 0.04 | | | | | 93.92 |
| 5 / 1 . | PC58 Xe | 4.91 | 0.00 | 66.89 | 19.07 | 0.00 | 9.38 | 0.70 | 0.15 | 0.00 | 0.02 | | 0.32 | | | | | 101.56 |

| | | | | | | | | | | | | | |
|---|---|---|---|---|---|---|---|---|---|---|---|---|---|
| 8 / 1 . | PC58 Xe | 4.82 | 0.00 | 66.47 | 19.44 | 0.00 | 9.37 | 0.68 | 0.08 | 0.00 | 0.03 | 0.72 | 101.86 |
| 9 / 1 . | PC58 Xe | 4.70 | 0.00 | 66.28 | 19.26 | 0.00 | 9.65 | 0.63 | 0.05 | 0.01 | 0.03 | 0.55 | 101.35 |
| 10 / 1 . | PC58 Xe | 4.14 | 0.00 | 57.57 | 16.74 | 0.00 | 8.40 | 0.60 | 0.08 | 0.00 | 0.02 | 0.45 | 88.16 |
| 11 / 1 . | PC58 Xe | 4.79 | 0.00 | 65.90 | 19.15 | 0.00 | 9.42 | 0.64 | 0.03 | -0.01 | 0.02 | 0.56 | 100.68 |
| 12 / 1 . | PC58 Xe | 5.04 | 0.00 | 65.37 | 19.44 | 0.00 | 9.09 | 0.68 | 0.02 | 0.00 | 0.01 | 0.65 | 100.52 |
| 13 / 1 . | PC58 Xe | 4.93 | 0.00 | 64.88 | 18.98 | 0.00 | 9.08 | 0.75 | 0.14 | 0.01 | 0.01 | 0.57 | 99.55 |
| 14 / 1 . | PC58 Xe | 4.99 | 0.00 | 65.29 | 18.99 | 0.00 | 9.15 | 0.83 | 0.32 | 0.00 | 0.01 | 0.40 | 100.12 |
| 15 / 1 . | PC58 Xe | 4.82 | 0.00 | 66.25 | 19.28 | 0.00 | 9.36 | 0.78 | 0.03 | 0.01 | -0.07 | 0.01 | 100.47 |
| **?** | | | | | | | | | | | | | |
| 1 / 1 . | PC58 Xe | 2.80 | 0.01 | 68.11 | 19.73 | 0.00 | 5.82 | 0.79 | 0.07 | 0.00 | -0.01 | 0.21 | 97.60 |
| 3 / 1 . | PC58 Xe | 4.12 | 0.00 | 64.68 | 18.87 | 0.00 | 8.60 | 0.73 | 0.02 | 0.00 | -0.03 | 0.25 | 97.33 |
| 6 / 1 . | PC58 Xe | 7.35 | 0.02 | 65.20 | 19.12 | 0.00 | 8.81 | 0.77 | 0.14 | 0.02 | -0.01 | 0.15 | 101.62 |
| 7 / 1 . | PC58 Xe | 2.19 | 0.01 | 70.50 | 20.51 | 0.00 | 6.36 | 0.72 | 0.08 | -0.01 | 0.00 | 0.28 | 100.73 |
| **Sanidine** | | | | | | | | | | | | | |
| 4 / 1 . | PC63 | 4.62 | 0.00 | 65.36 | 18.90 | 0.12 | 9.48 | 0.77 | 0.49 | 0.00 | -0.01 | 0.00 | 99.74 |
| 5 / 1 . | PC63 | 4.77 | 0.00 | 65.25 | 19.67 | 0.01 | 9.34 | 0.94 | 0.02 | 0.00 | -0.07 | 0.00 | 99.92 |
| 6 / 1 . | PC63 | 4.86 | 0.00 | 65.68 | 19.31 | 0.00 | 9.35 | 0.83 | 0.02 | 0.01 | -0.06 | 0.00 | 100.00 |
| **?** | | | | | | | | | | | | | |
| 1 / 1 . | PC63 | 5.07 | 0.03 | 62.88 | 15.17 | 0.01 | 5.72 | 1.71 | 5.48 | 0.00 | 0.35 | 0.00 | 96.41 |
| 2 / 1 . | PC63 | 5.88 | 0.20 | 65.57 | 17.89 | 0.32 | 7.39 | 1.28 | 1.65 | 0.01 | 0.57 | 0.47 | 101.38 |
| 3 / 1 . | PC63 | 3.63 | 0.00 | 60.82 | 17.67 | 0.31 | 8.54 | 0.81 | 0.01 | 0.01 | -0.01 | 0.64 | 92.64 |
| **Sanidine** | | | | | | | | | | | | | |
| 1 / 1 . | PC63 | 4.72 | 0.00 | 64.81 | 19.35 | 0.08 | 9.34 | 0.85 | 0.01 | -0.01 | -0.06 | 0.32 | 99.51 |
| 3 / 1 . | PC63 | 3.63 | 0.00 | 60.56 | 17.35 | 0.10 | 9.38 | 0.68 | 0.07 | 0.01 | 0.01 | 0.14 | 91.98 |
| 5 / 1 . | PC63 | 4.70 | 0.00 | 64.75 | 19.09 | 0.01 | 9.26 | 0.83 | 0.01 | 0.01 | -0.05 | 0.00 | 98.57 |
| 6 / 1 . | PC63 | 4.69 | 0.00 | 66.07 | 19.31 | 0.06 | 9.68 | 0.57 | 0.06 | 0.00 | -0.01 | 0.09 | 100.56 |

| | | | | | | | | | | | | | |
|---|---|---|---|---|---|---|---|---|---|---|---|---|---|
| 9 / 1 . | PC63 | 4.89 | 0.00 | 65.22 | 19.43 | 0.30 | 9.49 | 0.76 | 0.02 | 0.01 | 0.00 | 1.03 | 101.50 |
| 10 / 1 . | PC63 | 4.88 | 0.00 | 65.79 | 18.85 | 0.02 | 9.45 | 0.72 | 0.02 | 0.01 | 0.01 | 0.01 | 99.76 |
| **?** | | | | | | | | | | | | | |
| 2 / 1 . | PC63 | 5.04 | 0.13 | 64.89 | 17.65 | 0.49 | 7.48 | 1.11 | 1.47 | 0.01 | 0.33 | 0.69 | 99.52 |
| 4 / 1 . | PC63 | 4.86 | 0.03 | 65.21 | 18.91 | 0.01 | 8.65 | 0.82 | 0.78 | -0.01 | 0.04 | 0.07 | 99.41 |
| 7 / 1 . | PC63 | 2.61 | 0.00 | 70.30 | 20.17 | 0.19 | 6.49 | 0.58 | 0.05 | 0.00 | -0.01 | 0.50 | 101.06 |
| 8 / 1 . | PC63 | 4.06 | 0.00 | 64.50 | 18.63 | 0.07 | 8.86 | 0.66 | 0.02 | 0.01 | -0.06 | 0.13 | 96.93 |

*EMPA recorded on synthesized sanidine (in orange wt% oxide total lower than 96% or higher than 102%). Blanks mean that elements has not been analyzed.*

**Appendix F4/ EMPA of Xe/(Kr or Ar) gas bubbles and surrounding sanidine on Fe-poor zones of noble gases-bearing synthesized sanidine**

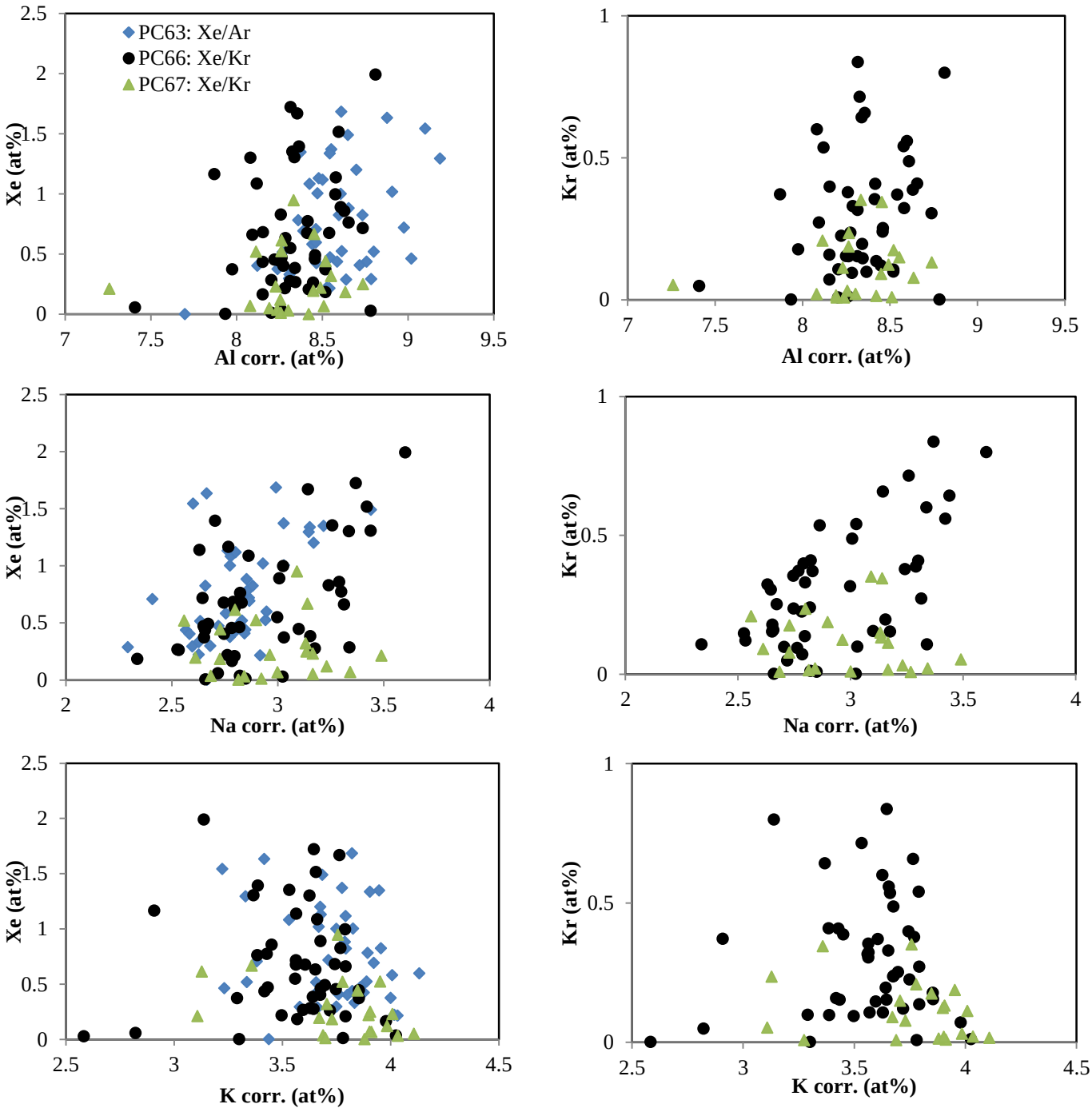


*Observed correlations for EMPA (oxide totals between 96% and 102%) of noble gases bubbles and surrounding sanidine on Fe-poor zones for Xe/(Kr, Ar)-bearing sanidine, PC63, PC66, PC67 (Table F1).*

## Appendix F5/ Image plate for X-ray diffraction on sanidine

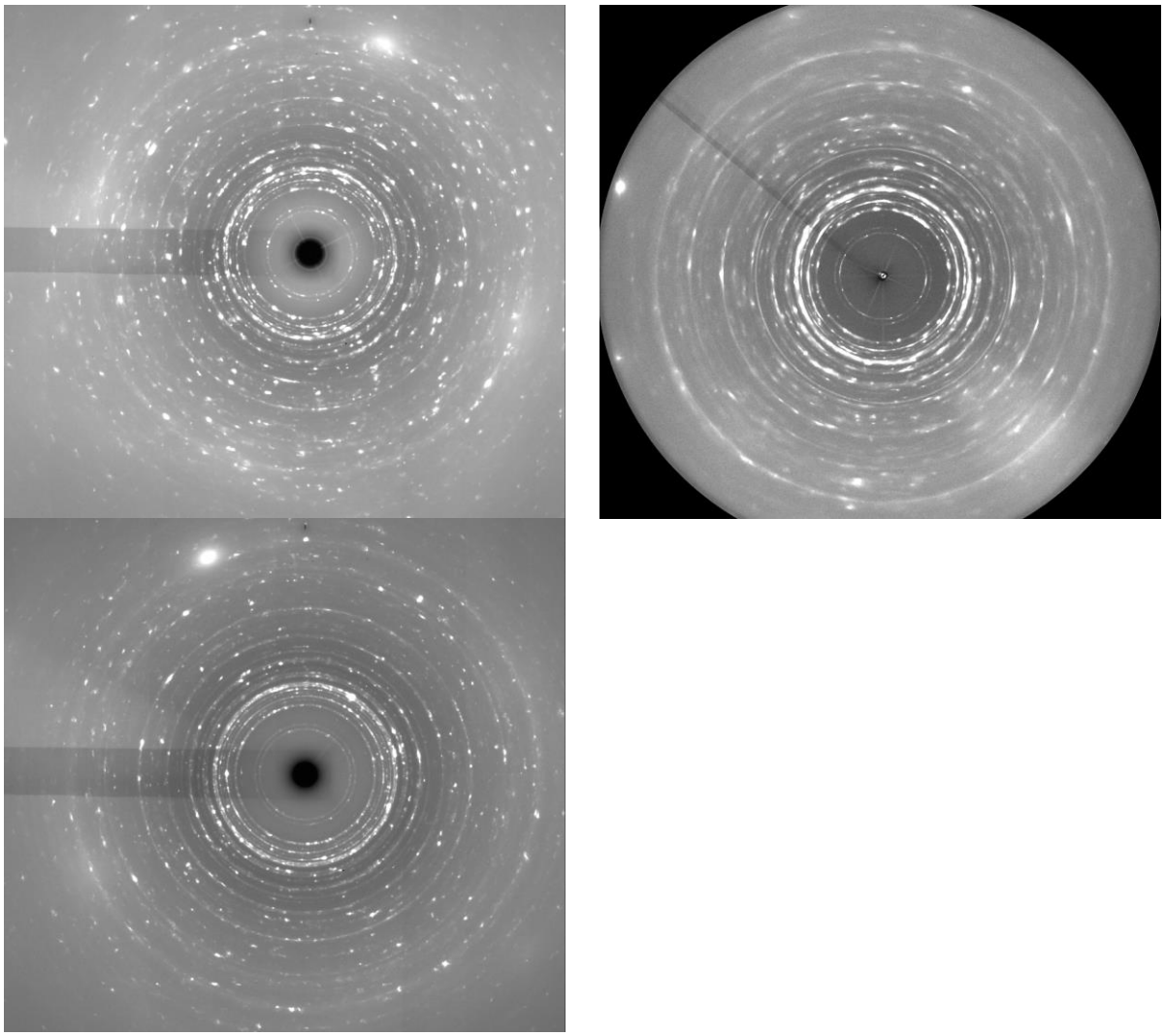

*Image plate for plain sanidine Itrongahi, P-cell6-plain at 0.7 GPa and 873 K (top left), for Xe/Kr-bearing sanidine Itrongahi, D-RT1-1-Xe/Kr at 2.5 GPa and 852 K (top right), and for Xe/Kr-bearing sanidine Itrongahi P-cell2-Xe/Kr at 2.5 GPa and 873 K (bottom left).*

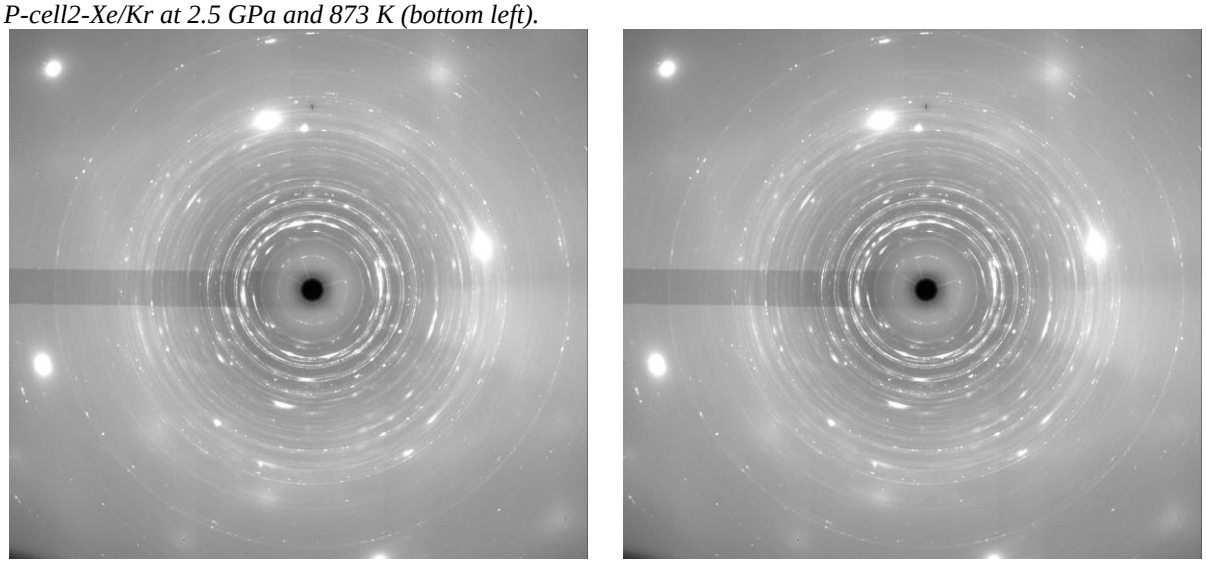

*Image plate for plain sanidine Nat., P-cell4-plain at 5.1 GPa and 1373 K (left), and for Xe-bearing sanidine Nat., P-cell4-Xe at 6.7 GPa and 1373 K (right).*

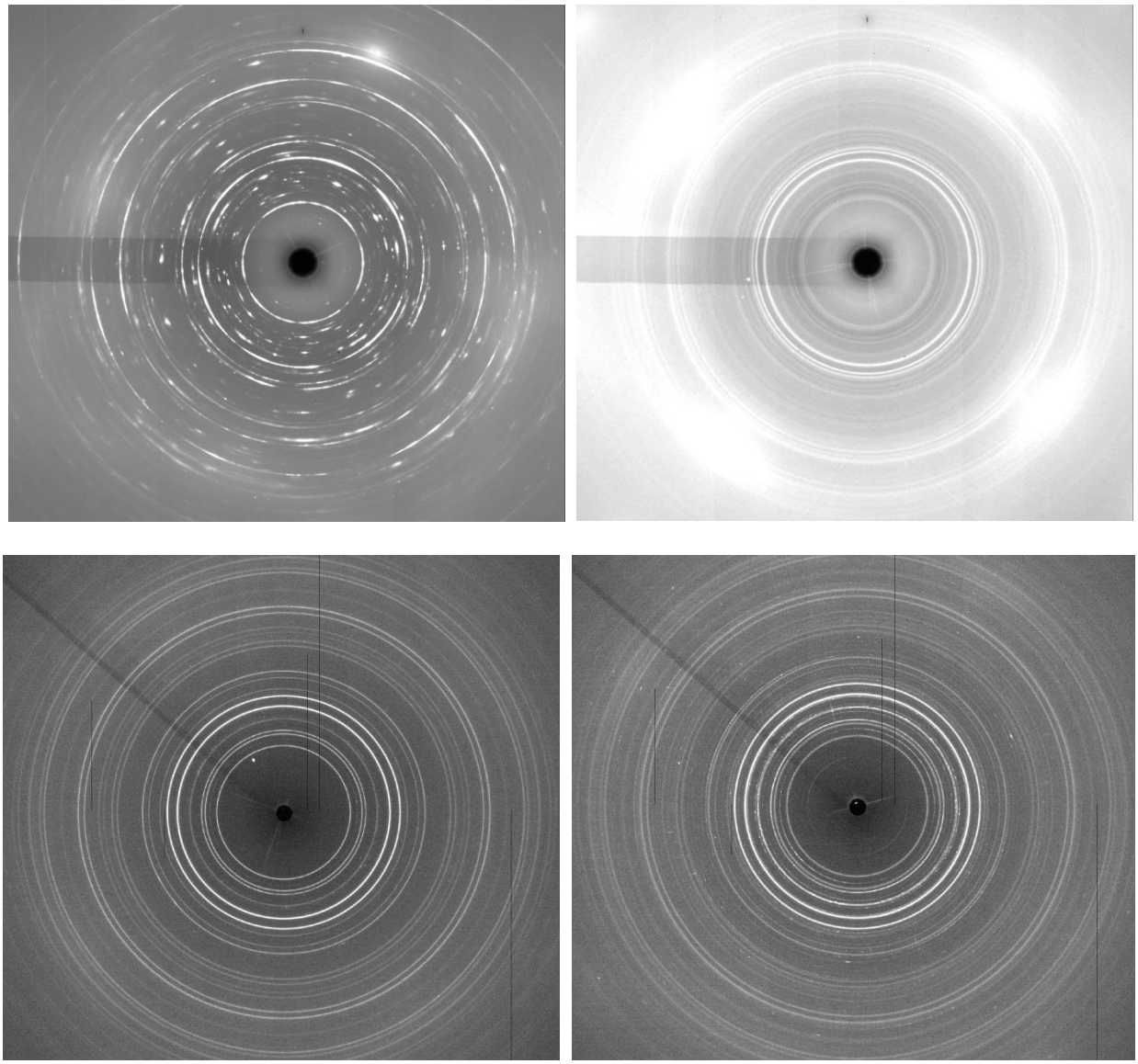

*Image plates of sample recrystallized from Xe/Ar-bearing hydrated sanidine Itrongahi glass P-cell6-Xe/Ar at 1073 K and 4.8 GPa (top right), of sample recrystallized from Xe/Ar-bearing hydrated sanidine Itrongahi glass P-cell3-Xe/Ar at 1254 K and 9.7 GPa, of sample recrystallized from plain hydrated sanidine Itrongahi glass D-HT2-1-plain at 5.6 GPa and 1158 K (bottom left), and of sample recrystallized from plain hydrated sanidine Itrongahi D-RT1-1 at 5.7 GPa and 1244 K (bottom right).*

**Appendix F6/ Raman analyses of recovered samples from *in situ* X-ray diffraction in DAC (P-cell4-plain, P-cell4-Xe, P-cell6-plain and P-cell6-Xe/Ar)**

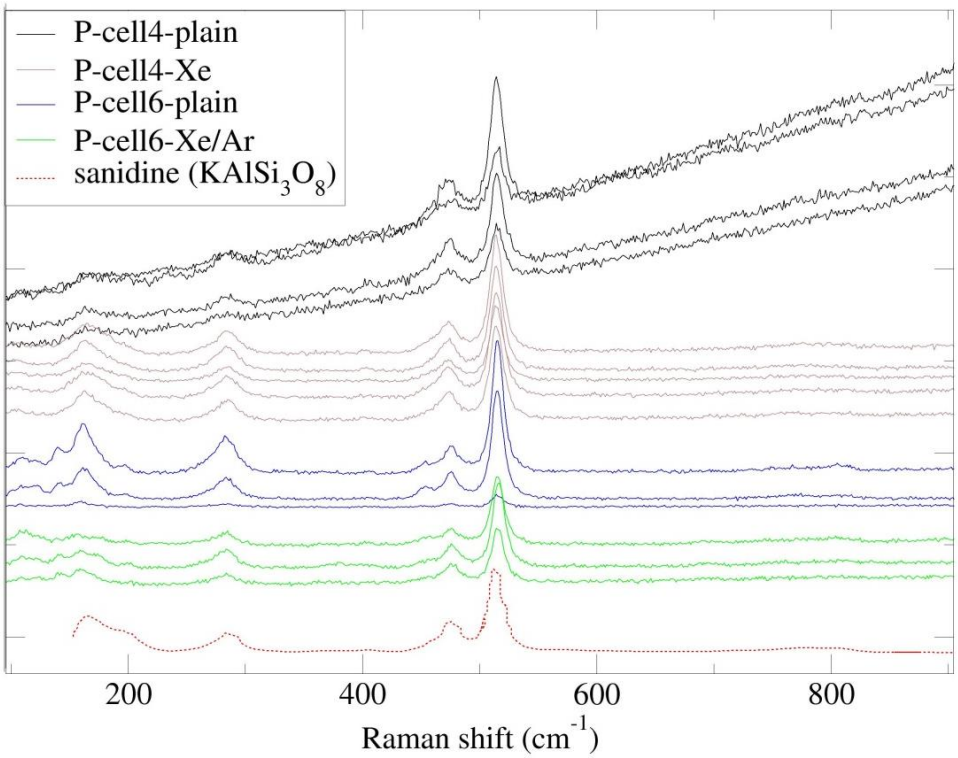


*Raman analyses performed on recovered gaskets. Background for P-cell4-plain is due to pollution from remaining pieces of graphite heater. Raman spectrum for sanidine from Freeman et al. (2008).*

## Appendix F7/ EMPA of recovered samples from *in situ* X-ray diffraction (P-cell6-plain, P-cell4-plain, P-cell4-Xe, P-cell6-Xe/Ar, P-cell3-Xe/Ar)

| 2017-05-29 | | | | | | | | | | | | | | | |
|---|---|---|---|---|---|---|---|---|---|---|---|---|---|---|---|
| **n° of analysis** | **Sample** | **$Na_2O$** | **MgO** | **$SiO_2$** | **$Al_2O_3$** | **Ar** | **$K_2O$** | **CaO** | **FeO** | **MnO** | **$TiO_2$** | **Kr** | **Xe** | **BaO** | **Total** |
| **Sanidine** | | | | | | | | | | | | | | | |
| 75 / 1 . | P-cell6-Xe/Ar dark zone | 0.24 | 0.08 | 66.10 | 19.79 | 0.01 | 14.58 | 0.01 | 0.00 | 0.01 | 0.02 | -0.01 | 0.00 | 0.05 | 100.90 |
| 76 / 1 . | P-cell6-Xe/Ar dark zone | 0.25 | 0.13 | 64.57 | 21.53 | 0.00 | 14.38 | -0.01 | 0.10 | 0.00 | 0.13 | -0.02 | 0.01 | 0.22 | 101.33 |
| 77 / 1 . | P-cell6-Xe/Ar dark zone | 0.36 | 0.30 | 61.96 | 23.83 | 0.01 | 14.39 | 0.01 | 0.10 | 0.00 | 0.19 | -0.02 | 0.00 | 0.01 | 101.17 |
| 78 / 1 . | P-cell6-Xe/Ar dark zone | 0.54 | 0.21 | 63.13 | 21.64 | 0.05 | 14.06 | 0.04 | 0.10 | 0.01 | 0.12 | -0.02 | 0.00 | 0.22 | 100.13 |
| 79 / 1 . | P-cell6-Xe/Ar dark zone | 0.25 | 0.23 | 63.58 | 21.63 | 0.01 | 8.30 | 0.07 | 0.12 | 0.01 | 0.31 | -0.02 | -0.01 | 0.02 | 94.54 |
| 80 / 1 . | P-cell6-Xe/Ar dark zone | 0.70 | 0.10 | 65.41 | 20.61 | 0.15 | 12.20 | 0.06 | 0.10 | 0.01 | 0.14 | -0.02 | 0.03 | 0.21 | 99.73 |
| 81 / 1 . | P-cell6-Xe/Ar dark zone | 0.20 | 0.12 | 63.93 | 21.88 | 0.01 | 14.62 | -0.01 | 0.10 | 0.00 | 0.17 | 0.00 | 0.00 | 0.10 | 101.14 |
| 82 / 1 . | P-cell6-Xe/Ar dark zone | 0.18 | 0.15 | 67.29 | 19.71 | 0.04 | 12.99 | 0.02 | 0.05 | -0.02 | 0.12 | 0.01 | 0.01 | 0.17 | 100.75 |
| 83 / 1 . | P-cell6-Xe/Ar dark zone | 0.27 | 0.09 | 67.39 | 18.51 | 0.00 | 14.29 | 0.03 | 0.09 | -0.01 | 0.09 | -0.01 | -0.02 | 0.03 | 100.79 |
| 84 / 1 . | P-cell6-Xe/Ar dark zone | 0.19 | 0.16 | 57.81 | 27.11 | 0.00 | 13.77 | 0.00 | 0.10 | 0.00 | 0.33 | -0.01 | 0.01 | 0.04 | 99.54 |
| **Sanidine** | | | | | | | | | | | | | | | |
| 85 / 1 . | P-cell6-Xe/Ar light zone | 0.29 | -0.01 | 66.55 | 18.44 | 0.02 | 15.64 | -0.01 | 0.03 | -0.02 | 0.02 | -0.03 | 0.03 | -0.01 | 101.03 |
| 86 / 1 . | P-cell6-Xe/Ar light zone | 0.23 | 0.00 | 65.63 | 19.15 | 0.01 | 16.33 | 0.00 | -0.02 | -0.02 | 0.05 | -0.03 | 0.00 | 0.10 | 101.50 |
| 87 / 1 . | P-cell6-Xe/Ar light zone | 0.25 | 0.01 | 65.97 | 18.75 | 0.01 | 16.14 | -0.03 | -0.05 | 0.01 | -0.01 | -0.02 | -0.01 | 0.13 | 101.26 |
| 88 / 1 . | P-cell6-Xe/Ar light zone | 0.24 | -0.01 | 66.06 | 19.03 | 0.01 | 16.28 | -0.02 | 0.05 | 0.01 | 0.02 | -0.02 | 0.00 | 0.06 | 101.77 |
| 89 / 1 . | P-cell6-Xe/Ar light zone | 0.26 | 0.06 | 65.40 | 19.39 | 0.01 | 15.89 | 0.03 | 0.04 | -0.01 | 0.04 | -0.03 | -0.01 | 0.22 | 101.34 |
| 90 / 1 . | P-cell6-Xe/Ar light zone | 0.27 | 0.12 | 62.64 | 21.40 | 0.01 | 15.57 | 0.01 | 0.11 | 0.01 | 0.09 | -0.01 | 0.01 | 0.08 | 100.34 |
| 91 / 1 . | P-cell6-Xe/Ar light zone | 0.34 | -0.01 | 65.58 | 18.99 | 0.03 | 16.01 | -0.01 | 0.00 | 0.01 | 0.02 | -0.01 | 0.02 | 0.05 | 101.04 |
| 92 / 1 . | P-cell6-Xe/Ar light zone | 0.24 | 0.00 | 65.40 | 18.92 | 0.01 | 16.25 | -0.02 | -0.03 | -0.01 | -0.01 | -0.03 | -0.01 | -0.02 | 100.82 |
| 93 / 1 . | P-cell6-Xe/Ar light zone | 0.28 | 0.02 | 65.51 | 18.72 | 0.02 | 16.31 | 0.01 | 0.05 | -0.01 | 0.01 | -0.01 | 0.00 | 0.10 | 101.03 |
| 94 / 1 . | P-cell6-Xe/Ar light zone | 0.44 | 0.88 | 61.76 | 19.76 | 0.01 | 15.10 | 0.07 | 0.10 | 0.00 | 0.28 | -0.02 | 0.03 | 0.05 | 98.48 |
| 95 / 1 . | P-cell6-Xe/Ar light zone | 0.41 | 0.09 | 64.41 | 19.28 | 0.01 | 15.75 | 0.02 | 0.04 | 0.02 | 0.13 | 0.00 | -0.01 | 0.10 | 100.25 |

| | | | | | | | | | | | | | | | |
|---|---|---|---|---|---|---|---|---|---|---|---|---|---|---|---|
| **Phase ?** | | | | | | | | | | | | | | | |
| 96 / 1 . | P-cell6-Xe/Ar light zone | 0.55 | 0.56 | 56.00 | 25.90 | 0.01 | 13.31 | 0.18 | 0.14 | 0.00 | 0.71 | -0.03 | 0.00 | -0.01 | 97.37 |
| **Sanidine** | | | | | | | | | | | | | | | |
| 97 / 1 . | P-cell6-plain | 1.17 | 0.02 | 66.51 | 18.86 | 0.00 | 14.90 | 0.00 | 1.04 | 0.02 | 0.01 | -0.04 | -0.01 | 0.07 | 102.60 |
| 98 / 1 . | P-cell6-plain | 0.50 | 0.02 | 66.47 | 18.87 | 0.00 | 15.00 | 0.00 | 0.82 | -0.01 | 0.08 | 0.00 | 0.00 | 0.16 | 101.94 |
| 99 / 1 . | P-cell6-plain | 0.83 | 0.03 | 66.59 | 19.00 | 0.00 | 15.50 | 0.00 | 0.82 | -0.01 | 0.00 | -0.01 | 0.02 | 0.07 | 102.86 |
| 100 / 1 . | P-cell6-plain | 0.76 | 0.02 | 66.07 | 19.23 | 0.00 | 15.21 | 0.00 | 0.81 | 0.00 | 0.04 | -0.01 | 0.00 | 0.03 | 102.17 |
| 101 / 1 . | P-cell6-plain | 0.93 | 0.02 | 66.74 | 19.26 | 0.00 | 15.20 | 0.00 | 0.89 | -0.02 | 0.01 | -0.01 | -0.01 | 0.06 | 103.12 |
| 102 / 1 . | P-cell6-plain | 0.52 | 0.02 | 65.02 | 18.82 | 0.01 | 14.66 | 0.02 | 0.64 | -0.01 | 0.02 | -0.02 | 0.01 | 0.10 | 99.84 |
| 103 / 1 . | P-cell6-plain | 0.42 | 0.02 | 66.17 | 19.31 | 0.00 | 15.77 | -0.01 | 0.67 | -0.01 | 0.01 | -0.02 | -0.01 | 0.05 | 102.40 |
| 104 / 1 . | P-cell6-plain | 0.34 | 0.01 | 65.72 | 18.92 | -0.01 | 15.89 | 0.01 | 0.91 | 0.00 | 0.03 | -0.01 | 0.02 | 0.12 | 101.98 |
| 105 / 1 . | P-cell6-plain | 1.01 | 0.00 | 66.34 | 18.98 | 0.00 | 14.98 | 0.01 | 0.79 | 0.01 | 0.02 | -0.01 | 0.00 | 0.06 | 102.19 |
| 106 / 1 . | P-cell6-plain | 0.83 | 0.02 | 66.00 | 19.08 | 0.00 | 15.29 | -0.02 | 0.79 | -0.01 | 0.05 | -0.02 | 0.01 | 0.08 | 102.16 |

| **2017-05-19** | | | | | | | | | | | | | | | |
|---|---|---|---|---|---|---|---|---|---|---|---|---|---|---|---|
| **n° of analysis** | **Sample** | **$Na_2O$** | **MgO** | **$SiO_2$** | **$Al_2O_3$** | **Ar** | **$K_2O$** | **CaO** | **FeO** | **MnO** | **$TiO_2$** | **Kr** | **Xe** | **BaO** | **Total** |
| **Sanidine** | | | | | | | | | | | | | | | |
| 21 / 1 . | P-cell4-plain | 5.20 | 0.01 | 65.09 | 19.34 | -0.01 | 9.51 | 0.56 | 0.19 | -0.01 | 0.04 | -0.02 | 0.01 | 0.43 | 100.38 |
| 149 / 1 . | P-cell4-plain | 4.56 | 0.00 | 65.81 | 20.13 | 0.00 | 9.65 | 0.68 | 0.16 | -0.01 | -0.01 | -0.02 | 0.00 | 0.47 | 101.46 |
| 150 / 1 . | P-cell4-plain | 5.45 | 0.00 | 65.55 | 19.92 | 0.00 | 8.91 | 0.65 | 0.20 | 0.00 | 0.00 | -0.02 | -0.01 | 0.37 | 101.05 |
| 151 / 1 . | P-cell4-plain | 5.05 | 0.00 | 64.34 | 19.43 | 0.00 | 9.73 | 0.50 | 0.24 | 0.02 | -0.02 | -0.02 | 0.01 | 0.49 | 99.80 |
| 152 / 1 . | P-cell4-plain | 5.42 | 0.00 | 65.16 | 19.88 | -0.01 | 9.10 | 0.72 | 0.28 | 0.01 | 0.00 | -0.03 | 0.01 | 0.40 | 100.99 |
| 153 / 1 . | P-cell4-plain | 5.09 | 0.00 | 65.39 | 19.66 | -0.01 | 9.93 | 0.47 | 0.20 | -0.02 | 0.05 | -0.02 | -0.01 | 0.19 | 100.98 |
| 154 / 1 . | P-cell4-plain | 5.13 | 0.00 | 66.12 | 19.74 | 0.00 | 9.66 | 0.57 | 0.20 | 0.03 | 0.02 | 0.01 | -0.02 | 0.40 | 101.89 |
| 155 / 1 . | P-cell4-plain | 5.12 | -0.01 | 66.09 | 20.00 | 0.00 | 9.34 | 0.62 | 0.20 | 0.00 | 0.03 | -0.01 | -0.01 | 0.43 | 101.84 |
| 156 / 1 . | P-cell4-plain | 4.94 | 0.00 | 65.93 | 19.81 | 0.01 | 9.93 | 0.53 | 0.17 | -0.01 | 0.04 | -0.01 | -0.01 | 0.50 | 101.86 |
| 157 / 1 . | P-cell4-plain | 5.16 | 0.02 | 64.23 | 20.07 | -0.01 | 9.04 | 0.87 | 0.28 | 0.01 | 0.07 | -0.03 | 0.02 | 0.38 | 100.14 |
| 158 / 1 . | P-cell4-plain | 5.68 | 0.00 | 63.83 | 19.12 | -0.01 | 9.13 | 0.43 | 0.15 | 0.01 | 0.01 | -0.02 | -0.01 | 0.25 | 98.60 |
| 159 / 1 . | P-cell4-plain | 4.58 | 0.00 | 59.20 | 17.15 | 0.00 | 8.95 | 0.41 | 0.10 | -0.04 | 0.03 | -0.04 | 0.02 | 0.46 | 90.88 |

**Sanidine**

| | | | | | | | | | | | | | | | |
|---|---|---|---|---|---|---|---|---|---|---|---|---|---|---|---|
| 22 / 1 . | P-cell4-Xe | 5.17 | 0.04 | 64.38 | 19.14 | 0.01 | 7.71 | 1.13 | 0.13 | 0.00 | 0.07 | 0.00 | 0.46 | 0.20 | 98.42 |
| 23 / 1 . | P-cell4-Xe | 5.25 | 0.03 | 67.15 | 20.11 | 0.00 | 7.41 | 1.11 | 0.02 | -0.01 | 0.03 | 0.00 | 0.50 | 0.25 | 101.82 |
| 24 / 1 . | P-cell4-Xe | 4.37 | 0.01 | 63.66 | 19.85 | -0.01 | 8.57 | 0.79 | 0.11 | 0.03 | 0.05 | -0.01 | 0.47 | 0.45 | 98.34 |
| 25 / 1 . | P-cell4-Xe | 4.20 | 0.02 | 65.61 | 20.26 | 0.01 | 8.15 | 0.93 | 0.12 | 0.00 | 0.04 | -0.01 | 0.52 | 0.39 | 100.23 |
| 26 / 1 . | P-cell4-Xe | 2.38 | 0.04 | 64.32 | 19.94 | 0.01 | 5.73 | 1.11 | 0.16 | 0.02 | 0.06 | -0.02 | 0.52 | 0.13 | 94.39 |
| 27 / 1 . | P-cell4-Xe | 4.68 | 0.66 | 60.11 | 18.51 | -0.01 | 7.72 | 0.93 | 0.27 | -0.02 | 0.04 | -0.01 | 0.36 | 0.33 | 93.58 |
| 28 / 1 . | P-cell4-Xe | 4.38 | 0.02 | 63.90 | 20.01 | 0.01 | 8.37 | 0.90 | 0.09 | 0.02 | 0.06 | -0.02 | 0.37 | 0.29 | 98.42 |
| 29 / 1 . | P-cell4-Xe | 4.09 | 0.01 | 64.65 | 19.84 | 0.01 | 8.31 | 0.86 | 0.09 | 0.01 | 0.07 | 0.00 | 0.55 | 0.31 | 98.78 |
| 30 / 1 . | P-cell4-Xe | 4.53 | 0.06 | 65.03 | 20.08 | 0.00 | 7.81 | 0.93 | 0.10 | 0.03 | 0.01 | -0.02 | 0.33 | 0.27 | 99.16 |
| 31 / 1 . | P-cell4-Xe | 4.52 | 0.02 | 66.09 | 20.42 | 0.00 | 8.22 | 0.74 | 0.28 | 0.00 | 0.00 | -0.01 | 0.31 | 0.24 | 100.80 |
| 32 / 1 . | P-cell4-Xe | 5.28 | 0.02 | 64.85 | 20.03 | 0.01 | 8.48 | 0.62 | 0.05 | 0.01 | -0.01 | -0.02 | 0.38 | 0.27 | 99.99 |
| 33 / 1 . | P-cell4-Xe | 5.33 | 0.01 | 65.49 | 20.45 | 0.00 | 8.12 | 0.69 | 0.05 | 0.01 | 0.05 | -0.01 | 0.47 | 0.24 | 100.90 |

**Atomic formula sanidine**

| | | | | | | | | | | | | | | | |
|---|---|---|---|---|---|---|---|---|---|---|---|---|---|---|---|
| 19 / 1 . | P-cell3-Xe/Ar | 0.23 | 0.02 | 65.02 | 18.38 | 0.29 | 12.69 | 0.01 | 0.06 | 0.01 | 0.04 | 0.02 | 0.71 | 0.12 | 97.58 |
| 34 / 1 . | P-cell3-Xe/Ar | 0.65 | 0.02 | 64.75 | 18.06 | 0.31 | 12.40 | 0.00 | 0.06 | 0.00 | 0.08 | 0.01 | 0.61 | 0.00 | 96.93 |
| 35 / 1 . | P-cell3-Xe/Ar | 0.61 | 0.02 | 64.38 | 18.21 | 0.28 | 11.33 | 0.02 | 0.00 | -0.02 | 0.06 | 0.00 | 0.57 | -0.02 | 95.45 |
| 36 / 1 . | P-cell3-Xe/Ar | 0.74 | 0.01 | 36.83 | 8.79 | 0.29 | 11.62 | 0.01 | 0.06 | 0.02 | 0.04 | 0.00 | 0.61 | 0.20 | 59.21 |
| 37 / 1 . | P-cell3-Xe/Ar | 1.21 | 0.02 | 62.77 | 20.76 | 0.26 | 9.55 | 0.00 | 0.02 | -0.01 | 0.05 | -0.01 | 0.55 | 0.11 | 95.29 |
| 38 / 1 . | P-cell3-Xe/Ar | 1.90 | 0.02 | 64.83 | 18.65 | 0.28 | 8.89 | 0.03 | -0.03 | 0.00 | 0.05 | -0.01 | 0.61 | 0.16 | 95.40 |
| 39 / 1 . | P-cell3-Xe/Ar | 1.04 | 0.01 | 62.21 | 18.96 | 0.29 | 13.36 | 0.02 | 0.02 | 0.03 | 0.03 | -0.01 | 0.62 | 0.05 | 96.61 |
| 40 / 1 . | P-cell3-Xe/Ar | 1.06 | 0.02 | 64.20 | 19.05 | 0.30 | 11.77 | 0.03 | -0.03 | -0.01 | 0.08 | -0.01 | 0.61 | 0.13 | 97.22 |
| 41 / 1 . | P-cell3-Xe/Ar | 2.23 | 0.03 | 58.21 | 19.28 | 0.31 | 16.14 | 0.02 | -0.03 | 0.00 | 0.05 | -0.02 | 0.59 | 0.23 | 97.05 |
| 42 / 1 . | P-cell3-Xe/Ar | 1.05 | 0.02 | 63.30 | 17.99 | 0.32 | 14.22 | 0.03 | 0.04 | 0.00 | 0.03 | 0.01 | 0.60 | 0.06 | 97.63 |

*EMPA recorded on recovered gasket after experiments (in orange wt% oxide total lower than 96% or higher than 102%). Blanks mean that element has not been analyzed.*

## Appendix F8/ Rietveld refinement for plain sanidine Itrongahi, P-cell6-plain

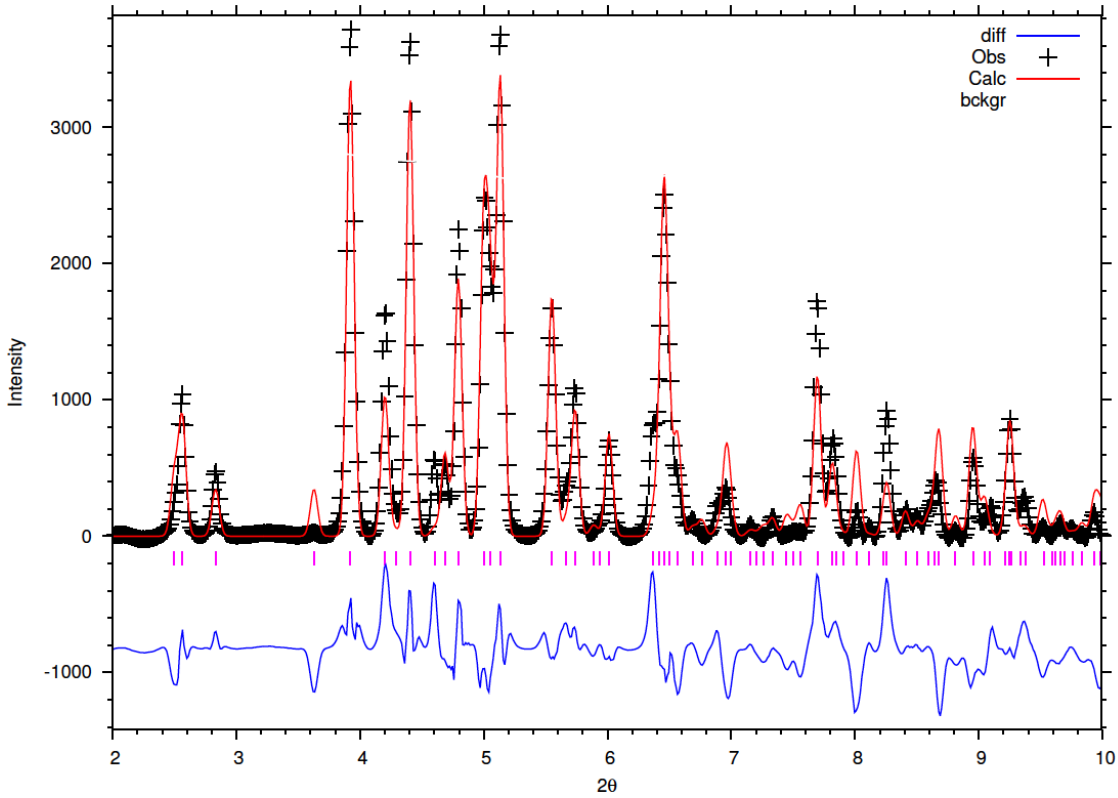


*Rietveld refinement for plain sanidine Itrongahi (P-cell6-plain) at 0.5 GPa and 676 K.*

## Appendix F9/ Rietveld refinements for sanidine Nat. (P-cell4-plain and P-cell4-Xe)

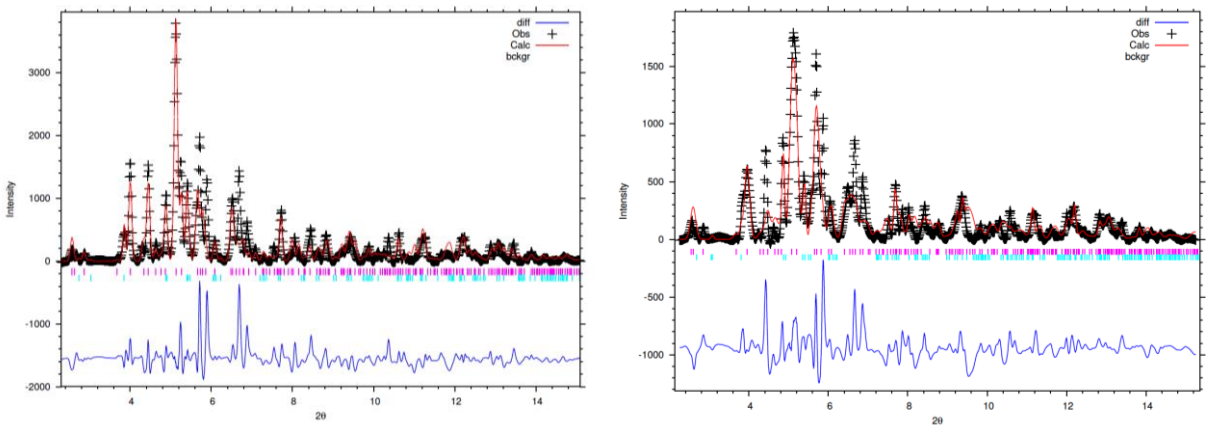


*Rietveld refinement for plain sanidine Nat. (P-cell4-plain) (left) at 5.1 GPa and 1373 K and Xe-bearing sanidine Nat. (P-cell4-Xe) at 3.1 GPa and 1473 K.*

## APPENDIX G/

## Appendix G1/ Average chemical composition of synthesized sanidine glasses

| Sample | $Na_2O$ | $SiO_2$ | $Al_2O_3$ | Ar | $K_2O$ | CaO | FeO | Kr | Xe | BaO | Total |
|---|---|---|---|---|---|---|---|---|---|---|---|
| **San Volk.** | 0.86 (2) | 66.3 (3) | 18.02 (9) | - | 15.6 (1) | -0.02 (1) | 0.78 (6) | - | - | 0.06 (3) | 101.6 (3) |
| **San Nat.** | 5.21 (9) | 66.0 (4) | 19.68 (8) | - | 9.2 (1) | 0.65 (5) | 0.22 (3) | - | - | 0.33 (7) | 101.4 (3) |
| **San It.** | 1.82 (5) | 65.0 (5) | 19.09 (7) | - | 14.0 (1) | -0.01 (1) | 0.17 (4) | - | - | 1.03 (9) | 101.2 (5) |
| **PC53** | 3.7 (5) | 64 (1) | 19.4 (5) | - | 8.2 (5) | 0.8 (4) | 0.4 (2) | - | 1.9 (2) | 0.30 (1) | 98.7 (5) |
| **PC69** | 4.8 (3) | 63.6 (5) | 19.2 (2) | - | 8.7 (4) | 0.78 (5) | -0.03 (9) | 0.52 (6) | 2.18 (4) | n.m. | 99.7 (7) |
| **PC70** | 5.1 (2) | 65.3 (6) | 19.4 (2) | 0.01 | 8.9 (2) | 0.80 (4) | 0.04 (5) | - | 0.05 (2) | 0.34 (7) | 99.8 (6) |
| **PC112A** | 1.7 (1) | 63.9 (8) | 19.2 (9) | - | 13.6 (5) | 0.02 (1) | 0.01 (1) | 0.03 (1) | 0.09 (2) | 1.05 (8) | 100 (1) |
| **PC112B** | 0.5 (2) | 67 (3) | 19.1 (6) | - | 11 (4) | 0.01 (2) | 0.2 (1) | 0.01 (1) | 0.06 (2) | 0.1 (1) | 99 (2) |
| **PC116A** | 0.65 (2) | 64.3 (5) | 18.5 (2) | 0.31 (2) | 12.6 (4) | 0.00 (1) | 0.00 (3) | - | 0.57 (4) | 0.07 (9) | 97.1 (6) |
| **PC116B** | 3 (2) | 62 (2) | 18.9 (8) | 0.06 (1) | 7 (1) | 0.8 (3) | 0.01 (1) | - | 0.16 (2) | 0.37 (6) | 92.1 (6) |
| **PC139*** | 0.8 | 66.3 | 18.3 | - | 13.8 | 0.03 | 0.03 | - | - | - | 100 |

*Average chemical compositions in wt% oxide retrieved for starting sanidine minerals, and for the different synthesized sanidine glasses. * analyses by EDX with SEM, less reliable than other EMP data.*

## Appendix G2/ EMPA of synthesized sanidine glasses

| **2017-05-29** | | | | | | | | | | | | | | | | | |
|---|---|---|---|---|---|---|---|---|---|---|---|---|---|---|---|---|---|
| **n° of analysis** | **sample** | $Na_2O$ | MgO | $SiO_2$ | $Al_2O_3$ | Ar | $K_2O$ | CaO | FeO | MnO | $TiO_2$ | Kr | Xe | BaO | $Cr_2O_3$ | NiO | $Re_2O_7$ | Total |
| **Glass** | | | | | | | | | | | | | | | | | | |
| 55 / 1 . | PC112A | 0.03 | 0.01 | 0.10 | 0.02 | -0.01 | 0.00 | 0.01 | 0.00 | 0.00 | -0.01 | 0.00 | 0.00 | 0.07 | | | | 0.25 |
| 56 / 1 . | PC112A | 3.03 | 5.08 | 62.65 | 14.93 | 0.01 | 1.17 | 0.13 | -0.02 | 0.01 | 0.01 | -0.02 | -0.01 | -0.01 | | | | 87.02 |
| 57 / 1 . | PC112A | 1.51 | 0.01 | 65.07 | 20.93 | 0.00 | 13.05 | 0.02 | 0.02 | 0.00 | 0.03 | 0.03 | 0.09 | 1.07 | | | | 101.86 |
| 58 / 1 . | PC112A | 1.79 | 0.01 | 65.02 | 20.20 | 0.00 | 13.86 | 0.02 | -0.01 | 0.00 | -0.03 | 0.05 | 0.16 | 0.92 | | | | 102.06 |
| 59 / 1 . | PC112A | 1.64 | 0.01 | 65.18 | 20.65 | 0.01 | 13.37 | 0.02 | 0.03 | 0.01 | -0.03 | 0.04 | 0.14 | 1.08 | | | | 102.22 |
| 60 / 1 . | PC112A | 1.34 | 0.00 | 65.94 | 21.39 | 0.00 | 12.28 | 0.01 | -0.01 | 0.00 | -0.04 | 0.04 | 0.09 | 1.01 | | | | 102.14 |

| | | | | | | | | | | | | | | | | | | |
|---|---|---|---|---|---|---|---|---|---|---|---|---|---|---|---|---|---|---|
| 61 / 1 . | PC112A | 1.36 | 0.01 | 65.30 | 21.27 | 0.00 | 12.48 | 0.03 | 0.00 | -0.01 | -0.03 | 0.03 | 0.09 | 0.96 | | | | 101.56 |
| 62 / 1 . | PC112A | 1.33 | 0.00 | 65.67 | 20.93 | 0.01 | 12.07 | 0.03 | 0.05 | -0.02 | -0.03 | 0.05 | 0.08 | 1.03 | | | | 101.26 |
| 63 / 1 . | PC112A | 1.27 | 0.00 | 65.74 | 21.03 | 0.00 | 11.84 | 0.02 | 0.02 | 0.00 | 0.01 | 0.06 | 0.11 | 1.01 | | | | 101.16 |
| 64 / 1 . | PC112A | 1.60 | 0.00 | 65.08 | 21.03 | 0.01 | 13.10 | 0.01 | 0.04 | -0.01 | 0.00 | 0.04 | 0.10 | 1.09 | | | | 102.12 |
| 65 / 1 . | PC112A | 1.31 | 0.01 | 65.61 | 21.19 | 0.01 | 12.21 | 0.00 | 0.00 | 0.00 | -0.02 | 0.06 | 0.06 | 0.94 | | | | 101.42 |
| 66 / 1 . | PC112A | 1.45 | 0.00 | 64.67 | 21.19 | 0.01 | 13.24 | 0.03 | 0.01 | 0.01 | -0.05 | 0.04 | 0.09 | 1.19 | | | | 101.94 |

| **2017-05-19** | | | | | | | | | | | | | | | | | | |
|---|---|---|---|---|---|---|---|---|---|---|---|---|---|---|---|---|---|---|
| **n° of analysis** | **sample** | **$Na_2O$** | **MgO** | **$SiO_2$** | **$Al_2O_3$** | **Ar** | **$K_2O$** | **CaO** | **FeO** | **MnO** | **$TiO_2$** | **Kr** | **Xe** | **BaO** | **$Cr_2O_3$** | **NiO** | **$Re_2O_7$** | **Total** |
| **Glass** | | | | | | | | | | | | | | | | | | |
| 50 / 1 . | PC116B | 0.82 | 0.01 | 65.73 | 19.32 | 0.05 | 3.75 | 0.84 | 0.00 | 0.01 | 0.03 | 0.01 | 0.11 | 0.26 | | | | 90.94 |
| 51 / 1 . | PC116B | 1.88 | 0.02 | 63.51 | 19.55 | 0.10 | 6.73 | 0.81 | 0.02 | 0.00 | 0.00 | 0.01 | 0.15 | 0.40 | | | | 93.17 |
| 52 / 1 . | PC116B | 1.74 | 0.02 | 63.98 | 19.97 | 0.05 | 6.68 | 0.79 | 0.02 | 0.04 | 0.05 | 0.01 | 0.19 | 0.45 | | | | 93.99 |
| 53 / 1 . | PC116B | 0.62 | 0.03 | 66.79 | 20.01 | 0.08 | 2.96 | 0.83 | -0.01 | 0.02 | 0.02 | -0.01 | 0.17 | 0.43 | | | | 91.95 |
| 54 / 1 . | PC116B | 0.84 | 0.02 | 66.07 | 19.73 | 0.08 | 3.88 | 0.79 | 0.01 | -0.01 | 0.04 | 0.00 | 0.16 | 0.35 | | | | 91.96 |
| 55 / 1 . | PC116B | 0.74 | 0.02 | 66.61 | 20.09 | 0.07 | 3.55 | 0.80 | 0.06 | 0.00 | 0.05 | 0.02 | 0.14 | 0.44 | | | | 92.57 |
| 56 / 1 . | PC116B | 1.88 | 0.03 | 62.76 | 19.55 | 0.07 | 6.88 | 0.81 | 0.01 | 0.00 | 0.04 | 0.01 | 0.15 | 0.39 | | | | 92.58 |
| 57 / 1 . | PC116B | 1.89 | 0.02 | 64.03 | 19.48 | 0.07 | 6.62 | 0.79 | -0.01 | -0.01 | 0.04 | -0.01 | 0.18 | 0.22 | | | | 93.33 |
| 58 / 1 . | PC116B | 1.61 | 0.02 | 63.11 | 19.70 | 0.06 | 6.39 | 0.79 | 0.01 | 0.00 | 0.03 | -0.01 | 0.16 | 0.26 | | | | 92.13 |
| 59 / 1 . | PC116B | 1.64 | 0.01 | 62.87 | 19.69 | 0.07 | 6.33 | 0.76 | 0.01 | 0.02 | 0.08 | 0.00 | 0.16 | 0.42 | | | | 92.05 |
| 60 / 1 . | PC116B | 1.71 | 0.02 | 63.04 | 19.61 | 0.06 | 6.48 | 0.83 | -0.04 | -0.01 | 0.02 | 0.00 | 0.15 | 0.23 | | | | 92.16 |
| 61 / 1 . | PC116B | 1.66 | 0.02 | 63.34 | 19.49 | 0.04 | 6.53 | 0.82 | 0.01 | -0.01 | 0.05 | 0.00 | 0.14 | 0.32 | | | | 92.42 |
| 62 / 1 . | PC116B | 1.61 | 0.02 | 63.88 | 19.65 | 0.06 | 6.17 | 0.83 | -0.01 | -0.02 | 0.07 | 0.00 | 0.15 | 0.38 | | | | 92.82 |
| 63 / 1 . | PC116B | 1.75 | 0.01 | 63.78 | 19.97 | 0.07 | 6.47 | 0.75 | 0.03 | 0.00 | 0.04 | -0.01 | 0.18 | 0.48 | | | | 93.51 |
| 64 / 1 . | PC116B | 1.59 | 0.02 | 64.03 | 19.56 | 0.07 | 6.17 | 0.84 | 0.03 | 0.01 | 0.05 | -0.01 | 0.16 | 0.33 | | | | 92.86 |
| 65 / 1 . | PC116B | 1.65 | 0.02 | 63.28 | 19.75 | 0.06 | 6.24 | 0.79 | 0.01 | -0.01 | 0.06 | 0.02 | 0.18 | 0.31 | | | | 92.36 |
| 66 / 1 . | PC116B | 1.85 | 0.02 | 63.24 | 19.66 | 0.05 | 6.59 | 0.80 | -0.02 | 0.01 | 0.06 | 0.00 | 0.14 | 0.32 | | | | 92.73 |
| 67 / 1 . | PC116B | 1.69 | 0.01 | 64.28 | 19.64 | 0.06 | 6.47 | 0.79 | -0.01 | -0.01 | 0.04 | -0.01 | 0.16 | 0.36 | | | | 93.50 |
| 68 / 1 . | PC116B | 1.44 | 0.02 | 63.23 | 19.74 | 0.05 | 6.23 | 0.80 | 0.01 | -0.03 | 0.05 | 0.01 | 0.17 | 0.38 | | | | 92.12 |
| 69 / 1 . | PC116B | 1.60 | 0.02 | 63.16 | 19.69 | 0.05 | 6.19 | 0.81 | 0.01 | -0.02 | 0.06 | -0.02 | 0.14 | 0.40 | | | | 92.13 |

| Glass | | | | | | | | | | | | | | | | | | |
|---|---|---|---|---|---|---|---|---|---|---|---|---|---|---|---|---|---|---|
| 43 / 1 . | PC116A | 0.37 | 0.00 | 67.64 | 18.56 | 0.34 | 7.42 | 0.01 | 0.00 | 0.04 | 0.03 | 0.00 | 0.57 | 0.13 | | | | 95.09 |
| 44 / 1 . | PC116A | 0.38 | 0.02 | 68.23 | 18.47 | 0.31 | 7.24 | 0.00 | 0.01 | 0.00 | 0.02 | 0.01 | 0.61 | 0.05 | | | | 95.33 |
| 45 / 1 . | PC116A | 0.68 | 0.04 | 64.08 | 18.10 | 0.32 | 13.17 | -0.01 | 0.02 | 0.02 | 0.06 | -0.01 | 0.60 | 0.03 | | | | 97.09 |
| 46 / 1 . | PC116A | 0.62 | 0.02 | 64.18 | 18.37 | 0.32 | 12.47 | -0.01 | 0.00 | 0.00 | 0.06 | -0.01 | 0.56 | 0.12 | | | | 96.70 |
| 47 / 1 . | PC116A | 0.35 | 0.01 | 67.35 | 18.56 | 0.31 | 6.80 | -0.01 | 0.00 | -0.02 | 0.02 | 0.00 | 0.52 | 0.07 | | | | 93.99 |
| 48 / 1 . | PC116A | 0.66 | 0.01 | 63.98 | 18.44 | 0.27 | 13.03 | -0.01 | 0.01 | 0.01 | 0.02 | 0.02 | 0.51 | 0.05 | | | | 96.99 |
| 49 / 1 . | PC116A | 0.64 | 0.02 | 63.91 | 18.30 | 0.31 | 12.16 | 0.01 | 0.02 | -0.01 | 0.02 | 0.00 | 0.56 | 0.05 | | | | 95.97 |
| 70 / 1 . | PC116A | 0.65 | 0.01 | 64.81 | 18.71 | 0.32 | 12.29 | 0.00 | 0.01 | 0.00 | 0.07 | 0.01 | 0.55 | -0.10 | | | | 97.40 |
| 71 / 1 . | PC116A | 0.66 | 0.02 | 65.08 | 18.65 | 0.33 | 12.62 | 0.01 | -0.04 | 0.01 | 0.08 | -0.01 | 0.53 | 0.01 | | | | 97.98 |
| 72 / 1 . | PC116A | 0.66 | 0.02 | 65.49 | 18.64 | 0.28 | 12.28 | 0.01 | 0.04 | 0.01 | 0.06 | 0.01 | 0.49 | 0.22 | | | | 98.20 |
| 73 / 1 . | PC116A | 0.66 | 0.01 | 64.18 | 18.28 | 0.31 | 12.80 | -0.01 | 0.00 | -0.02 | 0.02 | 0.01 | 0.57 | -0.03 | | | | 96.81 |
| 74 / 1 . | PC116A | 0.63 | 0.02 | 64.04 | 18.47 | 0.31 | 12.34 | 0.00 | -0.05 | 0.02 | 0.01 | 0.04 | 0.66 | 0.25 | | | | 96.76 |
| 75 / 1 . | PC116A | 0.61 | 0.02 | 64.23 | 18.52 | 0.32 | 12.29 | 0.00 | 0.02 | 0.01 | 0.04 | 0.00 | 0.59 | 0.02 | | | | 96.65 |
| 76 / 1 . | PC116A | 0.60 | 0.01 | 64.14 | 18.39 | 0.33 | 11.50 | 0.00 | 0.03 | 0.00 | 0.03 | 0.00 | 0.53 | 0.12 | | | | 95.67 |
| 77 / 1 . | PC116A | 0.66 | 0.02 | 64.07 | 18.39 | 0.32 | 12.28 | 0.00 | -0.01 | -0.04 | 0.02 | -0.01 | 0.62 | 0.10 | | | | 96.46 |
| 78 / 1 . | PC116A | 0.64 | 0.02 | 63.34 | 18.24 | 0.32 | 12.11 | 0.01 | 0.04 | 0.00 | 0.03 | -0.02 | 0.62 | 0.11 | | | | 95.45 |
| 79 / 1 . | PC116A | 0.65 | 0.02 | 64.07 | 18.42 | 0.32 | 12.87 | 0.02 | 0.00 | 0.03 | 0.02 | 0.00 | 0.58 | 0.09 | | | | 97.07 |
| 80 / 1 . | PC116A | 0.64 | 0.02 | 63.85 | 18.66 | 0.30 | 13.13 | 0.00 | 0.01 | 0.01 | 0.08 | 0.00 | 0.57 | 0.12 | | | | 97.38 |
| 81 / 1 . | PC116A | 0.68 | 0.01 | 64.62 | 18.61 | 0.33 | 13.01 | 0.00 | 0.01 | -0.01 | 0.03 | -0.01 | 0.59 | 0.14 | | | | 98.00 |
| 82 / 1 . | PC116A | 0.61 | 0.02 | 64.55 | 18.75 | 0.33 | 12.67 | 0.00 | -0.03 | -0.02 | 0.00 | 0.01 | 0.59 | 0.03 | | | | 97.53 |

| 2017-11-16 | | | | | | | | | | | | | | | | | | |
|---|---|---|---|---|---|---|---|---|---|---|---|---|---|---|---|---|---|---|
| **n° of analysis** | **sample** | **$Na_2O$** | **MgO** | **$SiO_2$** | **$Al_2O_3$** | **Ar** | **$K_2O$** | **CaO** | **FeO** | **MnO** | **$TiO_2$** | **Kr** | **Xe** | **BaO** | **$Cr_2O_3$** | **NiO** | **$Re_2O_7$** | **Total** |
| 136 / 1 . | PC112B | 0.18 | 0.02 | 74.09 | 20.40 | 0.01 | 3.94 | 0.03 | 0.36 | 0.02 | 0.01 | 0.01 | 0.06 | 0.05 | -0.02 | 0.01 | -0.11 | 99.20 |
| 285 / 1 . | PC112B | 0.25 | 0.02 | 70.06 | 19.87 | 0.01 | 5.51 | 0.02 | 0.37 | 0.02 | 0.03 | 0.01 | 0.06 | 0.16 | -0.01 | -0.05 | -0.10 | 96.39 |
| 286 / 1 . | PC112B | 0.32 | 0.03 | 69.36 | 19.89 | 0.02 | 6.55 | 0.02 | 0.29 | 0.00 | 0.04 | 0.02 | 0.09 | 0.14 | 0.01 | -0.01 | -0.09 | 96.77 |
| 287 / 1 . | PC112B | 0.27 | 0.03 | 70.78 | 20.06 | 0.01 | 5.73 | 0.02 | 0.24 | -0.01 | 0.02 | 0.03 | 0.07 | 0.06 | 0.00 | -0.01 | -0.08 | 97.33 |
| 288 / 1 . | PC112B | 0.25 | 0.01 | 70.85 | 20.02 | 0.01 | 5.71 | 0.00 | 0.24 | -0.02 | 0.02 | 0.01 | 0.07 | 0.13 | -0.01 | -0.05 | -0.16 | 97.32 |

| | | | | | | | | | | | | | | | | | | |
|---|---|---|---|---|---|---|---|---|---|---|---|---|---|---|---|---|---|---|
| 289 / 1 . | PC112B | 0.52 | 0.03 | 68.20 | 19.66 | 0.01 | 8.91 | 0.03 | 0.20 | -0.02 | 0.01 | 0.01 | 0.08 | 0.18 | -0.01 | -0.04 | -0.17 | 97.84 |
| 290 / 1 . | PC112B | 0.28 | 0.02 | 69.92 | 19.69 | 0.00 | 6.41 | 0.02 | 0.10 | -0.01 | 0.00 | 0.02 | 0.05 | 0.15 | -0.02 | 0.02 | -0.11 | 96.69 |
| 291 / 1 . | PC112B | 0.29 | 0.01 | 69.64 | 19.80 | 0.01 | 6.47 | 0.03 | 0.02 | -0.01 | 0.01 | 0.03 | 0.07 | 0.17 | 0.00 | 0.00 | -0.09 | 96.56 |
| 292 / 1 . | PC112B | 0.29 | 0.01 | 70.00 | 20.04 | 0.01 | 6.54 | 0.00 | 0.10 | -0.01 | 0.00 | 0.02 | 0.09 | 0.16 | 0.01 | 0.03 | -0.14 | 97.29 |
| 293 / 1 . | PC112B | 0.39 | 0.02 | 68.21 | 19.66 | 0.01 | 8.04 | -0.02 | 0.07 | -0.02 | -0.04 | 0.01 | 0.07 | 0.14 | 0.02 | 0.02 | -0.18 | 96.65 |
| 294 / 1 . | PC112B | 0.31 | 0.03 | 68.79 | 19.75 | 0.02 | 6.65 | 0.02 | 0.15 | 0.00 | 0.02 | 0.02 | 0.03 | 0.07 | 0.00 | -0.06 | -0.09 | 95.85 |
| 295 / 1 . | PC112B | 0.25 | 0.01 | 69.72 | 19.98 | 0.00 | 5.56 | -0.01 | 0.25 | 0.01 | 0.01 | 0.01 | 0.07 | 0.09 | 0.01 | -0.02 | -0.17 | 95.97 |
| 296 / 1 . | PC112B | 0.27 | 0.02 | 69.29 | 19.83 | 0.01 | 5.96 | -0.01 | 0.33 | -0.01 | -0.01 | 0.03 | 0.10 | -0.02 | -0.01 | 0.00 | -0.08 | 95.84 |
| 297 / 1 . | PC112B | 0.28 | 0.02 | 69.83 | 19.97 | 0.00 | 5.76 | -0.01 | 0.45 | -0.01 | -0.01 | 0.02 | 0.04 | -0.04 | 0.01 | -0.05 | -0.14 | 96.38 |
| 298 / 1 . | PC112B | 0.25 | 0.02 | 70.08 | 19.87 | 0.01 | 5.62 | 0.00 | 0.34 | -0.02 | 0.00 | 0.01 | 0.09 | 0.09 | 0.00 | 0.03 | -0.11 | 96.41 |
| 299 / 1 . | PC112B | 0.27 | 0.02 | 69.84 | 19.56 | 0.00 | 6.09 | 0.00 | 0.28 | -0.04 | 0.05 | 0.02 | 0.08 | 0.06 | -0.01 | -0.03 | -0.10 | 96.28 |
| 300 / 1 . | PC112B | 0.27 | 0.03 | 69.40 | 19.56 | 0.00 | 6.11 | 0.00 | 0.39 | 0.00 | 0.03 | 0.03 | 0.04 | -0.04 | -0.02 | 0.00 | -0.12 | 95.86 |
| 301 / 1 . | PC112B | 0.40 | 0.00 | 68.50 | 19.55 | 0.01 | 7.83 | 0.01 | 0.34 | 0.01 | 0.03 | 0.02 | 0.06 | 0.06 | 0.01 | -0.06 | -0.13 | 96.83 |
| 302 / 1 . | PC112B | 0.36 | 0.02 | 69.11 | 19.70 | 0.01 | 7.29 | 0.01 | 0.29 | -0.01 | -0.02 | 0.01 | 0.07 | 0.20 | 0.00 | 0.00 | -0.12 | 97.06 |
| 303 / 1 . | PC112B | 0.29 | 0.03 | 70.18 | 19.78 | -0.01 | 6.16 | 0.00 | 0.30 | 0.03 | -0.04 | 0.00 | 0.08 | -0.09 | 0.00 | -0.02 | -0.14 | 96.83 |
| 304 / 1 . | PC112B | 0.22 | 0.03 | 71.14 | 19.73 | 0.02 | 5.54 | 0.01 | 0.18 | -0.01 | 0.01 | 0.02 | 0.06 | -0.18 | -0.01 | 0.02 | -0.14 | 96.98 |
| 305 / 1 . | PC112B | 0.28 | 0.03 | 69.69 | 19.99 | 0.01 | 6.51 | 0.00 | 0.19 | -0.02 | -0.01 | 0.03 | 0.09 | 0.01 | -0.01 | 0.01 | -0.14 | 96.85 |

**2018-03-15**

| n° of analysis | sample | $Na_2O$ | MgO | $SiO_2$ | $Al_2O_3$ | Ar | $K_2O$ | CaO | FeO | MnO | $TiO_2$ | Kr | Xe | BaO | $Cr_2O_3$ | NiO | $Re_2O_7$ | Total |
|---|---|---|---|---|---|---|---|---|---|---|---|---|---|---|---|---|---|---|
| **?** | | | | | | | | | | | | | | | | | | |
| 8 / 1 . | PC116B | 0.97 | 0.02 | 63.11 | 19.18 | 0.06 | 4.69 | 0.86 | 0.00 | 0.00 | 0.03 | 0.01 | 0.20 | 0.48 | 0.00 | | | 89.61 |
| 9 / 1 . | PC116B | 1.43 | 0.02 | 61.41 | 19.09 | 0.07 | 6.50 | 0.82 | 0.00 | 0.01 | 0.08 | 0.00 | 0.18 | 0.46 | 0.00 | | | 90.06 |
| **Glass** | | | | | | | | | | | | | | | | | | |
| 11 / 1 . | PC116B | 4.34 | 0.01 | 59.01 | 18.15 | 0.07 | 8.08 | 0.80 | 0.02 | 0.00 | 0.02 | 0.01 | 0.18 | 0.46 | 0.00 | | | 91.16 |
| 12 / 1 . | PC116B | 4.51 | 0.01 | 58.89 | 18.00 | 0.04 | 8.16 | 0.88 | 0.00 | 0.00 | 0.02 | 0.00 | 0.16 | 0.44 | 0.00 | | | 91.11 |
| 13 / 1 . | PC116B | 4.57 | 0.00 | 59.56 | 18.03 | 0.06 | 8.15 | 0.84 | 0.02 | 0.01 | 0.00 | 0.00 | 0.18 | 0.32 | 0.00 | | | 91.74 |
| 14 / 1 . | PC116B | 4.61 | 0.02 | 59.81 | 18.38 | 0.07 | 8.04 | 0.79 | 0.00 | 0.00 | 0.08 | 0.00 | 0.19 | 0.50 | 0.00 | | | 92.48 |
| 15 / 1 . | PC116B | 4.57 | 0.03 | 59.70 | 17.92 | 0.06 | 8.13 | 0.80 | 0.00 | 0.00 | 0.04 | 0.00 | 0.16 | 0.24 | 0.00 | | | 91.64 |

| | | | | | | | | | | | | | | | | |
|---|---|---|---|---|---|---|---|---|---|---|---|---|---|---|---|---|
| 16 / 1 . | PC116B | 4.58 | 0.02 | 59.47 | 18.27 | 0.05 | 8.17 | 0.82 | 0.00 | 0.00 | 0.03 | 0.00 | 0.21 | 0.40 | 0.00 | 92.00 |
| 17 / 1 . | PC116B | 4.56 | 0.04 | 59.46 | 18.26 | 0.09 | 8.10 | 0.75 | 0.00 | 0.00 | 0.03 | 0.00 | 0.27 | 0.41 | 0.00 | 91.96 |
| 18 / 1 . | PC116B | 4.56 | 0.03 | 59.75 | 18.29 | 0.04 | 8.07 | 0.81 | 0.00 | 0.00 | 0.06 | 0.00 | 0.17 | 0.44 | 0.00 | 92.21 |
| 19 / 1 . | PC116B | 4.51 | 0.02 | 59.49 | 18.19 | 0.04 | 8.06 | 0.84 | 0.00 | 0.03 | 0.06 | 0.00 | 0.16 | 0.42 | 0.00 | 91.84 |
| 20 / 1 . | PC116B | 4.62 | 0.02 | 59.35 | 18.17 | 0.06 | 8.23 | 0.89 | 0.04 | 0.04 | 0.00 | 0.01 | 0.19 | 0.36 | 0.00 | 91.95 |
| 21 / 1 . | PC116B | 4.58 | 0.02 | 59.54 | 18.04 | 0.07 | 8.01 | 0.85 | 0.00 | 0.01 | 0.04 | 0.00 | 0.21 | 0.43 | 0.00 | 91.78 |
| 22 / 1 . | PC116B | 4.46 | 0.02 | 58.50 | 18.11 | 0.05 | 8.10 | 0.84 | 0.00 | 0.00 | 0.03 | 0.00 | 0.16 | 0.30 | 0.00 | 90.57 |
| 23 / 1 . | PC116B | 4.54 | 0.01 | 58.94 | 18.22 | 0.06 | 7.92 | 0.81 | 0.03 | 0.01 | 0.03 | 0.00 | 0.16 | 0.33 | 0.00 | 91.06 |
| 24 / 1 . | PC116B | 4.48 | 0.03 | 58.87 | 18.16 | 0.05 | 8.05 | 0.92 | 0.00 | 0.00 | 0.02 | 0.00 | 0.20 | 0.47 | 0.00 | 91.25 |
| 25 / 1 . | PC116B | 4.58 | 0.01 | 58.79 | 17.88 | 0.05 | 7.96 | 0.88 | 0.01 | 0.01 | 0.11 | 0.00 | 0.17 | 0.45 | 0.00 | 90.89 |
| 26 / 1 . | PC116B | 4.57 | 0.02 | 58.90 | 18.07 | 0.05 | 8.06 | 0.79 | 0.04 | 0.00 | 0.07 | 0.00 | 0.18 | 0.39 | 0.00 | 91.13 |
| 27 / 1 . | PC116B | 4.56 | 0.01 | 59.31 | 18.00 | 0.05 | 8.19 | 0.84 | 0.04 | 0.00 | 0.01 | 0.00 | 0.14 | 0.24 | 0.00 | 91.39 |
| 28 / 1 . | PC116B | 4.57 | 0.03 | 59.49 | 18.37 | 0.06 | 8.07 | 0.80 | 0.00 | 0.00 | 0.02 | 0.00 | 0.14 | 0.49 | 0.00 | 92.03 |
| 29 / 1 . | PC116B | 4.57 | 0.02 | 59.37 | 18.10 | 0.04 | 8.09 | 0.83 | 0.00 | 0.00 | 0.05 | 0.02 | 0.13 | 0.37 | 0.00 | 91.57 |
| 30 / 1 . | PC116B | 4.55 | 0.00 | 59.91 | 18.24 | 0.03 | 8.19 | 0.78 | 0.00 | 0.01 | 0.06 | 0.00 | 0.13 | 0.50 | 0.00 | 92.40 |
| 31 / 1 . | PC116B | 4.59 | 0.01 | 59.35 | 18.22 | 0.06 | 8.07 | 0.81 | 0.04 | 0.00 | 0.08 | 0.00 | 0.13 | 0.32 | 0.00 | 91.68 |
| **glass** | | | | | | | | | | | | | | | | |
| 32 / 1 . | PC70 | 5.22 | 0.03 | 64.82 | 19.65 | 0.01 | 9.02 | 0.81 | 0.00 | 0.01 | 0.01 | 0.00 | 0.02 | 0.27 | 0.00 | 99.88 |
| 33 / 1 . | PC70 | 5.25 | 0.03 | 64.89 | 19.54 | 0.01 | 9.03 | 0.77 | 0.02 | 0.03 | 0.08 | 0.00 | 0.06 | 0.33 | 0.00 | 100.04 |
| 34 / 1 . | PC70 | 5.34 | 0.03 | 65.27 | 19.65 | 0.01 | 9.04 | 0.84 | 0.00 | 0.00 | 0.00 | 0.00 | 0.05 | 0.35 | 0.00 | 100.58 |
| 35 / 1 . | PC70 | 5.22 | 0.03 | 65.58 | 19.60 | 0.01 | 9.01 | 0.75 | 0.00 | 0.00 | 0.01 | 0.00 | 0.03 | 0.24 | 0.00 | 100.47 |
| 36 / 1 . | PC70 | 5.28 | 0.02 | 64.34 | 19.32 | 0.02 | 8.84 | 0.84 | 0.05 | 0.00 | 0.04 | 0.00 | 0.07 | 0.50 | 0.00 | 99.32 |
| 37 / 1 . | PC70 | 5.29 | 0.02 | 64.09 | 19.40 | 0.01 | 9.06 | 0.83 | 0.00 | 0.00 | 0.02 | 0.00 | 0.03 | 0.38 | 0.00 | 99.12 |
| 38 / 1 . | PC70 | 5.27 | 0.01 | 65.02 | 19.54 | 0.01 | 9.24 | 0.84 | 0.00 | 0.00 | 0.00 | 0.01 | 0.03 | 0.26 | 0.00 | 100.23 |
| 39 / 1 . | PC70 | 5.34 | 0.04 | 64.74 | 19.60 | 0.01 | 9.09 | 0.77 | 0.02 | 0.04 | 0.04 | 0.00 | 0.06 | 0.19 | 0.00 | 99.93 |
| 40 / 1 . | PC70 | 5.23 | 0.03 | 65.34 | 20.00 | 0.02 | 9.17 | 0.82 | 0.03 | 0.01 | 0.00 | 0.00 | 0.04 | 0.28 | 0.00 | 100.98 |
| 41 / 1 . | PC70 | 5.31 | 0.02 | 64.55 | 19.75 | 0.01 | 9.07 | 0.84 | 0.03 | 0.00 | 0.02 | 0.00 | 0.07 | 0.29 | 0.00 | 99.97 |
| 42 / 1 . | PC70 | 5.21 | 0.03 | 64.64 | 19.46 | 0.02 | 8.91 | 0.77 | 0.02 | 0.03 | 0.08 | 0.00 | 0.06 | 0.39 | 0.00 | 99.61 |
| 43 / 1 . | PC70 | 5.28 | 0.03 | 65.35 | 19.57 | 0.02 | 9.04 | 0.76 | 0.04 | 0.00 | 0.03 | 0.00 | 0.05 | 0.25 | 0.00 | 100.42 |

| | | | | | | | | | | | | | | | | |
|---|---|---|---|---|---|---|---|---|---|---|---|---|---|---|---|---|
| 44 / 1 . | PC70 | 5.14 | 0.02 | 64.16 | 19.20 | 0.01 | 8.70 | 0.80 | 0.10 | 0.00 | 0.01 | 0.00 | 0.07 | 0.33 | 0.01 | 98.54 |
| 45 / 1 . | PC70 | 5.32 | 0.00 | 64.32 | 19.54 | 0.02 | 8.94 | 0.85 | 0.23 | 0.00 | 0.00 | 0.01 | 0.06 | 0.38 | 0.01 | 99.67 |
| 46 / 1 . | PC70 | 5.25 | 0.01 | 64.68 | 19.64 | 0.02 | 9.14 | 0.74 | 0.09 | 0.01 | 0.00 | 0.00 | 0.08 | 0.37 | 0.01 | 100.01 |
| 47 / 1 . | PC70 | 5.26 | 0.01 | 65.03 | 19.77 | 0.01 | 9.17 | 0.81 | 0.03 | 0.00 | 0.00 | 0.00 | 0.07 | 0.46 | 0.00 | 100.63 |
| 48 / 1 . | PC70 | 5.34 | 0.01 | 64.75 | 19.76 | 0.01 | 8.87 | 0.83 | 0.12 | 0.01 | 0.01 | 0.00 | 0.03 | 0.27 | 0.00 | 100.02 |
| 49 / 1 . | PC70 | 5.37 | 0.02 | 65.00 | 19.68 | 0.02 | 9.16 | 0.86 | 0.02 | 0.05 | 0.00 | 0.01 | 0.08 | 0.59 | 0.00 | 100.84 |
| 50 / 1 . | PC70 | 5.32 | 0.02 | 65.29 | 19.90 | 0.02 | 8.99 | 0.84 | 0.00 | 0.00 | 0.00 | 0.00 | 0.02 | 0.31 | 0.00 | 100.71 |
| 51 / 1 . | PC70 | 5.35 | 0.00 | 65.02 | 19.61 | 0.01 | 9.04 | 0.90 | 0.02 | 0.00 | 0.02 | 0.00 | 0.06 | 0.40 | 0.00 | 100.42 |
| **glass** | | | | | | | | | | | | | | | | |
| 52 / 1 . | PC112A | 1.81 | 0.02 | 63.65 | 19.09 | 0.00 | 14.11 | 0.00 | 0.03 | 0.01 | 0.00 | 0.01 | 0.11 | 0.98 | 0.00 | 99.82 |
| 53 / 1 . | PC112A | 1.87 | 0.01 | 63.06 | 18.70 | 0.00 | 14.08 | 0.00 | 0.01 | 0.01 | 0.00 | 0.01 | 0.11 | 1.26 | 0.00 | 99.12 |
| 54 / 1 . | PC112A | 1.79 | 0.00 | 63.99 | 18.59 | 0.01 | 13.83 | 0.01 | 0.02 | 0.02 | 0.00 | 0.04 | 0.10 | 1.01 | 0.00 | 99.41 |
| 55 / 1 . | PC112A | 1.81 | 0.01 | 63.69 | 18.73 | 0.01 | 13.82 | 0.00 | 0.06 | 0.00 | 0.00 | 0.02 | 0.09 | 1.06 | 0.00 | 99.29 |
| 56 / 1 . | PC112A | 1.78 | 0.00 | 64.33 | 18.77 | 0.01 | 14.03 | 0.04 | 0.00 | 0.00 | 0.00 | 0.04 | 0.12 | 0.96 | 0.00 | 100.07 |
| 57 / 1 . | PC112A | 1.79 | 0.01 | 63.92 | 18.80 | 0.00 | 13.92 | 0.00 | 0.01 | 0.00 | 0.01 | 0.01 | 0.11 | 1.11 | 0.00 | 99.69 |
| 58 / 1 . | PC112A | 1.82 | 0.00 | 64.75 | 18.73 | 0.00 | 13.99 | 0.02 | 0.04 | 0.01 | 0.00 | 0.04 | 0.08 | 1.17 | 0.00 | 100.65 |
| 59 / 1 . | PC112A | 1.79 | 0.00 | 63.20 | 18.59 | 0.00 | 13.90 | 0.00 | 0.03 | 0.00 | 0.00 | 0.03 | 0.06 | 1.13 | 0.00 | 98.74 |
| 60 / 1 . | PC112A | 1.77 | 0.02 | 62.75 | 18.29 | 0.00 | 13.87 | 0.03 | 0.02 | 0.01 | 0.00 | 0.01 | 0.07 | 1.07 | 0.00 | 97.90 |
| 61 / 1 . | PC112A | 1.74 | 0.01 | 62.91 | 18.40 | 0.00 | 13.70 | 0.04 | 0.00 | 0.01 | 0.02 | 0.03 | 0.09 | 0.95 | 0.00 | 97.88 |
| 62 / 1 . | PC112A | 1.75 | 0.01 | 62.45 | 18.42 | 0.01 | 14.15 | 0.03 | 0.00 | 0.02 | 0.00 | 0.01 | 0.08 | 1.17 | 0.00 | 98.11 |
| 63 / 1 . | PC112A | 1.73 | 0.01 | 63.64 | 18.60 | 0.00 | 13.68 | 0.02 | 0.00 | 0.00 | 0.04 | 0.03 | 0.06 | 1.15 | 0.00 | 98.97 |
| 64 / 1 . | PC112A | 1.74 | 0.01 | 62.42 | 18.33 | 0.01 | 13.67 | 0.03 | 0.00 | 0.00 | 0.00 | 0.02 | 0.09 | 0.95 | 0.00 | 97.27 |
| 65 / 1 . | PC112 | 1.81 | 0.01 | 63.64 | 18.52 | 0.00 | 14.10 | 0.02 | 0.01 | 0.01 | 0.00 | 0.02 | 0.08 | 1.08 | 0.00 | 99.29 |
| 66 / 1 . | PC112A | 1.82 | 0.00 | 63.73 | 18.68 | 0.01 | 14.11 | 0.00 | 0.00 | 0.00 | 0.00 | 0.02 | 0.11 | 0.84 | 0.00 | 99.31 |
| 67 / 1 . | PC112A | 1.78 | 0.01 | 64.81 | 18.78 | 0.01 | 13.80 | 0.01 | 0.00 | 0.00 | 0.00 | 0.02 | 0.08 | 1.03 | 0.00 | 100.33 |
| 68 / 1 . | PC112A | 1.79 | 0.00 | 63.77 | 18.48 | 0.01 | 13.91 | 0.02 | 0.01 | 0.00 | 0.00 | 0.02 | 0.08 | 1.03 | 0.00 | 99.11 |
| 69 / 1 . | PC112A | 1.76 | 0.00 | 63.73 | 18.95 | 0.01 | 13.79 | 0.03 | 0.00 | 0.02 | 0.00 | 0.01 | 0.06 | 1.00 | 0.00 | 99.36 |
| 70 / 1 . | PC112A | 1.76 | 0.01 | 63.27 | 18.60 | 0.01 | 13.81 | 0.01 | 0.01 | 0.01 | 0.07 | 0.02 | 0.07 | 1.20 | 0.00 | 98.84 |
| 71 / 1 . | PC112A | 1.76 | 0.00 | 63.19 | 18.72 | 0.00 | 13.71 | 0.00 | 0.01 | 0.00 | 0.00 | 0.03 | 0.10 | 1.04 | 0.00 | 98.56 |

| | | | | | | | | | | | | | | | | |
|---|---|---|---|---|---|---|---|---|---|---|---|---|---|---|---|---|
| 72 / 1 . | PC112A | 1.78 | 0.00 | 63.36 | 18.68 | 0.00 | 13.95 | 0.00 | 0.00 | 0.03 | 0.07 | 0.03 | 0.10 | 1.07 | 0.00 | 99.08 |
| **glass** | | | | | | | | | | | | | | | | |
| 187 / 1 . | PC112B | 0.64 | 0.02 | 65.82 | 18.94 | 0.02 | 14.66 | 0.07 | 0.08 | 0.00 | 0.00 | 0.02 | 0.07 | 0.14 | 0.01 | 100.49 |
| 188 / 1 . | PC112B | 0.29 | 0.04 | 70.73 | 19.41 | 0.00 | 7.60 | 0.06 | 0.16 | 0.01 | 0.02 | 0.00 | 0.07 | 0.00 | 0.02 | 98.40 |
| 189 / 1 . | PC112B | 0.66 | 0.00 | 64.07 | 18.52 | 0.00 | 14.94 | 0.00 | 0.07 | 0.01 | 0.01 | 0.00 | 0.00 | 0.45 | 0.00 | 98.73 |
| 190 / 1 . | PC112B | 0.75 | 0.01 | 64.95 | 17.74 | 0.00 | 15.09 | 0.00 | 0.22 | 0.06 | 0.00 | 0.04 | 0.02 | 0.00 | 0.00 | 98.88 |
| 191 / 1 . | PC112B | 0.71 | 0.04 | 63.95 | 18.23 | 0.01 | 15.59 | 0.04 | 0.25 | 0.00 | 0.00 | 0.01 | 0.01 | 0.45 | 0.00 | 99.28 |
| 192 / 1 . | PC112B | 0.73 | 0.02 | 63.23 | 18.35 | 0.03 | 15.63 | 0.00 | 0.23 | 0.05 | 0.06 | 0.01 | 0.08 | 0.07 | 0.00 | 98.49 |
| 193 / 1 . | PC112B | 0.56 | 0.02 | 67.38 | 18.38 | 0.00 | 15.36 | 0.00 | 0.29 | 0.04 | 0.12 | 0.00 | 0.04 | 0.14 | 0.03 | 102.35 |
| 194 / 1 . | PC112B | 0.54 | 0.02 | 68.82 | 18.87 | 0.03 | 15.04 | 0.00 | 0.19 | 0.03 | 0.09 | 0.02 | 0.04 | 0.00 | 0.00 | 103.68 |
| 195 / 1 . | PC112B | 0.56 | 0.03 | 69.03 | 18.21 | 0.03 | 14.48 | 0.00 | 0.43 | 0.07 | 0.07 | 0.04 | 0.05 | 0.00 | 0.02 | 103.02 |
| 196 / 1 . | PC112B | 0.47 | 0.02 | 66.27 | 18.99 | 0.01 | 15.15 | 0.00 | 0.33 | 0.00 | 0.02 | 0.00 | 0.04 | 0.29 | 0.03 | 101.62 |
| 197 / 1 . | PC112B | 0.55 | 0.03 | 65.49 | 18.35 | 0.00 | 15.24 | 0.05 | 0.36 | 0.06 | 0.06 | 0.03 | 0.03 | 0.00 | 0.01 | 100.26 |
| 198 / 1 . | PC112B | 0.48 | 0.02 | 66.79 | 19.46 | 0.00 | 15.53 | 0.00 | 0.30 | 0.00 | 0.00 | 0.00 | 0.02 | 0.42 | 0.00 | 103.02 |
| 199 / 1 . | PC112B | 0.65 | 0.04 | 68.20 | 18.35 | 0.01 | 15.14 | 0.03 | 0.25 | 0.00 | 0.02 | 0.00 | 0.05 | 0.03 | 0.00 | 102.76 |
| 200 / 1 . | PC112B | 0.49 | 0.03 | 68.65 | 18.46 | 0.02 | 15.03 | 0.01 | 0.00 | 0.06 | 0.00 | 0.01 | 0.14 | 0.00 | 0.00 | 102.90 |
| 201 / 1 . | PC112B | 0.51 | 0.05 | 66.19 | 18.99 | 0.02 | 15.25 | 0.02 | 0.39 | 0.11 | 0.07 | 0.00 | 0.08 | 0.00 | 0.00 | 101.68 |
| 202 / 1 . | PC112B | 0.20 | 0.03 | 74.05 | 19.19 | 0.03 | 5.97 | 0.00 | 0.38 | 0.12 | 0.01 | 0.04 | 0.07 | 0.00 | 0.00 | 100.08 |
| 203 / 1 . | PC112B | 0.49 | 0.03 | 64.59 | 18.54 | 0.00 | 14.75 | 0.00 | 0.31 | 0.00 | 0.00 | 0.00 | 0.06 | 0.00 | 0.02 | 98.78 |
| 204 / 1 . | PC112B | 0.46 | 0.03 | 63.23 | 18.84 | 0.02 | 15.48 | 0.01 | 0.45 | 0.00 | 0.01 | 0.01 | 0.14 | 0.07 | 0.00 | 98.74 |
| 205 / 1 . | PC112B | 0.69 | 0.03 | 63.12 | 18.65 | 0.00 | 15.07 | 0.00 | 0.31 | 0.01 | 0.06 | 0.00 | 0.07 | 0.18 | 0.01 | 98.19 |
| 206 / 1 . | PC112B | 0.69 | 0.00 | 66.42 | 18.08 | 0.03 | 15.37 | 0.00 | 0.07 | 0.00 | 0.05 | 0.00 | 0.08 | 0.01 | 0.00 | 100.81 |
| 207 / 1 . | PC112B | 0.75 | 0.01 | 66.01 | 18.59 | 0.01 | 15.25 | 0.02 | 0.11 | 0.03 | 0.00 | 0.00 | 0.10 | 0.22 | 0.02 | 101.11 |
| 208 / 1 . | PC112B | 0.76 | 0.03 | 65.85 | 18.10 | 0.05 | 15.59 | 0.00 | 0.16 | 0.02 | 0.00 | 0.00 | 0.08 | 0.19 | 0.00 | 100.82 |
| 209 / 1 . | PC112B | 0.80 | 0.02 | 65.26 | 17.86 | 0.03 | 15.57 | 0.05 | 0.10 | 0.02 | 0.00 | 0.00 | 0.07 | 0.00 | 0.00 | 99.77 |
| 210 / 1 . | PC112B | 0.56 | 0.02 | 65.26 | 19.21 | 0.01 | 15.53 | 0.03 | 0.09 | 0.01 | 0.07 | 0.00 | 0.12 | 0.07 | 0.00 | 100.97 |
| 211 / 1 . | PC112B | 0.64 | 0.02 | 65.17 | 18.64 | 0.00 | 15.14 | 0.02 | 0.15 | 0.08 | 0.02 | 0.02 | 0.04 | 0.20 | 0.00 | 100.14 |
| 212 / 1 . | PC112B | 0.67 | 0.02 | 64.33 | 18.80 | 0.01 | 15.31 | 0.00 | 0.09 | 0.00 | 0.00 | 0.01 | 0.04 | 0.16 | 0.00 | 99.44 |
| 213 / 1 . | PC112B | 0.82 | 0.03 | 65.94 | 18.45 | 0.00 | 15.51 | 0.00 | 0.14 | 0.00 | 0.11 | 0.01 | 0.09 | 0.42 | 0.03 | 101.57 |

| | | | | | | | | | | | | | | | | | |
|---|---|---|---|---|---|---|---|---|---|---|---|---|---|---|---|---|---|
| 214 / 1 . | PC112B | 0.71 | 0.02 | 64.31 | 18.29 | 0.00 | 15.37 | 0.00 | 0.07 | 0.04 | 0.13 | 0.00 | 0.00 | 0.15 | 0.02 | | 99.11 |
| 215 / 1 . | PC112B | 0.76 | 0.00 | 64.80 | 18.43 | 0.01 | 15.19 | 0.00 | 0.09 | 0.03 | 0.10 | 0.03 | 0.05 | 0.52 | 0.00 | | 100.00 |
| 216 / 1 . | PC112B | 0.79 | 0.03 | 63.68 | 18.28 | 0.00 | 15.17 | 0.00 | 0.00 | 0.02 | 0.00 | 0.00 | 0.00 | 0.10 | 0.02 | | 98.08 |
| 131 / 1 . | PC112B | 0.49 | 0.00 | 68.39 | 19.00 | 0.01 | 14.23 | 0.01 | 0.29 | 0.03 | 0.00 | 0.02 | 0.09 | 0.00 | 0.00 | | 102.56 |
| 132 / 1 . | PC112B | 0.56 | 0.02 | 67.04 | 18.59 | 0.00 | 14.94 | 0.00 | 0.42 | 0.02 | 0.07 | 0.00 | 0.10 | 0.00 | 0.00 | | 101.77 |
| 133 / 1 . | PC112B | 0.47 | 0.04 | 65.39 | 19.22 | 0.04 | 15.37 | 0.03 | 0.26 | 0.04 | 0.04 | 0.02 | 0.03 | 0.03 | 0.00 | | 100.98 |

**Previous EMPA (CAMECA SX5)**

| n° of analysis | Sample | $Na_2O$ | MgO | $SiO_2$ | $Al_2O_3$ | Ar | $K_2O$ | CaO | FeO | MnO | $TiO_2$ | Kr | Xe | BaO | $Cr_2O_3$ | NiO | $Re_2O_7$ | Total |
|---|---|---|---|---|---|---|---|---|---|---|---|---|---|---|---|---|---|---|
| **Glass** | | | | | | | | | | | | | | | | | | |
| 1 / 1 . | PC70 | 4.82 | | 66.77 | 18.84 | 0.02 | 8.84 | 0.81 | 0.06 | | | | 0.09 | | | | | 100.24 |
| 2 / 1 . | PC70 | 4.40 | | 63.56 | 18.54 | 0.02 | 8.48 | 0.83 | 0.06 | | | | 0.11 | | | | | 95.99 |
| 2 / 2 . | PC70 | 4.98 | | 66.70 | 18.95 | 0.02 | 8.68 | 0.85 | 0.07 | | | | 0.04 | | | | | 100.31 |
| 2 / 3 . | PC70 | 4.74 | | 66.09 | 19.40 | 0.01 | 8.54 | 0.77 | -0.03 | | | | 0.12 | | | | | 99.63 |
| 2 / 4 . | PC70 | 4.93 | | 66.19 | 19.09 | 0.02 | 8.70 | 0.66 | -0.04 | | | | 0.12 | | | | | 99.66 |
| 2 / 5 . | PC70 | 4.87 | | 66.25 | 19.54 | 0.01 | 8.88 | 0.63 | 0.07 | | | | 0.07 | | | | | 100.33 |
| 2 / 6 . | PC70 | 5.10 | | 66.50 | 19.48 | 0.01 | 9.09 | 0.77 | 0.08 | | | | 0.07 | | | | | 101.10 |
| 2 / 7 . | PC70 | 4.94 | | 65.18 | 19.47 | 0.02 | 8.70 | 0.83 | 0.15 | | | | 0.11 | | | | | 99.41 |
| 2 / 8 . | PC70 | 4.93 | | 65.68 | 19.02 | 0.02 | 8.38 | 0.88 | 0.04 | | | | 0.09 | | | | | 99.03 |
| 2 / 9 . | PC70 | 4.73 | | 66.13 | 19.13 | 0.02 | 8.71 | 0.79 | 0.08 | | | | 0.11 | | | | | 99.71 |
| 2 / 10 . | PC70 | 4.96 | | 65.78 | 18.98 | 0.02 | 8.74 | 0.83 | -0.11 | | | | 0.13 | | | | | 99.32 |
| 2 / 11 . | PC70 | 4.93 | | 65.97 | 19.17 | 0.02 | 8.85 | 0.84 | 0.17 | | | | 0.07 | | | | | 100.01 |
| 2 / 12 . | PC70 | 4.65 | | 66.57 | 19.64 | 0.01 | 8.78 | 0.85 | 0.06 | | | | 0.09 | | | | | 100.65 |
| 2 / 13 . | PC70 | 4.88 | | 65.82 | 19.62 | 0.02 | 8.56 | 0.77 | 0.00 | | | | 0.06 | | | | | 99.74 |
| 2 / 14 . | PC70 | 4.99 | | 65.95 | 19.48 | 0.02 | 8.88 | 0.75 | 0.10 | | | | 0.11 | | | | | 100.28 |
| 2 / 15 . | PC70 | 4.86 | | 65.98 | 19.58 | 0.01 | 8.30 | 0.76 | -0.03 | | | | 0.10 | | | | | 99.56 |
| 2 / 16 . | PC70 | 4.95 | | 64.58 | 19.44 | 0.01 | 8.20 | 0.74 | 0.07 | | | | 0.08 | | | | | 98.08 |
| 2 / 17 . | PC70 | 4.93 | | 65.60 | 19.80 | 0.01 | 8.95 | 0.72 | 0.11 | | | | 0.10 | | | | | 100.23 |
| 2 / 18 . | PC70 | 4.77 | | 65.83 | 19.34 | 0.02 | 8.46 | 0.83 | -0.06 | | | | 0.08 | | | | | 99.28 |
| 2 / 19 . | PC70 | 4.90 | | 65.44 | 18.97 | 0.02 | 9.29 | 0.82 | 0.03 | | | | 0.14 | | | | | 99.59 |

| | | | | | | | | | | | | | | | | | |
|---|---|---|---|---|---|---|---|---|---|---|---|---|---|---|---|---|---|
| 2 / 20 . | PC70 | 5.29 | | 65.64 | 19.26 | 0.02 | 8.16 | 0.84 | 0.07 | | | 0.09 | | | | | 99.37 |

**Previous EMPA (CAMECA SX5)**

| n° of analysis | Sample | $Na_2O$ | MgO | $SiO_2$ | $Al_2O_3$ | Ar | $K_2O$ | CaO | FeO | MnO | $TiO_2$ | Kr | Xe | BaO | $Cr_2O_3$ | NiO | $Re_2O_7$ | Total |
|---|---|---|---|---|---|---|---|---|---|---|---|---|---|---|---|---|---|---|
| **Glass** | | | | | | | | | | | | | | | | | | |
| 1 / 1 . | PC69 | 4.63 | | 63.32 | 19.31 | | 7.92 | 0.80 | 0.10 | | | 0.49 | 2.18 | | | | | 98.75 |
| 2 / 1 . | PC69 | 4.37 | | 63.47 | 19.34 | | 8.69 | 0.75 | -0.08 | | | 0.50 | 2.25 | | | | | 99.28 |
| 3 / 1 . | PC69 | 5.08 | | 63.22 | 19.05 | | 8.91 | 0.71 | 0.00 | | | 0.49 | 2.12 | | | | | 99.58 |
| 4 / 1 . | PC69 | 4.69 | | 63.95 | 18.99 | | 8.74 | 0.83 | -0.10 | | | 0.48 | 2.16 | | | | | 99.75 |
| 5 / 1 . | PC69 | 4.82 | | 62.93 | 19.13 | | 9.16 | 0.72 | 0.08 | | | 0.48 | 2.20 | | | | | 99.53 |
| 11 / 1 . | PC69 | 4.94 | | 64.43 | 19.34 | | 8.65 | 0.83 | -0.11 | | | 0.61 | 2.14 | | | | | 100.82 |
| 12 / 1 . | PC69 | 5.08 | | 63.77 | 18.96 | | 8.80 | 0.82 | -0.10 | | | 0.60 | 2.22 | | | | | 100.16 |
| **glass / bubble** | | | | | | | | | | | | | | | | | | |
| 6 / 1 . | PC69 | 4.40 | | 62.07 | 19.12 | | 8.39 | 0.79 | 0.11 | | | 0.56 | 2.53 | | | | | 97.98 |
| 7 / 1 . | PC69 | 3.91 | | 61.55 | 19.26 | | 9.00 | 0.85 | -0.03 | | | 0.73 | 3.57 | | | | | 98.85 |
| 8 / 1 . | PC69 | 4.66 | | 63.31 | 19.79 | | 8.47 | 0.86 | 0.01 | | | 0.52 | 2.27 | | | | | 99.89 |
| 9 / 1 . | PC69 | 5.08 | | 64.76 | 19.50 | | 8.37 | 0.68 | 0.04 | | | 0.51 | 2.31 | | | | | 101.25 |
| 10 / 1 . | PC69 | 3.04 | | 62.40 | 18.84 | | 7.42 | 0.73 | 0.18 | | | 0.95 | 4.70 | | | | | 98.26 |

*EMPA recorded on synthesized samples (in orange wt% oxide total lower than 96% or higher than 102%). Blanks mean that the element has not been analyzed.*

## Appendix G3/ EMPA of recovered sample from XAS experiments

| 2017-11-16 | | | | | | | | | | | | | | | | | |
|---|---|---|---|---|---|---|---|---|---|---|---|---|---|---|---|---|---|
| **n° of analysis** | **sample** | **$Na_2O$** | **MgO** | **$SiO_2$** | **$Al_2O_3$** | **Ar** | **$K_2O$** | **CaO** | **FeO** | **MnO** | **$TiO_2$** | **Kr** | **Xe** | **BaO** | **$Cr_2O_3$** | **NiO** | **$Re_2O_7$** | **Total** |
| 48 / 1 . | Rec. sample | 2.41 | 0.02 | 65.16 | 19.11 | 0.01 | 12.75 | 0.15 | 0.02 | -0.04 | -0.03 | -0.01 | 0.04 | 0.38 | -0.02 | 0.06 | -0.28 | 100.10 |
| 49 / 1 . | Rec. sample | 2.43 | 0.00 | 65.36 | 19.19 | 0.01 | 13.06 | 0.11 | -0.01 | -0.01 | 0.06 | 0.01 | 0.02 | 0.43 | -0.04 | -0.01 | -0.27 | 100.67 |
| 50 / 1 . | Rec. sample | 2.70 | 0.00 | 65.90 | 19.61 | 0.00 | 12.17 | 0.20 | 0.01 | -0.01 | -0.02 | 0.01 | 0.08 | 0.51 | -0.01 | 0.03 | -0.26 | 101.22 |
| 51 / 1 . | Rec. sample | 4.11 | 0.10 | 66.00 | 21.64 | 0.00 | 8.65 | 0.64 | 0.01 | -0.01 | 0.04 | 0.01 | -0.01 | 0.25 | -0.01 | 0.05 | -0.18 | 101.49 |
| 52 / 1 . | Rec. sample | 2.15 | 0.00 | 66.59 | 20.11 | 0.01 | 11.90 | 0.12 | 0.02 | 0.00 | 0.00 | 0.01 | 0.02 | 0.59 | -0.02 | 0.01 | -0.35 | 101.53 |
| 54 / 1 . | Rec. sample | 3.90 | 0.00 | 65.33 | 19.91 | 0.00 | 10.10 | 0.34 | 0.02 | 0.00 | -0.02 | 0.00 | 0.01 | 0.55 | -0.01 | 0.00 | -0.23 | 100.17 |
| 55 / 1 . | Rec. sample | 2.15 | 0.02 | 66.17 | 19.66 | 0.01 | 12.27 | 0.13 | 0.03 | -0.02 | 0.01 | 0.02 | 0.06 | 0.62 | -0.02 | -0.05 | -0.31 | 101.16 |
| 57 / 1 . | Rec. sample | 2.29 | 0.00 | 66.57 | 20.02 | 0.00 | 11.41 | 0.14 | 0.04 | -0.02 | -0.01 | 0.00 | -0.01 | 0.38 | -0.01 | -0.04 | -0.37 | 100.84 |
| 58 / 1 . | Rec. sample | 2.40 | 0.01 | 64.64 | 19.31 | -0.01 | 12.89 | 0.18 | -0.01 | 0.04 | -0.05 | 0.01 | -0.01 | 0.47 | -0.01 | 0.01 | -0.33 | 99.96 |
| 59 / 1 . | Rec. sample | 2.46 | 0.00 | 65.34 | 19.93 | -0.01 | 12.11 | 0.23 | 0.04 | -0.01 | -0.01 | 0.01 | 0.03 | 0.41 | -0.02 | 0.01 | -0.23 | 100.57 |
| 62 / 1 . | Rec. sample | 2.81 | 0.04 | 65.21 | 20.38 | 0.00 | 11.80 | 0.41 | 0.06 | -0.03 | 0.08 | 0.02 | 0.02 | 0.43 | -0.01 | -0.02 | -0.18 | 101.26 |
| 63 / 1 . | Rec. sample | 2.27 | 0.02 | 65.01 | 20.01 | 0.00 | 11.88 | 0.21 | 0.03 | -0.02 | 0.01 | 0.00 | 0.02 | 0.45 | -0.01 | 0.01 | -0.34 | 99.92 |
| 64 / 1 . | Rec. sample | 1.99 | -0.01 | 63.55 | 19.35 | 0.00 | 12.06 | 0.07 | 0.08 | -0.03 | 0.00 | -0.01 | 0.05 | 0.56 | -0.01 | 0.03 | -0.28 | 97.74 |
| 53 / 1 . | Rec. sample | 2.98 | -0.01 | 66.62 | 19.79 | 0.01 | 10.59 | 0.33 | 0.01 | -0.01 | 0.02 | 0.15 | 0.25 | 0.43 | -0.01 | 0.03 | -0.25 | 101.21 |
| 56 / 1 . | Rec. sample | 2.62 | 0.00 | 65.82 | 19.64 | 0.00 | 12.00 | 0.18 | 0.04 | 0.02 | 0.01 | 0.06 | 0.44 | 0.51 | -0.04 | -0.06 | -0.26 | 101.36 |
| 60 / 1 . | Rec. sample | 3.27 | 0.00 | 65.80 | 20.00 | 0.01 | 9.83 | 0.47 | 0.07 | 0.03 | 0.07 | 0.20 | 0.55 | 0.40 | 0.00 | -0.01 | -0.16 | 100.72 |
| 61 / 1 . | Rec. sample | 2.58 | 0.01 | 63.58 | 19.45 | 0.01 | 11.35 | 0.27 | 0.03 | 0.02 | 0.03 | 0.09 | 0.19 | 0.49 | 0.01 | 0.02 | -0.24 | 98.12 |
| 65 / 1 . | Rec. sample | 2.59 | 0.00 | 63.86 | 19.57 | 0.02 | 11.04 | 0.36 | 0.07 | 0.03 | 0.03 | 0.18 | 0.44 | 0.48 | 0.00 | 0.02 | -0.27 | 98.71 |
| 66 / 1 . | Rec. sample | 3.75 | 0.04 | 66.23 | 20.67 | 0.01 | 9.71 | 0.67 | 0.03 | -0.03 | 0.20 | 0.03 | 0.22 | 0.40 | -0.01 | 0.02 | -0.19 | 101.97 |
| 67 / 1 . | Rec. sample | 3.79 | 0.02 | 64.14 | 19.47 | 0.00 | 10.11 | 0.61 | 0.07 | 0.01 | 0.00 | 0.09 | 0.26 | 0.49 | 0.02 | 0.02 | -0.16 | 99.10 |
| 68 / 1 . | Rec. sample | 3.85 | 0.03 | 63.19 | 19.92 | 0.03 | 9.21 | 0.67 | 0.04 | -0.02 | 0.14 | 0.53 | 1.16 | 0.47 | -0.02 | -0.01 | -0.16 | 99.27 |
| 69 / 1 . | Rec. sample | 2.83 | 0.00 | 63.47 | 19.43 | 0.00 | 11.94 | 0.21 | 0.02 | 0.00 | -0.04 | 0.02 | 0.13 | 0.49 | -0.02 | 0.05 | -0.24 | 98.57 |

*EMPA recorded on recovered sample (Rec. sample) after XAS measurement in situ in PEP experiments.*

## APPENDIX I/ HAPLOGRANITE

Haplogranite samples were synthesized previously to this work, at 3.5 GPa, 24 hours, at 1100°C in presence of Xe/Ar (PC64 HPG), and at 1200°C in presence of Xe (PC57 HPG), using a mix of oxides given in Table 1. Plain sample (PC67 HPG) was synthetized at 3.5 GPa and 1100°C, 24 hours. EMPA of recovered samples for PC64 HPG and PC57 HPG are given in table 2.

| $Na_2O$ (wt%) | $SiO_2$ (wt%) | $Al_2O_3$ (wt%) | $K_2O$ (wt%) |
|---|---|---|---|
| 4.94 | 78.07 | 12.48 | 4.52 |

*Table 1: Composition of haplogranitic glass (from Leroy, PhD thesis, 2016)*

Crystalline Xe/Ar-bearing Haplogranite (PC64 HPG) presents an intriguing phase assemblage: a pentagonal (or hexagonal) hole is surrounded by metallic silicon and an Al-rich phase ($Si_{3.8}Al_{0.9}O_9$ approximately) (figure 1 and Table 2). Xe and Ar are mostly localized in the Al-rich phase and in bubbles surrounding the structure (figure 2). The surrounding assemblage is similar in texture and composition to gas-free HPG (PC67 HPG) and is mostly composed of feldspars. Geometry of the hole proves that a crystal was present and not a bubble. Radial fractures indicate an expansion of volume likely associated with a phase transformation. If noble gases have entered the composition of the previous disappeared phase (now a hole) it could explain why this phase has evaporated and transformed into metallic Si and the Al-rich phase back to room conditions. Two ultra-thin sections have been made (figure 3), although not yet observed as beam damage was evidenced on other Xe-rich samples, and cooled-stage will be preferred, not to damage ultra-thin sections. PC57 HPG is partially molten and do not present similar assemblage as PC64 HPG.

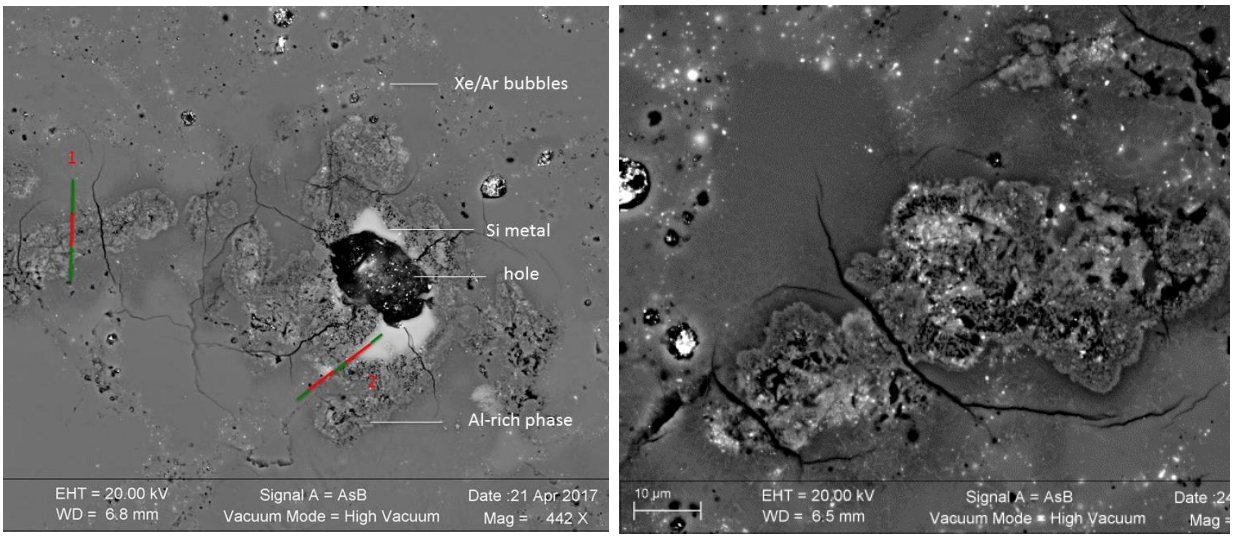


*Figure 1: SEM image in backscattered mode of recovered PC64 HPG with locations of ultra-thin sections indicated (in red the thin observable part of the section) (left). Zoom on Al-rich zones (right).*

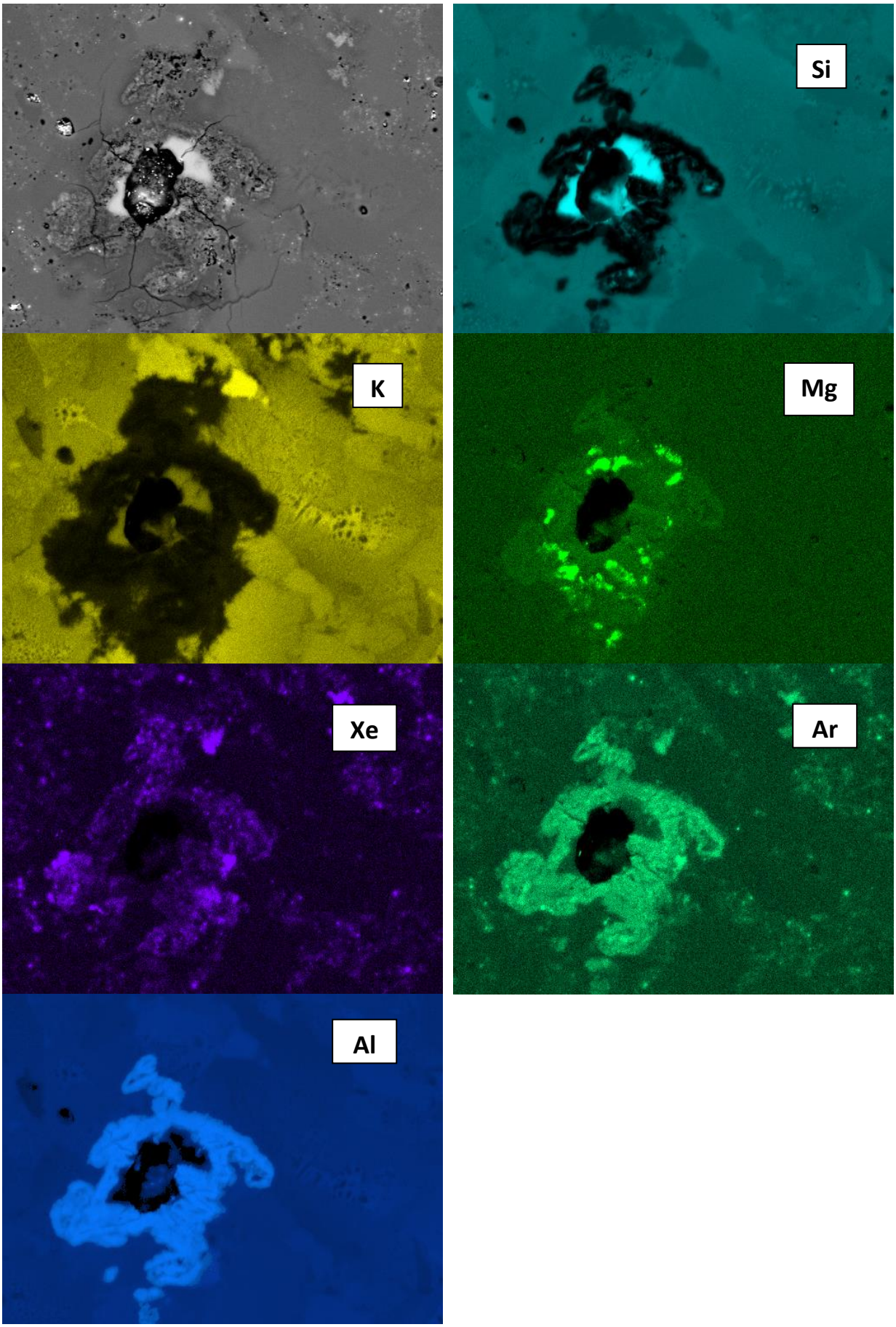


*Figure 2: Chemical mapping by SEM of PC64 HPG.*

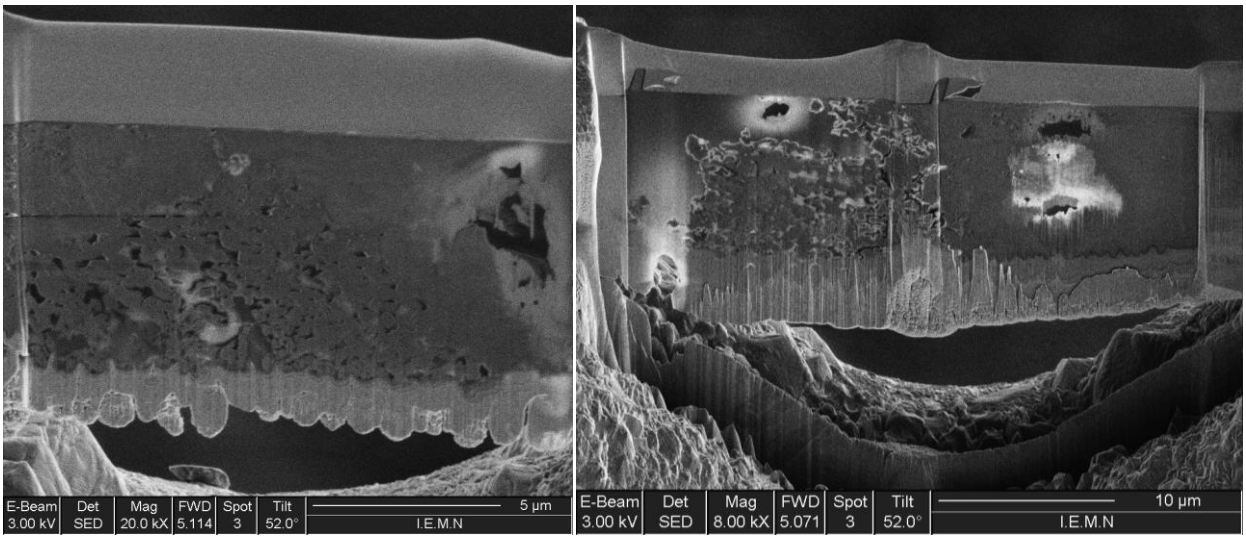


*Figure 3:Ultra-thin sections in backscattered mode by SEM-FIB (see positions in  figure 1).*

| Previous EMPA (CAMECA SX5) | | | | | | | | | | | | | |
|---|---|---|---|---|---|---|---|---|---|---|---|---|---|
| **n° of analysis** | **sample** | **$SiO_2$** | **$Na_2O$** | **$Al_2O_3$** | **$K_2O$** | **Xe** | **MgO** | **CaO** | **Ar** | **$TiO_2$** | **MnO** | **FeO** | **Total** |
| 3 / 1 . | PC64 HPG | 80.36 | 3.37 | 10.80 | 3.64 | 0.42 | | 0.04 | 0.09 | | | 0.08 | 98.81 |
| 4 / 1 . | PC64 HPG | 84.34 | 2.98 | 8.40 | 2.90 | 0.31 | | 0.08 | 0.08 | | | 0.11 | 99.20 |
| 5 / 1 . | PC64 HPG | 82.07 | 1.48 | 10.84 | 3.07 | 1.17 | | 0.06 | 0.35 | | | -0.06 | 98.98 |
| 6 / 1 . | PC64 HPG | 80.32 | 2.62 | 10.87 | 3.85 | 2.79 | | -0.05 | 0.79 | | | 0.03 | 101.21 |
| 7 / 1 . | PC64 HPG | 81.50 | 3.77 | 10.55 | 3.55 | 0.67 | | 0.08 | 0.18 | | | -0.13 | 100.17 |
| 8 / 1 . | PC64 HPG | 80.43 | 4.13 | 10.57 | 4.39 | 0.47 | | 0.04 | 0.08 | | | -0.10 | 100.00 |
| 9 / 1 . | PC64 HPG | 79.26 | 3.25 | 10.64 | 3.89 | 0.67 | | 0.01 | 0.08 | | | 0.00 | 97.81 |
| 10 / 1 . | PC64 HPG | 75.34 | 3.70 | 10.63 | 4.38 | 0.78 | | 0.03 | 0.10 | | | 0.10 | 95.05 |
| 11 / 1 . | PC64 HPG | 88.85 | 1.72 | 6.40 | 1.73 | 0.29 | | 0.01 | 0.12 | | | 0.01 | 99.14 |
| 12 / 1 . | PC64 HPG | 83.84 | 2.77 | 8.39 | 3.04 | 0.40 | | -0.01 | 0.19 | | | 0.03 | 98.65 |
| 13 / 1 . | PC64 HPG light grey rosette | 82.58 | 0.10 | 13.73 | 0.23 | 0.25 | | 0.04 | 0.06 | | | 0.16 | 97.15 |
| 14 / 1 . | PC64 HPG light grey rosette | 204.62 | -0.04 | 1.89 | 0.05 | 0.01 | | 0.03 | 0.01 | | | 0.04 | 206.60 |
| 15 / 1 . | PC64 HPG light grey rosette | 16.95 | 0.03 | 74.95 | -0.01 | 1.34 | | 0.00 | 0.25 | | | 0.33 | 93.84 |
| 16 / 1 . | PC64 HPG light grey rosette | 69.54 | 7.07 | 18.59 | 6.87 | 0.03 | | -0.03 | 0.01 | | | 0.08 | 102.17 |

| Previous EMPA University of Edinburgh | | | | | | | | | | | | | |
|---|---|---|---|---|---|---|---|---|---|---|---|---|---|
| **n° of analysis** | **sample** | **$SiO_2$** | **$Na_2O$** | **$Al_2O_3$** | **$K_2O$** | **Xe** | **MgO** | **CaO** | **Ar** | **$TiO_2$** | **MnO** | **FeO** | **Total** |
| 1 / 1 . | PC64 HPG | 80.50 | 3.76 | 12.78 | 4.58 | 0.19 | 0.00 | 0.01 | 0.26 | 0.02 | 0.00 | 0.02 | 102.17 |
| 2 / 1 . | PC64 HPG | 80.50 | 3.78 | 11.51 | 4.12 | 0.13 | 0.00 | 0.01 | 0.09 | 0.01 | 0.00 | 0.01 | 100.20 |
| 3 / 1 . | PC64 HPG | 84.73 | 3.22 | 10.79 | 3.16 | 0.30 | 0.00 | 0.01 | 0.33 | 0.03 | 0.00 | 0.02 | 102.70 |
| 4 / 1 . | PC64 HPG | 78.16 | 3.65 | 13.57 | 4.54 | 0.25 | 0.00 | 0.01 | 0.23 | 0.02 | 0.01 | 0.01 | 100.54 |
| 5 / 1 . | PC64 HPG | 75.21 | 2.97 | 14.64 | 5.24 | 0.68 | 0.00 | 0.01 | 0.60 | 0.05 | 0.01 | 0.03 | 99.68 |
| 6 / 1 . | PC64 HPG | 72.55 | 0.92 | 14.58 | 3.53 | 1.25 | 0.01 | 0.01 | 1.08 | 0.07 | 0.00 | 0.06 | 94.50 |
| 7 / 1 . | PC64 HPG | 73.74 | 5.71 | 15.89 | 5.92 | 0.03 | 0.00 | 0.02 | 0.05 | 0.01 | 0.01 | 0.00 | 101.38 |
| 8 / 1 . | PC64 HPG | 82.34 | 3.05 | 10.61 | 3.70 | 0.29 | 0.00 | 0.01 | 0.24 | 0.02 | 0.01 | 0.03 | 100.40 |
| 9 / 1 . | PC64 HPG | 80.94 | 1.95 | 12.72 | 4.17 | 0.80 | 0.00 | 0.01 | 0.75 | 0.05 | 0.00 | 0.05 | 101.71 |
| 10 / 1 . | PC64 HPG | 79.28 | 0.28 | 16.46 | 0.91 | 1.07 | 0.01 | 0.01 | 0.96 | 0.07 | 0.00 | 0.07 | 99.50 |

| | | | | | | | | | | | | | |
|---|---|---|---|---|---|---|---|---|---|---|---|---|---|
| 1 / 1 . | PC57 HPG white | 80.76 | 1.74 | 14.68 | 5.69 | 0.61 | 0.03 | 0.04 | 0.00 | 0.06 | 0.01 | 0.06 | 103.90 |
| 2 / 1 . | PC57 HPG white | 72.39 | 5.50 | 15.17 | 5.13 | 0.54 | 0.03 | 0.05 | 0.00 | 0.06 | 0.00 | 0.05 | 99.13 |
| 3 / 1 . | PC57 HPG white | 75.63 | 5.29 | 13.86 | 4.53 | 0.47 | 0.03 | 0.04 | 0.00 | 0.06 | 0.00 | 0.04 | 100.12 |
| 4 / 1 . | PC57 HPG white | 73.29 | 5.65 | 15.03 | 5.09 | 0.54 | 0.04 | 0.05 | 0.00 | 0.06 | 0.00 | 0.08 | 100.00 |
| 5 / 1 . | PC57 HPG white | 72.94 | 5.61 | 14.89 | 5.21 | 0.60 | 0.04 | 0.05 | 0.00 | 0.07 | 0.00 | 0.06 | 99.69 |
| 6 / 1 . | PC57 HPG grey | 73.24 | 5.28 | 15.06 | 5.14 | 0.53 | 0.04 | 0.05 | 0.00 | 0.06 | 0.01 | 0.03 | 99.63 |
| 7 / 1 . | PC57 HPG grey | 80.07 | 4.41 | 10.92 | 3.67 | 0.33 | 0.02 | 0.05 | 0.00 | 0.06 | 0.01 | 0.03 | 99.68 |
| 8 / 1 . | PC57 HPG grey | 73.51 | 5.64 | 14.92 | 5.04 | 0.54 | 0.04 | 0.06 | 0.00 | 0.07 | -0.01 | 0.03 | 100.04 |
| 9 / 1 . | PC57 HPG grey | 71.59 | 7.08 | 17.92 | 4.54 | 0.01 | 0.00 | 0.02 | 0.00 | 0.01 | 0.01 | 0.01 | 101.19 |
| 10 / 1 . | PC57 HPG grey | 73.45 | 5.50 | 15.16 | 5.05 | 0.64 | 0.04 | 0.05 | 0.00 | 0.08 | 0.00 | 0.06 | 100.26 |
| 11 / 1 . | PC57 HPG dark | 99.14 | 0.37 | 0.93 | 0.30 | 0.04 | 0.00 | 0.01 | 0.00 | 0.01 | 0.00 | 0.01 | 100.83 |
| 12 / 1 . | PC57 HPG dark | 99.80 | 0.12 | 0.36 | 0.13 | 0.02 | 0.00 | 0.01 | 0.00 | 0.01 | 0.01 | -0.01 | 100.46 |
| 13 / 1 . | PC57 HPG dark | 100.95 | 0.10 | 0.27 | 0.07 | 0.01 | 0.00 | 0.00 | 0.00 | 0.00 | -0.01 | 0.00 | 101.40 |
| 14 / 1 . | PC57 HPG dark | 75.98 | 5.25 | 14.16 | 4.86 | 0.47 | 0.03 | 0.04 | 0.00 | 0.06 | 0.00 | 0.05 | 101.08 |
| 15 / 1 . | PC57 HPG dark | 74.98 | 5.51 | 14.43 | 5.02 | 0.47 | 0.03 | 0.05 | 0.00 | 0.06 | -0.01 | 0.03 | 100.74 |
| | | | | | | | | | | | | | |
| 1 / 1 . | PC57 HPG white | 71.99 | 5.30 | 14.88 | 5.20 | 0.56 | 0.04 | 0.05 | 0.00 | 0.06 | 0.01 | 0.05 | 98.32 |
| 2 / 1 . | PC57 HPG dark | 101.45 | 0.06 | 0.18 | 0.04 | 0.00 | 0.00 | 0.00 | 0.00 | 0.01 | 0.00 | 0.01 | 101.74 |
| 3 / 1 . | PC57 HPG grey | 72.97 | 7.28 | 17.75 | 4.66 | 0.00 | 0.00 | 0.02 | 0.00 | 0.00 | 0.00 | 0.01 | 102.70 |

*Table 2: EMPA recorded on recovered PC64 HPG and PC57 HPG (in orange wt% oxide total lower than 96% or higher than 102%). Blanks mean that the element has not been analyzed.*

## APPENDIX J/ WAVELLITE

Attempt was made to synthesize Xe-bearing wavellite during this work (Table 1) as wavellite has been shown to retain high Xe content in the Okhlo natural nuclear reservoir (Meshik et al., 2000). However, no Xe-bearing wavellite have been synthesized. Recovered sample (PC127A and PC127B) indicates that behavior of wavellite at high pressure and temperature is complex as wavelite rapidly destabilizes (Giskow et al., 2004[22]), indeed wavellite can only be observed in hydrothermal type conditions of low temperature, for instance as a secondary mineral after quenching of experiments run at 200°C with hydrous fluids (Drüppel et al., 2007). Experiment at 1 GPa and 1000°C is on the verge of the wavellite melting point, indeed in one capsule a glass was recovered (PC127B) whereas in the other (PC127A) a crystalline assemblage was observed (probably due to temperature gradient inside the cell assembly). For PC127A a complex crystalline assemblage is observed (figure 1): corundum, an alumino-phosphate phase, a Al/F-rich phase and a destabilized Si-bearing alumino-phosphate phase with presence of vanadium.

| Name | gas mix | *P* (GPa) | *T* (°C) | Duration (hours) | powder (mg) | gas (mg) | weight loss after piercing (mg) |
|---|---|---|---|---|---|---|---|
| PC127A | Xe/Kr | 1 | 1000 | 5 | 13.8 | 2 | 0.6 |
| PC127B | Xe/Ar | 1 | 1000 | 5 | 13.9 | - | 1.6 |

*Table 1: Synthesis conditions for the two wavellite samples*

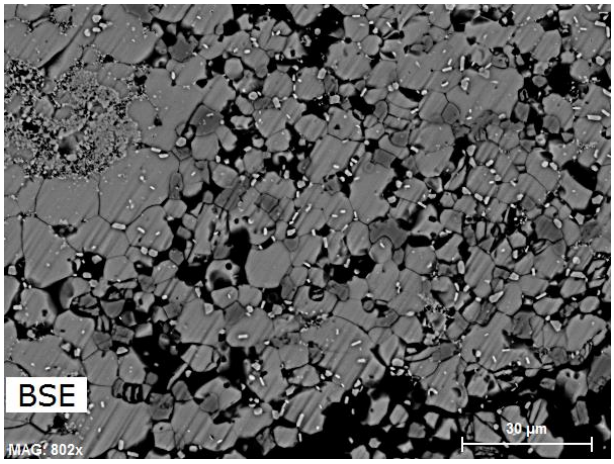


*Figure 1: PC127A, (alumino-phosphate wavellite as starting material (matrix of intermediate grey) with corundum (bright phase), fluoro-aluminate (dark grey) and a destabilized Si alumino-phosphate phase (top left).*

[22] Firing at 250°C of $Al(H_2PO_4)_3$ leads to anhydrous aluminophosphate.